A study on the effects of interparticle interactions on the dynamics, rheology and aging of colloidal systems out of equilibrium

Nick N. Koumakis

Submitted for the degree of Doctor of Philosophy

Department of Materials Science and Technology
University of Crete

February 2011

Committee:

George Petekidis[1,2] (Supervisor)

George Fytas[1,2]

Dimitris Vlassopoulos[1,2]

Maria Vamvakaki[1,2]

Benoit Loppinet[1]

John F. Brady[3]

Kostas Karatasos[4]

1. Institute of Electronic Structure and Laser (IESL), Foundation of Research and Technology (FORTH), Heraklion, Crete, Greece

2. Department of Materials Science and Technology, University of Crete, Heraklion, Crete, Greece

3. Chemical Engineering Department, California Institute of Technology, Pasadena, California, U.S.A.

4. Chemical Engineering Department, Aristotle, University of Thessaloniki, Greece

Acknowledgements

This work, from the first experiments to the composition of this thesis, has been an arduous process, both enjoyable and difficult. In this period of time, I was fortunate enough to have George Petekidis as my supervisor, who would listen to my ideas and thoughts, patiently providing constructive criticism and giving me direction when needed. My initiation to the world of simulations and the understanding that comes with it would not have been possible without the immeasurable assistance of John Brady, who provided the foundations of my code and supported my endeavors with many discussions, both during his stay in Greece and my visit to Caltech. Many thanks go to Dimitris Vlassopoulos for his contribution to my rheological background and Kostas Karatasos for his help in my beginnings of analyzing simulation data.

I would also like to thank Andy Downard for supplying and supporting his Brownian Dynamics code, which served as a basis of understanding for my own implementations; Christopher (Kiki) Klein and Simon Rogers for stimulating discussions on the intricacies of stresses within the period during oscillatory rheology and James Swan for his eye-opening discussions on lubrication forces and Stokesian Dynamics.

It has been a habit of mine to engage in scientific discussions with fellow scientists in the laboratory. Over the years great discussions have been had with Manos Anyfandakis, Antreas Pamvouksoglou, Uli Jonas, Panagiotis Voudouris, Anastasia Rissanou, Pierre Ballesta, Vassiliki Michailidou, Evelyne van Ruymbeke, Frederic Renou, Benoit Loppinet, Nikos Gomopoulos and Manolis Steiakakis to name just a few. In addition to the many scientific discussions we have had, I would also like to sincerely thank and applaud my current officemates, Andreas Poulos and Domenico Truzzolillo, for their superhuman endurance and tolerance concerning my temporary insanity in the few months before giving in this thesis.

Throughout this undertaking, a milder but perhaps more permanent version of madness was defined by my personality, the brunt of which was inflicted on Nikki for the past years. For this and her unwavering support in my effort to complete this work, she has my everlasting gratitude.

I would like to express my thanks to my parents, my family and my friends, many of whom I've already mentioned, for their understanding and support of my colloidal obsession of the past few years.

As a final note, I would like to truly thank the members of my committee for their evaluation of this lengthy thesis, especially those who are traveling to Crete in order to attend my defense.

This work was supported by the Greek General Secretariat for Research and Technology (Basic Research Program PENED,-03ED566).

"Mechanisms of Yielding and Flow in Colloidal Glasses, Crystals and Gels"

Abstract

The phase behavior of a suspension of monodisperse colloidal hard spheres is determined solely by its volume fraction, φ. At low concentrations we find a liquid state and at higher concentrations it forms an ordered crystal as a way to maximize entropy. At a transition volume fraction of about 0.59 the system becomes kinetically trapped in a metastable glassy state. Addition of a high concentration non-adsorbing linear polymer depletant causes attractions between the particles, inducing microstructurally heterogeneous frozen gel states at intermediate volume fractions and attractive glasses at high φ's. Under non-linear shear, solid-like suspensions of hard spheres, either glasses, crystals or gels, yield and flow, the stress response to the applied strain reflecting the microstructural changes and microscopic particle motions. This study focuses on the linear and the non-linear properties under shear (transient and steady state), both microscopic and rheological, of solid-like colloidal suspensions, encompassing the hard sphere glasses, shear induced crystals, attractive glass and gels states. To this end, we use rheology, Brownian Dynamics simulations, along with the light scattering Echo technique.

«Μελέτη της επίδρασης των διαμοριακών αλληλεπιδράσεων στη δυναμική, τη ρεολογία και τη γήρανση κολλοειδών συστημάτων εκτός ισορροπίας»

Σύνοψη

Η φασική συμπεριφορά ενός αιωρήματος μονοδιάσπαρτων σκληρών σφαιρών καθορίζεται μόνο από το κλάσμα όγκου του. Σε χαμηλές συγκεντρώσεις είναι σε υγρή φάση και σε πιο μεγάλες ανασυντάσσεται σε κρύσταλλο για να μεγιστοποιήσει την εντροπία. Στο μεταβατικό κλάσμα όγκου των 0.59, το σύστημα εγκλωβίζεται κινητικά σε μια μετασταθή υαλώδη κατάσταση. Η προσθήκη μη προσροφώμενων, υψηλής συγκέντρωσης, γραμμικών πολυμερών προκαλεί ελκτικές δυνάμεις αποκλεισμού ανάμεσα στα σωματίδια, επιφέροντας δομικά ετερογενής καταστάσεις πηκτώματος, σε ενδιάμεσα κλάσματα όγκου, και ελκτικούς ύαλους σε μεγαλύτερα. Υπό την εφαρμογή μη γραμμικής διάτμησης, στερεές καταστάσεις σκληρών σφαιρών, είτε ύαλου, κρύσταλλου ή πηκτώματος, υγροποιούνται και ρέουν, με την μετρούμενη τάση να αντικατοπτρίζει τις μικροσκοπικές κινήσεις και αλλαγές στη δομή. Αυτή η διατριβή εστιάζει στις γραμμικές και μη γραμμικές καταστάσεις υπό διάτμηση (μεταβατικές και σταθερές), εξετάζοντας τις μικροσκοπικές και ρεολογικές ιδιότητες στερεών κολλοειδών αιωρημάτων. Τα μελετώμενα συστήματα συμπεριλαμβάνουν ύαλους σκληρών σφαιρών, κρυστάλλους επαγόμενους υπό διάτμηση, πηκτώματα και ελκτικούς ύαλους, τα οποία εξετάζονται με την χρήση ρεολογίας, προσομοιώσεων Brownian δυναμικής και την τεχνική σκέδασης φωτός Echo.

Summary

The phase behavior of a suspension of monodisperse colloidal hard spheres is determined solely by its volume fraction, φ. At low concentrations it is in a liquid state and at higher concentrations it forms an ordered crystal as a way to maximize entropy. At a transition volume fraction of about 0.59 the system becomes kinetically trapped in a metastable glassy state, although the application of external fields such as shear on a monodisperse glass may form a shear aligned crystal. Addition of a high concentration non-adsorbing linear polymer depletant causes attractions between the particles, inducing microstructurally heterogeneous frozen gel states at intermediate volume fractions and attractive glasses at high φ's. Under non-linear shear, solid-like suspensions of hard spheres, either glasses, crystals or gels, yield and flow, the stress response to the applied strain reflecting the microstructural changes and microscopic particle motions. This study focuses on the linear and the non-linear transient and steady state properties under shear, both microscopic and rheological, of solid-like colloidal suspensions, encompassing the hard sphere glasses, shear induced crystals and attractive glass and gels states.

The transient response of hard sphere glasses was examined in a start-up shear experiment with experimental rheology and Brownian Dynamics (BD) simulations, exhibiting a stress peak at strains corresponding to yielding. The stress peak was found to increase in amplitude at high rates and lower φ, while the position of the peak increased with rate and generally remained unchanged with φ. The structural changes seen in the pair correlation function associated these findings with the structural elongation and distortion of the particle cages during shear. The examination of the stress after cessation of shear showed relaxations which became pronounced for larger rates. The structure and the dynamics during relaxation were found to revert back to the state at rest at rates similar to the relaxation of stress.

The response of hard spheres under oscillatory shear was also investigated, both experimentally and through Brownian dynamics simulations. We found two distinct regimes in terms of stress responses, dynamics and structure under shear, one for the lower frequencies and a second for the higher frequencies of oscillation, the transition related to the time scale of the in cage beta relaxation. At low frequencies, motions were found to be Brownian activated, with the particle out of cage mobility being supported by Brownian motion. However, at high frequencies, motions were found to be activated by collisions as particles are pushed out of their cages due to shear induced collisions. The yield strains were generally found to mirror these time scales, showing lower values in the Brownian activated and larger values in the collision/shear activated regime. Around the yield point a complex

dependency of displacements with frequency of oscillation was observed, with particles exhibiting of cage diffusive behavior at the low frequency regime, but being trapped within their cages at the high frequency regime. In addition, new methods for analysis of the elastic and viscous components of stresses during oscillatory experiments were introduced and examined.

Using BD simulations, we compared the displacements under oscillatory shear in a shear-induced crystal, oriented parallel to shear, with those in a glass at the same volume fraction. We found that due to the sliding layers, the crystal exhibits anisotropic displacements with cooperative motion of x-z layers of particles sliding over each other, significantly different to the isotropic displacements found in the glass. Through examination of the glass and two orientations of crystal we concluded that the experimental transition from glass to crystal with increasing strain, as well as the selection of crystal orientation is governed by the minimization of stresses and displacements. Additionally, through the use of the LS-Echo technique coupled with rheology, we examined the shear-induced particle motions in glasses and the corresponding shear induced crystals revealing strong correlations to BD simulations results.

While the hard sphere glass shows a single simple yielding process at a strain corresponding to the maximum distortion of the cage, of about 10% strain, attraction dominated glasses show a two-step yielding process at different ranges of strain. It has been suggested that the first step at low yield strain corresponds to the breaking of the attractive bonds between the particles and the second at larger strain to the cage breaking process. We experimentally followed the transition from an attractive glass with a two-step yielding process to lower volume fraction gels showing a similar complex yielding. The range of attraction was also changed, modifying the strain of the primary and secondary yield points.

BD simulations under steady shear were also carried out for depletion gels correlating the non linear stress response to the structural changes. The first low strain peak is verified to refer to the initial particle collisions (bond breaking), while the second stress peak refers to larger scale structural rearrangements. Stresses were found to significantly depend on the initial structural properties and the rejuvenation protocol. At steady state for low shear rates a collapse of clusters onto each other was observed, creating large voids, while at larger rates the inhomogenieties are reduced. Moreover, we have used a new measure to monitor the gel structures, the void distribution function, which is an efficient measure of long range heterogeneous structure.

CONTENTS

1. Introduction. . . . . Pg. 1
1.1 General Introduction. . . . . Pg. 1
1.2 Hard Sphere Colloids. . . . . Pg. 3
1.3 Depletion Attractions. . . . . Pg. 7
1.4 Model Systems under Shear: Rheology and Microscopic Properties. . Pg. 10
1.5 References. . . . . Pg. 16

2. Systems, Techniques and Methods. . . . . Pg. 25
2.1 Sterically Stabilized PMMA Spheres. . . . . Pg. 25
2.2 Sample Preparation. . . . . Pg. 25
2.3 Background - Rheology. . . . . Pg. 27
2.4 Rheometer Setup. . . . . Pg. 32
2.5 Light Scattering Echo. . . . . Pg. 33
2.6 DWS Echo Setup. . . . . Pg. 36
2.7 Brownian Dynamics Simulation. . . . . Pg. 36
2.8 References . . . . . Pg. 44

3. Hard Spheres: General Rheology and Dynamics at Rest. . . . . Pg. 45
3.1 Introduction. . . . . Pg. 45
3.2 Linear Viscoelasticity and Frequency Sweeps. . . . . Pg. 45
3.3 Non Linear Strain Sweeps and Yielding. . . . . Pg. 48
3.4 Flow Curves and Transient Tests. . . . . Pg. 51
3.5 Simulations at Rest. . . . . Pg. 53
3.6 References. . . . . Pg. 62

4. Stresses, Dynamics and Structure during Transient Shear: Start-up and Cessation of Flow. . . . . Pg. 65
4.1 Introduction/Experimental. . . . . Pg. 66
4.2 Experiments. . . . . Pg. 68
4.3 Brownian Dynamics Simulations. . . . . Pg. 75
4.4 Chapter Conclusions. . . . . Pg. 96

4.5 References. . . . . Pg. 97

5. Oscillatory Shear on Glasses: Stresses, Structure and Dynamics. . . . . Pg. 99
5.1 Introduction/Experimental. . . . . Pg. 100
5.2 Experiments. . . . . Pg. 106
5.3 Brownian Dynamics Simulations. . . . . Pg. 121
5.4 Lissajous Analysis. . . . . Pg. 145
5.5 Chapter Conclusions. . . . . Pg. 154
5.6 References. . . . . Pg. 155

6. Simulation of Hard Sphere Crystals under Oscillatory Shear. . . . . Pg. 159
6.1 Introduction/Simulation Method. . . . . Pg. 160
6.2 Glass vs. Crystal at Rest. . . . . Pg. 162
6.3 Glass vs. Parallel Crystal under Oscillatory Shear. . . . . Pg. 164
6.4 Parallel Crystal under Oscillatory Shear. . . . . Pg. 175
6.5 Parallel vs. Perpendicular Crystals under Oscillatory Shear. . . . . Pg. 184
6.6 Chapter Conclusions. . . . . Pg. 191
6.7 References. . . . . Pg. 192

7. Experimental Rheology and LS-Echo during the Shear Induced Crystallization of Hard Sphere Glasses. . . . . Pg. 195
7.1 Introduction/Experimental. . . . . Pg. 195
7.2 Oscillatory Rheology. . . . . Pg. 197
7.3 LS-Echo. . . . . Pg. 200
7.4 Chapter Conclusions. . . . . Pg. 210
7.5 References. . . . . Pg. 211

8. Experimental Rheology of Attractive Colloids. . . . . Pg. 213
8.1 Introduction/Experimental. . . . . Pg. 214
8.2 Oscillatory Rheology. . . . . Pg. 217
8.3 Steady Shear Rheology. . . . . Pg. 229
8.4 Changing the Size Ratio and Aging Effects. . . . . Pg. 237
8.5 Chapter Conclusions. . . . . Pg. 245

8.6 References. . . . . Pg. 246

9. Simulations of Sheared Attractive Gels: Stresses and Structure under Shear. . . . . Pg. 251

9.1 Introduction/Implementation. . . . . Pg. 251

9.2 Start up Shear: Stresses. . . . . Pg. 256

9.3 Start up Shear: Structural Properties. . . . . Pg. 260

9.4 Chapter Conclusions. . . . . Pg. 274

9.5 References. . . . . Pg. 275

10. Conclusions. . . . . Pg. 277

A. Appendix. . . . . Pg. 285

A.1 Simulation Box anisotropy. . . . . Pg. 285

A.2 Taylor Dispersion. . . . . Pg. 290

A.3 High Pe' Crystal Stresses. . . . . Pg. 292

A.4 Rheometer Resonance. . . . . Pg. 293

A.5 References. . . . . Pg. 294

Chapter 1 – Introduction & Background

1.1 General Introduction

Colloids

In 1861 the Scottish scientist Thomas Graham coined the term colloid in order to distinguish between dispersed gelatin-like materials that were unable to pass through a membrane and small molecules that could. He named the gelatin type materials "colloids", from the Greek "κόλλα" meaning "glue". In a modern perspective, colloids are defined as particles dispersed in a continuous phase with sizes between typically 10 nm and 1000 nm in at least one dimension. Colloidal motions were first examined in 1827, when the botanist Robert Brown observed irregular motion of pollen grains of colloidal size in water when studying them under an optical microscope. This motion, exhibiting random diffusive characteristics and now known as Brownian, is a result of collisions of solvent molecules with the colloidal particles.

In modern society, colloidal science has provided a sizable array of applications in technologically and biologically relevant areas (Hunter, 2001). The inks used in ball point pens and ink jet printers, many cosmetics and paints owe their special properties to their colloidal character. A common application of colloidal principles is the preparation of products which are able to remain homogeneous after long shelf periods. Knowledge of the colloidal properties of soils allows scientists to induce optimum plant growth and increase fertility levels. In biology, colloids manifest in the form of biopolymers (nucleic acids, proteins and polysaccharides), cell membranes and other cell components, while the flow properties of blood are understood in terms of a colloidal dispersion of red corpuscles in a liquid. Moreover, specifically designed colloids allow delivery and controlled release of drugs into specific areas and organs (Fanun, 2010).

Colloidal suspensions show phase behaviors which are analogous to atomic or molecular systems and thus may serve accordingly as ideal model systems for studying various phenomena with an accuracy and depth on a microscopic scale that is hard to reach for atomic or molecular systems. The mesoscopic size of colloidal particles, which is comparable to the wavelength of light, allows them to be studied with both light scattering (Berne and Pecora, 1976) and optical microscopy (Prasad, Semwogerere et al., 2007). Since their dynamics are strongly slowed down in comparison with atomic or molecular systems, any occurring

microscopic processes can be followed in detail, even allowing the experimental probing of individual particle motions.

The added possibility of tuning the size and interactions of colloidal particles combined with the accessibility of the particles to a variety of experimental techniques make them a lucrative atomic modeling system. Suspensions of colloidal hard spheres may be used as model systems (Poon, 2004), offering insight into many fundamental phenomena of condensed matter physics such as the equilibrium phase transitions (Poon, 2002) and mechanically frustrated states such as glasses and with the implementation of attractions, also gel and attractive glass transitions (Pusey, 1991; Pusey, 2008). The glass transition is perhaps the greatest unsolved problem in condensed matter physics (Pusey, 1991); the main question is how to reconcile the amorphous liquid-like structure, with solid-like mechanical properties. The defining feature of any glass is very low particle mobility within a disordered solid, many orders of magnitude smaller than that of a corresponding fluid.

More specifically, colloids may provide a valuable model system for the examination of the glass transition (van Megen and Underwood, 1993). In addition to the time and length scale accessibility inherent in colloidal systems, they show many properties that mimic the behavior of more traditional molecular glass formers. Thus, considerable insight is gained into features that are general to the glass transition such as motion cooperativity and dynamic heterogeneity (Kegel and van Blaaderen, 2000; Weeks, Crocker et al., 2000). However, colloidal glasses also possess features that are particular to their soft matter nature. Perhaps the most remarkable is shear melting. Because of the large particle size, colloids form soft solids and thus with the application of shear one can induce flow (Petekidis, Vlassopoulos et al., 2003) and study non linear rheological properties, something not easily accomplished with molecular glasses.

Rheology and Colloids

In a sense we are all experienced rheologists; while pouring ordinary honey in a cup of herbal tea, we observe the viscous behavior of a simple Newtonian fluid; pressing on a doorbell of a friendly neighbor, we feel the force of a Hookean solid as the spring inside compresses; the ordinary practice of squeezing toothpaste out of a tube causes what was initially a solid, to flow like a liquid. Each material has its own unique mechanical response to the application of stress or deformation, the study of this being rheology.

Colloidal dispersions are one of the simpler classes of materials for which the interplay between the viscoelastic mechanical properties and externally applied stresses can be investigated. Their ability to flow and yield under shear deformation is the basis of their widespread utility, since they can be solid-like under quiescent conditions and flow like a liquid when under strong shear, while their mechanical behavior depends sensitively on their internal structure and dynamics. Shear induced flow is only one means of driving a solid-to-fluid transition within the generic jamming ‘‘phase’’ diagram (Liu and Nagel, 1998), where strong similarities should exist among the shear, concentration, and temperature induced fluidizations. However, a detailed understanding of shear induced fluidization and the differences to the other, more common, methods requires familiarization with the microscopic behaviors related to shear melting and their correlation to the mechanical response.

This thesis presents a study of the stress and microscopic response under shear of model colloidal systems containing model hard sphere particles. We examine glassy hard spheres under steady and oscillatory shear as well as their shear induced crystal counterparts under oscillatory shear. With the addition of linear polymer we induce depletion attractions between particles and are able to study attractive glasses and gels under various shear conditions. We use Brownian dynamic simulations and the Light Scattering Echo technique to examine the microscopic dynamics of the systems and correlate them to the stress responses.

1.2 Hard Sphere Colloids

Hard Sphere Particles

The system studied in this work is ideally the simplest conceivable particle dispersion. Colloidal hard spheres are ideally microscopic particles moving within a medium with Brownian motion that interact with an infinite repulsive potential when they touch. Figure 1.1 shows the potential V(r) as $V(0<r<2R)=\infty$ and $V(r>2R)=0$, where R is the particle radius. Hard spheres have no attractive or long range repulsive energy so we only need to consider entropy to calculate their free energy and determine the phase behavior (Hoover and Ree, 1968; Poon and Pusey, 1995). We can thus characterize this system by the number density of the particles alone. This is expressed in colloid volume fraction $\varphi = \frac{4}{3}\pi R^3 \frac{N}{V}$.

As mentioned in the introduction, Van der Waals attractive forces may cause colloidal particles to aggregate irreversibly (Hunter, 2001). This attraction between colloids is sufficiently long ranged (r^{-1} for $r<R$) to be able to affect particles in the size range of colloids. The resulting attractive potential has strength proportional to the refractive index mismatch between solvent and particle (Hamaker constant), that can be many times that of the thermal

energy of the particles. This makes it important to stabilize the colloids to prevent aggregation.

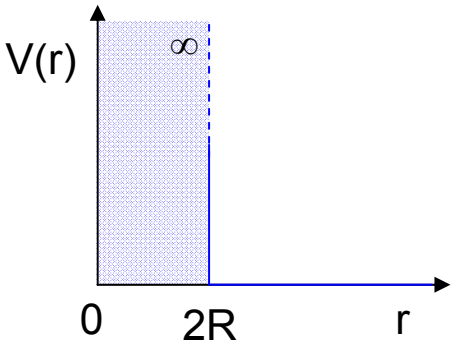

Figure 1.1: The pair potential of hard sphere particles of uniform radius R and centre to centre separation r.

The method used to specifically stabilize the particles in this work is steric stabilization. Small polymer chains are densely grafted on the surface of the colloidal particles. When two particles dispersed in a solvent that is good to the polymer chains approach, the polymer layers interpenetrate resulting in the reduction of entropy of individual chains. This causes a strong repulsion between the two polymer layers preventing the particles from getting close enough for the Van der Waals forces to become significant. If the grafting density and length of the chains are properly tailored, the resulting potential for sterically stabilized particles is a good approximation of a hard sphere potential.

Phase Diagram

As mentioned before, there is no temperature/energy scale for hard spheres, so there is only one parameter which completely determines the phase behavior. This is the particle volume fraction Φ. Hard spheres exhibit a liquid phase at volume fractions beneath 0.494, where the particles are free to diffuse and explore the whole volume available. A liquid-crystal coexistence phase is observed at volume fractions ranging from 0.494 to 0.545 and a fully crystalline structure from 0.545 to about 0.58 (Pusey and van Megen, 1986; Pusey, Zaccarelli et al., 2009). Due to the large particle sizes of these colloidal crystals, they are extremely weak compared to atomic crystals and can be destroyed by gently shaking the sample cell. As hard spheres cannot overlap, the maximum packing in an ordered state is $\Phi_{MAX} \approx 0.74$. If the particles form an amorphous random close packed structure then the maximum packing fraction is $\Phi_{RCP} \approx 0.64$ (Schaertl and Sillescu, 1994). The liquid-crystal coexistence phase has a linear dependence of crystal volume to volume fraction that makes it possible from the relevant heights of the phases to accurately determine volume fraction (Ackerson, 1990).

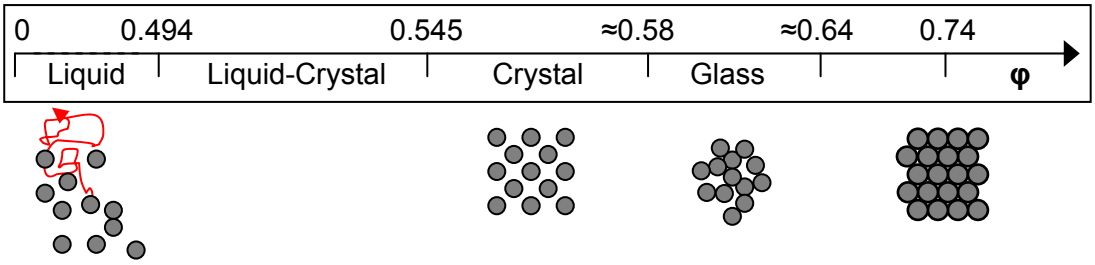

Figure 1.2 Phase behaviour of a suspension of monodisperse hard spheres

Entropy is the driving force behind the crystallization of hard sphere colloids. It may seem counterintuitive that the increase of entropy leads to an ordered state, however the crystal structure gives freedom of movement to each particle around their lattice site by increasing individual free volume. Even though the particles are in an ordered state, the increase of entropy due to individual motion and free volume is greater than the reduction of the configurational entropy (Pusey, Zaccarelli et al., 2009).

The experimental implementation of hard spheres introduces radial polydispersity on the particles, defined as the standard deviation of the radius:

$$\sigma = \frac{\sqrt{\overline{R^2} - \overline{R}^2}}{\overline{R}} \qquad (1.1)$$

As polydispersity rises, crystallization dynamics become slower as different particles sizes are not easily accommodated in the crystal lattice. At about 10% polydispersity, the distribution of sizes is too large and crystallization is suppressed (Poon and Pusey, 1995; Schöpe, Bryant et al., 2007; Pusey, Zaccarelli et al., 2009).

By increasing the volume fraction further the hard sphere particles reach a non ergodic metastable state. For φ above 0.58, the particles are unable to move into the entropically favorable crystal positions due to space restrictions and become trapped in a dynamically arrested glass phase (Pusey and van Megen, 1987; Pusey, 2008);. Figure 1.2 shows the hard sphere phase diagram. Recent molecular dynamics simulations have brought up a discussion on the definition of the glass transition volume fraction and the appearance of crystallization in the glass regime (Zaccarelli, Valeriani et al., 2009). While highly polydisperse hard sphere systems are unable to crystallize, the arrested glassy state at high φ remains unchanged.

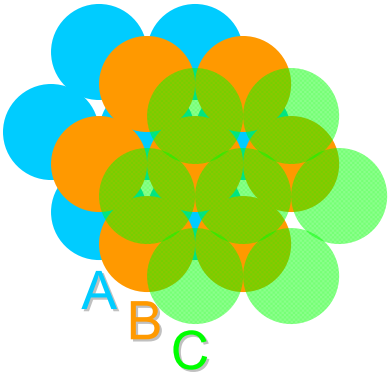

Figure 1.3: FCC crystal representation.

The crystal structures in which hard spheres initially assemble to when left at rest are a mixture of face-centred cubic (FCC) and hexagonally close packed (HCP) regions that are randomly oriented (Pusey, Megen et al., 1989). As seen in figure 1.3 the FCC crystal is defined by hexagonal layers of spherical particles one on top of the other. The HCP crystal is similar, but instead of the three repeating layers of the FCC (ABCAB…), the HCP has two (ABAB…). If left for long periods of time, it was found that this mixture of random HCP and FCC structures will gradually age into a pure FCC crystal, the absolute minimum of energy (Kegel and Dhont, 1999; Martelozzo, Schofield et al., 2002). Small mechanical perturbations also seemed to favour the FCC structure.

Additionally, suspensions of colloidal hard spheres may be used as model systems (Poon, 2004), offering insight into many fundamental phenomena of condensed matter physics such as the equilibrium phase transitions (Poon, 2002) and frustrated states such as glasses and with the implementation of attractions, also gels transitions (Pusey, 1991; Pusey, 2008).

Metastable Glass Transition

As described, simple hard sphere suspensions are considered to become non-ergodic at a volume fraction greater than the glass transition volume fraction ($\varphi \approx 0.58$). However, recently steady-state dynamics have been detected above this volume fraction for relatively polydisperse hard sphere suspensions (Pham, Petekidis et al., 2006). Beyond this point, although long-range diffusion is essentially frozen (Van Megen and Underwood, 1994; Brambilla, El Masri et al., 2009), dynamic heterogeneities may allow slow non-diffusive relaxations related with activated hoping mechanisms (Kegel and van Blaaderen, 2000; Saltzman and Schweizer, 2006).

By observing the positions of the fastest and slowest particles (Weeks, Crocker et al.,

2000) it was found that just below the glass transition the motions of the fast-moving particles were strongly correlated spatially in clusters. As the glass transition was approached these domains grew in size, although when entering the glass phase, the average size of these clusters was reduced, providing a dynamic signature of the glass transition (Weeks and Weitz, 2002a; Weeks and Weitz, 2002b). The mobile particles have been found to be weakly correlated with regions of lower density although this is not a strong enough correlation to be predictive of the dynamics in advance (Conrad, Starr et al., 2005), i.e. local structural analysis is not able to infer dynamical properties.

The dynamic heterogeneities near and above the glass transition have also been discussed by (Weeks, Crocker et al., 2007) and shown to have large distance spatial correlations of a few particle diameters which increase with φ, although showing no divergent behavior near or above the glass transition. It has been suggested that the appearance of heterogeneities is universal in glassy materials (Chaudhuri, Berthier et al., 2007). Moreover, in the work of (Conrad, Dhillon et al., 2006) it has been proposed that the motion of the slowest particles strongly contributes to the bulk elasticity.

1.3 Depletion Attractions

The repulsive potential of hard sphere colloids may be modified by the addition of non adsorbing linear polymer resulting in a short range attraction potential. As schematically shown in figure 1.4a, the center of a polymer coil is excluded from a region around the hard sphere colloid, the depletion zone at a range of approximately R_g, the polymer radius of gyration. He overlap of the particle depletion zones for adjacent colloids increases the free volume available to the polymer chains. Therefore as particles are brought together, the entropy of the individual polymer chains is increased as the overall excluded volume is decreased. This effect may be also understood in terms of osmotic pressure, since the polymer cannot enter the excluded volume between the particles, the differential pressure from the polymers on the colloids pushes the particles together, effectively inducing attractions.

As taken from the ideal model of Asakura and Oosawa (Asakura and Oosawa, 1954; Aarts, Tuinier et al., 2002), the attraction potential range is given by the polymer radius of gyration, while the strength is proportional to the pressure from the polymers in the free volume and the overlap volume between the particles as:

$$\frac{U_{dep}(r)}{K_B T} = \begin{cases} +\infty & : r \le 2R \\ -\frac{\Pi}{K_B T} \cdot V_{Overlap}(r) & : 2R < r \le 2R(1+q_s) \\ 0 & : r > 2R(1+q_s) \end{cases} \qquad (1.2)$$

The ratio of the polymer to the colloid radius is $q = \xi = R_g / R$, which for in the case of the ideal theory, is equal to the attraction range (q_s) and thus the overlap volume between the colloids is given by the simple geometric overlap volume of two spheres as (Aarts, Tuinier et al., 2002):

$$V_{Overlap}(r) = \left[1 - \frac{3r}{4R(1+q_s)} + \frac{1}{2}\left(\frac{r}{2R(1+q_s)}\right)^3\right]\frac{\pi}{6}\left[2R(1+q_s)\right]^3 \qquad (1.3)$$

while the pressure may be calculated by assuming that the polymer behaves as an ideal gas. This results in a depletion potential of the form shown in figure 1.4b.

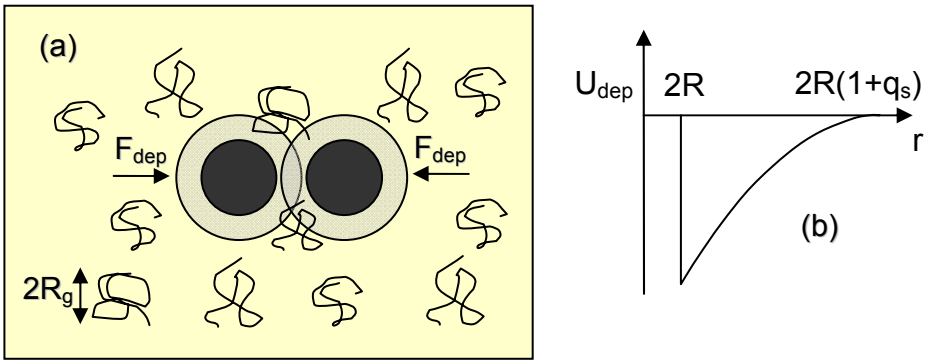

Figure 1.4: a) Representation of depletion attractions in polymer colloid mixtures and b) pair depletion potential schematically plotted with the distance between two particles.

However, the polymer pressure is a complex function of the polymer concentration in the free volume around the colloids, c_{pfree}, and may be calculated by (Aarts, Tuinier et al., 2002):

$$\frac{\Pi}{K_B T} = \left(\frac{4}{3}\pi R^3\right)^{-1} \int_0^y \frac{\partial \Pi}{\partial y} dy \qquad (1.4)$$

with $y = c_{pfree} / c^* = (c_p / c^*) / \alpha$, where c_p is the polymer concentration (gr/ml) in the sample volume and $c^* = \frac{3M_w}{4\pi N_A R_g^3}$, the overlap concentration of the polymer coils. The α parameter is the ratio of free volume available for the polymer to the total volume ($V_{free}=\alpha V$) given by (Aarts, Tuinier et al., 2002):

$$\begin{aligned} \alpha &= (1-\varphi)\exp\left[-\left(A'd + B'd^2 + C'd^3\right)\right] \\ A' &= 3q_s + 3q_s^2 + q_s^3 \\ B' &= (9/2)q_s^2 + 2q_s^3 \\ C' &= 3q_s^3 \\ d &= \varphi/(1-\varphi) \end{aligned} \qquad (1.5)$$

For the case of ideal polymers and taking into account the polymer coil-coil interactions (Aarts, Tuinier et al., 2002), the range of attraction is $q_s = \xi^* = \left(1 + \frac{6}{\sqrt{\pi}}q + 3q^2\right)^{1/3} - 1$, while the polymer pressure derivative is equal to $\partial\Pi/\partial y = q^{-3}$, simply proportional to the number density of polymer chains.

The generalized free volume theory (GFVT) (Lekkerkerker, Poon et al., 1992; Fleer and Tuinier, 2007) may also be implemented, which adds the sphere curvature effects to and gives more accurate results in terms of polymer interactions in the semi dilute regime. The theory is implemented as changes in the range of interactions and polymer pressure as (Fleer and Tuinier, 2007):

$$q_s = \xi^* = 0.865\left(q\Big/\sqrt{1+3.95y^{2\gamma}}\right)^{0.88} \qquad (1.6)$$

$$\partial\Pi/\partial y = q^{-3}\left[1 + 3.77y^{3\gamma-1}\right] \qquad (1.7)$$

with γ being the de Gennes exponent, equal to 0.77.

These colloid polymer mixtures have a rich phase diagram that depends not only on the volume fraction and polymer concentration, but also on the range of attraction, solvent quality and polydispersity (Poon, 1998; Poon, 2002; Bergenholtz, Poon et al., 2003; Shah, Chen et al., 2003a; Fasolo and Sollich, 2005a; Fasolo and Sollich, 2005b). With the addition of polymer, interparticle attraction increases causing particles to bond and increase bond escape time (Smith, Petekidis et al., 2007; Laurati, Petekidis et al., 2009) creating stable percolated structures that lead to colloidal gelation (Chen and Schweizer, 2004; Zaccarelli, 2007). An example of a phase diagram for a small polymer to colloid size ratio (ξ≈0.1) is shown in figure 1.5

When adding moderate attractions in a hard sphere glass, a re-entrant transition to a liquid state emerges as attractions may bring some particles together opening-up space for others to move (Pham, Puertas et al., 2002; Pham, Egelhaaf et al., 2004). With higher attractions, the system moves to another kinetically frustrated state of an attractive glass

with particles strongly bonded to each other. In both repulsive and attractive glasses, caging of particles by their neighbors dominates the structural, dynamic and mechanical response, the most obvious structural length scale in such highly packed systems being smaller than a particle size. On the other hand, at low volume fraction arrested states the density inhomogeneities are caused by attractions rather than entropic caging and are related with a characteristic lengthscale of few to several particle diameters.

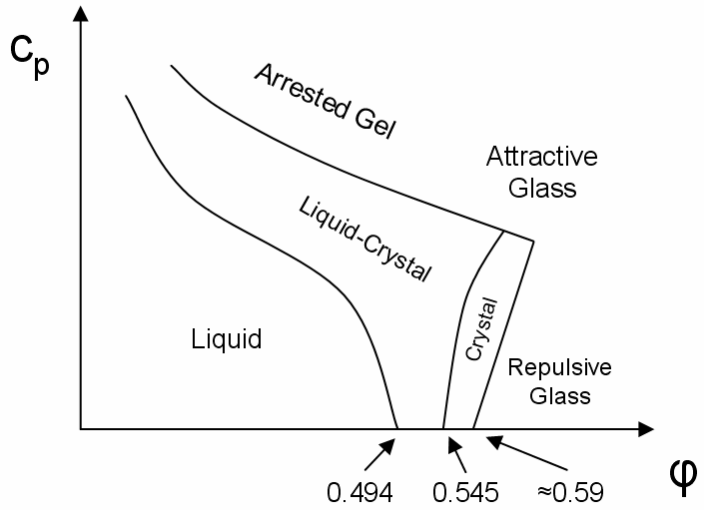

Figure 1.5: Schematic phase diagram for a mixture of hard spheres and non adsorbing linear polymer for a small size ratio of $\xi \approx 0.1$.

1.4 Model Systems under Shear: Rheology and Microscopic Properties

Hard sphere Glasses

Hard sphere glasses are an interesting system generally exhibiting solid like response at rest, while showing complex features under non linear shear. In (Koumakis, Schofield et al., 2008) we studied the linear elasticity of hard sphere dispersions near and above the glass transition, finding a power law increase of elasticity as a function of the distance from maximum packing, while successfully applying the Mode Coupling Theory for the frequency dependence of the moduli as done in (Mason and Weitz, 1995) for silica hard spheres near the glass transition. Creep and recovery experiments (Petekidis, Vlassopoulos et al., 2004) as well as some oscillatory shear measurements coupled with DLS echo (Petekidis, Moussaid et al., 2002; Petekidis, Vlassopoulos et al., 2003) were used to examine the non linear properties of a polydisperse hard sphere glass and concluded that it can tolerate a high amount of strain (10%-15%) before yielding irreversibly as related to breaking of the hard sphere entropic cages. Moreover, the non harmonic response of hard sphere glasses under oscillatory shear is

reported by (Le Grand and Petekidis, 2008) and compared to the response of systems with softer repulsive interaction potentials.

There has also been recent scientific activity in the experimental determination of the microscopic properties of concentrated hard sphere glasses under shear. With the use of confocal microscopy coupled with under steady shear (Besseling, Weeks et al., 2007) showed a sub linear power law dependence for the shear induced diffusion coefficient with increasing shear rate. Moreover, recent work (Besseling, Isa et al., 2010) relates the shear banding instability in high concentration glasses to shear concentration coupling, while mapping the occurrence of banding with applied rate and volume fraction. Using MCT, simulations and microscopy the work of (Zausch, Horbach et al., 2008) relates the transient stress peak from start up experiments to the appearance of a transient super diffusive regime. Through microscopy and steady shear (Schall, Weitz et al., 2007) identified localized irreversible shear transformation zones and determined their formation energy and topology, while (Eisenmann, Kim et al., 2010) related the microscopic motions of the particles under shear to a modified Stokes-Einstein relation which replaces the thermal energy with shear energy. Additionally, the dynamic heterogeneities under steady shear have also been analyzed for a super cooled liquid by (Chen, Semwogerere et al., 2010).

Recent theoretical advances for concentrated colloidal systems under a shear include the Soft Glassy Rheology (SGR) model (Sollich, 1998; Fielding, Sollich et al., 2000), which is able to capture main features of non-linear rheological tests. An interesting idea to come forth is the Strain Rate Frequency Superposition (SRFS) principle (Wyss, Miyazaki et al., 2007), which relates the linear oscillatory viscoelasticity with the non linear response, although concerns on its validity have been raised (Erwin, Rogers et al.). On the other hand, much more rigorous approaches such as MCT were extended to describe steady (Fuchs and Cates, 2009) and oscillatory shear (Miyazaki and et al., 2006; Brader, Siebenburger et al., 2010) non-linear tests. A complete microscopic theory of glassy colloidal suspensions under stress giving variables including elastic moduli, viscosity and yield strains was presented in the work of (Kobelev and Schweizer, 2005c). Still, however, the detailed physical mechanisms responsible for yielding in colloidal systems and the way this is affected by interparticle interactions is not fully disclosed. A recent review (Brader, 2010) generally examines colloids under shear with respect to their rheology, structure and microscopic rearrangements.

Although theory has been applied to the oscillatory stress response of glasses, it is still in the early stages, failing to capture the details of transient non linear stresses. Moreover, experiments have yet to examine the frequency dependence of the non harmonic stresses,

while the microscopic changes behind the stress responses are mostly speculative. In chapters 3, 4 and 5 we examine the response of glassy hard spheres at rest and under shear, experimentally and through Brownian Dynamics simulations, using the microscopic information from the simulations to describe the phenomenology of the stress responses.

In **chapter 3**, we present an **overview** of the **linear and non linear rheological responses** of **hard sphere glasses** from relevant literature and the current work. Additionally, the **microscopic motions** for the **state at rest** from the **Brownian dynamics simulations** is presented as a basis of understanding before the motions under shear are discussed in chapters 4 and 5.

In **chapter 4**, we study a **steady shear start-up experiment** on **hard sphere glasses**, both **experimentally** and with BD **simulations**, examining the amplitude and strain of the stress overshoot as a function of volume fraction and shear rate, while correlating with the transient super diffusion and structural changes. Additionally, we report on the **stress relaxation at the cessation of shear**.

In **chapter 5**, we use similar techniques to study the response of **glasses** under **oscillatory shear** in **experiments** and **simulations**, correlating the **non harmonic stresses** with the **microscopic rearrangements**, especially as a function of frequency. Two distinct regimes are found as a function of oscillation frequency during the application of non linear shear, which refer to both the non harmonic stress response and the microscopic motions under shear. We also examine the possibility of retrieving *a priori* the microscopic information from analyses of the instantaneous viscoelastic properties during the non linear oscillatory shear.

Shear induced Crystals

While crystallization in quiescent hard sphere systems occurs within hours or days as randomly oriented crystallites, under oscillatory shear, crystallization may occur within a few minutes and is oriented with the flow(Ackerson and Pusey, 1988). Depending on the studied volume fraction, the created crystal may be transient ($\varphi<0.454$), partial ($0.454<\varphi<0.545$) or monocrystalline ($\varphi>0.545$) (Haw, Poon et al., 1998a), while it flows in complicated fashion with crystal layers sliding one over the other (Ackerson, 1990). It has been found for dense suspensions of hard spheres ($\varphi>0.545$) under oscillatory strain that two different orientations of crystals arise depending on the strain of oscillation; while high strains ($\gamma_0>50\%$) produce a monocrystal with the closed packed direction parallel to shear, low strains ($\gamma_0<50\%$) produce a distribution of crystallites with orientations around a crystal with the closed packed

direction perpendicular to shear (Ackerson and Pusey, 1988; Haw, Poon et al., 1998a; Haw, Poon et al., 1998b).

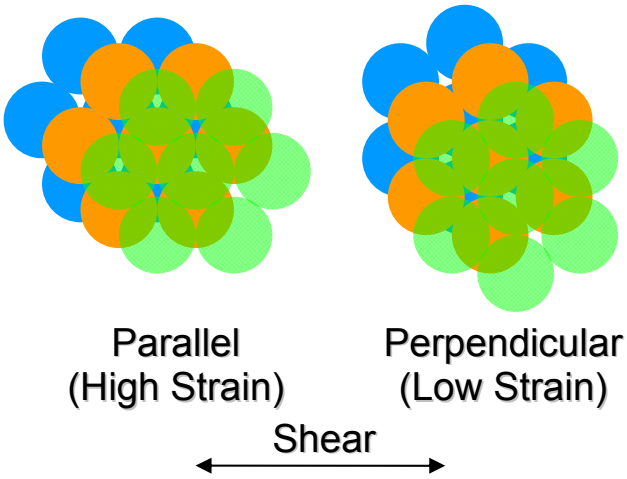

Figure 1.6: Representation of close packed direction of crystal parallel and perpendicular to shear.

Figure 1.6 shows a representation of the closed packed direction of the crystal at high and low strains. At low strains (Haw, Poon et al., 1998a) would see that the crystal would have some sort of "polycrystallinity" as the sample would not be fully oriented in the perpendicular direction, but would have "grains" which had a preferred direction which was perpendicular to the shear direction. At high strains the sample would reorient parallel to shear and the "polycrystallinity" would disappear. In the case of the cone and plate geometries used in (Koumakis, Schofield et al., 2008), crystallization manifested only as a crystal with the closed packed direction parallel to shear, possibly due to spatial constrictions for the perpendicular crystal in a rotational configuration. In (Komatsugawa and Nosé, 1995) there is a discussion on the physical interpretation of the change of orientation from perpendicular at low strains to parallel to shear at high strains.

Static light scattering in addition to oscillatory shear was used by (McMullan and Wagner, 2009) to examine the time dependent growth of a crystal under shear, while exploring the parameters for optimum crystallization. Light scattering echo and optical microscopy were used to examine hard sphere glasses under oscillatory shear strain by (Haw, Poon et al., 1998b), finding the crystal growth time scales for high φ glass. Two dimensional simulations of repulsive and attractive systems under shear revealed an optimal shear rate where crystallization speed is enhanced over the one at rest (Cerda, Sintes et al., 2008). Brownian dynamics simulations were carried out on crystal nucleation with the application of steady shear and an umbrella sampling technique, which found that shear suppresses nucleation and leads to a larger critical nucleus, which promotes crystallization (Blaak, Auer et al., 2004a;

Blaak, Auer et al., 2004b). The work of (Smith, Petekidis et al., 2007) examined the shear induced ordering in an attractive gel with microscopy and light scattering echo and proposed a model for particle escape time and crystallization.

Furthermore, (Duff and Lacks, 2007) executed a range of different simulation techniques to examine the mechanism of shear induced ordering on jammed systems and deduced that ordering occurs as shear pushes the system to lower energy minima. There is an interesting review on colloidal shear induced ordering by (Vermant and Solomon, 2005), while a more recent review of nucleation in 2D and 3D crystals at rest and under external fields has been written by (Gasser, 2009).

Previous work on the rheological behavior of shear induced crystallization in hard sphere glasses (Koumakis, Schofield et al., 2008), has shown that the viscoelastic moduli of shear induced crystals have smaller values than the amorphous/glass of the same φ, although qualitatively similar frequency behaviour. However, when compared to the same distance from maximum packing, the ordered structure exhibits larger elastic moduli. The yield strains of the crystal were additionally observed to be smaller than those of their counterpart amorphous.

Light scattering experiments (Ackerson and Pusey, 1988; Ackerson, 1990) showed the structures and geometric flow characteristics of the hard sphere crystal under shear. (Derks, Wisman et al., 2004) studied colloidal crystallization with a confocal microscope using a counter rotating cone plate shear cell and was able to image the shear behavior of hard sphere crystals by looking at a stationary plane. Moreover, confocal microscopy was used to measure the mean squared displacements of a crystal under steady shear by (Derks, Wu et al., 2009) noting the zig zag and collective layer motions of a crystal, while discussing the crystal melting with a dynamic Lindemann criterion and the measured long and short time shear induced diffusion coefficients. Later work (Yu, Derks et al., 2009) with confocal microscopy experiments on crystallization and melting under shear discovered that crystal melting occurs in domains and that crystallization under shear is not based on nucleation. The differences in the microscopic motions of glass and crystal under shear though have not be thoroughly examined, while there is interest in understanding the interplay of applied oscillation frequency and strain amplitude during yielding.

In **chapter 6**, BD **simulations** are implemented on **shear induced hard sphere crystal** structures **under oscillatory shear**. The microscopic motions of the crystal are compared to findings of chapter 5 on the same volume fraction glass as a complement to the rheological

findings of (Koumakis, Schofield et al., 2008). As done in (Komatsugawa and Nosé, 1995) the parallel and perpendicular crystals are also examined, although now in the context of stresses and displacements as taken from the simulations. The microscopic displacements of the crystal are also examined in volume fractions above the maximum packing of the glass.

In **chapter 7**, we use the experimental **light scattering DWS Echo** technique to extract the **microscopic information** on the particle motions for **the glass and the shear induced crystal**. The dynamics from the DWS Echo experiments are then compared to the simulation results of chapter 6, exhibiting strong qualitative similarities.

Attractive Glasses and Gels

Previous rheological experiments (Pham, Petekidis et al., 2006; Pham, Petekidis et al., 2008) in colloid-polymer mixtures at high particle volume fractions have shown that an attractive glass exhibits a two step yielding with increasing oscillatory strain amplitude as opposed to the single yielding in a repulsive glass. The first step was attributed to bond breaking while the second one to cage breaking in the glassy state. As the strain amplitude is increased beyond the linear regime, particles are able to change bonding neighbors by escaping from interparticle attraction, thus leading to energy dissipation and partial yielding. When higher strains are applied to the system, the cages are distorted and finally break giving rise to a second yielding point.

Theoretical studies based on combined Mode Coupling and activated hoping theories (Kobelev and Schweizer, 2005b; Kobelev and Schweizer, 2005a) in various regimes of the attractive colloids phase diagram have calculated the elasticity of arrested states and determined the critical yield stress and strain. More recently an elastic model based on a hierarchical arrest scheme (Zaccone, Wu et al., 2009) has provided insight in the contribution to the mesoscopic elasticity from particle-particle interactions and cluster structures. However, no theoretical work to date has predicted or is able to describe the two step yielding observed experimentally. Apart from those on attractive glasses (Pham, Petekidis et al., 2006; Pham, Petekidis et al., 2008), experimental studies, have been performed in various regimes of the phase diagram mainly focusing on the linear rheology (Shih, Shih et al., 1990; Grant and Russel, 1993; Wolthers, van den Ende et al., 1997; Shah, Chen et al., 2003b; Laurati, Petekidis et al., 2009; Conrad, Wyss et al., 2010) for a wide range of attractive systems. Moreover, the structure under shear has been investigated using microscopy (Varadan and Solomon, 2003; Smith, Petekidis et al., 2007) and light scattering (Varadan and Solomon, 2001; Mohraz and Solomon, 2005) as well as in microrheological yielding experiments with the use of optical tweezers (Furst

and Pantina, 2007). Finally we should note that bridging aspects of theory and experiments, simulations under transient(Whittle and Dickinson, 1997; Rzepiela, van Opheusden et al., 2004) and steady state shear(Whittle and Dickinson, 1997; Silbert, Melrose et al., 1999) have probed the shear induced disruption of the gel network as a function of shear rate. Still the yielding mechanisms in colloidal gels, especially in the intermediate particle volume fractions where multiple length scales are present are far from well understood.

In **chapter 8,** we **investigate the transition**, from a **cage dominated to bond dominated kinetic arrest** with **experimental rheology**. This is achieved by probing samples that have the same attraction strength but different colloidal volume fraction. Thus by lowering the latter one could have expected to eliminate the cage effect and recover a single step yielding. In reality though, the **transition from an attractive glass to a gel** was proven to be far from simple as particle cages turn into particle clusters and interconnected networks (Krall and Weitz, 1998; Lu, Conrad et al., 2006; Lu, Zaccarelli et al., 2008; Laurati, Petekidis et al., 2009). In order to unravel this complexity, we additionally examined the time evolution (ageing) of linear and non linear mechanical properties and the changes caused by increasing the range of attraction.

Moreover, we used Brownian Dynamics **simulations** in **chapter 9**, with variables similar to those of the experimental system to elucidate the **transient structural changes** during the **application of shear on a gel** and their relation to the stress response. The steady state structures during shear are found to be correlated to the applied rate, while the transient stresses are quite sensitive to the shear history of the gel. Through this work, the original simple bond and cage breaking idea (Pham, Petekidis et al., 2006; Pham, Petekidis et al., 2008) is refined for attractive glasses and extended to lower volume fraction gels (Koumakis and Petekidis, 2011).

1.5 References

Aarts, D. G. A. L., R. Tuinier and H. N. W. Lekkerkerker (2002). "Phase behaviour of mixtures of colloidal spheres and excluded-volume polymer chains." Journal of Physics Condensed Matter **14**(33) 7551-7561.

Ackerson, B. J. (1990). "Shear induced order and shear processing of model hard sphere suspensions." J. Rheol. **34**(4) 553-590.

Ackerson, B. J. and P. N. Pusey (1988). "Shear-Induced Order in Suspensions of Hard Spheres." Phys. Rev. Lett. **61** 1033.

Asakura, S. and F. Oosawa (1954). "On interaction between two bodies immersed in a solution of macromolecules." The Journal of Chemical Physics **22**(7) 1255-1256.

Bergenholtz, J., W. C. K. Poon and M. Fuchs (2003). "Gelation in model colloid-polymer mixtures." Langmuir **19**(10) 4493-4503.

Berne, B. J. and R. Pecora (1976). Dynamic Light Scattering. New York, Wiley-Interscience Publications.

Besseling, R., L. Isa, P. Ballesta, G. Petekidis, M. E. Cates and W. C. K. Poon (2010). "Shear Banding and Flow-Concentration Coupling in Colloidal Glasses." Physical Review Letters **105**(26) 268301.

Besseling, R., E. R. Weeks, A. B. Schofield and W. C. K. Poon (2007). "Three-Dimensional Imaging of Colloidal Glasses under Steady Shear." Physical Review Letters **99**(2) 028301.

Blaak, R., S. Auer, D. Frenkel and H. Lowen (2004a). "Crystal Nucleation of Colloidal Suspensions under Shear." Phys. Rev. Lett. **93** 068303

Blaak, R., S. Auer, D. Frenkel and H. Löwen (2004b). "Homogeneous nucleation of colloidal melts under the influence of shearing fields." Journal of Physics: Condensed Matter **16**(38) S3873.

Brader, J. M. (2010). "Nonlinear rheology of colloidal dispersions." Journal of Physics: Condensed Matter **22**(36) 363101.

Brader, J. M., M. Siebenburger, M. Ballauff, K. Reinheimer, M. Wilhelm, S. J. Frey, F. Weysser and M. Fuchs (2010). "Nonlinear response of dense colloidal suspensions under oscillatory shear: Mode-coupling theory and Fourier transform rheology experiments." Physical Review E **82**(6) 061401.

Brambilla, G., D. El Masri, M. Pierno, L. Berthier, L. Cipelletti, G. Petekidis and A. B. Schofield (2009). "Probing the equilibrium dynamics of colloidal hard spheres above the mode-coupling glass transition." Physical Review Letters **102**(8) 085703.

Cerda, J. J., T. Sintes, C. Holm, C. M. Sorensen and A. Chakrabarti (2008). "Shear effects on crystal nucleation in colloidal suspensions." Physical Review E **78**(3) 031403.

Chaudhuri, P., L. Berthier and W. Kob (2007). "Universal Nature of Particle Displacements close to Glass and Jamming Transitions." Physical Review Letters **99**(6) 060604.

Chen, D., D. Semwogerere, J. Sato, V. Breedveld and E. R. Weeks (2010). "Microscopic structural relaxation in a sheared supercooled colloidal liquid." Physical Review E **81**(1) 011403.

Chen, Y. L. and K. S. Schweizer (2004). "Microscopic theory of gelation and elasticity in polymer-particle suspensions." Journal of Chemical Physics **120**(15) 7212-7222.

Conrad, J. C., P. P. Dhillon, E. R. Weeks, D. R. Reichman and D. A. Weitz (2006). "Contribution of Slow Clusters to the Bulk Elasticity Near the Colloidal Glass Transition." Physical Review Letters **97**(26) 265701.

Conrad, J. C., F. W. Starr and D. A. Weitz (2005). "Weak Correlations between Local Density and Dynamics near the Glass Transition." The Journal of Physical Chemistry B **109**(45) 21235-21240.

Conrad, J. C., H. M. Wyss, V. Trappe, S. Manley, K. Miyazaki, L. J. Kaufman, A. B. Schofield, D. R. Reichman and D. A. Weitz (2010). "Arrested fluid-fluid phase separation in depletion systems: Implications of the characteristic length on gel formation and rheology." Journal of Rheology **54**(2) 421-438.

Derks, D., H. Wisman, A. v. Blaaderen and A. Imhof (2004). "Confocal microscopy of colloidal dispersions in shear flow using a counter-rotating cone–plate shear cell." J. Phys. Condens. Matter **16** S3917–S3927

Derks, D., Y. L. Wu, A. Van Blaaderen and A. Imhof (2009). "Dynamics of colloidal crystals in shear flow." Soft Matter **5**(5) 1060-1065.

Duff, N. and D. J. Lacks (2007). "Shear-induced crystallization in jammed systems." Phys. Rev. E **75**(3) 031501.

Eisenmann, C., C. Kim, J. Mattsson and D. A. Weitz (2010). "Shear Melting of a Colloidal Glass." Physical Review Letters **104**(3) 035502.

Erwin, B. M., S. A. Rogers, M. Cloitre and D. Vlassopoulos "Examining the validity of strain-rate frequency superposition when measuring the linear viscoelastic properties of soft materials." Journal of Rheology **54**(2) 187-195.

Fanun, M. (2010). Colloids in drug delivery, Boca Raton, FL.

Fasolo, M. and P. Sollich (2005a). "Effects of colloid polydispersity on the phase behavior of colloid-polymer mixtures." Journal of Chemical Physics **122**(7) 074904.

Fasolo, M. and P. Sollich (2005b). "Effects of polymer polydispersity on the phase behaviour of colloid-polymer mixtures." Journal of Physics Condensed Matter **17**(6) 797-812.

Fielding, S. M., P. Sollich and M. E. Cates (2000). "Aging and rheology in soft materials." J. Rheol. **44**(2) 323-369.

Fleer, G. J. and R. Tuinier (2007). "Analytical phase diagram for colloid-polymer mixtures." Physical Review E **76**(4) 041802.

Fuchs, M. and M. E. Cates (2009). "A mode coupling theory for Brownian particles in homogeneous steady shear flow." Journal of Rheology **53**(4) 957-1000.

Furst, E. M. and J. P. Pantina (2007). "Yielding in colloidal gels due to nonlinear microstructure bending mechanics." Physical Review E **75**(5) 050402.

Gasser, U. (2009). "Crystallization in three-and two-dimensional colloidal suspensions." Journal of Physics Condensed Matter **21**(20).

Grant, M. C. and W. B. Russel (1993). "Volume-fraction dependence of elasti moduli and transition temperatures for colloidal gels." Physical Review E **47**(4): 2606 2606-2614.

Haw, M. D., W. C. K. Poon and P. N. Pusey (1998a). "Direct observation of oscillatory shear-induced order in colloidal suspensions." Phys. Rev. E **57** 6859.

Haw, M. D., W. C. K. Poon, P. N. Pusey, P. Hebraud and F. Lequeux (1998b). "Colloidal glasses under shear strain." Phys. Rev. E **58** 4673.

Hoover, W. G. and F. H. Ree (1968). "Melting Transition and Communal Entropy for Hard Spheres." J. Chem. Phys. **49**(8) 3609.

Hunter, R. J. (2001). Foundations of Colloid Science, Oxford University Press.

Kegel, W. K. and J. K. G. Dhont (1999). "''Aging'' of the structure of crystals of hard colloidal spheres." J. Chem. Phys. **112** 3431.

Kegel, W. K. and a. A. van Blaaderen (2000). "Direct Observation of Dynamical Heterogeneities in Colloidal Hard-Sphere Suspensions." Science **287**(5451) 290-293.

Kobelev, V. and K. S. Schweizer (2005a). "Dynamic yielding, shear thinning, and stress rheology of polymer-particle suspensions and gels." Journal of Chemical Physics **123**(16) 164903.

Kobelev, V. and K. S. Schweizer (2005b). "Nonlinear elasticity and yielding of depletion gels." Journal of Chemical Physics **123** 164902.

Kobelev, V. and K. S. Schweizer (2005c). "Strain softening, yielding and shear thinning in glassy colloidal suspensions." Phys. Rev. E **71** 021401.

Komatsugawa, H. and S. Nosé (1995). "Nonequilibrium molecular dynamics simulations of oscillatory sliding motion in a colloidal suspension system." Physical Review E **51**(6) 5944.

Koumakis, N. and G. Petekidis (2011). "Two step yielding in attractive colloids: transition from gels to attractive glasses." Soft Matter (In Press) DOI:10.1039/c0sm00957a.

Koumakis, N., A. B. Schofield and G. Petekidis (2008). "Effects of shear induced crystallization on the rheology and ageing of hard sphere glasses." Soft Matter **4**: 2008 2008-2018.

Krall, A. H. and D. A. Weitz (1998). "Internal dynamics and elasticity of fractal colloidal gels." Physical Review Letters **80**(4) 778-781.

Laurati, M., G. Petekidis, N. Koumakis, F. Cardinaux, A. B. Schofield, J. M. Brader, M. Fuchs and S. U. Egelhaaf (2009). "Structure, dynamics, and rheology of colloid-polymer mixtures: From liquids to gels." Journal of Chemical Physics **130**(13) 134907.

Le Grand, A. and G. Petekidis (2008). "Effects of particle softness on the rheology and yielding of colloidal glasses." Rheologica Acta **47**(5-6) 579-590.

Lekkerkerker, H. N. W., W. C. K. Poon, P. N. Pusey, A. Stroobants and P. B. Warren (1992). "Phase Behaviour of Colloid + Polymer Mixtures." Europhysics Letters **20**(6) 559.

Liu, A. J. and S. R. Nagel (1998). "Nonlinear dynamics: Jamming is not just cool any more." Nature **396**(6706) 21-22.

Lu, P. J., J. C. Conrad, H. M. Wyss, A. B. Schofield and D. A. Weitz (2006). "Fluids of clusters in attractive colloids." Physical Review Letters **96**(2) 028306.

Lu, P. J., E. Zaccarelli, F. Ciulla, A. B. Schofield, F. Sciortino and D. A. Weitz (2008). "Gelation of particles with short-range attraction." Nature **453**(7194) 499-503.

Martelozzo, V. C., A. B. Schofield, W. C. K. Poon and P. N. Pusey (2002). "Structural Aging of crystals of hard-sphere colloids." Phys. Rev. E **66** 021408.

Mason, T. G. and D. A. Weitz (1995). "Linear Viscoelasticity of Colloidal Hard Sphere Suspensions near the Glass Transition." Phys. Rev. Lett. **75** 2770.

McMullan, J. M. and N. J. Wagner (2009). "Directed self-assembly of suspensions by large amplitude oscillatory shear flow." Journal of Rheology **53**(3) 575-588.

Miyazaki, K. and et al. (2006). "Nonlinear viscoelasticity of metastable complex fluids." EPL (Europhysics Letters) **75**(6) 915.

Mohraz, A. and M. J. Solomon (2005). "Orientation and rupture of fractal colloidal gels during start-up of steady shear flow." Journal of Rheology **49**(3) 657-681.

Petekidis, G., A. Moussaid and P. N. Pusey (2002). "Rearrangments in hard-sphere glasses under oscillatory shear strain." Phys. Rev. E **66** 051402.

Petekidis, G., D. Vlassopoulos and P. N. Pusey (2003). "Yielding and flow of colloidal glasses." Faraday Discuss **123** 287-302.

Petekidis, G., D. Vlassopoulos and P. N. Pusey (2004). "Yielding and flow of sheared colloidal glasses." Journal of Physics Condensed Matter **16**(38) S3955-S3963.

Pham, K. N., S. U. Egelhaaf, P. N. Pusey and W. C. K. Poon (2004). "Glasses in hard spheres with short-range attraction." Physical Review E **69**(1 1) 115031-1150313.

Pham, K. N., G. Petekidis, D. Vlassopoulos, S. U. Egelhaaf, W. C. K. Poon and P. N. Pusey (2008). "Yielding behavior of repulsion- and attraction-dominated colloidal glasses." Journal of Rheology **52**(2) 649-676.

Pham, K. N., G. Petekidis, D. Vlassopoulos, S. U. Egelhaaf, P. N. Pusey and W. C. K. Poon (2006). "Yielding of colloidal glasses." Europhysics Letters **75**(4) 624-630.

Pham, K. N., A. M. Puertas, J. Bergenholtz, S. U. Egelhaaf, A. Moussaïd, P. N. Pusey, A. B. Schofield, M. E. Cates, H. Fuchs and W. C. K. Poon (2002). "Multiple glassy states in a simple model system." Science **296**(5565) 104-106.

Poon, W. (2004). "Colloids as Big Atoms." Science **304**(5672) 830-831.

Poon, W. C. K. (1998). "Phase separation, aggregation and gelation in colloid-polymer mixtures and related systems." Current Opinion in Colloid and Interface Science **3**(6) 593-599.

Poon, W. C. K. (2002). "The physics of a model colloid-polymer mixture." Journal of Physics Condensed Matter **14**(33) R859-R880.

Poon, W. C. K. and P. N. Pusey (1995). Phase Transitions of spherical colloids. Observations and Simulations of Phase Transitions of Complex Fluids. M. Baus, Kluwer Academic Publishers**:** 3-51

Prasad, V., D. Semwogerere and E. R. Weeks (2007). "Confocal microscopy of colloids." Journal of Physics Condensed Matter **19**(11).

Pusey, P. N. (1991). Liquids, Freezing and the Glass Transition. Les Houches Session 51. D. Lesvesque, J. P. Hansen and J. Zinn-Justin. North-Holland, Amsterdam.

Pusey, P. N. (2008). "Colloidal glasses." Journal of Physics Condensed Matter **20**(49) 494202.

Pusey, P. N., W. v. Megen, P. Bartlett, B. J. Ackerson, J. G. Rarity and S. M. Underwood (1989). "Structure of crystals of hard colloidal spheres." Phys. Rev. Lett. **63**(25) 2753-2756.

Pusey, P. N. and W. van Megen (1986). "Phase behaviour of concentrated suspensions of nearly hard colloidal spheres." Nature **320**(6060) 340-342.

Pusey, P. N. and W. van Megen (1987). "Observation of a glass transition in suspensions of spherical colloidal particles." Phys. Rev. Lett. **59**(18) 2083.

Pusey, P. N., E. Zaccarelli, C. Valeriani, E. Sanz, W. C. K. Poon and M. E. Cates (2009). "Hard spheres: crystallization and glass formation." Philosophical Transactions of the Royal Society A: Mathematical, Physical and Engineering Sciences **367**(1909) 4993-5011.

Rzepiela, A. A., J. H. J. van Opheusden and T. van Vliet (2004). "Large shear deformation of particle gels studied by Brownian dynamics simulations." Journal of Rheology **48**(4) 863-880.

Saltzman, E. J. and K. S. Schweizer (2006). "Activated hopping and dynamical fluctuation effects in hard sphere suspensions and fluids." The Journal of Chemical Physics **125**(4) 044509-19.

Schaertl, W. and H. Sillescu (1994). "Brownian dynamics of polydisperse colloidal hard spheres: Equilibrium structures and random close packings." J. Stat. Phys. **77** 1007.

Schall, P., D. A. Weitz and F. Spaepen (2007). "Structural Rearrangements That Govern Flow in Colloidal Glasses." Science **318**(5858) 1895-1899.

Schöpe, H. J., G. Bryant and W. v. Megen (2007). "Effect of polydispersity on the crystallization kinetics of suspensions of colloidal hard spheres when approaching the glass transition." J. Chem. Phys.(127) 084505.

Shah, S. A., Y. L. Chen, K. S. Schweizer and C. F. Zukoski (2003a). Phase behavior and concentration fluctuations in suspensions of hard spheres and nearly ideal polymers. Journal of Chemical Physics, AIP. **118:** 3350-3361.

Shah, S. A., Y. L. Chen, K. S. Schweizer and C. F. Zukoski (2003b). "Viscoelasticity and rheology of depletion flocculated gels and fluids." Journal of Chemical Physics **119**(16) 8747-8761.

Shih, W. H., W. Y. Shih, S. I. Kim, J. Liu and I. A. Aksay (1990). "Scaling Behavior of the Elastic Properties of Colloidal Gels." Physical Review A **42**(8) 4772-4779.

Silbert, L. E., J. R. Melrose and R. C. Ball (1999). "The rheology and microstructure of concentrated, aggregated colloids." Journal of Rheology **43**(3) 673-700.

Smith, P. A., G. Petekidis, S. U. Egelhaaf and W. C. K. Poon (2007). "Yielding and crystallization of colloidal gels under oscillatory shear." Phys. Rev. E **76**(4) 041402.

Sollich, P. (1998). "Rheological constitutive equation for a model of soft glassy materials." Physical Review E **58**(1) 738.

van Megen, W. and S. M. Underwood (1993). "Glass-Transition in Colloidal Hard-Spheres - Mode-Coupling Theory Analysis." Phys. Rev. Lett. **70**(18) 2766-2769.

Van Megen, W. and S. M. Underwood (1994). "Glass transition in colloidal hard spheres: Measurement and mode-coupling-theory analysis of the coherent intermediate scattering function." Physical Review E **49**(5) 4206-4220.

Varadan, P. and M. J. Solomon (2001). "Shear-Induced Microstructural Evolution of a Thermoreversible Colloidal Gel." Langmuir **17**(10) 2918-2929.

Varadan, P. and M. J. Solomon (2003). "Direct visualization of flow-induced microstructure in dense colloidal gels by confocal laser scanning microscopy." Journal of Rheology **47**(4) 943-968.

Vermant, J. and M. J. Solomon (2005). "Flow-induced structure in colloidal suspensions." J. Phys. Condens. Matter **17** R187-R216.

Weeks, E. R., J. C. Crocker, A. C. Levitt, A. Schofield and D. A. Weitz (2000). Three-Dimensional Direct Imaging of Structural Relaxation Near the Colloidal Glass Transition. **287:** 627-631.

Weeks, E. R., J. C. Crocker and D. A. Weitz (2007). "Short and long-range correlated motion observed in colloidal glasses and liquids." Journal of Physics: Condensed Matter **19**(20) 205131.

Weeks, E. R. and D. A. Weitz (2002a). "Properties of Cage Rearrangements Observed near the Colloidal Glass Transition." Phys. Rev. Lett. **89**(9) 095704.

Weeks, E. R. and D. A. Weitz (2002b). "Subdiffusion and the cage effect studied near the colloidal glass transition." Chemical Physics **284**(1-2) 361-367.

Whittle, M. and E. Dickinson (1997). "Stress overshoot in a model particle gel." The Journal of Chemical Physics **107**(23) 10191-10200.

Wolthers, W., D. van den Ende, V. Breedveld, M. H. G. Duits, A. A. Potanin, R. H. W. Wientjes and J. Mellema (1997). "Linear viscoelastic behavior of aggregated colloidal dispersions." Physical Review E **56**(5) 5726-5733.

Wyss, H. M., K. Miyazaki, J. Mattsson, Z. Hu, D. R. Reichman and D. A. Weitz (2007). "Strain-Rate Frequency Superposition: A Rheological Probe of Structural Relaxation in Soft Materials." Physical Review Letters **98**(23) 238303.

Yu, L. W., D. Derks, A. Van Blaaderen and A. Imhof (2009). "Melting and crystallization of colloidal hard-sphere suspensions under shear." Proceedings of the National Academy of Sciences of the United States of America **106**(26) 10564-10569.

Zaccarelli, E. (2007). "Colloidal gels: Equilibrium and non-equilibrium routes." Journal of Physics Condensed Matter **19**(32) 323101.

Zaccarelli, E., C. Valeriani, E. Sanz, W. C. K. Poon, M. E. Cates and P. N. Pusey (2009). "Crystallization of Hard-Sphere Glasses." Phys. Rev. Lett. **103**(13): 135704.

Zaccone, A., H. Wu and E. Del Gado (2009). "Elasticity of Arrested Short-Ranged Attractive Colloids: Homogeneous and Heterogeneous Glasses." Physical Review Letters **103**(20) 208301.

Zausch, J., J. Horbach, M. Laurati, S. U. Egelhaaf, J. M. Brader, T. Voigtmann and M. Fuchs (2008). "From equilibrium to steady state: the transient dynamics of colloidal liquids under shear." Journal of Physics: Condensed Matter **20**(40) 404210.

Chapter 2 – Systems, Techniques and Methods

2.1 Sterically Stabilized PMMA Spheres

The hard sphere particles used in this work consist of polymethylmethacrylate (PMMA) cores sterically stabilized by thin (≈10 nm) chemically grafted layers of poly-12-hydroxystearic acid (PHSA) chains. The particles were dissolved in three different solvents: cis-decahydronaphtalin (cis-decalin), Octadecene and Bromonaphthalene. Specifically, cis-decalin was used as it has been experimentally studied widely and found to be a good approximation of hard spheres (Bryant, Williams et al., 2002). For long time rheological experiments and the DWS echo technique, particles were dissolved in Octadecene, eliminating the effect of solvent evaporation, while being turbid enough to give multiple scattering. We have recently found (briefly shown in chapter 8), that the interactions between particles in Octadecene were not completely hard, showing some attractions possibly due to Van der Walls attractions related with the high particle-solvent refractive index mismatch. In order to correct for this mismatch, but still keep solvent evaporation to a minimum, we use a solvent mixture of Octadecene and Bromonaphthalene which closely approaches the refractive index of cis-decalin.

2.2 Sample Preparation

In order to determine the volume fraction for a monodisperse hard sphere sample, the usual procedure is to reach the coexistence regime through dilution or evaporation and derive a value from the crystal to liquid ratio of the sample (Pusey, Zaccarelli et al., 2009). Details on how the volume fraction is calculated from the coexistence can be found in the paper of (Ackerson, 1990). In the cases of high refractive index mismatch of the used solvent (Octadecene), rapid sedimentation when using large spheres or polydisperse samples the coexistence region could not be found. For these samples calibration of the volume fraction was made by using the random close packing volume fraction, derived from computer simulations (Schaertl and Sillescu, 1994). To achieve random close packing, the samples were first centrifuged until all the excess solvent was expelled from the colloid and the sample was separated to the randomly close packed colloid and the supernatant solvent. The standard deviation of the volume fraction derived this way is $\sigma_\varphi=\pm0.006$ as each centrifugation, even of the same batch, achieves a different packing fraction each time.

The rest of the sample concentrations were determined by successive dilutions of the same sample batch. This means that even though the absolute volume fraction of a sample may generally have a non negligible error because of reproducibility deviations of random close packing, the error in the determination of the volume fractions in the same batch by successive dilutions is small (of the order of the weight determination error, typically much less than 0.1% for each dilution).

Changing the solvent of a suspension of hard spheres is achieved by successive random close packing through centrifugation and replacement of the supernatant with the desired solvent. Depending on the ratio of added solvent to the random closed packed colloid, switching solvents may take a few cleanings, for example at least 5 cleanings would be needed if the ratio is 2:1 or 7 if the ratio is 1:1 for the old solvent to be reduced to less than 0.001% of total volume fraction. In the case of the used solvent mixture of Octadecene and Bromonaphtalene, the sample is first cleaned in Octadecene and then Bromonaphtalene is added until the mixture has reached the desired ratio between solvents. The volume or mass ratio of the two solvents in the colloidal dispersion is then determined by measuring the refractive index of the supernatant after an initial homogenisation and then subsequent packing through centrifugation. Small changes in particle size (swelling) may occur when using Bromonaphthalene, therefore a protocol of one week waiting time before any measurements has been established. Since changes in the ratio of solvents may cause particle sizes to change, dilution for a specific batch of particles is done only from the initial supernatant of the solvent mixture.

Hard Sphere Dispersions

The following equation was used to calculate volume fractions when dilution or evaporation occurred:

$$\Phi = \Phi_0 \left[1 + \frac{m_s}{m_c} \left(1 + \frac{\Phi_0 (\chi - 1)}{1 + a\chi} \right) \right]^{-1}, \text{ where } \chi = \frac{\rho_c}{\rho_s} \quad (2.1)$$

with Φ as the new volume fraction, Φ_0 the old volume fraction, m_s the mass of the added solvent, m_c the mass of the colloidal suspension, ρ_c the density of the dry colloid and ρ_s the density of the solvent. α is a parameter used to compensate for the fact that the spheres do not have the same density when in solvent, but have an increased radius due to the stabilizing layer. For the colloid ρ_c=1.188 gr/cm^3 in all cases, and for the solvents $\rho_{decalin}$=0.897 gr/cm^3, $\rho_{octadecene}$=0.788 gr/cm^3, $\rho_{Bromonaphthalene}$=1.480 gr/cm^3 while solvent mixtures have the corresponding average density. For α we used a typical value of α=0.12.

Colloid-Polymer Mixtures

In the case of making colloid-polymer mixtures, a solution of polymer was added to the colloid suspension reaching a desired volume fraction Φ and overall polymer concentration C_p, which is the mass of polymer per unit volume of sample. If the mass of the polymer solution is m_{ps} and its concentration C_{ps} then the polymer concentration in the mixture is:

$$C_p = C_{ps}\left[1+\frac{m_c}{m_{ps}}\left(1+\frac{\Phi_0(\chi-1)}{1+a\chi}\right)^{-1}\right]^{-1} \quad (2.2)$$

The new volume fraction Φ of the mixture is found from eq. 2.1 by replacing m_s with m_{ps}. As for equation 2.1 for any evaporation or when diluting a mixture of polymer and colloids with solvent, the new polymer concentration C_p changes compared to the old one C_{p0} as:

$$C_p = C_{p0}\left[1+\frac{m_s}{m_c}\left(1+\frac{\Phi_0(\chi-1)}{1+a\chi}\right)\right]^{-1} \quad (2.3)$$

2.3 Background - Rheology

Rheology is a science that deals with the flow and mechanical properties of materials. The name comes from the Greek word "ροή", which means "flow". It has been extensively used for characterizing polymers and aiding in the industrial processing of polymeric products. The macroscopic properties probed by rheology can be used to glimpse into the microscopic structure and relate to important time and size scales. This information is extracted from the material through deformation and subsequent measurement of the force response, or reversely application of force and measurement of the deformation.

Linear Viscoelasticity

Consider the deformation geometry of simple shear, sketched in Fig. 2.1. The material being sheared is between two flat rigid surfaces. The adhesion between the material and the surfaces is assumed to be strong enough that there is no slippage at either surface. The shear stress σ_{xy} (called here σ for short) in this simple shear is defined as the ratio of the applied force and the cross-sectional area of the surfaces A, which is also the area of any plane perpendicular to the y-direction within the material being sheared.

$$\sigma = \frac{F}{A} \quad (2.4)$$

The shear strain is defined as the displacement of the top plate Δx relative to the thickness of the sample h (see Fig. 2.1).

$$\gamma = \frac{\Delta x}{h} \quad (2.5)$$

By defining the stress and strain in this fashion, each part of the entire sample being sheared has identical shear stress σ and shear strain γ as long as the material shears uniformly.

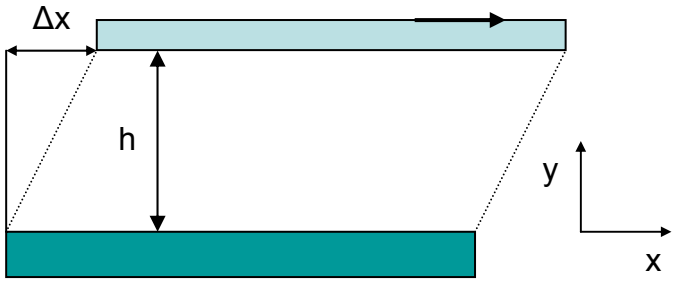

Figure 2.1: Deformation in simple shear requires application of equal and opposite forces to the two plates. The figure is a 2-dimensional representation.

If the material between the surfaces is a perfectly elastic solid, the shear stress σ and shear strain γ are proportional, with the constant of proportionality defining the shear modulus G.

$$G = \sigma / \gamma \qquad (2.6)$$

Since the stress has units of force/area and the strain is dimensionless, the modulus has units of force/ area. Equation 2.6 is Hooke's Law of Elasticity and it is valid for all solids at sufficiently small strains.

On the other hand, if the material between the surfaces is a simple liquid, the stress is identically zero at any constant strain γ. In liquids, the stress is determined by the shear deformation rate. The rate of change of shear strain with time called the shear rate.

$$\dot{\gamma} = \frac{d\gamma}{dt} \qquad (2.7)$$

If the top plate moves with a constant velocity v, the shear rate is $\dot{\gamma}$=v/h. For simple liquids, the shear stress σ is linearly proportional to shear rate $\dot{\gamma}$, with the constant of proportionality defining the shear viscosity η.

$$\eta = \sigma / \dot{\gamma} \qquad (2.8)$$

This relation is Newton's Law of Viscosity and liquids that obey it are referred to as Newtonian liquids.

Materials such as polymers and colloidal suspensions are viscoelastic, meaning that they have intermediate properties between Newtonian liquids and Hookean solids, behaving as liquids at certain applied rates and solids at others.

Oscillatory Shear

A simple viscoelastic measurement that has become very easy to implement with the advent of modern rheometers is oscillatory shear. For strain controlled rheometers, a sinusoidal strain with angular frequency ω is applied to a sample in the simple shear geometry.

$$\gamma(t) = \gamma_0 \sin(\omega t) \qquad (2.9)$$

The principle advantage of this technique is that the viscoelastic response of any material can be probed directly on different time scales (l/ω) of interest by simply varying the angular frequency ω. If the material studied is a perfectly elastic solid, then the stress in the sample will be related to the strain through Hooke's Law (2.6).

$$\sigma(t) = G\gamma(t) = G\gamma_0 \sin(\omega t) \qquad (2.10)$$

The stress is perfectly in-phase with the strain for a Hookean solid, as shown in Fig. 2.2.

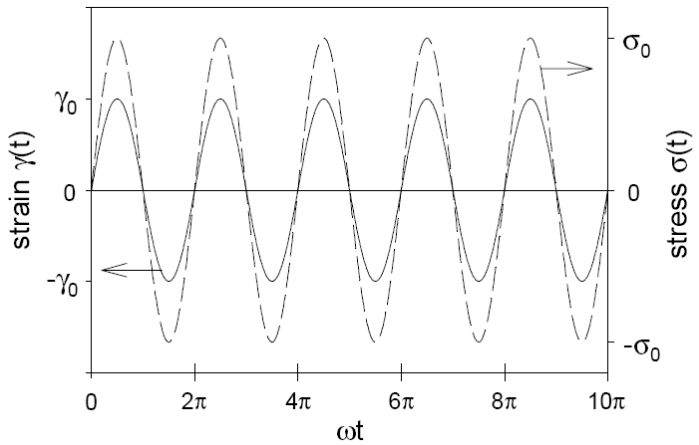

Figure 2.2: Oscillatory strain (solid curve and left axis) and oscillatory stress (dashed curve and right axis) are in-phase for a Hookean solid.

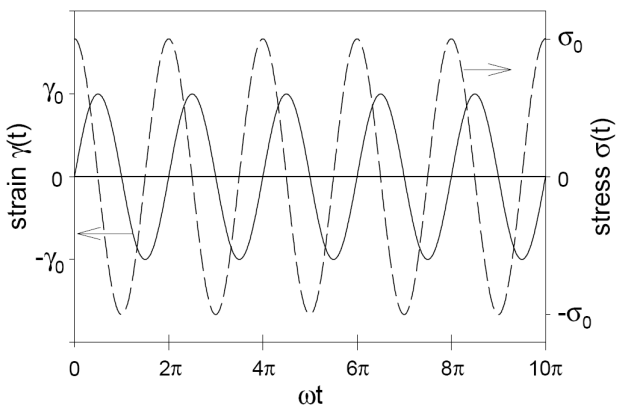

Figure 2.3: Oscillatory strain (solid curve and left axis) and oscillatory stress (dashed curve and right axis) are out-of-phase for a Newtonian liquid. The stress leads the strain by phase angle δ == π /2.

On the other hand, if the material being studied is a Newtonian liquid, the stress in the liquid will be related to the shear rate through Newton's Law (2.8).

$$\sigma(t) = \eta \frac{d\gamma(t)}{dt} = \eta\gamma_0\omega\cos(\omega t) \qquad (2.11)$$

The stress in a Newtonian liquid still oscillates with the same angular frequency ω, but is out-of-phase with the strain by π /2, as shown in Fig. 2.3. More generally, the linear response of a viscoelastic material always has the stress oscillating at the same frequency as the applied strain, but the stress leads the strain by a phase angle δ.

$$\sigma(t) = \sigma_0 \sin(\omega t + \delta) \qquad (2.12)$$

In general, δ can be frequency dependent, with any value in the range 0 < δ < π /2. The two simple cases already treated correspond to the limits allowed for the phase angle. Solids that obey Hooke's Law have δ = 0 at all frequencies, while liquids that obey Newton's Law have δ = π /2 at all frequencies. Since the stress is always a sinusoidal function with the same frequency as the strain, we can separate the stress into two orthogonal functions that oscillate with the same frequency, one in-phase with the strain and the other out-of-phase with the strain by π /2.

$$\sigma(t) = \gamma_0[G'(\omega)\sin(\omega t) + G''(\omega)\cos(\omega t)] \qquad (2.13)$$

The above equation defines G'(ω) as the storage modulus and G"(ω) as the loss modulus. Equation 2.13 can be related to Eq. 2.12 for the stress in oscillatory shear using the trigonometric identity for the sine of a sum.

$$\sin(\omega t + \delta) = \cos\delta\sin(\omega t) + \sin\delta\cos(\omega t) \qquad (2.14)$$

This suggests that the storage and loss moduli can be related to the phase angle and the modulus amplitude σ_0/γ_0 at each frequency ω.

$$G' = \frac{\sigma_0}{\gamma_0}\cos\delta \qquad (2.15)$$

$$G'' = \frac{\sigma_0}{\gamma_0}\sin\delta \qquad (2.16)$$

The ratio of storage and loss moduli is the tangent of the phase angle, called the loss tangent.

$$\tan\delta = \frac{G'}{G''} \qquad (2.17)$$

The storage and loss moduli are the real and imaginary parts of the complex modulus $G^*(\omega)$.

$$G^*(\omega) = G'(\omega) + iG''(\omega) \quad (2.18)$$

Peclet Number

In order to quantify the effect of shear on a material, the Peclet number is introduced. It is mostly used for colloidal suspensions and is a measure of the relative importance of convective motion of shear flow to diffusive Brownian motion. It is a dimensionless number that is given by the shear rate $\dot{\gamma}$ multiplied by the time needed for a particle to diffuse a distance proportional to its radius (a factor of 6), $Pe = \dot{\gamma} \cdot \tau_B$, where $\tau_B = R^2 / D$ is the Brownian diffusion time. For the dilute regime $\tau_B = 6\pi\eta_S R^3 / K_B T$ and $Pe = 6\pi\eta_S R^3 \dot{\gamma} / K_B T$ (bare Peclet). At Pe<<1, the Brownian diffusion is more important than the shear rate and the system's state closely resembles the system at rest. If Pe>1, the shear rate becomes important compared to Brownian motion and the system moves out of equilibrium giving rise to structural changes.

In the case of oscillatory measurements we define $Pe' = \omega \cdot \tau_B$, which refers to the relevant frequency of oscillatory shear when compared to the Brownian time scale. In contrast to the simple Pe, the Pe' is only the equivalent of a non dimensional ω and Pe'>1 does not correspond to a system out of linearity, rather it describes that the frequency of oscillation is comparable/faster than the Brownian time. We may define a Pe in oscillatory shear by taking the maximum rate within the period and calculating $Pe = \dot{\gamma}_{\max} \cdot \tau_B = \gamma_0 \cdot \omega \cdot \tau_B$. The resulting number will only be relevant if γ_0 is in the non linear regime.

In the case of dense hard sphere suspensions the short time self diffusion is not equal to the diffusion in the dilute regime, rather it is reduced by a significant factor due to hydrodynamic interactions (Sierou and Brady, 2001). Since the actual Brownian time of the sample scales all other resulting times, when examining the effects of shear, the hydrodynamic effect should be taken into account. Therefore we may distinguish between two Brownian times and/or Peclet numbers. The first, which are called "bare", refer to the dilute regime and its Brownian time can simply be calculated by the particle radius and solvent viscosity. The second, called "dressed", take into account the hydrodynamic interactions between particles and reflect the smaller short-time self-diffusion coefficient, $D_s(\varphi)$. While the bare Pe is relatively simple to calculate, the calculation of the dressed Pe requires the knowledge of the φ dependence of $D_s(\varphi)/D_0$.

Experimental Geometries

When working with commercial rheometers, the geometries differ from the simple shear geometry shown previously. Although the simple shear geometry is easy to understand, it is

very hard to implement experimentally. To solve various implementation issues, experimental rheology turned to rotating geometries such as the parallel plate and cone plate geometries shown in figure 2.4 and also the couette geometry.

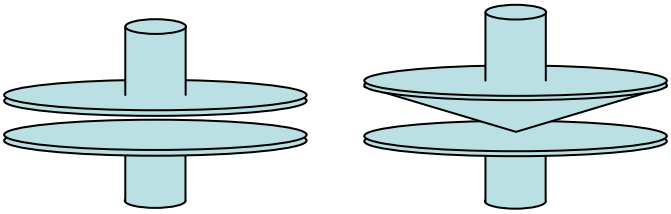

Figure 2.4: Illustration of the parallel plate (left) and cone plate (right) geometries used in experimental rheology.

The main difference between the two geometries is that the cone and plate has a homogenous strain field, whereas the parallel plates do not. This is especially important when performing non-linear measurements, as the validity of the response relies heavily on the assumption that the whole sample responds to applied strain in the same way. For linear measurements this assumption is true even in the case of parallel plates that apply non-homogenous strain. Cone and plate geometries were mostly used in this work as we focus on non-linear rheology.

2.4 Rheometer Setup

In general, two rheometers were used in this work: A Rheometric Scientific strain controlled ARES Rheometer (Dual Transducer with a Measuring Torque Range: 0.004-10 gr·cm with the first transducer and 0.04-100 gr·cm with the second) and an Anton Paar MCR-501 stress control rheometer, with a very good strain control loop (Applied Torque Range: 0.01-100 gr·cm). All the measurements were made at a constant temperature of 20±0.01˚C stabilised with a Peltier system in both rheometers. An exception was made in the case of the Echo measurements where no temperature control was used due to vibrations of the water bath cooling system affecting measurement stability. In this case the room temperature was stabilized to about 20±1˚C.

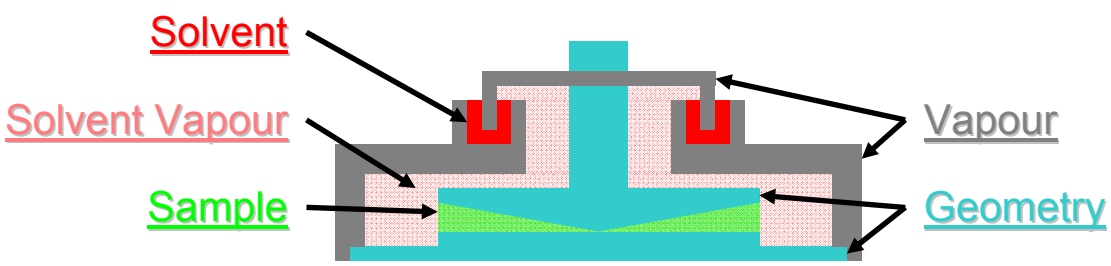

Figure 2.5: Representation of vapor saturation trap.

For the samples in cis-decalin and the mixture of Octadecene and Bromonaphthalene the area around the sample was sealed with a home made vapour saturation trap (as seen in figure 2.5). The vapour trap consists of two main pieces, a cylindrical aluminium piece which sits on the bottom plate and has a trough for putting in the sample solvent and second piece which is fitted on the top plate. The two pieces are fitted in such a way as to not touch, which would cause measurements to be affected, but allow the low viscous solvent to seal the vapours inside the trap. For measurements done in the stress controlled Anton Paar, a slightly different design of the trap was used. In order to avoid the condensation of the solvent vapour either on the sample (causing dilution) or on the inside of the trap (causing evaporation), the room temperature was regulated to be as close as possible to the stabilized sample temperature. By keeping a stable room temperature, sample measurements without the effects of dilution or evaporation would allow a few hours (cis-decalin) to a few days (mixture of Octadecene and Bromonaphthalene) of measurements.

2.5 Light Scattering Echo

To complement the rheological techniques and see what is happening on a microscopic level to the glass when it is sheared into a crystal, we performed Light Scattering Echo experiments. This technique, like classic dynamic light scattering, examines the degree of correlation of the scattered light between two times, forming the time autocorrelation function $g_2(\tau) \equiv \langle I(t)I(t+\tau)\rangle / \langle I(t)\rangle^2$ of the scattered intensity, $I(t)$ (Berne and Pecora, 1976). As this correlation in light is related with microscopic particle movement, it shows the correlation between particle positions. When a correlation function shows total de-correlation for a time **τ**, this means that the structure after time **τ** has changed in comparison to its initial structure over length scales which are determined by the scattering conditions. At rest this would mean that the system has rearranged itself in such a way that there is no correlation between the particles' positions after time **τ**.

When applying oscillatory shear, the sample de-correlates as the medium is distorted by flow and partially re-correlates at intervals multiple to the period of oscillation when the flow field has returned to its initial position. The amount of correlation which is recovered gives a measure of the amount of particles which returned to their initial position after one period of oscillation.

In the case of transparent samples, the single scattering limit, the scattering at a particular wavevector are determined with $q = (4\pi n / \lambda)\sin(\theta / 2)$ as the wavevector, where λ is the wavelength, θ the scattering angle and n the refractive index. The length scale probed in this

case is $2\pi/q$. On the other hand for opaque samples as in our case, the technique of Diffusing Wave Spectroscopy (DWS) is used in the limit of strong multiple scattering (Weitz and Pine, 1993). In this case, the dependence on the scattering wavevector is lost and the measured correlation and relaxation times depend on the scattering geometry (transmission or backscattering), as well as the number of scattering events N, the geometry of the incident beam and the intrinsic dynamics of the sample (Weitz and Pine, 1993). The length scale probed by DWS is smaller than classic DLS and is $\sqrt{\frac{6}{N}}\frac{\lambda}{2\pi}$.

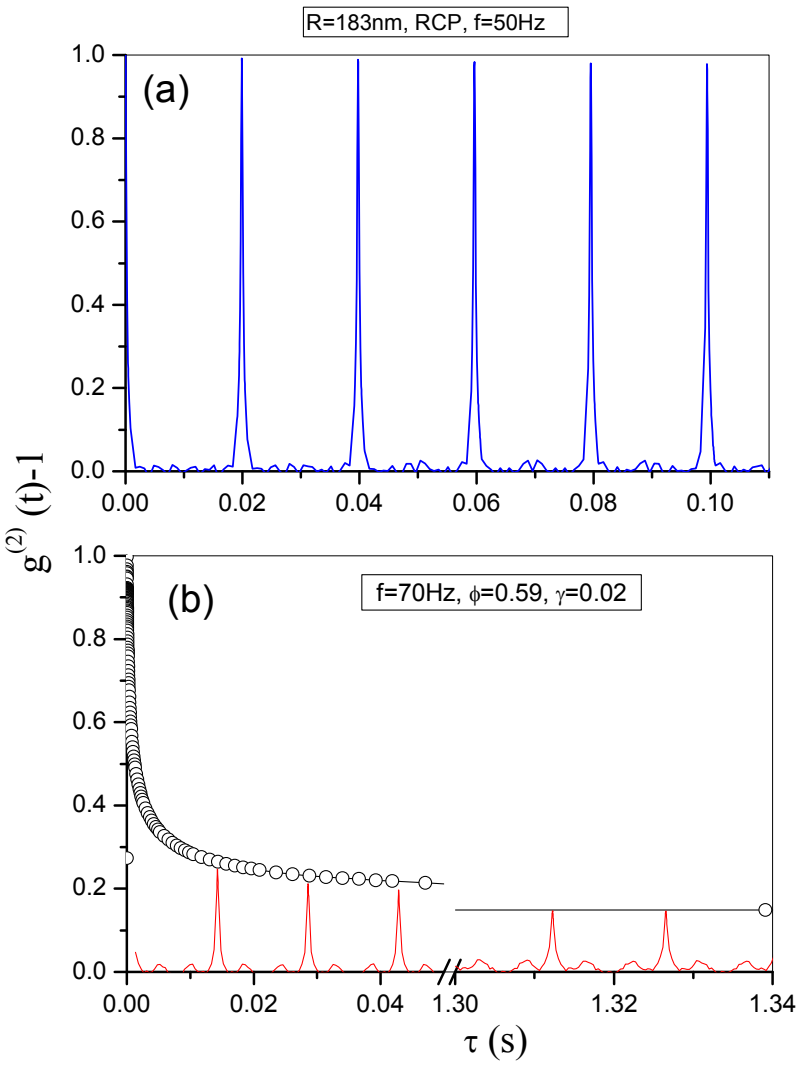

Figure 2.6: Echoes in the linear regime of random closed packed spheres (top) showing purely elastic response with no decay and a lower volume fraction (bottom) where we see decay due to Brownian motion (Petekidis, Moussaid et al., 2002).

As mentioned, the autocorrelation function of the intensity $g_2(\tau)$ decays with the application of oscillatory shear. If after one period of oscillation T (or mT), the scatterers return to their original positions, meaning a purely reversible deformation, the light speckle pattern reverts

to its original configuration and $g^{(2)}(mT)-1=1$. This is seen in figure 2.6a as an echo experiment that was performed on a sample of hard spheres near the random close packing where essentially no Brownian motion is present. The correlation function reveals 'echoes' of amplitude 1 at delay times equal to integer multiples m of the period of oscillation T. However, if the shear and/or the intrinsic motion induce some irreversible re-arrangements and the particles do not return to their initial positions, the echoes will have amplitudes that are smaller that 1. This can be seen in figure 2.6b, where the Brownian motion causes the echoes to decay. We can decouple the shear induced from the Brownian re-arrangements by comparing the decay of the correlation function at rest to the echoes, again shown in the figure.

In the simple case of a non-sheared dilute suspension of particles undergoing Brownian motion, in the strong multiple scattering limit, it is shown (Weitz and Pine, 1993) that the correlation function approximately decays as an exponential according to:

$$\sqrt{g^{(2)}(\tau)-1} \approx \exp\left(-\frac{1}{6}Nk^2\left\langle \Delta r^2(\tau)\right\rangle\right) \qquad (2.19)$$

where N is the average number of times a photon is scattered, $k=2\pi n/\lambda$ is the propagation vector of light and $\left\langle \Delta r^2(\tau)\right\rangle$ is the particle's mean square displacement. Even though light scattering generally measures the collective motion of particles, it has been argued for large particles that DWS largely measures the self diffusion (Weitz and Pine, 1993).

If we apply oscillatory shear to the sample, we induce displacements additional to those due to Brownian motion, thus for the echo measurement we can write:

$$\sqrt{g^{(2)}(\tau)-1} \approx \exp\left(-\frac{1}{6}Nk^2\left[\left\langle \Delta r^2(\tau)\right\rangle_B+\left\langle \Delta r^2(\tau)\right\rangle_S\right]\right) \text{ for } \tau=mT \qquad (2.20)$$

where $\left\langle \Delta r^2(\tau)\right\rangle_B$ is the displacement attributed to Brownian motion and $\left\langle \Delta r^2(\tau)\right\rangle_S$ the displacement associated with the additional shear induced diffusion.

Since the length scale probed by DWS is proportional to $\sqrt{\frac{6}{N}}\frac{\lambda}{2\pi}$, small motions will cause $g^{(2)}(\tau)-1$ to decay to zero if the scattering events N are too many. For this we are forced to work with a small number of scattering events, where Eq. 2.19 may not be valid. Even though working between the limit of single scattering and strong multiple scattering is difficult, there has been work on double scattering (Sorensen, Mockler et al., 1976). It has been argued by (Petekidis, Moussaid et al., 2002) that for the transmission geometry, the dynamics are very

similar to those measured by DWS at an approximated N=2 and by eliminating single scattering with a polarizer one can give a reasonable description of $g^{(2)}(\tau)$. In truth, results of the relevant chapter 7 show that interpretation of results from the backscattering DWS need further analysis, as will be discussed there.

2.6 DWS Echo Setup

The LS echo experiments were carried out on the ARES strain controlled rheometer in the backscattering setup shown in figure 2.7, able to carry out rheological and scattering experiments simultaneously. For the DWS Echo measurements for the shear induced crystallization study, transparent geometries were needed and although some tests were made using the simpler setup of parallel glass plates, inhomogeneous strain throughout the sample led to partial crystallization and consequently problematic measurements. Thus a homemade transparent Plexiglas cone was constructed which had a diameter of 38mm, an angle of 0.03 rad and was insoluble in the solvents used during these experiments. This cone was used as the rotating part of the geometry, while a stationary parallel glass plate was used for the top. In the setup, as shown in figure 2.7, a red laser (λ=633nm) shines from the top and the scattered light intensity is measured at backscattering. A photon multiplier tube is used to acquire the intensity of the scattered light and measure the echoes. In order to cut off reflections and single scattering events, a crossed polarizer is put between the sample and the detector.

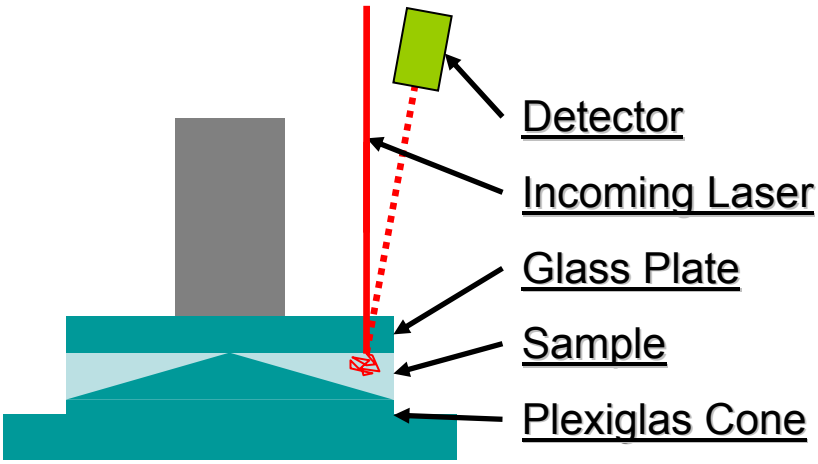

Figure 2.7: Representation of echo experimental setup.

2.7 Brownian Dynamics Simulation

In addition to rheology and light scattering echo, a number of Brownian dynamics simulations were conducted on hard sphere systems under both steady and oscillatory shear to complement the findings of the experimental techniques. The code used here assumes

Brownian diffusion of particles with hard sphere interactions. Hydrodynamic effects are ignored as the computational cost is high and their effect at low Peclet numbers should be negligible (Foss and Brady, 1999). A simple description of how the algorithm works is as follows: The algorithm positions a predetermined number of particles in a three dimensional box either randomly, or in specific positions. It then displaces them sequentially in a random Brownian step and applies a predetermined deformation. The Brownian step and the deformation, which is nothing more than a strain displacement in the velocity direction, change in magnitude according to the size of the predetermined time step. The hard sphere potential is enforced when particles overlap at the end of each time step by pulling them back across the line that connects their centres back to contact, while enforcing force conservation. The algorithm then repeats the displacements and overlap checks, creating a repeating cycle. The positions of the particles are saved in predetermined intervals for any further analysis.

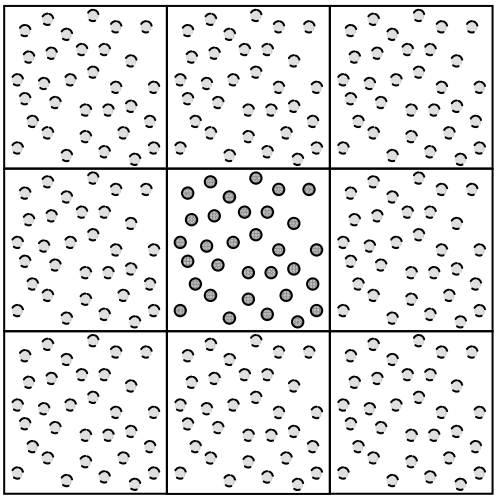

Figure 2.8: 2-D Representation of periodic boundary conditions. The surrounding boxes are copies of the centre box, the darker particles in the centre box are 'real' and the lighter ones on the outside boxes are 'imaginary' copies. The 'real' particles on the edge of the box can interact with the 'imaginary' particles in their proximity and act accordingly.

In order to avoid misleading surface and size effects in the simulated system, periodic boundary conditions are applied. When periodic boundary conditions are applied in a box, a particle can move freely to the edge and if it passes the edge boundary, it then appears on the opposite side of the box. Similarly, a particle on the edge of the box interacts with the particles on the opposite side of the box, even if they are "imaginary" or "ghost" particles. This allows the study of systems without many of the complications of wall or boundary effects, effectively simulating an infinitely large system with an infinite amount of particles and as such, resembling a real system. Figure 2.8 shows a representation of the periodic boundary conditions. In the case of shear, the imaginary particles' shear velocity changes as

compared to their real images as shown in figure 2.9 to keep the periodicity in order. Care should be taken as any probed length scale in the system should be much smaller than the simulation box.

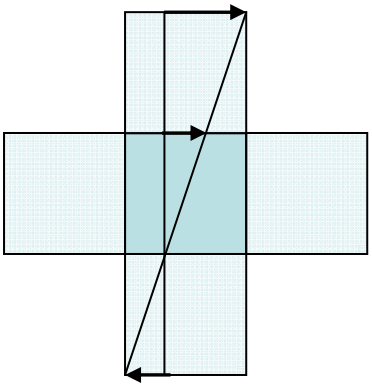

Figure 2.9: In the event of shear, the imaginary particles in the top and bottom boxes are sped up or slowed down as shown by the shear profile to keep the periodic boundary conditions in order.

Simulation Method

Brownian dynamics is a simulation method used in the study of suspensions that simulates colloids at the particle level and ignoring hydrodynamic interactions. This allows simulations of larger and more complicated systems, in comparison to the more acute but computationally consuming Stokesian dynamics simulation (Foss and Brady, 1999). The size of colloidal particles is such that there is a clear separation of time and length scales between the particles and the fluid molecules, therefore the fluid can be treated as a continuum, but the particles are still small enough to be affected by collisions with the fluid molecules and are thus still Brownian.

Thus, Brownian dynamics can be described as a simplification of Stokesian dynamics, where hydrodynamic interactions between particles are neglected. For N rigid particles of radius R and density ρ in a medium of viscosity η moving with velocity **U**, we examine states where the Reynolds number is Re<<1 (the dimensionless ratio of inertial forces $\rho U^2/R$ to viscous forces $\eta U/R^2$). The motion of the particles is described by the N-body Langevin equation:

$$\mathbf{m}\frac{d\mathbf{U}}{dt} = \mathbf{F}^H + \mathbf{F}^B + \mathbf{F}^P \quad \text{(Eq. 2.21)}$$

where **m** is the generalized mass/moment tensor, **U** is the particle translational/rotational velocity vector, $\mathbf{F}^H$ is the hydrodynamic force vector, $\mathbf{F}^B$ is the stochastic force vector that gives rise to Brownian motion, and $\mathbf{F}^P$ is the deterministic non-hydrodynamic force vector. Since inertia is not important in colloidal dispersions (Re<<1) the equation reduces to:

$$0 = \mathbf{F}^H + \mathbf{F}^B + \mathbf{F}^P \quad \text{(Eq. 2.22)}$$

Additionally for BD and negligible hydrodynamic interactions, the hydrodynamic force reduces to Stokes drag $\mathbf{F}^H = -6\pi\eta R\mathbf{U}$ (Eq. 2.23).

The form of the stochastic or Brownian force $\mathbf{F}^{\mathbf{B}}$ that arises from the thermal fluctuations in the fluid is given by the fluctuation-dissipation theorem:

$$\begin{aligned} \overline{\mathbf{F}^B(t)} &= 0 \\ \overline{\mathbf{F}^B(t)\mathbf{F}^B(t+\tau)} &= 2K_B T(6\pi\eta R)\mathbf{I}\delta(t) \end{aligned} \qquad \text{(Eq. 2.24)}$$

The over bars denote an ensemble average over the thermal fluctuations in the fluid, K_BT is the thermal energy, and δ(t) is the Dirac delta function. The non-hydrodynamic force vector can be separated into the particle interaction components, the hard sphere interaction occurring at contact and any additional potential:

$$\mathbf{F}^P = \mathbf{F}^{HS} + \mathbf{F}^{Ext} \text{ (Eq. 2.25).}$$

The particle evolution equation is obtained by integrating equation 2.22 twice over a time step **Δx** to finally get the displacement vector under shear:

$$\begin{aligned} \Delta x = Pe\langle\mathbf{U}\rangle\Delta t + \mathbf{X}(\Delta t) + F^P\Delta t = Pe\langle\mathbf{U}\rangle\Delta t + \mathbf{X}(\Delta t) + \Delta\mathbf{x}^{HS} + \Delta\mathbf{x}^{Ext} \\ \text{and } \overline{\mathbf{X}} = 0, \quad \overline{\mathbf{X}(\Delta t)\mathbf{X}(\Delta t)} = 2D\mathbf{I}\Delta t, \quad D = \frac{kT}{6\pi\eta a} \end{aligned} \qquad \text{(Eq. 2.26)}$$

This equation shows that at each time step the displacement is equal to the sum of the displacement from the imposed velocity <**U**> (shear), the random Brownian displacement (**X**(Δt)) the displacement due to interparticle hard potential (Δx^{HS}) and any additional forces (Δx^{Ext}). To get the equation, it was assumed that there are no hydrodynamic interactions and as such rotational and translational motions are decoupled. **X** is non-dimensionalised by the particle radius R, the time t by the Brownain time $\tau_B = R^2/D$ and <**U**> by D/R.

At each time step, the positions of the particles are updated first by adding the displacements due to the Brownian and external forces, and second by an iterative method which corrects collisions by applying the hard-sphere force/displacement ($\mathbf{\Delta x^{HS}}$). This hard-sphere collision scheme is based on the "potential-free" algorithm of (Heyes and Melrose, 1993) in which the overlap between pairs of particles is corrected by moving the particles with equal force along the line of centres, back to contact. This algorithm is "potential free" concerning the hard repulsion in that it does not require a specific declaration of a pair potential, although it implements the hard-sphere potential which is infinite if the particles are overlapping and zero otherwise.

Instead of drawing random displacements from a Gaussian profile, we may use **Ψ** as a random vector of which each element is selected from a uniform distribution of random numbers

ranging from -1 to 1 with a mean value of zero, then $\mathbf{X}(\Delta t) = \sqrt{2D\Delta t}\mathbf{\Psi}\sqrt{3}$. This method produces a Gaussian distribution of displacements after a few time steps.

By making all the equations non-dimensional, then for every time step and for no additional potential, each particle moves by:

$$\begin{aligned} \Delta x &= \sqrt{2\Delta t}\Psi\sqrt{3} + \Delta x_{Shear} \\ \Delta y &= \sqrt{2\Delta t}\Psi\sqrt{3} \\ \Delta z &= \sqrt{2\Delta t}\Psi\sqrt{3} \end{aligned} \quad \text{(Eq. 2.27)}$$

where Ψ is a random number ranging from -1 to 1 with a mean value of zero, x is the velocity direction and y is the velocity gradient direction.

In the case of a simple steady shear, $\Delta x_{Shear} = Pe \cdot \mathrm{y} \cdot \Delta t$ and $Pe = \dot{\gamma} \cdot t_B = \dot{\gamma} \cdot R^2/D$, meaning that for Pe=1, 100% strain will be reached in a time scale of t_B. For the case of oscillatory shear where $\gamma = \gamma_0 \cdot \sin(\omega t)$ a different Pe must be used as discussed in the introductory chapter. Thus we define Pe', which corresponds to an oscillation frequency with the instantaneous shear of each particle calculated as:

$$\begin{aligned} &\text{For } \gamma = \gamma_0 \cdot \sin(Pe' \cdot t), \\ &\Delta x_{Shear} = Pe' \cdot \gamma_0 \cdot \cos(Pe' \cdot t) \cdot \mathrm{y} \cdot \Delta t \\ &\text{and } Pe' = \omega R^2/D = 2\pi t_B/T \end{aligned} \quad \text{(Eq. 2.28)}$$

where γ_0 is the peak amplitude of shear and ω is the frequency of oscillation. If we compare the maximum shear rate in the oscillation with the steady rate, the relation between the two Pe is given by $Pe=\gamma_0 Pe'$.

According to(Foss and Brady, 2000) in order to calculate the stress, the algorithm directly calculates the pairwise interparticle forces that would have resulted in the hard sphere displacements during the course of a time step. By examining Eq. 2.22 and equating the contribution due to interparticle force with the hard sphere displacement we get in dimensional form:

$$\mathbf{F}^P = 6\pi\eta R \frac{\Delta x^{HS}}{\Delta t} \quad \text{(Eq. 2.29)}$$

This is simply the average Stokes drag on the particle during the course of the hard-sphere displacement. Once the interparticle forces from each collision are known, they can be used to calculate the stress. The bulk stress, which is defined as the average stress over the volume V containing N particles is given by (Foss and Brady, 2000):

$$\langle \mathbf{\Sigma} \rangle = -\langle p \rangle_f \mathbf{I} + 2\eta(1 + \tfrac{5}{2}\phi)\langle \mathbf{E} \rangle - NkT\mathbf{I} - N\langle \mathbf{x}\mathbf{F}^P \rangle \quad \text{(Eq. 2.30)}$$

and $\langle p \rangle_f$ is the average fluid pressure, $-NkT\mathbf{I}$ is the isotropic stress associated with the Brownian thermal motion and $2\eta(1+\frac{5}{2}\phi)\langle \mathbf{E} \rangle$ is the hydrodynamic contribution to the stress that reduces to the single particle Newtonian Einstein correction, where $\langle \mathbf{E} \rangle$ is the rate of strain tensor. All the rheologically interesting behaviour is contained in the $\langle \mathbf{xF}^P \rangle$ contribution. Since this work focuses on shear response, as taken from rheometer, only one of the tensor values is examined. To calculate the contribution of each particle to the stress we use this non-dimensional equation (normalized with K_BT/R^3):

$$\Sigma_{xy} = -\frac{r_x \Delta y^{HS}}{V \Delta t} \quad \text{(Eq. 2.31)}$$

Therefore the overall measured stress, σ_{xy} is the sum of the contributions of all particles. The specific simulation method has been used and described in detail in (Foss and Brady, 2000).

At rest and for relatively low Pe, Brownian dynamics simulations should be able to qualitatively capture stresses and displacements, even with the absence of hydrodynamics(Foss and Brady, 1999; Brady, 2001). The addition of the depletion potential in the simulations will be discussed in the relevant chapter.

Cell lists

Even though computing the pairwise interactions between particles may be achieved through examination of each and every pair of particles, this tends to be computationally inefficient and of O[N(N-1)/2]. By dividing the simulation domain into cells with an edge length of at least the range of the interaction potential and computing the interaction between the particles in the same (red) and in the adjacent (green) cells (fig 2.10), a smaller computation cost of O[N] is attained. Since the cell length is at least the length of the interaction range in all dimensions, no interacting particles can be missed.

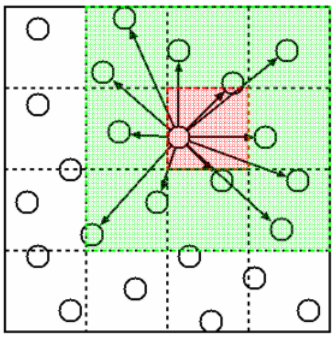

Figure 2.10: 2-D Representation of cell list pairwise computations. Particles are separated according to their positions in the simulation box in cells. Particles in a cell check for interactions with other particles only within their own (red) or neighbouring cells (green).

Calculations of Structural and Dynamical Properties

The pair distribution function (PDF) describes the distribution of distances between pairs of particles contained within a given volume. For two arbitrary sets of N_a and N_b particles, it is calculated by the following equation:

$$g\left(r,\overrightarrow{r_{ab}}\right)=\frac{V}{4\pi r^2 N_a N_b}\left\langle\sum_{i=1}^{N_a}\sum_{j=1}^{N_b}\delta\left(r-\left|\vec{r_i}(t)-\vec{r_j}(t)\right|\right)\right\rangle_t \quad \text{(Eq. 2.32)}$$

where r is the examined pair distance, V the volume of the cell, $\vec{r_i}$ and $\vec{r_j}$ the positions of the particles. For a homogeneous particle distribution, equal sets of particles and r>R, the particle radius we find g(r)=1. However, for the dense systems we examine, g(r) shows various peaks indicating the increase of probability in finding a particle at that distance.

The Mean Squared Displacement (MSD) gives a statistical measure of the distance a particle has moved in a specific time. If x_i is the non-affine position (by subtraction of affine shear field motion) of a particle i in the x direction and N is the total number of particles then the MSD is generally calculated by using the following equations:

$$\left\langle\Delta x^2(\tau)\right\rangle=<\frac{1}{\mathrm{N}}\sum_{i=1}^{N}[x_i(t+\tau)-x_i(t)]^2>_\tau \text{ and} \quad \text{(Eq. 2.33)}$$
$$\left\langle\Delta r^2(\tau)\right\rangle=\left\langle\Delta x^2(\tau)\right\rangle+\left\langle\Delta y^2(\tau)\right\rangle+\left\langle\Delta z^2(\tau)\right\rangle$$

where x_i is substituted with y_i and z_i for the different axis.

Because of the finite system size, the high density of the system and subsequent small displacements over long times, subtraction of the centre of mass motion is needed as a correction (Koumakis, 2007), such as:

$$\left\langle\Delta x^2\right\rangle_\tau=<\frac{1}{\mathrm{N}}\sum_{i=1}^{N}\left[\left(x_i(t+\tau)-x_i(t)\right)-\frac{1}{\mathrm{N}}\sum_{i=1}^{N}\left[x_i(t+\tau)-x_i(t)\right]\right]^2>_\tau \quad \text{(Eq. 2.34)}$$

It is important to note that by subtracting the affine motion at every time step, the effect of Taylor dispersion is lost (Taylor, 1954). Although all mean squared displacements are discussed with the affine motion subtracted, this effect may be especially important in the case of oscillatory shear. Further details are given in the Appendix.

The one sided, self Van Hove function (Van Hove, 1954), $G_S(\Delta x,\tau)$, is the probability density function of a particle's displacement distance for a specified elapsed time. The probability distribution of a particle moving a distance between $\Delta(\Delta x)=\Delta x_b-\Delta x_a$ for an elapsed time τ is specified as:

$$P\left(\Delta(\Delta x),\tau\right)=\frac{1}{N}\left\langle\sum_{i=1}^{N}\delta\left(\Delta x-\left|x_i\left(t+\tau\right)-x_i\left(t\right)\right|\right)\right\rangle_t=\frac{\mathrm{N}(\Delta x,\tau)}{\mathrm{N}} \quad \text{(Eq. 2.35)}$$

where Δx is the distance a particle has moved in a time scale τ, averaged over time. The probability density function, $G_S(\Delta x,\tau)$, is then given by $P\left(\Delta(\Delta x),\tau\right)=\int_{\Delta x_a}^{\Delta x_b}G_S\left(\Delta x,\tau\right)d\Delta x$ where $\int_0^{\infty}G_S\left(\Delta x,\tau\right)d\Delta x=1$.

For a single sphere in a Newtonian fluid, both the probability distribution and density functions should have a Gaussian profile, i.e. a curve that fits the function $f(x)=\frac{A}{w\sqrt{\pi/2}}e^{-2\left(\frac{x}{w}\right)^2}$, where A and w are fitting parameters for the area and the width of the curve respectively. The lowest order deviation of the Van Hove function from Gaussian behavior is given by

$$a_{2x}\left(\tau\right)=\frac{\left\langle\Delta x^4\left(\tau\right)\right\rangle_{N,t}}{3\left\langle\Delta x^2\left(\tau\right)\right\rangle_{N,t}^2}-1,\ a_{2r}\left(\tau\right)=\frac{3\left\langle\Delta r^4\left(\tau\right)\right\rangle_{N,t}}{5\left\langle\Delta r^2\left(\tau\right)\right\rangle_{N,t}^2}-1 \quad \text{(Eq. 2.36)}$$

averaged over particles and time, where a_{2x} is the for a single dimension and a_{2r} for radial displacements. Non-zero values mean that G_s exhibits non-Gaussian behavior.

Examples

Examples of simulated systems at rest are shown in figure 2.11. The amorphous polydisperse glassy hard sphere system is the focus of chapters 4 and 5. Chapter 6 focuses on the monodisperse FCC crystal under shear, while chapter 9 examines low volume fraction attractive gels under shear.

Amorphous Glass (φ=0.62) FCC Crystal (φ=0.62) Strong Attractive Gel (φ=0.25)

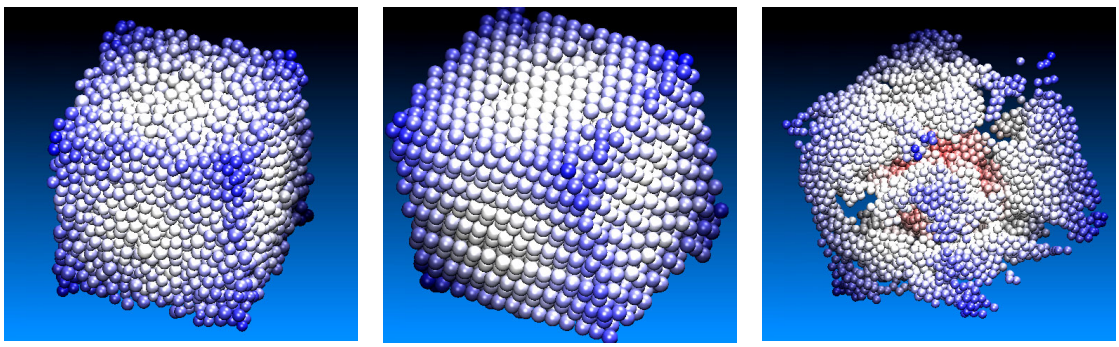

Figure 2.11: Images of different types of simulated systems as shown above the images.

2.8 References

Ackerson, B. J. (1990). "Shear induced order and shear processing of model hard sphere suspensions." J. Rheol. **34**(4) 553-590.

Berne, B. J. and R. Pecora (1976). Dynamic Light Scattering. New York, Wiley-Interscience Publications.

Brady, J. F. (2001). "Computer simulation of viscous suspensions." Chemical Engineering Science **56**(9) 2921-2926.

Bryant, G., S. R. Williams, L. Qian, I. K. Snook, E. Perez and F. Pincet (2002). "How hard is a colloidal ‘‘hard-sphere’’ interaction?" Phys. Rev. E **66** 060501

Foss, D. R. and J. F. Brady (1999). "Self-diffusion in sheared suspensions by dynamic simulation." J. Fluid Mech. **401** 243-274.

Foss, D. R. and J. F. Brady (2000). "Brownian Dynamics simulation of hard-sphere colloidal dispersions." Journal of Rheology **44**(3) 629-651.

Heyes, D. M. and J. R. Melrose (1993). "Brownian dynamics simulations of model hard-sphere suspensions." Journal of Non-Newtonian Fluid Mechanics **46**(1) 1-28.

Koumakis, N. (2007). Shear Induced Crystallization of a Colloidal Glass. Department of Materials Science and Technology, University of Crete. **MSc**.

Petekidis, G., A. Moussaid and P. N. Pusey (2002). "Rearrangments in hard-sphere glasses under oscillatory shear strain." Phys. Rev. E **66** 051402.

Pusey, P. N., E. Zaccarelli, C. Valeriani, E. Sanz, W. C. K. Poon and M. E. Cates (2009). "Hard spheres: crystallization and glass formation." Philosophical Transactions of the Royal Society A: Mathematical, Physical and Engineering Sciences **367**(1909) 4993-5011.

Schaertl, W. and H. Sillescu (1994). "Brownian dynamics of polydisperse colloidal hard spheres: Equilibrium structures and random close packings." J. Stat. Phys. **77** 1007.

Sierou, A. and J. F. Brady (2001). "Accelerated Stokesian Dynamics simulations." Journal of Fluid Mechanics **448**(-1) 115-146.

Sorensen, C. M., R. C. Mockler and W. J. Sullivan (1976). Phys. Rev. A **14** 1520.

Taylor, G. (1954). Conditions under Which Dispersion of a Solute in a Stream of Solvent can be Used to Measure Molecular Diffusion. **225:** 473-477.

Van Hove, L. (1954). "Correlations in Space and Time and Born Approximation Scattering in Systems of Interacting Particles." Physical Review **95**(1) 249.

Weitz, D. A. and D. J. Pine (1993). Diffusing-wave spectroscopy. Dynamic Light Scattering: The Method and Some Applications W. Brown, Clarendon Press**:** 652–720.

Chapter 3 – Hard Spheres: General Rheology and Dynamics at Rest

3.1 Introduction

The purpose of this chapter is to introduce the general rheological response of concentrated dispersions of hard sphere glasses, both linear and non linear, and then describe the dynamics at rest as taken from Brownian dynamics simulations. Most of the rheological data to be shown in this chapter is taken from previous studies and presented as an overview of hard sphere glass behavior under shear. The simulations on the other hand, are results of this work that although do not provide many novel findings, were needed to initialize the simulations under shear and serve as a starting point for the understanding of more complicated states under shear flow.

We begin examination of the rheology by showing the linear oscillatory viscoelasticity, with the frequency, volume fraction dependence and particle size renormalizations. Afterwards, we will discuss non linear oscillatory response, the emergence of non harmonic stress and the volume fraction dependence of yield strains. Additionally, we will examine transient steady rate tests as well as steady state flow curves and their correlation to particle dynamics. Creep and recovery experiments will also be discussed. Simulation results of the dynamics at rest at various volume fractions will then be shown as well as various analyses of the data examining the dynamic heterogeneities.

3.2 Linear Viscoelasticity and Frequency Sweeps

When applying oscillatory shear in the linear regime of strains, the microstructural properties of the probed material are not affected by the application of shear and the measured viscoelastic properties reflect the state at rest. Variation of the oscillation frequency allows one to probe the material at different time scales, retrieving the viscoelasticity at those time scales, as well as indirectly probing the microscopic properties.

A dynamic frequency sweep (DFS) as shown in figure 3.1, is a probe of viscoelasticity in the linear regime at various frequencies, keeping a constant strain while varying the frequency. In this specific case, we show the results of a high volume fraction glass (black, circles) and its shear induced crystal (red, squares), with the elastic (solid) and viscous (open) moduli from the work of (Koumakis, Schofield et al., 2008). The elastic and viscous moduli, or G’ and G’’

respectively, in the case of the glass and the crystal, show almost constant values within the examined time scales, with G' greater than G''. The details show G' having a small increasing slope with frequency and G'' exhibiting a minimum in the case of the glass.

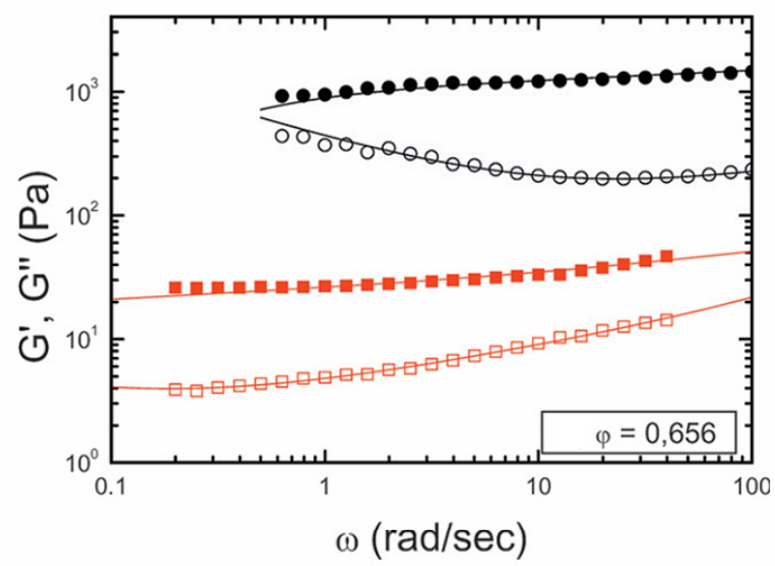

Figure 3.1: Linear dynamic frequency sweeps of a glass (black, circles) and the same volume fraction shear induced crystal (red, squares) from the work of (Koumakis, Schofield et al., 2008) showing the elastic (solid) and viscous (open) moduli. Lines are Mode Coupling Theory (MCT) fits to the data from (Mason and Weitz, 1995).

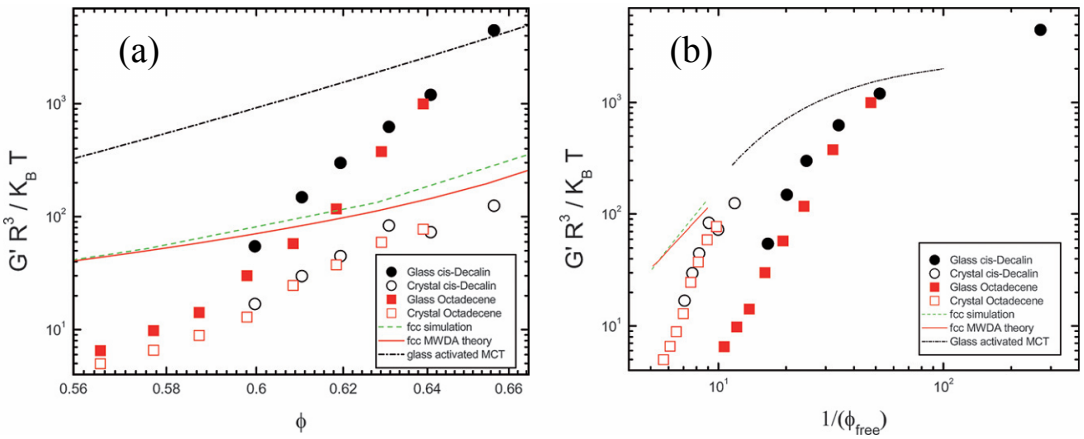

Figure 3.2: The scaled linear dynamic elastic moduli (at ω=1rad/sec) of glasses (solid points) and shear induced crystals (open points) as shown in legend, from the work of (Koumakis, Schofield et al., 2008) for two different solvents (cis-Decalin with circles and Octadecene for squares) as a function a) of volume fraction and b) the inverse free volume ($\varphi_{free}=\varphi_{max}-\varphi$). Activated MCT theory is from (Kobelev and Schweizer, 2005) (black, dash-dot line), while crystal elasticity is from (Laird, 1992) (theory, red, solid line) and (Pronk and Frenkel, 2003) (simulations, green, dashed line).

From these curves we generally observe that both the glass and the crystal exhibit a solid-like response in a large range of frequencies, characteristic of structurally frozen system. The crystal has much smaller viscoelastic stresses than the glass due to ordering and thus larger available space per particle at the same φ. The small slope of G' may be attributed to slightly increased particle motions in small frequencies, while the minimum of G'' may be connected to the transition between the in cage and out of cage relaxation times of the particles as shown by MCT (van Megen and Underwood, 1993; Mason and Weitz, 1995). Using the Generalized Stokes Einstein (GSE) equation, we may directly correlate the viscoelastic properties to the motions and dynamics of the particles at rest as will be shown further in the text.

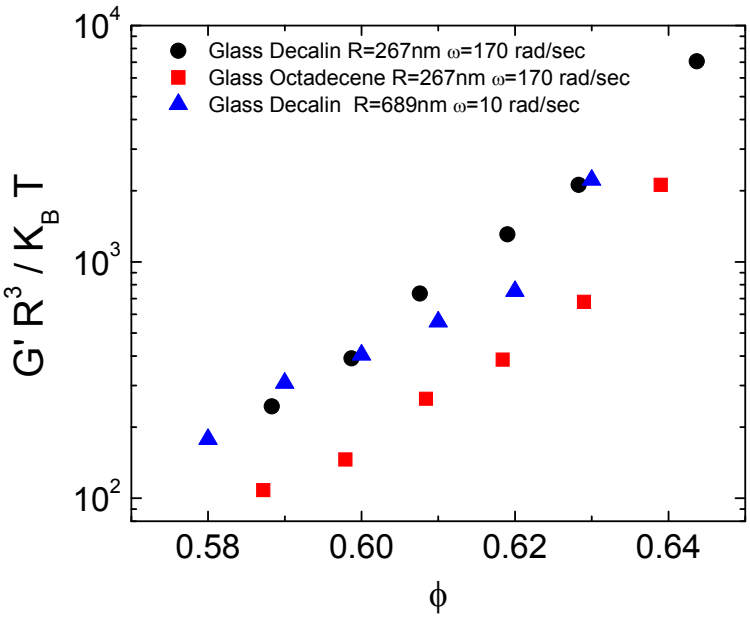

Figure 3.3: Superposition of linear elastic moduli for two different sphere sizes (267nm and 689nm) at similar time scales (or Pe') from (Koumakis, 2007). The high frequencies for the small spheres have been extrapolated from frequency sweeps.

Extracting the values of G' for both the crystal and the glass at a specific frequency in the DFS, we plot them as a function of φ in figure 3.2a. For both systems, G' increases with volume fraction, as there is less space available for particles to move and larger number of particles per unit volume, leading to a stronger solid like response. In figure 3.2b, the same data is plotted against the inverse free volume, $\varphi_{free}=\varphi_{max}-\varphi$, where for the glass $\varphi_{max}=\varphi_{RCP}=0.66$ and for the crystal $\varphi_{max}=0.74$. The ordered crystal shows larger moduli than the glass at the same distance from maximum packing, as the ordered structure produces a stronger solid for the same average free volume per particle. It was also found that the values and dependencies produced by theory on the glasses and on the crystal was not able to give

the qualitative φ dependence as received from the experiments, although the orders of magnitude were correct.

When examining different sphere sizes we are able to superimpose the viscoelastic moduli by non dimensionalizing the time scales and the values of elasticity. The superposition is possible as the hard sphere repulsion potential does not change with particle size or with temperature. Therefore, time scales may be normalized by the Brownian time ($t_B=R^2/D_0$) of the particles, which governs all other time scales in the system, while the stresses/moduli may be normalized by the thermal energy and particle size (K_BT/R^3). Figure 3.3 has an example of this superposition from (Koumakis, 2007), showing the elastic moduli as a function of φ for different sphere sizes. The moduli have been scaled by K_BT/R^3 and taken so as to have the same frequencies when normalized by the Brownian time.

3.3 Non Linear Strain Sweeps and Yielding

By applying larger oscillatory strains, the microstructure of a hard sphere glass may be disturbed leading to changes in the viscoelastic moduli. A Dynamic Strain Sweep (DSS) is a test which keeps a constant frequency, but varies the applied strain. An example of such a test is shown in figure 3.4, as taken from the work of (Pham, Petekidis et al., 2008) for hard sphere glasses. At small strains, the viscoelastic properties remain constant with G' greater than G'' defining the linear regime where the cage is only slightly deformed. As strains increase above about 1-2% strain, the elastic modulus starts decreasing, while the viscous modulus increases which leads to a crossover with G''>G' and a liquid state. The increase of G'' at even higher strains leads to a peak and then a subsequent transition to a steady state decrease of both G' and G''.

The transition of the hard sphere glass from a solid-like into a liquid-like response is called yielding and is microscopically associated with the braking of the glassy "cages". In a strain sweep there are various ways to define the strain at which yielding occurs, as are marked on the figure 3.4. Thus we may define strain (i) as the onset of yielding (γ≈1%), where the non linearities begin to become apparent by the first changes of the linear properties. At point (ii) we can define the crossover strain (γ≈10%), where the elastic modulus becomes equal to the viscous modulus, clearly marking the point where the system rheologically transitions from a solid into a liquid. Finally, point (iii), the peak of G'', may also be defined as a critical strain (γ≈10%), where the viscous loss during the cage breaking process is maximum. The features of the various yield points as defined, have been found to show different dependencies

(Koumakis, Schofield et al., 2008) and may stem from different aspects of the yield mechanism.

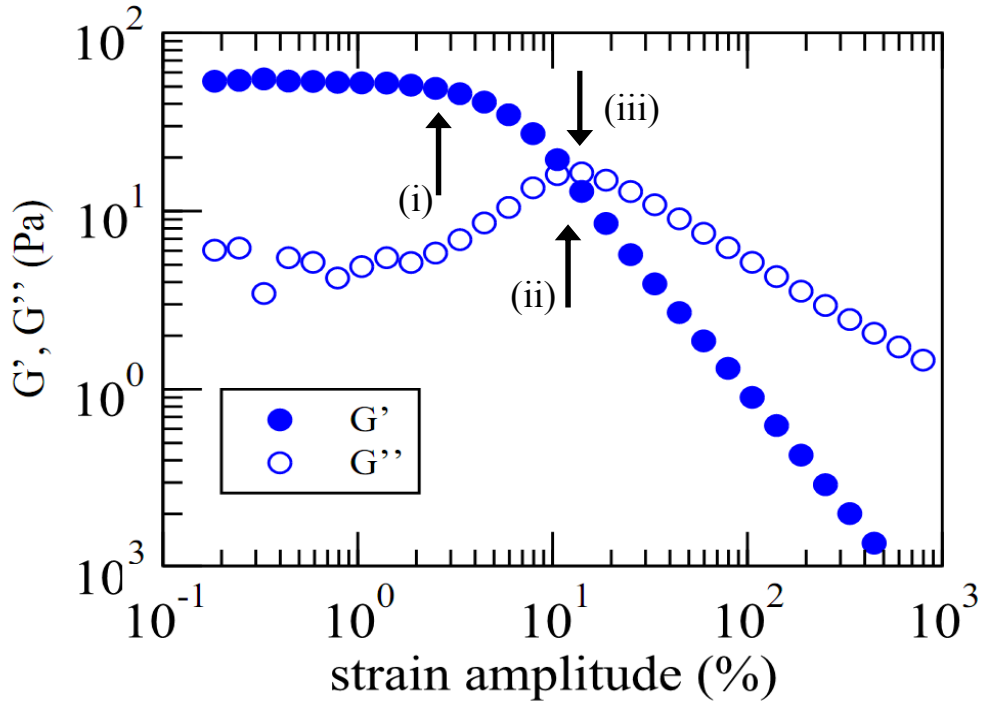

Figure 3.4: Non linear strain sweep for a glass at ω=1rad/sec showing the elastic (solid) and viscous (open) moduli for φ=0.60 from the work of (Pham, Petekidis et al., 2008). Vertical arrows refer to the various definitions of the yield strain.

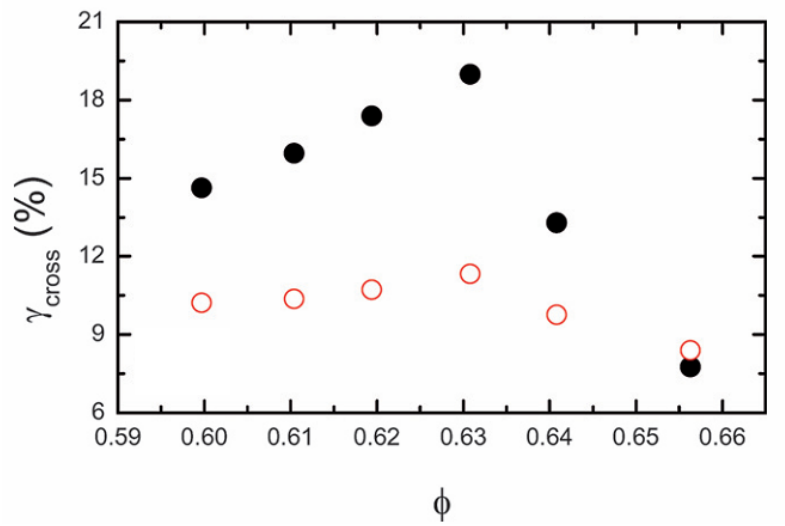

Figure 3.5: Crossover yield strains versus φ from dynamic frequency sweeps for glasses (solid) and shear induced crystals (open) from (Koumakis, Schofield et al., 2008).

The yield strains corresponding to the crossover of the viscoelastic moduli and the onset of irreversible rearrangements have been found to have a similar dependence to φ (Petekidis,

Moussaid et al., 2002; Koumakis, 2007). As shown in figure 3.5 taken from (Koumakis, Schofield et al., 2008), the crossover yield strain of the glass is generally larger than that of the crystal, while both show a peak as a function of φ. The crystal has a smaller yield strain than the glass due to the sliding layer motion decreasing the strain needed to induce flow as described in literature (Koumakis, Schofield et al., 2008). The maximum in the yield strain is the result of two competing mechanisms. In the glass state, as the volume fraction decreases, the cages loosen up and the yield strain starts decreasing until the system becomes a liquid where it goes to zero. On the other hand, as the glass increases towards maximum close packing, tighter cages are formed that lower the yield strain and thus make the material more brittle.

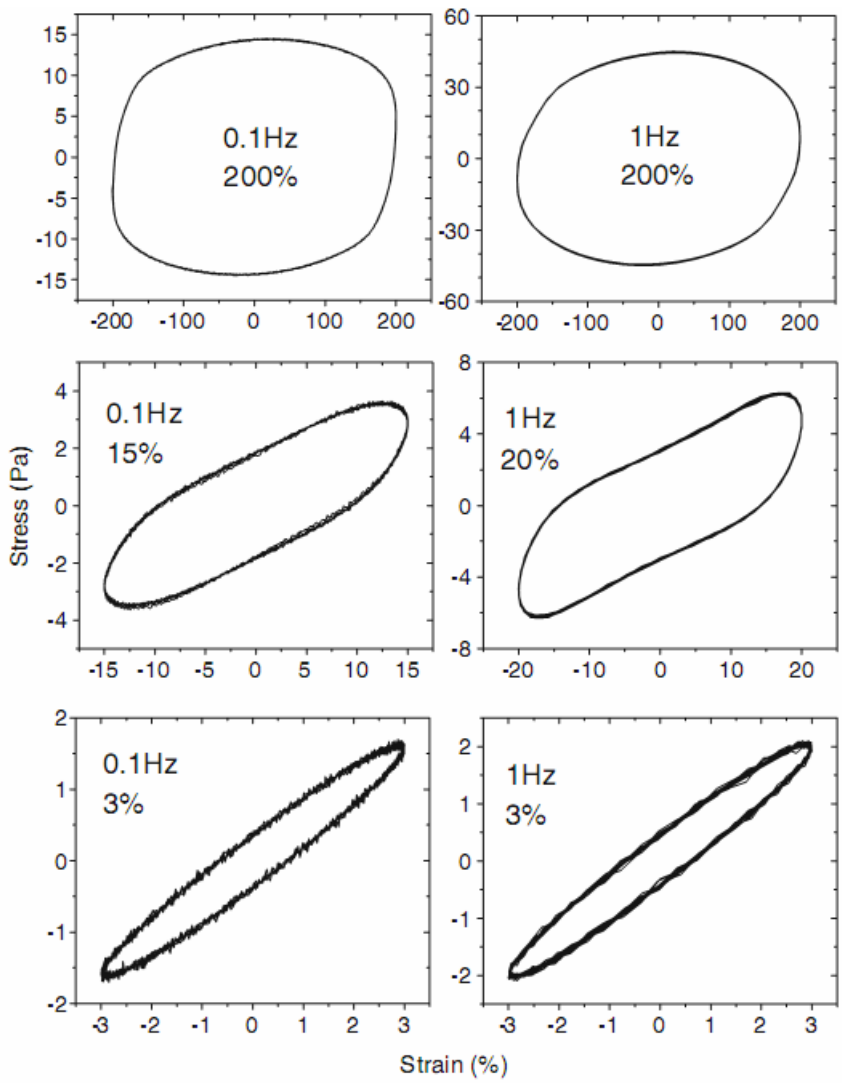

Figure 3.6: Lissajous figures of the non harmonic oscillatory stress response of glassy hard spheres suspensions from the work of (Le Grand and Petekidis, 2008). Applied frequencies and strains are shown on the respective figures.

As a final note on the dynamic rheological properties under large amplitude oscillatory shear, we must state that while the analysis of the stress response from the application of a simple sinusoidal strain assumes a simple harmonic response, this is not the case. An example of the non linear stress responses of hard sphere glasses in the form of stress-strain Lissajous figures is shown in figure 3.6 as taken from (Le Grand and Petekidis, 2008). For a simple harmonic response, the expected Lissajous figure should have the geometrical shape of an ellipsoid, but as can be seen in the figure, for strains above yield this is not the case. The appearance of non harmonic responses above yield, make the interpretation of strain sweeps such as 3.4 more complicated, as the definitions of the elastic and viscous moduli are based on simple sinusoidal stress responses. These complex responses are extensively discussed for the hard sphere system in chapter 5.

3.4 Flow Curves and Transient Tests

A conceptually simpler way of applying shear to a system is by using a constant steady rate. While the stress response for a constant rate at long times is generally also constant, the startup of shear from the state at rest produces a transient stress response. For a glassy hard sphere system, a typical such stress response is seen in figure 3.7 as a function of strain. This transient response is very similar to the strain sweep seen in figure 3.4 in the sense that we find a linear regime, a yielding event and a steady state. Initially there is a linear increase of stress, reflecting the simple elastic response of the system before any microstructural changes occur. As strain is increased, the stresses depart from linear behavior showing a stress peak which is then followed by a steady stress response.

As for the strain sweep we are able to describe various points in the transient test which correspond to various yield strains and additionally mark the stress peak and steady state stresses. We can describe three points for the yielding, (i) the onset of non linear behavior, (ii) the peak of the stress and (iii) the beginning of the steady state. Although some features of these yield strains seem similar to the dynamic case, it is not certain if they reflect exactly the same microscopic mechanisms. By varying φ and applied shear rate, the described strains and stresses vary considerably. The phenomenology and microscopic mechanisms of the startup curves for hard sphere glasses are the subject of chapter 4.

For hard sphere glasses, the steady states of the startup experiments at various rates generally show complex behaviors with applied rate. Various steady rate sweeps (SRS) or flow curves from varying volume fractions of hard sphere suspensions are shown in figure 3.8, taken from the work of (Petekidis, Vlassopoulos et al., 2004). For simple Newtonian liquids, the stress is

found to be linearly proportional to the applied rate, as seen for the lowest volume fractions ($\varphi<0.50$). As φ is increased though, the flow curves show local power law slopes that are less than one (sub linear), and at the highest φ show plateau values of stress for low rates. The stress plateau defines the yield stress, the stress needed to induce flow in the system.

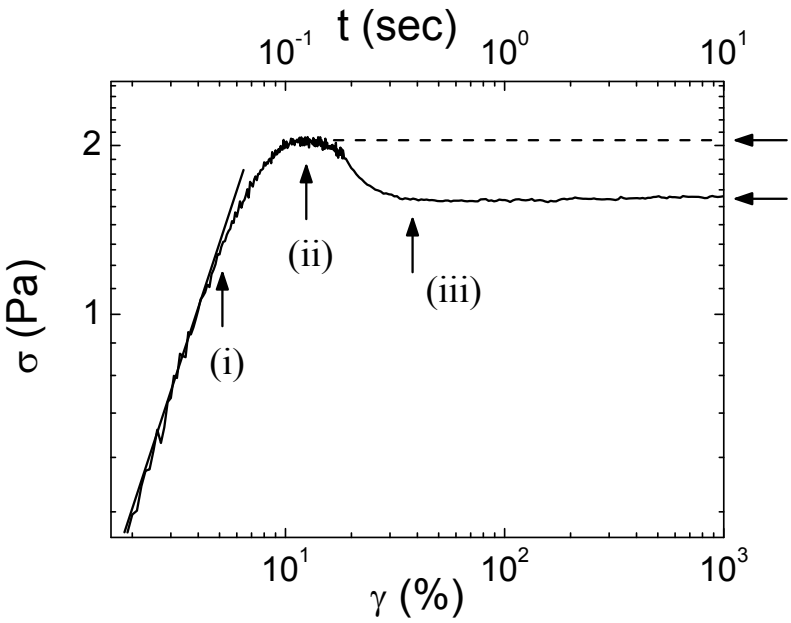

Figure 3.7: Transient/start-up steady rate shear stress response at a rate of $1s^{-1}$ for a hard sphere glass at $\varphi=0.60$. Vertical arrows show the various yield strains, while horizontal arrows show the peak and steady state stresses.

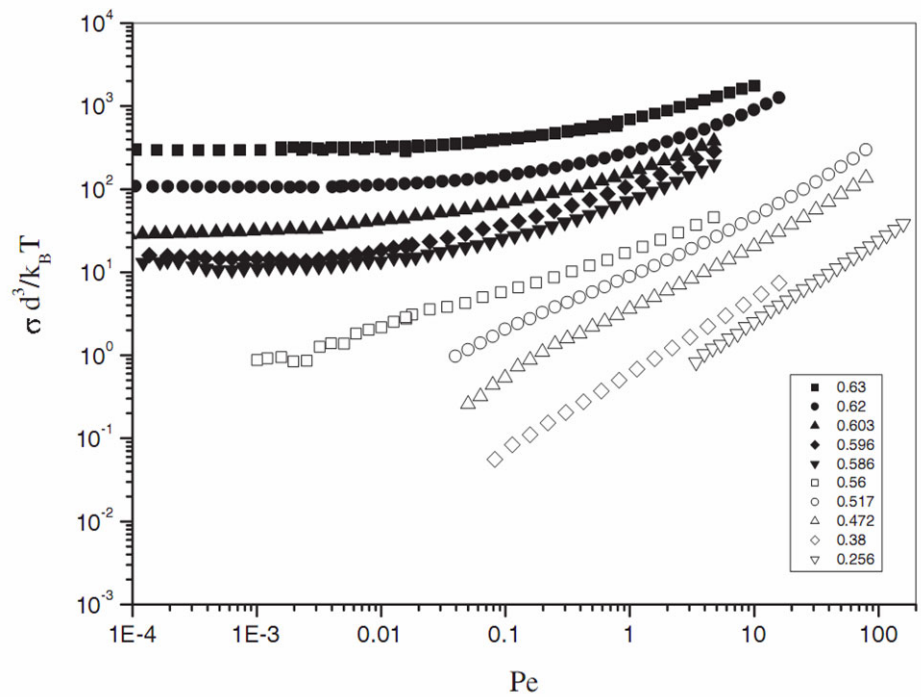

Figure 3.8: Steady rate flow curve showing the (normalized) stress response at various φ as a function of rate from (Petekidis, Vlassopoulos et al., 2004).

3.5 Simulations at Rest

Displacements and Relaxation Times

Here we examine the dynamics of glassy hard sphere colloids as taken from Brownian dynamics simulations. As discussed, these results are from BD simulations performed as a part of this work for the initialization of the states under shear (Chapter 5 and 6). They are also presented to provide an initial understanding of the hard sphere glassy dynamics before application of shear is discussed. Below we present the behavior at rest for multiple φ, below and above the glass transition showing the dynamical properties through the mean squared displacements, the out of cage relaxations and the non Gaussian parameter. We also examine the radial distribution function of various sets of particles based on their mobility as a way to determine the spatial properties of the dynamic heterogeneities. The methods of calculating these variables from the particle positions are found in the relevant section of chapter 2.

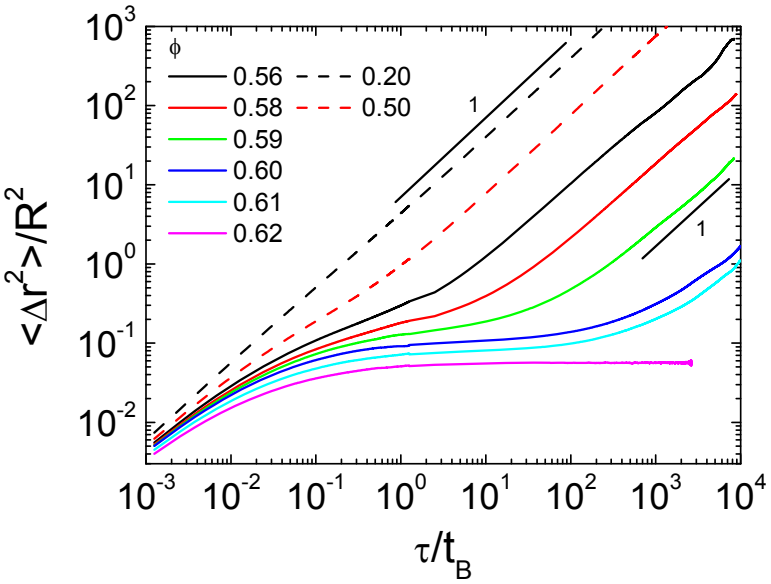

Figure 3.9: The steady state mean squared displacements at rest as a function of time from BD simulations from dilute volume fractions up to the glass regime.

In order to avoid crystallization during the simulations polydispersity was added. Polydispersity in these simulations is represented by a discrete Gaussian distribution of radii having 80 components with a root mean squared deviation of 10%. The shown simulations were carried out in a cubic box with 1005 particles both at rest and under shear. The particles were randomly placed and left for some time (a maximum of $300t_B$) to reach an equilibrium state, quantified by unchanging mean squared displacements. Simulations were run with a

time step of $2\pi\ 10^{-4}\ t_B$ or less, while structural properties, displacements and stresses under shear were averaged over at least 50 t_B.

The mean squared displacements from Brownian Dynamics simulations at rest are shown in figure 3.9 for different volume fractions of non crystallizing polydisperse particles. For the dilute regime, the lowest volume fraction shown, we see simple diffusive motion with a power law slope of unity. As volume fraction is increased towards the glass we find two distinct regimes of particle motion. At small time scales, the particles move only short distances that are related to the motion inside the "cages" formed by neighboring particles (β relaxation). Once the time scales and motions become long enough, particles come into contact and collide with their neighbors reducing their mobility and thus the slope of the displacements below unity. At even longer time scales, since the particles have a finite probability to escape their cages, the displacements become diffusive again exhibiting out of cage relaxations (α relaxation). As volume fractions are increased the time the particles are trapped in their cages increases, also increasing the α relaxation, up to a point where the time scale of the relaxation, t_α, diverges. At this point, where particles become trapped in their cages and may not escape with diffusive motion, the glass transition may be defined. Without further quantification, in figure 3.9 the glass transition within this time window, appears to be between φ=0.60 and φ=0.61 when the secondary relaxation ceases to be diffusive. These long time non diffusive displacements refer to heterogeneous out of cage motions which are localized and are related with the motion of only a few particles and are called dynamic heterogeneities (Kegel and van Blaaderen, 2000; Weeks, Crocker et al., 2000).

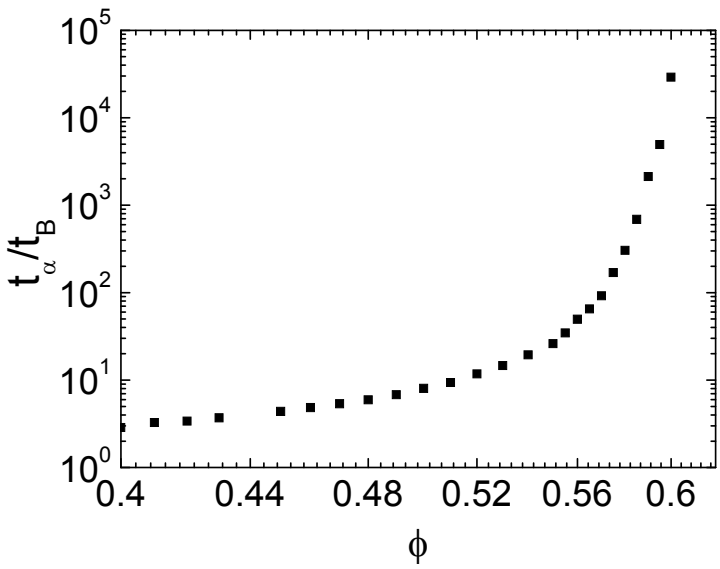

Figure 3.10: The steady state relaxation times as a function of φ, taken from mean squared displacements at rest from BD simulations close to the glass regime.

Although these simulations lack hydrodynamics, which would horizontally shift the curves towards larger time scales by a factor related to the volume fraction dependence of the short time self diffusivity (Sierou and Brady, 2001), the extracted trends should be correct and comparable to experiments(Foss and Brady, 2000). Additionally, the work of (Zaccarelli, Valeriani et al., 2009) shows that the addition of polydispersity in a hard sphere colloidal glass shows little or no deviation of the MSD at rest from a monodisperse system.

Within a simplified version of the Generalized Stokes-Einstein equation (Mason, 2000), we may relate the dynamic viscoelastic moduli (frequency sweeps) shown in figure 3.1 to the microscopic particle rearrangements by:

$$G^*(\omega = 2\pi/\tau) \propto 1/<\Delta r^2(\tau)> \qquad \text{(Eq. 3.1)}$$

$$\frac{G''(\omega)}{G'(\omega)} = \tan\left[(\pi/2)\frac{d[\ln(<\Delta r^2(\tau = 1/\omega)>)]}{d\ln\tau}\right] \qquad \text{(Eq. 3.2)}$$

Therefore, one can use the MSD in a glassy system to determine its viscoelastic moduli a various frequencies. The experimental data of figure 3.1, corresponds to time scales at the plateau of the MSD, which suggest a relatively constant elasticity and a minimum of G''. According to equations (Eq. 3.1) and (Eq. 3.2), the slight decrease of G' at lower ω (and thus G*) corresponds to an increase of $<\Delta r^2(\tau)>$ at longer times. Moreover, the minimum of G'' corresponds to the minimum power law slope of $<\Delta r^2(\tau)>$, which relates to the time scale of a particle exploring its glassy cage and marks the transition between the in cage and out of cage relaxation times. In the case of high φ glasses, where no true long time out of cage relaxation exists (non diffusive), this corresponds to the beginning of increased long time displacements due to dynamic heterogeneities.

The limits of very high frequencies or short times will correspond to generally large moduli with G''>G', while the lowest frequencies and longest times where out of cage motions take place the moduli will decrease again showing viscous behavior (G''>G'). Although not strictly in a system of hard spheres, the whole range of frequencies measured for a single sample may be seen in the work of (Crassous, Regisser et al., 2005).

If the displacements are diffusive at long times then we can extract a characteristic time for long time out of cage diffusion as $D_{Long}=R^2/t_\alpha=<\Delta r^2>/(6\tau)$, and $t_\alpha= (6\tau R^2)/<\Delta r^2>$. Figure 3.10 shows the out of cage relaxation time as extracted from the BD simulations, which we find increases substantially with increasing volume fraction and seems to diverge at the glass

transition volume fraction. Similar results as shown here were also obtained experimentally by (Brambilla, El Masri et al., 2009). It is important to note that at this time scale (t_α), especially for glasses, particles have not necessarily diffused by a squared distance of $6R^2$, due to the complicated motions as seen in fig 3.9.

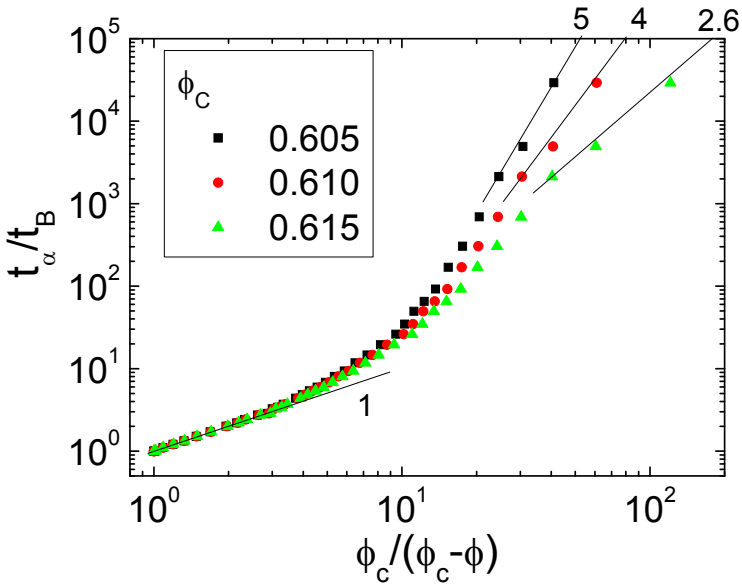

Figure 3.11: The steady state relaxation times as shown in figure 3.1 as a function of the distance from the glass transition. The glass transition is varied in order to show the sensitivity to its choice.

In figure 3.11 we plot t_α with the inverse distance from a critical φ_C, assumed to be the glass transition. Here we see a strong power law increase close to the glass transition which is particularly sensitive to the choice of the critical φ_C. The final extracted power law slopes of 4 and 5 have no particular theoretical meaning, although detailed experiments and simulations (Brambilla, El Masri et al., 2009; Brambilla, El Masri et al., 2010) have produced a final slope of 1 and a $\varphi_c \approx 0.614$ and compare to the theoretical prediction of 2.6 from MCT. Therefore we find that extraction of the glass transition from the divergence of such time scales is not trivial. From a technical standpoint and following the plotted trends, in order to simulate and extract the out of cage relaxation time, t_α, of volume fractions that are larger than 0.60 would require prohibitively long computational times.

Dynamic Heterogeneities

Particles undergoing random diffusive motion should show displacement distribution profiles, or Van Hove functions, which have Gaussian characteristics. However in the case of concentrated dispersions of figure 3.9, the particles are not diffusive for all time scales, thus expecting deviations from Gaussian behavior. In figure 3.12 we show the Van Hove functions for the x-axis of φ=0.56 at time scales of the short and long time diffusivities as well as a non

diffusive intermediate time scale. While the displacement profiles for the diffusive regions are Gaussian, the intermediate time scales corresponding to the non ergodicity plateau show deviations. Deviations from Gaussian behavior in these systems has been attributed to dynamic heterogeneities(Kegel and van Blaaderen, 2000; Weeks, Crocker et al., 2000; Weeks, Crocker et al., 2007), which occur when clustered groups of particles move at different speeds than the bulk. We note that since the displacements for the glasses and liquids at rest are isotropic, the findings are equivalent in all directions.

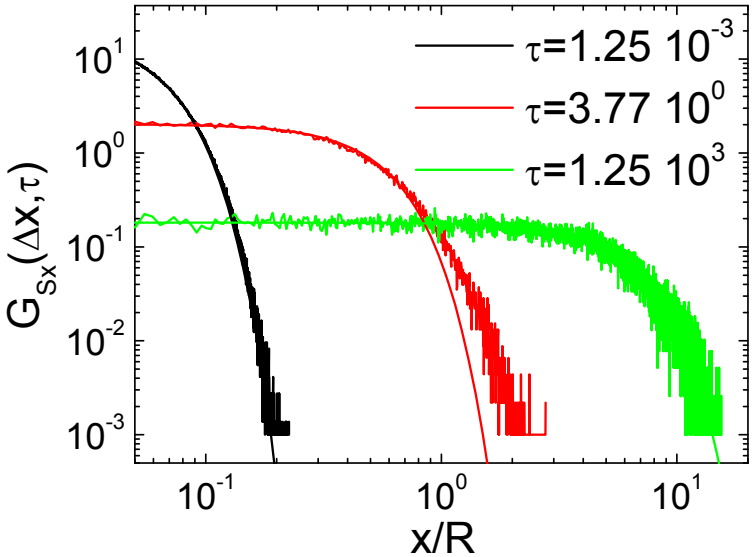

Figure 3.12: The single sided Van Hove self correlation function for the displacements in the x-axis φ=0.56 at various time scales encompassing the short time diffusivity (black), an intermediate transition (red) and the long time diffusivity (green). Gaussian fits are shown as lines of the same color.

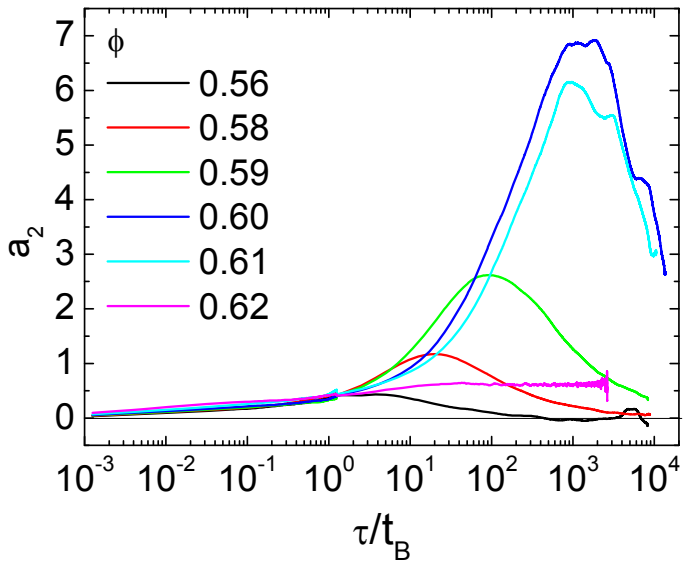

Figure 3.13: The non Gaussian parameter a_2, of the displacements shown in 3.9.

We may quantify the deviation from Gaussian statistics by calculating the a_2 parameter as shown in figure 3.13. In the case of a system at rest, the parameter gives measure of the dynamic heterogeneities present in the simulated system. At small times with in-cage diffusion, heterogeneities are low as all processes are diffusive. As the probed time is increased, heterogeneities increase due to the collisions with neighboring particles and particle frustration. At lower φ, the onset of out of cage diffusion accompanied by a drop of heterogeneities. Thus the maximum of the a_2 parameter may be an indicator of the transition between in cage and out of cage motion. In the case of the highest φ glass (0.62), the a_2 is almost constant with time having small values instead of a growing maximum, suggesting the absence of a secondary out of cage relaxation at longer time scales.

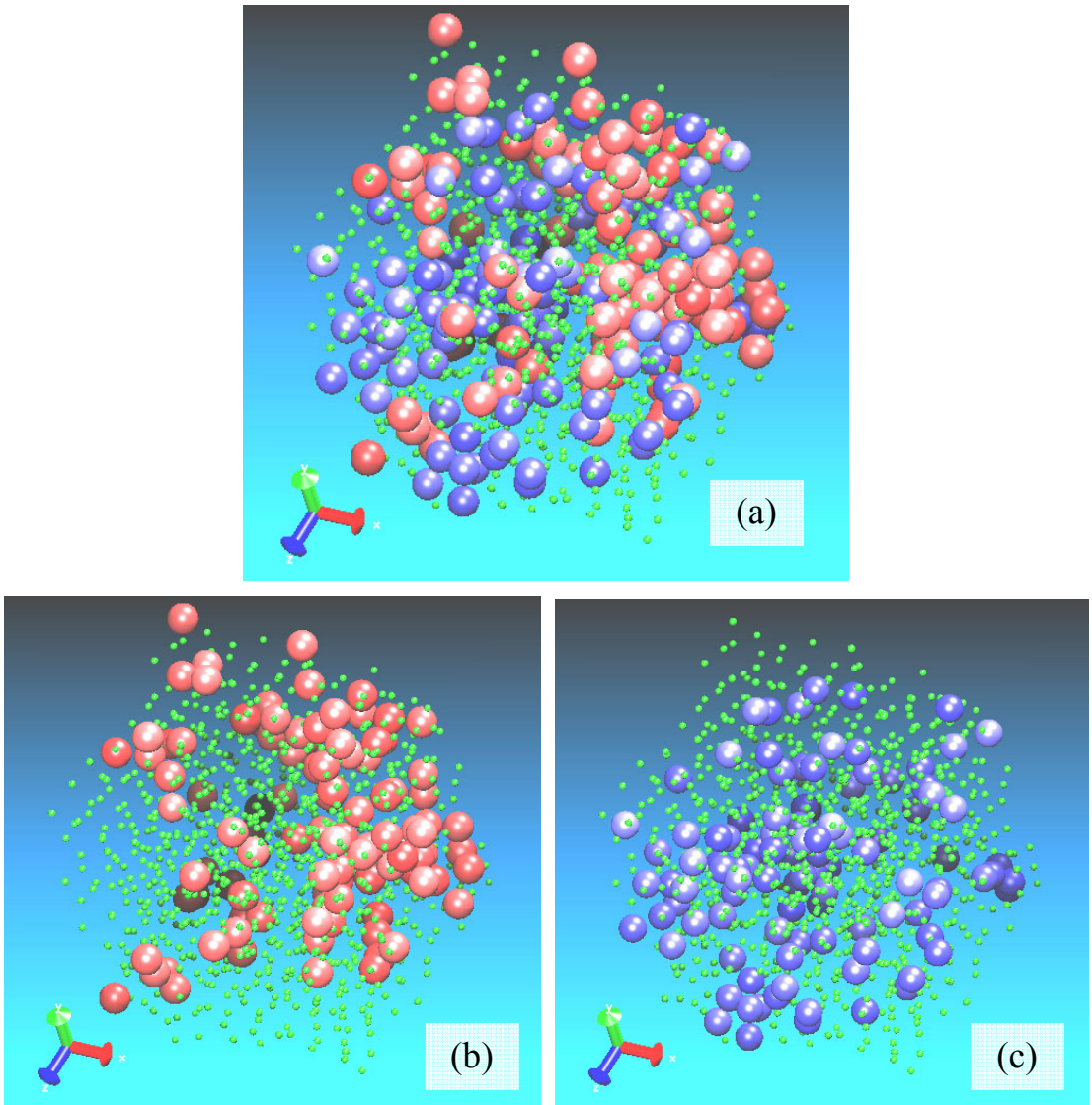

Figure 3.14: Characteristic images of the 10% fastest (red, full size), slowest (blue, full size) and other particles (green, ¼ radii) as defined by the g(r) of previous figures 3.11 and 3.12 for φ=0.56 at the time scale of $\tau=3.77t_B$, the maximum of a_2. Images show a) both distributions of fast and slow, b) only the 10% fastest and c) only the 10% slowest.

The volume fraction dependence of the a_2 peak has been associated with the glass transition(Weeks, Crocker et al., 2000), which in accordance to findings of figure 3.11, must be slightly above φ=0.60. Dynamic heterogeneities as detected in experiments refer to two distinct populations of particles, those that follow motions mainly within the cages and those which undergo faster out of cage jumps due to cooperative motions. Therefore, the maximum of a_2 most probably occurs due to the superposition of two types of displacements.

While the a_2 parameter gives an average measure of the deviation of Gaussian behavior and has been linked to dynamic heterogeneities, it does not give information on the spatial distribution of the heterogeneities. As done in (Weeks, Crocker et al., 2000) we separate a percentage of particles that show the largest and/or slowest displacements within for a specific time scale. The images of figure 3.14 show a snapshot of the 10% fastest and slowest particles for φ=0.56 in the time scale of the maximum of a_2. The fastest and slowest particles are full size in red and blue respectively, while the rest of the particles are of ¼ radii in green. The clustering of the red and blue particles is evident, moreover there are indications of particle strings connecting the clusters.

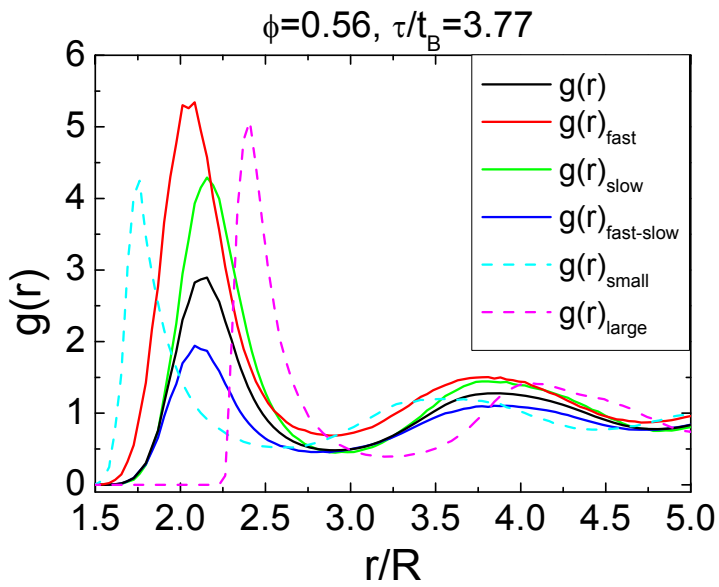

Figure 3.15: The radial distribution function g(r) for various sets of particles as described in the text and shown in the legend for φ=0.56 and a time scale corresponding to the maximum of a_2 for the applicable sets of particles.

A well known way of examining the structure of a particle system is by calculating the radial distribution function g(r) as shown in chapter 2. In this case, we have modified the overall distribution to calculate the distribution function of specific sets of particles, based on their

dynamic characteristics. Thus with the application of g(r) we quantify the heterogeneous structures of particles of different speeds as seen in figure 3.14.

Specifically in figure 3.15 we show the overall g(r) in comparison to various sets of only 10% of all the particles, which are chosen based on varying criteria. Thus, the average g(r) of φ=0.56 is plotted along with the g(r) of the 10% fastest, slowest, smallest and largest particles. Additionally the g(r) of the fastest subset is compared to the slowest subset. The fastest and slowest particles are determined in this case by sorting the amount of displacements for each particle in a time scale of $\tau=3.77t_B$, near the maximum of a_2. Looking at the first neighbor peak at around r=2R, we find the smallest value for $g(r)_{fast\text{-}slow}$, followed by the overall g(r), $g(r)_{slow}$ and the highest value for $g(r)_{fast}$. The smaller particles have the first peak shifted to the smaller r/R while the larger particles' g(r) is shifted to larger values.

The increased values of $g(r)_{fast}$ over g(r) shows that the fastest 10% of particles show a higher probability than the average to be within the first, second and third (not shown) neighbors. This means that faster particles tend to form clusters and subsequently that dynamic heterogeneities can be characterized by both temporal and spatial properties. The height of the first maximum of g(r) can be used to quantify the spatial extent of the heterogeneities.

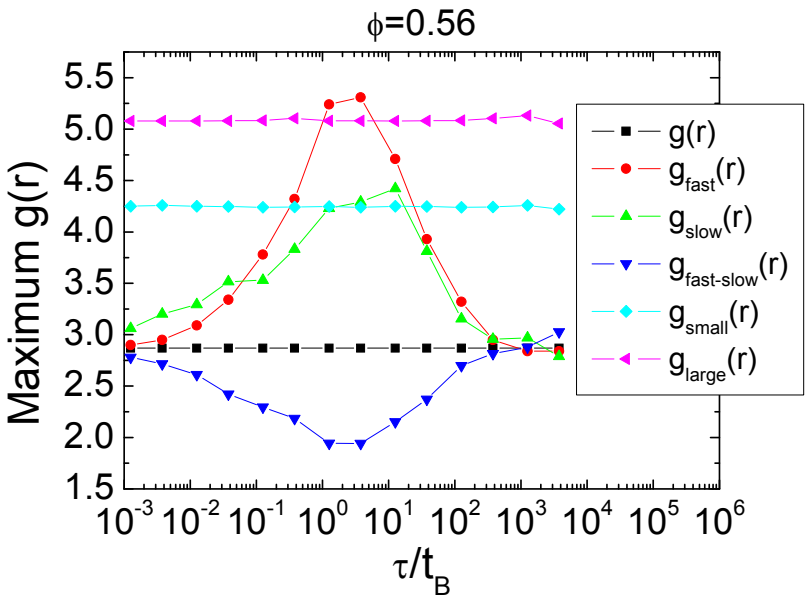

Figure 3.16: The first maximum of the g(r) for the various sets of particles as described in the text and as shown in legend versus time for φ=0.56.

Slower particles exhibit similar clustering and heterogeneous behavior, although less that the faster particles, while $g(r)_{fast\text{-}slow}$ shows an expected drop from the average, because faster and slower particle clusters are separated from each other. The largest and smallest particle radial

distribution functions are also examined in order to decouple the heterogeneities from size effects. The peaks are shifted in the radius axis according to the size and the probability peak increases in both cases, because of the smaller particle distribution than the average. The work of (Weeks, Crocker et al., 2007) uses spatial correlation functions linked to dynamics in order to determine the extent of the heterogeneities. These may give more detailed information and will be implemented in further analyses of the simulations.

As discussed, the first maximum of the g(r) can be used to spatially quantify the heterogeneities. Figure 3.16 shows the time dependence of the g(r) peaks of the different particle groups for φ=0.56. The faster and slower particles show the maximum clustering at about $4t_B$, which is the same value of the peak of a_2, thus we find that the displacement's deviation from Gaussian behavior also corresponds to the largest spatial clustering of the dynamically deviating particles. The lack of time dependence on the peak of the larger and smaller particles shows that particle sizes are decoupled from the dynamical heterogeneities. As with the a_2, at small and large times where diffusive behavior dominates, the g(r) of the fastest and slowest particles shows the lack of heterogeneous behavior by approaching the g(r) of the bulk.

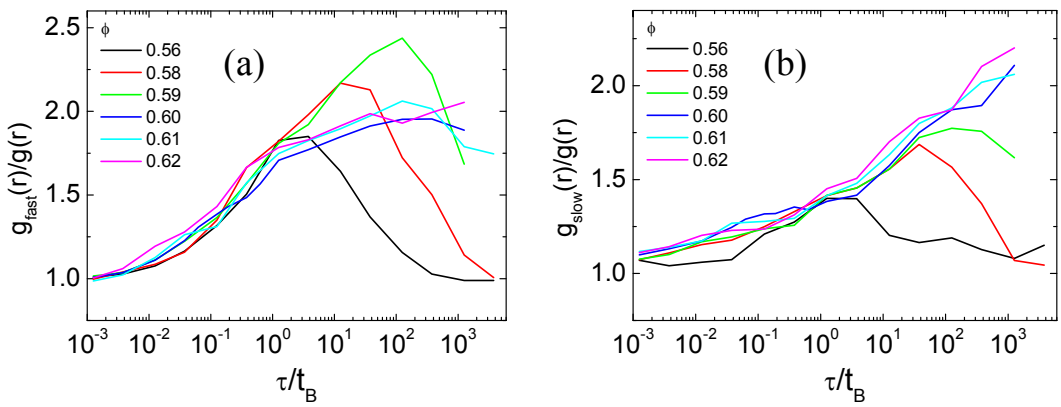

Figure 3.17: The first maximum of the g(r) for a) the 10% fastest particles and b) the 10% slowest particles normalized by the values of the maximum of g(r) in the bulk as a function of time for various φ as shown in the legend.

In figure 3.17, we plot the maximum of g(r) for the fastest and slowest particles for various φ as a function of time, but in contrast to figure 3.16 we have now normalized with the average g(r) of the bulk. The normalization is done to decouple the effect of φ on the heights of the peaks, which may complicate the interpretation of the data. Spatial clustering for the fastest particles (3.17a) shows an increase with time and a peak, generally following the qualitative behavior of a_2 until φ=0.59. Above this φ we find a simple increase to a plateau. Spatial

clustering for the slower particles in 3.17b shows similar dependencies but smaller values, which become comparable to the faster particles at higher φ.

Between the various φ's, a_2 shows significant qualitative differences with the maxima of g(r). The a_2 parameter (figure 3.13), increases with φ and suddenly drops to a stable value at 0.62. With respect to time, these findings indicate similar mechanisms governing the deviations from Gaussian behavior with the spatial inhomogeneities, although showing differences with respect to changing φ. As will be seen in other chapters, with the use of this analysis, the a_2 parameter is not just an indicator of dynamic heterogeneities, but may also indicate deviation from Gaussian behavior due to high shear.

3.6 References

Brambilla, G., D. El Masri, M. Pierno, L. Berthier and L. Cipelletti (2010). "Brambilla et al. Reply." Physical Review Letters **105**(19) 199605.

Brambilla, G., D. El Masri, M. Pierno, L. Berthier, L. Cipelletti, G. Petekidis and A. B. Schofield (2009). "Probing the Equilibrium Dynamics of Colloidal Hard Spheres above the Mode-Coupling Glass Transition." Physical Review Letters **102**(8) 085703.

Crassous, J. J., R. Regisser, M. Ballauff and N. Willenbacher (2005). "Characterization of the viscoelastic behavior of complex fluids using the piezoelastic axial vibrator." Journal of Rheology **49**(4) 851-863.

Foss, D. R. and J. F. Brady (2000). "Structure, diffusion and rheology of Brownian suspensions by Stokesian Dynamics simulation." Journal of Fluid Mechanics **407**(-1) 167-200.

Kegel, W. K. and a. A. van Blaaderen (2000). "Direct Observation of Dynamical Heterogeneities in Colloidal Hard-Sphere Suspensions." Science **287**(5451) 290-293.

Kobelev, V. and K. S. Schweizer (2005). "Strain softening, yielding and shear thinning in glassy colloidal suspensions." Phys. Rev. E **71** 021401.

Koumakis, N. (2007). Shear Induced Crystallization of a Colloidal Glass. Department of Materials Science and Technology, University of Crete. **MSc**.

Koumakis, N., A. B. Schofield and G. Petekidis (2008). "Effects of shear induced crystallization on the rheology and ageing of hard sphere glasses." Soft Matter **4**: 2008 2008-2018.

Laird, B. B. (1992). "Weighted density functional theory calculation of elastic constants for face centered cubic and body centered cubic hard sphere crystals." J. Chem. Phys. **97**(4) 2699.

Le Grand, A. and G. Petekidis (2008). "Effects of particle softness on the rheology and yielding of colloidal glasses." Rheologica Acta **47**(5-6) 579-590.

Mason, T. G. (2000). "Estimating the viscoelastic moduli of complex fluids using the generalized Stokes–Einstein equation." Rheologica Acta **39**(4) 371-378.

Mason, T. G. and D. A. Weitz (1995). "Linear Viscoelasticity of Colloidal Hard Sphere Suspensions near the Glass Transition." Phys. Rev. Lett. **75** 2770.

Petekidis, G., A. Moussaid and P. N. Pusey (2002). "Rearrangments in hard-sphere glasses under oscillatory shear strain." Phys. Rev. E **66** 051402.

Petekidis, G., D. Vlassopoulos and P. N. Pusey (2004). "Yielding and flow of sheared colloidal glasses." Journal of Physics Condensed Matter **16**(38) S3955-S3963.

Pham, K. N., G. Petekidis, D. Vlassopoulos, S. U. Egelhaaf, W. C. K. Poon and P. N. Pusey (2008). "Yielding behavior of repulsion- and attraction-dominated colloidal glasses." Journal of Rheology **52**(2) 649-676.

Pronk, S. and D. Frenkel (2003). "Large difference in the Elastic Properties of fcc and hcp Hard Sphere Crystals." Phys. Rev. Lett. **90** 255501.

Sierou, A. and J. F. Brady (2001). "Accelerated Stokesian Dynamics simulations." Journal of Fluid Mechanics **448**(-1) 115-146.

van Megen, W. and S. M. Underwood (1993). "Glass-Transition in Colloidal Hard-Spheres - Mode-Coupling Theory Analysis." Phys. Rev. Lett. **70**(18) 2766-2769.

Weeks, E. R., J. C. Crocker, A. C. Levitt, A. Schofield and D. A. Weitz (2000). Three-Dimensional Direct Imaging of Structural Relaxation Near the Colloidal Glass Transition. **287:** 627-631.

Weeks, E. R., J. C. Crocker and D. A. Weitz (2007). "Short and long-range correlated motion observed in colloidal glasses and liquids." Journal of Physics: Condensed Matter **19**(20) 205131.

Zaccarelli, E., C. Valeriani, E. Sanz, W. C. K. Poon, M. E. Cates and P. N. Pusey (2009). "Crystallization of Hard-Sphere Glasses." Phys. Rev. Lett. **103**(13): 135704.

Chapter 4 – Stresses, Dynamics and Structure during Transient Shear: Start-up and Cessation of Flow

Abstract

The transient response of model hard sphere glasses is examined during the application of steady rate start-up shear and subsequent cessation of shear using experimental rheology and Brownian Dynamics (BD) simulations. With elapsed time the glasses exhibit an initial elastic increase, a stress peak at the yield point of approximately 10% strain and a constant stress steady state. The stress peak was found to increase in amplitude at high rates and lower φ, while the position of the peak increased with rate and generally remained unchanged with φ.

Although at rest the displacements of the glass show a plateau, the length scale of in-cage motion, at the steady state under shear the BD Simulations generally showed that long time motions become diffusive as the cages are broken and particles flow past each other. Moreover, the long time diffusion coefficient showed large dependence on applied rate, but much smaller dependence on the studied φ. At short times, the displacements decreased with elapsed strain when compared to the state at rest, the decrease being more pronounced with increasing φ and Pe. These short time motion constrictions are associated with the shear induced out of cage motion, as forcing a particle out of cage increases long time diffusivity, but also hinders in cage motion through spatial constriction. A transient super diffusive regime was found to occur at intermediate time scale displacements, which becomes more pronounced with increasing φ. This is related to the transient nature of the start up shear and the transition from the displacements at rest to diffusive long time displacements under shear.

Examination of the structural properties under shear from BD simulations showed that compared to the structure of other planes, the steady state g(r) in the xy plane (velocity – velocity gradient) is most affected becoming highly anisotropic. The transient g(r) of the xy plane at low strains starts isotropic, turning into a distorted structure as strain increases and showing flow lines along the extension axis when strains increase above yield, signifying out of cage diffusion. While cage distortion is more significant at high rates, low rates still distort the structure although do not elongate the cage. The peak of the stress response is found to be correlated to the inability of particles to escape their cages and relax the stress, before the maximum distortion of the cage occurs which forces them out due to applied shear.

The examination of the stress after cessation of shear showed relaxations which became more pronounced for larger rates while generally becoming slower as φ is increased and particle motions become hindered. The structure and the dynamics during relaxation were found to revert back to the state at rest at rates similar to the relaxation of stress.

4.1 Introduction/Experimental

Introduction

In this chapter we study the transient stress response of hard sphere glasses along with the stress relaxation at cessation of shear, using both experimental rheology and Brownian dynamics simulations. The former allows rheological characterization of the system under shear, while the latter directly provides information on the microstructure and dynamics. A steady shear rate was applied and the stress response was measured against strain (or equivalently time). These steady experiments are conceptually simpler than oscillatory strain sweeps, as the rate remains constant throughout the test.

The position and intensity of a stress overshoot in a steady rate experiment contains information on the yield strain and stress of a measured system. Peaks such as these have been seen experimentally in a variety of soft matter including polymers (Osaki, Inoue et al. 2000; Islam and Archer 2001; Ravindranath and Wang 2008), worm-like micelles (Padding, Boek et al. 2008), nanocomposites (Letwimolnun, Vergnes et al. 2007; Akcora, Liu et al. 2009), colloidal gels (Mohraz and Solomon 2005) and colloidal glasses (Derec, Ducouret et al. 2003; Carrier and Petekidis 2009). They have been theoretically predicted (Sollich 1998) and have additionally been probed by simulations (Rottler and Robbins 2003; Padding, Boek et al. 2008; Zausch, Horbach et al. 2008). Although system specific explanations vary, the basic idea is of an elastic energy storage mechanism which causes increase of stress before the peak and a dissipative energy release mechanism after the peak which fluidizes the system.

Experimental/Simulations

The hard spheres used in this chapter have a radius of R_C=267nm and were suspended in cis-trans decalin, giving a bare Brownian time of t_B=0.3sec. The suspensions were prepared according to the standard procedure described in chapter 2, with the volume fraction determined from the coexistence regime and diluted from φ_{RCP}=0.680±0.005. The rheometer used was the stress controlled Anton Paar MCR-501 with a Peltier temperature stabilization at T=20°C. The smallest acquisition time used for this rheometer in the transient tests was 0.1sec

to minimize error. Hence for the step rate tests low strain information was lost when the inverse rate was comparable or lower than the acquisition time. Two cone and plate geometries of different diameter where used to allow accurate measurements of low stress samples (low φ, large cone) and avoid thickening when loading for high volume fraction samples (small cone). The large cone is 50mm in diameter with an angle of 0.0175rads, while the small cone is 25mm in diameter and has an angle of 0.035rads. The cone truncations are 0.102mm and 0.050mm respectively. Before each examined rate, a rejuvenation protocol was enforced which consisted of series of tests starting from a high negative shear rate, a small waiting time, the same positive shear rate and a waiting time of 200sec. The high rate used was varied from $10s^{-1}$ at low φ to smaller rates at high φ to avoid thickening effects. This particular sequence was used in order to (roughly) correspond with the rejuvenation protocol of larger spheres in a shear cell used for microscopy experiments (Laurati, Mutch et al.). Some results of these experiments will be briefly shown further in the chapter.

φ	0.56	0.58	0.60	0.62
$D_S(\varphi)/D_0$	0.133	0.115	0.095	0.069

Table 4.1: The self diffusion $D_S(\varphi)/D_0$ that links experimental $Pe_0=Pe_{bare}$ to the $Pe_{sims}=Pe_{dressed}$, with $Pe_0= D_S(\varphi)/D_0 \cdot Pe_{sims}$ and $t/t_{B0}= t/(D_S(\varphi)/D_0 \cdot t_{Bsims})$.

Since the BD simulations do not incorporate hydrodynamic interactions, in order to compare the rheological experiments and the BD simulations at rest and under shear a normalization of time scales is needed. The defining time scale in the hard sphere system is the Brownian time $t_B=R^2/D_S$, a measure of the time it takes for a particle to diffuse its own size, where D_S is the short time diffusion coefficient. The experimental self short time diffusion coefficient cannot be extracted from the dynamics of each run; rather the diffusion is imposed by the simulation as the value of the coefficient when dilute (D_0). While in experiments, unless the dynamics are measured or theoretical calculations used, the short time diffusion coefficient is generally unknown and has a smaller value than in the dilute due to hydrodynamic interactions. This means that the simulations are normalized by a t_{Bsims} that reflects the real value of the Brownian time in the specific experiment/run, while rheological experiments can only be normalized by the value of Brownian time in the dilute t_{B0}. Simulations with the implementation of hydrodynamics have been done quantifying the change in short time self diffusion coefficients with φ by (Sierou and Brady 2001). We can thus link the Brownian time and Peclet numbers of experiments (t_{B0}, Pe_0) and simulations (t_{Bsims}, Pe_{sims}) as $Pe_0=D_S(\varphi)/D_0 \cdot Pe_{sims}$ and $t/t_{B0}= t/(D_S(\varphi)/D_0 \cdot t_{Bsims})$, where $D_S(\varphi)/D_0$ is the normalized short time

self diffusion coefficient that has been interpolated from the data of (Sierou and Brady 2001). Table 4.1 shows the values of $D_S(\varphi)/D_0$ for the φ used in the simulations, with an φ_{RCP}=0.64.

4.2 Experiments

Linear Moduli

The simplest of rheological characterizations for the samples examined here is in the form of linear viscoelastic values. Figure 4.1 plots the elastic and viscous moduli, G' and G'', of the different volume fractions normalized with sphere size and thermal energy against frequency, ω, or equivalently $Pe'_0=\omega t_{B0}$. All the samples show an elastic response with G'>G'' at all frequencies, and G' having a small slope, especially for the higher φ, throughout the probed frequency regime. The small increase of G' for the higher φ at the lowest frequency is most probably due to aging of the sample and/or minor evaporation. The loss modulus shows the characteristic minimum, which moves to smaller times as φ increases, in agreement with previous findings (Koumakis, Schofield et al. 2008). The smallest φ at the lowest ω shows G' approximately equal to G'' and is expected to become liquid like (G''>G') at lower frequencies. The physical mechanisms related to the power law slope of G' and the minimum of G'' have been discussed in chapter 3.

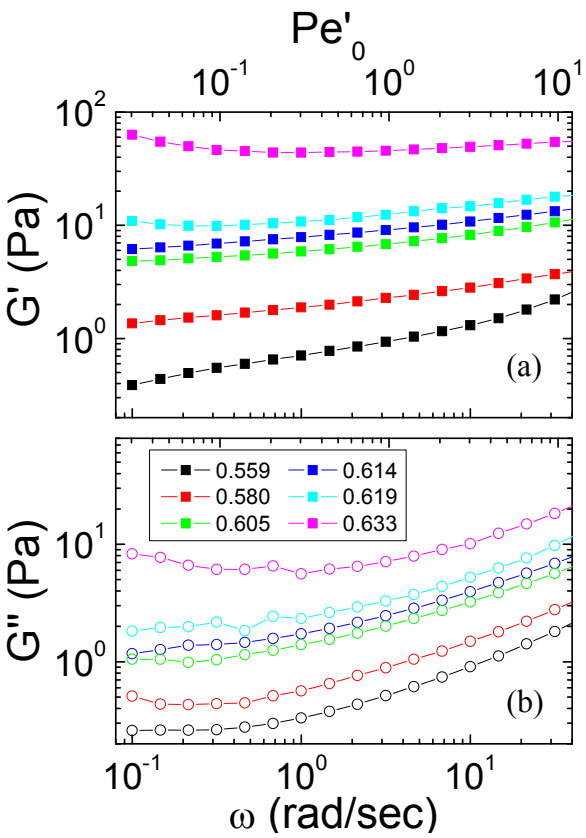

Figure 4.1: Linear frequency sweeps at different φ. Solid symbols represent the elastic moduli while open symbols the viscous moduli.

Figure 4.2a plots the normalized elastic moduli vs φ and figure 4.2b shows the elastic moduli against $1/(\varphi_{RCP}-\varphi)$, the reciprocal free volume. Figure 4.2a shows that φ dependence of the elastic moduli show an exponent of $m_{exp}=30\pm3$. A previous study has argued that the determining quantity of physical properties in a hard sphere glass is not the absolute volume fraction, but rather the distance from the maximum close packing (Koumakis, Schofield et al. 2008). Thus when looking at the elastic properties with the distance from maximum packing (4.2b) a lower slope of $m_{free}=4.1\pm0.2$ is found, with data points having less fitting error to the power law than the simple φ dependence.

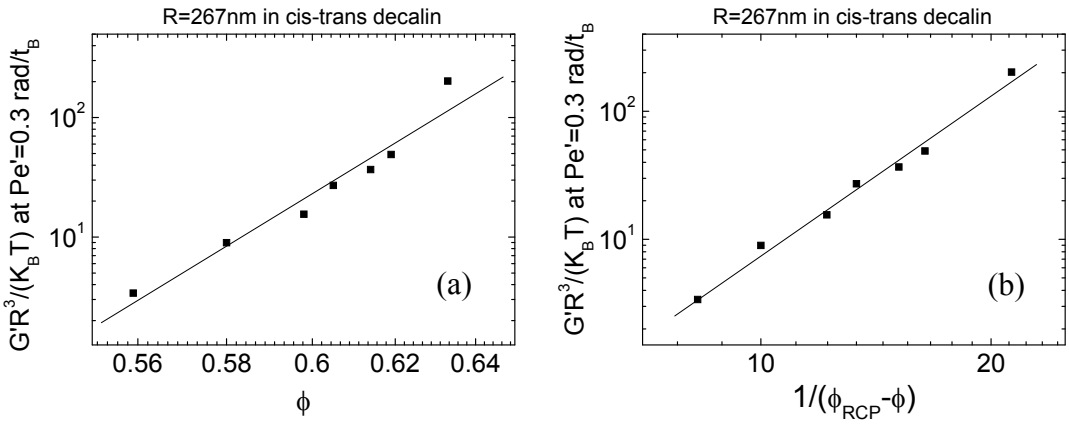

Figure 4.2: Elastic moduli at ω=1 rad/sec or $Pe'_0=0.3$ plotted a)with φ and b)with the inverse free volume $1/(\varphi_{RCP}-\varphi)$, where $\varphi_{RCP}=0.680$ as calculated experimentally. Power law fits have slopes of approximately 30 for a) and 4.1 for b).

According to simple scaling by the GSE, the increase of G' corresponds to the reduction of $\langle\Delta r^2\rangle$, and so when increasing φ there is a decrease in displacements due to less available free volume. Therefore scaling the elastic moduli by the free volume fraction seems like a logical choice. By estimating the average distance Δ between particles, $\Delta \sim \left[\left(\phi_{RCP}/\phi\right)^{1/3}-1\right]$, and inserting it into the GSE we find a simple power law dependence of G* (or G') of $m_{free}=2.1$ instead of the experimental $m_{free}=4.1$. An explanation for this deviation would be that the reduction of the elastic modulus at low frequencies by dynamic heterogeneities is more pronounced at lower φ, giving a larger slope in the experimental data. The prediction of the activated hoping MCT model (Kobelev and Schweizer 2005) for an exponential volume fraction dependence of the elastic modulus of a hard sphere glass yields larger values than the ones shown here by about an order of magnitude, with the power law slope increase being less than experiments with a value of $m_{theo}=15$ instead of the experimental $m_{exp}=30$. Moreover, characterisation of inter-particle interactions may be done through the power law

exponent $G' \sim \varphi^m$, by $U(r) \sim 1/r^{-3(m-1)}$. Systems with softer interactions are known to exhibit smaller exponents in the range of m=4-6 (Ozon, Petekidis et al. 2006), while the prediction of activated hopping MCT (Kobelev and Schweizer 2005) implies a weaker exponential volume fraction dependence which could be rationalised, in the present volume fraction range, with a power law exponent of $m_{theo}=15$.

Start-up Shear: Transient and Steady State Stresses

Figure 4.3a shows the stress versus strain in step rate experiments at φ=0.605 with different rates, while 4.3b shows step rate data at $Pe_0=0.0019$ and various volume fractions. The experiments show an initial increase, a peak in most cases and a steady state plateau for larger strains (γ>30%). Qualitatively, the main points of interest are the peak strain increase with increasing rate (4.3a), the stress overshoot becoming more pronounced with increasing rate (4.3a) and the decrease of the peak with increasing φ (4.3b). Quantitatively, the strains of the peak stresses in figure 4.3 are shown in figure 4.4, which indeed show an increase of γ_{peak} with rate, while the φ dependence shows relatively constant values at equal rates.

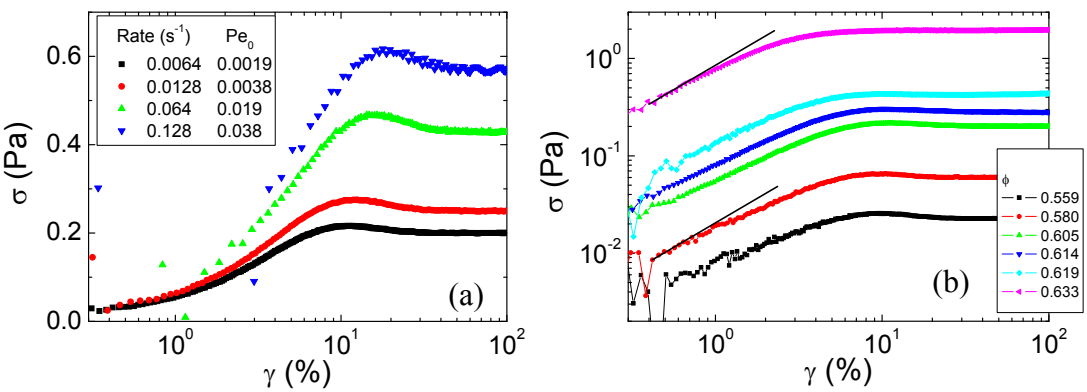

Figure 4.3: a) Step rate startup experiments of φ=0.605 for different rates. b) Step rate startup experiments of multiple φ at a fixed rate of $Pe_0=0.0019$ (or $\dot{\gamma}=0.0064s^{-1}$). For clarity, a) is shown in a linear-log plot while b) in a log-log plot. The lines in b) are a power slope of unity.

In figure 4.5 the flow curve of the different φ is shown along with the transient peak and steady state stresses from the step rates of figure 4.3. The flow curve was measured right after loading, while each point was taken with a delay time of 10sec to minimize the overall time of the test. Accordingly the smallest rates ($Pe_0<0.01$) may not show steady state values as the accumulated strain for each point is less or comparable to the yield strain. Although the shown steady state points ideally should be very close to the flow curve data, possible evaporation or aging during the tests has increased the stresses, especially at the highest φ. Shear banding (or slip) is not an issue in these measurements as according to (Besseling, Isa et al. 2010), we probe rates and φ that are in a stable flow regime.

At high φ there is Bingham like behavior showing a yield stress plateau at very low rates, which may reach a slope of unity at high rates, larger than the rates available in the experimental window. The lowest φ sample (0.559) exhibits a flow regime both at high and low rates. This also correlates with the linear oscillatory data where a G'/G'' crossover is observed at Pe'_0=0.03rad/t_{B0}, with an expected terminal flow regime at lower frequencies. Since, in this plot the steady state and transient peaks do not distinguish well between each other, we plot in figure 4.6 the peak and steady state stresses separately. Figure 4.6a shows the peak and steady state stresses as a function of φ, showing a general increase with φ and applied rate. Figure 4.6b plots the fraction of the peak stress to the steady state, showing a decrease with increasing φ and decreasing rates. Note that at the highest volume fraction we do not observe a stress overshoot for the rates measured. The decrease of the ratio has an apparent linear relation to φ.

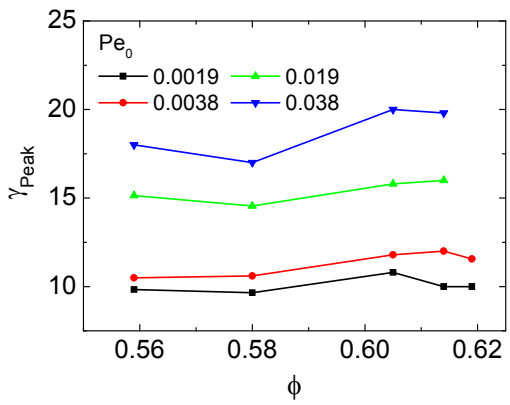

Figure 4.4: Strain values of the peaks seen in the previous figure plotted against φ for different rates.

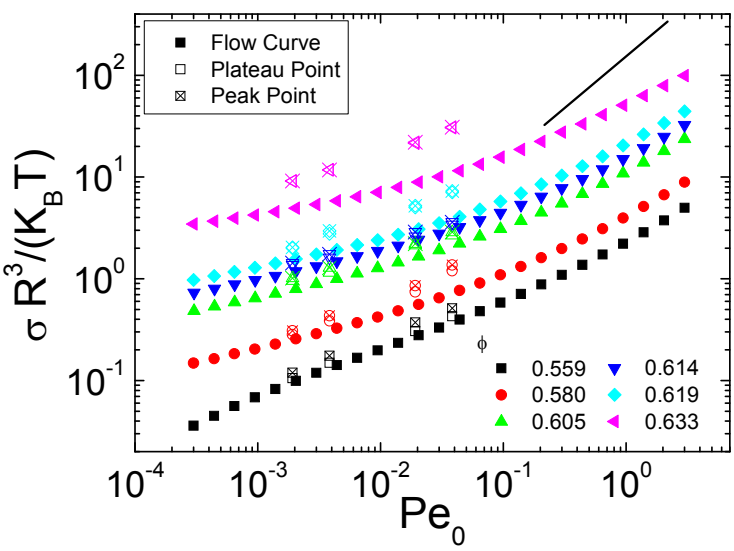

Figure 4.5: Flow curve of the different examined φ. Steady state and transient peak stresses are additionally plotted as seen in figure 4.3. Line shows a power law slope of unity.

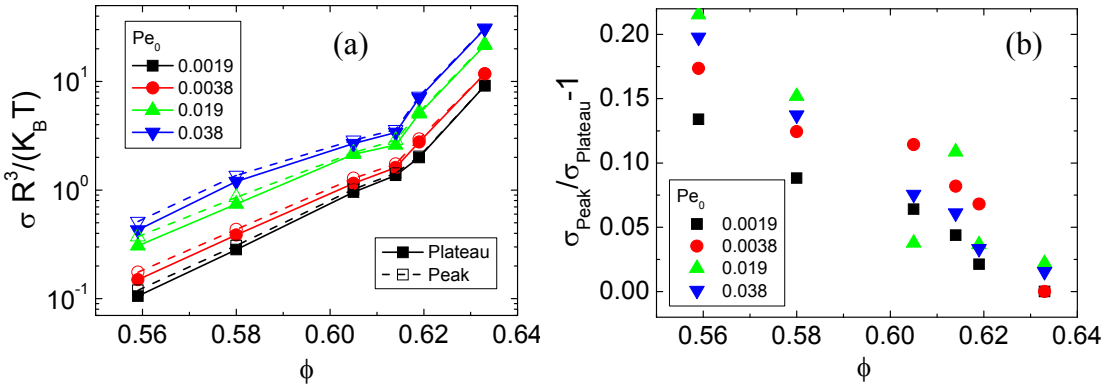

Figure 4.6: a) Steady state and transient peak stresses for different rates plotted with φ and b) $\sigma_{peak}/\sigma_{plateau}$-1 with φ for the same rates indicating the loss of the peak at high φ as well as low rates.

As discussed the initial stress increase should reflect an energy storage mechanism related with the elasticity of the system, while the peak corresponds to an energy dissipation mechanism that leads to fluidization and the plateau stress. Assuming a simple elastic response, the initial increase should show a linear increase with time, or equivalently a power slope of unity. As seen in fig. 4.3b, this is not the case with the slope being smaller than one, reflecting the viscous component of the sample in these time scales.

We can assume a simple equation for the viscoelasticity in the linear regime, $\sigma = \sigma_{elast} + \sigma_{visc} = G\gamma + \eta\dot{\gamma}$, under the assumption that during the experiment the viscoelasticity (G, η) does not change. If $\dot{\gamma}$ remains constant then $\frac{d\log(\sigma)}{d\log(\gamma)} = \frac{G\gamma}{\sigma}$, which means that the power law slope in each point of the step rate, along with the total stress, may be used to decompose the total stress into elastic and viscous components. Thus any step rate experiment with an initial slope less than one infers a viscous contribution to stresses.

Cessation of Shear: Stress Relaxation

Here we present stress relaxation data measured after the cessation of the step rate test, while keeping the strain rate constant at a value of zero. At approximately 100% strain, corresponding to the steady state, shear was stopped and the stress response was measured over time. The stress relaxation at φ=0.605 as a function of time is plotted in figure 4.7a. The plot shows that a long time relaxation is observed after low rates, although at short times, stresses show a more complicated behavior with relaxations of different rates crossing each other. Figure 4.7b shows the same relaxations, with the stresses normalized by the steady state value as determined just before the cessation of shear. Here we also have the time normalized

by the Brownian time t_{B0} as discussed. This clearly shows the speedup of relaxation with increasing shear rate, with the highest rates showing a fast stress drop to a few percent of the stress after cessation of flow. The volume fraction dependence of the relaxation for a single rate with Pe_0=0.019 is shown in figure 4.8 with the normalized stress and time as before. With the decrease of φ the stress seems to relax faster with the final stress after ~100sec decreasing towards zero for the lowest φ measured (0.559), whereas at the highest φ (0.633) it seems that a non zero stress plateau is reached. An overview of these results can be seen in figure 4.9, where the normalized stresses are taken after $100t_{B0}$ and plotted against rate (4.9a) and volume fraction (4.9b), showing stronger relaxations occurring at higher Pe'_0 and smaller φ.

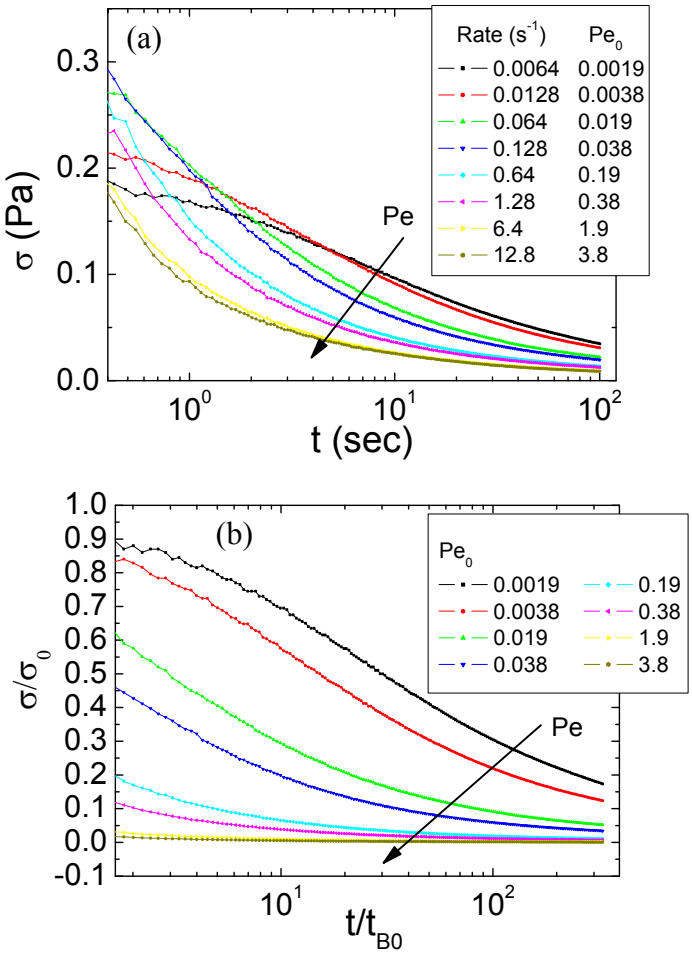

Figure 4.7: Stress relaxations of φ=0.605 after cessation of shear for different rates by plotting a) the stress values with time (in sec) and b) the stress values normalized by the stress at the end of the step rate with time normalized by t_{B0}.

The measured stress relaxation values seen in fig. 4.7a are correlated to relaxations of purely elastic stresses as the rate is zero and should mirror the structural rearrangements of anisotropic hard sphere cages that have been formed due to shear. The idea is that the slow relaxation is caused by particle motions that restructure the initial anisotropy to a state closer

to rest. For an ergodic viscoelastic medium that is fluid like at long times (low φ), one would expect the relaxation to eventually reach a zero value (fig 4.8 and 4.9). In the case of a non-ergodic hard sphere glass, it is not clear if the stresses ever relax to a zero state or equivalently if the initial shear induced anisotropy relaxes back to the isotropic structure at rest.

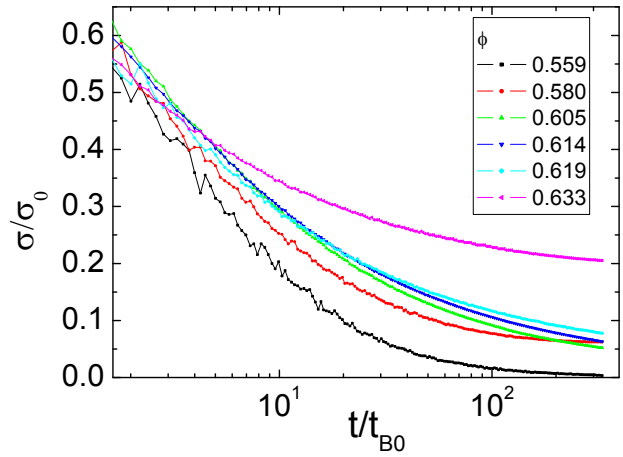

Fig 4.8: Normalized stress relaxations of different φ after cessation of shear for a fixed rate of Pe_0=0.019.

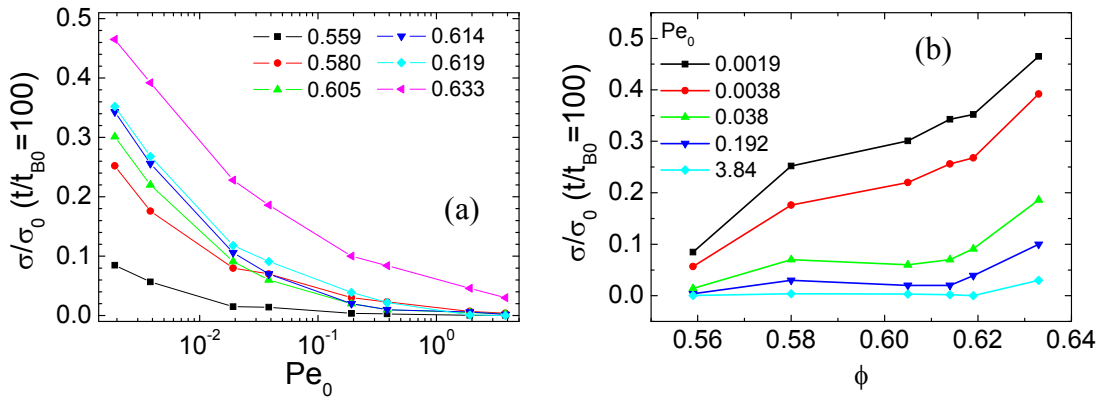

Figure 4.9: Normalized stress relaxation values at a time scale of t/t_{B0}=100 after cessation of shear of a) different φ versus Pe_0 and b) different Pe_0 versus φ.

As we vary the rate, the instantaneous structure and the dynamics during shear must in some way reflect the non-linear stress response of the system. At high rates a solid like system at rest showing a yield stress at low rates becomes fluid like under high shear. The relaxations reflect this by exhibiting small stress drops at low shear rates (solid like response), while showing stronger relaxation at higher rates (fluid like response). Alternately one may consider the structural properties of the system under shear. At low rates near the yield stress, the structure is minimally distorted, thus the entropic restoring force is small and stresses exhibit small or slow relaxations. In the case of high rates and large structural anisotropies, the restoring force at cessation of shear is large, showing stronger and faster relaxations. The

structural and dynamic properties will be examined further in this chapter with the aid of simulations, linking stresses and microscopic information.

4.3 Brownian Dynamics Simulations

Start-up Shear: Transient Stresses

By using BD simulations we attempt to elucidate the microscopic changes, both structural and dynamic, that occur during start-up shear and relaxation at cessation of shear. A range of four different φ with N=5405 particles were examined, both in the glassy regime and below of φ=0.56, 0.58, 0.60 and 0.62. Two rates of Pe=0.1 and 1 were used for all φ, along with Pe=10 for φ=0.58, all reaching up to γ=100%. To improve statistics for the structural properties, as well as stress calculations, Pe=0.1 and 1 of φ=0.58 were run 5 times with different initial configurations and averaged.

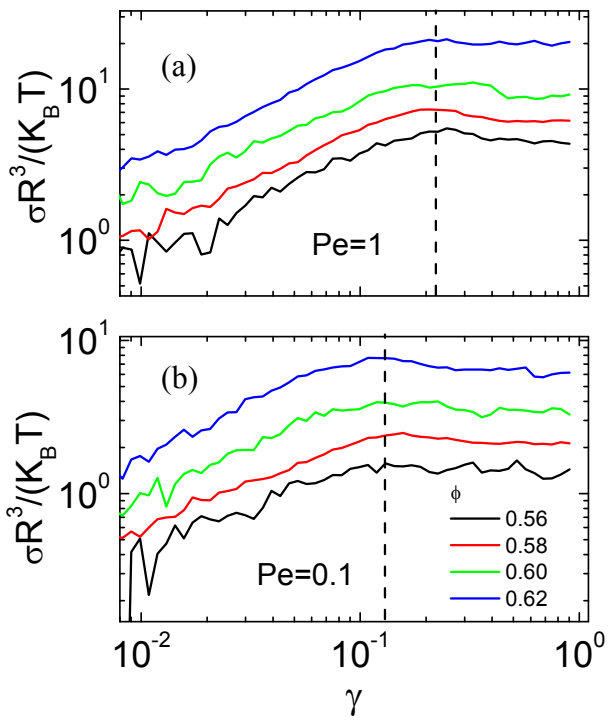

Figure 4.10: Hard sphere collision stresses as taken from simulations for N=5405 at φ=0.56, 0.58, 0.60 and 0.62 for a) Pe=0.1 and b) Pe=1. Lines show the approximate position of the stress peaks. For φ=0.58, stresses were averaged over 5 runs, while the others are just from single runs.

Figure 4.10 shows the stress for the start up experiments of the different φ for Pe=1 (4.10a) and Pe=0.1 (4.10b). The findings are similar to those of the experiment, although in the case of the simulations, statistical noise is high. There is a general increase of stresses with increasing φ, but there is no clear trend of the peak stresses or strains between φ. When

comparing the two rates shown, a clearer picture is emerging for the strain corresponding to the stress peak which increases at higher Pe. A different set of runs having less particles, but more runs per φ and rate, showed the height of the peak φ dependence more clearly and were found to qualitatively agree with experimental findings. Unfortunately, those runs did not export the structural information; therefore we do not show them in favor of consistency.

Start-up Shear: Particle Displacements

In general the calculation of particle displacements shows smaller statistical error than the stresses, as the latter is an instantaneous property owing its values to changes in a single step, while the former associates motion between multiple frames. Hence, the calculated mean squared displacements in this section are clearer than the stresses. Since during this calculation the system is not in a steady state, a time average of mean squared displacements can not provide information on the transient dynamics and the related microstructural changes during start-up shear. Thus for most of the figures we calculate two time type particle displacements using the following equation, modified from chapter 2:

$$\left\langle \Delta y^2\left(t,t_w\right)\right\rangle_N = \frac{1}{\mathrm{N}}\sum_{i=1}^{N}\left[\left(y_i(t_w+\Delta t)-y_i(t_w)\right)-\frac{1}{\mathrm{N}}\sum_{i=1}^{N}\left[y_i(t_w+\Delta t)-y_i(t_w)\right]\right]^2 \quad (4.1)$$

which gives the average displacement between two times, with $\mathbf{t_w}>0$ the elapsed time from the beginning of shear, **t** is the absolute elapsed time with $\mathbf{\Delta t=t-t_w}$ being the time frame for the displacement. Note that there is no averaging over time, only over the number of particles N. Instead of t_w and t, γ_w and γ may equivalently be used, which denotes elapsed strain instead of elapsed time. Note that the waiting time, t_w, here has a different meaning to what is usually described in aging experiments; i.e. the elapsed time after rejuvenation as shown in chapter 8 for attractive systems. Generally, only $<\Delta y^2>$, of the velocity gradient direction, is shown for the sake of simplicity, while it is also specifically chosen in order to compare with recent experimental confocal studies (Laurati, Mutch et al.), although $<\Delta z^2>$ and affine $<\Delta x^2>$ ($\Delta x=x_i-y_iPe$) show similar properties as will be discussed below.

In figure 4.11 we plot the particle displacements (4.11a) and the non Gaussian parameter (4.11b) of the y axis for φ=0.62 for two Pe under shear and for the system at rest. In addition, the stress response is shown in the inset. As mentioned, the data under shear represents the average over all particles, N, during a time of $\mathbf{\Delta t=t-t_w}$. For both Pe under shear in fig. 4.11a, at small $\mathbf{t_w}$, $<\Delta y^2>$ shows an initial increase following the behavior at rest, which becomes diffusive (slope of unity) at longer $\mathbf{t-t_w}$. At large $\mathbf{t_w}$, corresponding to the steady state, $<\Delta y^2>$ matches the diffusive behavior for long $\mathbf{t-t_w}$, whereas at small $\mathbf{t-t_w}$, it shows lower values compared to the displacements at rest. The non Gaussian parameter (fig. 4.11b) has similar

values to rest for small $\mathbf{t_w}$, additionally showing a reduction to zero at large $\mathbf{t\text{-}t_w}$ (diffusive) and exhibiting an increase for large $\mathbf{t_w}$ and small $\mathbf{t\text{-}t_w}$. Note that for short $\mathbf{t_w}$, although the system is under shear it has not reached the yield point and has not started flowing yet. This corresponds to the regime where the stress increases almost linearly with time (fig. 4.10).

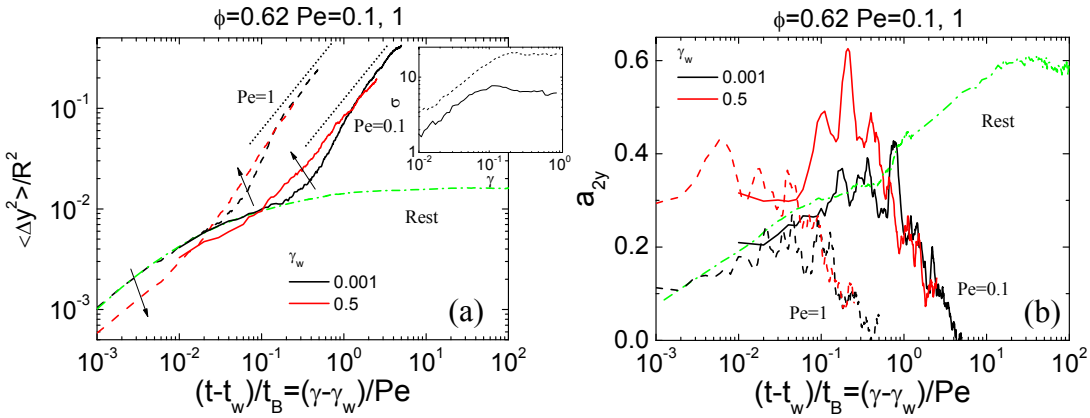

Figure 4.11: Results of hard sphere BD simulations on the particle dynamics at rest (dash-dot) and under shear at Pe=0.1 (solid line) and Pe=1 (dashed line) for short initial (γ_w=0.001, black) and long steady state (γ_w=0.5, red) elapsed strains (γ=Pe t) for φ=0.62 with a) MSD in the y axis and b) non Gaussian parameter a_2. Inset shows the measured stress (Single run). Dash-dot green lines show the state at rest, while dotted lines in a) show the power law slope of 1.

At long time scales (γ>30%), both rates due to many collisions between particles and out of cage displacements, exhibit a diffusive behavior with displacements following a linear increase versus time and the non Gaussian parameter approaching zero. At the steady state ($\boldsymbol{\gamma_w}$=0.5) and for short times, a decrease of particle displacements is observed compared to those at rest, suggesting a constriction of particle mobility under shear which is more pronounced at higher rates. The a_2 parameter corroborates this by showing pronounced deviations from Gaussian behavior at these time scales. Since the constriction occurs due to shear in the steady state after the onset of flow, it seems to be related to the out of cage motion. For $\boldsymbol{\gamma_w}$=0.001 and mid values of $\boldsymbol{\gamma\text{-}\gamma_w}$, there is what appears to be a super diffusive behavior with the MSD vs $\mathbf{t\text{-}t_w}$ having a local power law slope of greater than unity. Although, this may be an apparent effect as the values are not taken at steady state and both displacements and time scales are changing while the system is yielding, it does indicate a transition from the microscopic dynamics prior to yield, to those after yielding when the sample flows. This effect seems less pronounced with increasing rate, possibly because the transition of yielding occurs in a range of time scales where the state at rest has displacements values nearer to the steady state under shear.

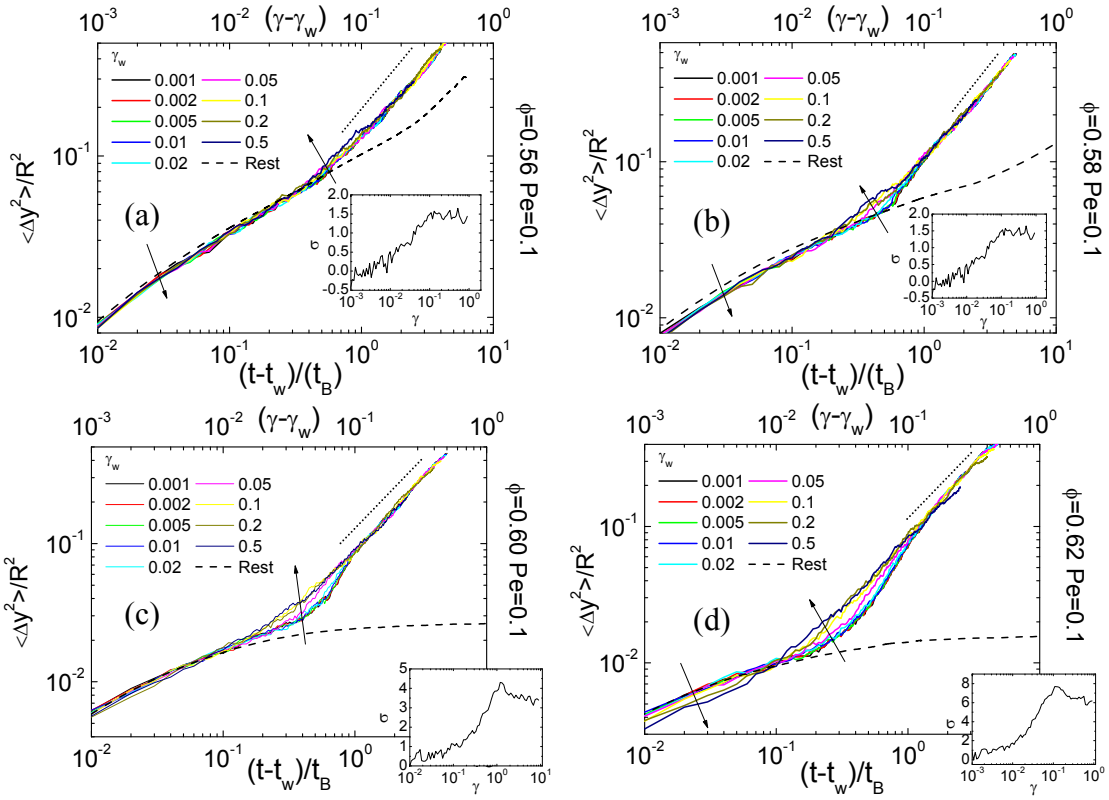

Figure 4.12: Results of hard sphere BD simulations (single runs) on the particle dynamics at rest and under shear at Pe=0.1 for different elapsed times/strains (γ=Pe t) for a) φ=0.56, b) 0.58 , c) 0.60 and d) 0.62 as noted on the graphs. The dotted lines show the power law slope of unity, while insets show the measured stress.

Figures 4.12 and 4.13 show the displacements as in 4.11a, however showing multiple γ_w for different φ's and at Pe=0.1 (fig. 4.12) and Pe=1 (fig. 4.13). The behavior of particle displacement for all φ's is qualitatively as described in fig. 4.11, while effects of constriction and the apparent or "transient" super diffusion become less apparent for at lower φ's. The constriction is related to the rate as its increase introduces to increased collisions, while the higher φ's means higher particle proximity and thus again increased collisions. Drop of small time or instantaneous diffusivity with increasing rate has also been seen at lower volume fraction in the liquid regime by Stokesian Dynamics simulations(Foss and Brady 2000).

The transient super diffusion is directly linked to the local power law slope of the displacements at rest. As this slope approaches unity the changes in displacements between rest and steady state are smaller, thus the super diffusion effect is weaker. Most notably the effect is reduced at low φ where the slope is generally large and also at high rates where smaller time scales are probed and in cage motion is stronger exhibiting large slopes. The transient super diffusive behavior also correlates with the appearance of the stress overshoot.

However as we see in figures 4.13 and 4.14, quantitative connections might not be simple since the magnitudes of the two effects are not directly proportional.

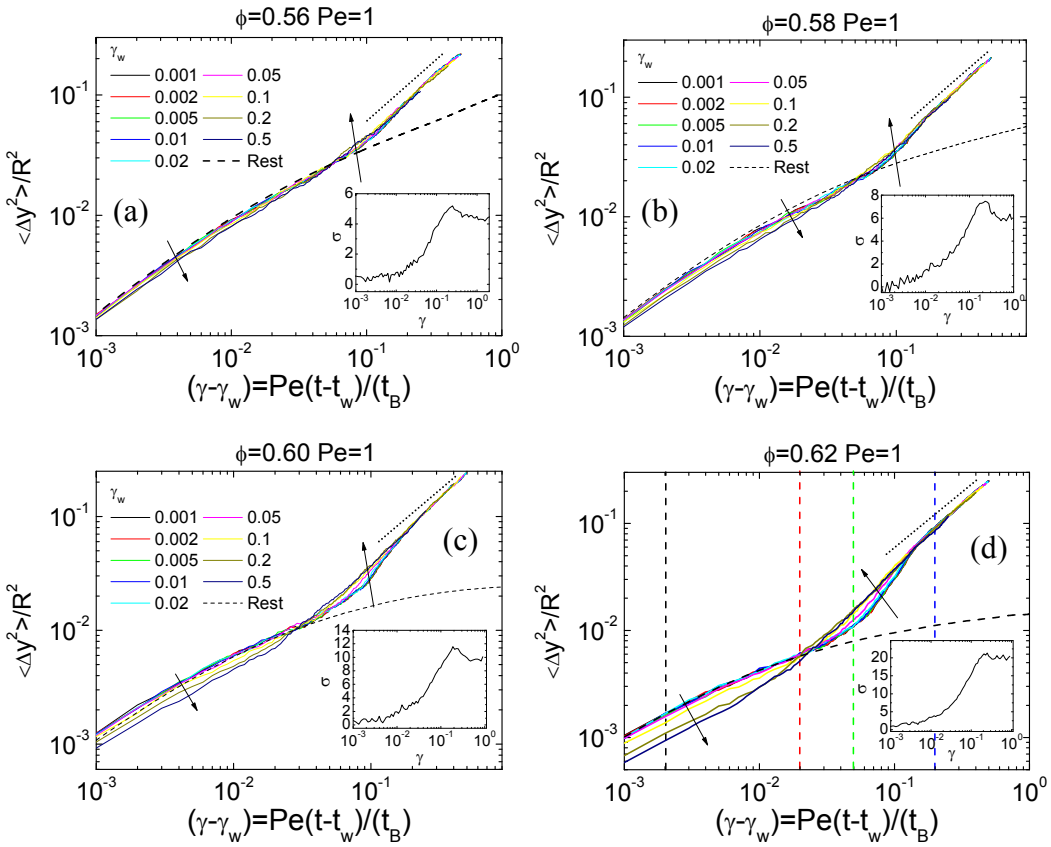

Figure 4.13: Results of hard sphere BD simulations (single runs) on the particle dynamics at rest and under shear at Pe=1 for different elapsed times/strains (γ=Pe t) for a) φ=0.56, b) 0.58, c) 0.60 and d) 0.62 as noted on the graphs. The dotted lines show the power law slope of unity, while insets show the measured stress. Note the strong drop of short time displacements for strains above yield. The vertical dashed lines in d) correspond to the γ-γ_w examined in the next figure.

The strain of the onset of non linearities as seen on figures 4.12 and 4.13 can be estimated by the deviation of displacements from those at rest for the smallest γ-γ_w at a specific γ_w. For example at φ=0.62 in figure 4.13 the onset of non linear behavior occurs in the area of $0.05<\gamma_w<0.10$. A more quantitative estimation of non linear onset can be achieved as seen in figure 4.14a, where displacement values of equal $\Delta\gamma=\gamma-\gamma_w$ are plotted as a function of the elapsed strain γ. In order to characterize the onset, γ is used instead of γ_w, since $\gamma>\gamma_w$ and thus relates with the first appearance of non linear behavior. Similarly, if one desires to characterize the steady state the value of γ_w must be used which defines the smallest strain.

The short time constriction of the particle mobility under shear for $\Delta\gamma$=0.002 can clearly be seen in 4.14a, where the displacements are initially equal to the ones at rest, while with

increasing strain they decrease to smaller values. The change of these displacements at low **Δγ** can be used to estimate a yield strain, which is graphically defined as the intersection point of the extended lines referring to the initial state and the steady decrease. Similarly, a steady state strain can be defined by the intersection of the long time steady state and the steady decrease. Extracted values for the various φ and Pe are shown in fig. 4.14b. A yield strain may also be extracted from figures of 4.12 and 4.13 as the strain where the γ_w=0.001 curve deviates from the displacement at rest. However, statistical errors in the data do not allow accurate estimation of the yield strain.

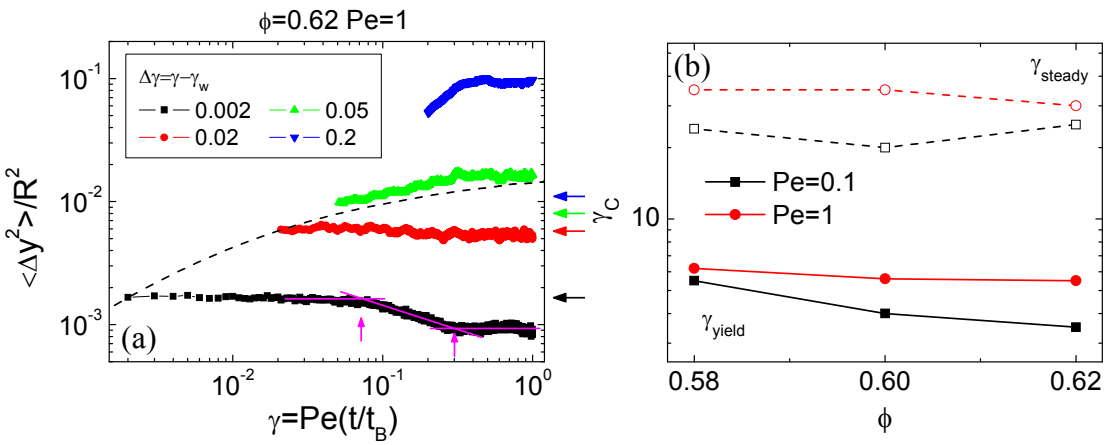

Figure 4.14: a) Displacements for specific elapsed strain/time intervals $\Delta\gamma=\gamma-\gamma_w$=0.002, 0.02, 0.05, 0.2 (increasing from bottom to top) versus the elapsed strain at Pe=1 and φ=0.62. The horizontal arrows show the corresponding time interval displacements at rest (increasing from bottom to top), while the dotted line shows the displacements at rest. The vertical magenta arrows show the microscopic onsets of yield and steady state. b) The strain values corresponding to the onsets of yield (solid) and steady state (open) for Pe=0.1 (black, squares) and Pe=1 (red, circles) are extracted from data as shown in a) and plotted against φ.

As **γ** increases in fig. 4.14a, the features seen in figures 4.12 and 4.13 become more apparent, additionally showing information on smaller time scales (especially for **Δγ**=0.2), inaccessible by the previous representation. For smaller **Δγ,** we see the effect of in cage mobility constriction, with particle displacements at the steady state becoming smaller than at rest, while reversely for larger **Δγ**, the displacements increase over those at rest as out of cage motions occur. The yield and steady strains of fig. 4.14b, show relatively unchanging values, much like the experimental data of the stress peaks. It is interesting to note that while the two extracted strains map the range of the transition between linear strain and steady state, their average roughly corresponds to the strain of the stress peak.

In figure 4.15, the MSD of the y axis, a_2 parameter and stresses are shown, averaged over 5 runs of different initial configurations, in relation to the γ_{yield} and γ_{steady} of fig 4.14b and rest. The displacements at rest show diffusive out of cage relaxation at the longest times, verified by the slope of the displacements and by the non-Gaussian parameter. As already discussed, the displacements under shear for small γ_w follow the displacements at rest until the onset of non-linearities, which may be identified with the yield point, while at larger γ_w constriction effects are observed at short times (or $\Delta\gamma$'s). Once the steady state is reached, for all γ_w (or t_w) diffusive behavior is displayed. For the a_2 parameter the dependencies are similar, with the constriction at small strains and large γ_w related with an increase of a_2, whereas at long times with a reduction to zero. The area between the arrows roughly denotes the transition between linear stress response and the steady state flow. While the arrows showing the γ_{yield} point to a location where the displacements have already deviated from those at rest, the arrow indicating γ_{steady} point straight to where the a_2 goes to zero.

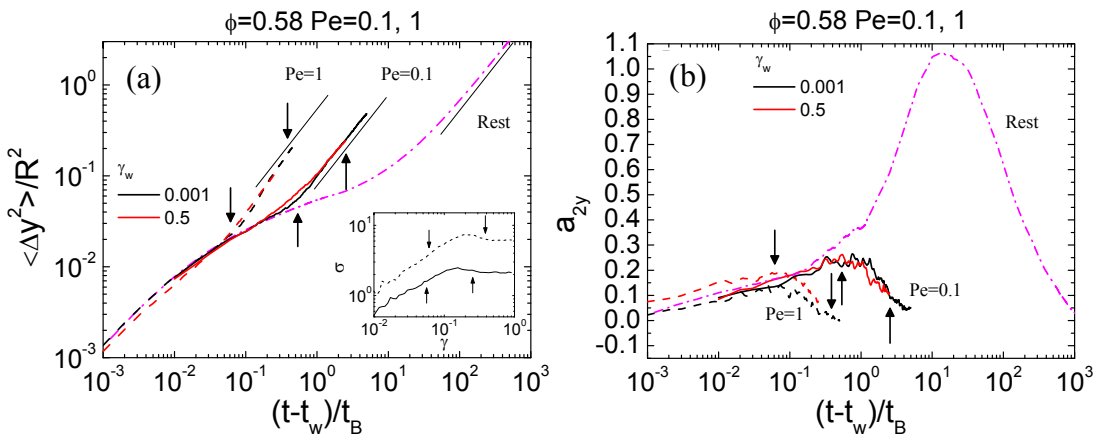

Figure 4.15: a) MSD in the y axis and b) non Gaussian parameter a_{2y} for φ=0.58 at Pe=0.1 (solid) and Pe=1 (dashed) for γ_w=0.001 (black) prior to yield and γ_w=0.5 (red) at steady state, averaged over 5 runs. Dash-dot magenta lines correspond to the MSD at rest. Inset in a) shows stresses vs strain, while the vertical arrows both in the inset and main graphs indicate the γ_{yield} and γ_{steady} from fig 4.14b, while thin solid lines indicate a power law slope of 1.

The displacements discussed up to now were limited to the y axis (gradient direction). In figure 4.16a we show the displacements for all the axes at γ_w=0.5 normalized by the elapsed time (Δt), or equivalently an effective shear induced diffusion coefficient, while figure 4.16b shows the steady state self-diffusion coefficients under shear normalized by D_0 at the long time values of 4.16a. Displacements in the x and y axes are in general similar (Δx^2 slightly larger than Δy^2), while the z axis deviates from the other two at longer times and shows a smaller plateau value near the steady state. The normalized shear induced diffusion coefficients, $D_i/D_0=\langle\Delta x_i^2\rangle/(2t/t_B)$, clearly show for all φ's and Pe, such a drop (approximately

10%) of displacements in the z axis. This will be explained further with the examination of the structure under shear. Of interest is the qualitatively different φ dependence behavior of the diffusion coefficients under shear for the two Pe. While Pe=0.1 exhibits a decrease of D/D_0 with increasing φ, at Pe=1 we rather observe an increase. As will be shown in the case of oscillatory shear in a wider range of Pe, different applied Pe probe different timescales of motion in comparison to the state at rest. The diffusivities at low Pe reflect the motion of the particles at rest, thus higher φ's have lower diffusivities. At higher Pe the diffusivities increase and become proportional to particle collisions, which should also be more pronounced with increasing φ.

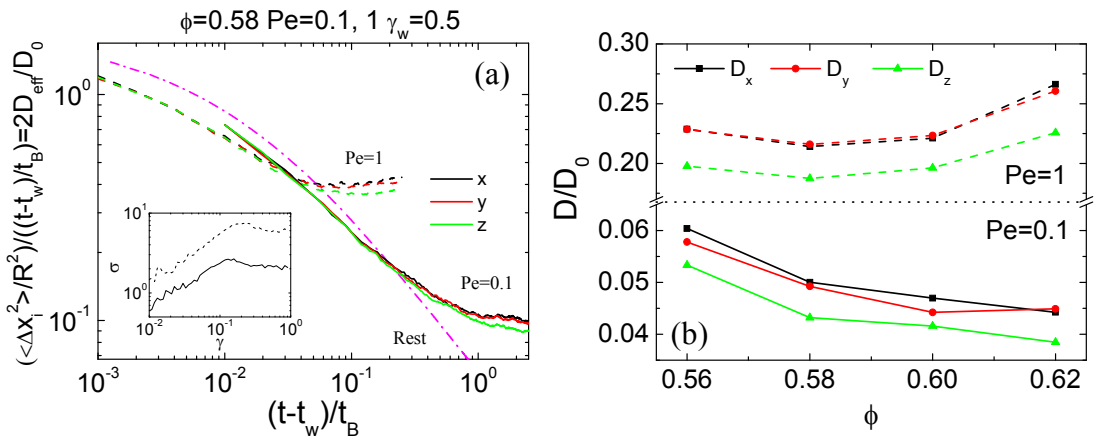

Figure 4.16: a) MSD for all axis normalized by Δt producing an effective normalized diffusion coefficient ($2D_{eff}/D_0$) of φ=0.58 at Pe=0.1 and Pe=1 for long (γ_w=0.5) waiting strains. Solid lines show Pe=0.1, dashed lines show Pe=1 while the dash-dot magenta line is at rest. The axes are colored as shown in the legend. b) Shear induced diffusivity at steady state versus φ for all axes and Pe.

Start-up Shear: Confocal Microscopy

Using confocal microscopy on a dense hard sphere suspension, recent work (Laurati, Mutch et al.) shown in fig. 4.17, finds similar phenomenology of the dynamics under steady shear as discussed for the Brownian dynamics simulations. Although the probed time scales are larger due to experimental constraints and the small time constrictions are lost, the appearance of a transient super diffusion at small waiting time as well as the increase of diffusivity over rest at long times is evident.

Theoretical, simulation and experimental work on the transient start-up stresses has been made by (Zausch, Horbach et al. 2008). In this work they correlate the appearance of the transient super diffusive behavior with that of the stress peak. While this connection may be valid to some extent, we find that the correlation between the two is not simple; rather it exhibits a complicated coupling to changes in φ and applied rate as seen in figures 4.12 and

4.13. As shown, we find that as φ is decreased or Pe is increased, the stress peak is more pronounced, but the transient super diffusion is lost. Therefore, the appearance of the super diffusion is a function of the dynamics at rest at the time scale of the peak, while the stress peak, as will be shown, is a function of the structural changes during the transient shear.

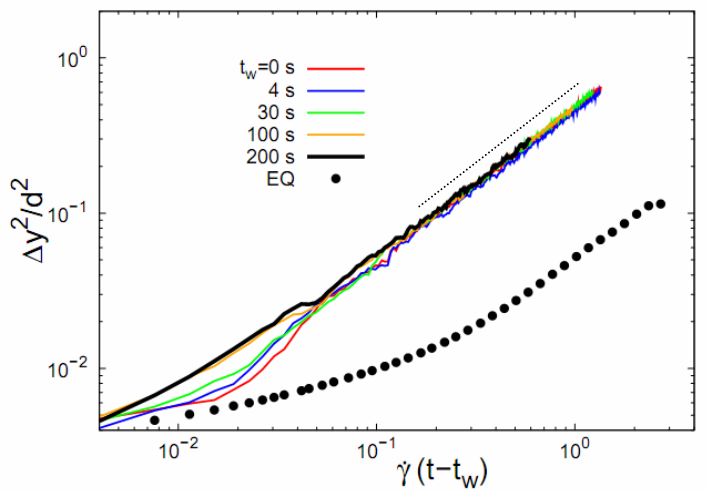

Figure 4.17 Experimental data of MSD of φ=0.56 at Pe_0=0.019 showing similar evolution of values with waiting time as in simulations.

Start-up Shear: Structure

While the dynamics are an important part of the story, both the transient and steady state (Foss and Brady 2000; Brady 2001) structural information of the particles under shear is of great interest. The simple radial particle distribution function is unable to capture the anisotropy under shear, showing relative invariance from the state at rest. By examining what occurs at the three different planes (xy, xz and zy), a much clearer picture emerges. The images to be shown are 2D slices of the radial distribution function in the respective planes of 1.4 radii in width and an area of 10x10 radii. The xy plane shows the most interesting features. The final images are arbitrarily normalized, although images shown in the same figure have been normalized by the same coefficients. Images are shown in false Red-Green-Blue colors, with blue being low intensity and red being high. To achieve greater clarity, some images have the respective image at rest subtracted as indicated.

Introducing the 2D images of g(r), figure 4.18a shows the xy plane g(r) for φ=0.56 under shear of Pe=1. The image is averaged at the steady state between γ=0.5-1. The xy plane anisotropy under shear presents itself as a generally higher intensity along the compression axis shown as a red line, with a drop of intensity along the vertical of the compression axis (extension axis), shown with a green line. The intensities are shown in more detail for figure

4.18b, where the g(r) along the compression and extensional axes are compared to the isotropic condition at rest. The compression axis shows the largest peak at contact, followed by the state at rest and lastly the extension axis. After the first peak, the state at rest has the most well defined minima and maxima, followed by the compression and finally the extension axis. Although the positions of the first maxima are hard to distinguish, it is clear that the subsequent minima and maxima exhibit changes from at rest, with the compression axis showing a shift to smaller r/R and the extension axis a shift to larger r/R.

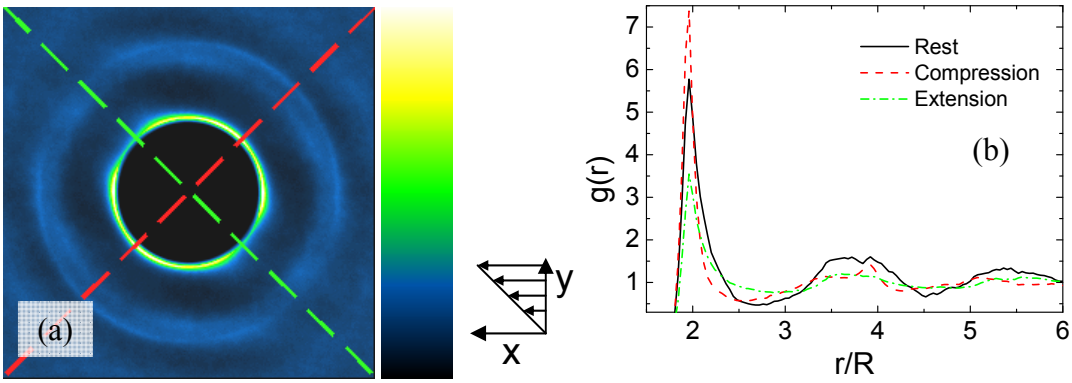

Figure 4.18: a) Image of g(r) in the xy plane for φ=0.56 and Pe=1 averaged at the steady state for strains 50%-100%, with the compression axis shown as a red line and the extension axis as a green line. The intensity scale and direction of the shear field is shown on the right. b) Graph of g(r) for the same conditions along the compression axis, the extension axis and at rest.

The steady state description of g(r) shows that along the compression axis a large number of collisions occur, indicated by the increased height of the first peak and the positional shift of the subsequent minima and maxima. In the extension axis however, there are fewer collisions. Furthermore as the drop in the first maximum and the positional shift to larger distances indicate, a larger flow of particles is revealed by the "smearing" of the g(r) (smaller maxima and larger minima) in the extension axis.

Figure 4.19 shows the xy plane g(r) for Pe=0.1 and Pe=1 atφ=0.56, 0.58, 0.60 and 0.62, averaged at the steady state between γ=0.5-1. A trend emerges from these images which show sharper characteristics at higher Pe and higher φ (narrower peaks), although the anisotropy becomes optically more apparent at Pe=1 and lower φ. The structural information of this figure can be correlated to the dynamic information of figures 4.12 and 4.13. The property that directly correlates to the structural anisotropy is the constriction at small times, related to the number of collisions which occur under shear. For the lower Pe and φ, the Brownian motion becomes significant and the anisotropic effect of shear is reduced, while increasing Pe and φ lead to more collisions. The anisotropy however becomes visually more apparent at lower φ as the broadening of the peaks allows for larger intensity variations in the image.

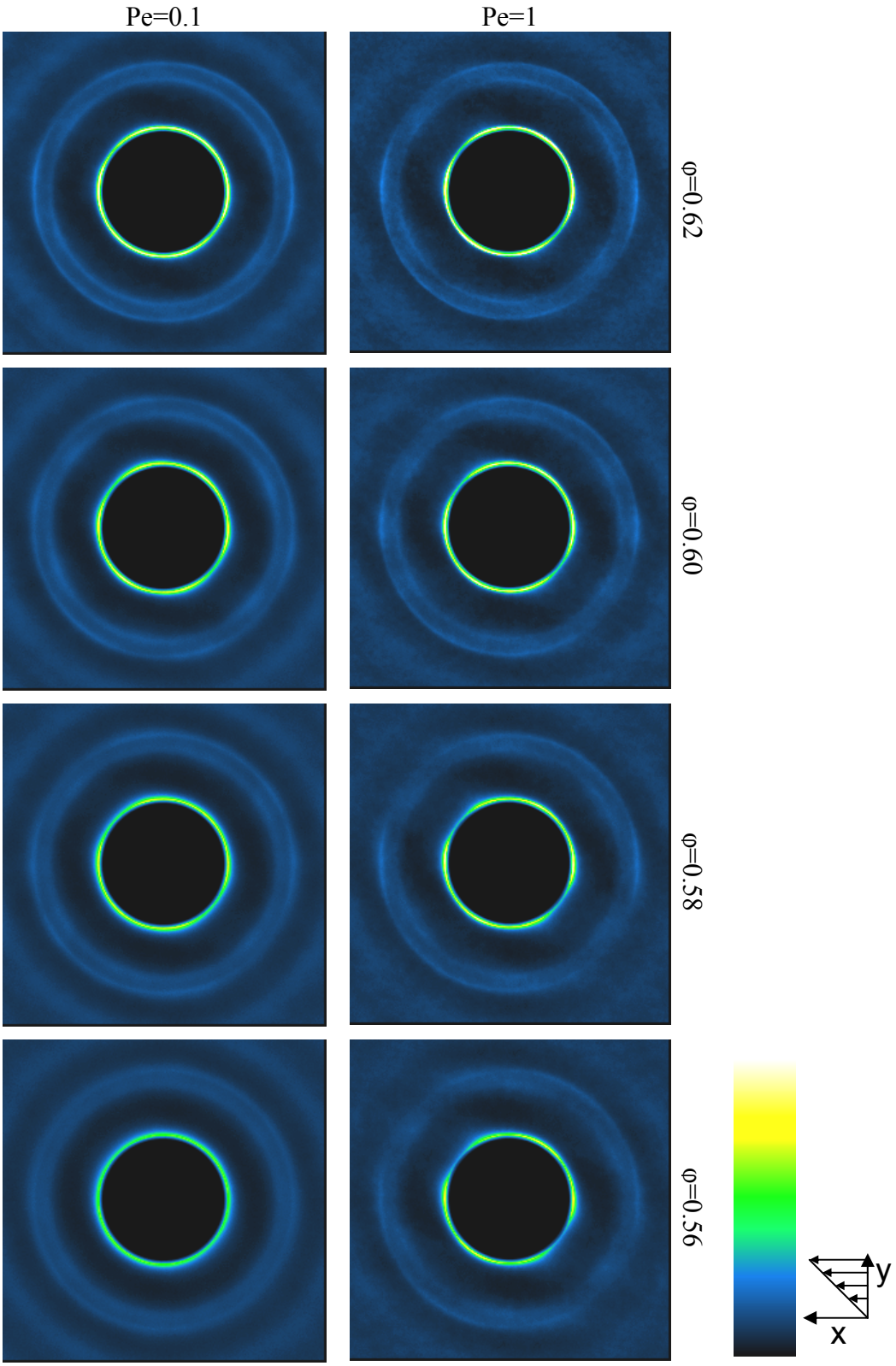

Figure 4.19: g(r) in the xy plane for φ=0.56, 0.58, 0.60 and 0.62 (bottom to top) with Pe=0.1 (left) and Pe=1 (right) averaged at the steady state for strains of 50%-100%.

Figure 4.20 shows the stress response of φ=0.58 at Pe=1 averaged over 5 runs along with the transient values of the g(r) at select strains. Strains of 1%, 10%, 20% and 40% were chosen as to be a) in the linear regime, b) during the onset of non-linear behavior, c) at the height of the peak and d) at the steady state respectively. Figure 4.21 shows the same images in detail, both with and without the state at rest subtracted. As strain is increased, the anisotropy becomes more pronounced, starting from a small increase of the first maximum of g(r) in the compression axis at 1%. At 10%, the increase widens and the anisotropy appears at the second peak, while the first maximum in the extension axis spreads toward the first minimum. Increasing to 20%, the compression axis shows an even wider increase, with the extension axis showing a spread reaching close to the secondary peak, while the intensity in the whole axis is more diffused. At the steady state (40%) the g(r) seems to stop changing with the most significant difference being the appearance of slightly stronger intensity "lobes" in the x-axis of the first and second maxima, along with stronger diffuse intensity in the extension axis.

By correlating the transient microstructural information with the stress and displacements a more complete picture emerges. At small strains (≈1%) the stress increases steadily and the structure shows some small distortion, while the displacements show no deviation from those at rest, indication a linear deformation regime. At higher strains (≈10%), the beginning of non linear stress response, displacements show the appearance of constricted particle mobilities at short times (4.14b) and out of cage motions at longer times (4.15a). g(r) reflects this with the stronger intensity of the first maximum in the compression axis (constriction) along with the spreading of the first maximum towards the second in the extension axis (out of cage motion). The out of cage motion is not dominant at this point, as the first maximum in the extension axis has not yet spread out to reach the second. At even higher strains (≈20%), corresponding to the peak stress, the longer time displacements are almost diffusive while short time constriction has nearly reached steady state. The xy plane g(r) is consistent with this behavior, with the compression axis of the first maximum showing more prominent intensities, while exhibiting diffuse particle locations along the extension axis due to large contribution from out of cage motion. At the steady state strain (≈40%), the measured stress is reduced from the peak value (≈20%), although the microscopic displacement and structural changes are generally small, reaching the final steady state values for the short (constriction) and long (diffusive) time displacements, with the g(r) exhibiting more diffuse particle locations along the extension axis and small intensity lobes on the x-axis as described.

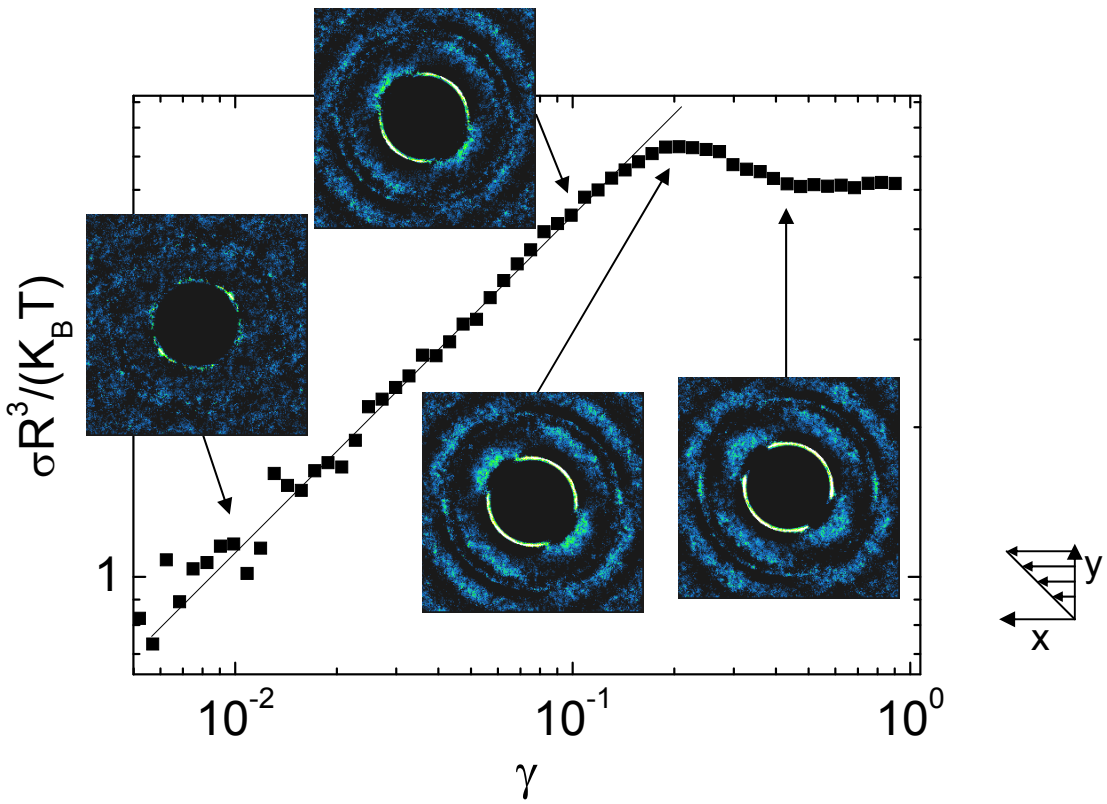

Figure 4.20: Stress versus strain for φ=0.58 and Pe=1, with superposition of g(r) in the xy plane (with subtraction of the g(r) at rest) at strains of 1%, 10%, 20% and 40% averaged over 2%.

While the increase of constriction seen in the compression axis of g(r), corresponds to an increase of stress with increasing strain due to cage elasticity, the out of cage motion should reflect viscous loss. Thus in the linear regime and up to 10% where there is little or no out of cage diffusion, the elastic behavior dominates with a strong increase of stress with strain. As out of cage rearrangements become more dominant, the stress peak is reached with cages almost reaching maximum distortion. As the applied rate is comparable to the Brownian motion (Pe=1), some particles remain trapped within cages even though maximum distortion has been attained. Consequently a stress drop occurs as the strain increases further, associated with the out of cage motion of particles that were still trapped within the cages at the peak stress, allowing a relaxation of stored stress. The final "lobes" in the x-axis of the g(r) reflect the areas of slightly higher stress as particles collide and steady state out of cage motion occurs. Similar structural information, although with higher statistical noise, is found for smaller Pe=0.1, scaled to the smaller strains as found by the γ_{yield} and γ_{steady} of fig. 4.14b.

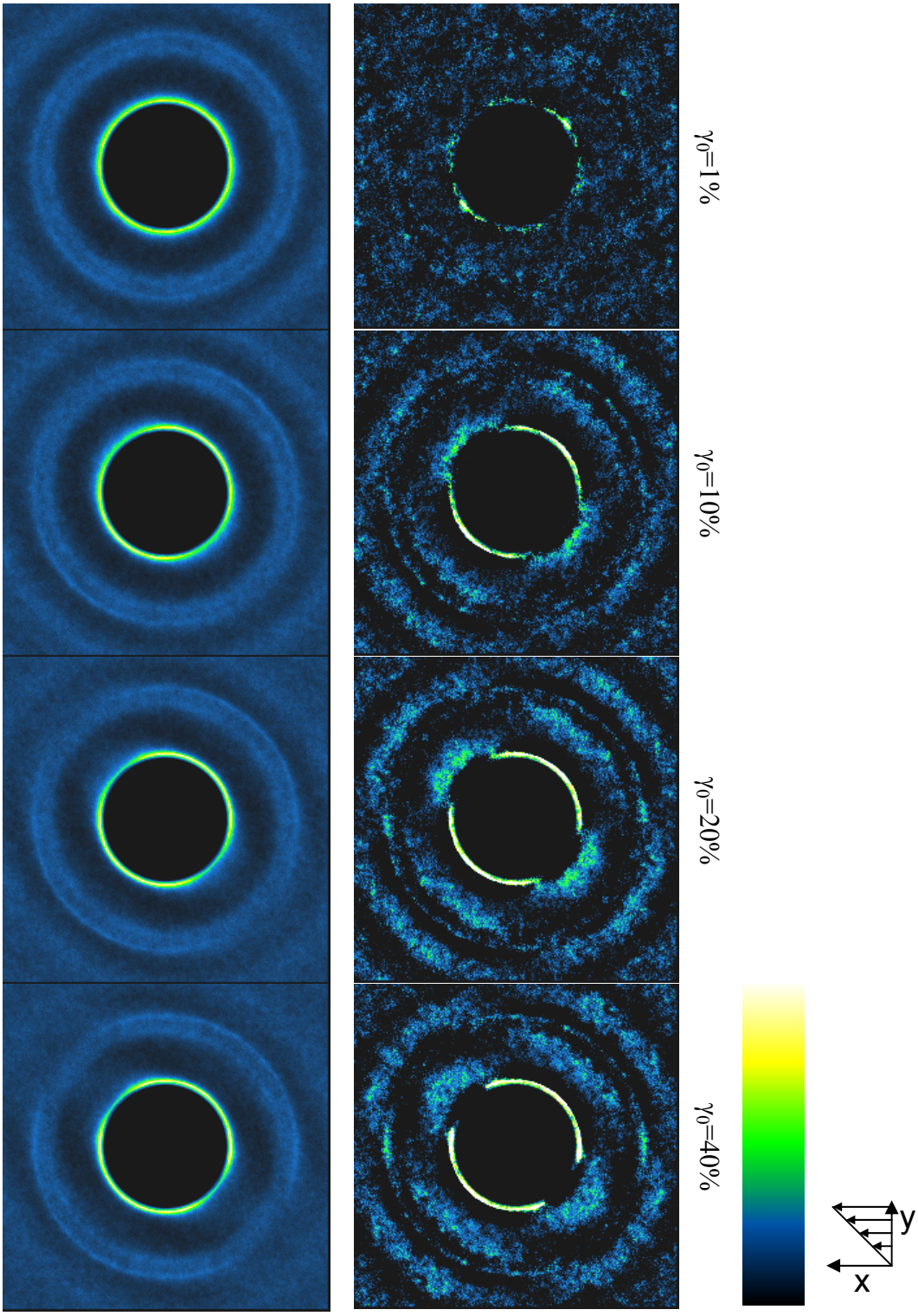

Figure 4.21: The g(r) in the xy plane at strains of 1%, 10%, 20% and 40% from top to bottom as seen in figure 4.20. On the left are the full images, while on the right are the images after subtraction of the g(r) at rest. Note that out of cage escape begins after 10% strain elapses.

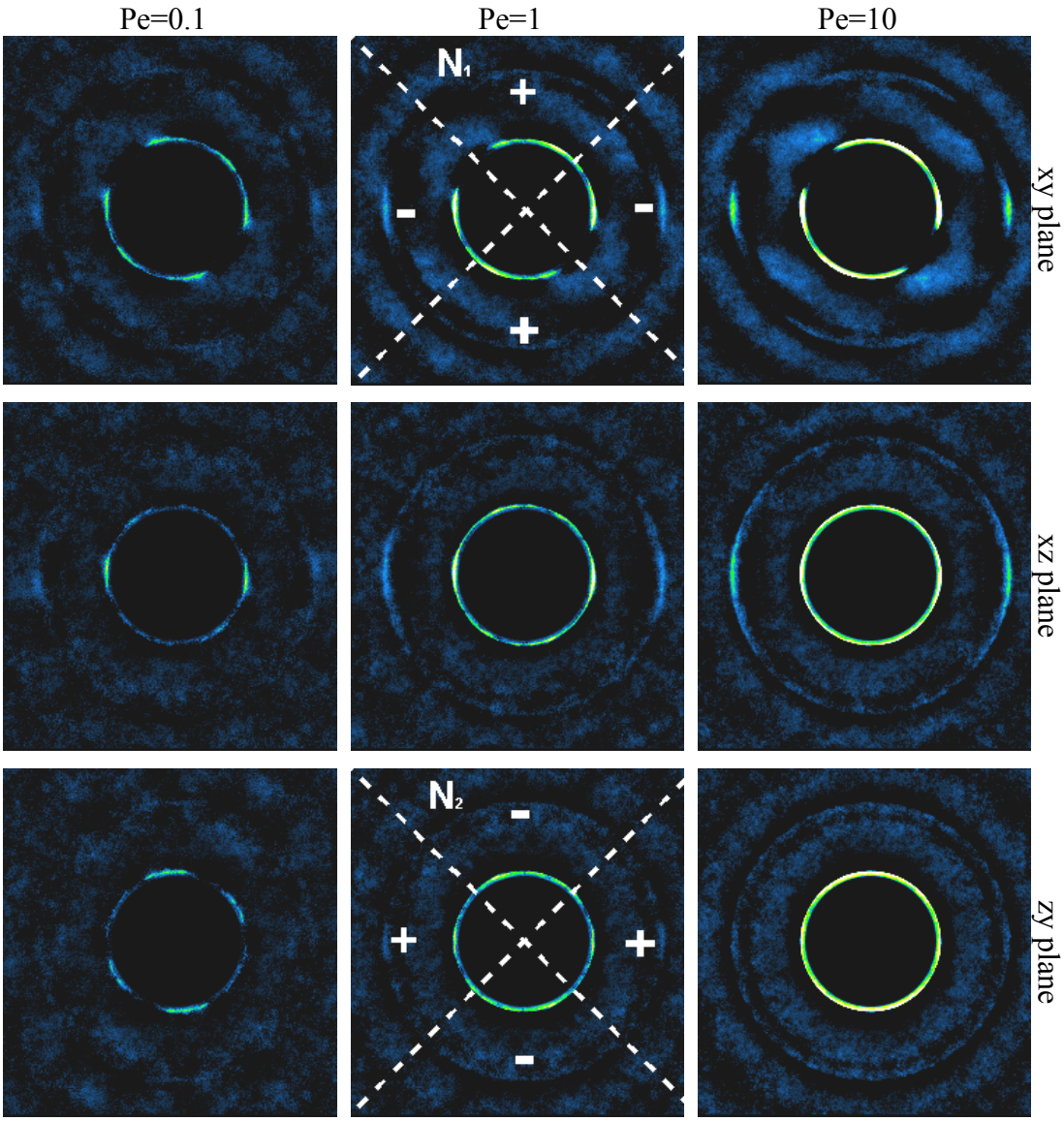

Figure 4.22: g(r) for φ=0.58 with Pe=0.1, 1 and 10 (From left to right) in the xy, xz and zy planes (from top to bottom) averaged at the steady state for strains of 50%-100% and shown after subtraction of the g(r) at rest. The normal stress contributions of the g(r) planes on N_1 and N_2 are selectively shown.

Therefore we find that the mechanism behind the stress peaks lies in the persistence of structural cage elasticity, since the maximum cage distortion occurs before all particles are able to undergo out of cage relaxation. This intuitively translates to the high shear leading to more elongated cages during the stress peak, which are partly or even totally destroyed at the steady state. This argument is strengthened by the experimental and simulations finding that smaller rates and higher φ's produce smaller stress peaks. The former is a matter of particles having more time to diffuse out of their cage with Brownian motion thus there is less elongation, while the latter occurs because as φ is increased, less available space makes any

cage distortion more difficult. As shown in figure 4.18b, further analysis could examine the g(r) in the compression and extension axes of the xy plane during the transient strain increase.

While much of the information lies in the xy plane g(r), there is still value in looking in the other planes. Figure 4.22 shows the steady state of the xy, xz and zy planes for Pe=0.1, 1 and 10 for φ=0.58 after subtracting the state at rest. The different rates show similar features when looking at the same plane, although with less intensity as Pe is decreased. The xy (shear-velocity gradient) plane shows features as extensively discussed, while the xz (shear-vorticity) shows a general increase of the first and second maxima of g(r) with a higher localized intensity along the x axis. The zy (vorticity-velocity gradient) plane shows mirrors the features of the xy plane, with the localized intensity increasing in the y axis. These findings correspond to the smallest value of shear displacements in the z axis and small differences between x and y axes (fig.4.16a), as higher intensities in the respective directions correspond to higher displacements. The slight anisotropic peaks for the zy plane at Pe=0.1 is most probably an artifact of localized ordering at some point during shear, although this is not a general phenomenon.

Through the use of MCT, (Zausch, Horbach et al. 2008) connect the appearance of the stress peak to the local transient super diffusion and a negative value of a generalized dynamical shear modulus G(t). In their formalization of G(t), they connect the decrease of stress after the peak to an approximate time dependent isotropic structure factor. Although we found the connection of the stress peak to the transient super diffusion to be quite complex, our structural data during and after the peak do show strong correlation to the transient stress response. Unlike the theoretical approximation, the structural information extracted from the simulations is highly anisotropic (fig. 4.21). It thus would be of interest to use the structural data from these simulations, or possibly from experimental confocal microscopy, to examine the validity of the theory using exact anisotropic structural data for the prediction of the stress and microscopic displacements responses.

Start-up Shear: Normal Stresses

The first and second normal stress differences are defined as $N_1 = \sigma_{xx} - \sigma_{yy}$ and $N_2 = \sigma_{yy} - \sigma_{zz}$, where σ_{xx}, σ_{yy} and σ_{zz} are the diagonal components of the stress tensor which have negative values. The average of the diagonal components also give the suspension pressure $\Pi = -(\sigma_{xx} + \sigma_{yy} + \sigma_{zz})/3$. Figure 4.23a shows the transient N_1 and N_2 with elapsed strain at Pe=1 and φ=0.58, along with the x-axis pressure component for different Pe. Although the general behavior observed is reminiscent of the σ_{xy} stresses, we find that N_1 has positive values, while

N_2 has negative values. The sign of the normal stress differences can be understood by examining the structure under shear. Figure 4.22 schematically shows the relation of the g(r) intensity to N_1 and N_2 for the xy and zy planes as done in (Foss and Brady 2000). Generally, the increase of intensity along an axis means larger pressure values and thus a decrease of the corresponding diagonal stress element. Consequently, N_1 is positive and N_2 is negative as the g(r) at contact shows more intensity along the y axis of the corresponding images.

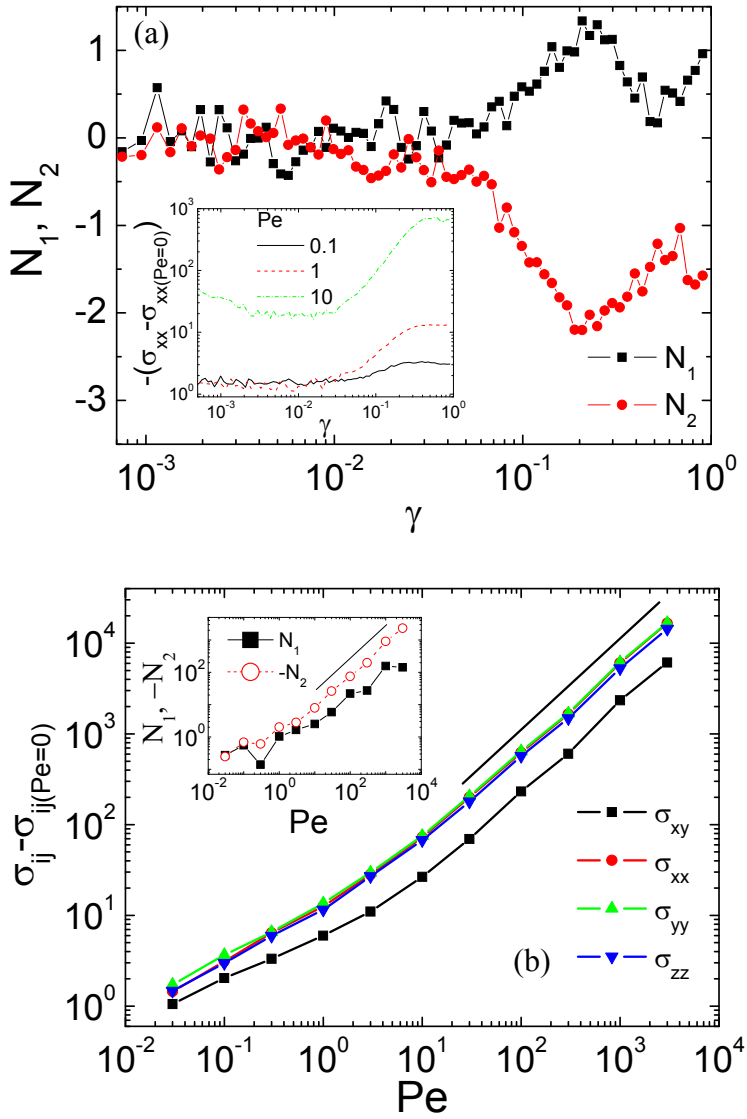

Figure 4.23: a) Transient normal stresses differences N_1 and N_2 vs γ of φ=0.58 for Pe=1. Inset shows the transient behavior of the x-axis pressure components ($-\sigma_{xx}$) after subtracting the state at rest with γ for Pe=0.1, 1 and 10. b) The stress response and the steady state pressure components for all axes as a function of Pe after subtracting the state at rest. Inset shows the normal stresses N_1 and $-N_2$. Lines show a power law slope of one.

Figure 4.23b depicts a rate dependence (flow curve type) of pressures and stresses from simulations at φ=0.58 as taken from steady state values. In order to shorten simulation times, the flow curve was made as in experiments by starting at high rates from a configuration at rest, waiting for a steady state and then using the last configuration of the high rate to run the lower rate. In this way the equilibration time for a steady state was smaller, but each rate was not taken from a startup experiment. After subtracting the pressure stresses at rest, we find that they qualitatively show similar behavior to the σ_{xy} stresses, a slope near unity at high rates, while reducing the slope at lower rates. In the case of φ=0.58, the stresses at the limit of Pe→0 will not show a plateau as for larger φ's, but will rather exhibit a Newtonian slope of 1 as at large time scales (small rates) the particles are fully diffusive exhibiting liquid like behavior. The normal stresses N_1 and $-N_2$ in the inset show similar dependencies, although the noise level is high. The findings here are in general agreement to those found at φ=0.45 from (Yurkovetsky and Morris 2008).

Cessation of Shear: Stress Relaxations, Structure and Dynamics

The stresses and particle relaxation after the cessation of shear were examined with the BD simulations for the various Pe and φ. Again the stresses, dynamics and structural changes are probed. Figure 4.24 shows the stress relaxation for φ=0.62 with the stresses normalized by the stress just before cessation, while the inset shows the non normalized stresses. The relaxation after the high rate shear (Pe=1) is faster, while the two stress relaxations reach a non-zero value at the longest time. Thus we find that for the simulations the general phenomenology is the same as the experimental relaxations at large φ. Specifically, at φ=0.62, the stresses become approximately equal for $t/t_B>1$ (inset of fig. 4.24).

Figure 4.25 depicts the g(r) of the xy plane after subtracting the state at rest during the relaxation for intervals of $t/t_B=0.1$, 1 and 10 after shear cessation. For $t/t_B=0$ the initial distortion of the cage during shear is stronger for high Pe (not shown) as the structures are for all intents the same as the structures during shear. With time the structure relaxes showing smaller intensities as it resemble those at rest. At the longest time scales the structures have not fully relaxed, showing a shadow of the structure during shear. Comparing the structures at the two rates we see larger intensities at initial times, while at longer times show similar intensities. Thus the structural intensities seem to correspond to the stress relaxations of the two rates.

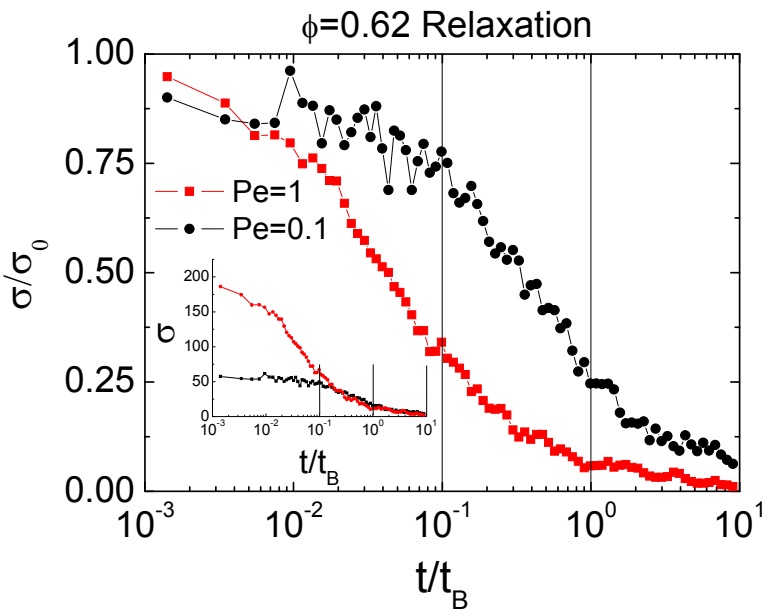

Figure 4.24: Stress relaxation of φ=0.62 after cessation of shear at Pe=0.1, 1 as given from simulations normalized by the stress before cessation. Inset shows the non normalized values, while vertical lines refer to the time scales of fig. 4.25.

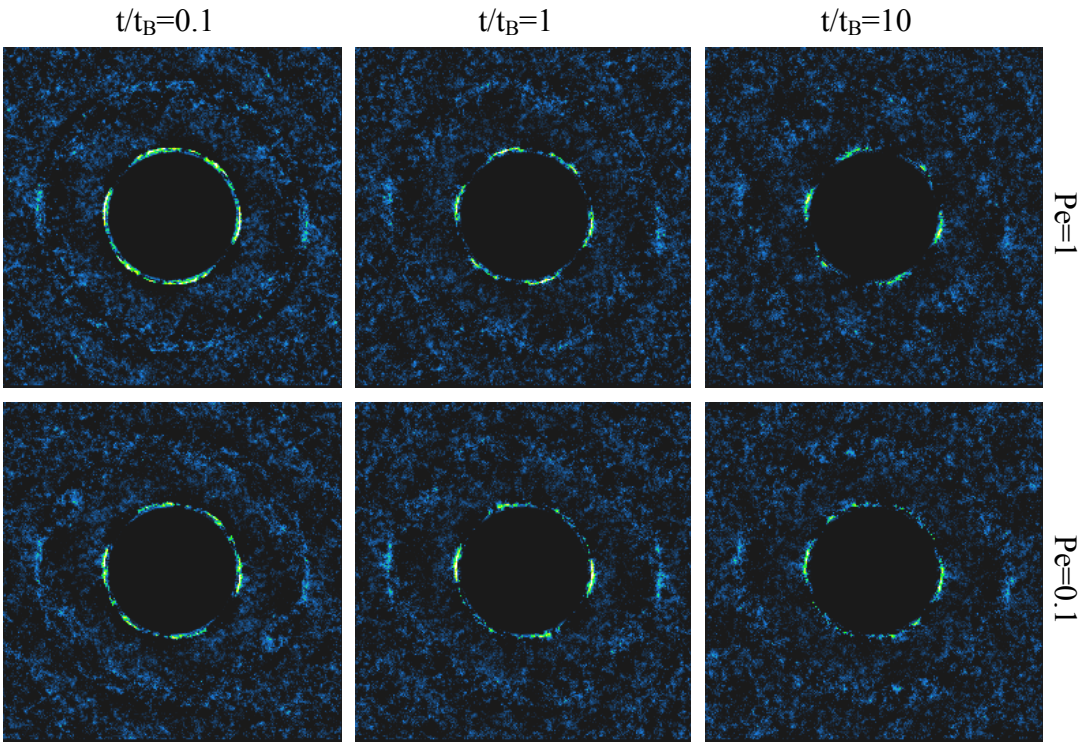

Figure 4.25: g(r) in the xy plane during relaxation subtracting the state at rest for φ=0.62 with Pe=0.1 and 1 (from bottom to top), at t/t_B=0.1, 1 and 10 (from left to right) after stopping shear, averaged over $\Delta t/t_B$=0.02.

The mean squared particle displacements after cessation of shear can be seen in figure 4.26 in the fashion of 4.12, 4.13 and 4.14a. Figure 4.26 compares the steady state displacements at

rest and under shear with the evolving displacements during relaxation, after shear at Pe=1 for φ=0.62 at a short (t_w=0.001) and long (t_w=5) waiting time. Initially, at small waiting and elapsed time the displacements during relaxation are very similar to the displacements during shear, showing an apparent constriction in motion. As time passes and the system progresses though relaxation, the values of the displacements deviate from the curve under shear leaning towards the curve at rest. At larger waiting times, the shorter Δt show close resemblance to the curve at rest, while at longer Δt displacements shows some deviations. Figure 4.26b shows the time evolution of $<\Delta y^2>$ for different Δt as they approach the state at rest, showing that a steady state is mostly achieved after about t/t_B=5 with larger Δt taking more time.

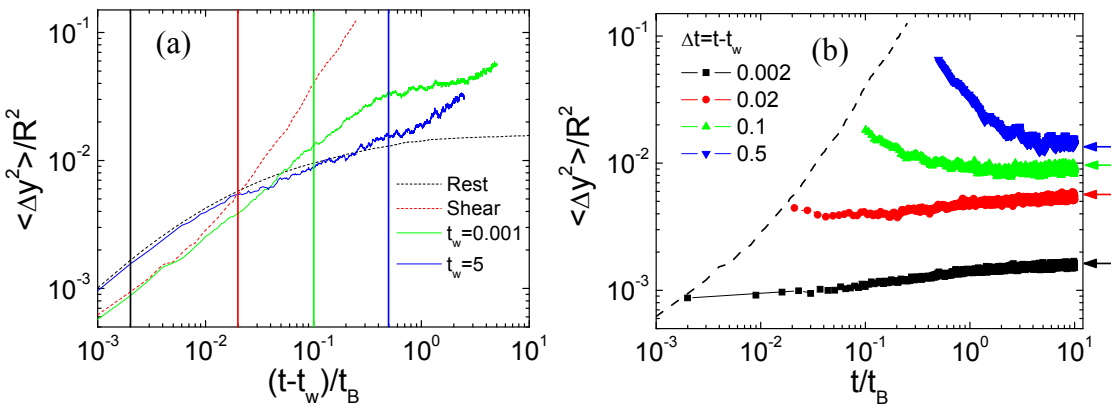

Figure 4.26: Displacements during relaxation of φ=0.58 after cessation of shear at Pe=1 with a) displacements as a function of elapsed time after waiting short (t_w=0.001) and long time (t_w=5), while comparing to the displacements at rest and under steady state shear and b) displacements with time at specific Δt=t-t_w=0.002, 0.02, 0.1, 0.5 intervals. Vertical colored lines in a) correspond to the Δt used in b), while horizontal arrows in b) show the displacements at rest for the specific Δt.

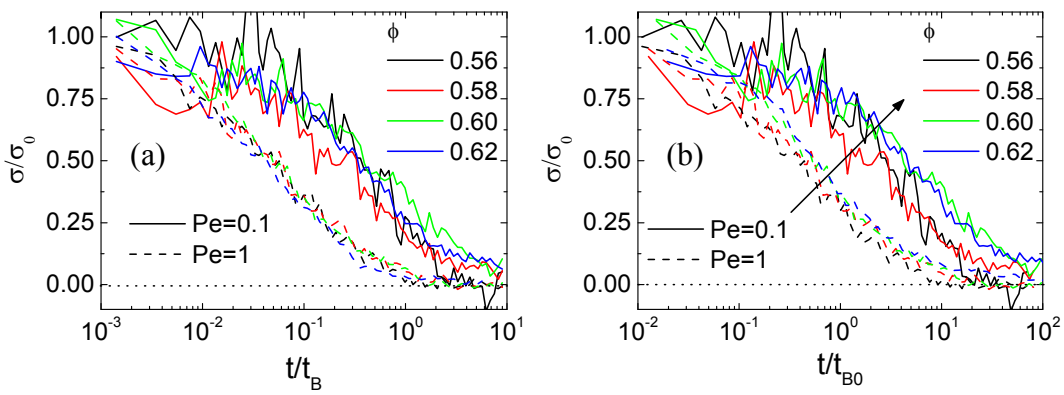

Figure 4.27 Normalized stress relaxations of φ=0.56, 0.58, 0.60 and 0.62 after cessation of shear at both Pe=0.1 and 1 as given from simulations plotted against a) t/t_B and b) t/t_{B0}.

Analysis of the displacements reveals that the relaxation occurs by initially reverting the short time motions of the system back to those at rest and then slowly changing the longer time displacements. The short time constrictions under flow refer to particles having less space while being forced out of cage, thus initially particles which were in the process of jumping out of cage return to an in cage configuration. Afterwards collective longer range motions occur, relaxing a large portion of the stress and slowly diminishing long time displacements. Additionally, the difference in the relaxation time for different rates can be traced back to the constriction effect. At higher rates, relaxation after cessation occurs at a smaller time scales, which can be attributed to the constriction effect and the large number of particles undergoing out of cage motion during shear at any instant. Moreover, at φ=0.62, even though the steady state is mostly achieved after about t/t_B=5, some residual stresses remain as seen in figure 4.24. These may or may not eventually relax with slower collective motions, but we suspect that any subsequent relaxations of stress and displacements are correlated to the out of cage motions of the system, either fully diffusive or through dynamic heterogeneities.

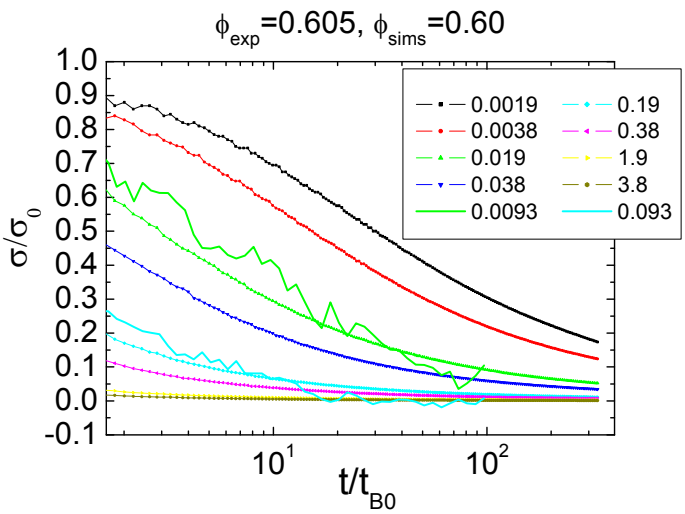

Figure 4.28 Comparison of normalized stress relaxation from experimental φ=0.605 and simulation φ=0.60 with the time scales of the simulations changed as shown in table 4.1.

Figure 4.27a shows the relaxation of stresses for multiple φ and Pe=0.1 and 1 for normalized values of stresses. Even though noise in the measurements is quite high (these are single runs), the curves of different volume fractions fall onto each other. Based on previous discussion, since short time relaxation is related to the shear induced diffusivity and since there is relative invariance in the long time shear induced diffusivity with φ (fig. 4.16b) the superposition of the curves appears valid. In the experiment though, at the same rates the different volume fractions have different relaxations (fig. 4.8). This effect may be due to the different in cage diffusion constants of each φ and thus different applied rate and relaxation

time scale. An example of the shift in relaxation is given in 4.27b, where the relaxation time scales are shifted to simulate experimental data. Unfortunately, using the existing data we are not able to compare the applied Pe as would be shifted in experimental measurements of different φ and constant shear rate, which would make the differences between φ more pronounced. Figure 4.28 shows an instance of superposition of simulation and experimental relaxation stresses for similar values of rates and φ. While the overlap shown may not be generalized with the current experimental and simulation data, it lays down the qualitative agreement between the two.

4.4 Chapter Conclusions

To conclude this chapter, we find that the stress peak in experiments becomes stronger at high Pe and lower φ, although in simulations due to statistical errors this is not as clear. We also find that the strain of the peak increases with Pe and remains generally unchanged with φ, in both experiments and simulations. The relative height the peak as well as the strain is found by structural changes in the pair correlation function to be associated with the structural elongation of the cage during shear.

Simulations generally show that short time displacements decrease with elapsed strain, being more pronounced with increasing φ and Pe. These constrictions are associated with shear induced out of cage motion, as forcing a particle out of cage increases long time diffusivity, but also hinders in cage motion through constriction. A transient super diffusive regime occurs at intermediate time scale displacements, which becomes more pronounced with increasing φ, although less pronounced with increasing Pe. This is related to the transient nature of the start up shear and the transition from the displacements at rest to diffusive long time displacements under shear. Moreover, the long time diffusion coefficient showed large dependence on applied rate, but much smaller dependence on the studied φ.

During shear the steady state g(r) in the xy plane (velocity – velocity gradient) is most affected becoming highly anisotropic, while the xz plane (velocity - vorticity) only shows some compression in the velocity (x) axis. Similarly the zy plane g(r) shows distortion/compression only in the y plane. This correlates to the slightly smaller values of the z-axis diffusion coefficients and pressure stresses under shear. The transient g(r) of the xy plane at low strains is isotropic, turning into a distorted structure as strain increases and showing flow lines along the extension axis when strains increase above yield signifying out of cage diffusion. While cage distortion is more significant at high rates, low rates still distort the structure although do not elongate the cage.

Both experimentally and in simulations, the stress relaxation after cessation of shear is faster for larger Pe while generally becomes slower as φ is increased. Both structural and dynamic analyses from simulations reveal the speed of relaxation to be positively correlated to the shear induced out of cage diffusion coefficient. It is also found that the structure and dynamics revert back to the state at rest at a rate similar to the relaxation of stress.

4.5 References

Akcora, P., H. Liu, S. K. Kumar, J. Moll, Y. Li, B. C. Benicewicz, L. S. Schadler, D. Acehan, A. Z. Panagiotopoulos, V. Pryamitsyn, V. Ganesan, J. Ilavsky, P. Thiyagarajan, R. H. Colby and J. F. Douglas (2009). "Anisotropic self-assembly of spherical polymer-grafted nanoparticles." Nature Materials **8**(4): 354-359.

Besseling, R., L. Isa, P. Ballesta, G. Petekidis, M. E. Cates and W. C. K. Poon (2010). "Shear Banding and Flow-Concentration Coupling in Colloidal Glasses." Physical Review Letters **105**(26): 268301.

Brady, J. F. (2001). "Computer simulation of viscous suspensions." Chemical Engineering Science **56**(9): 2921-2926.

Carrier, V. and G. Petekidis (2009). "Nonlinear rheology of colloidal glasses of soft thermosensitive microgel particles." Journal of Rheology **53**(2): 245-273.

Derec, C., G. Ducouret, A. Ajdari and F. Lequeux (2003). "Aging and nonlinear rheology in suspensions of polyethylene oxide–protected silica particles." Physical Review E **67**(6): 061403.

Foss, D. R. and J. F. Brady (2000). "Structure, diffusion and rheology of Brownian suspensions by Stokesian Dynamics simulation." Journal of Fluid Mechanics **407**(-1): 167-200.

Islam, M. T. and L. A. Archer (2001). "Nonlinear rheology of highly entangled polymer solutions in start-up and steady shear flow." Journal of Polymer Science, Part B: Polymer Physics **39**(19): 2275-2289.

Kobelev, V. and K. S. Schweizer (2005). "Strain softening, yielding and shear thinning in glassy colloidal suspensions." Phys. Rev. E **71**: 021401.

Koumakis, N., A. B. Schofield and G. Petekidis (2008). "Effects of shear induced crystallization on the rheology and ageing of hard sphere glasses." Soft Matter **4**: 2008-2018.

Laurati, M., K. Mutch and S. U. Egalhaaf (Unpublished).

Letwimolnun, W., B. Vergnes, G. Ausias and P. J. Carreau (2007). "Stress overshoots of organoclay nanocomposites in transient shear flow." Journal of Non-Newtonian Fluid Mechanics **141**(2-3): 167-179.

Mohraz, A. and M. J. Solomon (2005). "Orientation and rupture of fractal colloidal gels during start-up of steady shear flow." Journal of Rheology **49**(3): 657-681.

Osaki, K., T. Inoue and T. Isomura (2000). "Stress overshoot of polymer solutions at high rates of shear." Journal of Polymer Science, Part B: Polymer Physics **38**(14): 1917-1925.

Ozon, F., G. Petekidis and D. Vlassopoulos (2006). "Signatures of Nonergodicity Transition in a Soft Colloidal System." Ind. Eng. Chem. Res. **45**: 6946-6952.

Padding, J. T., E. S. Boek and W. J. Briels (2008). "Dynamics and rheology of wormlike micelles emerging from particulate computer simulations." The Journal of Chemical Physics **129**(7): 074903-11.

Ravindranath, S. and S. Q. Wang (2008). "Universal scaling characteristics of stress overshoot in startup shear of entangled polymer solutions." Journal of Rheology **52**(3): 681-695.

Rottler, J. and M. O. Robbins (2003). "Shear yielding of amorphous glassy solids: Effect of temperature and strain rate." Physical Review E **68**(1): 011507.

Sierou, A. and J. F. Brady (2001). "Accelerated Stokesian Dynamics simulations." Journal of Fluid Mechanics **448**(-1): 115-146.

Sollich, P. (1998). "Rheological constitutive equation for a model of soft glassy materials." Physical Review E **58**(1): 738.

Yurkovetsky, Y. and J. F. Morris (2008). "Particle pressure in sheared Brownian suspensions." Journal of Rheology **52**(1): 141-164.

Zausch, J., J. Horbach, M. Laurati, S. U. Egelhaaf, J. M. Brader, T. Voigtmann and M. Fuchs (2008). "From equilibrium to steady state: the transient dynamics of colloidal liquids

Chapter 5 – Oscillatory Shear on Glasses: Stresses, Structure and Dynamics

Abstract

The non-linear oscillatory response of glassy hard sphere suspensions has been examined, both experimentally with rheology and through Brownian dynamics simulations. We found two distinct regimes in terms of stress responses, dynamics and structure under shear, one for the lower frequencies and a second for the higher frequencies of oscillation, the transition related to the time scale of the in cage beta relaxation or equivalently the minimum of G'' in a linear frequency sweep. In terms of rheological response, dynamic strain sweeps going well into the non linear regime show maxima of G'' at strains of about 10% for low frequencies, while higher frequencies exhibit maxima at strains of 100%. The parameters which characterize the third harmonic stresses within the period, I_3/I_1 and δ_3, may quantify the transition between these regimes, the first through a characteristic minimum, while the second more reliably with a transition at high strains from a thinning to a hardening regime.

Furthermore, a dynamic strain sweep with what appeared to be two peaks of G'' and thus inferring two distinct yielding processes was observed in a narrow range of frequencies and high volume fraction. These yielding processes are found to be related to the non harmonic properties of the stress response by showing a transition from a low frequency response at low strains to a high frequency response at high strains.

The stress-strain Lissajous figures were observed to have characteristic shapes in each regime, with the low frequencies showing trapezoid like shapes, with an elastic stress increase of about 10% strain after the maxima of strain and then almost constant stress. The higher frequencies showed a distinct area of reduced stresses in comparison to a simple harmonic response after the maximum of strain, due to reduction of particle collisions, with a range of 50% strain, while additionally showing a viscous response for the rest of the curve.

When increasing the strain, displacements also increased as more particles were able to undergo out of cage motions, while spatial dynamic inhomogenieties and the non Gaussian parameter showed an increase during yielding and then a decrease at larger strains. At the largest strains, displacements were found to occur due to out of cage motion homogenously throughout the system, while for strains around yield the particles were divided into two

populations: one that exhibits in cage displacements and a second that exhibit out of cage displacements. For applied strains that cause the shear induced diffusivity to increase above the diffusivity at rest, we find super diffusive behavior, between the short and long time diffusivities under shear.

Diffusivity at high oscillatory strains showed a linear increase with frequency in the high frequency regime mirroring the viscous loss due to shear activated particle rearrangements. However, in the low frequency regime, diffusivity increased with a power law slope of less than one, depending on the distance from maximum packing, with Brownian activated out of cage displacements. Moreover, intermediate strains near yielding show a much more complex behavior of displacements, with particles showing out of cage diffusive behavior in the low frequency regime, but being trapped within their cages in the high frequency regime. Although in the latter case the non Gaussian parameter is large, the displacements are found to be spatially homogenous between particles in the system.

For a super cooled liquid near the glass transition and in the context of the BD simulations, we recognize three regimes for diffusivity and stresses under high strain or steady state shear. At the highest rates, diffusivity and stresses follow a power law slope of one with applied rate as the stress response is governed by interparticle collisions. For rates corresponding to the displacement plateau at rest, the stress slope is reduced to zero as the entropic cage plasticity is measured, with the diffusivity showing a slope of less than one. At the lowest rates, the long time diffusivity is probed, exhibiting a slope of zero for the diffusion and a slope of unity for the stresses as the system behaves as a fluid.

Lastly, new methods for analysis of the elastic and viscous components of stresses during oscillatory experiments are brought forward and examined against relaxations functions of elastic stresses. The comparisons show that although the new methods are an improvement upon existing decompositions, they still lack the necessary sophistication to extract meaningful physical properties for arbitrary stress responses.

5.1 Introduction/Experimental

Introduction

A simple way of examining the viscoelasticity of a material is by the application of an oscillatory shear field and the measurement of the time-dependent stress response. Compared to other rheological experiments, oscillatory shearing has distinct practical advantages, which makes it an appealing method for rheological characterization. For small strain amplitudes the

shear stress is a simple harmonic function, with a fundamental frequency equal to that of the applied strain, while the small disturbance in the microstructure is mirrored in the linear viscoelastic properties. General aspects of the viscoelastic character of the material can thus be inferred from the magnitudes of the moduli as a function of frequency.

In the nonlinear regime, the stress response to a sinusoidal application of strain contains higher harmonic contributions, which arise from the nonlinearity of the stress as a function of the strain (Wilhelm, 2002). Possibly the first instance of decomposing the oscillatory stresses using the third harmonic can be found in (Philippoff, 1966). Thus, for many complex materials, analysis of the stress response using the fundamental frequency of the applied strain alone is not sufficient for describing its mechanical properties. Analysis based only on the first harmonic complex modulus as a function of frequency can thus be expected to give a partial characterization of a system's mechanical response (Cho, Hyun et al., 2005; Ewoldt, Clasen et al., 2007; Ewoldt, Hosoi et al., 2008; Cho, Song et al., 2010; Ewoldt and McKinley, 2010; Ewoldt, Winter et al., 2010). Fourier transform (FT) rheology, originating in the works of (Onogi, Msuda et al., 1970; Wilhelm, 2002; Klein, Spiess et al., 2007), aims to quantify the nonlinear response of complex fluids by analyzing the harmonic structure of the stress signal measured in large amplitude oscillatory shear LAOS experiments.

Concentrated colloidal systems, glasses in particular, although being generally elastic in character, exhibit a complex transient response to oscillatory shear in which the viscous dissipation mechanism present at small strain amplitudes crosses over to a plastic flow as the amplitude is increased (Carrier and Petekidis, 2009; Brader, Siebenburger et al., 2010; Ewoldt, Winter et al., 2010; Renou, Stellbrink et al., 2010; Rogers and Vlassopoulos, 2010). The onset of plastic flow gives rise to a strong increase in the amplitudes of the higher harmonics. Complicated viscous responses for hard sphere systems have also been reported (Le Grand and Petekidis, 2008).

The purpose of the experimental and simulation work shown in this chapter is to highlight the non-linear oscillatory response of hard sphere glasses in the context of different time scales and correlate them to the state at rest. Additionally, we examine some existing analysis methods used for the non linear stress behavior within the period and propose new methods based on our findings in order to associate stress behavior to microscopic processes.

Fourier Analysis

The simple principles of Fourier analysis of the stress response are as follows. By applying an oscillatory strain field of the form, $\gamma = \gamma_0 \sin(\omega t)$, we retrieve a stress response which may be analyzed by decomposition into the higher harmonics of the frequency as:

$$\sigma(t) = \sigma_e(t) + \sigma_v(t) = \gamma_0 \sum_{n=1}^{\infty} G'_n \sin(n\omega t) + \gamma_0 \sum_{n=1}^{\infty} G''_n \cos(n\omega t) = \gamma_0 \sum_{n=1}^{\infty} G_n^* \sin(n\omega t - \delta_n) \quad (5.1)$$

Here n, which is an odd number due to symmetry conditions (Bird, Armstrong et al., 1987), denotes the number of the higher harmonic present in the response. G'_n and G''_n are the moduli of each harmonic (i.e G'_1=G'), while δ_n is the phase difference of each harmonic from the phase of the applied strain. The stress response for individual harmonics is then:

$$\sigma_n(t) = \gamma_0 \left(G'_n \sin(n\omega t) + G''_n \cos(n\omega t) \right) = \gamma_0 G_n^* \sin(n\omega t - \delta_n) \quad (5.2)$$

The stresses are also separated into elastic, σ_e, and viscous, σ_v, stresses which are described by closed loops in stress-strain and stress-strain rate Lissajous figures respectively (Cho, Hyun et al., 2005). Moreover, the intensity of each harmonic is given by $I_n = \sqrt{G_n'^2 + G_n''^2}$. Since in principal the stress shows symmetry with respect to strain reversal i.e. with $\sigma(\gamma, \dot{\gamma}) = -\sigma(-\gamma, -\dot{\gamma})$, no even harmonics should be present in eq. 5.1.

Thus we may quantify the non linear behavior using the intensity ratios of the higher harmonics to the first. When the ratio I_n/I_1 shows a value close to zero, the state is mostly linear, while when the ratio rises, non linearities also become significant. In effect though, since this chapter deals with non linearities that are dominated by the third harmonic, we mainly use I_3/I_1 as a measure of non linear behavior.

Based on the values of the non linear stresses (n>1) at the maximum strain and the maximum strain rate we may define different states of non linearity under oscillatory shear (Ewoldt, Hosoi et al., 2008). If $\sigma_{n>1}(\gamma_{\max}) > 0$ then we identify the sample in this state as strain hardening, while when $\sigma_{n>1}(\gamma_{\max}) < 0$, we may characterize it as strain softening. Similarly with the rate, we may define $\sigma_{n>1}(\dot{\gamma}_{\max}) > 0$ to be shear thickening and $\sigma_{n>1}(\dot{\gamma}_{\max}) < 0$ to be shear thinning.

These descriptors give a physical phenomenological meaning to the shape of the curves in terms of where the non linearities appear within the period. Thus they refer to the increase

(hardening) or decrease (softening) of the elastic stress and the increase (thickening) or decrease (thinning) of the viscous stress due to the addition of higher harmonics, always in comparison to the first harmonic.

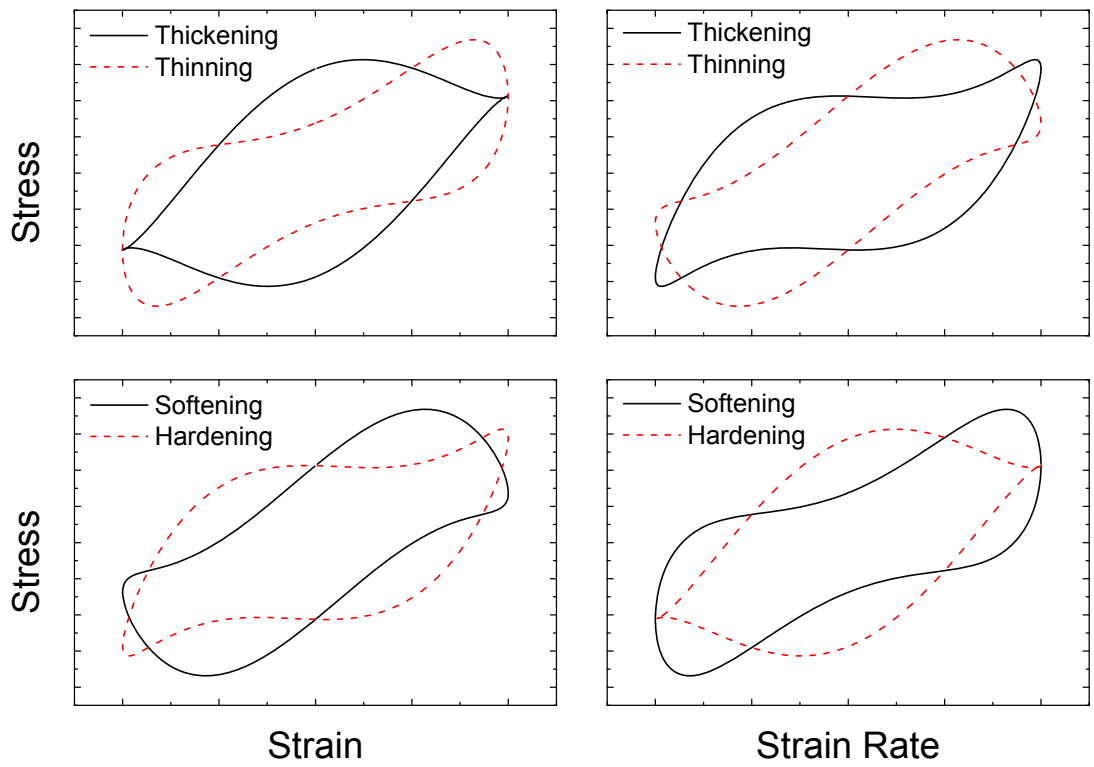

Figure 5.1: Numerical plots showing examples of different third harmonic phases as shown in legend. The equations followed for strain and stress are $\gamma=\gamma_0\sin(\omega t)$ and $\sigma=I_1\sin(\omega t-\pi/4)+I_3\sin(3\omega t-\delta_3)$, while δ_3 varies as $-\pi/2$, 0, $\pi/2$ and π for shear thinning, strain softening, shear thickening and strain hardening respectively and $I_3/I_1=0.15$.

From such definitions, states of hardening and softening are mutually exclusive as are thickening and thinning, while it is common to describe states of non linearity by both rate and strain definitions. For example a state may exhibit both thickening and hardening, while the ratio of the stresses at the maxima of stress and rate will show the dominant effect. Again, in the case of the measurements and simulations of this chapter, since non linearity is dominated by the third harmonic, we use the phase δ_3 to quantify the descriptors.

As an example we add a third harmonic response to an existing simple harmonic response, using specific values of $I_3/I_1=0.15$ and G'=G'', as shown in figure 5.1. The Stress-Strain and Stress-Rate Lissajous type figures of the four descriptors is shown based on simple equations of $\gamma=\gamma_0\sin(\omega t)$ for the strain and $\sigma=I_1\sin(\omega t-\pi/4)+I_3\sin(3\omega t-\delta_3)$ for the stress. δ_3 varies as $-\pi/2$,

0, $\pi/2$ and π for shear thinning, strain softening, shear thickening and strain hardening respectively.

In comparison to existing literature (Ewoldt, Hosoi et al., 2008), the phase δ_3 gives the ratio of e_3 (e_3=G'$_3$) to ν_3 (ν_3=G''$_3/\omega$), thus defining whether the elastic or viscous component of non linearity is stronger. The e_3 and ν_3 parameters may be used to extract further physical meaning from the shape of the Lissajous curve. However, in this work we use the I_3 and δ_3 simply as parameters for characterizing the shape of the curves and to track changes with the variation of strain and frequency. Therefore, concerning the stress response we will avoid any further in depth analysis and instead use the structural and microscopic motions information from the BD simulations further in the chapter in order to physically explain the data.

Experimental

Two different hard sphere sizes were examined. Polydisperse non crystallizing PMMA hard spheres dispersed in Octadecene (R=358nm) as well as a mixture of Octadecene and Bromonaphthalene (R=130nm, solvent mass ratio 1:0.446) were prepared as discussed in chapter 2. Initially the sample volume fractions were calculated by the distance from maximum packing φ_{RCP}=0.670 as estimated by an approximate radial polydispersity of 10% and as shown in table 5.1. Given that the two particle sizes need to be compared, the sample volume fractions have been scaled to reflect similar values of linear elasticity, thus the φ presented reflect a dilution from maximum packing of φ_{RCP}=0.687 for the smaller spheres in the mixture of solvents and φ_{RCP}=0.650 for the larger spheres in Octadecene. The differences may occur due to the standard deviation of φ for each packing ($\Delta\varphi=\pm0.006$), although more importantly, due to the differences of the actual radial polydispersity for the two spheres and possibly the particle interaction potential in the two solvents. Thus we examine three samples as shown in table 5.2 of smaller spheres with φ=0.602, 0.620 and 0.639 and two of the larger spheres with φ=0.620 and 0.600.

Rheological measurements were conducted on the ARES strain controlled rheometer with the addition of the solvent vapor trap for evaporating solvents. The data from within the period was extracted from the analog torque and strain signal output, as well as using the software of the instrument. In order to acquire the non linear data, each strain was measured for multiple periods, from 4-20 depending on the applied frequency, while always ensuring that the points for each acquired period were above 300.

	R_c=130nm, φ_{RCP}=0.670			R_c=358nm, φ_{RCP}=0.670	
φ	0.588	0.605	0.624	0.618	0.639

Table 5.1: Calculations of φ for the samples used in this chapter as taken from an initial random close packing of φ_{RCP}=0.670 for a polydispersity of 10%.

As discussed in the chapter 2 we define the bare $Pe'_0=t_{B0}\omega$ and calculate for the larger spheres t_{B0}=0.90sec, while for the smaller spheres t_{B0}=0.04sec. By using the two different sphere sizes, we are able to probe a greater range of time scales and thus frequencies. As in chapter 4 we correlate simulations with experiments and thus Pe'_0 and Pe' with a factor $D(\varphi)/D_0$. This factor can also be used to normalize experimental responses of different φ's with each other. Since here the maximum packing fraction differs between sphere sizes, the values presented in table 5.2 are different for the two sizes and different from chapter 4.

	R_c=130nm, φ_{RCP}=0.687			R_c=358nm, φ_{RCP}=0.650	
φ	0.602	0.620	0.639	0.600	0.620
$Pe'_{0bare\ (\omega=1rad/sec)}$	0.040	0.040	0.040	0.898	0.898
$D_s(\varphi)/D_0$	0.130	0.113	0.096	0.101	0.080
$Pe'_{dressed\ (\omega=1rad/sec)}$	0.308	0.354	0.417	8.895	11.230

Table 5.2: Time multiplication factor $\mathbf{c=D_s(\varphi)/D_0}$ that links experimental $Pe'_0=Pe'_{bare}$ to the $Pe'=Pe'_{sims}=Pe'_{dressed}$, with $Pe'_0=c\cdot Pe'_{sims}$ and $t/t_{B0}= t/(c\cdot t_{Bsims})$, as well as Pe'_{0bare} and Pe' at ω=1rad/sec.

Simulations

In order to avoid crystallization during the simulation runs, an effect especially pronounced with the application of non linear oscillatory shear, polydispersity was added. Polydispersity in these simulations is represented by a discrete Gaussian distribution of radii having N/13 components with a root mean squared deviation of 10%, where N is the number of total particles, while the denominator value of 13 is specifically chosen as it allows close representation of the distribution with varying N. Distributions of 3%, 5% and 7% were also tested. In these cases amorphous configurations did not always crystallize at rest, but the application of non linear oscillatory shear, especially at high Pe', induced crystallization which had strong defects and were not necessarily FCC parallel or perpendicular to shear direction (i.e. with the 111 plane of the crystal lying on the xz plane) as seen in experiments.

All of the shown simulations were carried out in a cubic box with 1005 particles both at rest and under shear, while some runs were additionally performed with 1440 or 4860 particles. The particles were randomly placed and left for some time (a maximum of $300t_B$) to reach

equilibrium before applying shear. Simulations were run with a time step of $2\pi\ 10^{-4}\ t_B$ or less, while structural properties, displacements and stresses under shear were averaged over at least 10 oscillations. Acquisition of data for each simulation point under oscillatory shear consisted of application of the oscillation from a state at rest and then waiting for a steady state.

5.2 Experiments

Strain/Frequency Sweeps

We begin the presentation of data with the linear viscoelasticity of the samples used. Since the purpose of this study is not a comprehensive analysis of the volume fraction dependence of viscoelasticity, but rather a general description of it, only a few φ have been studied. Figure 5.2a and 5.2b shows the frequency sweeps of the small and large spheres respectively. Both the stresses and the time scales have been normalized as discussed above and in chapter 2, the stresses showing increasing values with increasing φ. The frequency dependence shows viscoelastic properties which are expected from hard sphere glasses (Koumakis, Schofield et al., 2008) as additionally discussed in chapters 3 and 4. The minimum of G'', which is associated within MCT (Mason and Weitz, 1995) and the Generalized Stokes Einstein equation (Mason, 2000) as a transition between the in cage (β) and out of cage (α) relaxations, is seen to slightly move to smaller time scales with increasing φ, better seen in 5.2a. While in glassy hard spheres, α-relaxation due to out of cage diffusion is strictly speaking expected to be infinite, the minimum may also reflect long time non diffusive displacements due to dynamic heterogeneities. The slope of G' becomes smaller with increasing φ due to the decreasing contribution of Brownian motion at longer time scales. While we should be able to overlap the curves of the different sized spheres on a single figure, the differences between the solvents and the uncertainties of the absolute volume fractions, suggest the need for a more detailed study of φ.

The non linear response is initially probed by strain sweeps at different frequencies, giving the elastic and viscous moduli (figs. 5.3 and 5.4 for the smaller and larger spheres respectively). The onset of non linearities begins at around 1% strain, with higher φ showing an earlier onset. Figure 5.4a (low Pe'_0) exhibits simple features for yielding as seen in many colloidal systems; the decrease of G' with increasing strain and the simultaneous appearance of a peak in G'' at approximately 10% strain as well as the constant power law slopes at high strains with G' having roughly twice the slope of G''. The terminal slopes of G' and G'' of the different tests and samples are gathered in table 5.3.

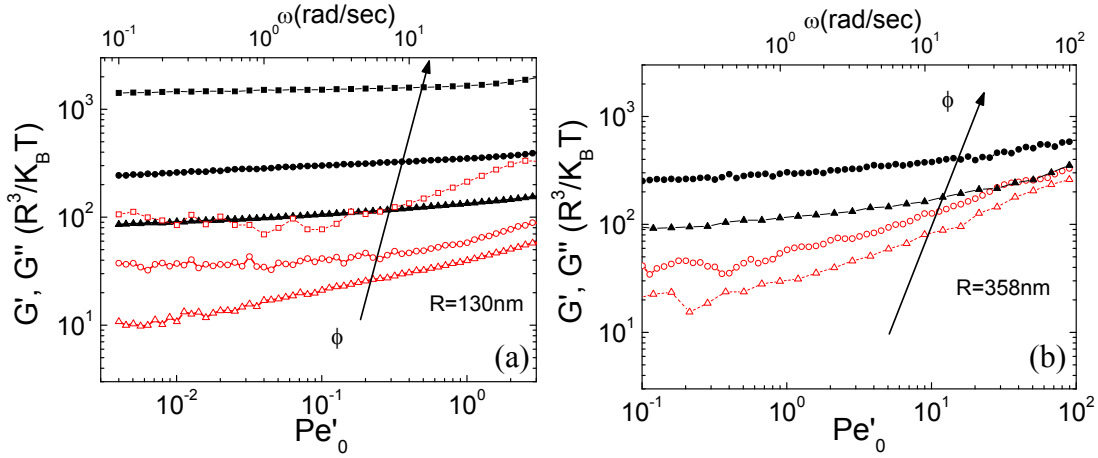

Figure 5.2: Frequency sweeps of hard spheres showing the elastic (solid, black) and viscous (open, red) moduli of a) smaller spheres (130nm) of φ=0.602, 0.620 and 0.639 in a mixture of Bromonaphthalene and Octadecene and b) larger spheres (358nm) at φ=0.600 and 0.620 in Octadecene.

The curves in figures 5.3b and 5.4 however appear to exhibit richer yielding features. The higher φ of 5.3b clearly shows two distinct peaks in the G'' with increasing strain, while in fig. 5.4 the higher Pe'_0 shows a broad peak of G'' at higher strains than normal (≈100%) and an additional peak for G'. These findings are unusual in view of hard sphere interactions and have been associated so far only with attractive colloidal systems (Pham, Petekidis et al., 2006) in chapters 8 and 9. Below we show that such peaks are unrelated to attractions and will be discussed and elucidated within the context of non linear stresses inside the period of oscillation utilizing BD simulations that show the microscopic rearrangements and structural changes. Upon closer observation of the curves, it appears that a single peak of G'' dominates the lower Pe' at strains of about 5-10%, while at high Pe' a single but broader peak dominates at strains of 30-100% with an added shoulder for G'. With this in mind, the two peaks of figure 5.3, give the impression of an intermediate frequency response where both types of peaks are able to appear.

In order to elucidate the origin of the described yielding behavior in oscillatory shear we examine the deviation of the stresses from a simple sinusoidal response. In figure 5.5 there is an example of the decomposition of an experimental stress response in a simple sinusoidal response (first harmonic) and the sum of the first and third harmonic responses. A simple application of the first harmonic deviates quite a lot from the measured stress and although may give a qualitative measure of the elastic and viscous behavior, it fails to capture the details of the non linear stresses. The addition of the third harmonic makes a better fit on the experimental data, but again fails to capture the details. In order to truly capture all the information of an arbitrary periodic stress response, an infinite amount of harmonics is needed. Despite these observations, the analysis of the data that will be presented mainly

focuses on the changes of the third harmonic of the stress, which carries the bulk of information for the non linearities in the scope of this study.

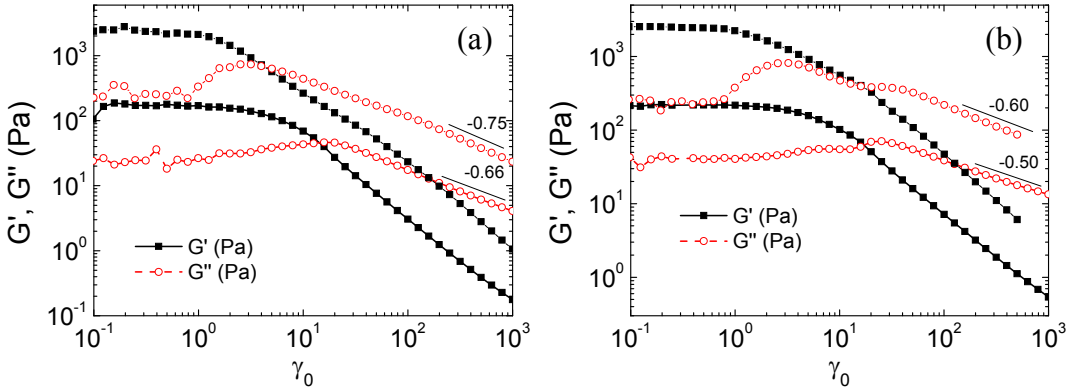

Figure 5.3: Strain sweeps showing the elastic (solid, black) and viscous (open, red) moduli of the smaller spheres (130nm) at φ=0.602 and 0.639 at a) ω=1rad/sec or Pe'_0=0.04 and b) ω=10rad/sec or Pe'_0=0.4. The power law slopes at high strains are also shown for the viscous moduli.

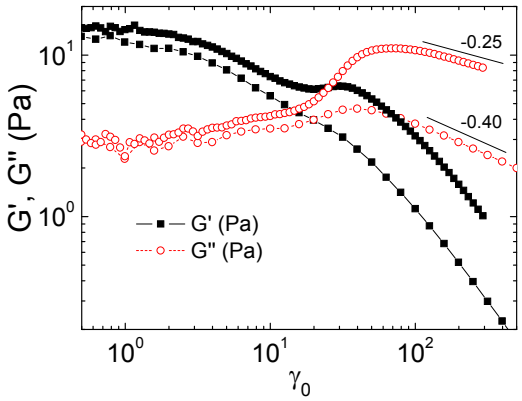

Figure 5.4: Strain sweeps showing the elastic (solid, black) and viscous (open, red) moduli of the larger spheres (358nm) at φ=0.600 at ω=0.1rad/sec and 1rad/sec or Pe'_0=0.2 and 2. The power law slopes at high strains are also shown for the viscous moduli.

While the appearance of higher harmonics complicates the simple physical meaning of viscoelasticity in the non linear regime, the value of G'' still gives a clear measure of the energy lost in a period independently of any higher harmonics. This is easily clarified by the understanding that the integral of stress with strain in a closed loop (energy lost) produces zero values for all components of the odd harmonics, both elastic and viscous, except for the viscous component of the first (G'') (Onogi and Matsumoto, 1981). Thus even with the complications of higher harmonics, the values of G'' in the strain sweeps is clearly defined and thus can provide information on the non linear behavior under oscillatory shear independently of the amplitude of the higher harmonics.

φ (R=130nm)	Pe'$_0$=0.04 G', G''	Pe'$_0$=0.4 G', G''	φ (R=358nm)	Pe'$_0$=0.09 G', G''	Pe'$_0$=0.9 G', G''
0.602	-1.21, -0.66	-1.09, -0.50	0.600	-1.22, -0.40	-1.16, -0.25
0.620	-1.35, -0.71	-1.21, -0.54	0.620	-1.29, -0.55	-1.08, -0.27
0.639	-1.40, -0.75	-1.28, -0.60			

Table 5.3: Large strain power law slopes of elastic and viscous moduli, as taken from the preceding strain sweeps for the examined samples and oscillation frequencies.

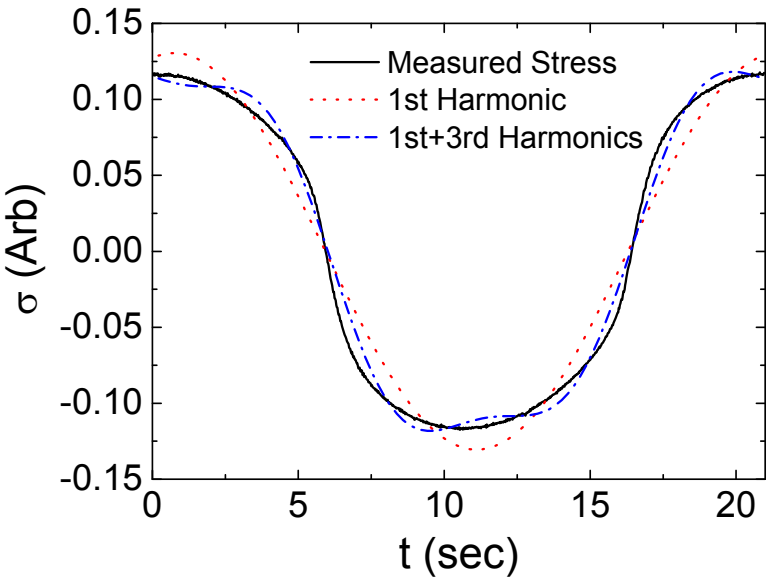

Figure 5.5: Example of a non linear stress response at ω=0.3rad/sec and γ_0=100% for small spheres (R_c=130nm) at φ=0.64 with time. Measured stresses (arbitrary units) are shown in comparison to the first harmonic stress and the sum of the first and third harmonic stresses.

Table 5.3 gathers the terminal slopes of both G' and G'' for all strain sweeps shown. A general phenomenological description follows that the slopes increase with higher φ and become smaller with higher Pe'$_0$. As discussed, the slopes of G'' produced by the strain sweeps have a simple physical interpretation associated with them and are easier to explain, unlike the slopes of the elastic moduli which also affected by the higher harmonic components of the stress response.

A simple explanation can be found from a steady shear flow curve (Chapter 4, fig. 4.6). At low rates, viscosity decreases with a large slope (less than -1) as the system is shear thinned, but as the rate is increased the large slope slowly increases to approach zero as the terminal viscosity is approached and the system behaves as a Newtonian fluid, i.e. when the viscosity is constant with applied rate (or equivalently when the stress increase is linear). Plastic flow

may be defined as the flow occurring at the lowest rate showing an almost constant stress, the yield stress, with changing rate. Similarly in oscillatory shear, as the frequency is increased the G'' terminal slope at high strains approaches zero (Newtonian flow). Reversely, with increasing concentration, stronger thinning occurs at the frequencies producing slopes closer to -1 (Plastic flow). This implies that the terminal slopes of G'' as measured a strain sweep are in fact not terminal, but will eventually approach zero at the limit of very high strains as in a simple flow curve. In truth, for concentrated systems of hard spheres, the high rate terminal slope of the stress for steady shear experiments to date have always been found to be less than one. However the simulations of chapter 4 (fig. 4.24) clearly show a slope of one at the highest rates. While this view is simplistic and avoids addressing the non harmonic and transient stresses within the period, subsequent findings in this chapter support this general idea.

Non Harmonic Behavior and Lissajous Plots

Although showing the characteristics of the higher harmonics (I_n and δ_n) will give a fingerprint of the behavior at the specific ω and γ_0, it is paramount to assess the properties of the system under shear from the shape of the curve, as physical properties are difficult to ascribe to the numbers in question. Figures 5.6 and 5.7 show Pipkin type diagrams (stress vs strain) of the non linear behavior at three strains of γ_0=10, 30 and 100% and three frequencies for the two different sized spheres as shown on the figures and in their captions. The two figures have similar values of Pe'_0 and seem to probe similar time scales. At the lowest Pe' (fig 5.7) the Lissajous exhibit a trapezoid shape which becomes squarer with increasing strain. The increase of stress that occurs from maximum strain to maximum stress has a range of about 5-10% strain that occurs for all γ_0. As Pe' is increased, the figures become more ellipsoid like, smoothing out the angles of the lower Pe'. At even higher Pe' (fig 5.6), the shapes begin to deviate from their ellipsoid features by exhibiting what appear to be areas of reduced stress when compared to a simple harmonic (seen in further analysis in fig. 5.50) after the occurrence of the strain maxima (the first and third quadrant of the curve). These stress drops have a range of 30-50% strain and are reminiscent of less concentrated non-Brownian sphere behavior under oscillatory shear as seen in (Gadala-Maria and Acrivos, 1980).

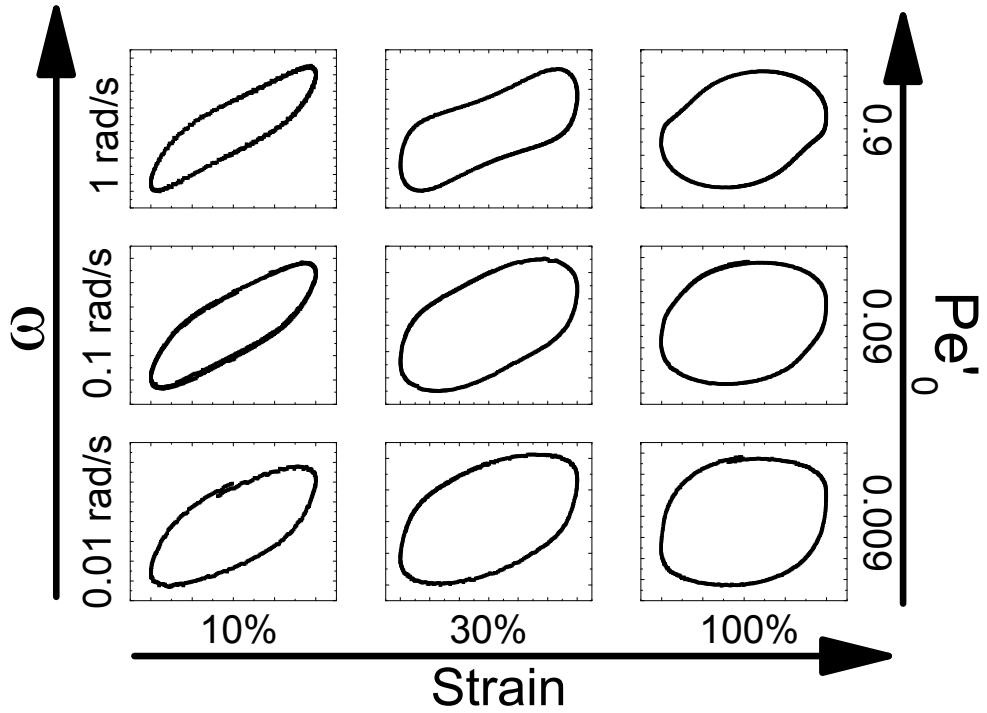

Figure 5.6: Pipkin type diagram (stress vs strain) showing strains of 10%, 30% and 100% at different frequencies (ω and Pe'_0) for larger spheres of R=358nm at φ=0.62.

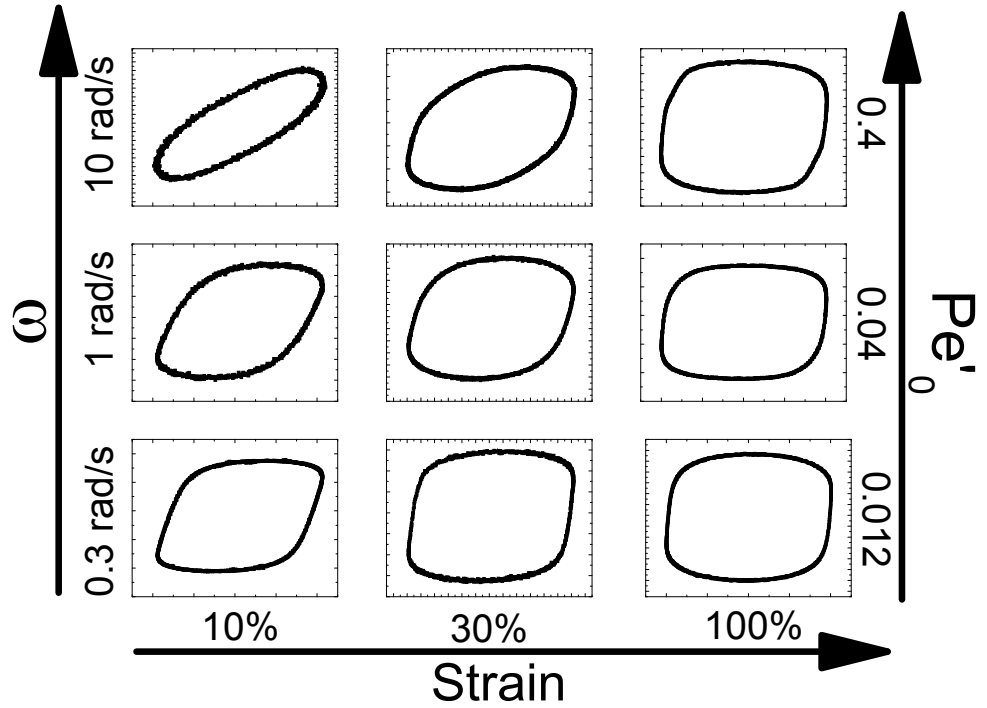

Figure 5.7: Pipkin type diagram (stress vs strain) showing strains of 10%, 30% and 100% at different frequencies (ω and Pe'_0) for smaller spheres of R=130nm at φ=0.64.

With this simple observation of the Lissajous shapes we find two distinct yielding regimes of non linear behavior dominated by the applied frequency or Pe'. The applied strain does not

seem to change the general yielding shape, but only the number of features that can be seen. For example, the high Pe' and low strains are not able to show the extent of the stress reduction, which at the highest strains is found to be of the order of 50% strain. From the preceding discussion, and as will be shown later in more detail, since non linearities can be quantified by I_3/I_1 we find that low frequencies will generally exhibit large values (trapezoid, fig. 5.7), followed by a minimum at intermediate values (ellipsoid, fig. 5.6 & 5.7) and an increase again at high frequencies (fig. 5.6). Generally, the phases are more difficult to interpret, although by comparison with figure 5.1 it is clear that within the period intermediate strains show strain hardening behavior at the lowest Pe', while the highest Pe' they show shear thinning behavior. These results show a span of Pe' wider than initially estimated by Pe'_0, which may be due to the difference in φ and will be discussed.

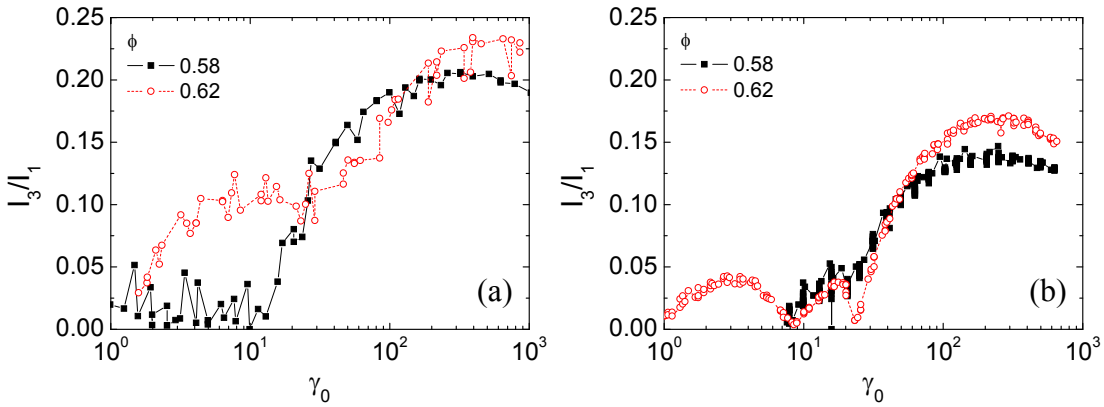

Figure 5.8: The strain sweeps of figure 5.3 showing the non linear component I_3/I_1 of the smaller spheres (130nm) at φ=0.60 and 0.64 at a) ω=1rad/sec and b) ω=10rad/sec.

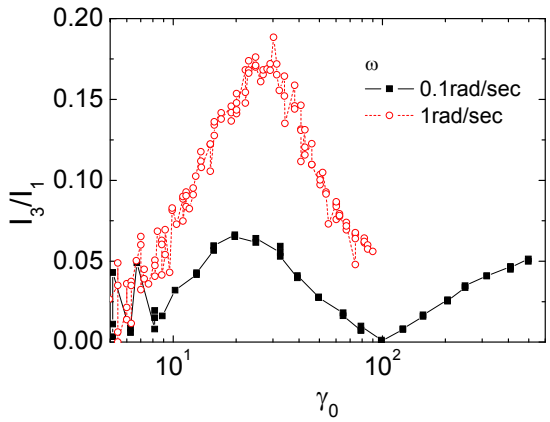

Figure 5.9: The strain sweeps of figure 5.4 showing the non linear component I_3/I_1 of the larger spheres (358nm) at φ=0.62 at ω=0.1rad/sec and 1rad/sec.

Even though the values of I_n and δ_n do not generally have clear physical meanings, it still is important to examine these values as they do give important information on the dependencies

(ω, γ_0, φ) of non linearities under oscillatory shear. Thus figure 5.8 and 5.9 show the I_3/I_1 contribution to the stresses for the strain sweeps shown in figures 5.3 and 5.4 respectively. Similarly figs 5.10 and 5.11 show the third harmonic phase δ_3. The variations in intensity of the third harmonic seem to follow some of the features of the corresponding strains sweeps. In the linear regime the values are close to zero, while showing an increase at the beginning of non linearity. In some of the cases, a strong variation in the slope of I_3/I_1 with strain shows a corresponding variation in the G' and G''. In other cases, the minima that appear can be simply explained by the changes in the Lissajous shape due to increasing strain, as discussed for the Pipkin diagrams. For example, in figure 5.7 for ω=1rad/sec as one increases strain, the system changes from a trapezoid shape at low strains to more square shape at higher strains. In between the two limits, a minimum in I_3/I_1 will occur as the shape closely approaches an ellipsoid.

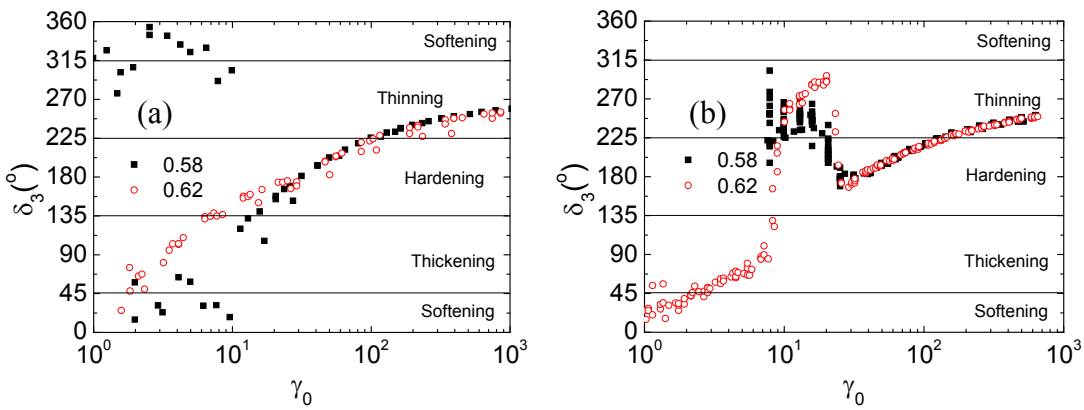

Figure 5.10: The strain sweeps of figure 5.3 showing the phase of the third non linear component δ_3 of the smaller spheres (130nm) at φ=0.60 and 0.64 at a) ω=1rad/sec and b) ω=10rad/sec.

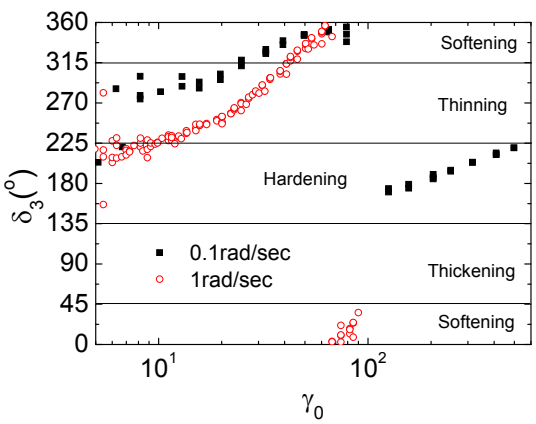

Figure 5.11: The strain sweeps of figure 5.4 showing the phase of the third non linear component δ_3 of larger spheres (358nm) at φ=0.62 at ω=0.1rad/sec and 1rad/sec.

Phases are similarly problematic, although more robust in their meaning as they refer to the position of deviations from the ellipsoid shape and not the intensity of non linearity which may change along with the simple viscoelastic contribution. Thus it is logical when in figure 5.10, δ_3 begins from a strain softening behavior with the maximum stress occurring near the maximum strain, as the trapezoid shape extends towards this strain. At high strains, δ_3 approaches a shear thinning behavior as the initial increase asymptotically shifts to a square shape. Similarly in 5.11, δ_3 reflects the position of the stress decrease.

It must be noted that in the representation of δ_3, the various areas which have been highlighted as softening, thinning, hardening and thickening, do not represent sharp transitions from one area to another. They rather show the area of the dominant effect; i.e. one can have both an effect of thinning and hardening at the same time and when $\delta_3=225^o$, both effects are of equal intensity.

Since I_3 and δ_3 simply reflect the shape of the Lissajous, any maxima, minima or changes in values do not necessarily detect transitions of the non linear behavior. Indeed, the bulk of observed features in this study simply state the gradual changes of the Lissajous shapes. An exception arises for φ=0.64 (and to a lesser degree for φ=0.62) in the strain sweeps of figs 5.3b, 5.8b and 5.10b. At around 20-30% strain a second peak of G'' appears, I_3/I_1 is abruptly reduced to zero and δ_3 also shows a sudden change from thinning to hardening. The higher strain Lissajous of ω=10rad/sec of figure 5.7 shows a general trapezoid/square shape, but apparently the discussed small stress decrease of high Pe' also appears. In this specific intermediate frequency and φ, both general types of non linear behavior are seen in the Lissajous, while G' and G'' reflect this in the strain sweep by showing the two peaks of G'', one for each yielding regime.

In order to elucidate the character of the two yielding regimes at different frequencies, we measured the stress response at a range of frequencies, while keeping a constant non-linear applied strain amplitude. In figures 5.12 and 5.13 we show the results of the non-linear measurements for the larger spheres and φ=0.62 at γ_0=30% and 100%. As expected from figure 5.7, the I_3/I_1 of 5.12a shows large values at low and high frequencies along with a minimum approaching zero at intermediate values. The two strains generally show similar behavior with the major difference being the shifted positions of minima. The differences in the minima do not refer to a shift between the two regimes for the two strains, but rather capture the different shapes of the curves due to varied strain. As an example, while in fig 5.12a at Pe'_0=0.9 the 100% strain shows a minimum, figure 5.7 and figure 5.13b shows that the specific point is well within the high Pe' regime. Perhaps a more accurate representation

of the shift is given by δ_3 in figure 5.12b which shows the deviation from a plateau value and thus the transition into a different regime at approximately Pe'_0=0.1.

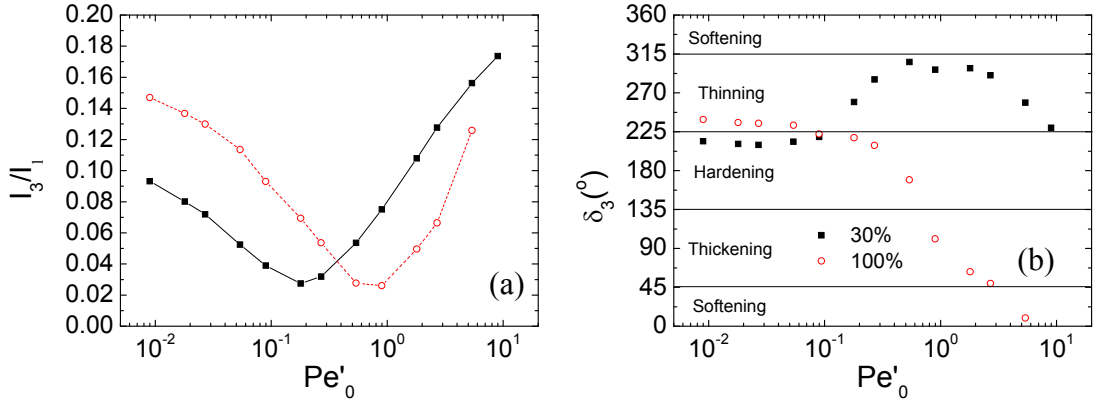

Figure 5.12: Non linear components with changing frequency for φ=0.62 for larger spheres (R=358nm) at γ_0=30% (solid, black) and 100% (open, red) showing the non linear component a) I_3/I_1 and b) phase δ_3.

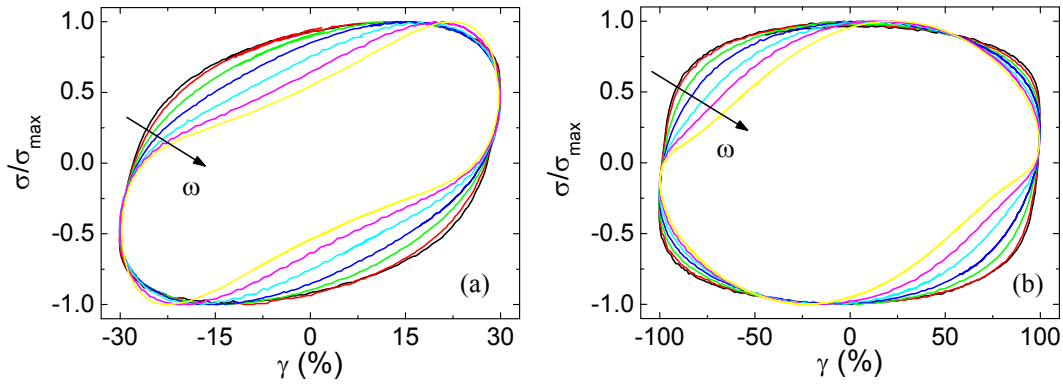

Figure 5.13: Normalized stress-strain Lissajous figures of φ=0.62 for larger spheres (R=358nm) at a) γ_0=30% and b)100% corresponding to experimental data of figure 5.12 (every two points).

Similarly figures 5.14 and 5.15 show the frequency dependence of two strains for the smaller spheres and larger φ. In 5.14a there is a much more complicated picture with I_3/I_1 showing undulations that, upon examination of the respective Lissajous figures (5.15b), do not show a strong differentiation in shape. The undulations seen especially at 100% seem to refer to the subtle changes in shape towards a trapezoid with sharper corners at the lowest frequencies. At γ_0=30%, similar reasons construct the curve of 5.14a. At the highest Pe'_0 of figure 5.14b, we see a strong deviation from the "plateau" values of δ_3, which at higher frequencies should lead to the transition seen in the larger spheres.

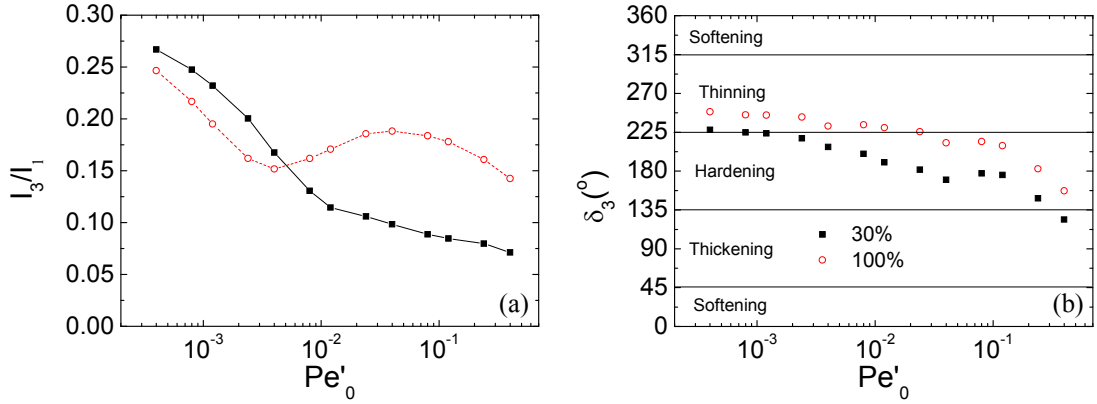

Figure 5.14: Non linear components with changing frequency for φ=0.64 for larger spheres (R=130nm) at γ_0=30% (solid, black) and 100% (open, red) showing the non linear component a) I_3/I_1 and b) phase δ_3.

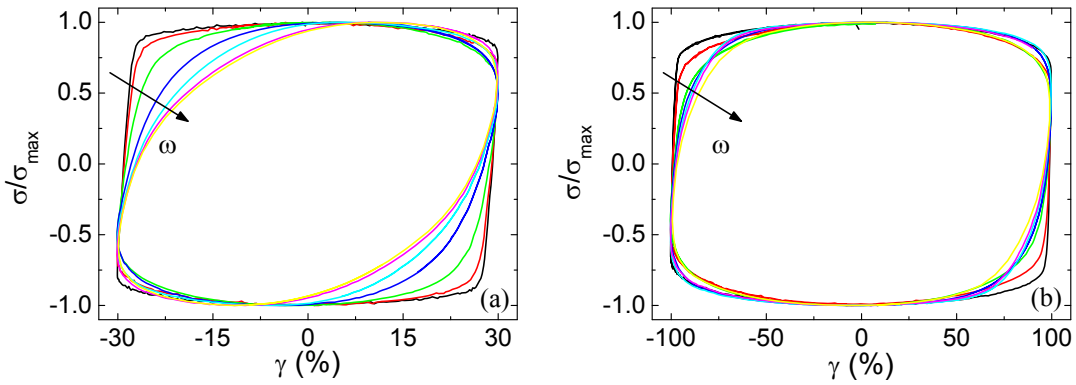

Figure 5.15: Normalized stress-strain Lissajous figures of φ=0.64 for smaller spheres (R=130nm) at a)γ_0=30% and b)100% corresponding to experimental data of figure 5.14 (every two points).

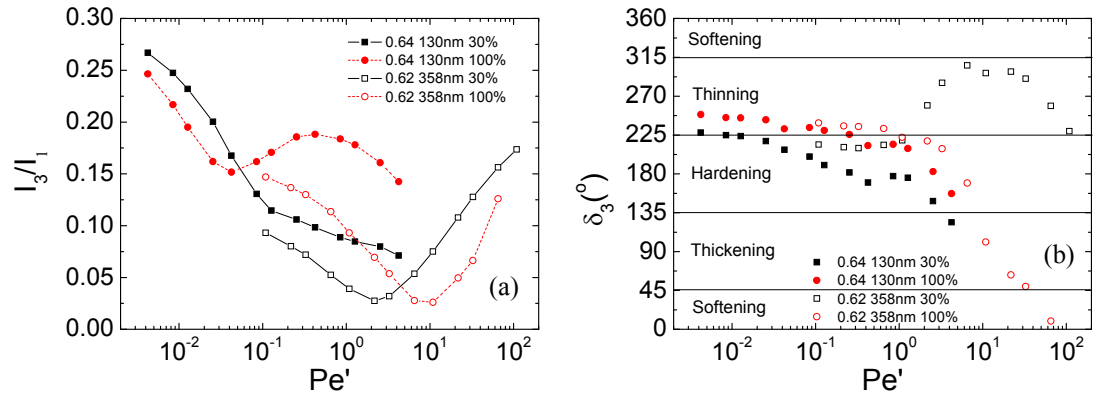

Figure 5.16: Non linear component I_3/I_1 with changing Pe' (dressed) of φ=0.64 for smaller spheres and φ=0.62 for larger spheres for γ_0=30% (solid) and 100% (open).

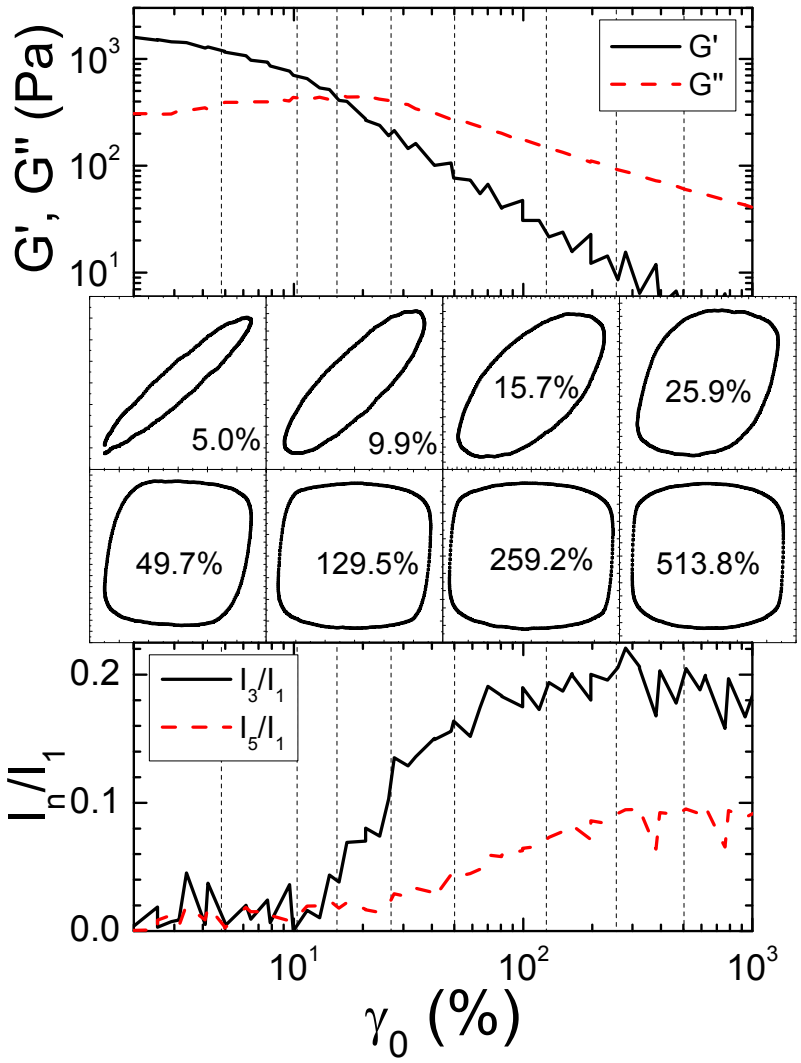

Figure 5.17: Dynamic strain sweep data of φ=0.602 for R=130nm (ω=1rad/sec or Pe'_0=0.04) showing the viscoelastic moduli with strain (top), the contribution of the higher harmonics I_3/I_1 and I_5/I_1 (bottom) and the Lissajous stress-strain figures (middle) at select strains as indicated by vertical lines and strain values within each figure.

When results of the two size spheres are plotted together with a Pe' referring to the time scales of the specific φ, as in figure 5.16, the data at first glance seem to be incompatible. We believe that the incompatibilities stem from the difference in yield strains, a consequence of different volume fractions. The high φ (small spheres) has a smaller yield strain and thus smaller linear regime allowing less time for the system to relax its structure during oscillation at a fixed frequency. In this way the Lissajous shapes and higher harmonics are more susceptible to changes as different frequencies are probed. Even though these are different φ, the phases of fig. 5.16b show a deviation at the same Pe', which is the start of the transition to the high Pe' regime. For γ_0=100% the phases almost superimpose, while for γ_0=30% they deviate differently, possibly due to the proximity of the strain to yielding. It is important to note, as discussed in the introduction of this chapter, that the descriptors given by the third

harmonic phase (thickening, thinning etc.) are incomplete without the higher harmonics, although here the deviations should be small.

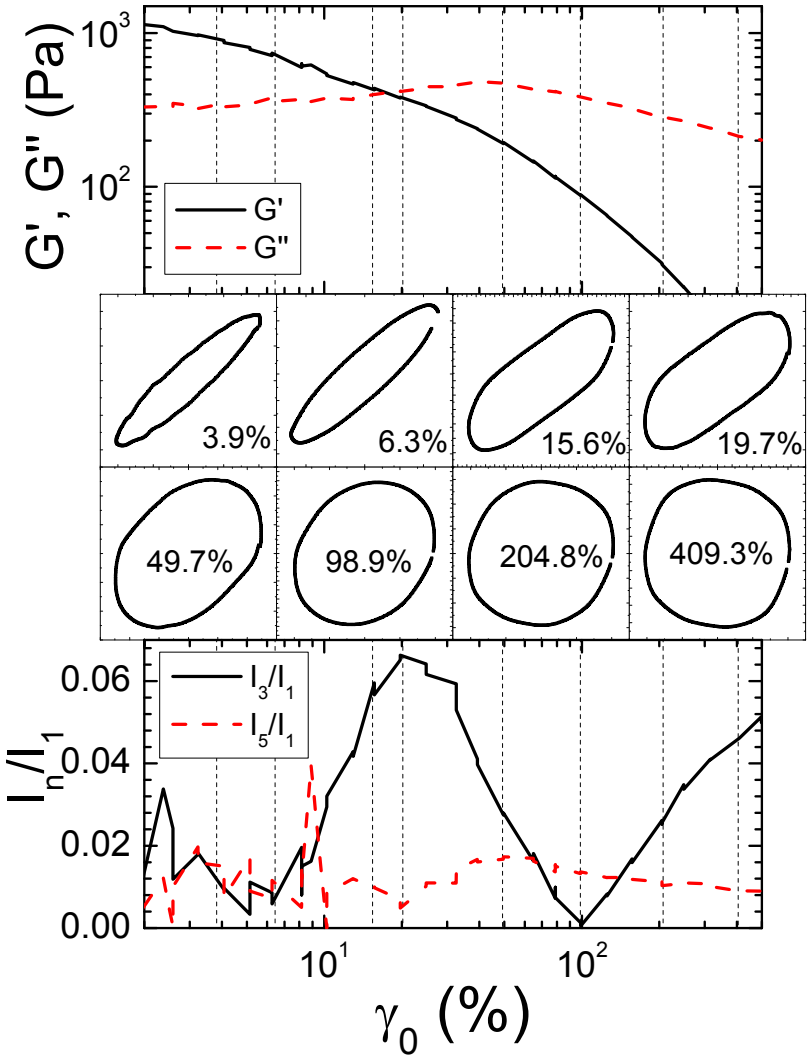

Figure 5.18: Dynamic strain sweep data of φ=0.600 for R=358nm (ω=0.1rad/sec or Pe'_0=0.2) showing the viscoelastic moduli with strain (top), the contribution of the higher harmonics I_3/I_1 and I_5/I_1 (bottom) and the Lissajous stress-strain figures (middle) at select strains as indicated by vertical lines and strain values within each figure.

Summary and Comparison of Non-Harmonic Behaviors

The previously discussed strain sweeps exhibiting single peaks of G'' at low strains (fig. 5.17, low Pe'), at high strains (fig. 5.18, high Pe') and with two peaks (fig. 5.19, intermediate Pe' and high φ) are now presented in detail and compared to each other. These figures show the elastic and viscous moduli, along with the non linear parameter I_3/I_1 and Lissajous figures corresponding to key positions within the strain sweep. This detailed presentation allows one to qualitatively see the evolution of the non linearities.

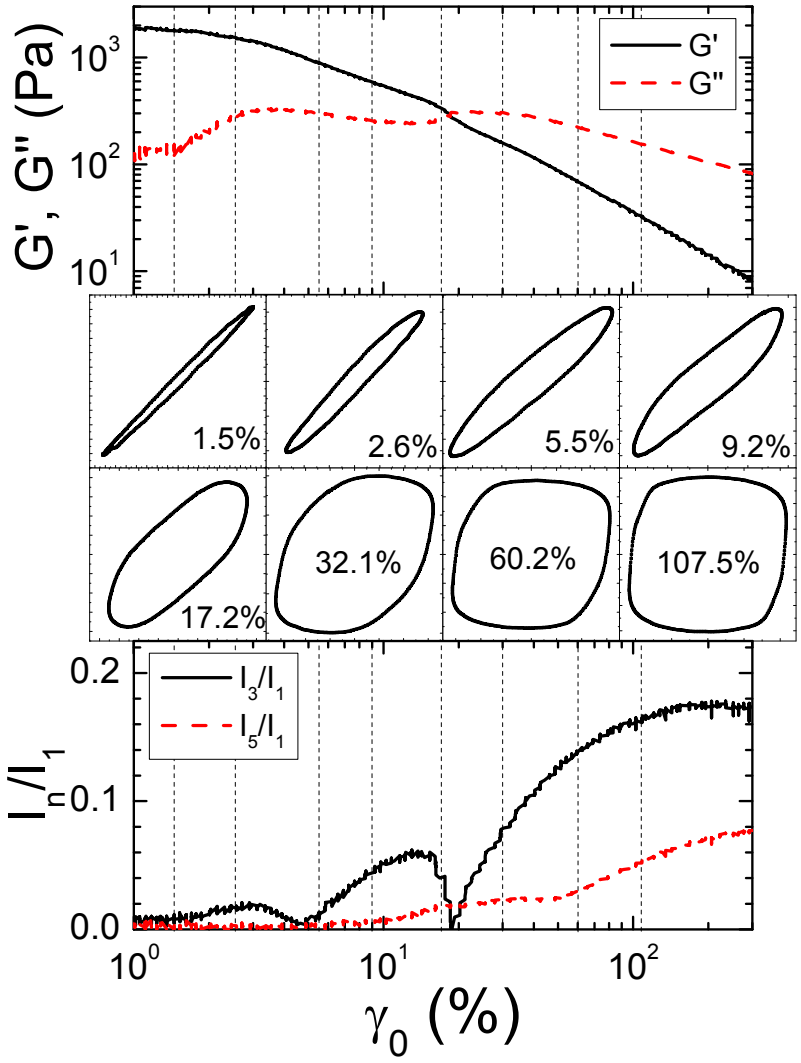

Figure 5.19: Dynamic strain sweep data of φ=0.639 for R=130nm in the area of the two peaks (ω=10rad/sec or Pe'_0=0.4) showing the viscoelastic moduli with strain (top), the contribution of the higher harmonics I_3/I_1 and I_5/I_1 (bottom) and the Lissajous stress-strain figures (middle) at select strains as indicated by vertical lines and strain values within each figure.

In 5.17, a trapezoid shape begins emerging above 10% strain, showing a monotonic increase and subsequent plateau of I_3/I_1 and I_5/I_1. Fig. 5.18 similarly shows an increase of the non linear parameters above 10%, but in this case they describe the appearance of the high Pe' stress drop at the strain maxima. The maximum of I_3/I_1 at about 20% in this case actually represents the extent of the stress drop, with the reduction of I_3/I_1 at higher strains showing the reduction of non linearity. The peaks of G'' in the two figures originate from the shape variations of the low (5.17) and high (5.18) Pe' regimes respectively. In the case of the two peaks of G'' (5.19) in the intermediate Pe' regime, under γ_0=10% there is little or no appearing high Pe' regime stress drop in the Lissajous curves, while as strain and thus average

strain rate both increase, a transition to the high Pe' regime occurs. Moreover, the Pe' where this strain sweep occurs is at the transition from low to high Pe' regime (fig 5.16b); Increasing rates of higher strains may allow the transition to occur much like in the case of a constant strain and increasing oscillation frequency.

In fig 5.20 the Lissajous of four characteristic non linear oscillatory responses encompassing the high and low Pe' limit as well as large (100%) and small (30%) applied strains are shown. In addition we plot the total elastic and viscous decompositions taken from the fundamental as well as the higher harmonic contributions as discussed in literature (Cho, Hyun et al., 2005). A main finding of this analysis refers to the elastic stress at the maxima of strain and the difference between the two Pe' regimes. While in the low Pe' regime a higher slope than the average is observed (5.20c, 5.20d), the high Pe' regime reversely shows a lower slope (5.20a, 5.20b). Although these decompositions are mathematically well defined, the actual physical meaning behind these decompositions is quite vague. Further in this chapter, with the help of simulations and further experiments, we try to understand these decompositions and possibly improve upon them.

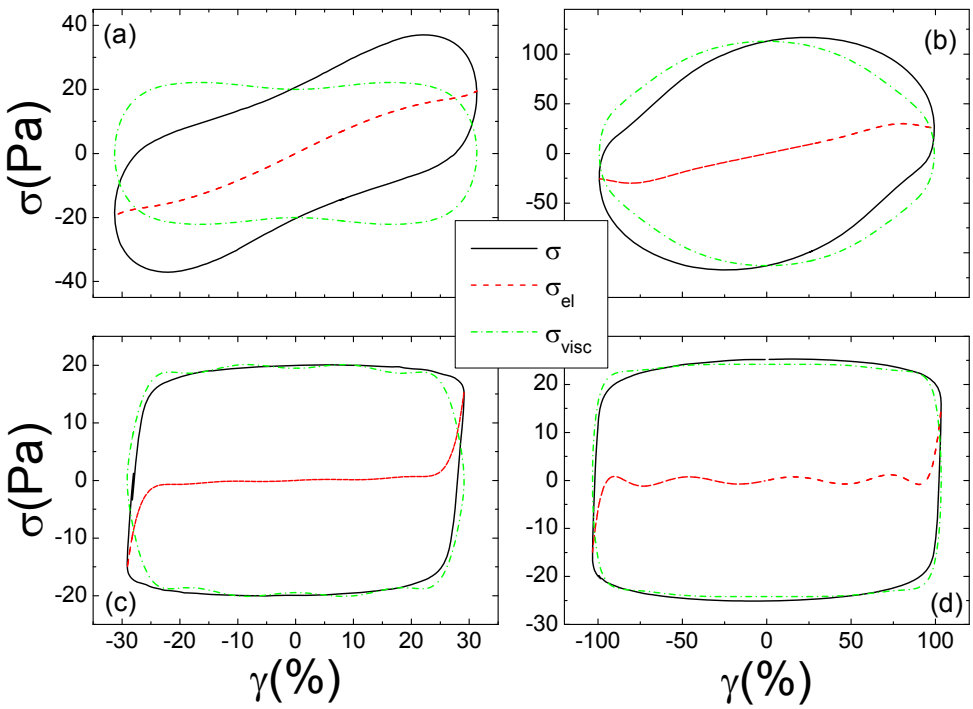

Figure 5.20: Lissajous of four general non linear oscillatory responses as shown in previous figures with ω=1rad/sec (Pe'_0=2) and large spheres (R=358nm, High Pe' regime) for a) γ_0=30% and b) γ_0=100%, while ω=0.3rad/sec (Pe'_0=0.012) and small spheres (R=130nm, Low Pe' regime) for c) γ_0=30% and d) γ_0=100%. The elastic and viscous stress components are also shown (Cho, Hyun et al., 2005).

5.3 Brownian Dynamics Simulations

Stresses under Shear

The experimental rheological results clearly show two distinct non linear regimes with changing frequency. Although the phenomenology of this is established, there is no clear understanding of the physical processes that cause these two regimes to occur. Brownian dynamics simulations are thus used to investigate the microscopic and microstructural changes behind the observed phenomena, by examination of the stresses, dynamics and structures during oscillations, on average and within the period. The stress data coming from the simulations are found to qualitatively agree with the experiments, as seen for chapter 4. The analyses of the stresses are performed in a similar manner to the experimental data calculating the first harmonic G', G'' moduli, the higher harmonic I_3/I_1 and phase δ_3, as well as examining the Lissajous figures.

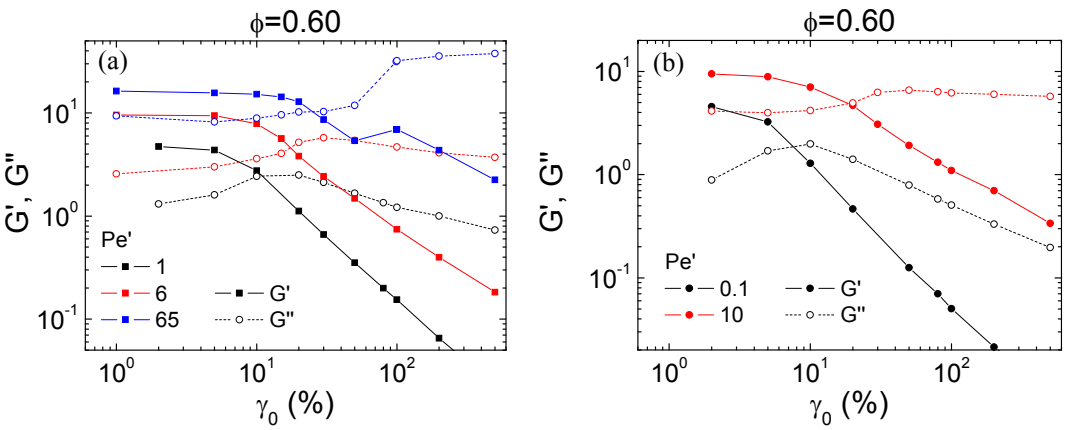

Figure 5.21: Strain sweeps showing the elastic (solid) and viscous (open) moduli of φ=0.60 for a) Pe'=1, 6 and 65 and b) Pe'=0.1 and 10.

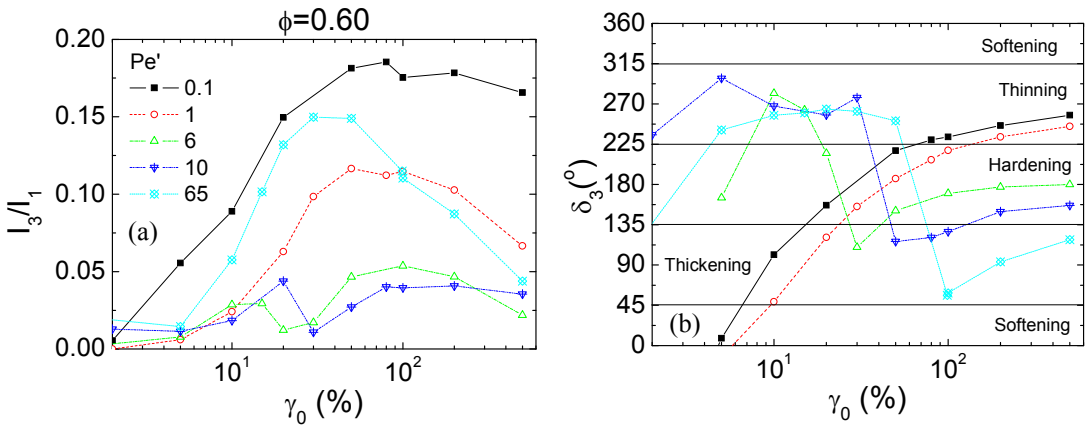

Figure 5.22: The strain sweeps of fig 5.21 for φ=0.60 at Pe'=0.1, 1, 6, 10 and 65 showing the non linear components a) I_3/I_1 and b) phase δ_3.

We first look at a single volume fraction in the glass regime (φ=0.60) by following dynamic "strain sweeps" for a few different Pe'=0.1, 1, 10, 6 and 65, as seen in figures 5.21 and 5.22. Unfortunately, the long time of the simulation runs do not allow large numbers of strains per strain sweep as in the case of experiments, but the general features seen in experiments are still observed. For the lower Pe', non linear behavior begins with a peak in G'' occurring at strains of about 10%, followed by shear thinning with constant decreasing slopes for G' and G''. As Pe' is increased, the slope of G' and G'' during thinning increases and the peak of G'' moves to higher $\gamma_0 \approx 100\%$ as in experiments (figs 5.3 and 5.4). The two peaks of G'' seen in figure 5.3b are not obvious in the simulations, even at Pe'=6 at the closest estimated calculation (Table 5.2) and as furthermore determined later in the text from the δ_3 vs γ_0 figure 5.22b and the δ_3 vs Pe' figure 5.26b. In truth however, the amount of available strains are not enough to discern these details in the sweep.

The non linear components of these strain sweeps are presented in figure 5.22. The I_3/I_1 seen here roughly corresponds to the experimental data of figures 5.8 and 5.9, showing a non monotonic frequency dependence of the curves with decreasing values from low to intermediate Pe' (0.1-10) and then increasing again at Pe'=65. Various features, maxima and minima, can also be correlated with the change in frequency, low Pe' showing a rather monotonic increase with strain to a plateau value, intermediate strains showing various minima, while highest Pe' showing a maximum at $\gamma_0 \approx 30\%$. However, unless a detailed experimental volume fraction characterization is performed, it is not possible to make a consistent quantitative comparison between simulations and experiment, as small variations in φ produce non trivial differences in the extracted non linear quantities and the estimated time scales.

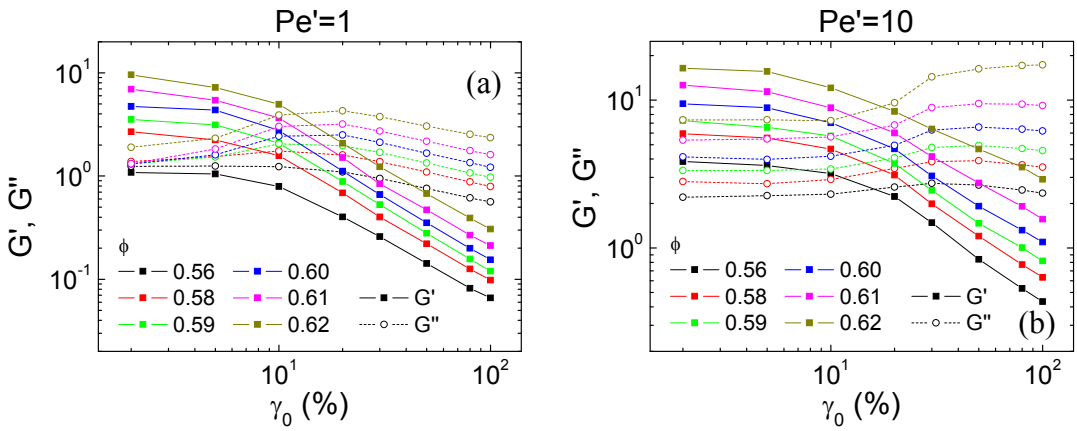

Figure 5.23: Strain sweeps showing the elastic (solid) and viscous (open) moduli of multiple φ for a) Pe'=1 and b) Pe'=10.

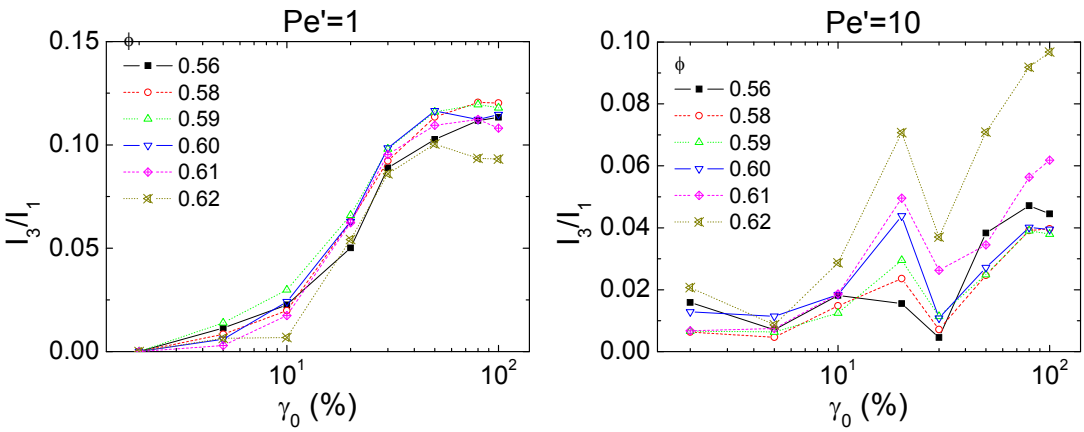

Figure 5.24: The strain sweeps of fig 5.23 for multiple φ showing the non linear component I_3/I_1 for a)Pe'=1 and b)Pe'=10.

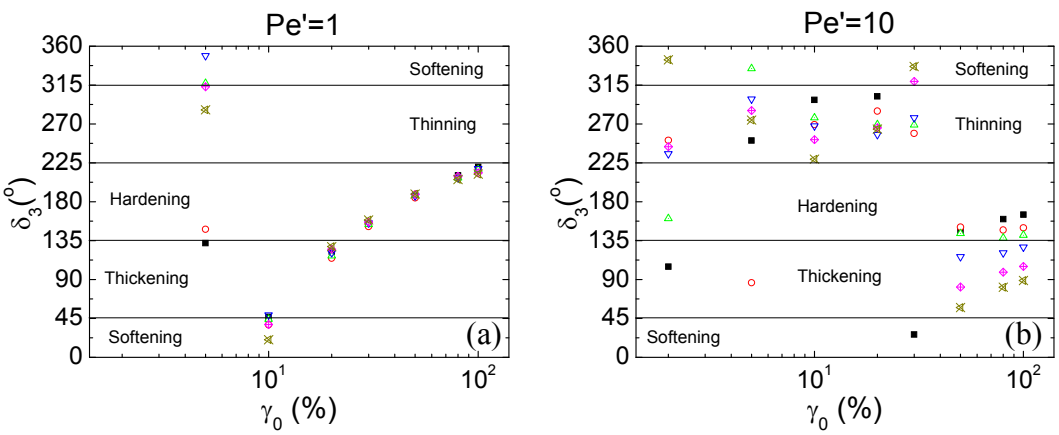

Figure 5.25: The strain sweeps of fig 5.23 for multiple φ (legend as in fig 5.24) showing the non linear component δ_3 for a) Pe'=1 and b) Pe'=10.

The phase δ_3 from the simulations of 5.22b similarly shows correlations to experimental data as seen in 5.10 and 5.11. The low Pe' exhibit a monotonic increase towards a plateau in the shear thinning regime at high γ_0, while as Pe' increases this plateau moves towards values in the shear thickening regime with values at low γ_0 beginning in the thinning regime. Although lacking statistics and having few points, the abrupt jumps in δ_3 seen in fig 5.10b, which are indicators of the two peaks in G'', are possibly seen in Pe'=6.

In figures 5.23 (G', G''), 5.24 (I_3/I_1) and 5.25 (δ_3) for Pe'=1 and 10, we similarly examine multiple φ from below the glass transition of φ=0.56 up to 0.62. The viscoelastic moduli show simple dependencies with φ, with an increase of the elastic and viscous moduli with φ for both Pe'. The peak of G'' for Pe'=1 at about 10% becomes more pronounced with increasing φ and does not seem to change its position. The terminal power law slopes at high γ_0 do not

change strongly and remain at values of about -1.2 and -0.45 for G' and G'' respectively, although possibly due to the lack of hydrodynamic interactions in BD, these values deviate significantly from experimental values. Experiments (fig 5.3) show that the slopes do change with φ, which is most probably due to the difference in the experimental dressed Pe' between φ sheared at the same ω (Table 5.2). The higher Pe'=10 shows the peak of G'' at higher γ_0, as shown before, with the peak becoming substantially stronger with increasing φ and not reaching a terminal state at the final point of γ_0=100%.

The third harmonic intensities seen in figure 5.24 closely resemble experimental data from 5.8, showing a monotonic increase with strain for Pe'=1 (lower frequency regime), while capturing the peak at intermediate strains and subsequent increase for Pe'=10 (higher frequency regime). At Pe'=1 the intensities are generally unaffected φ, while at Pe'=10 a general increase in non linearity with φ is observed, although keeping the qualitative picture with changing strain quite similar. The similarities observed between experiment and simulation with regard to I_3/I_1, also extend to the phases δ_3 of figure 5.25 and the experimental data of 5.10. We see a similar stability with φ as for I_3/I_1 for Pe'=1, although at Pe'=10 there is a φ dependence seen especially at the high γ_0 limit, which shows a transition of the plateau from the hardening regime at low φ to the thickening regime at high φ.

The frequency dependence of the non linear properties for a fixed φ at γ_0=30% and 100% is shown in figure 5.26, similarly to the experimental results of 5.16. As stated before, although the I_3/I_1 shows a minimum in fig 5.26a similarly to experiments, a quantitative comparison is hampered by uncertainty due to the experimental determination of φ and the absence of hydrodynamic interactions in BD. It is interesting though to note that the minima occur at similar time scales (Pe'≈10). The phases (δ_3) show a stronger correlation with experiments, with the curve of γ_0=30% starting at low strains between thinning and hardening, decreasing and then showing an abrupt shift up to the thinning regime. For γ_0=100%, there is a decrease of the phase starting at low Pe' from the thinning regime almost reaching the softening regime at the highest Pe'. Experiments at high Pe' do not show plateau values for the phase, which most possibly is because of the proximity to the high rate hydrodynamic thickening which cannot be captured with these simulations. The high rate hydrodynamic thickening regime, related with particle hydroclusters, should not to be confused with the thickening regime of the third harmonic phase, which refers to the deviation from simple harmonic oscillatory stress within the cycle.

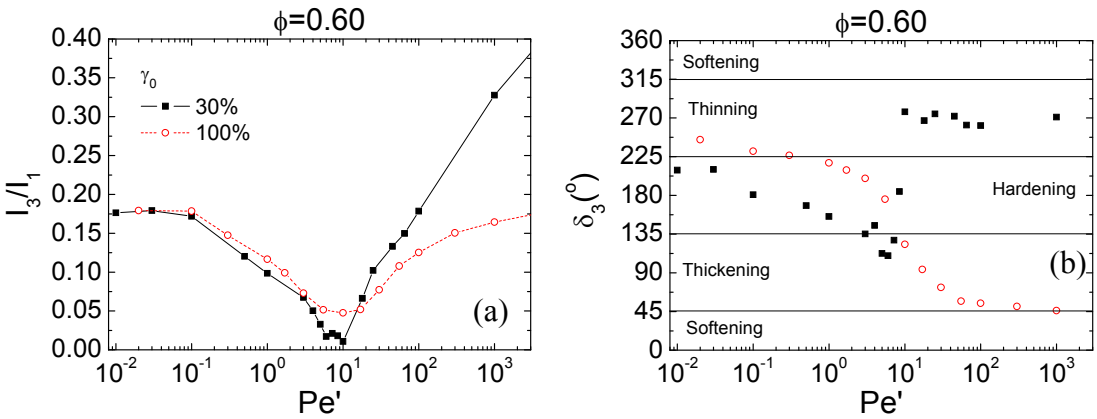

Figure 5.26: Non linear frequency sweeps of φ=0.60 for γ_0=30% and 100% showing the non linear component a) I_3/I_1 and b) phase δ_3.

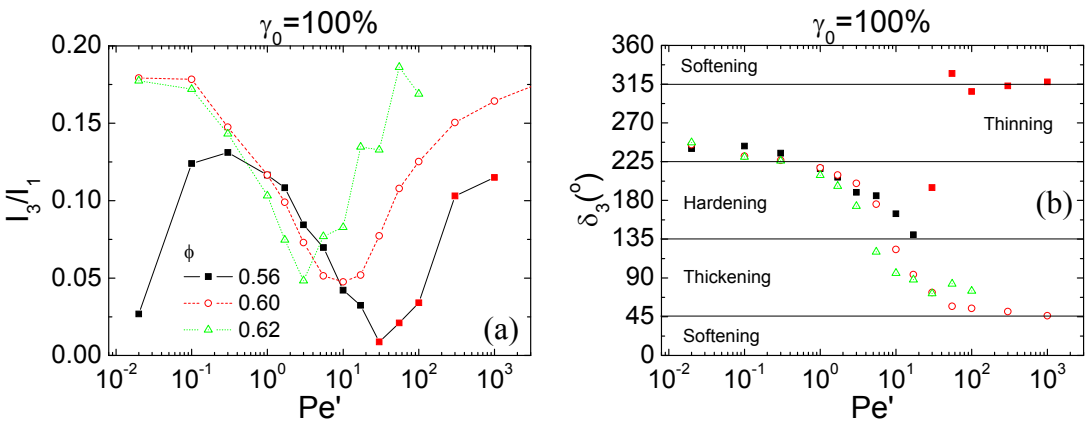

Figure 5.27: Non linear frequency sweeps of φ=0.56, 0.60 and 0.62 for γ_0=100% showing the non linear component a) I_3/I_1 and b) phase δ_3. Note that the points of φ=0.56 (solid, square) for Pe'>17 in red, show shear ordering as seen in (Foss and Brady, 2000a) for low φ under steady shear.

In figure 5.27 we examine the frequency dependence of the non linear properties at γ_0=100% for φ=0.56, 0.60 and 0.62. Initially we see that I_3/I_1 in fig. 5.27a shows a similar shape with the minimum at intermediate Pe' shifting to lower values with increasing φ, while higher φ's non linearities increase. At the lower φ=0.56, high Pe' lead to shear ordering (marked in red), identical to the ordering seen under similar simulations conditions of high Pe and φ, although under steady shear (Foss and Brady, 2000a). It may be surprising that ordering occurs at all since the polydispersity is high, but apparently the nature of the specific ordering, which appears only in the velocity gradient and vorticity (yz) plane, allows it. It is expected that any ordering causes many changes to the stress response and thus for Pe'>20, the data cannot be compared to the amorphous state. In the case of the lowest Pe', φ=0.56 shows a strong drop of non-linear response as expected, because at long time scales as shown in chapter 3 (fig. 3.9), φ=0.56 behaves as a simple liquid (t_α/t_B≈100). Similar findings should be expected for φ=0.60

at much longer time scales ($t_\alpha/t_B \approx 10000$). The phase of the third harmonic δ_3 generally shows similar φ dependence and as I_3/I_1 exhibiting a shift to smaller Pe' with φ.

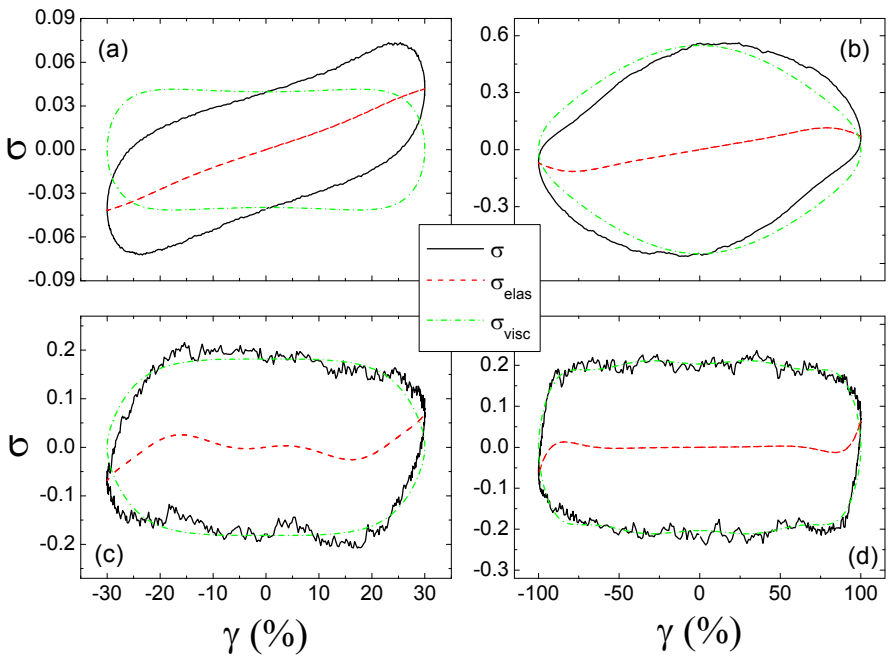

Figure 5.28: Lissajous of four general non linear oscillatory responses with Pe'=65 and φ=0.60 for a) γ_0=30% and b) γ_0=100%, while Pe'=0.02 for c) γ_0=30% and d) γ_0=100%. The stresses have additionally been split into elastic and viscous components (Cho, Hyun et al., 2005).

Similar to the experiments, four general representative Lissajous for the BD simulations are shown in figure 5.28. As for the experimental case, low Pe' show a trapezoid shape with an increasing elastic stress at the strain maxima, while high Pe show the stress reduction and decreasing elastic stress at the strain maxima. The lack of hydrodynamics generally does not seem to influence the non-linear components or the general shapes of the curves as understood from the comparison to the previous experimental data (fig. 5.20).

Dynamics under Shear: Strain Dependence

Similarly to chapter 4, we examine the non-affine motion of hard sphere particles under shear, although unlike chapter 4, we do not examine transient values of displacements as in chapter 4; rather we average displacements over many periods. It should be clarified that unless the time scales that are examined are multiples of the period (τ=nT), results will include information of motions that occur within the period. Moreover in addition to the results presented below, experimental measurements examining the microscopic motions of polydisperse hard sphere glasses under oscillatory shear have also been carried out using the technique of LS-Echo (Petekidis, Moussaid et al., 2002).

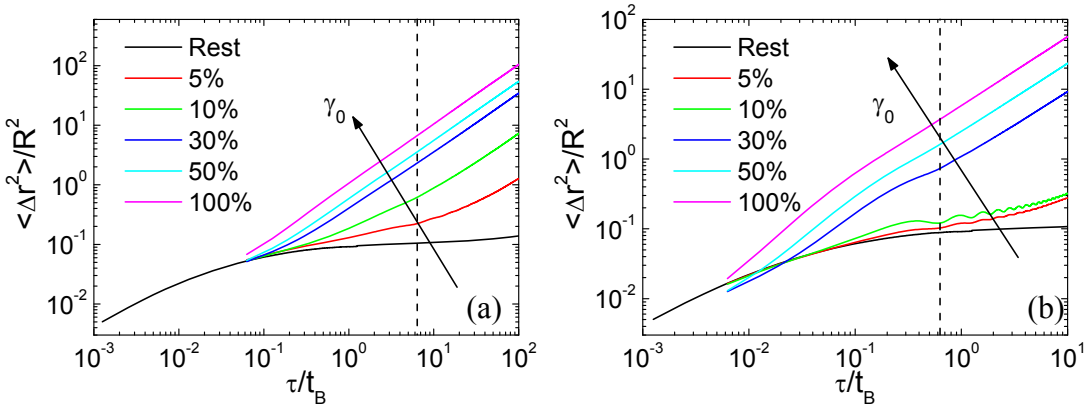

Figure 5.29: MSD versus time of φ=0.60 for select γ_0 at a) Pe'=1 and b) Pe'=10. Vertical dotted line corresponds to the time scale of one period of oscillation.

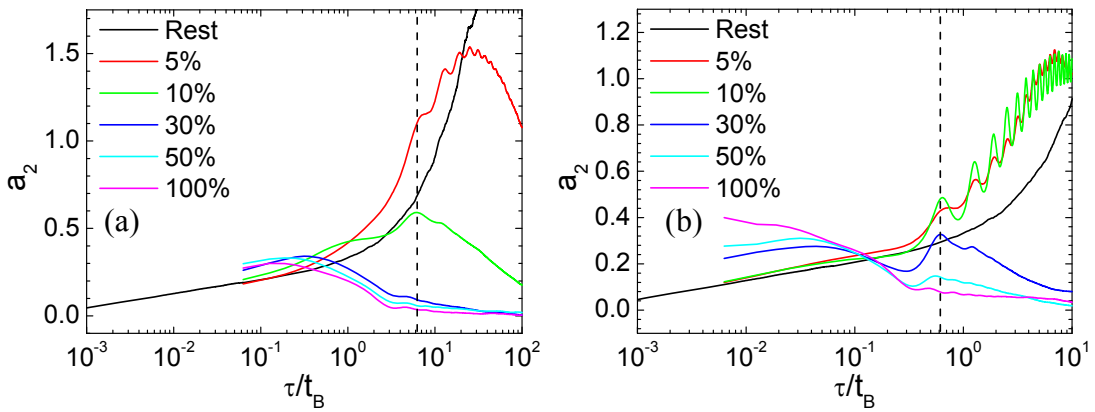

Figure 5.30: Non Gaussian parameter a_2 versus time of φ=0.60 for select γ_0 at a) Pe'=1 and b) Pe'=10. Vertical dotted line corresponds to the time scale of one period of oscillation.

In figure 5.29 we examine particle displacements for φ=0.60 at Pe'=1 and Pe'=10 (the corresponding rheological properties are shown in fig 5.21 and 5.22). Both Pe' show that with increasing strain, the displacements deviate from the state at rest, finally showing long time diffusive behavior at large strains above the crossover strain (with G''>G') and simultaneously increasing the diffusion coefficient with strain. The higher strains at Pe'=10 show constriction at small time scales, also seen under steady shear in chapter 4 (fig. 4.12). Interestingly, the higher strains at Pe'=10, where the diffusion coefficient under shear (τ>T) becomes comparable or larger to D_0, also show transient super diffusive behavior for τ<T. This super diffusive behavior is inferred (Foss and Brady, 2000b; Foss and Brady, 2000a; Pine, Gollub et al., 2005) or directly shown (Sierou and Brady, 2004) by results of older simulations, as the long self diffusion coefficient under shear increases above the self diffusion coefficient at the dilute limit. Although not shown in chapter 4, this type of super diffusion is seen under steady shear. The oscillations that occur for high Pe' and low strains

(showing minima at τ=nT) are not an artifact of the simulations, rather correspond to specific particle motions caused by the high frequency oscillations. These effects are more apparent at higher Pe' and will be discussed below. The displacements under shear are found to be generally isotropic, although some small differences will be discussed below.

The non Gaussian parameter a_2 for the displacements shown in fig. 5.29 is plotted in fig. 5.30. We find that for both Pe', at small non linear strains (G'>G''), a_2 increases, while when the displacements become diffusive (at G'<G'') the a_2 parameter is decays towards zero. At the lowest time scales there is an increase of the parameter with increasing rate, corresponding to the constrictions at high shear rates as seen in chapter 4. The oscillations in the a_2 parameter, as opposed to the ones seen in the MSD, can also be seen at low Pe' and stem from the MSD averaging which adds up displacements from time scales that are not integer multiples of the oscillation period.

In the case of oscillatory shear, determining a diffusion coefficient in the traditional sense may not by applicable. The changing rate within the period actually affects the displacements that occur for time scales smaller than a single period, thus the long time displacements do not originate from small continuous random steps, but from random steps biased by the changing rate within the period. We may calculate an effective diffusion coefficient by dividing the displacements that occur in multiples of the period with the elapsed time ($<\Delta r^2(nT)>/(nT)$). Even then, these values will only show diffusive behavior if there is a linear relation between $<\Delta r^2(nT)>$ at vs τ, which is not necessarily true at the lowest strains.

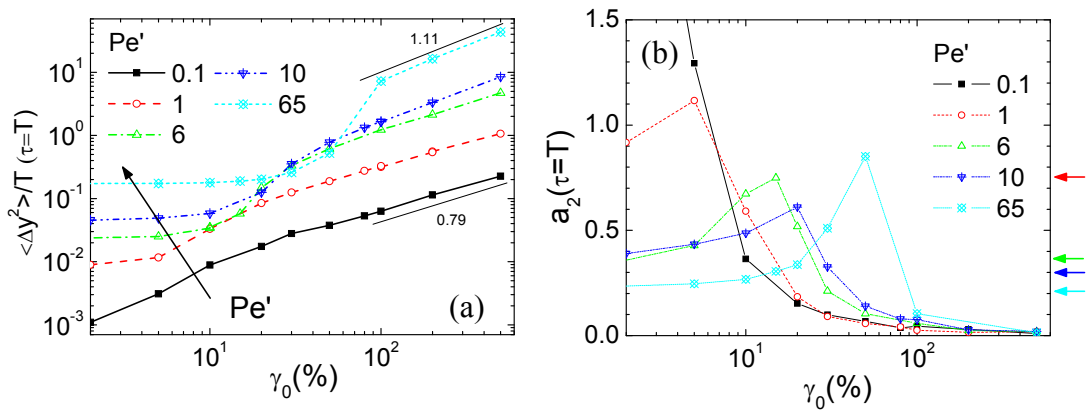

Figure 5.31: Data from the strain sweeps of figure 5.21 for particle motions at φ=0.60 with a)the particle displacements per period $<\Delta y^2>/T$ and b)the α_2 parameter at various Pe' for τ=T. Calculation of terminal power law slopes is shown for a). The horizontal colored arrows in b) correspond to the values of a_2 at rest for the time scales of the respectively colored Pe'.

Accordingly, in figure 5.31a we show the displacements per period, $<\Delta y^2>/T$, for the strain sweeps of fig. 5.21. As said, while $<\Delta y^2>/T$ is an effective diffusion coefficient, for the low and intermediate strains of this graph, the displacements are not diffusive. In the linear regime, measurements start with plateau values as the displacements reflect the state at rest and increase with increasing strain, finally reaching a terminal power law slope. The terminal slopes vary from 0.8 at the lowest Pe' to 1.1 at the highest Pe' and will be explained in detail further in the text. Due to the changes of the onset of non linearity (yield strain) for different Pe', displacements of different frequencies overlap as generally we see that increasing Pe' means an increase of yield strain. We additionally extract the non Gaussian parameter at the time scale of one period as shown in 5.31b. At the smallest strains the non Gaussian parameter has the values of the state at rest, while showing an increase generally correlated to beginning of yield, the increase of I_3/I_1 and also to sudden changes in δ_3. At the highest strains where the displacements show diffusive behavior (power law slope of 1 with τ), the a_2 parameter is reduced close to zero, a determining factor of diffusivity.

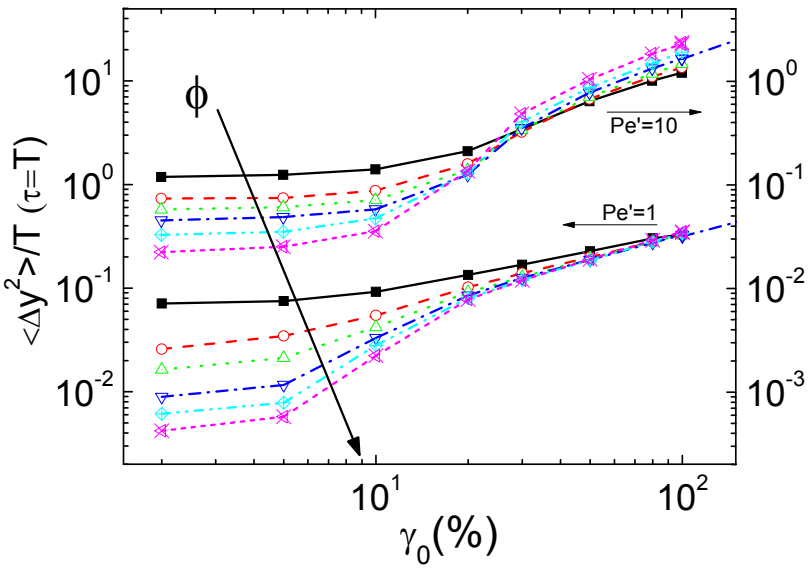

Figure 5.32: Data from strain sweeps of figure 5.23 showing the $<\Delta y^2>/T$ of φ=0.56, 0.58, 0.59, 0.60, 0.61 and 0.62 at Pe=1 and Pe=10. The right axis (Pe=10) is shifted by a factor of 10 compared to the left axis (Pe=1).

Similarly to the I_3/I_1 and δ_3 of figures 5.24a and 5.25a, the displacements for Pe'=1 at the various φ (fig 5.32) show almost equal non linear displacements and non Gaussian parameter between each other with the high strain displacements reaching similar values. In the linear regime though, there are large differences due to the corresponding values at rest of the different φ. For Pe'=10 (figs 5.24a, 5.25a) the differences are stronger and although yield strains are not significantly different (fig 5.23b) within the accuracy of the points, there are

increased displacements for higher φ at high γ_0. This indicates that as the Brownian motion becomes less important, the shear induced displacements are dominated by particle collisions and increased with higher particle density.

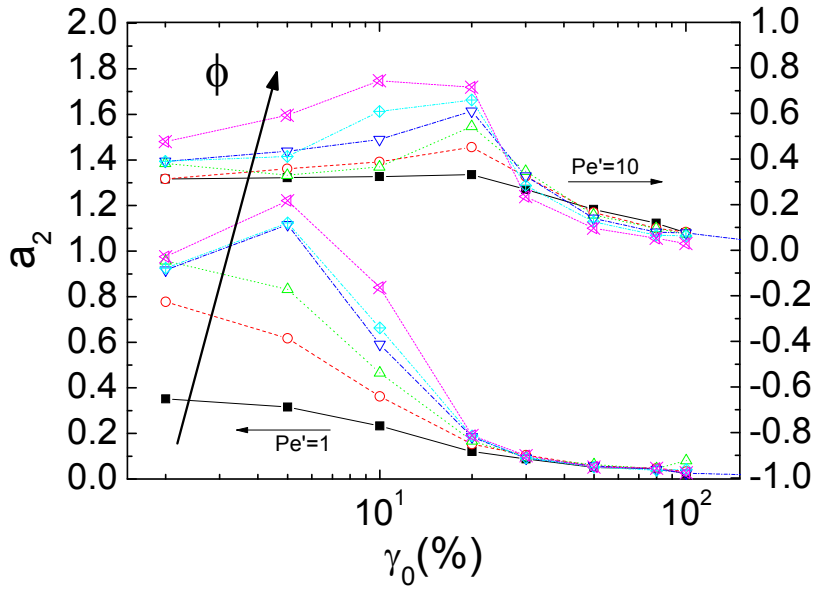

Figure 5.33: Data from strain sweeps of figure 5.23 showing the a_2 parameter of φ=0.56, 0.58, 0.59, 0.60, 0.61 and 0.62 at Pe=1 and Pe=10.

The a_2 parameter (fig 5.33) shows similar phenomenology as in 5.31b for all φ, with an initial peak as strain increases and then a drop to zero at high strains/rates. With the increase of displacements at higher φ, the non Gaussian parameter also reaches the diffusive limit of zero at smaller γ_0. The peak of a_2 seems correlated with the rate of increase of MSD vs γ_0 for the different φ. We speculate that the a_2 parameter increases because of the broadening of the distribution of displacements during oscillations near yielding; there is greater variation of displacements, because the percentage of the applied strain within the period above yield is comparable to that below yield.

Although the a_2 parameter gives measure of the average distribution of displacements and describes the amount of deviation from Gaussian behavior, it does not give any spatial information on the distribution within the simulation space. Thus as shown in chapter 3, we may give measure of the spatial distribution of heterogeneous displacements by selecting and highlighting a subgroup of the particles determined by the amount of displacements in a specific time scale of each particle (Weeks, Crocker et al., 2000). In figure 5.34 we show snapshots of particle positions of a glass (φ=0.60) under shear (Pe'=10), highlighting the 10% fastest (red) and 10% slowest (blue) particles, while downsizing the 80% rest of the particles to ¼ radii, determining the speed from displacements within one period. In this way we get a

qualitative image of the spatial distribution of the heterogeneities. In the linear regime, resembling the state at rest and also at intermediate strains, the distribution of the fastest and slowest particles shows clustering, more so for the faster particles. At the highest strain the distributions become random, as the a_2 parameter also shows a decrease to zero.

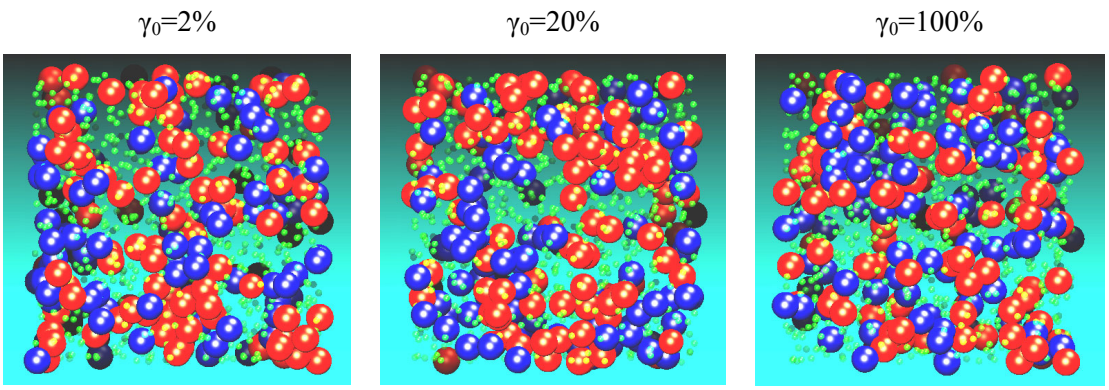

Figure 5.34: Snapshot of particle positions in an oscillatory shear simulation at Pe'=10 and φ=0.60 with varying γ_0, showing the 10% fastest particles in red (full size), the 10% slowest particles in blue (full size) and the rest of the particles in green (transparent, 1/4 radii). The particle velocities are measured within the time scale of one period.

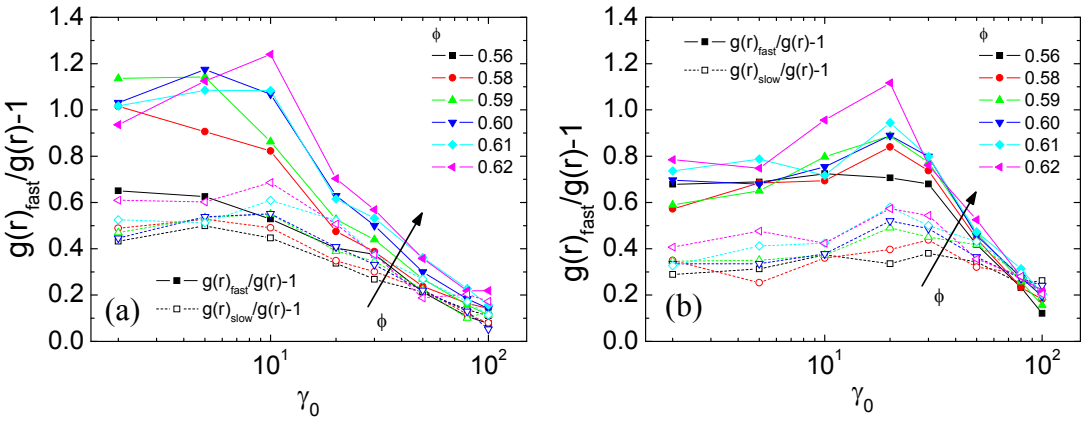

Figure 5.35: Data from strain sweeps of figure 5.23 showing the maximum of g(r) for the 10% fastest and the 10% slowest particles normalized by the overall g(r) within one period of φ=0.56, 0.58, 0.59, 0.60, 0.61 and 0.62 at a)Pe'=1 and b)Pe'=10.

Spatial information on the dynamic heterogeneities may be gained, as shown in chapter 3 (fig. 3.16) for the case at rest, by extracting the maxima of g(r) of the 10% fastest and of the 10% slowest particles and comparing them to the overall g(r). In figure 5.35 we plot these maxima as $g(r)_{fast}/g(r)-1$ and $g(r)_{slow}/g(r)-1$ so as to reach zero when $g(r)_{fast}=g(r)$ or $g(r)_{slow}=g(r)$. Generally we find that the spatial information of the dynamic heterogeneities shows similar behavior to the non Gaussian parameter of figure 5.33, especially for the case of $g(r)_{fast}$. Again

we see a peak of clustering with increasing strain and then a subsequent drop towards zero as the dynamic distribution of heterogeneities is homogenized. The slower particles are less clustered and show a less discernable peak with increasing strain, while both fast and slow heterogeneities generally show an increase with φ.

The clustering of dynamically heterogeneous particles occurs because of the cooperative nature of motion near and above the glass transition. In order for one particle to move, especially in the case of out of cage motion, the particles next to it must also move. Therefore in examining the spatial distribution of the fastest particles, they will statistically be found near each other. In the case of the slowest particles, an opposite phenomenon occurs; since they generally lack significant motion, they tend to be found far from the faster particles and again in clusters. This mechanism in the slower particles, though, produces weaker clustering.

As in the case of the a_2 parameter, the $g(r)_{fast}$ shows a peak at strains near yielding again due to particle populations being divided to high speed out of cage motions and low speed in cage motions. The peak occurs as the increase of strain makes this division stronger than the state at rest, before going to zero at the highest strains. Although at first glance the a_2 parameter seems to give the same information as the spatial distribution, this is not the case. By definition, when a_2 is zero the spatial distribution of heterogeneities must be random, but when a_2 is above zero the spatial distribution may show clustering or may again be random. A case of the a_2 parameter being uncorrelated to the spatial distribution will be examined further in the text.

Having discussed the average rheological and microscopic motion properties of different volume fractions and rates we now will discuss some implications of these findings on the viscous energy lost within the period. In order to see the correlation between the viscous stresses and the displacements we plot the power law terminal slopes of $\sigma_{viscous}=\gamma_0 G''$ and $D_y(\tau=T)$ from the data of the strain sweeps shown in 5.21 and 5.23. Figure 5.36 shows the slopes of $\varphi=0.60$ versus Pe' (5.36a) and of Pe'=1 versus φ (5.36b). As discussed in comparison to a steady rate flow curve, low rates in a glassy material show unchanging stress (Plastic flow), while high rates show a simple fluid stress slope of one (viscous flow). Indeed for the high γ_0 slopes we find in figure 5.36a that high Pe' have a viscous stress slope approaching unity and show decreasing values as Pe' is reduced. On the other hand the diffusivities show a constant value of approximately 0.7 at low values of Pe', while increasing towards unity at higher values.

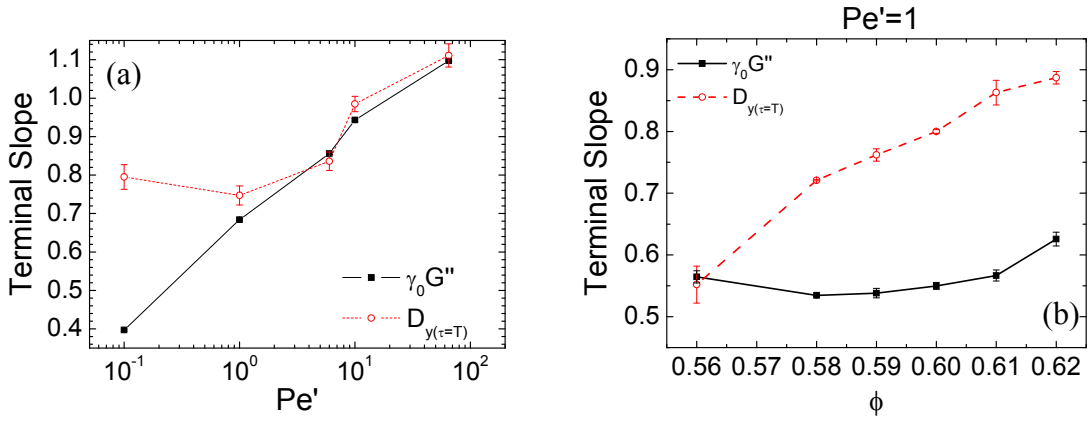

Figure 5.36: The large strain power law slopes of the viscous stress (γ_0 G'') versus γ_0 along with the diffusion coefficients in the y-axis D_y versus γ_0, for a) φ=0.60 plotted against Pe' and for b) Pe'=1 plotted against φ.

In the limit of high $\dot{\gamma}$, even though glassy, the system may reach a sheared state where both the viscous stresses and the long time self diffusivity have a linear relation to $\dot{\gamma}$. In this Newtonian fluid state, diffusivity and stresses are linearly correlated because the viscous loss of energy occurs primarily due to diffusive motion. This is seen in 5.36a for the higher Pe' where γ_0G'' and D_y have similar slope values.

As Pe' becomes smaller, a second component to the energy loss within the period is introduced. This component seems to have a smaller dependence with $\dot{\gamma}$ than diffusivity (or none), adding up to the viscous stress slopes we observe in figure 5.36a. In a glass ($t_\alpha \rightarrow \infty$) as the applied rate is decreased, there should always be a non-zero dependence of the diffusivity on the shear rate as the shear pushes the particles out of their cages. This dependence becomes unimportant with regard to the stresses, as at low rates the structural/plastic stresses become much more prevalent. Therefore we find that the deviation of the viscous stresses within the period from the diffusivities is due to the plasticity of glasses under shear and elastic/structural stresses.

For figure 5.36b, when looking at a specified Pe'=1 and varying φ, low φ show similar values between the slopes of diffusivity and viscous stress, while as φ is increased the deviation between the two increases. Generally we find that as φ increases, the slope of the viscous stress remains constant, while that of the diffusion increases indicating the larger effect of collisions with higher particle density. The similarity of the values for φ=0.56 is due to the proximity of the time scale to out of cage diffusivity.

Dynamics under Shear: Frequency Dependence

As seen in the experimental and simulation data, we find interesting stress results for the frequency dependence of the non linear oscillatory measurements. In figure 5.37 we examine the MSD for select Pe' at γ_0=30% (5.37a) and γ_0=100% (5.37b). While for high γ_0=100% we see a simple increase of diffusivity with Pe', low γ_0=30% show a non-monotonic change with an increase and a subsequent decrease of diffusivity. High γ_0=100% and high Pe' also show super diffusive behavior for some τ<T as the system under shear increases its out of cage diffusivity above the self diffusion in the dilute regime, as discussed previously. Additionally, we observe that low γ_0 show oscillations in the MSD for high Pe'.

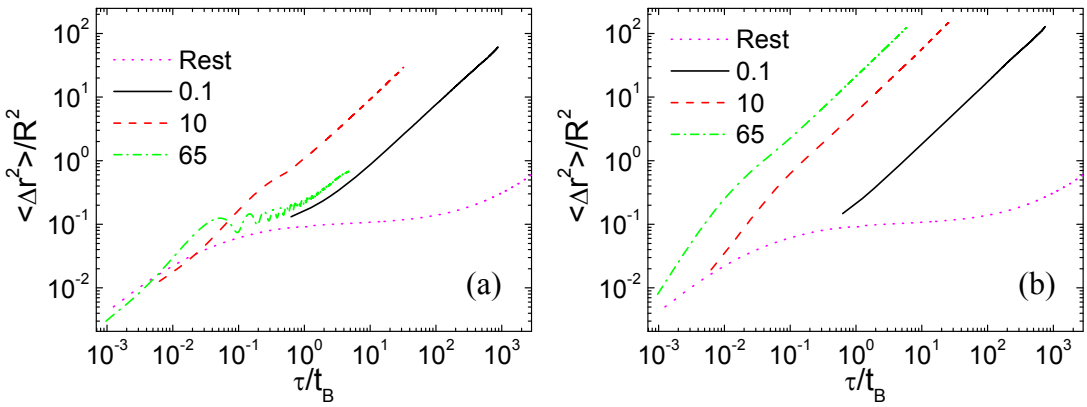

Figure 5.37: MSD versus time of φ=0.60 for select Pe' at a) γ_0=30% and b) γ_0=100%.

If we take the displacements per period of 5.37 and normalize them by the period, we get a value akin to a diffusion coefficient as shown in figure 5.38, while showing the non Gaussian parameter and representative van Hove functions in 5.39 and 5.40 respectively. Generally we find that the displacements are slightly anisotropic with the direction of shear (x) having the largest values, followed by the velocity gradient (y) and finally the vorticity direction (z). At γ_0=100% and at low Pe' we observe a power law slope that is less than unity (approximately 2/3), while at high Pe' we see a slope of unity showing simple fluid like behavior. In both high and low Pe' of γ_0=100%, the non Gaussian parameter and van Hove functions show simple random motion statistics with the a_2 parameter showing values close to zero.

At γ_0=100% but low Pe' (and also Pe), since Brownian motion is generally the dominant driving force, escape occurs the instant the cage has deformed enough for a particle to escape. Therefore, we postulate that random diffusive motion occurs through Brownian activated cage escape, the slope that is less than unity, for these shearing time scales, most possibly being a complicated function of φ. This also means that the yield strain for small Pe' will also be

relatively low, as observed in the experimental (figs 5.3 and 5.4) and simulation data (fig 5.21). At γ_0=30% and low Pe' we see a similar slope of about 2/3 for identical reasons; being that simple random motions with small a_2 values, occur by mechanism of Brownian activated cage escape.

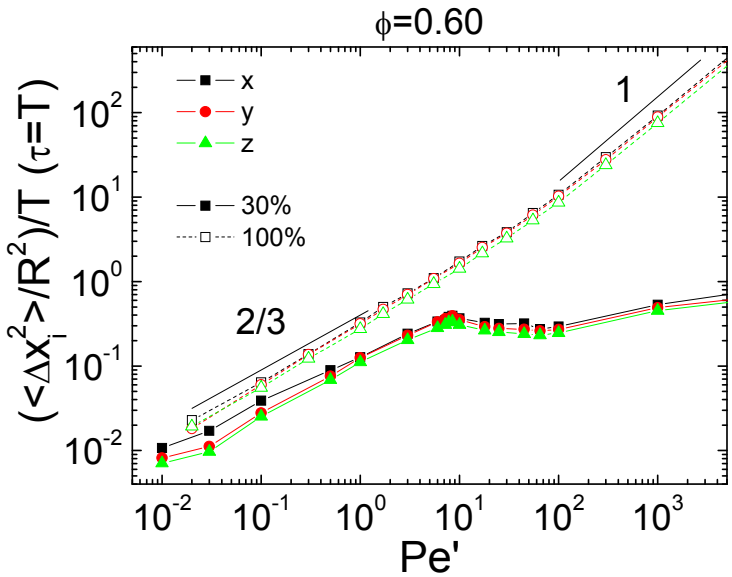

Figure 5.38: The average displacements within one period normalized by the period ($<\Delta x_i^2>/T$) during oscillatory shear with constant non linear γ_0 as a function of Pe' for φ=0.60 at γ_0=30% and 100%.

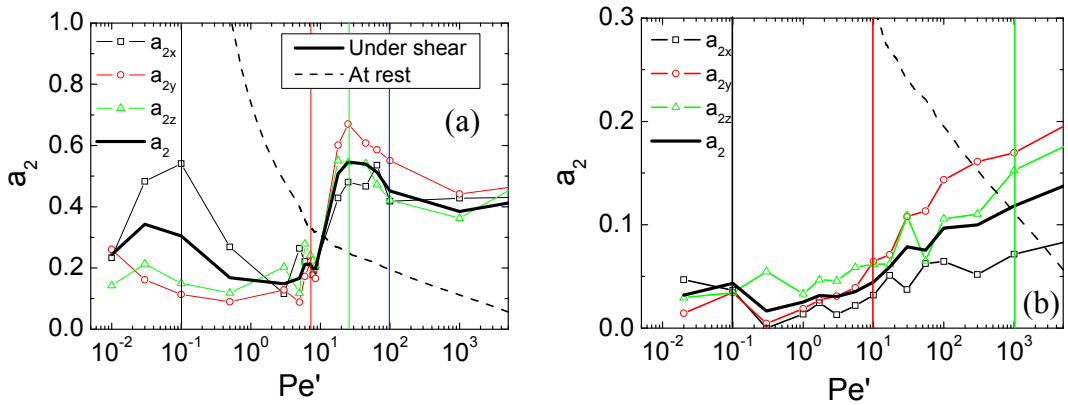

Figure 5.39: The a_2 parameter in all axes for a time scale of one period during oscillatory shear with constant non linear γ_0 as a function of Pe' for φ=0.60 at γ_0=30% and the values at rest for comparison. Vertical lines denote the Pe' examined in the next figure.

At γ_0=100% and high Pe', since Brownian motion become negligible, random diffusive motion occurs through shear collisions between particles. At these time scales, even if the cage has opened, particle Brownian motion is not fast enough for a particle to escape and has to be pushed out by shear induced collisions, thus random motion becomes linearly

proportional to shear rate/Pe'. This linear proportionality has been seen in the limit of non Brownian particles (Infinite Pe) by (Sierou and Brady, 2004). In contrast to the low Pe' Brownian activated cage escape, this diffusive motion is collision activated. Thus in the case of higher frequencies, yield strains become larger.

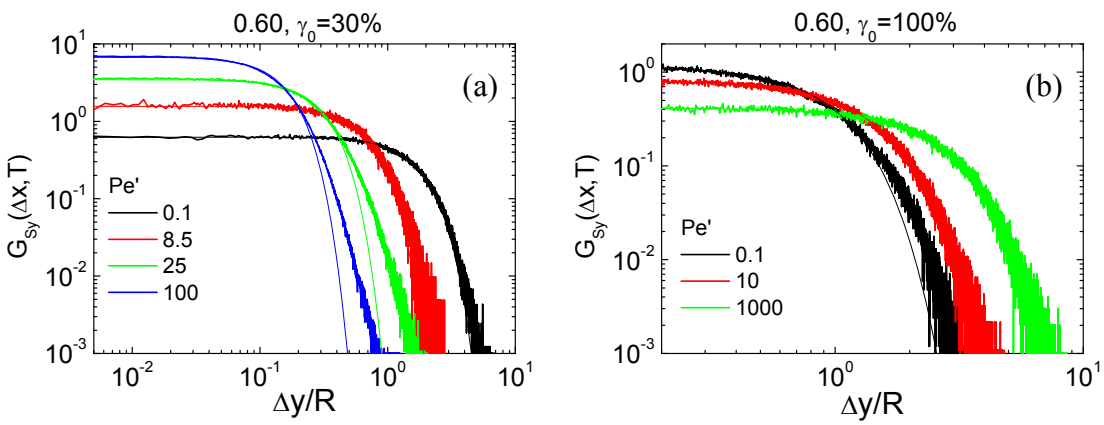

Figure 5.40: Single sided Van Hove self correlation for φ=0.60 at γ_0=30% for displacements in one period for select Pe'=0.1, 8.5, 25 and 100, as highlighted in previous figure.

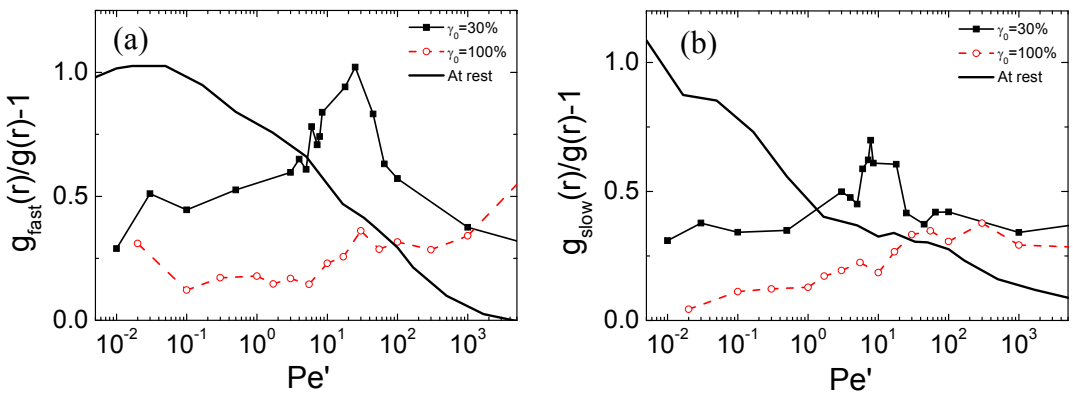

Figure 5.41: The normalized maximum of g(r) at a time scale of one period with constant non linear γ_0=30% (solid points) and 100% (open points) as a function of Pe' for φ=0.60 for a) the 10% fastest and b) the 10% slowest particles, with comparison to the state at rest (solid line) at the same time scales.

For γ_0=30% and higher Pe' we find that there is first a drop of diffusivity and then a subsequent weak increase. This difference when compared to the higher γ_0=100%, possibly occurs due to the drop of yield strain for the higher frequencies, meaning that γ_0=30% shows deviant behaviour because of the proximity to yielding. This strain also does not show true diffusive behavior for Pe'>10, showing increased values of a_2 and large deviations from Gaussian behavior as seen from the van Hove functions. At even higher Pe', "diffusivity" does not increase linearly with Pe' and high a_2 values persist. Since random motion for the higher Pe' is tied to shear collisions, relatively low strains (γ_0=30%) seem not to induce

enough collisions for simple random motion to occur, showing the drop of "diffusivity" and the peak of a_2, because particle populations are segregated between in cage and out of cage motions.

The spatial information of the dynamic inhomogenieties in figure 5.41 generally shows correlation with the non Gaussian a_2 parameter for γ_0=100% and for the lower Pe' at γ_0=30%. This essentially means that both fast and slow moving particles become localized, which allows us to surmise segregation of particle populations into clusters of fast and slow moving particles as in the case of rest and as discussed for figure 5.35.

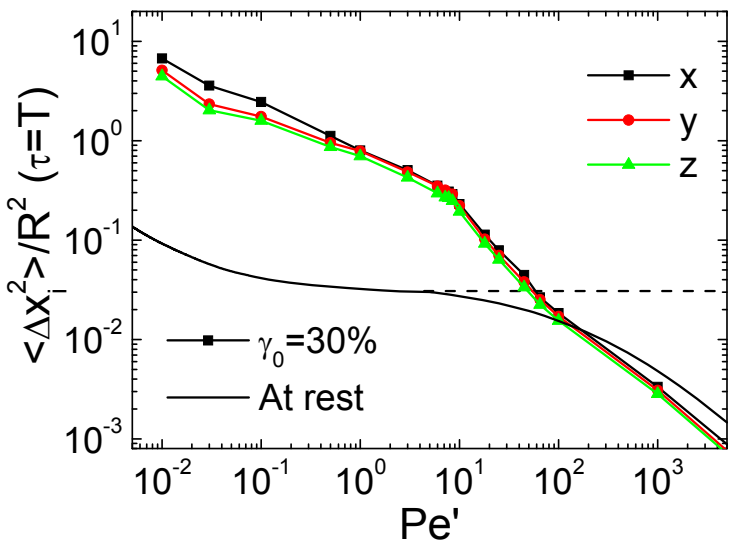

Figure 5.42: The average displacements within one period during oscillatory shear with constant non linear γ_0=30% as a function of Pe' for φ=0.60, additionally showing $<\Delta x^2>$ for the state at rest with Pe'=$2\pi/\tau$. The horizontal dashed line shows the approximate magnitude of in cage displacements based on the state at rest.

Interest lies in the case of higher Pe' and γ_0=30%, where the spatial distribution of inhomogeneities shows a decreasing function towards zero, while a_2 remains constant. This finding is important as it states that the abnormal distribution of motions does not originate from populations of particles moving at different speeds, rather that statistically all particles homogeneously deviate from a simple random walk type motion. This shows that non Gaussian behavior in this regime does not originate from dynamic inhomogeneities, but rather shows a homogeneous particle behavior with correlation to the applied shear. At a previous of $<\Delta r^2>$ vs τ (fig 5.37) we saw that low γ_0=30% also showed oscillations in the MSD for higher Pe'. This is the source of the increase in the a_2 parameter and refers to a portion of particles which follows the sheared oscillatory motion and returns to their initial positions after an oscillation as if they haven't been sheared at all.

In order to elucidate the motions under oscillatory shear for γ_0=30%, we examine the displacements as seen in figure 5.38 with the displacements at rest at the same time scales as $<\Delta x^2>$ vs Pe'=$2\pi/\tau$ in figure 5.42. Looking at the lower Pe', the shear induced displacements are larger than that the motions at rest and a simple extrapolation shows that the shear induced diffusion will become equal to the long time diffusion coefficient at rest (taken from chapter 3, fig. 3.10) at approximately Pe'=10^{-7}. At the highest Pe', displacements under shear become smaller than the in cage displacements at rest. This shows that not only there is a lack of out of cage collision assisted diffusion, but there is also an additional reduction of displacements. Thus even at γ_0=30% strain, not only do the particles return to their initial cages after a single period, but also show less displacements than at rest because constrictions from collisions.

Therefore the drop between the high Pe' and low Pe' regimes, refers to a transition from low Pe' Brownian activated diffusion, which shows higher displacements than at rest, to a regime that shows only in cage displacements with less displacements than at rest. As seen before in figure 5.37 of $<\Delta r^2>$ vs τ, at time scales that are not multiples of the period there are still non trivial displacements within the period, but because of the collision activated random motions, unless the particles are thrown out of their cage, they are forced to return to their initial position.

By correlating figures 5.26 and 5.42 we find that the minimum in the I_3/I_1 of the rheological response corresponds to the time scale of the plateau of the MSD at rest. This finding importantly states that the two regimes of high and low Pe' can be independently predicted by knowledge of the motions at rest. By examination of the linear dynamic frequency sweeps and their correlation to the dynamics at rest through the GSE relation, we may relate the minimum of G'' to the transition of the two non linear regimes. Indeed from the experimental data of figures (5.3, 5.12 and 5.14), we find that the transition occurs at a frequency within an order of magnitude of the minimum of G''.

We found that the low Pe' diffusivity slope of 5.38 for γ_0=100% is approximately 2/3, although the meaning of this slope has not been understood. Hence in figure 5.43 we examine the φ dependence of the diffusion coefficients under shear with varying Pe'. At high Pe', in the collision activated regime, the slopes of all φ show a simple liquid like behavior with a power law slope of unity, with smaller values of diffusivity for smaller φ reflecting less collisions for the smaller densities. At low Pe' however, the slopes differentiate for the different φ, with increasing values of 0.57, 0.71 and 0.8 for increasing φ=0.56, 0.60 and 0.62. In the case of the lowest φ=0.56, the values of diffusivity tend towards a plateau at the

smallest values of Pe'. This plateau is equal to the long time diffusivity at rest, which at these sheared time scales becomes more important than the shear induced diffusivity.

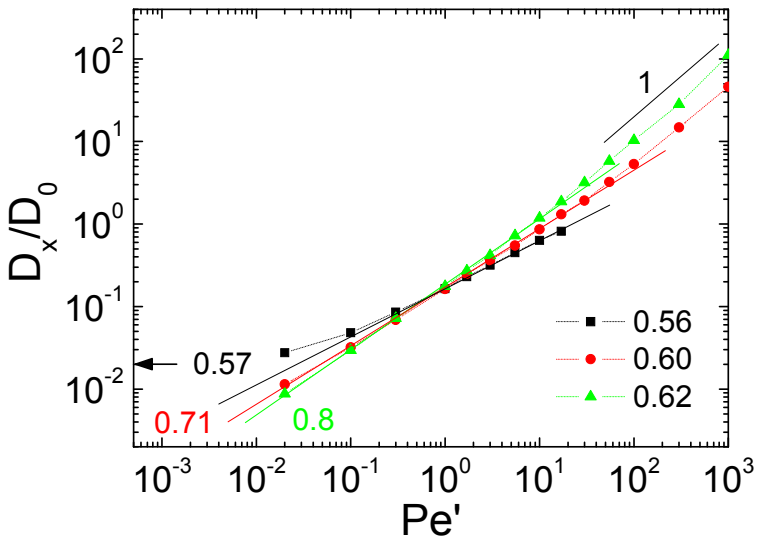

Figure 5.43: The average long time x-axis diffusion coefficients during oscillatory shear with constant non linear γ_0=100% of φ=0.56, 0.60 and 0.62 as a function of Pe'. Power law slopes at low Pe' are shown with values of 0.57, 0.71 and 0.80 with increasing φ. The horizontal arrow points to the out of cage diffusion coefficient of φ=0.56, while higher Pe' values of φ=0.56 are not shown due to ordering as discussed.

In this regime of low Pe', random motions are activated by Brownian hopping and so the slopes may reflect the distance needed in elapsed strain between each hopping event, or the distance the particles need to travel to allow hopping to occur, both reflected by the yield strain. Since high φ are more dense, more hopping events are likely to occur, reflected by the larger slope. Similar slopes for the diffusivity, not equal to unity, have been seen in steady shear (Besseling, Weeks et al., 2007). It may be possible that the low Pe' slope of diffusivity also reflects long range cooperative restructuring under shear, something not reflected in the self diffusion, which becomes more difficult at higher φ. It is expected that as one increases φ towards maximum packing the slope increases towards unity, effectively reaching a limit where Brownian activated particle motion under shear can not be distinguished from collision activated motion, due to high particle proximity.

Based of findings from figures 5.36 and 5.43 and previous chapters 3 and 4, we propose a schematic (fig 5.44) of the general behavior of diffusivities and stresses under shear for hard sphere suspensions near and above the glass transition, ignoring the effects of hydrodynamic thickening. For this qualitative discussion, Pe' is approximated to Pe for the case of very high non linear strains, where $\gamma_0 >> \gamma_{yield}$. At the highest rates, the non Brownian particle limit of

regime (iii), diffusivity and stresses increase linearly with shear rate (the high shear viscosity plateau) (Breedveld, van den Ende et al., 2001; Breedveld, van den Ende et al., 2002; Sierou and Brady, 2004), as the occurring motions of the particles are collision activated and the stresses are proportional to the amount of particle collisions. As the rate is decreased towards time scales comparable to the MSD plateau of the system at rest, regime (ii), the stresses also reach a plateau (yield stress) reflecting the plasticity of the system. In this regime of applied rates, the shear induced diffusivity has a non zero power law slope value, reflecting the Brownian activated out of cage motion. This value is dependent upon φ and we find that value of this slope increases towards unity as φ is increased towards maximum packing. At time scales where out of cage diffusion occurs, the system reverts to a simple Newtonian fluid (regime (i)) with the stress showing a local power law slope of unity. Any shear induced diffusion in this case becomes unimportant when compared to the long time diffusion at rest and the diffusivity reaches an unchanging plateau value equal to the long time diffusivity at rest. In the case of a glass, regime (i) is not applicable since there is no out of cage diffusivity. As φ is decreased beneath the glass transition, regime (i) appears, with regime (ii) becoming smaller. Eventually regime (ii) should disappear, allowing only regimes (i) and (iii) down to the limit of φ→0.

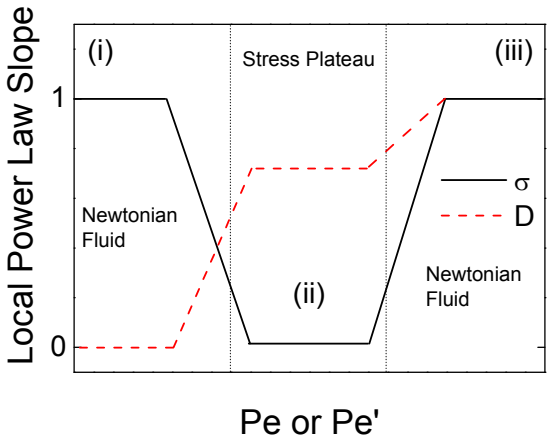

Figure 5.44: Scheme showing the local power law slopes of the stress and diffusion coefficient under shear against Pe or Pe'(for high γ_0) plotted vs Pe or Pe'.

Dynamics under Shear: Within the period

Although the dynamics under shear have been examined as averages within the period, in order to understand the stresses within the period (Lissajous), we must also study the instantaneous dynamics and structural properties. In figure 5.45 we show the applied strain, measured stress and short time displacements within the period for γ_0=30% and 100% in the low Pe' regime of φ=0.60. Since the system has a large amount of time to relax, there is an

elastic increase of stress with the reversal of strain that has a persistence of about 10%; the yield strain of the material. Within the period this occurs after the maxima of strain at Pe't/t_B=π/2 and 3π/2. At these low Pe', as discussed, we see Brownian activated displacements, which are roughly proportional to the strain rate and also isotropic. We also observe a strong correlation of the stress within the period to the displacements.

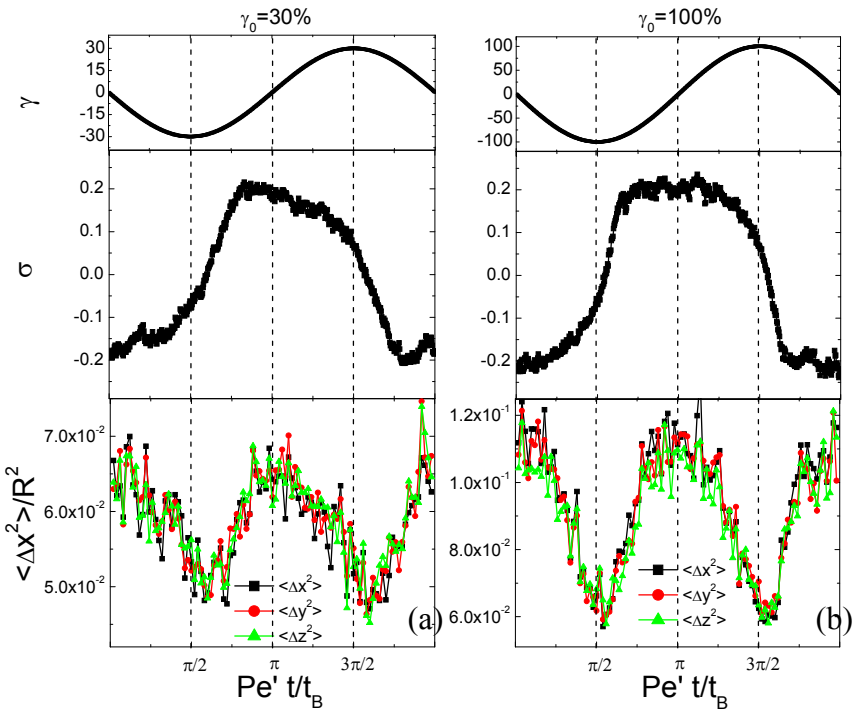

Figure 5.45: Time evolution within the period of strain, stress and short time displacements (τ=T/100) of φ=0.60 and Pe'=0.02 for a) γ_0=30% and b) γ_0=100%.

From the discussions up to this point, the trapezoid shape at low Pe', seen both in experiments and in simulations, refers to a system that is in a quasi steady state under shear, showing an elastic increase of stresses at the reversal of strains with an approximate range of about 10% strain, and a steady state shear stress varying slightly with rate. In the case of these low Pe' and shear rates, it seems that the stresses of the system under shear mostly reflect the plasticity (or entropic elasticity) of the glassy cage while having a small contribution from the out of cage displacements. The stresses after the elastic increase should closely resemble the stresses taken from a flow curve under steady shear at the same applied rates (Rogers and Vlassopoulos, 2011).

In figure 5.46 we show the same strains as in figure 5.45, although now for the high Pe' regime. In this regime we have a familiar stress drop after the maxima of strain at Pe't/t_B=π/2 and 3π/2, which has a range of about 50%. Instantaneous displacements do not show a simple proportionality to the strain rate or stress, especially in the case of γ_0=30%. However, as

discussed these high Pe' on average show simple collision activated displacements, and thus displacements should be linearly proportional to the strain rate.

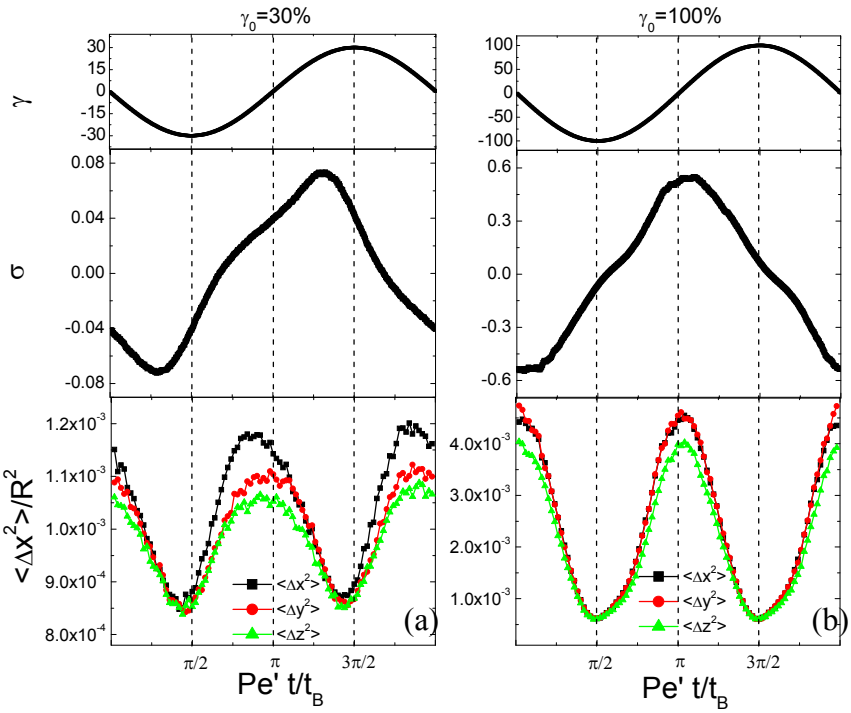

Figure 5.46: Time evolution within the period of strain, stress and short time displacements (τ=T/100) of φ=0.60 and Pe'=65 for a) γ_0=30% and b) γ_0=100%.

The negligible contribution of the Brownian motion introduces complexity to the stresses, causing the reduced stresses with the reversal of strain and a similar reduction in instantaneous displacements. Since particle motion generally takes place though shear induced collisions, we believe that both the reduced displacements and stresses occur after the strain reversal because there are fewer collisions between particles. Fewer collisions occur because the spatial landscape has not been randomized by Brownian motion, since during the increase of strain the particles clear their sheared path of other particles, thus on the reversal of strain there is less resistance and fewer collisions. For large γ_0=100%, after the stress reduction, displacements become proportional to the shear rate and the stress exhibit collision activated motion. Hence, the average stresses and displacements within the period for high γ_0 show a simple linear relation to applied frequency or strain.

Therefore we find that the stress reduction at high Pe', seen both in experiments and in simulations, refers to a system that is under shear and far from a relaxed state at any point during shear, the particles driven purely by the applied strain. The reduced stresses at the reversal of strains have a large approximate range of about 50% strain, and a steady state

shear stress varying almost linearly with rate. In the case of these high Pe' and shear rates, it seems that the stresses of the system under shear mostly reflect and relate to the out of cage displacements and shear induced collisions (viscous energy loss) rather than plasticity or entropic elasticity.

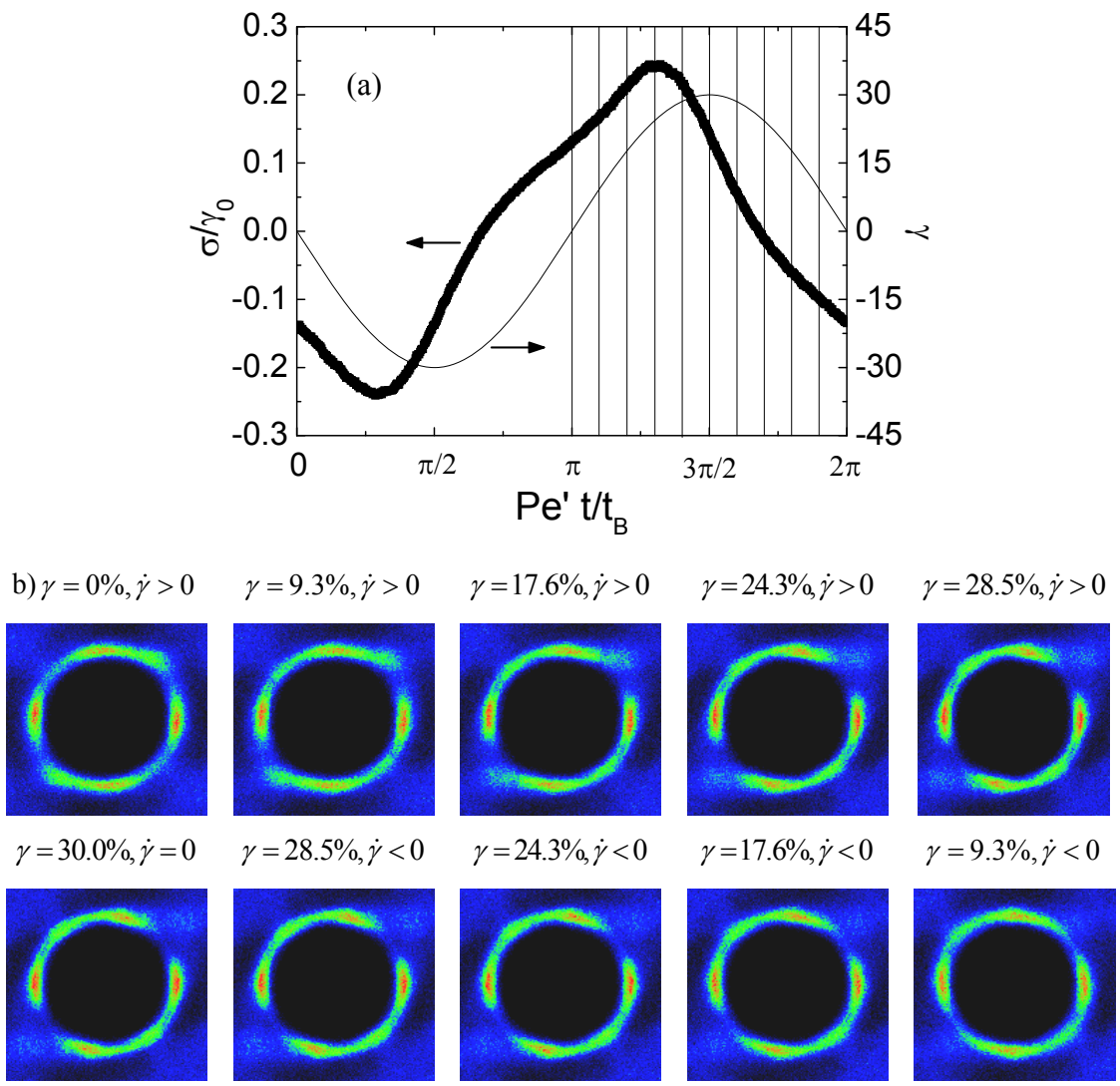

Figure 5.47: a) The evolution within a period of stress and strain for Pe'=65 and γ_0=30% at φ=0.60, b) The pair correlation function for the xy plane for instances within the period as highlighted with vertical lines in a), starting from Pe't/t_B=π and ending in 2π.

Microstructure under Shear: Within the Period

As in chapter 4, we examine the microstructural properties of the colloids under shear, in order to correlate the structural properties with the stresses within the period. As for low Pe in chapter 4, small strains and small Pe' do not show significant changes in the pair correlation function (g(r)) and are not available for examination, although we do expect distortion of the structure even for the smallest rates. We concentrate on the xy plane (velocity-velocity

gradient), as information of the distorted structure is more apparent there. Since the system is under oscillatory shear, we expect the structures to be highly transient in nature and therefore many snapshots of the structures are needed.

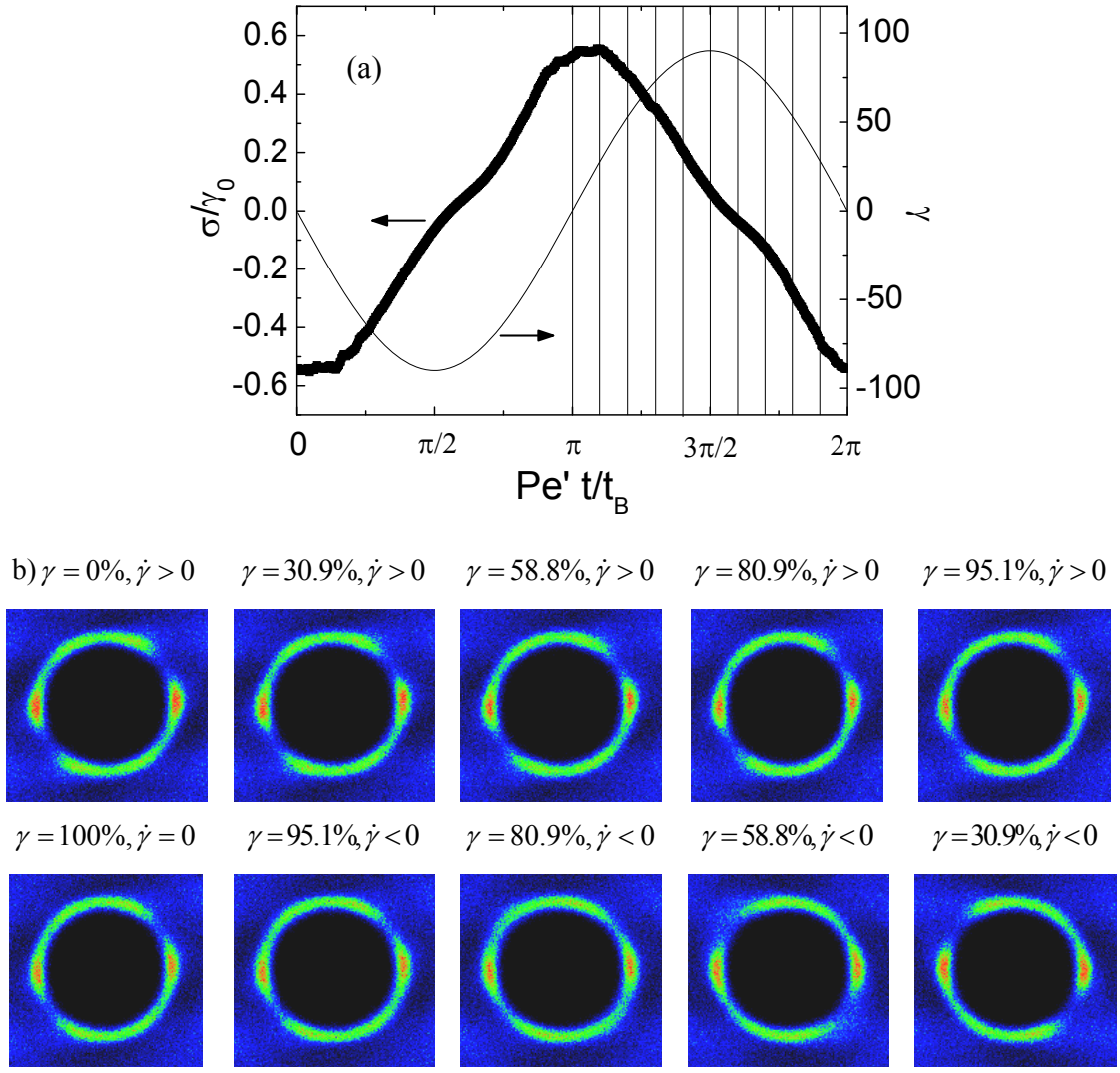

Figure 5.48: a) The evolution within a period of stress and strain for Pe'=65 and γ_0=100% at φ=0.60, b) The pair correlation function for the xy plane for instances within the period as highlighted with vertical lines in a), starting from Pe't/t_B=π and ending in 2π.

We show the stresses, applied strains and pair correlation functions in the xy plane for the high Pe' regime of γ_0=30% (fig. 5.47) and γ_0=100% (fig. 5.48). Figures 5.47a and 5.48a depict the applied strain and stress responses also marking with vertical lines the positions where the structural properties are extracted and shown in figs 5.47b and 5.48b. The structures of only half the oscillation are shown, but the symmetry of oscillation may give us the rest of the structures, though mirrored because of opposite strain and strain rate. The stress reduction that we see at the reversal of strain and the explanation of fewer collisions due to

the induced structure from previous shear can be clarified by using the images of g(r) in the xy plane.

The structure within the period for both high and low strains shows that even though strain rate is reversed, the previous structure is retained for a large amount of elapsed strain after the reversal. For figure 5.47 we see that by decreasing strain from γ=30% to γ=17.6% there are only small changes in the structure, while reaching steady state at γ=-17.6% (seen in the mirrored image), after an elapsed strain of about 50%. The stress is correlated to the changes of the structure, showing only a small stress increase for the portion of the period with unchanging structure. Similar results can be seen in 5.48 for γ_0=100%, where the structure before the reversal again persists for more that 50% strain. Moreover, there are indications that the structure during shear for γ_0=30% may not have the chance to fully evolve into a steady state, since for γ_0=100% the structure evolves over strains of more than 50%. This supports the finding that high Pe' at γ_0=30% do not show out of cage displacements, as the cage structure has not fully evolved allowing out of cage motions due to collisions.

5.4 Lissajous Analysis

Discussion

Based on the previous analysis of structure and dynamics for the hard sphere glasses, we are able to describe the non harmonic behavior of the stresses and ascribe elastic stresses, based on the structure and/or entropic cage elasticity, and viscous stresses, based on diffusivity and shear induced collisions. At low Pe' we expect the entropic (elastic) stresses to always be proportional to the total stress response as each point is in a quasi steady state, even during the reversal of strain. The stress due to displacements (viscous) should be generally small and proportional to the rate, mirroring the out of cage motion within the period. In the case of high Pe', we expect the viscous (displacements) stresses to be dominant in the portions of the period that have large collisions; the portions beyond the stress reduction where the structure has reached a steady state. During the stress drop of the reversal, we expect the structural stresses to be more apparent. After 50% strain has elapsed from the reversal and the structure has reached a steady state the structural stress should not change. In the case of high Pe', we differentiate the elastic stress into a structural stress as opposed to the entropic stress of low Pe', as the high rates don't allow for contribution from Brownian motion.

The elastic and viscous stresses as seen in previous figures (5.20 and 5.28) from the analysis done by Cho and Ewolt cannot be representative of microstructural changes in the context of this work neither for the viscous nor for the elastic stresses, because of a simple exclusion.

The analysis imposes an elastic and viscous symmetry for the same values of strain. For example in the case of high Pe', we expect different elastic and viscous stresses based on the microscopic properties before and after the strain reversal. Hence, at the same strains an analysis which imposes viscous and elastic components with equal (or opposite) components is not applicable. In this subsection we attempt to modify the existing analysis techniques to account for the microscopic information available from the simulations.

Proposing modified methods of Lissajous analysis:

A) G'_{inst} and G''_{inst}

The main problem in proposing an elastic stress that does not have an equal value of equal stresses and is not equivalent to the one previously shown is that under some circumstances, it must give an open loop within the period (in a Lissajous) with some loss or gain of energy within the circle. In this case, it cannot be strictly called an elastic stress, as this implies no loss of energy in the period. This argument may be overlooked if one defines an instantaneous elasticity, which is not bound by a closed loop in the period, but is always proportional to the strain. In this way an open loop of elastic stress may occur. Similarly an instantaneous viscous stress may be defined that is proportional to the strain rate. Thus we define a non linear oscillatory stress and analyze it into an elastic and viscous component by:

$$\sigma = \sigma_{G'inst} + \sigma_{G''inst} = \gamma_0 G'_{inst}(t)\sin(\omega t) + \gamma_0 G''_{inst}(t)\cos(\omega t) \quad (5.3)$$

where we define G'_{inst} and G''_{inst} as the instantaneous elastic and viscous moduli.

In essence the particular analysis assigns different values of the elastic and viscous moduli at each moment of the period, such so each instantaneous stress and its derivative belongs to a linear stress curve. In this way each point in the curve is treated and analyzed without any symmetry constrictions. As a requirement for the validity of the analysis, in the limit of a linear response, the values of G'_{inst} and G''_{inst} remain at a constant value equal to the representative viscoelastic constants, while the average of the elastic and viscous stresses for a specific strain equal their counterparts of the previous analysis.

Using this method, we analyze the four representative Lissajous of high and low Pe' and γ_0 as shown in figure 5.49. We find that this modified analysis method shows promise by exhibiting complex viscous and elastic stresses within the period. Unfortunately, even by relaxing the constraint of symmetry for equal strains there is an additional constraint. This analysis still uses the existing definition of an elastic stress which is reduced to a zero value at γ=0. Again this does not fit with previous microscopic information which shows that at low Pe' and high strains, the stress is mainly entropic in origin showing large plastic stresses even

when γ=0. Even at high Pe' structural stresses are expected to be small, but non zero, at any point of the oscillation.

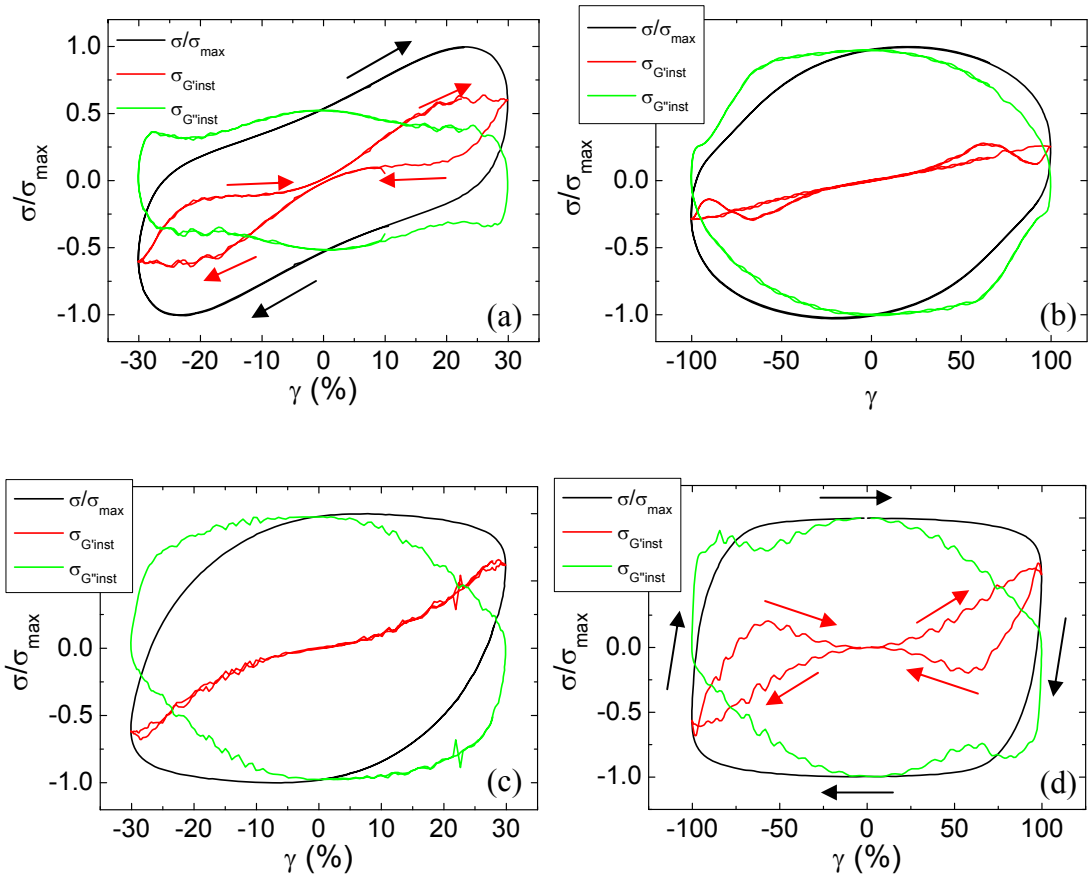

Figure 5.49: Lissajous of four general non linear oscillatory responses (as seen in fig 5.20) with ω=1rad/sec and large spheres (High Pe') at φ=0.64 for a) γ_0=30% and b) γ_0=100%, while ω=1rad/sec and small spheres (low Pe') for c) γ_0=30% and d) γ_0=100%. The stresses have additionally been split into elastic and viscous stresses as described in the text. The colored arrows show the direction of shear.

The specific analysis though is not without some success. At high Pe' and high strains we find a drop in stresses at the reversal of strain, although based on the simulations, the response after initial restructuring shows a non changing structure (constant structural stress) and displacements which are proportional to the applied rate (constant viscous loss). By taking the instantaneous viscoelastic properties (fig 5.50b) we can show that even though the applied strain is highly non linear, the stress reduction due to the reversal has a very specific range of γ=50%, while the rest of the response is constant and unchanging for the rest of the period (0-π/2 and π-3π/2). This can be clearly seen in figure 5.50a, where the instantaneous viscoelastic properties of γ=0 remain constant over much of the period. Thus by using this analysis we may infer the stability of the microstructural properties in a specified region without prior knowledge of any microscopic information.

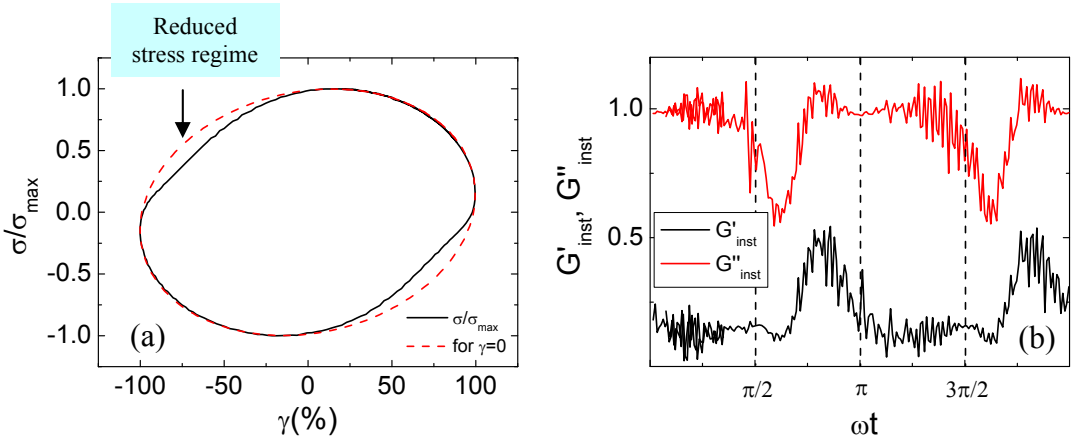

Figure 5.50: Non linear oscillatory response with ω=3rad/sec and γ_0=100% for large spheres (high Pe') at φ=0.62 with a) the Lissajous Stress strain plot and b)the instantaneous elastic and viscous moduli within a period. The stresses of a full cycle that correspond to G'_{inst} and G''_{inst} at γ=0% have additionally been plotted in a), highlighting the reduced stress regime after maximum strain.

As discussed, the previous method of analysis although novel, still has an arbitrary constriction, for the purposes of microscopic stresses, of the elastic stress being zero at γ=0. In the case of linear applied strains, or even strains near yielding, this constriction is valid as a simple elastic response, according to Hook's Law (σ=γG), should have a value of zero for γ=0. In the instance of arbitrarily changing properties and yielding within the period though, the value of zero strain may be assigned to any point. For example in the case of high strains but low Pe', since each point is in a quasi steady state, we could easily assume a zero value of strain for purposes of determining the cage elasticity, at the strain maxima.

B) σ_e and σ_v

We thus define an elastic stress that varies within the period but does not necessarily have an association to the elapsed strain within the period, removing the constriction of σ_{elas}=0 at γ=0. We do this by calculating a viscous stress that is by definition proportional to strain rate and finding the elastic stress by subtracting the viscous stress from the total as:

$$\sigma = \sigma_e + \sigma_v = \sigma_e + \eta\dot{\gamma} = \sigma_e(\dot{\gamma}) + \eta(\dot{\gamma})\dot{\gamma} \quad (5.4),$$

where σ_e and η may change arbitrarily with the rate.

By taking the derivative we find:

$$\frac{d\sigma}{d\dot{\gamma}} = \frac{d\sigma_e}{d\dot{\gamma}} + \dot{\gamma}\frac{d\eta}{d\dot{\gamma}} + \eta \quad (5.5)$$

In the limit where $d\sigma_e/d\dot{\gamma} + \dot{\gamma}d\eta/d\dot{\gamma} << \eta$ (5.6) then through 5.4 and 5.5 we have:

$$\sigma_v = \frac{d\sigma}{d\dot{\gamma}}\dot{\gamma} \text{ and } \sigma_e = \sigma - \frac{d\sigma}{d\dot{\gamma}}\dot{\gamma} \quad (5.7).$$

This analysis mathematically defines the viscous stress as the amount of stress proportional to the rate of shear, while the remaining stress is defined as elastic and may be applied either for steady or arbitrary shear. Based on previous microscopic information, in a flow curve of a glassy material this analysis would correctly predict $\sigma_v=\sigma_{total}$ at the limit of highest rates where the power law slope is unity, while $\sigma_e=\sigma_{total}$ at the limit of low rates where the slope is zero. An example of this is shown in figure 5.51, although rates do not reach the limit of high Pe. This analysis originates from the idea and implies that the viscous stress is related to the stress due to displacements (hydrodynamic stress), while the elastic stress is due to structure/entropy (Brownian stress). It fails in regions where there are rapid changes of elastic stresses or viscosity as stated by eq. 5.6, and is ill defined for transient states. In the case of hydrodynamic thickening where viscosity increases with shear rate, this simple separation also fails, returning negative values for the elasticity. The two analyses of equations 5.3 and 5.7 are connected through the simple relation $\sigma_{G'inst}=\sin^2(\omega t)\sigma_e$.

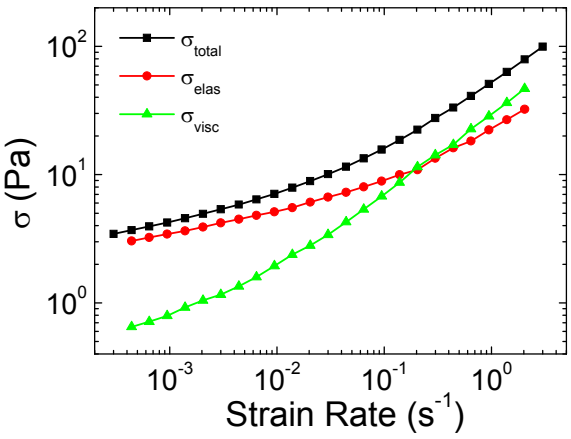

Figure 5.51: Flow curve of hard sphere glass examined in chapter 4 of φ=0.633, separating the stresses into elastic and viscous according to equation 5.7.

Even though this analysis conceptually corrects the error of $\sigma_e(\gamma=0)=0$ in an oscillatory experiment and predicts the microscopic stresses at the limits of a flow curve, there are issues in its implementation. Foremost we find that in the case of an oscillatory experiment, the calculation of stresses diverge at $\gamma=0$. Moreover, an important technical issue is concerned with the propagation of noise when analyzing experimental data. Figure 5.52 shows the implementation of the analysis of equation 5.7, applying smoothing of the experimental points before the analysis, while discarding the diverging points for $\gamma=0$. The analysis seems to capture the premise that for low Pe' and high strains the elastic (Brownian or entropic)

stresses around γ=0 are comparable to the total stresses, while the viscous (hydrodynamic or diffusive) stresses are relatively small. A large error in the analysis arises from the violation of equation 5.6, especially near the maxima of strain where the derivative of the elastic stress is large. In principle the derivatives of 5.6 can be factored in the calculation of the viscous and elastic stresses, but the stress responses would have to be modeled in order to produce analytical expressions without statistical noise.

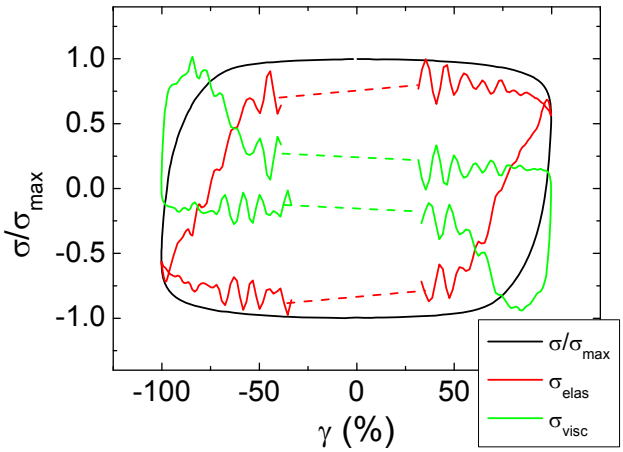

Figure 5.52: Lissajous of non linear oscillatory response with ω=1rad/sec and γ_0=100% for small spheres (low Pe') at φ=0.64. The stresses have additionally been split into elastic and viscous stresses as described in the text. Dotted lines are guides to the eye.

Relaxations within the period

A way to experimentally examine and define an elastic/entropic stress is to abruptly stop the experiment and measure the instantaneous relaxing stress. In literature (Mackay and Kaffashi, 1995; Dullaert and Mewis, 2005), tests such as these have been performed to extract information on and separate the hydrodynamic and Brownian stresses as described in Stokesian Dynamics simulations (Foss and Brady, 2000b). The instantaneous stress that remains after cessation of a shearing experiment is in principle the Brownian stress, which is related to the transient structure under shear, while the hydrodynamic stress is the difference between the Brownian and the total stress referring to stresses caused purely by the application of shear. In the context of the simulations and discussions here, the Brownian stress would roughly correspond to the entropic/elastic stress, while the hydrodynamic stress would correspond to the diffusive/viscous stresses.

Here we experimentally attempt to separate the elastic-like contribution from the total stress by stopping the non linear oscillatory experiments at various points within the period and measuring the resulting stresses. Previous studies (Dullaert and Mewis, 2005) have modeled the rheometer transducer and removed the filter in order to get the small time scales

(t<0.01sec) required to actually extract the initial instantaneous stress relaxation. Modeling the transducer and removing the filter is a lengthy procedure, not in the scope of this work, thus instead we show the evolution of the relaxing stress with time which should qualitatively give measure of the elastic stresses. An example of the measured stress before and during such a relaxation is shown in fig 5.53. Before each relaxation, a few oscillations (5-10) were made in order for the system to reach a steady state.

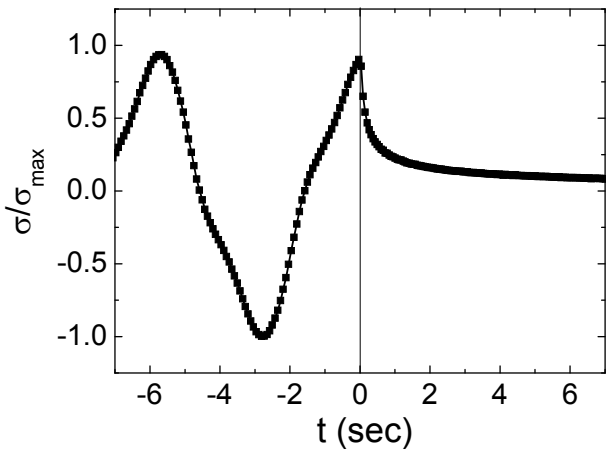

Figure 5.53: Relaxation within the period example of ω=1rad/sec and large spheres (High Pe') at φ=0.62 for γ_0=30%. At t=0sec the strain is kept stable at the specific strain of the period and the stress relaxation is followed.

The relaxation of stress occurs as discussed in chapter 4 through slow out of cage diffusion, with the remaining stress reflecting the anisotropic structure due to the previously applied shear. Thus we expect the relaxation stress to qualitatively show the entropic/structural stresses during the oscillation. Here we show the Lissajous figures of low Pe' for low γ_0=30% in figure 5.54 and high γ_0=100% in 5.55, in conjunction with the relaxation stresses after specific time intervals from the cessation of shear. We find that in both cases the elastic stress evolution is qualitatively very similar to the total stress, which shows an elastic increase right after the stress maximum of about 10% strain in length and a subsequent steady state where the entropic elasticity and structure does not change.

In figure 5.56 we see the relaxations within the period of high Pe' and low strain oscillations, showing an interesting experimental change between the entropic and total stress ratio within the period. During the stress reduction, right after the reversal of strains, we find that the elastic stresses are comparable to the total stresses since as seen from the simulations, almost no out of cage diffusion occurs. As the stress increases after that and collisions occur, the elastic stresses don't increase substantially, but the viscous component increases as there is dissipation due to out of cage motions. If one examines the details of the relaxed stresses,

after the reversal and for about 10% elapsed strain, the stresses actually relax to negative stresses. This according to 5.47b is due to the previous unchanged shear induced structure.

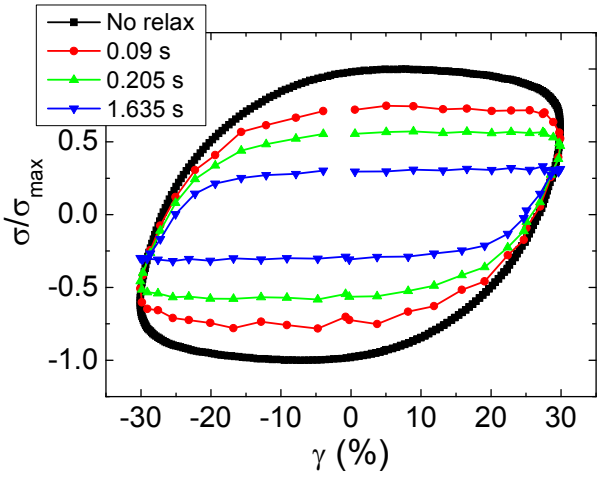

Figure 5.54: Stresses under shear and stresses during relaxation within the period of ω=1rad/sec and small spheres (Low Pe') at φ=0.64 for γ_0=30%.

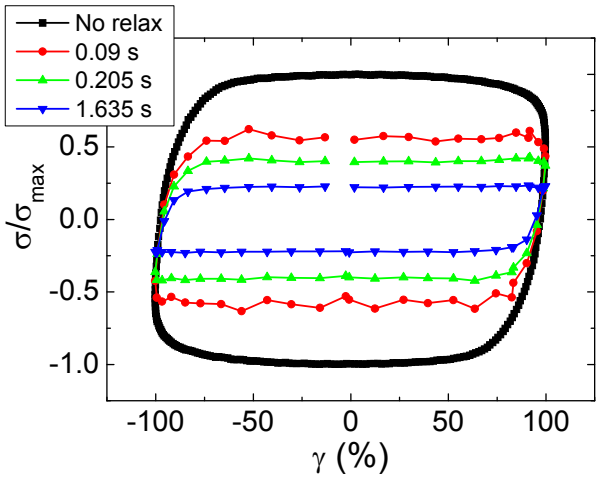

Figure 5.55: Stresses under shear and stresses during relaxation within the period of ω=1rad/sec and small spheres (Low Pe') at φ=0.64 for γ_0=100%.

In figure 5.57 we see the relaxations within the period of high Pe' and high strain oscillations. Here the elastic stress shows an evolution of about 50% from the strain maximum after which it stays constant until reversal as corroborated by the structural changes seen for the simulations in figure 5.3b. We find that the elastic stresses generally have small values due to the dominance of viscous out of cage motions. Therefore we conclude that the findings from the relaxation experiments are as expected from the structural and dynamic properties and examination from simulations.

The relaxations within the period qualitatively give measure of the results of an ideally suited analysis of the Lissajous stress into elastic stress should have. The experimental results show that despite their shortcomings, both the proposed analyses correctly report some of the expected and measured elastic and viscous stresses, and are an improvement upon existing methods. However, great care must be taken to understand the limitations implementing of such simplistic techniques on the complex problem of non linear oscillatory shear. Indeed for systems which are strongly driven out of equilibrium it is debatable if any decomposition of stresses is able to give meaningful data without prior knowledge of expected microscopic properties.

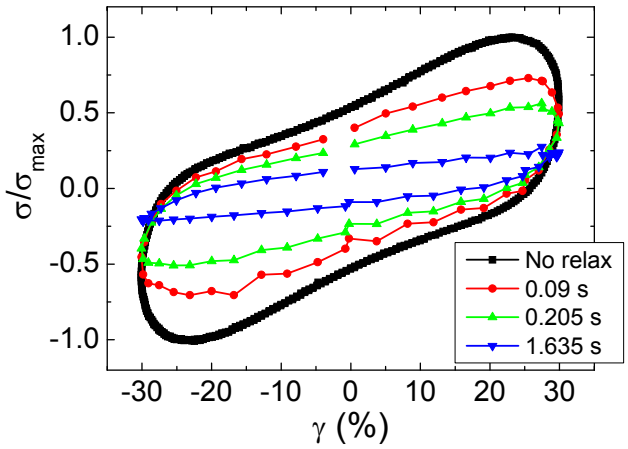

Figure 5.56: Stresses under shear and stresses during relaxation within the period of ω=1rad/sec and large spheres (High Pe') at φ=0.62 for γ_0=30%.

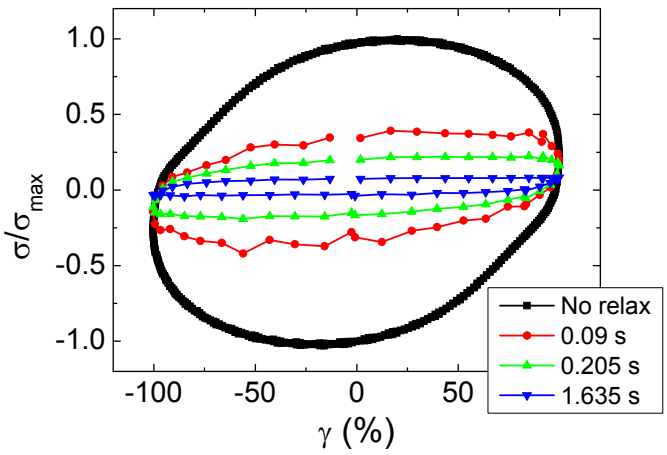

Figure 5.57: Stresses under shear and stresses during relaxation within the period of ω=1rad/sec and large spheres (High Pe') at φ=0.62 for γ_0=100%.

5.5 Chapter Conclusions

We have examined the non linear oscillatory response of glassy hard sphere suspensions in a wide range of frequencies, both experimentally and through Brownian dynamics simulations. We find two distinct regimes, one for the lower frequencies and a second for the higher frequencies (or Pe'), the transition related to the time scale of the in cage beta relaxation and the minimum of G'' in a linear frequency sweep.

In terms of rheological response, dynamic strain sweeps going well into the non linear regime show maxima of G'' at strains of about 10% for low frequencies, while higher frequencies exhibit maxima at strains of 100%. The parameters which characterize the third harmonic, I_3/I_1 and δ_3, may quantify the transition between these regimes, the first through a characteristic minimum, while the second more reliably with a transition at high strains from a dominant shear thinning regime to that of strain hardening. Furthermore, a dynamic strain sweep with what appeared to be two peaks of G'' and thus inferring two distinct yielding processes was observed in a narrow range of frequencies and high volume fractions. These yielding processes are found to be related to the non harmonic properties of the stress response by showing a transition from a low frequency response at low strains to a high frequency response at high strains. Moreover, the stress-strain Lissajous figures have characteristic shapes in each regime. The low frequencies show trapezoid like shapes, with an elastic stress increase for about 10% strain after the rate reversal and a subsequent constant stress. The higher frequencies show a distinct area of reduced stresses compared to a simple harmonic response after the maximum of strain, due to reduction of particle collisions, with a range of 50% strain, while additionally showing a viscous response for the rest of the curve.

When increasing the strain, displacements also increase as more particles are able to undergo out of cage motions, while spatial dynamic inhomogenieties and the non Gaussian parameter show an increase during yielding and then a decrease at larger strains. At the largest strain amplitude displacements are due to out of cage motion and occur homogenously throughout the system, while for strains around yielding the particles are divided into two populations: one that exhibit in cage displacements and a second that exhibit out of cage displacements. High applied strains and rates cause constrictions of particles leading to fewer displacements than at rest for short times due to increased collisions. For applied strains above yield resulting to the shear induced diffusivity higher than that at rest, we find transient super diffusive behavior, between the short and long time diffusivities under shear.

The shear induced diffusivity at high strains shows a linear increase with frequency in the high frequency regime, while increasing with a power law slope of less than one in the low frequency regime. On the other hand, in the limit of maximum packing we may expect no distinction between the diffusivity of the high and low frequency regime, since both should have a slope of one. Moreover, at intermediate strains near yielding a much more complex behavior of particle displacements is observed, with particles showing out of cage diffusion in the low frequency regime, but appear trapped within their cages in the high frequency regime. Although in the latter case the non Gaussian parameter is large, the displacements are found to be spatially homogenous between particles in the system.

For a super cooled liquid near the glass transition, we recognize three regimes for the shear induced diffusivity and stresses under high strain amplitude or steady state shear. At the highest rates, both diffusivity and stresses follow a power law slope of one with applied rate as the stress response is governed by interparticle collisions. For rates corresponding to the non-ergodic plateau of the particle displacements at rest, the stress slope is reduced to zero as a plastic deformation of the entropic cage is probed, with the diffusivity showing a slope of less than one. At the lowest rates, the long time diffusivity is probed, leading to a slope of zero for the diffusion and a slope of unity for the stresses as a function of rate since the system behaves as a fluid.

Lastly, new methods for analysis of the elastic and viscous components of stresses during oscillatory experiments were introduced and examined in relation to stress relaxations after cessation of shear within the oscillation. The comparison showed that although the new methods are an improvement upon existing decompositions, they still lack the necessary sophistication to extract meaningful physical properties for arbitrary stress responses.

5.6 References

Besseling, R., E. R. Weeks, A. B. Schofield and W. C. K. Poon (2007). "Three-Dimensional Imaging of Colloidal Glasses under Steady Shear." Physical Review Letters **99**(2) 028301.

Bird, R., R. Armstrong and O. Hassager (1987). Dynamics of Polymeric Liquids: Volume 1 Fluid Mechanics. New York, Wiley.

Brader, J. M., M. Siebenburger, M. Ballauff, K. Reinheimer, M. Wilhelm, S. J. Frey, F. Weysser and M. Fuchs (2010). "Nonlinear response of dense colloidal suspensions under oscillatory shear: Mode-coupling theory and Fourier transform rheology experiments." Physical Review E **82**(6) 061401.

Breedveld, V., D. van den Ende, M. Bosscher, R. J. J. Jongschaap and J. Mellema (2002). "Measurement of the full shear-induced self-diffusion tensor of

noncolloidal suspensions." The Journal of Chemical Physics **116**(23) 10529-10535.

Breedveld, V., D. van den Ende, R. Jongschaap and J. Mellema (2001). "Shear-induced diffusion and rheology of noncolloidal suspensions." The Journal of Chemical Physics **114**(13) 5923-5936.

Carrier, V. and G. Petekidis (2009). "Nonlinear rheology of colloidal glasses of soft thermosensitive microgel particles." Journal of Rheology **53**(2) 245-273.

Cho, K. S., K. Hyun, K. H. Ahn and S. J. Lee (2005). "A geometrical interpretation of large amplitude oscillatory shear response." Journal of Rheology **49**(3) 747-758.

Cho, K. S., K.-W. Song and G.-S. Chang (2010). "Scaling relations in nonlinear viscoelastic behavior of aqueous PEO solutions under large amplitude oscillatory shear flow." Journal of Rheology **54**(1) 27-63.

Dullaert, K. and J. Mewis (2005). "Stress jumps on weakly flocculated dispersions: Steady state and transient results." Journal of Colloid and Interface Science **287**(2) 542-551.

Ewoldt, R. and G. McKinley (2010). "On secondary loops in LAOS via self-intersection of Lissajous–Bowditch curves." Rheologica Acta **49**(2) 213-219.

Ewoldt, R., P. Winter, J. Maxey and G. McKinley (2010). "Large amplitude oscillatory shear of pseudoplastic and elastoviscoplastic materials." Rheologica Acta **49**(2) 191-212.

Ewoldt, R. H., C. Clasen, A. E. Hosoi and G. H. McKinley (2007). "Rheological fingerprinting of gastropod pedal mucus and synthetic complex fluids for biomimicking adhesive locomotion." Soft Matter **3**(5) 634-643.

Ewoldt, R. H., A. E. Hosoi and G. H. McKinley (2008). "New measures for characterizing nonlinear viscoelasticity in large amplitude oscillatory shear." Journal of Rheology **52**(6) 1427-1458.

Foss, D. R. and J. F. Brady (2000a). "Brownian Dynamics simulation of hard-sphere colloidal dispersions." Journal of Rheology **44**(3) 629-651.

Foss, D. R. and J. F. Brady (2000b). "Structure, diffusion and rheology of Brownian suspensions by Stokesian Dynamics simulation." Journal of Fluid Mechanics **407**(-1) 167-200.

Gadala-Maria, F. and A. Acrivos (1980). "Shear-Induced Structure in a Concentrated Suspension of Solid Spheres." J. Rheol. **24**(6) 799-814.

Klein, C. O., H. W. Spiess, A. Calin, C. Balan and M. Wilhelm (2007). "Separation of the Nonlinear Oscillatory Response into a Superposition of Linear, Strain Hardening, Strain Softening, and Wall Slip Response." Macromolecules **40**(12) 4250-4259.

Koumakis, N., A. B. Schofield and G. Petekidis (2008). "Effects of shear induced crystallization on the rheology and ageing of hard sphere glasses." Soft Matter **4**: 2008 2008-2018.

Le Grand, A. and G. Petekidis (2008). "Effects of particle softness on the rheology and yielding of colloidal glasses." Rheologica Acta **47**(5-6) 579-590.

Mackay, M. E. and B. Kaffashi (1995). "Stress Jumps of Charged Colloidal Suspensions, Measurement of the Elastic-like and Viscous-like Stress Components." J. Coll. Int. Sc. **174** 117-123.

Mason, T. G. (2000). "Estimating the viscoelastic moduli of complex fluids using the generalized Stokes–Einstein equation." Rheologica Acta **39**(4) 371-378.

Mason, T. G. and D. A. Weitz (1995). "Linear Viscoelasticity of Colloidal Hard Sphere Suspensions near the Glass Transition." Phys. Rev. Lett. **75** 2770.

Onogi, S. and T. Matsumoto (1981). "Rheological properties of polymer solutions and melts containing suspended particles." Polym. Eng. Rev. **1** 45-87.

Onogi, S., T. Msuda and T. Matsumoto (1970). "Non-Linear Behaviour of Viscoelastic Materials. I. Disperse Systems of Polystyrene Solution and Carbon Black." Trans. Soc. Rhoel. **14** 275-294.

Petekidis, G., A. Moussaid and P. N. Pusey (2002). "Rearrangments in hard-sphere glasses under oscillatory shear strain." Phys. Rev. E **66** 051402.

Pham, K. N., G. Petekidis, D. Vlassopoulos, S. U. Egelhaaf, P. N. Pusey and W. C. K. Poon (2006). "Yielding of colloidal glasses." Europhysics Lett. **75**(4) 624-630.

Philippoff, W. (1966). "Vibrational Measurements with Large Amplitudes." Trans. Soc. Rheol. **10** 317-334.

Pine, D. J., J. P. Gollub, J. F. Brady and A. M. Leshansky (2005). "Chaos and threshold for irreversibility in sheared suspensions." Nature **438**(7070) 997-1000.

Renou, F., J. Stellbrink and G. Petekidis (2010). "Yielding processes in a colloidal glass of soft star-like micelles under large amplitude oscillatory shear (LAOS)." Journal of Rheology **54**(6) 1219-1242.

Rogers, S. A. and D. Vlassopoulos (2010). "Frieze group analysis of asymmetric response to large-amplitude oscillatory shear." Journal of Rheology **54**(4) 859-880.

Rogers, S. A. and D. Vlassopoulos (2011). In Press.

Sierou, A. and J. F. Brady (2004). "Shear-induced self-diffusion in non-colloidal suspensions." Journal of Fluid Mechanics(506) 285-314.

Weeks, E. R., J. C. Crocker, A. C. Levitt, A. Schofield and D. A. Weitz (2000). Three-Dimensional Direct Imaging of Structural Relaxation Near the Colloidal Glass Transition. **287:** 627-631.

Wilhelm, M. (2002). "Fourier-Transform Rheology." Macromolecular Materials and Engineering **287**(2) 83-105.

Chapter 6 – Simulation of Hard Sphere Crystals under Oscillatory Shear

Abstract

Using Brownian dynamics simulations of hard sphere particles, high volume fraction shear-induced crystals were examined under oscillatory shear. Comparisons of the microscopic motions at rest and under shear were made between a crystal and the same volume fraction glass. For the amorphous and crystalline structures at rest we found that although the short time displacements for the crystal is higher than that of the glass, the dynamic heterogeneities in the glass may allow increase of the displacements above those of the crystal for longer times. Thus while in the crystal particles are completely confined in their cage with the MSD showing a clear plateau, in the glass large scale out of cage motion is observed via dynamic heterogeneities.

When comparing the displacements under oscillatory shear of the glass and the crystal oriented parallel to shear, it was found that the crystal has anisotropic displacements compared to the isotropic displacements in the glass. The crystal displacements are due to cooperative motion of velocity-vorticity layers of particles sliding over each other, thus exhibiting a yield strain less than that of the glass. Past the yield point, the long time shear induced displacements of the glass are found to be larger, while stresses are highly correlated to instantaneous shear induced displacements in both crystal and glass. Thus we conclude that during the experimental shear of a monodisperse glass, the large out of cage displacements allow the system to explore the energy landscape and find the minima in energy, stresses and displacements by configuring particles into a crystal oriented parallel to shear.

Through the examination of the crystal under oscillatory shear, we have found that the displacements of the crystal increase with decreasing frequency, although showing qualitatively similar displacements as a function of applied strain. The yield strain of the crystal is less for lower oscillation frequencies as Brownian motion has time to act upon the system under shear and allow the sliding of the crystal layers. The equivalent of an effective diffusion coefficient was shown to exhibit a power law scaling with frequency of less that one at lower frequencies, an effect of similar origin to the corresponding frequency dependence of a hard sphere glass, the slope being dependent on φ or more accurately the distance from maximum packing. The stress responses of the crystal under oscillatory shear in experiments and simulations were qualitatively similar at low frequencies, with the largest differences

possibly occurring due to the lack of hydrodynamic interactions in the BD simulations as well as crystal defects of the experimental system.

When experimentally shearing a monodisperse hard sphere glass, two different crystal orientations occur; a FCC crystal with the close packed direction parallel to shear at high strains and a crystal with the close packed direction perpendicular to shear at low strains. Similarly to the creation of a crystal from a glass, the low strain perpendicular and high strain parallel to shear crystals may occur due to minimization of stresses and displacements similarly to the shear induced crystallization of a glass. The crystal perpendicular to shear exhibits low stresses and MSD at low non linear strains (10%-20%), while parallel to shear shows slightly larger stresses in the same regions. At higher strains, the sliding layers of the parallel crystal are more efficient in minimizing stresses and the perpendicular crystal is no longer stable. Thus starting from an amorphous glassy system, at low strains a crystal perpendicular to shear is formed, which becomes unstable at larger strains and reorients into a crystal parallel to shear.

6.1 Introduction/Simulation Method

While crystallization in quiescent hard sphere systems occurs within hours or days, under oscillatory shear, crystallization may occur within a few minutes and is oriented with the flow (Ackerson and Pusey 1988). Flow of the shear induced crystals occurs in complicated fashion with crystal layers sliding one over the other (Ackerson 1990). It has been found for dense suspensions of hard spheres (φ>0.545) under oscillatory strain that two different orientations of crystals arise depending on the strain of oscillation; while high strains (γ_0>50%) produce a monocrystal with the closed packed direction parallel to shear (figure 6.1a), low strains (γ_0<50%) produce a distribution of crystallites with orientations around a crystal with the closed packed direction perpendicular to shear (figure 6.1b) (Haw, Poon et al. 1998; Haw, Poon et al. 1998). In the case of the cone and plate geometries used in (Koumakis, Schofield et al. 2008), crystallization manifested only as a crystal with the closed packed direction parallel to shear, possibly due to spatial constrictions for the perpendicular crystal in a rotational configuration.

Previous work on the rheological behavior of shear induced crystallization in hard sphere glasses (Koumakis, Schofield et al. 2008), found that the viscoelastic moduli of shear induced crystals have smaller values than the amorphous/glass of the same φ, although qualitatively similar linear frequency behaviour. When compared to the same distance from maximum

packing, the ordered structure had larger elastic moduli. The yield strains of the crystal were additionally observed to be smaller than the amorphous structure.

The purpose of this work is the detailed determination of the microscopic rearrangements under oscillatory shear and their relation with the mechanical properties for the shear induced crystals formed from a hard sphere glass. We also study the major differences with the amorphous glass of polydisperse hard spheres. For this purpose we performed BD simulation in glassy and FCC crystals with close packing parallel or perpendicular to shear.

Although in the experimental systems the crystals where created by the application of shear, initial testing with simulations showed that crystallization in a finite simulation box creates crystals which are skewed and randomly oriented, even under shear. This occurs as the propagation of the crystal due to Brownian motion occurs faster than shear alignment. Additionally, since the crystal is anisotropic, the periodic box must be of dimensions tailored to fit multiples of the FCC crystal unit cell.

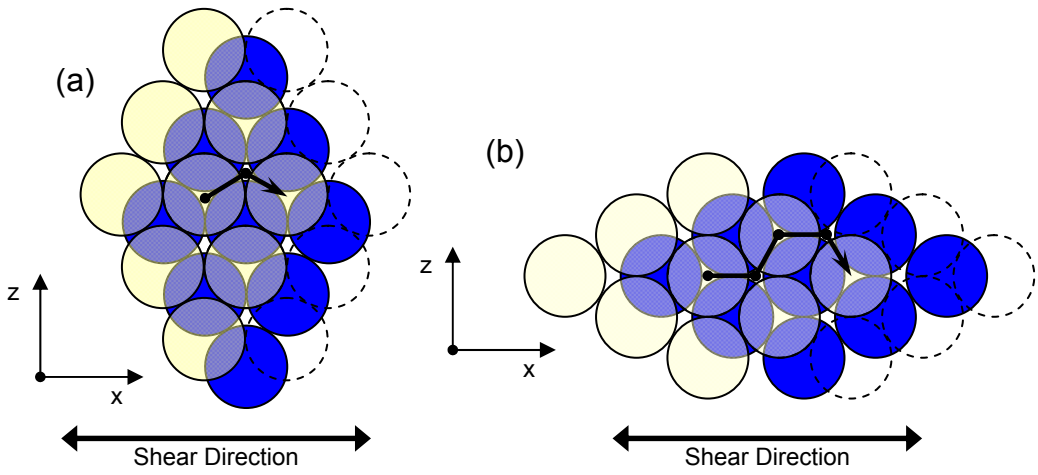

Figure 6.1: Schemes showing a) the simple slipping layer yielding process of a crystal with the close packed direction parallel to shear and b) the complex slipping layer yielding process of a crystal with the close packed direction perpendicular to shear.

Therefore, the simulated hard sphere FCC crystals were initially constructed to the appropriate specifications and then left to reach equilibrium at rest for $t=5t_B$ before applying shear. Depending on the simulation, the (111) plane was positioned on the velocity-vorticity plane with the closed packed direction of the spheres set either parallel (fig. 6.1a) or perpendicular (fig. 6.1b) to the shear direction. As shown in the appendix, there is a dependence of the simulation results on the anisotropy of the simulated box. In general it was found that isotropic boxes are more suitable for looking at systems at rest, while the highly

anisotropic ones for looking at crystal systems under shear. Thus, two types of simulated boxes for the crystal are shown in this paper, one relatively isotropic with 1440 particles and one highly anisotropic (longer in the velocity gradient direction) with 4860 particles. We denote them as 10-12-12 and 6-135-6, representing the number of particle layers in the velocity (x), velocity gradient (y) and vorticity (z) directions respectively. In order to better replicate the experimental conditions, the 6-135-6 system has a random FCC layering in the y-axis.

The amorphous polydisperse glass was simulated in a cubic box with 1440 or 1005 particles both at rest and under shear and a Gaussian distribution of radii with 10% standard deviation to suppress crystallization. The particles in both the amorphous and crystal system were randomly placed and left for some time (a maximum of $300t_B$) to reach a equilibrium before applying shear. Simulations were run with a time step Δt of $2\pi\ 10^{-4}\ t_B$ or less and displacements under shear were averaged over at least 15 oscillations. The particle polydispersity in the simulations is reproduced by a discrete Gaussian distribution having N/13 components with a root mean squared deviation of 10% for the radii, where N is the number of total particles, while the denominator value of 13 is specifically chosen as it allows close representation of the distribution with varying N

6.2 Glass vs. Crystal at Rest

Figure 6.2 shows the mean squared displacements (MSD) of the simulated crystal and glass at rest for various volume fractions both below and above the glass transition. The latter is expected to be slightly above 0.60 as shown in chapter 3 (fig 3.11), as judged by the out of cage relaxation time scale. The crystal shows an initial diffusive increase of the MSD reflecting an in cage beta relaxation and then a plateau. The amorphous configurations show an initial increase (beta), a region of smaller slope and then depending on φ, a strong increase of the MSD or weaker increase. The former corresponds to lower φ out of cage alpha relaxation, while the latter suggests the suppression of out of cage diffusion (between φ=0.60-0.62), with the existence of dynamic heterogeneities as discussed in chapter 3.

Depending on the time scale of probing and the volume fraction, amorphous structure may have a higher MSD than crystal at long times, but less at short times. Both the amorphous and the crystal generally have isotropic displacements at rest which increase in amplitude as φ is decreased. The inset shows the non-Gaussian parameter a_2, as defined in chapter 2, for φ=0.62 for the crystal and the glass. The non-Gaussian behavior is more pronounced in the glass, while its increase with time has been discussed in chapter 3. The crystal on the other hand,

shows a small undulation at relatively small times and then settles at an a_2 value of zero, showing full Gaussian behavior.

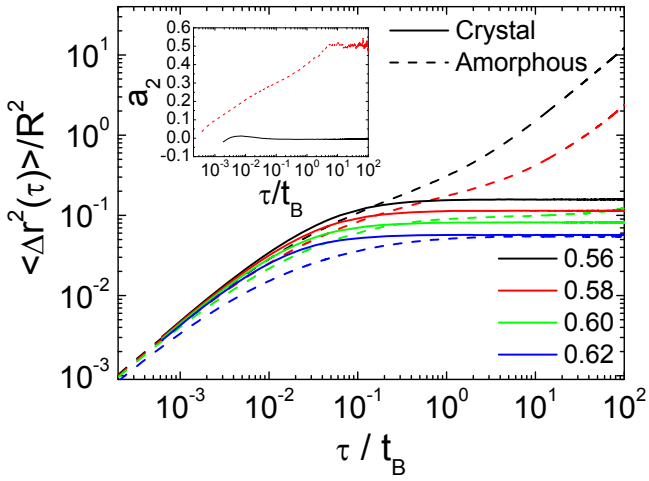

Figure 6.2: Mean squared displacements of amorphous polydisperse configurations and FCC crystal configurations (10-12-12) at rest for different φ. Inset shows the non-Gaussian parameter, a_2, for φ=0.62 at rest for the crystal and the glass.

As φ is increased, the available volume for each particle within its cage decreases causing a general drop of short time particle displacements. At high volume fractions, where there is small or no out of cage α-relaxation, the MSD in a glass is always less than that of the crystal. This occurs because the average available free volume for each particle is always less in the glass when compared to the crystal of the same volume fraction (Koumakis, Schofield et al. 2008). As the volume fraction is decreased though, the α-relaxation becomes important and due to the increase at long times, the amorphous configurations have exhibit larger MSDs at longer times.

The non-Gaussian parameter of the glass seen in the inset is large due to inhomogenieties and collisions; however the crystal shows almost at all times simple Gaussian behavior. Unlike the dynamic heterogeneities seen in the metastable glass, displacements of the crystal particles are spatially homogeneous. The small undulation corresponds to the time scale of the particles encountering the crystal cage where the MSD turns to a plateau and displacements are constricted.

6.3 Glass vs. Parallel Crystal under Oscillatory Shear

Glass vs Crystal under Shear: Mean Squared Displacements

In figure 6.3a we show the MSD of a glass and a crystal parallel to shear at φ=0.62 with time at a specific strain of 30% and a Pe' of 1. In the case of the glass, the displacements are isotropic, with the $<\Delta x^2>$, $<\Delta y^2>$ and $<\Delta z^2>$ curves being approximately equal. In the case of the crystal however, the curves follow different paths showing the highly anisotropic behavior in a crystal under shear. Displacements in all directions are approximately the same at short times, corresponding to in cage motion, but at longer times, where out of cage motion due to shear occurs, $<\Delta x^2>$ exhibits the highest increase, followed by $<\Delta z^2>$ and last $<\Delta y^2>$, which remains almost stable. The small increase of $<\Delta y^2>$ at long times is most probably due to Mermin-Wagner fluctuations (Mermin 1968) as shown in the Appendix. The effect of Taylor dispersion on the motion of the crystal under shear should be minimal as displacements in the velocity gradient direction are small in comparison to the displacements of the shear direction, as discussed in the Appendix.

Figure 6.3b depicts the MSD for the different directions with respect to shear at a specific time equal to one period ($t=T=2\pi t_B$) for the φ=0.62 glass and crystal. Again the anisotropy of the crystal under shear is clear when compared to the glass. At strains greater than 5%, the beginning of yielding (Koumakis, Schofield et al. 2008), the particle displacements in the glass initially show a sharp and then a weaker increase with strain. Similarly the crystal shows substantial changes above the yield strain. The greatest increase is in the x direction and persists up to 100%. However the MSD in the z-axis, slowly decreases with increasing strain after the initial jump. The y-axis displacements do not show abrupt changes around the yield point, but exhibits a slight decrease at higher strains. The inset depicts the average displacement behavior ($<\Delta r^2>$) in the glass and the crystal with applied strain again at τ=T. The main finding apparent from figure 6.3b is that while the glass and crystal exhibit similar overall displacements in the linear regime (see also fig 6.2), at strains above the yield the glass has significantly larger displacements which furthermore increase faster with strain than the crystal.

The glass in fig. 6.3a qualitatively shows a much different behavior than the crystal. As mentioned, a major difference is the isotropic displacements of the glass, both in short and long times. The short times which correspond to in-cage motion, exhibit weaker displacements than the crystal, because of the decreased free volume per particle (Koumakis, Schofield et al. 2008), similar to the situation at rest. At longer times, which are comparable to the period of oscillation, shear induced out of cage displacements occur showing a diffusive

character. The shear induced diffusion in the glass, unlike that of the crystal, occurs at a single particle level. The similar values of long time displacements for the crystal in the x-axis and for the glass are coincidental as can be seen in the strain dependence of fig. 6.3b.

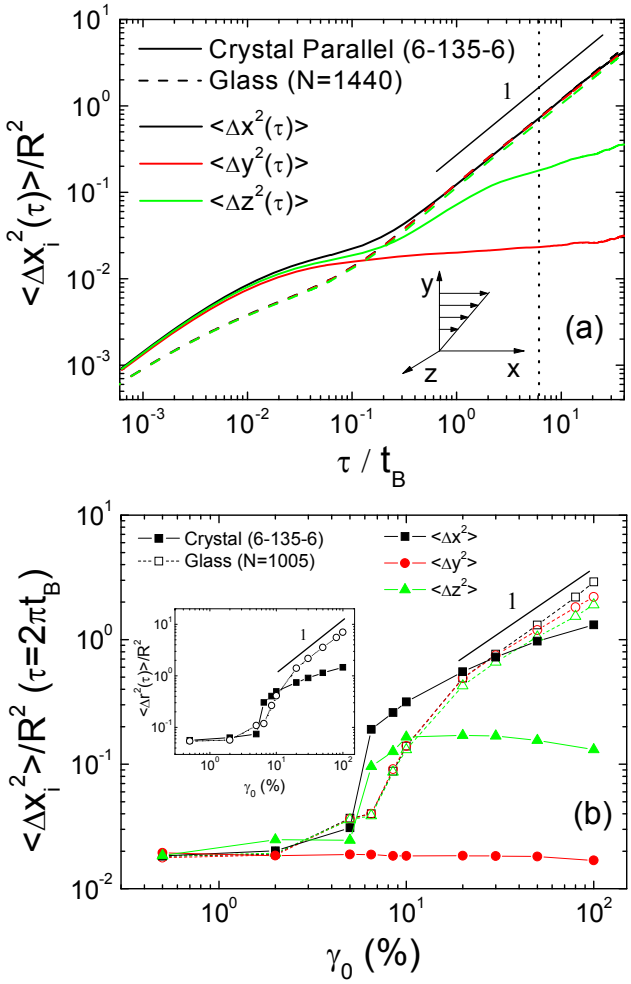

Figure 6.3: Mean square displacements of a glass and crystal parallel to shear at φ=0.62 under oscillatory shear at Pe'=1 with a) the MSD at different directions vs time at 30% strain and b) the MSD at different directions vs Strain at $\tau=T=2\pi t_B$ and overall displacements vs Strain at $\tau=T=2\pi t_B$ (inset). The vertical dotted line in a) refers to the time scale of points in b), while the solid lines in both a) and b) are power law slopes of 1.

By looking at a specific time scale, in this case the period of oscillation (τ=T), we may examine the MSDs in relation to the maximum strain γ_0 and the shear rate $\dot{\gamma}$ (figure 6.3b). The displacements in the glass start with low values at low strains, reflecting the low in-cage plateau. The sharp increase above the yield strain (>5%) with an exponent of greater than 1, is related to the glass cage that starts to "melt" as particles start to diffuse out of their cage under the influence of shear (the $\langle\Delta r^2\rangle$ vs τ exponent is approaching unity at long times). In the glass, diffusive behavior is observed in this time scale for values of γ_0>10%. The linear

increase ($<\Delta r^2>$ vs γ_0 exponent of roughly 1) seen at higher strains (>10%) is due to the γ_0 and $\dot{\gamma}$ increase of diffusivity (Foss and Brady 2000; Besseling, Weeks et al. 2007; Besseling, Isa et al. 2009) and is found to have a power law slope dependence on the frequency and volume fraction as discussed for oscillatory shear in chapter 5.

With the help of the scheme of fig. 6.1a, which depicts the crystal layers and sliding mechanism and in agreement with previous findings and suggestions (Ackerson 1990; Derks, Wu et al. 2009), one can explain the MSD findings in figures 6.3a and 6.3b. In the glass, particles have random isotropic positions, so at rest and under shear, the displacements in the x, y and z directions are almost isotropic (Foss and Brady 2000; Besseling, Weeks et al. 2007; Besseling, Isa et al. 2009), as also shown in chapters 4 and 5. In the case of the crystal, however even though the positional anisotropy of the particles does not cause any strong anisotropic displacements at rest, it shows strong anisotropy under shear.

As shown in fig. 6.1a, in a crystal the particles under shear are confined to their crystal layers in the x-z plane. Shear causes the particle layers to slide over each other, giving rise to the displacements seen in fig. 6.3a and 6.3b. The figures show that at strains above yield, the largest displacements in the crystal are in the x direction (velocity), as the layers slide in this direction. The z direction (vorticity) has the second largest displacements, due to the layer zig-zag motion that allows the sliding to take place. The confinement in the x-z plane means that the smallest displacements occur in the y direction (velocity gradient), which can be attributed to in-cage diffusion. In fig. 6.3a, $<\Delta x^2>$ shows diffusive behavior for long times, reaching a power law of one, though it should be clarified that such diffusion occurs through the motion of layers as whole rather than individual particles as will be shown below. The out of cage $<\Delta z^2>$ shows a strong initial increase directly related to the zig-zag motion, while the weaker long time increase should be related to a longer time scale layer hopping. Finally, we note that the increase of $<\Delta y^2>$ at longer times is due to an artifact of the large anisotropy of the box and is discussed in the Appendix.

While having isotropic displacements at low strains, the crystal exhibits high anisotropy above the yield strain (>5%). The increase in $<\Delta x^2>$ above yield strain occurs, as discussed, because of increased displacements due to sliding layers. Above the yield strain there is also a sudden increase of $<\Delta z^2>$, from the zig-zag motion of the layers, although the values dwindle with increasing strain as higher shear rates constrict the motion to specific pathways lowering the in-cage Brownian motion. Similarly, $<\Delta y^2>$ decreases as the higher rate sliding layer motion constricts random Brownian motion in the y-axis as well.

The overall displacements in the inset of fig. 6.3b show that although the MSD of the glass and crystal are comparable in the linear regime, the glass shows significantly more long time displacements in the non linear regime than the crystal. At γ_0>10%, particles in a glass rearrange a diffusively at the time scale of one period and $<\Delta r^2>$ vs τ shows a linear increase. At γ_0 > 20% particles in a crystal rearrange anisotropically with average displacements always less than in the glass. A peculiar finding is that the exponents of $<\Delta r^2>$ vs γ_0 and also $<\Delta x^2>$ vs γ_0 are about 0.6, while at this time scale $<\Delta x^2(\tau)>$ suggests a diffusive behavior ($<\Delta x^2>\sim\tau$). As discussed in chapter 5 for the glass, this non-trivial exponent is affected by the distance from maximum packing i.e. it is φ dependent.

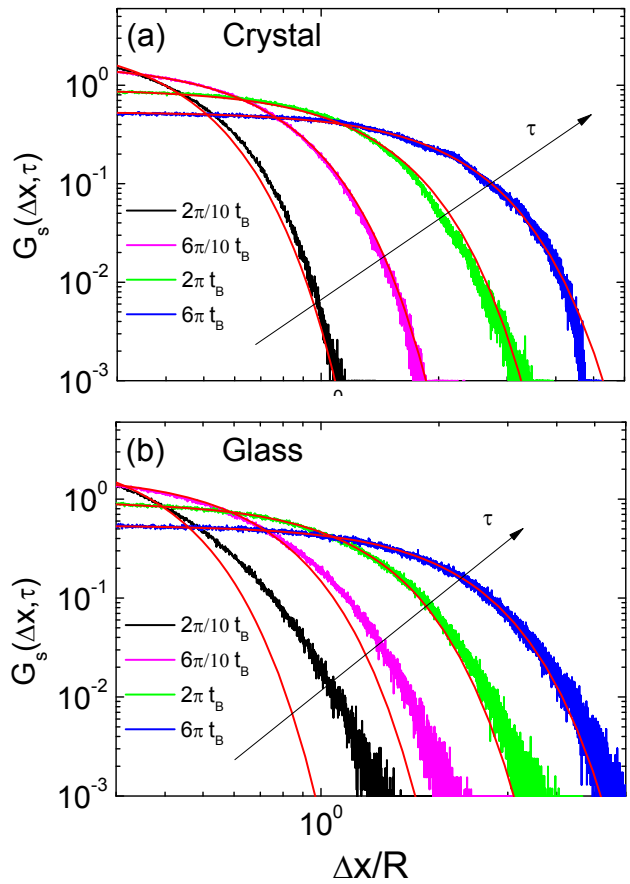

Figure 6.4: x-axis single sided Van Hove self correlation functions (probability density function) at φ=0.62 under oscillatory shear at Pe'=1 and 30% strain amplitude at various time scales $\tau/t_B=2\pi/10$, $6\pi/10$, 2π and 6π with $T=2\pi$ for a) the crystal parallel to shear and b) the glass.

Experimental findings of (Derks, Wu et al. 2009) on a crystal under steady shear showed a linear increase of both long and short time diffusivity. This is not the case for our findings as we extract a sub-linear slope of 0.6 for long time displacements, while short time

displacements related to in cage diffusivity show almost no changes when compared to rest. As stated in their work, the extracted short time diffusivity was estimated by using the shortest experimentally accessible time scale and thus may also include out of cage motions. Additionally, the long time diffusivities were examined in a small range of shear rates, which may have given an apparent linear dependence with rate. Moreover, their experiments were carried out under the application of steady shear, which may qualitatively change particle motions in comparison to oscillatory shear.

The higher MSD values in the crystal around γ_0=10% can be explained by the difference of yield strains between crystal and glass. The onset of yield in the glass shows a smaller strain than the in crystal, although the crystal yields more abruptly in a smaller range of strains due to the slipping layers, thus the particle displacements in the crystal are higher than in the glass around the crystal yield strain. This is seen in the rheological measurements of (Koumakis, Schofield et al. 2008), with the onset of yield being earlier for the glass, while reversely the solid to liquid transition occurring sooner for the crystal. Such behavior may not be observed if we probe a higher volume fraction glass with a smaller yield strain. Additionally, it is important to note that as the probed time scale decreases, thus monitoring in-cage motion, the qualitative differences between a glass and crystal should also decrease, as may be inferred from figure 6.3a. Generally we find that the average long time particle displacements in the crystal under shear are smaller than in the glass of the same volume fraction. At shorter times though, which reflect the in-cage motions, particle displacements in the crystal are larger than those in the glass due to the increased free space.

Glass vs Crystal under Shear: Non Gaussian Behavior

In order to quantify the deviation of the displacements under shear from Gaussian statistics we plot Van Hove probability density functions along with the non Gaussian parameter a_2 as described in chapter 2. Fig. 6.4 shows the x axis Van Hove functions of the crystal (6.4a) and glass (6.4b) at Pe'=1 and γ_0=30% as seen for the MSD in fig. 6.3a with the corresponding Gaussian fits. The time scales probed range from within the period (at T/10) to a multiple of the period (at 3T). The crystal roughly shows Gaussian behavior for all time scales, while the glass shows stronger deviations as time scales become smaller within the period. Figure 6.5 shows the a_2 parameter as a function of time for the crystal and glass under shear again at Pe'=1 and γ_0=30% and at rest. The crystal under shear shows similar values to rest for the smallest times, while for larger times, although still before the time of a period, there is a peak. Larger times move towards a zero value with a high statistical error. The glass under shear as discussed in detail in chapter 5, exhibits higher values of a_2 than at rest at small

times, which increase and shows a peak for time scales less than an oscillation period. At times larger than a period, the glass particle displacements become Gaussian.

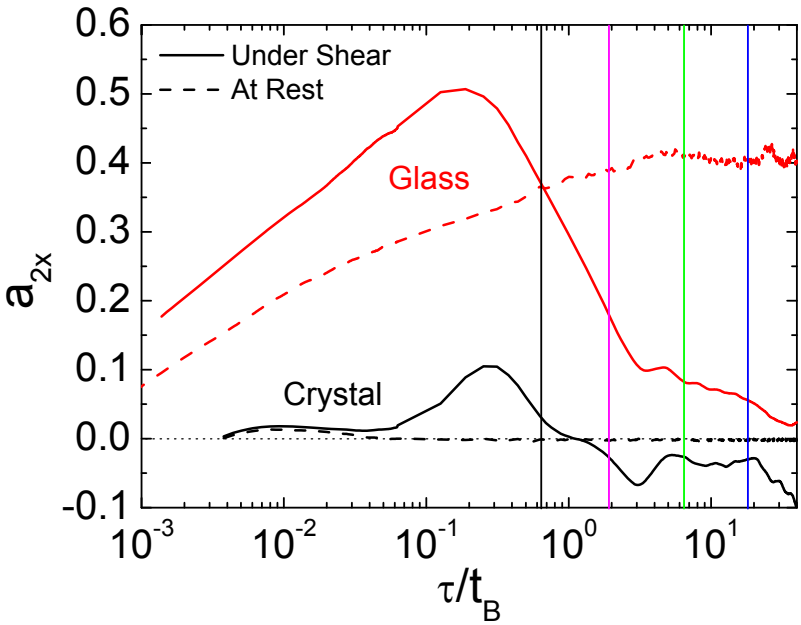

Figure 6.5: Non Gaussian parameter in the x-axis versus time for the crystal parallel to shear (black) and the glass (red) at φ=0.62 for Pe'=1 and γ_0=30% as in fig. 6.3a and at rest. The vertical lines correspond to the time scales probed in figures 6.4a and 6.4b.

The slope of unity for the x axis displacements of the crystal (fig. 6.3a) at long (and short) times together with behavior of the Van Hove function (6.4a) and the a_2 parameter (6.5) suggests that particle displacements are Gaussian at these time scales. For the glass (fig. 6.3a) the displacements at long time increases linearly with time, while a_2 is close to zero, suggesting diffusive out of cage motion due to shear. However at shorter times the displacements are non Gaussian. In figure 6.5, the non Gaussian parameter of the glass under shear increases with time prior to flow, because of dynamic inhomogenieties at rest as well as the non Gaussian contribution from particle collisions due to shear and then drops to zero (as seen in chapter 5), when out of cage diffusivity becomes important at long times.

Similarly, the crystal with minimal non-Gaussian behavior at rest shows a peak at the time scale that marks the transition from the in-cage diffusion to the shear induced sliding layer diffusion. Moreover, in 6.4a, the Van Hove correlation functions for the crystal shows some undulations at long times due to statistical error. The same statistical errors can be seen in the a_2 parameter of the crystal (6.5). This is due to the fact that after the crystal yields, we are

probing the concerted motion of sliding layers, thus essentially averaging the x-axis motion of only 135 layers, instead of 4860 particles.

Cooperative Motions of Crystal under Shear

To investigate how cooperative particle displacements occur in a sheared crystal, we calculate the mean squared displacements of each particle in the crystal after subtraction of the motions of their x-z plane neighbors. In order to do this we modify the equation for the calculation of the MSD from chapter 2 as:

$$\left\langle \Delta x_{neib}{}^{2} \right\rangle_{\tau} = < \frac{1}{\mathrm{N}} \sum_{i=1}^{N} \left[\left(x_i(t+\tau) - x_i(t) \right) - \frac{1}{Z} \sum_{k(i)}^{Z} \left[x_{k(i)}(t+\tau) - x_{k(i)}(t) \right] \right]^2 >_{\tau} \quad (6.1)$$

where Z is the total number of other particles. In this case, Z=6 and the *k* particles are identified as the closest neighboring particles of the same x-z layer at the beginning of the simulation and remain the same throughout the calculation. Specifically, a Z number of *k* particles are chosen from the initial configuration when satisfying these conditions in relation to the *i* particles: $|\vec{r}_i - \vec{r}_k| : \min$ and $|y_i - y_k| : \min$.

Figure 6.6 shows particle displacements under shear relative to their x-z layer cage neighbors for the crystal parallel to shear at φ=0.62, at low (γ_0=10%) and high (γ_0=100%) strains with Pe'=1. Displacements in the velocity gradient direction (y) have not been plotted, because $<\Delta y_{neib}^2>$ is statistically similar to $<\Delta y^2>$ as the single particle motion in this axis is uncorrelated to its neighbors (for this φ). The relative displacements seem to remain practically constant at all times under shear, except in the case of $<\Delta x_{neib}^2>$ for 100% where an increase at longer times is observed in the linear regime (γ_0=2%) and similarly to the displacements at rest, $<\Delta x_{neib}^2> \approx <\Delta z_{neib}^2>$. In the non-linear regime, at $\gamma_0 \geq 10\%$, $<\Delta x_{neib}^2>$ steadily increases with increasing strain, while $<\Delta z_{neib}^2>$, decreases. The Van Hove functions for γ_0=30% for the x-axis displacements at various time scales shown in the inset are practically identical and of Gaussian character.

The relatively constant values of $<\Delta x_{neib}^2>$ and $<\Delta z_{neib}^2>$ under shear compared to their respective $<\Delta x^2>$ and $<\Delta z^2>$ show that indeed the previously discussed displacements occur as collective motions of whole x-z layers and do not correspond to individual particle motion. This means that the values of $<\Delta x_{neib}^2>$ and $<\Delta z_{neib}^2>$ only reflect the changes in the in-cage Brownian motion of the particles, since particles are trapped in their layers. Consequently, the decrease of $<\Delta x_{neib}^2>$ or $<\Delta z_{neib}^2>$ corresponds to a constriction of the cage in the specific direction, while an increase will suggest an elongation. Hence fig. 6.6 indicates a constriction

of the cage with increasing strain in the z-axis, in addition to that seen before in the y-axis (fig 6.3b).

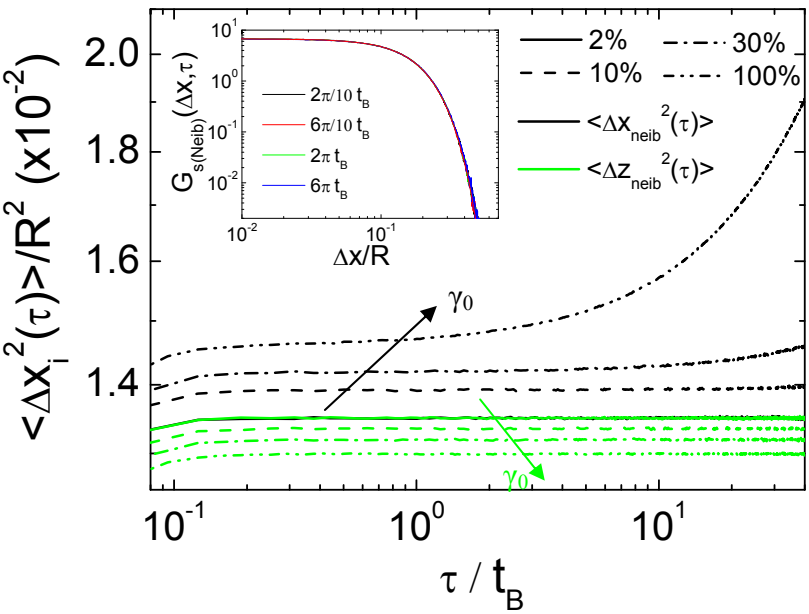

Figure 6.6: Mean squared displacements under shear from a crystal parallel to shear at φ=0.62 and Pe'=1 for γ_0=2%, 10%, 30% and 100% strain amplitudes. Values of $<\Delta y_{neib}^2(\tau)>$ have been omitted as they are statistically equal to $<\Delta y^2(\tau)>$. The inset shows the Van Hove function of the relative displacements for γ_0=30% in the x axis at different times and a Gaussian fit.

The increase of $<\Delta x_{neib}^2>$ at high strain and longer times points to an elongation, which is possibly an inlayer cage stretching due to strong collisions. More accurately it hints towards a fluctuating cage distortion, instead of a simple static elongation, which requires more than a single period of oscillation for a particle to probe its length. The alternative of inlayer out of cage displacements has been ruled out by neighbor enumeration at the end of the analysis, which shows that no overtaking events occur. Assuming this increase is due to inlayer cage stretching, in the limit of infinite time, relative displacements, $<\Delta x_{neib}^2>$, should reach a second plateau. This has not been directly seen, but there are some indications of a plateau value for applied strains at around 10%. Unfortunately, verification of this would generally require simulated time scales of a few orders of magnitude more.

Additionally we find that for these time scales, the displacements are quite far from the Lindemann criterion of crystal melting (Lindemann 1910), which would need $\sqrt{\langle \Delta x_{neib}^2 \rangle} > 0.26R$, whereas the maximum value shown in figure 6.6 is $\sqrt{\langle \Delta x_{neib}^2 \rangle} \simeq 0.14R$. Indeed from the state at rest of figure 6.2, the limit of φ=0.545, where the crystal is expected

to melt, we may estimate $\sqrt{\langle \Delta x_{neib}{}^2 \rangle} = 0.26R$. Moreover, as seen from the Van Hove function inset, the relative crystal displacements in the x-axis are Gaussian for γ_0=30%. The rest of the different strains and axis show similar Gaussian behavior at all shown time scales.

Glass vs Crystal under Shear: Dynamics and Stresses within the Period

The simulated MSDs under oscillatory shear examined up to this point, were averaged between configurations throughout the period that did not have equal shear rates. A next step would be to look into the particle motions under shear within the oscillation period and additionally examine their correlation to shear stress. Since experimentally the echoes are not able to probe the rearrangements that occur within the period, simulations are best suited. Figure 6.7 shows the instantaneous MSD, $<\Delta x_i^2>_{inst}$, and shear stresses of the crystal and the glass for φ=0.62, γ_0=30% and Pe'=1, in order to understand the rearrangements within the period of oscillation in the non linear regime. $<\Delta x_i^2>_{inst}$ are determined by averaging displacements over a small part of the period ($\tau=2\pi/100=T/100$).

In both the cases of crystal parallel to shear (fig. 6.7a) and amorphous glass (fig. 6.7b) the displacements are quite complex and change within the period of oscillation, contrary to the more trivial case of the linear regime (γ_0<2% - not shown). Due to anisotropy and layer displacements, the crystal does not exhibit stresses and displacements that are simply proportional to the rate, but seem to depend on both the elapsed strain and the rate (fig. 6.7a). When the rate is zero and the strain is maximum at $t/t_B=\pi/2$, the crystal is like at rest (for relatively low Pe'), as the small rate allow relaxation from previous shear history. Although the stress values decrease afterwards with a negative shear rate, the actual stress resistance increases. After this point, the resistance increases until about 20% of elapsed strain, where we observe a peak and then a subsequent decrease of resistance. There are some undulations of the stress and then a reversal of the process at zero shear rate (60% of elapsed strain). As seen in previous experimental work, the crystal generally has less stresses than glass in the non linear regime(Koumakis, Schofield et al. 2008). The displacements in the different axes show a behavior that roughly corresponds to that of the stress. The glass displacements are somewhat simpler than the crystal following the rate of shear and the stresses more closely. The crystal displacements however are more complicated exhibiting peaks and valleys at specific points in the oscillation in correlation to similar findings in the shear stress.

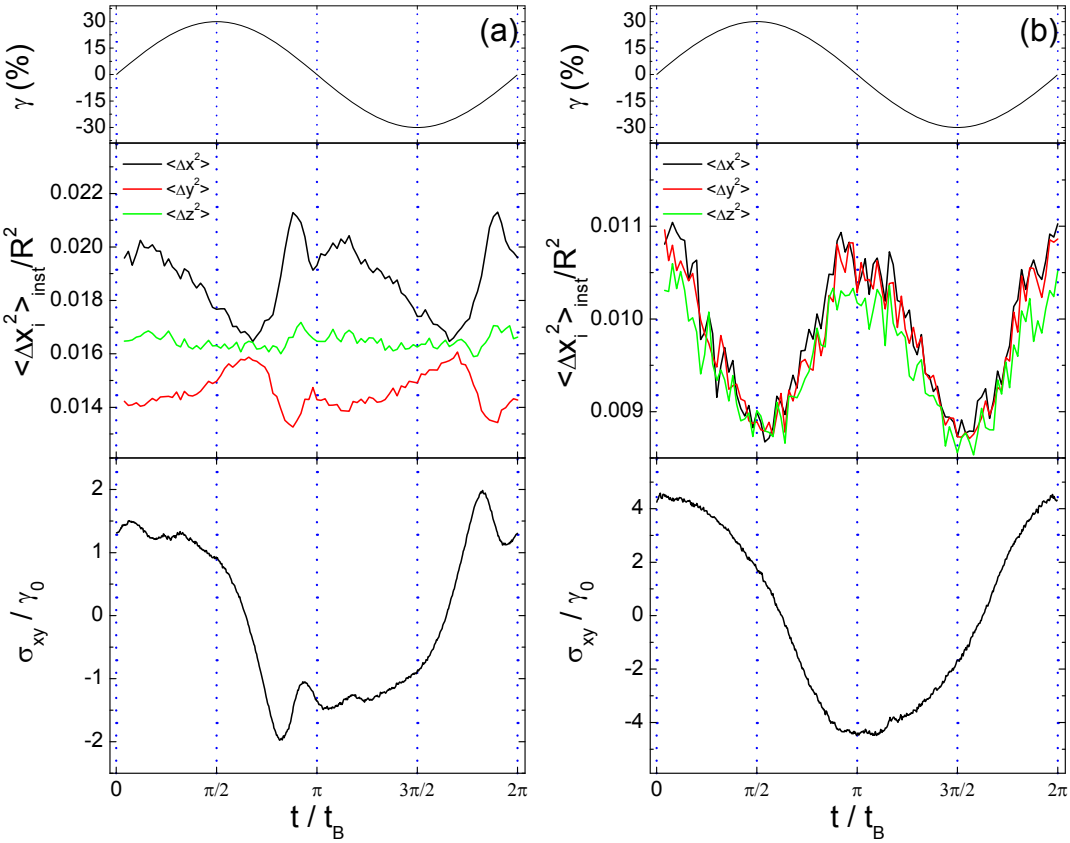

Figure 6.7: Mean squared displacements at $\tau=2\pi t_B/100$ ("instantaneous" MSD) for each axis at $\varphi=0.62$, Pe'=1 and $\gamma_0=30\%$ within the period (top) and normalized stress (bottom) versus time of a) the crystal parallel to shear and b) the same φ glass

As stated, the glass (fig. 6.7b) has isotropic displacements and stresses which are roughly proportional to the rate. When the isotropic glass is sheared in the non-linear regime, the system is shear melted and flows with particles forced out of their cages. The proportionality of the stress to the shear rate shows viscous behavior and thus the increased displacements under shear correspond to the energy dissipation related to viscous stresses and out of cage displacements (chapter 5). The complex behavior of the crystal within the period can be explained by the anisotropy and sliding layer yielding process. As described, there is a peak in the stress response approximately after 20% strain has elapsed from the point of zero shear rate. The x-axis instantaneous displacements show a slightly delayed, but sharp increase, along with the occurrence of the peak of the strain. Thus as the motion in the x-axis corresponds to layer sliding, we conclude that the stress peak corresponds to the storage of energy as the system is strained and then the release of this energy when the layers begin to slide. The y-axis shows a minimum instead of a peak, due to the constriction that occurs during the sliding. In this axis, the absence of significant displacements in the z-axis, the direction of the zig-zag motion, relates to the smaller speed of motion compared to the other

directions. The undulations after the first peak are caused by subsequent sliding of the layers, which are present only in the crystal because of the reproducibility of the structure with increasing strain and that should not be apparent in the amorphous glass.

The instantaneous particle displacements within the period in the crystal, on average, are larger than in the glass, while reversely the stresses in the glass are larger than in the crystal. This occurs because the measured stress does not correspond to the absolute values of the instantaneous MSD; rather they roughly correspond to the change of displacements from the random Brownian motion average at that time scale. Since $<\Delta x \Delta y>$ at rest is zero and the displacements in the x and y directions are uncorrelated, we are able to directly get $\sigma_{xy} \sim <\Delta x \Delta y>_{(\tau \rightarrow 0)}$ from the simulation method. However, σ_{xy} is generally is not directly relatable to $<\Delta x^2>$, $<\Delta y^2>$ or $<\Delta z^2>$ as random Brownian motion also contributes to these values.

Glass vs Crystal under Shear: Discussion

Another way of examining the properties of the crystal and the glass and quantitatively comparing the viscoelastic properties with the MSD is using the Generalized Stokes Einstein (GSE) equation from (Mason 2000) as described in chapter 3. The GSE relates the complex shear modulus with mean square displacements as $G^*(\omega = 2\pi/\tau) \propto 1/<\Delta r^2(\tau)>$. Thus the plateau value of the mean square displacement, quantifying the localization of the particle should be inversely proportional to the elastic modulus. However we observe that at Pe'=1 (or $\tau=2\pi$) and linear strains for $\varphi=0.62$, the isotropic plateau MSD, for the glass and the crystal is comparable (as in fig. 6.2), but elastic modulus of glass is larger than that of crystal. Therefore in contradiction to the GSE relation from (Mason 2000), while the crystal and the glass in simulations have similar MSD, the moduli are quite different. In this formulation, it may be that the changes in the structural properties (i.e. amorphous vs ordered) and thus the elastic constants are not taken into account, although this is not yet clear.

Generally, we know that the FCC crystal is the entropically favorable configuration of concentrated hard sphere dispersions (Kegel and Dhont 1999; Pusey, Zaccarelli et al. 2009). When in the glass regime, the particles find themselves kinetically trapped and unable to rearrange into the minimum free energy state. The application of shear provides the particles in the glass regime the ability to rearrange and explore the energy landscape with large and isotropic MSD as seen in fig. 6.3. Eventually the particles find the minimum free energy (maximum of entropy) and as seen in experimental studies (Ackerson and Pusey 1988; Ackerson 1990; Haw, Poon et al. 1998; Haw, Poon et al. 1998; Koumakis, Schofield et al.

2008), the system crystallizes with specific orientation compared to shear. As seen in figs. 6.3 and 6.7, the crystal that is created under shear has both less shear stress and fewer displacements which are additionally anisotropic.

6.4 Parallel Crystal under Oscillatory Shear

Crystal under Shear: Frequency Dependence of Displacements

Now turning our focus solely to the crystal parallel to shear, figure 6.8a shows the strain dependence of the MSD for two different frequencies, Pe'=0.1 and Pe'=1, at φ=0.62 separately in the three axis, while figure 6.8b shows the x-axis for Pe'=0.1, 1 and 10. The extracted MSDs are at a time scale of one period ($20\pi\ t_B$ for Pe'=0.1, $2\pi\ t_B$ for Pe'=1 and $2\pi/10\ t_B$ for Pe'=10). For Pe'=1 the data in fig. 6.8 is the same as plotted and described for fig. 6.3b. The curves for all directions and Pe'=0.1 in 6.8a have larger values than for Pe'=1 and the onset of non linearities is smaller for Pe'=0.1 (>2%). Additionally, between the two frequencies the displacements have qualitatively similar shapes. Similarly in 6.8b, displacements increase with decreasing frequency and again non linear behavior begins at lower strains for lower frequencies.

The increase of the displacements at lower Pe' is due to the larger time scale per period that allows Brownian motion to enhance the shear induced displacements during sliding. This is also seen experimentally in glasses under shear (Petekidis, Moussaid et al. 2002) and as discussed previously in chapter 5. Looking at both 6.8a and 6.8b, it seems that the yield strain for lower Pe' is smaller, which should again be related to the longer time scale per period and the larger contribution of Brownian motion which assists the random sliding of layers. This is concurrent to experimental rheology (Petekidis, Vlassopoulos et al. 2003) and simulations (Chapter 5) of hard sphere glasses where yield strain increases with frequency. At the smallest Pe' there is a minimum yield strain, being the least amount of distortion needed to allow Brownian motion layer escape. Similarly for the highest Pe' there is a maximum yield strain which corresponds to the largest allowed distortion before the crystal layer has slid to the next layer position.

As done in chapter 5 for the glass in oscillatory shear, we examine the displacements of the crystal under large amplitude oscillatory shear at a specific strain against the applied frequency. The displacements divided by the period in figure 6.9, show an increase with a slope of about 0.6 at the lowest frequencies. At about Pe'=3, similarly to the case of γ_0=30% for the glasses, there is a drop in effective diffusivity and a subsequent increase. When compared to the state at rest (fig 6.10), the longest time scales (smaller Pe') show large

displacements under shear, whereas at smaller time scales the shear induced displacements become identical to those at rest.

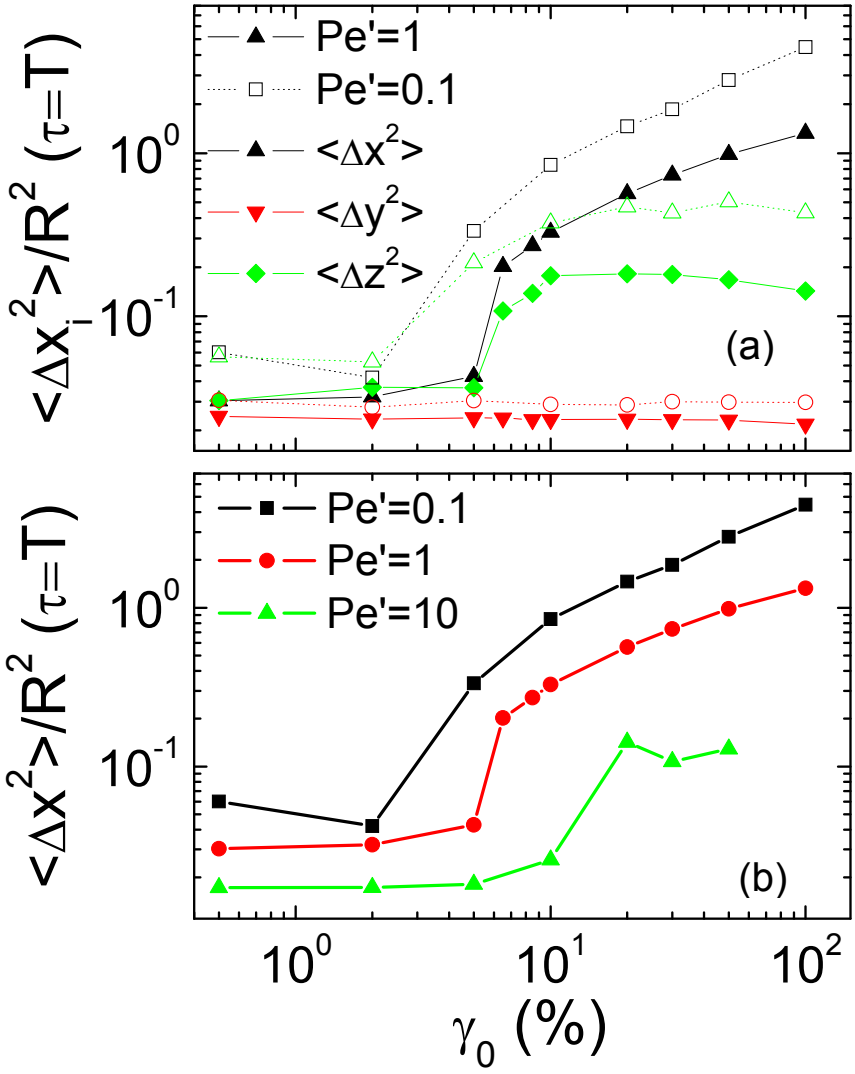

Figure 6.8: Mean squared displacements vs strain for a crystal parallel to shear at φ=0.62 for a time of a single oscillation period in a) all axis and two different Pe' (0.1 and 1) and b) only the x axis and three different Pe' (0.1, 1 and 10).

As seen for the glass, the non Gaussian parameter of fig 6.11a is close to zero for small Pe', an indication of simple shear induced diffusive behavior. At the reduction of displacements (Pe'≈10), a_2 shows a peak, seen in detail by the deviation of the van Hove functions from Gaussian behavior (6.11b).

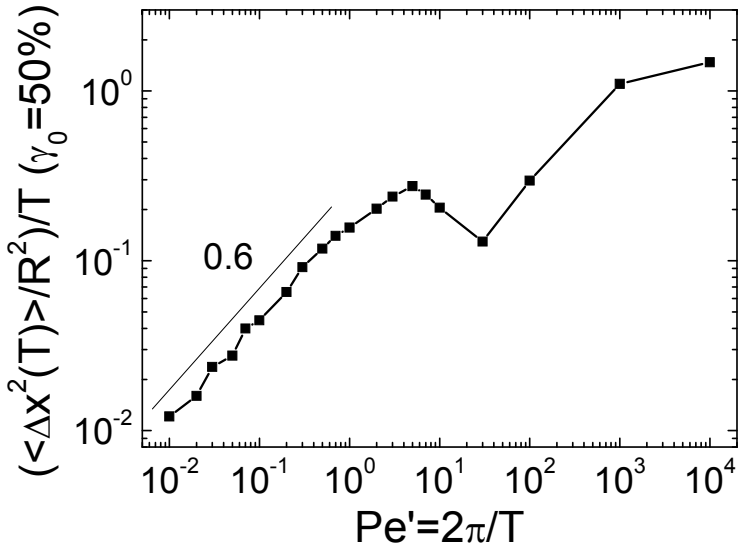

Figure 6.9: Effective diffusion coefficient in the x-axis for a time (t=T) averaged over the period vs Pe' for the crystal parallel to shear at γ_0=50% and φ=0.62.

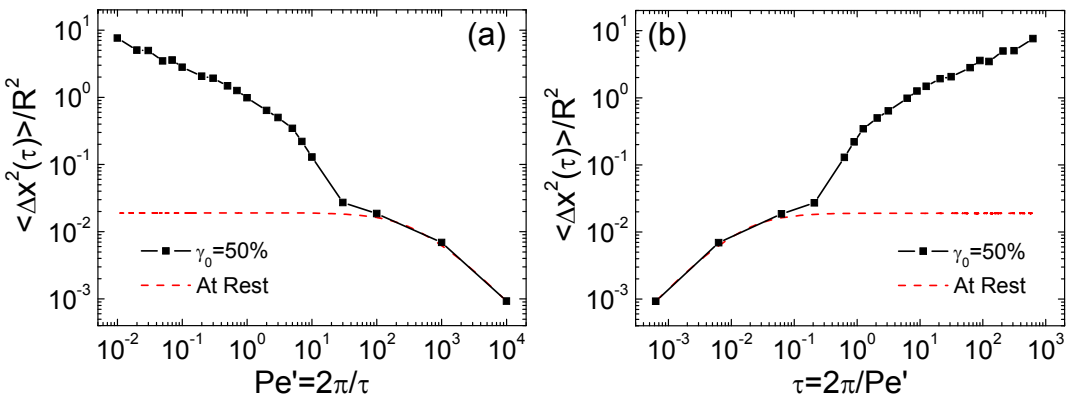

Figure 6.10: x-axis MSD for a time of a single period a) as a function of Pe' and b) as a function of time for a crystal parallel to shear with γ_0=50% and φ=0.62, the data of figure 6.9, compared with the displacements at rest for the same time scales.

At low Pe' and γ_0=50% we find that the layers of the crystal exhibit random diffusive motion in the x axis showing a power law behavior with applied frequency as $D_x=\langle\Delta x^2(T)\rangle/T\sim Pe'^{0.6}$. At higher Pe', much like in the case of low strain oscillatory shearing of glasses (chapter 5), the displacements show non diffusive motions. Based on the conclusions of the amorphous glasses and by linking the slipping motion of the layers to out of cage displacements, we may understand this behavior in crystals under shear as follows.

Based on the findings of chapter 5, at low frequencies and shear rates the slipping motion of the layers is Brownian activated, which means that when the applied strain reaches a critical

value, random Brownian motion allows the layers to slide, thus showing Gaussian displacements in the form of a random walk type motion, much larger than in the state at rest. Although one may expect a linear relation of the diffusivity and the applied rate, in the context of the behavior of glass in chapter 5, the smaller power law slope of 0.6 may be related to the distance from maximum packing. Specifically, the slope may signify the lower probability for a random cooperative sliding occurrence as Pe' is increased due to the available particle space, expressed as a slope of less than unity.

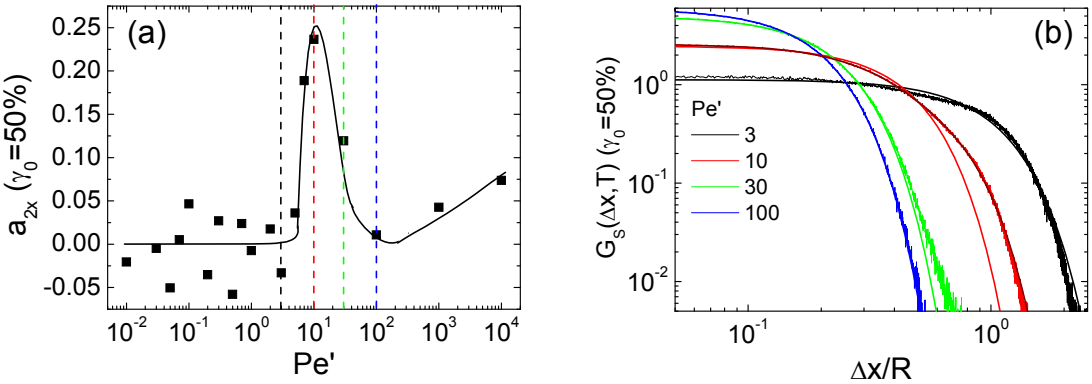

Figure 6.11: a) Non-Gaussian parameter a_2 at γ_0=50% and different Pe' for the x-axis b) Van Hove functions and Gaussian fits as for a) for selected Pe'. Solid line in a) is a guide to the eye, while colored dotted vertical lines indicate the frequencies shown in b).

At the highest Pe', the applied shear becomes comparable to the Brownian motion, and even though there is layer sliding motion within the period ($\gamma_0 > \gamma_{yield}$), the particles (and the layers) return to their initial configurations after each oscillation moving only small distances due to their self diffusion. The random component of motion at the highest Pe' is lost due to the ordered nature of the crystal, as the shear creates specific low collision pathways for the crystal layers to slide, returning to their initial positions after each oscillation.

In the intermediate Pe', the displacements show a transition from one regime to another, exhibiting strong non Gaussian behavior. In this regime, since the displacements at rest are comparable to the displacements under shear, particles/layers are separated into two populations. Those which undergo sliding motion show large displacements, while those exhibiting only in cage motion show small ones. This is clearly seen for Pe'=10 in 6.11b, where two Gaussian functions where additionally used to fit the data, showing a very good superposition.

Crystal under Shear: Displacements near Yielding

Finding the approximate yield strain with simulations for a certain Pe' and φ as done in fig 6.8 requires many independent runs. Therefore to qualitatively discuss the yield strains of the crystal at a certain Pe' with changing φ, we probe different φ each with a single run at a strain close to yield. The displacements for each φ may be used an indirect probe, qualitatively showing the trend of the yield strain. Figures 6.12a and 6.12b show particle displacements under shear vs time for φ=0.56, 0.58, 0.60, 0.62, 0.66, 0.68, 0.70 and 0.72 at Pe'=1 and γ_0=10%. The figures are separated in two regimes; one at low φ around the glass transition (fig. 6.12a) and one for higher φ reaching up to close packing (fig. 6.12b). At short times we observe a decrease of displacements in all directions with increasing volume fraction, similar to the dependencies at rest. For long times, the x and z axes (velocity and vorticity directions respectively) display an increase of displacements with φ, while the y axis (gradient direction) shows a decrease. The higher φ exacerbates the directional anisotropy of the MSDs, showing $<\Delta x^2>$ as being the largest and $<\Delta y^2>$ the smallest both at short and long times.

Figure 6.13a plots the displacements in the time scale of one period versus the inverse distance from maximum packing from the simulations runs seen in 6.12a and 6.12b. There is an increase with φ of the displacements in the x and z axis with a terminal slope of 0.5, while the y axis displacements decrease to a plateau value. The same displacements by subtraction of the xz plane neighbors are shown in figure 6.13b. Probing the in cage motion, these displacements show equal values for all directions decreasing with a power law slope of -2 with the inverse distance from maximum packing.

The displacements in one period seen in figure 6.12 and in more detail in 6.13a increase for the x and z axis (velocity and vorticity directions) showing more displacements with increasing φ, even though the available space for particle motion is less. The increased mobility at higher φ, strongly indicates the decrease of yield strain with φ as seen in experimental rheological data (Koumakis, Schofield et al. 2008). This argument can only be used in the case of constant shear conditions (Pe' and γ_0) as different Pe' exhibit different yield strains. The MSD in the y-axis of 6.13a approaches a plateau value that reflects the least amount of motion required for layers to slide over one another at the maximum packing volume fraction limit.

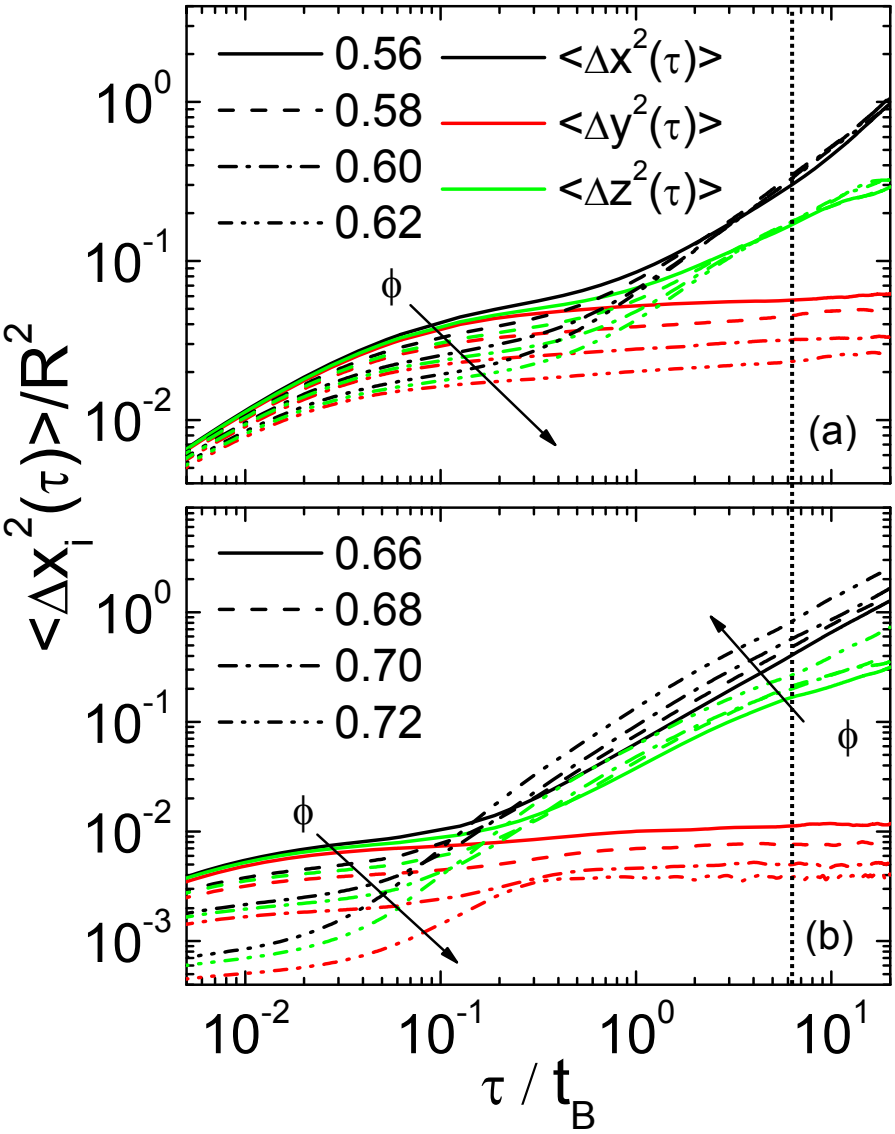

Figure 6.12: Mean squared displacements of crystal parallel to shear at Pe'=1 with γ_0=10% for a) φ=0.56, 0.58, 0.60 and 0.62 and b) φ=0.66, 0.68, 0.70 and 0.72. Vertical dotted line indicates the time scale corresponding to figure 6.13.

Lastly ,the general decrease of short time MSD seen in figure 6.12 as well as the decrease of MSD compared to neighbors in 6.13b reflects the decrease of available in cage particle space as φ increases. By estimating the average distance Δ between particles, $\Delta \sim \left[\left(\phi_{MAX} / \phi \right)^{1/3} - 1 \right]$, we find that the dependence of the squared average distance to the distance from packing follows a power law slope as $\Delta^2 \sim \left[\phi_{MAX} / \left(\phi_{MAX} - \phi \right) \right]^{-2}$ at the limit of φ→φ_{MAX}, which agrees with the slope in 6.13b.

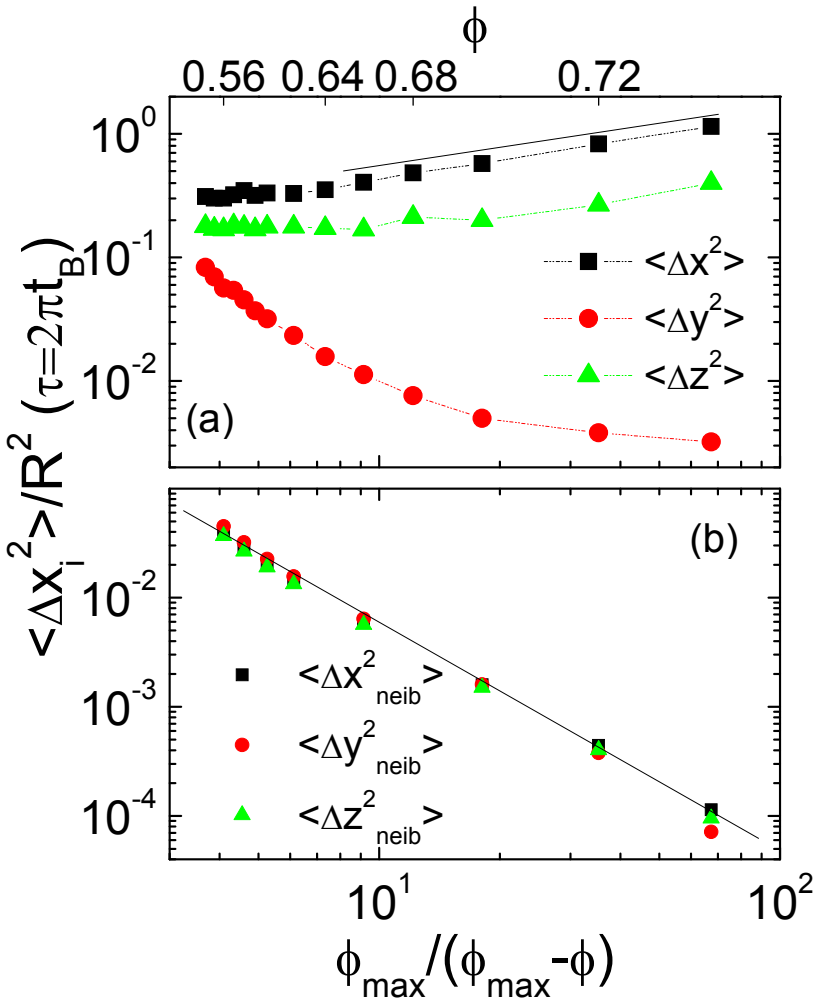

Figure 6.13: Mean squared displacements under shear versus distance from maximum packing (φ_{max}=0.741) of crystal parallel to shear for Pe'=1 and a time of one period $T=2\pi t_B$ with a strain of 10% with a) single particle displacements and b) displacements relative to the x-z layer neighbors. Line in a) is a power law slope of 0.5 while in b) a slope of -2.

Crystal under Shear: Displacements well above Yielding

Similarly to the previous figures (6.12 and 6.13), in figure 6.14 we show the displacements of a few φ at constant shear conditions of Pe'=1 and a higher strain of γ_0=100% which is well above the yield strain. Figure 6.14a shows the displacements with time for different φ (as in 6.12), while 6.14b shows the relative displacements, $<\Delta x^2(\tau)>_{neib}$, for the same conditions. The phenomenology of 6.14a is similar to that in 6.12a with the long time MSD in x and z directions increasing with φ, while decreasing in y (gradient) as discussed before due to decrease of yield strain.

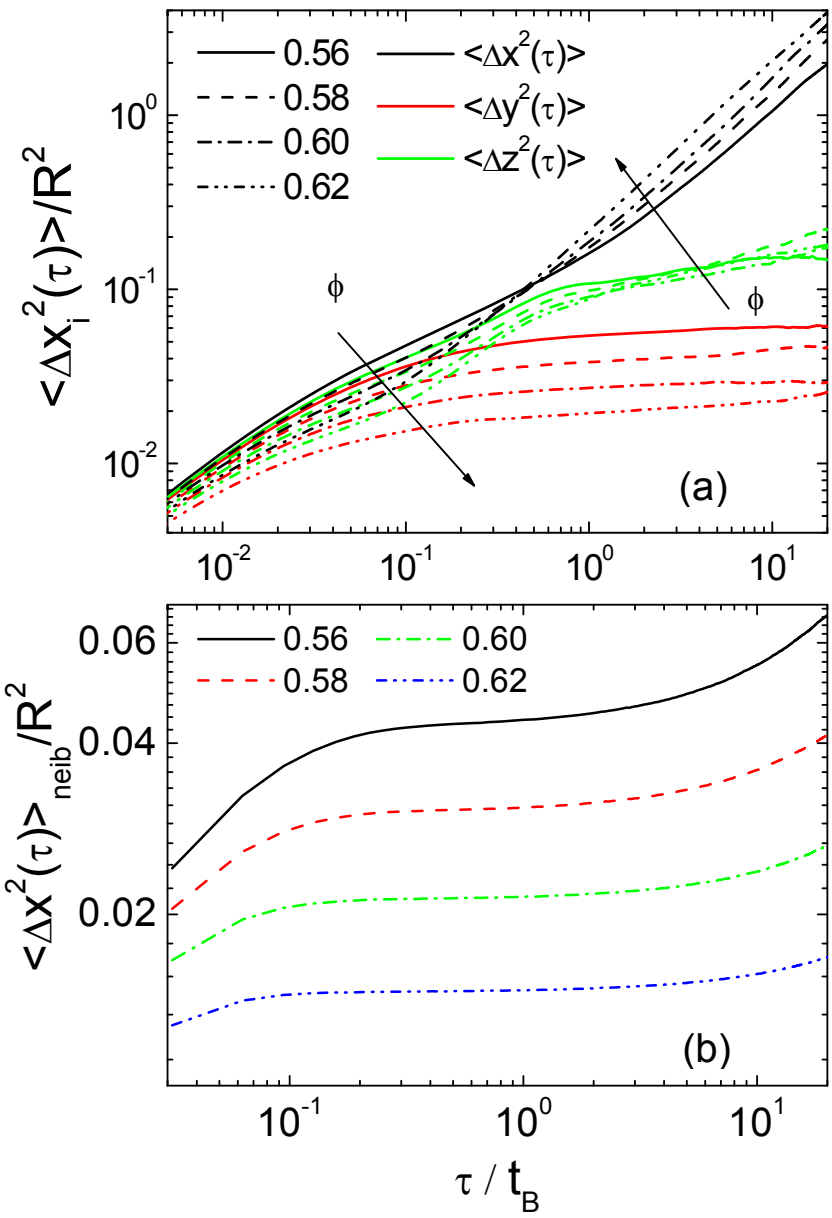

Figure 6.14: Mean squared displacements of crystal parallel to shear at Pe'=1 with γ_0=100% for φ = 0.56, 0.58, 0.60 and 0.62 with a) overall displacements and b) the x-axis displacements relative to the center of layer cage

As in fig. 6.6, which showed an increase of the x-axis in cage displacement at long times with increasing γ_0, in figure 6.14b, $<\Delta x^2(\tau)>_{neib}$ shows a similar increase. Here $<\Delta x^2(\tau)>_{neib}$ for γ_0=100% shows a stringer increase at long times as φ is decreased. This finding supports the argument previously given (discussion of figure 6.6), that the long time increase corresponds to the elongation of the cage under shear in the x direction. As φ is decreased, the available space increases allowing easier elongation of the cage at high strains.

Crystal under Shear: Comparison to experiments

The similarities and differences between the stresses measured in rheological experiments and determined by simulations may be seen in figure 6.15. Although simulation stresses in the crystal generally show many peaks, here we show low Pe' and low φ simulation results, where many features are smoothed out and the qualitative similarities between experiments and simulation are more apparent. Figure 6.15a show the simulation results for φ=0.56 and Pe'=0.1 at γ_0=10%, 30% and 50%, while 6.15b shows experimental data at ω=10 rad/sec for the 270nm monodisperse spheres at the same strains. The stresses from simulations show a trapezoid Lissajous shape with similar elastic slope at high strains and an identical stress plateau at zero strain, for all γ_0. Experiments produce similar but smoothed out Lissajous shapes, with the main difference being the increase of the stress at zero strain with increasing γ_0.

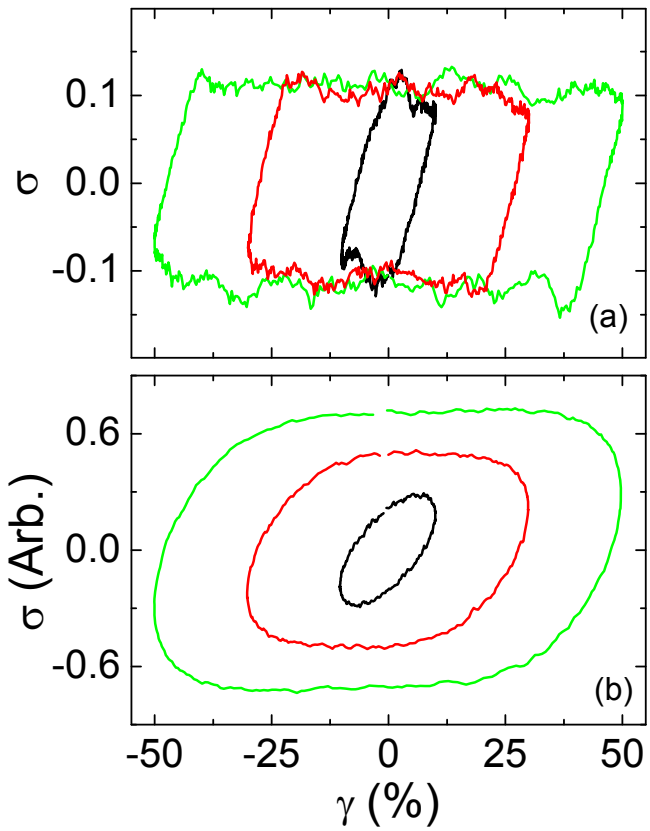

Figure 6.15: Lissajous (Stress vs strain) plot for φ=0.56 at different γ_0 a) from BD simulations at Pe'=0.1 and b) from experiments with 270nm spheres in Octadecene at ω=10 rad/sec.

In the simulations (6.15a), because of sliding layers, stresses remain relatively constant with increasing strain amplitude, and when the rate is reversed, there is a sharp drop to negative values and immediate reversal. In the case of the experiment (6.15b), a similar shape occurs, but now due to the hydrodynamic drag, the plateau exhibits larger stresses with the increase of

strain and thus shear rate. Moreover, possibly due to crystal defects in a real system or partial crystallization, due to the rotational cone and plate geometry, the reversal is smoothed out. The lack of short range hydrodynamic drag (lubrication forces) in the simulations may also prevent the crystal from breaking apart at larger rates (Pe>>1) and strains (γ_0>>100%) as seen experimentally, which is discussed briefly in the appendix, although in most shown cases we are below this limit. Additionally, we would like to clarify that there is a definite increase of the plateau stress with rate in the simulations, albeit quite small and only distinguishable between large variations of Pe'.

6.5 Parallel vs. Perpendicular Crystals under Oscillatory Shear

In oscillatory shear experiments of concentrated hard sphere systems with non rotational parallel plates, FCC crystals with the close packed direction parallel (fig. 6.1a) and perpendicular (fig. 6.1b) to shear have been found to occur at different strain regimes (Haw, Poon et al. 1998). Starting from an amorphous configuration, low strain amplitudes produce a crystal with a distribution of orientation around a preferred orientation of the closed packed direction perpendicular to shear (fig. 6.1b). Higher strains of γ_0>50% reorient the existing crystal and produce a macroscopic crystal with the closed packed direction parallel to shear (fig. 6.1a). By lowering the strain with this specific structure, the system does not revert back to being amorphous or to the crystal perpendicular to shear. Previous work of (Komatsugawa and Nosé 1995) has discussed that this orientation change occurs through energy changes due to geometrical constraints. This work explains these orientation changes in terms of stresses and displacements under shear and comments on the lack thereof in the experimental observations on rotational geometries.

In figure 6.16 we compare the oscillatory stress response in Lissajous curves of the crystals with parallel and perpendicular to shear direction for low and high strains at Pe'=1 for a φ=0.62. The shapes of the curves are complicated, reflecting the monocrystallinity and yield properties of the system. At the low strain regime (6.16a) the two crystal orientations exhibit similar Lissajous shapes, with the elastic stress slope being equal at the maxima of strain. Beyond the simple elastic response the crystals yield, revealing smaller stresses for the crystal perpendicular to shear. At the high strain regime (6.16b), the elastic response at the strain maxima again is similar; however strains beyond yield show very different behaviors. The crystal parallel to shear shows stresses with decaying oscillations around a rate independent stress until strain reversal. In contrast, the crystal perpendicular to shear produces a strong

increase of stress, much higher than the crystal parallel to shear, which then shows an oscillating decay to a high and rate dependent stress value.

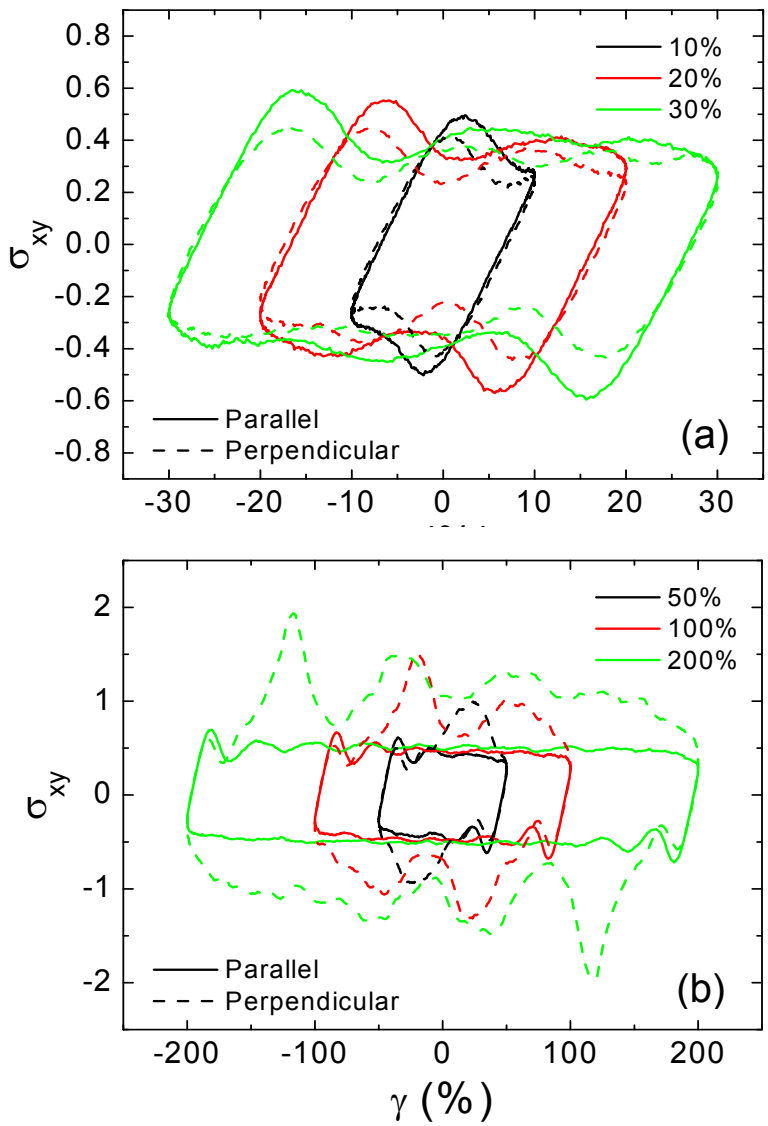

Figure 6.16: Lissajous (Stress-Strain) curves of crystals parallel and perpendicular to shear for φ=0.62 at Pe'=1 for a) low non linear strains of 10%, 20% and 30% and b) high non linear strains of 50%, 100% and 200%

Thus, at the beginning of the non linear regime (low strains, figure 6.16a), the crystal parallel to shear has larger stresses than the crystal perpendicular to shear, whereas for larger strains not only is this reversed but the crystal perpendicular to shear produces very strong stress peaks (figure 6.16b). This is correlated with the perpendicular to parallel switch observed in experiments. It seems that the smaller stresses for small strains allow a preferential perpendicular orientation, while at larger strains this orientation gives prohibitive stresses, causing a switch to the crystal parallel to shear. If strains are then reduced, although the

perpendicular crystal flows easier, there is no driving force to cause the system to change orientations. Additionally, the linear regime stresses between the two orientations, although not shown, are identical as expected from simple FCC elasticity tensors (Laird 1992). Thus, the elastic slopes at the maxima of strain seen for both orientations in fig. 6.16 are equal and represent linear elastic deformation. It is important to note that the stresses for such crystals are not generally equal in all directions.

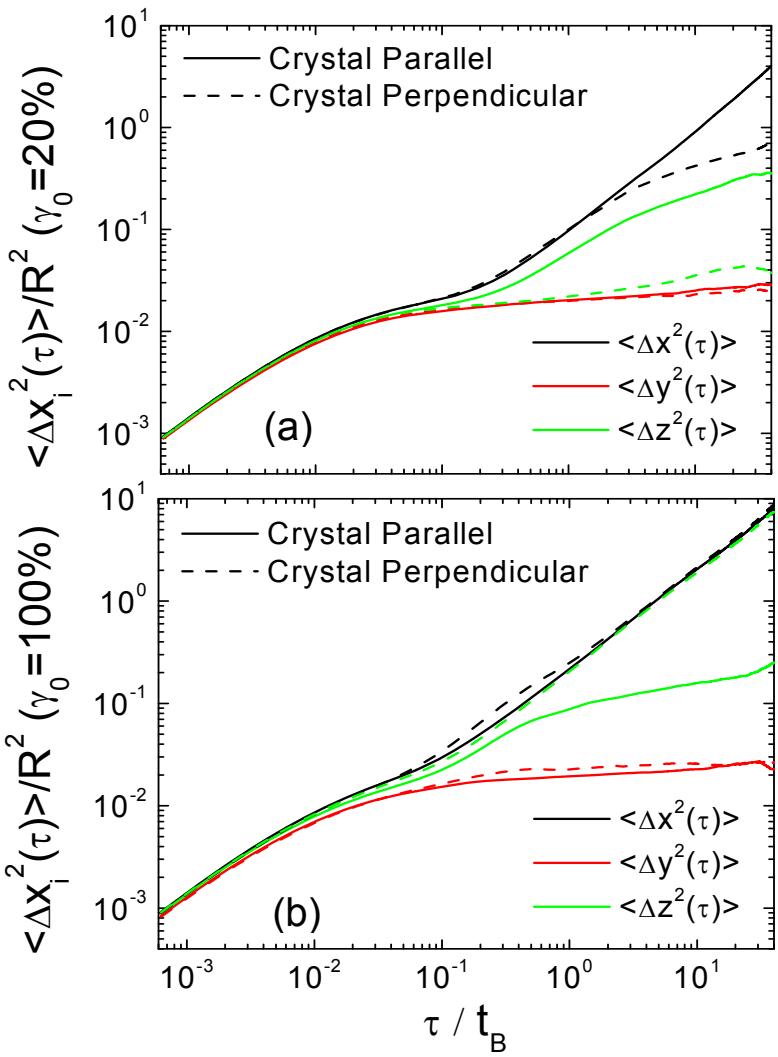

Figure 6.17: Mean squared particle displacements from crystals parallel and perpendicular to shear at φ=0.62 under oscillatory shear with a Pe' of 1 at a) γ_0 = 20% and b) γ_0 = 100%

The time dependence of the MSDs under shear for the two orientations for Pe'=1 at low γ_0=20% and high γ_0=100% can be seen in fig. 6.17. While the in-cage/short time displacements of the two crystals are equal for low and high strains, at longer times they show differences. Similarly to the stress findings of the fig. 6.16, the long time MSDs (t>T) for the crystal perpendicular to shear are in average less at low strains, while larger at high strains.

More specifically compared to its parallel counterpart, at low strains $<\Delta x^2>$ and $<\Delta z^2>$ become less for the perpendicular crystal and for high strains they increase. In both cases $<\Delta y^2>$ remains the same in both orientations.

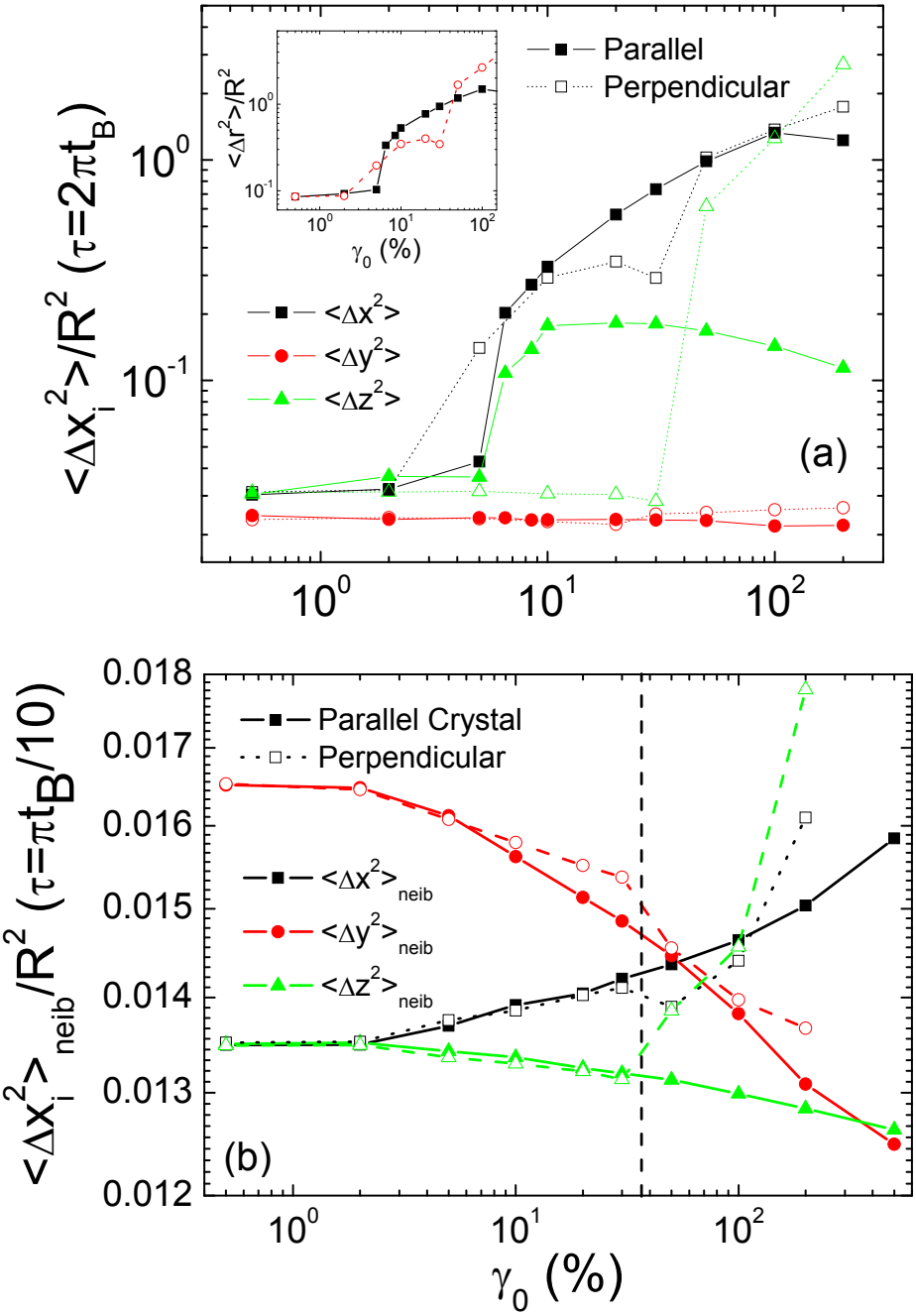

Figure 6.18: Mean squared displacements versus applied strain of crystals parallel and perpendicular to shear at φ=0.62 and Pe'=1 a) for a time slice of $2\pi t_B$ (1 period), inset shows $<\Delta r^2(T)>$ versus γ_0, b) the displacements relative to the same layer cage at a time of $\pi t_B/10$ (the plateau vs. τ). while the vertical dashed line in (b) denotes the abrupt change in displacements of the perpendicular crystal.

The MSD strain dependence of the orientations at Pe'=1 is shown in 6.18a along with the MSD calculated by subtracting neighbor motion in 6.18b. Starting from small γ_0, the crystal with perpendicular orientation shows a high $<\Delta x^2>$ at smaller strains than the parallel one, thus exhibiting a smaller yield strain. Until γ_0=30%, the displacements in the perpendicular crystal are smaller with $<\Delta z^2>$ being constant, while for γ_0>50%, they sharply increase above those of the parallel crystal. The MSD relative to the neighbors are similar for both orientations up to γ_0=50%, but reveal an abrupt increase for the perpendicular crystal above this strain.

The displacements of the different crystal orientations under shear follow the findings of the stresses from fig. 6.16. The displacements of the perpendicular crystal in small strains (γ_0<50%) are less than the parallel, while the stresses are also less. When strains are increased above a certain point ($\gamma_0 \geq 50\%$) the crystal perpendicular to shear exhibits much higher displacements and stresses, additionally giving rise to crystal instabilities with the motion relative to neighbors being severely increased. This is an important indicator of instability as internal stresses are high enough to disrupt the internal layer arrangement.

Figures 6.19 and 6.20 show the stresses and instantaneous displacements within the period for the crystals parallel and perpendicular to shear for a low strain of 20% (fig. 6.19) and a high strain of 100% (fig. 6.20). As discussed earlier for low strains (6.16a), the two orientations have similar stress features although the perpendicular crystal exhibits lower absolute values. The instantaneous displacements at low strains also show similar features in the x and y axis as shown in 6.7a. However there is a marked difference in the z axis, where there are strong minima for the perpendicular crystal. For the high strains of fig. 6.20, the stresses are shown as in fig. 6.16b, where the crystal perpendicular to shear shows abrupt stress peaks. The high strain displacements of the crystal parallel to shear mimic the low strain behavior, although now the z axis has more significant changes. The perpendicular crystal in this case shows that the displacements are only anomalous in the z axis.

Going back to figure 6.1, we schematically show the sliding behavior under shear of the parallel (6.1a) and perpendicular (6.1b) crystals. The layers of the crystal parallel to shear have only one slipping angle relative to the shear direction, $\pi/6$. However, the layers of the crystal perpendicular to shear have two slipping angles, the first one having a zero value and the second one being $\pi/3$. While even a zero angle would need a finite amount of stress to allow sliding of layers, as the angle is increased, the stress needed to slide the layers is also increased. Thus at low nonlinear strains the crystal perpendicular to shear has lower stresses (zero angle) and smaller displacements.

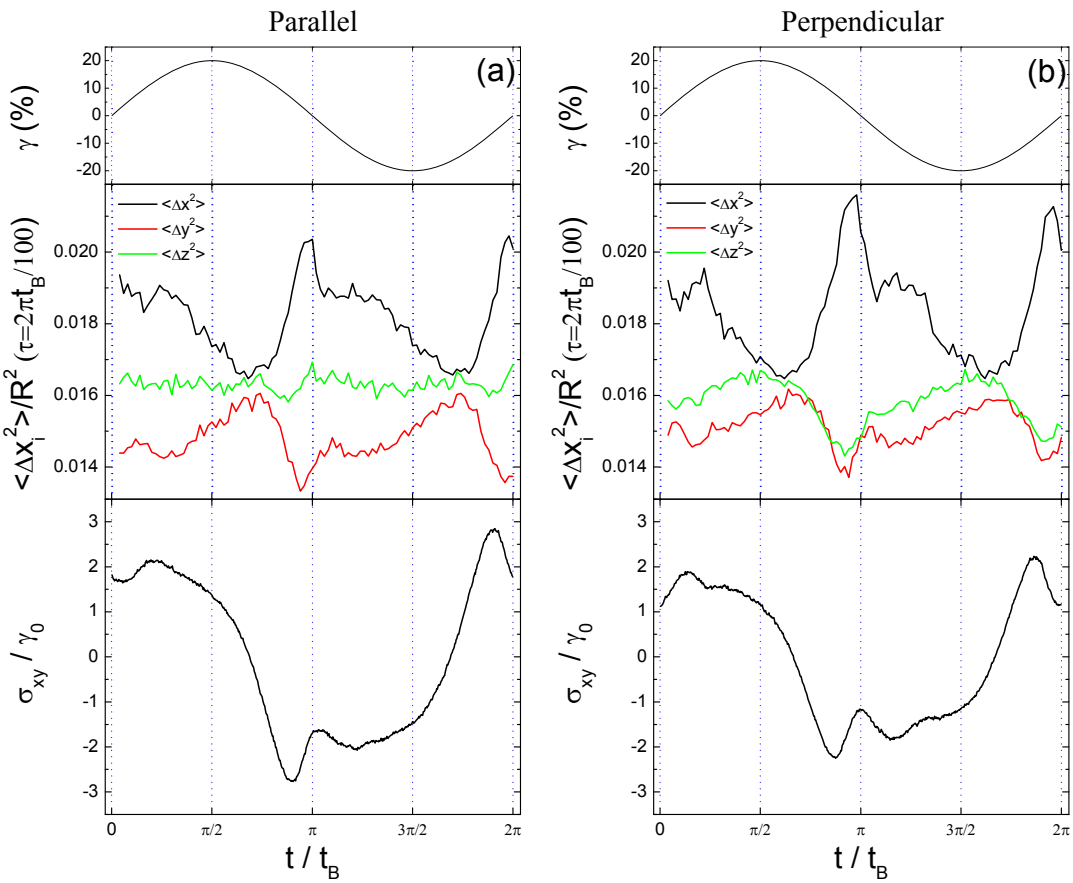

Figure 6.19: Mean squared displacements at $\tau=2\pi t_B/100$ ("instantaneous" MSD) for each axis at $\varphi=0.62$, Pe'=1 and $\gamma_0=20\%$ within the period (top) and normalized stress (bottom) versus time of a) the crystal parallel to shear and b) the crystal perpendicular to shear.

As strain is increased, the perpendicular crystal is forced to explore an area of much larger stress ($\pi/3$ angle), which causes displacement instabilities in the z axis (figs 6.17, 6.18, 6.19 and 6.20). Experimentally these instabilities force the crystal to reorient parallel to shear. Then a smaller sliding angle ($\pi/6$) is involved, which allows smoother layer motion with less stresses. The crystal experimentally remains in this orientation for all strains, as there are no instabilities. In real systems however at very high strains the crystal is destroyed by hydrodynamic lubrication forces as will be discussed. Below the smaller yield strain of the perpendicular crystal is also due to the initial zero angle slipping mechanism.

From the simulations we have found that the crystal parallel to shear is stable at all strains which is congruent with experimental observations (Haw, Poon et al. 1998). The crystal perpendicular to shear is stable only at small non-linear strains, while has high instabilities (in the y axis) at higher strains. It was also found that the crystal perpendicular to shear exhibits less stresses and MSDs than the crystal parallel to shear at low strains. Thus we concluded

that the shear induced crystal experimentally is created first with a perpendicular orientation (less displacements and stresses), which then changes to parallel (reorientation due to instabilities in the perpendicular one). Since the crystal parallel to shear is still very efficient in reducing stresses under shear, crystal does not revert back to the perpendicular orientation at low strains.

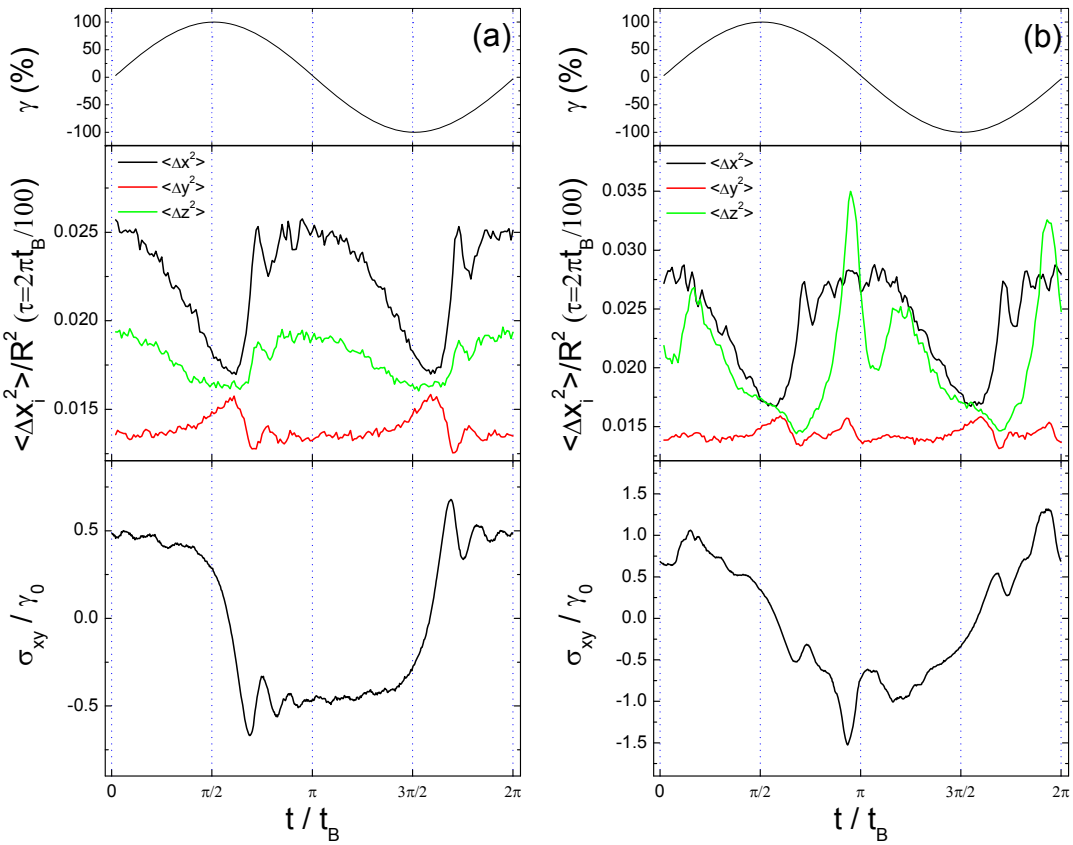

Figure 6.20: Mean squared displacements at $\tau=2\pi t_B/100$ ("instantaneous" MSD) for each axis at $\varphi=0.62$, Pe'=1 and $\gamma_0=100\%$ within the period (top) and normalized stress (bottom) versus time of a) the crystal parallel to shear and b) the crystal perpendicular to shear.

Even at the highest strains (500%) the simulated crystal parallel to shear shows no instabilities (Appendix). The slipping layer is such that whatever strain or Pe' is applied, the crystal is stable. At higher rates and strains there are actually less instabilities, as there is less Brownian motion to complicate the shear alignment of the crystal. The experimental instabilities for the parallel crystal, causing destruction of the crystal at high strains, are most probably hydrodynamic in origin(Yu, Derks et al. 2009). The lubrication stresses, which are not implemented in the Brownian dynamics code, could cause jamming of particles and subsequent breaking of the crystals. However, the instabilities of the crystal perpendicular to

shear are spatial in origin (excluded volume) and are thus captured by the Brownian Dynamics simulations.

The lack of any perpendicular crystal in the rheometer cone-plate geometry is possibly due to the curvature in the x-z plane, as there may be higher energies/stress for creation of crystal (Koumakis 2007; Koumakis, Schofield et al. 2008). Additionally, the reason there is no full crystallization at lower strains, however long the elapsed time of shear, is related to the experimental finding that in a parallel plate shear cell there is a distribution of crystal orientations around the perpendicular at low strains (Haw, Poon et al. 1998). Since the perpendicular crystal is unable to form in the rotational geometry, only a small portion of parallel crystal is allowed, which by increasing the strain grows into a full crystal.

6.6 Chapter Conclusions

Glass vs. crystal at rest

For the amorphous and crystalline structures at rest we found that although the short time MSD for the crystal is higher than that of the glass, the dynamic heterogeneities in the glass may allow increase of the MSD above those of the crystal for longer times. Thus while in the crystal particles are completely confined in their cage with the MSD showing a clear plateau, in the glass large scale out of cage motion is observed via dynamic heterogeneities. When approaching the limit of random close packing (≈0.66) the crystal MSD should always be larger that of a same φ glass because of the larger distance from maximum packing (≈0.74).

Glass vs. parallel crystal under oscillatory shear

When comparing the displacements of the crystal oriented parallel to shear and the glass under oscillatory shear we concluded that, due to the sliding layers the crystal has anisotropic displacements compared to the isotropic displacements found in the glass. The crystal displacements are due to cooperative motion of x-z layers of particles sliding over each other, although high rates cause cage elongation in the shear direction seen as an increase of $<\Delta x^2>$ relative to the x-z neighbors at long times. The yield strain of the crystal is found to be less than the glass, due to sliding layer motion. Past the yield point, the long time shear induced displacements of the glass are found to be larger, while stresses are highly correlated to instantaneous shear induced displacements in both crystal and glass. Thus we conclude that during the experimental shear of a monodisperse glass, the large out of cage displacements allow the system to explore the energy landscape and find the minima in energy, stresses and displacements by configuring particles into a crystal oriented parallel to shear.

Parallel crystal under oscillatory shear

Through the examination of the parallel crystal under oscillatory shear, we have found that the MSD of the crystal increases with decreasing Pe', although showing qualitatively similar displacements as a function of applied strain. The yield strain of the crystal is less for lower oscillation frequencies as Brownian motion has time to act upon the system under shear and allow the sliding of the crystal layers. The $<\Delta x^2(T)>/T$ at γ_0=30%, the equivalent of an effective diffusion coefficient, was shown to exhibit a power law scaling as $Pe'^{0.6}$ for φ=0.62 at the lower frequencies, an effect of similar origin to the corresponding frequency dependence of the hard sphere glass of chapter 5, the slope being dependent on φ or more accurately the distance from maximum packing.

Additionally we showed that the crystal under shear exhibits a decrease in yield strain with increasing φ, which leads to an increase in long time MSD. Analysis of displacements relative to x-z neighbors also shows that the elongation of the cage under shear in the x-axis is inversely proportional to φ. The stress responses of the crystal under oscillatory shear in experiments and simulations are qualitatively similar at low frequencies, with the largest differences possibly occurring due to the lack of hydrodynamic interactions in the BD simulations as well as crystal defects of the experimental system.

Parallel vs. perpendicular crystals under oscillatory shear

The experimental transition from glass to crystal with increasing strain as well as the selection of crystal orientation is governed by the minimization of stresses and displacements in the hard sphere system. Similarly, the low strain perpendicular and high strain parallel to shear crystals may occur due to minimization of stresses and displacements. The crystal perpendicular to shear exhibits low stresses and MSD at low non linear strains (10%-20%), while parallel to shear shows slightly larger stresses in the same regions. At higher strains, the sliding layers of the parallel crystal are more efficient in minimizing stresses and the perpendicular crystal is no longer stable. Thus starting from an amorphous glassy system, at low strains a crystal perpendicular to shear is formed, which becomes unstable at larger strains and reorients into a crystal parallel to shear.

6.7 References

Ackerson, B. J. (1990). "Shear induced order and shear processing of model hard sphere suspensions." J. Rheol. **34**(4): 553-590.

Ackerson, B. J. and P. N. Pusey (1988). "Shear-Induced Order in Suspensions of Hard Spheres." Phys. Rev. Lett. **61**: 1033.

Besseling, R., L. Isa, E. R. Weeks and W. C. K. Poon (2009). "Quantitative imaging of colloidal flows." Advances in Colloid and Interface Science **146**(1-2): 1-17.

Besseling, R., E. R. Weeks, A. B. Schofield and W. C. K. Poon (2007). "Three-Dimensional Imaging of Colloidal Glasses under Steady Shear." Physical Review Letters **99**(2): 028301.

Derks, D., Y. L. Wu, A. Van Blaaderen and A. Imhof (2009). "Dynamics of colloidal crystals in shear flow." Soft Matter **5**(5): 1060-1065.

Foss, D. R. and J. F. Brady (2000). "Brownian Dynamics simulation of hard-sphere colloidal dispersions." Journal of Rheology **44**(3): 629-651.

Haw, M. D., W. C. K. Poon and P. N. Pusey (1998). "Direct observation of oscillatory shear-induced order in colloidal suspensions." Phys. Rev. E **57**: 6859.

Haw, M. D., W. C. K. Poon, P. N. Pusey, P. Hebraud and F. Lequeux (1998). "Colloidal glasses under shear strain." Phys. Rev. E **58**: 4673.

Kegel, W. K. and J. K. G. Dhont (1999). "‘‘Aging’’ of the structure of crystals of hard colloidal spheres." J. Chem. Phys. **112**: 3431.

Komatsugawa, H. and S. Nosé (1995). "Nonequilibrium molecular dynamics simulations of oscillatory sliding motion in a colloidal suspension system." Physical Review E **51**(6): 5944.

Koumakis, N. (2007). Shear Induced Crystallization of a Colloidal Glass. Department of Materials Science and Technology, University of Crete. **MSc**.

Koumakis, N., A. B. Schofield and G. Petekidis (2008). "Effects of shear induced crystallization on the rheology and ageing of hard sphere glasses." Soft Matter **4**: 2008-2018.

Laird, B. B. (1992). "Weighted density functional theory calculation of elastic constants for face centered cubic and body centered cubic hard sphere crystals." J. Chem. Phys. **97**(4): 2699.

Lindemann, F. A. (1910). Phys. Z. **11**: 609.

Mason, T. G. (2000). "Estimating the viscoelastic moduli of complex fluids using the generalized Stokes–Einstein equation." Rheologica Acta **39**(4): 371-378.

Mermin, N. D. (1968). "Crystalline Order in Two Dimensions." Physical Review **176**(1): 250.

Petekidis, G., A. Moussaid and P. N. Pusey (2002). "Rearrangments in hard-sphere glasses under oscillatory shear strain." Phys. Rev. E **66**: 051402.

Petekidis, G., D. Vlassopoulos and P. N. Pusey (2003). "Yielding and flow of colloidal glasses." Faraday Discuss **123**: 287-302.

Pusey, P. N., E. Zaccarelli, C. Valeriani, E. Sanz, W. C. K. Poon and M. E. Cates (2009). "Hard spheres: crystallization and glass formation." Philosophical Transactions of the

Royal Society A: Mathematical, Physical and Engineering Sciences **367**(1909): 4993-5011.

Yu, L. W., D. Derks, A. Van Blaaderen and A. Imhof (2009). "Melting and crystallization of colloidal hard-sphere suspensions under shear." Proceedings of the National Academy of Sciences of the United States of America **106**(26): 10564-10569.

Chapter 7 – Experimental Rheology and LS-Echo during Shear Induced Crystallization of Hard Sphere Glasses

Abstract

The LS-Echo technique coupled with rheology has been used to examine the shear-induced motions of glasses and their corresponding shear induced crystals. Comparing the results on the glass and the crystal, we observe that although at low strains the crystal shows increased particle displacements than glass due to relative to the higher free volume around a particle (in-cage motion), at higher strains the crystal shows reduced particle rearrangements due to the anisotropic sliding layer motion. A qualitative comparison between the BD simulations on crystals and the experiments show good agreement at the high frequency regime, where a characteristic minimum of shear induced diffusivities as a function of frequency is observed.

7.1 Introduction/Experimental

In the previous chapter with the use of Brownian dynamics simulations we examine various aspects of the dynamics under shear of the shear induced crystal, while also comparing it to the same volume fraction glass. The purpose of this work is to experimentally determine and verify the microscopic rearrangements in the crystals under oscillatory shear and the major differences with the glass using rheology and LS Echo (Petekidis, Moussaid et al., 2002; Smith, Petekidis et al., 2007). Additionally we investigate the connection between such microscopic rearrangements with regard to the corresponding rheology and the glass-crystal transition under shear.

We use strain sweeps of increasing and then decreasing strain in order to create shear induced crystallization as studied by (Koumakis, Schofield et al., 2008). However here, due to the scattering geometry, the observation of Bragg peaks in transmission is not possible here. Instead we use the rheological results of the strain sweeps and optical observation of the sample under shear as a method of detecting ordering.

Relatively monodisperse (σ=0.05) PMMA hard spheres dispersed in Octadecene (R=267nm) were prepared as discussed in chapter 2. Due to high refractive index mismatch the sample volume fractions were calculated by the distance from maximum packing φ_{RCP}=0.660 as

estimated by an approximate radial polydispersity of 5% from (Schaertl and Sillescu, 1994). We examine two samples as shown in table 7.1 with φ=0.605 and 0.615. Rheological measurements were conducted on the ARES strain controlled rheometer at ambient room temperature, stabilizing at 20 ± 2^0C, using the backscattering DWS Echo setup as described in chapter 2. The data from within the period were extracted using the analog torque and strain outputs. In order to acquire the non linear data and echo data, as well as reach the equilibrium state during the crystallization process, each strain in the strain sweeps was measured for multiple periods (above 20) and multiple points per decade of strain (O(100)). Each echo correlation function was measured for a relatively large amount of time encompassing several strain values, 600sec for f=1.6Hz (ω=10rad/s) and 300sec for f=16Hz (ω=100rad/s), giving 4 to 8 points per decade during a strain sweep. Rejuvenation of the sample consisted of a low rate steady shear rotation for the destruction of any crystallinity (Koumakis, Schofield et al., 2008).

As discussed in the chapter 2 we define the bare $Pe'_0=t_{B0}\omega$ and calculate for the spheres in Octadecene t_{B0}=0.37sec. As in previous chapters we correlate simulations with experiments and thus Pe'_0 and Pe' with a factor $D(\varphi)/D_0$. Since here the maximum packing fraction differs between the crystal and the glass, the values presented in table 7.1 are different between the two. In reality, the factor $D(\varphi)/D_0$ for the crystal is a rough estimation, since we have not found any other calculations or measurements on the short time diffusivity for an ordered crystal at such high φ.

	Amorphous, φ_{RCP}=0.660		Crystal, φ_{MAX}=0.741	
φ	0.605	0.615	0.605	0.615
Pe'_{0bare} (ω=1rad/sec)	0.370	0.370	0.370	0.370
$D_s(\varphi)/D_0$	0.139	0.130	0.196	0.190
$Pe'_{dressed}$ (ω=1rad/sec)	2.662	2.855	1.888	1.947

Table 7.1: Time multiplication factor $c=D_s(\varphi)/D_0$ that links experimental $Pe'_0=Pe'_{bare}$ to the $Pe'=Pe'_{sims}=Pe'_{dressed}$, with $Pe'_0=c\cdot Pe'_{sims}$ and $t/t_{B0}= t/(c\cdot t_{Bsims})$, as well as Pe'_{0bare} and Pe' at ω=1rad/sec.

High (16Hz) and low (1.6Hz) frequency strain sweeps were carried out for the two volume fractions in order to create the crystal, while simultaneously measuring the LS-Echo correlation functions. LS-Echo data where also collected for a range of frequencies at a constant non linear strain value of γ_0=50%. In this chapter we will initially present the rheological data (Viscoelastic moduli, I_3/I_1 and Lissajous plot) of increasing and decreasing

strain amplitude for the crystallization process in the two frequencies and the two volume fractions. We will continue by introducing the LS-Echo measurements and show the strain dependence of the echo heights for these measurements. Finally we will attempt to make a more quantitative analysis using diffusing wave spectroscopy theory and transmute the correlation function under shear to diffusivities for comparison with the BD simulations.

7.2 Oscillatory rheology

Creation of Crystal: Rheological Measurements

In figure 7.1 we show dynamic strain sweeps at 1.6 Hz for volume fractions of φ=0.605 and 0.615, which on increasing strain amplitude probe the viscoelastic properties of a glass as it turns into a crystal, and with decreasing strain probe the shear induced crystal. The strain sweeps have been taken with many points per decade and a large measurement time per point. Although this is to ensure a steady state under shear, the effects of long time measurements on the samples are evident, with the oscillations of the viscoelastic properties in 7.1b. These are due to room temperature fluctuations (of about 15 minutes) following the air conditioning cycles.

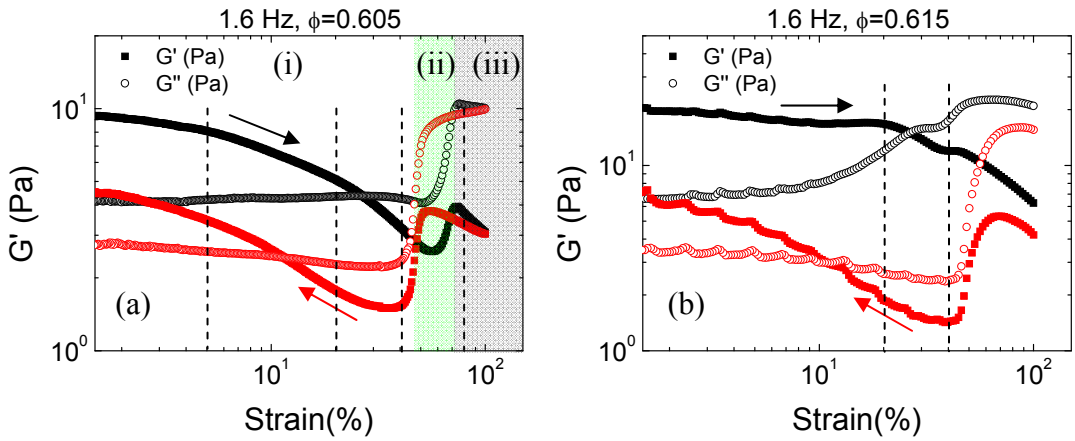

Figure 7.1: Dynamic Strain Sweep of 1.6 Hz starting from the glass and increasing strain (black) and decreasing strain to the crystal (red) for a) φ=0.605 and b) φ=0.615. Arrows note the direction of shear. Vertical dashed lines correspond to the strains of the Lissajous of 7.2b and 7.3b. Shaded areas in a) refer to structures under shear as discussed in text with i) showing stable glass or crystal, ii) unstable crystal and iii) amorphous glass. The tests were conducted with 160 points per decade and 15sec per point for a) and 80 points per decade and 60sec per point for b).

A detailed description of this process for hard sphere particles of the same size, but suspended in cis-decalin can be found in (Koumakis, 2007; Koumakis, Schofield et al., 2008). At low strains (area (i) of fig. 7.1a), following the black curve, the system is amorphous/glassy and as strain is increased passed the crossover point (G'=G'') it starts to partially crystallize. Upon entering area (ii), the crystal which is formed up to this point shows structural instabilities due

to high shear rates. At the highest strains of (iii) the particles are unable to sustain any form of ordering and break down into an amorphous glass possibly due to hydrodynamic effects as discussed in the appendix (A.3). On decreasing strain (red curve) in area (iii), the amorphous structure remains, but as area (ii) is entered, the crystal structure is reformed. Upon entering area (i) the crystal is able to stabilize under shear and the rest of the curve probes the non linear properties of the shear induced crystal. Similar dynamic strain sweeps can be seen for the higher φ shown in figure 7.1b.

Although the strain sweeps were carried out with a large number of points and for long time, the measured viscoelastic properties upon increasing strain suggest that the glass does not fully crystallize but a decrease of strains is needed. Hence a better crystal is formed upon decreasing the strain rather than increasing it. This is due to the very narrow range of strains where full crystallinity may be achieved before structural instabilities begin (Koumakis, Schofield et al., 2008).

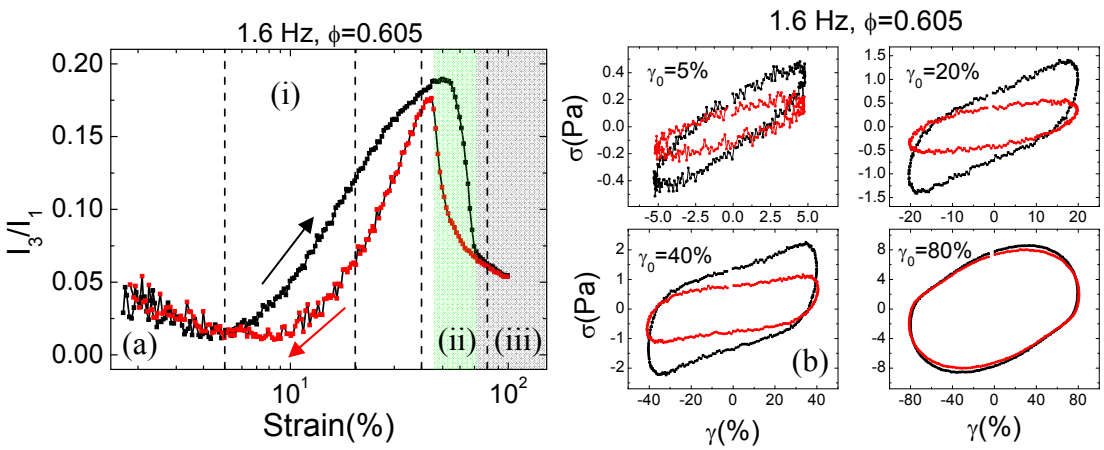

Figure 7.2: a) Third Harmonic of stress response and b) Lissajous curves in selected strains from the dynamic strain sweeps of figure 7.1a. Arrows in a) refer to the direction of shear, while shaded areas are discussed in text. Vertical dashed lines in a) refer to the strains probed in b). In both a) and b) black color refers to increasing strain, while red to decreasing strain.

As described in chapter 5, the shape of the Lissajous figures and the higher Fourier components may provide information on the microscopic time scales in comparison to the frequency of applied shear. Thus we show the non harmonic stress response during the strain sweep (of figure 7.1) as described by I_3/I_1, as well as the Lissajous plots at specific strains which may be seen in figures 7.2 (φ=0.605) and 7.3 (φ=0.615). In general similar behavior is seen for both φ's. Furthermore, when comparing to findings of chapter 5 regarding the Lissajous shapes, we observe that we are in the high Pe' regime. Comparing the glass and the crystal we observe strong differences in the non harmonic behavior. Even though the crystal

exhibits a smaller yield strain than the glass, the non harmonic response for the same strain amplitudes is smaller. Both the reduction of non harmonic effects and the drop of yield strains for the crystal are possibly due to the larger distance from maximum packing and the appearance of the slipping layers allowing flow with reduced stresses.

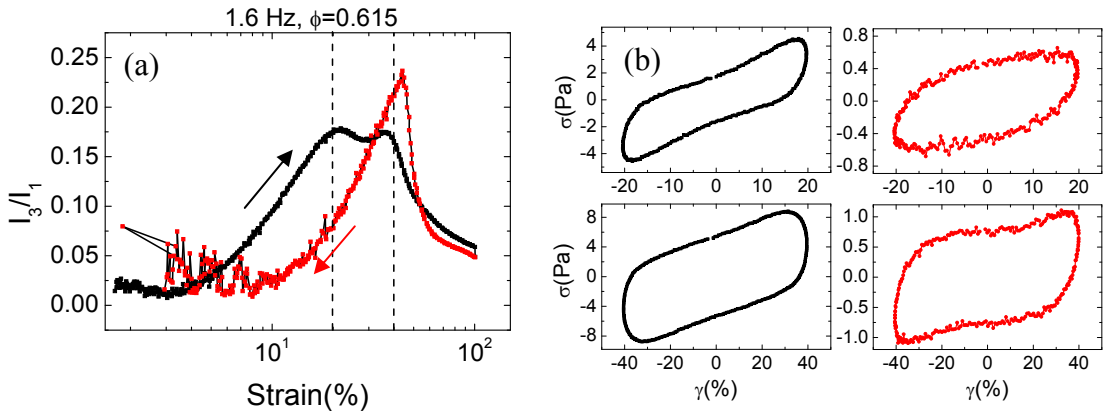

Figure 7.3: a) Third Harmonic of stress response and b) Lissajous curves in select strains from the dynamic strain sweep of figure 7.1b. Arrows in a) refer to the direction of shear, while vertical dashed lines in a) refer to the strains probed in b). In both a) and b) black color refers to increasing strain, while red to decreasing strain.

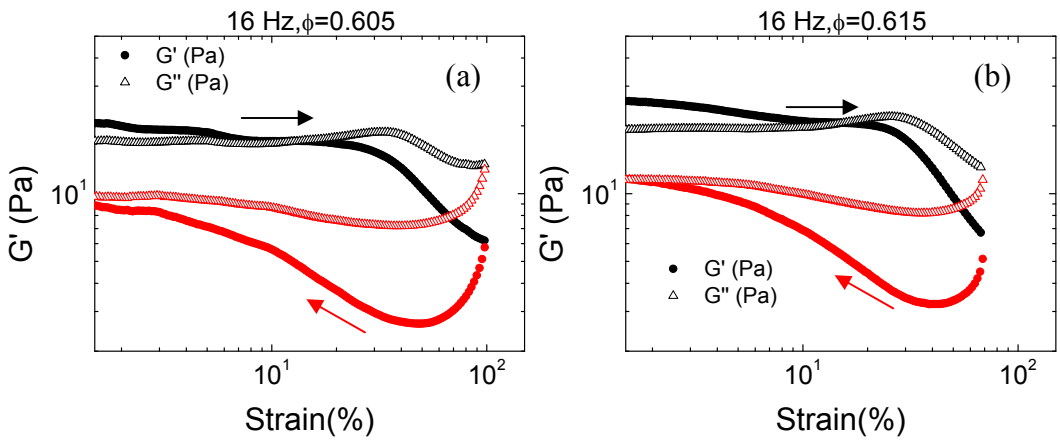

Figure 7.4: Dynamic Strain Sweep of 16 Hz starting from the glass and increasing strain (black) and decreasing strain to the crystal (red) for a) φ=0.605 and b) φ=0.615. Arrows note the direction of shear.

Strain sweeps at 16Hz were additionally performed for the two volume fractions as seen in figure 7.4. In this case 80 points per decade with 15 sec per point were used. The findings in such high frequency are similar to the previous, although here measurements we restricted measurements up to area (ii). Thus the glassy system during strain increase becomes semi-crystalline above the crossover strain and upon decreasing strain is fully crystallized. As will be shown with LS-Echo experiments, specifically for φ=0.615 (7.4b), the "glassy" regime upon increasing strain, seems to sustain crystalline patches as rejuvenation was not able to

fully shear melt the sample to a simple glass. Higher harmonic (FT) response is not shown here since at such high frequencies it is affected by "resonance" response of the rheometer transducer as described in the appendix (A.4).

Previous work with a parallel plate shear cell (Haw, Poon et al., 1998), has shown that full crystallization takes place at strains just above yielding, making a comparison between a glass and a crystal of the same sample in non linear strains impossible. The reason we are able to make this experimental comparison is because the glass is not able to fully develop into a crystal in the rotational plates of the rheometer until strains much larger than yielding are reached (Koumakis, 2007; Koumakis, Schofield et al., 2008). However we would like to emphasize that in a strain sweep starting from a glass, the crystallization percentage increases incrementally with larger strains and so the rheological and microscopic information above the crossover strain actually represent a mixture of both glass and crystal.

7.3 LS-Echo

Glass vs Crystal under Shear: Strain Dependence and Analysis

LS echo measurements were conducted simultaneously with the rheological measurements shown above, as a way to probe both rheology and dynamics at the same time, as was done with the Brownian Dynamics simulations in previous chapters (4, 5 and 6). Figure 7.5 shows the intensity autocorrelation functions under shear for selected strains, during the experiment of figure 7.1a upon strain increase. As described in the introductory chapter, the correlation function shows echoes at multiples of the oscillation period (inverse frequency). The height of the echoes is reversely related either to the number of particles that undergo irreversible rearrangements during the time scale of one period or to the amount of phase difference of the scattered light introduced due to the average shear induced displacements. In the case of linear measurements, the echoes should follow the correlation function at rest, while as strain is increased and irreversible rearrangements set in, the echoes should decrease in amplitude.

As seen in the inset, the width of each echo is related to the applied strain; the larger the strain and strain rate, the thinner the echo. The reciprocal of the half width at half height taken from the first echo can yields the decay rate Γ (Figure 7.6). We find that the decay rate increases linearly with the strain as also seen in the work of (Petekidis, Vlassopoulos et al., 2003). This is expected since the decay rate is proportional to strain rate; moreover, to a first approximation we may assume that the scattering conditions, the transmition of light through the sample and thus the number of scattering events are constant with strain. This is acceptable as a homogeneous strain field should cause a linear increase in the decay rate of

the echoes, independently of the structure of the material as long as there is no slip (Hébraud, Lequeux et al., 1997; Petekidis, Moussaid et al., 2002). Thus figure 7.6 is a good indication of the absence of slip during such measurements. Equivalently we may extract the decay rate Γ from the initial decay of the echo, but in this case at the limit of zero strain the decay rate will be equal to the initial Brownian decay of the system at rest.

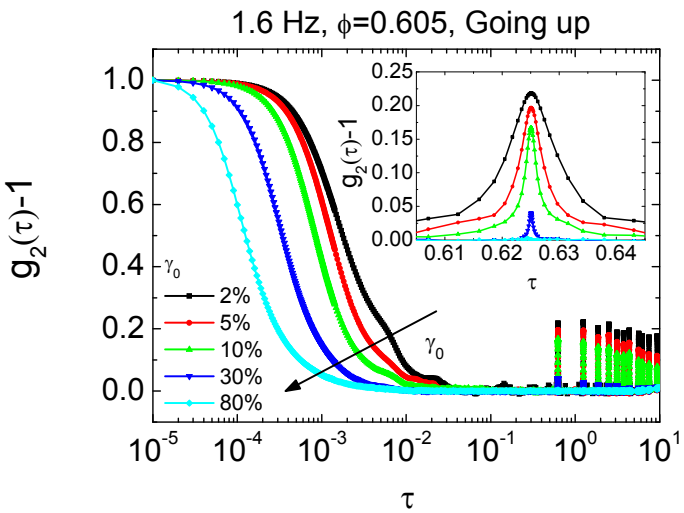

Figure 7.5: Results of LS-Echo scattering experiment during the strain sweep of figure 7.1a with selected correlation functions of increasing strain. The arrow shows the change in the curves with increasing strain, while the inset has a detailed view of the first echo peaks from the same data.

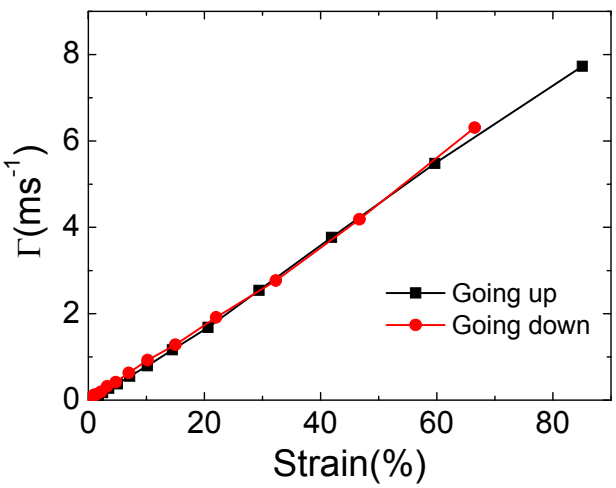

Figure 7.6: Results of the LS-Echo scattering experiment during the strain sweep of figure 7.1a showing the rate of the first echo decay extracted from the half-width half-height of the peak. The line is a guide to the eye.

A measure of the irreversible rearrangements may be deduced from the height of the first echo ($g_2(\tau=T)-1$), when plotted against strain as shown in figure 7.7 for previous

measurements (Koumakis, 2007) performed on a different sample batch of the same system. These experiments have showed that the glass under oscillatory shear upon increasing strain amplitude exhibits different rearrangements compared to the crystal during decreasing strain. Hence, $g_2(T)$-1 follows different paths for the up and down sweeps. The glass starts with higher echo peaks which decrease towards zero at the highest strains, while the crystal shows larger echo values at high strains and smaller ones in the linear regime.

In the linear regime it was proposed that the crystal shows smaller values due to increased in-cage Brownian motion, while in the non linear regime, the crystal showed larger values due to fewer irreversible rearrangements from sliding layer motion.

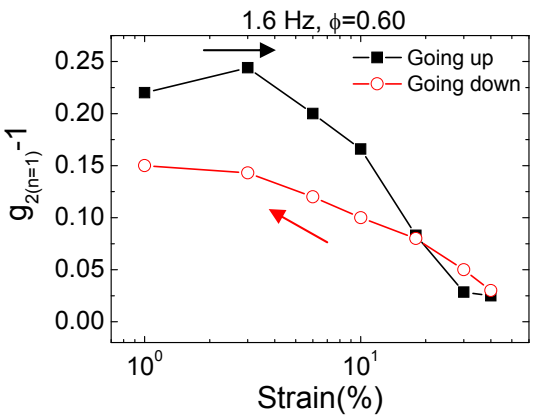

Figure 7.7: LS-Echo results of previous work (Koumakis, 2007) at 1.6 Hz showing the peak values of the first echo for increasing (glass/amorphous) and decreasing (crystal) strain for φ=0.60.

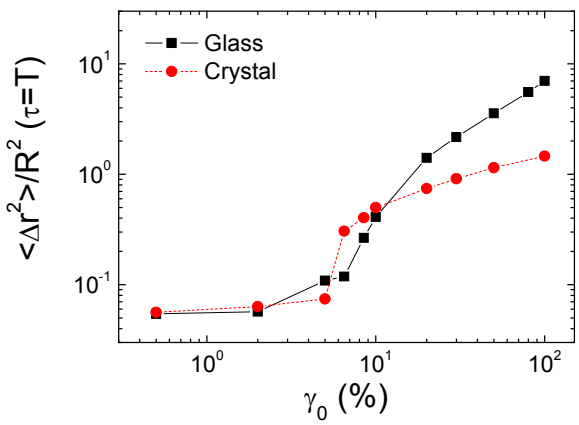

Figure 7.8: Overall particle displacements $<\Delta r^2>/R^2$ at $\tau=T=2\pi t_B$ vs strain extracted from simulations (chapter 6) in a glass and crystal parallel to shear at φ=0.62 under oscillatory shear at Pe'=1.

Indeed, results on the mean squared displacements from simulations in the glass and crystal (fig. 7.8) show similar findings as discussed in chapter 6. At low strains, particle displacements follow those at rest with the glass showing fewer in cage displacements than

the crystal. In the non-linear regime though, displacements in the crystal become less than those in the glass as shear induced ordering is driven to the minimization of stresses as well as particle rearrangements.

Further LS-Echo measurements were carried out for φ=0.605 and φ=0.615 at 1.6 and 16Hz, which in general give similar results to the previous work shown in fig. 7.7. In figure 7.9 we show the LS-Echo data for the peak of the first echo ($g_2(\tau=T)-1$) for the strain sweeps of figures 7.1a (1.6Hz) and 7.4a (16Hz) at φ=0.605 and similarly in figure 7.10 we present the results of φ=0.615 related to the strain sweeps of figures 7.1b (1.6Hz) and 7.4b (16Hz). In both volume fractions and both frequencies, we find the same general behavior as described above: At low strains weaker particle rearrangements are probed in the glass than in the crystal whereas at high strains the situation is reversed. For both glass and crystal, we find that at higher frequencies the first echo peak shows a weaker reduction with strain than at the lower frequencies, with such behavior being more evident in the crystal.

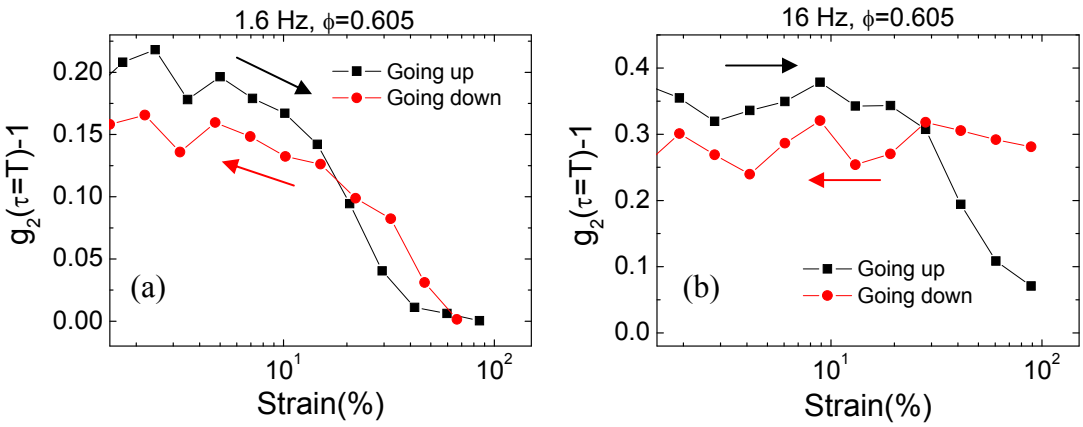

Figure 7.9: Results of LS-Echo scattering experiment of φ=0.605 during the strain sweeps of a) figure 7.1a at 1.6Hz and b) figure 7.4a at 16Hz with the peak of the first echo during increasing and decreasing strain.

From the particle motions of the crystal and the glass at rest as examined in the simulations of chapter 6, longer times show equal or larger motions than short times. Therefore, it is expected that in the linear regime, lower frequencies and thus larger time scales will have equal or smaller echo values than higher frequencies. Indeed figure 7.9 for φ=0.605 shows such behavior. However in fig. 7.10, we observe that at 16Hz the linear regime (low strain) values of $g_2(T)$ is smaller than that for 1.6Hz. As mentioned previously, this is most probably due to partial crystallization of the sample, remaining after the rejuvenation protocol.

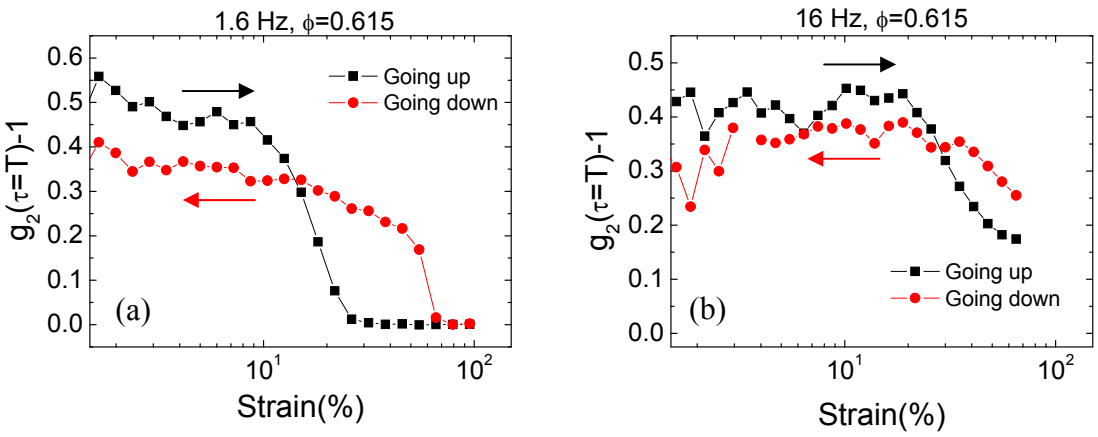

Figure 7.10: Results of LS-Echo scattering experiment of φ=0.615 during the strain sweeps of a) figure 7.1b at 1.6Hz and b) figure 7.4b at 16Hz with the peak of the first echo during increasing and decreasing strain.

Comparing the strain dependence of the peaks of the first echoes (figures 7.9 and 7.10) to the corresponding rheological data, we find that the echoes of the glass show a strong decay with the increase of applied strain, which corresponds to the crossover strain, the strain at which the system becomes liquid like. The crystal on the other hand exhibits a lower crossover strain than the glass, but shows a much weaker decay. The reduction of the crystal yield strain is attributed to the sliding layers, which allow the crystal to flow at smaller strains than the glass, however the sliding layers additionally reduce the amount of particle motion during flow resulting in larger echo values than the glass.

The peaks of the echoes which occur at multiples of the period, ($g_2(nT)$-1), as extracted from measurements such as shown in figure 7.5, represent the correlation function under oscillatory shear. At multiples of the period, stroboscopic detection of the scattered light allows the probing of particle motions without the effect of affine motion. This is not exactly the same as subtracting the applied shear, which is done in the simulations, as discussed in the appendix (A.2), although in the case of crystals under shear the differences are expected to be minimal.

Therefore, we additionally plot the echo peaks as a function of time for various strains, $g_2(nT)$-1, and use a Kohlrausch-Williams-Watts (KWW) function of the form $\sqrt{g_2(nT)-1} = A\exp\left[-(t/\tau)^b\right]$ in order to fit the field autocorrelation function as shown in figure 7.11. Although the range of times is not large we may get an indication of the strain dependence of the relaxation times under oscillatory shear. The analysis shows decrease of the relaxation time, faster motions, with increasing strain, as expected and understood from simple observation of the first echoes. The decrease of the stretching exponent, b, shows an

increase of the distribution of relaxation time, which may refer to the increase of the a_2 parameter with increasing strain, as seen in the BD simulations of glasses under oscillatory shear in chapter 5.

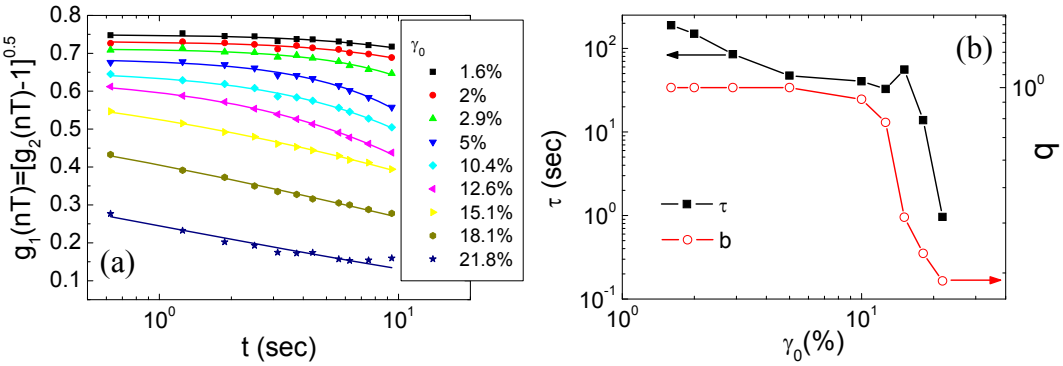

Figure 7.11: Results of LS-Echo scattering experiment during the strain sweep of figure 7.1b (φ=0.615, f=1.6Hz) with a) the field autocorrelation peak of the nth echo plotted against time for select strains, during the increase of strain in a glassy state and exponential fits of the form $\sqrt{g_2(nT)-1} = A\exp\left[-(t/\tau)^b\right]$. b) The fitting parameters of the exponential fit of a) plotted against strain with A=0.70±0.05.

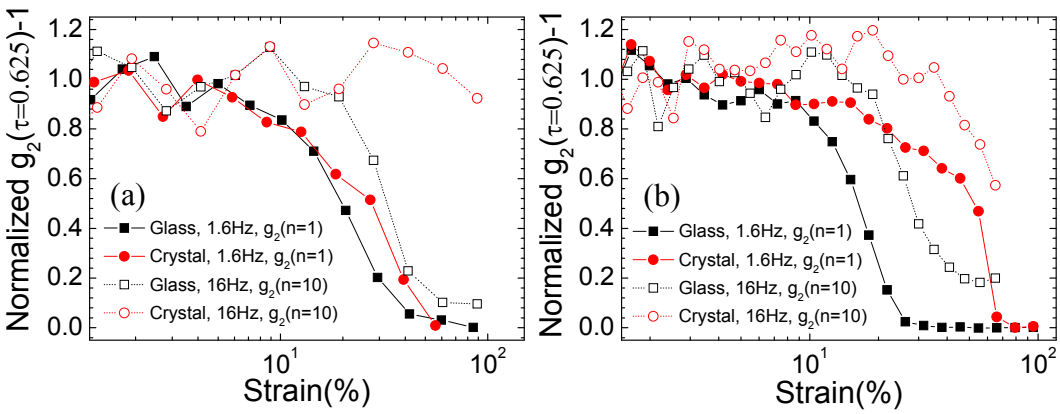

Figure 7.12: Results of LS-Echo scattering experiment of a) φ=0.605 and b) φ=0.615 showing the echo heights at the same correlation time τ=0.625sec for 1.6 and 16Hz, while normalized with the echo value in the limit of γ_0=0 (linear regime).

Another approach to examining the frequency dependence of the echo response is by comparing the echoes at different frequencies, but at the same correlation time. In figure 7.12 we show for both volume fractions the amplitudes of the echoes with strain, i.e. for 1.6Hz the value of the first echo amplitude, while for 16Hz the value of the tenth echo corresponding to τ=0.625sec. Moreover we have normalized the echo peaks with the average echo values as γ_0 approaches zero; the linear regime. We find that the higher frequency generally shows weaker

decrease of the echo peaks with increasing strain. At the high Pe' regime of these measurements, this may be associated with the reversibility at intermediate strains as seen for the simulations of the glass in chapter 5 and of the crystal in chapter 6.

Crystal under Shear: Frequency Dependence and Analysis

In order to compare with the simulation results of chapter 6, we carried out LS-Echo experiments on the shear induced crystal under non linear shear at different frequencies. In figure 7.13 we show, $g_2(nT)$-1, plotting the echo peaks with time for a crystal under shear at two φ for γ_0=30% and a range of frequencies from f=0.16 to 16 Hz. We see that while the higher frequencies seem to superimpose, $g_2(nT)$-1 deviate from each other as frequencies become smaller and time scales grow larger. This means that at high frequencies, particle displacements under shear are similar, while as frequencies decrease, shear induced displacements also increase.

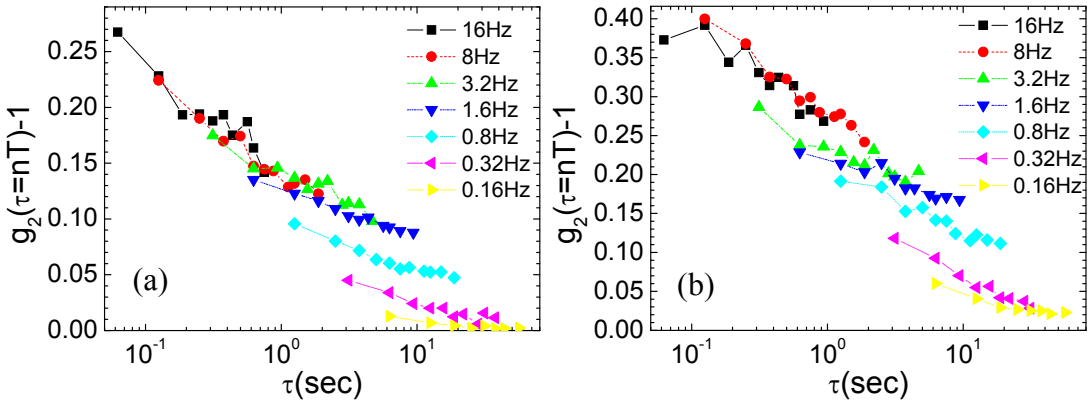

Figure 7.13: Results of LS-Echo scattering experiments at constant γ_0=30% and varying frequencies for the crystal as shown in the legend with the intensity autocorrelation peak of the echoes plotted against time, for a) φ=0.605 and b) φ=0.615.

These findings are very similar to results from the previous chapter 6 seen in figure 7.14, where the motions for the state at rest is compared to the motions at the same time scales under oscillatory shear. At high frequencies displacements are equal to the displacements at rest as no irreversible rearrangements occur, however as Brownian motion becomes more important, crystal layers are able to permanently slide past one another, through Brownian activated motions, giving rise to irreversible layer rearrangements. Since high frequency oscillations do not induce irreversible layer motions, the time dependence of $g_2(nT)$-1 for the higher frequencies as seen in fig 7.13 will be equal to each other and the state at rest.

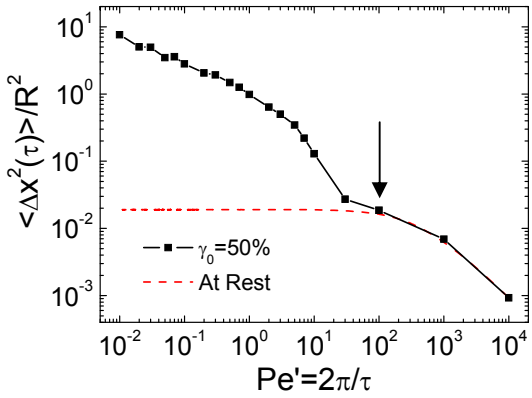

Figure 7.14: BD simulation results for a crystal at φ=0.62 parallel to shear sheared at γ_0=50%, from chapter 6. The x-axis MSD at a time of one period vs Pe' is shown together with the displacements at rest for the same time scales. The vertical arrow shows the approximate point of deviation of the state at rest and state under shear.

One can roughly estimate the point where the superposition of echoes between frequencies deviates in figure 7.13 as about f=5Hz, between the measured curves of 3.2 and 8Hz. The equivalent point in fig. 7.14 would be at Pe'=100 as noted in the figure. By foregoing the small differences between the φ of simulations and experiments, we can combine these numbers to give us an experimental estimate of t_B (within an order of magnitude). Therefore since Pe'=ω t_B=2πf t_B, we then find $t_{Bdressed}$≈3sec, which is quite comparable to the values given in table 7.1.

In order to make quantitative comparisons to the simulations though, we must transform the correlation function into mean squared displacements. For extracting the MSD information from the experimental LS-Echo experiments, we use two equations/methods originating from the principles of Diffusive Wave Spectroscopy (DWS) at rest (Weitz and Pine, 1993). By approximating the light propagation through a very highly scattering medium as a diffusive process, the probability of the different photon paths is determined, allowing the calculation of the intensity (g_2(t)) and field (g_1(t)) autocorrelation functions $\left(g_1(t)=\sqrt{g_2(t)-1}\right)$. The latter in the backscattering geometry is:

$$g_1(t)=\frac{\sinh\left[\left(\frac{L}{l^*}-\frac{z_0}{l^*}\right)\sqrt{\frac{6t}{\tau}}\right]+\frac{2}{3}\sqrt{\frac{6t}{\tau}}\cosh\left[\left(\frac{L}{l^*}-\frac{z_0}{l^*}\right)\sqrt{\frac{6t}{\tau}}\right]}{\left(1+\frac{8t}{3\tau}\right)\sinh\left[\frac{L}{l^*}\sqrt{\frac{6t}{\tau}}\right]+\frac{4}{3}\sqrt{\frac{6t}{\tau}}\cosh\left[\frac{L}{l^*}\sqrt{\frac{6t}{\tau}}\right]} \quad (7.1)$$

The mean free path l is the average distance between scattering events, while the transport mean free path l^* is the length scale over which the direction of light propagation is

randomized. The value z_0 describes an instantaneous source of diffusing light at a distance of $<z_0>\approx l^*$ inside the sample, while L is the thickness of the sample. The decay of the autocorrelation is related to the diffusion coefficient through $k_0^2\left\langle \Delta r^2(t)\right\rangle = 6t/\tau$, where $\tau = \left(k_0^2 D\right)^{-1}$ and $k_0 = 2\pi/\lambda$, λ the wavelength of the light beam.

At the limit of $L>>l^*$ the above equation becomes:

$$g_1(t) = \frac{\exp\left[-\frac{z_0}{l^*}\sqrt{\frac{6t}{\tau}}\right]}{1+\frac{2}{3}\sqrt{\frac{6t}{\tau}}} \quad (7.2)$$

And this can be further approximated by:

$$g_1(t) = e^{-\gamma\sqrt{6t/\tau}} \quad (7.3)$$

where in most cases $\gamma = \left\langle z_0\right\rangle / l^* + 2/3 \approx 2.1$.

The above assumes that the thickness of the sample is much larger than the transport mean free path of the light *($L>>l^*$)*. Using the simple equation $g_1(t) = e^{-\gamma\sqrt{k_0^2\left\langle \Delta r^2(t)\right\rangle}}$, we can acquire from experimental data for $g_2(t)$ mean squared displacements in a straight forward manner. An example of the extracted displacements with time can be seen in figure 7.15 for a specific set of data. The simple exponential equation 7.3 shows a power law slope increase of only 0.15. The important issue which arises with the findings of this method is that the experimental displacements under shear in the non linear regime do not show diffusive behavior. This is indicated by the MSD that do not follow a power law slope of unity (or close to unity) with time in the log-log plot of 7.15 as expected from the simulations of the previous chapter.

On the other hand we know that the approximation of $L>>l^*$ used in the specific equation is not true here. Indeed the sample thickness within the rheometer geometry where the laser beam illuminates the sample is L≈500μm, which is of the order of l^* of this sample (l^*≈300μm). Thus in order to calculate the displacements, a second method is to implement equation 7.1 using τ and L/l^* as fitting parameters, assuming that $<z_0>/l^*$ remains constant and moreover supposing that displacements for the crystal exhibit diffusive behavior in the non linear regime under shear. Thus by definition, the analysis using the complex equation 7.1 gives a power law slope of unity as shown in figure 7.15.

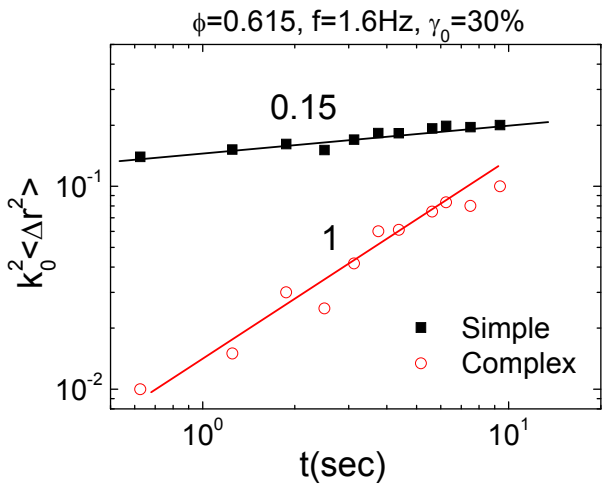

Figure 7.15: Translating experimental echo peaks of φ=0.615, f=1.6Hz and γ_0=30% to mean squared displacements through equation 7.3 (Simple) and equation 7.1 (Complex) using L/l^*=2.5 as a fitting parameter in the latter case.

Figure 7.16 shows a quantitative comparison of the experimental and simulation MSD, using the discussed analysis methods. We plot $(<\Delta r^2(\tau=T)>/R^2)/(T/t_B)$ which has the meaning of an effective diffusion coefficient, since simple diffusivity may not be the case for all points shown. We find that the experimental diffusivities are at least an order of magnitude less than the simulation data. Thus using the approximate solution for $g_2(t)$ in the multiple scattering conditions (Eq. 7.3) there is a qualitatively similar Pe' dependence of the effective diffusivities in experiments and simulations only for the highest Pe'. Using the more complex equation fit (Eq. 7.1) we find more qualitative similarities with a characteristic minimum in diffusivity at approximately the same frequencies, observed in experiments similarly to simulations.

For φ=0.605, the L/l^* fitting values varied from 1.1-2.7, while for φ=0.615 from 1.5-4.0, showing a general increase with larger applied frequencies. First of all, the range of L/l^* deduced is reasonable, although the actual l^* for the specific sample was not determined, although as mentioned it is expected to be from 200-300μm based on transmission measurements. Since the sample thickness (L) does not change, the increase of l^* with φ may be attributed to the increase in density which causes stronger scattering, while the changes with frequency could be due to the change of local structure at high shear rates as shown in chapters 4 and 5 and the creation of larger density fluctuations during shear.

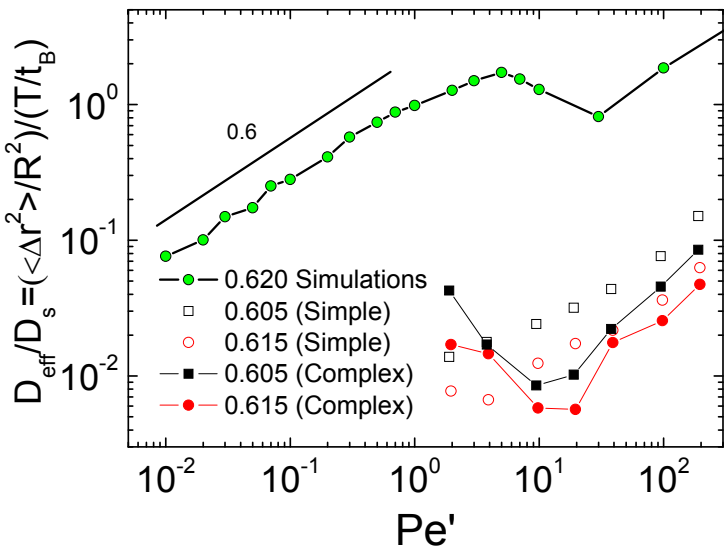

Figure 7.16: Quantitative comparison of experimental and simulation MSD data (as a normalized effective diffusion coefficient) of crystal under shear at γ_0=30% for experiments and γ_0=50% for simulations (chapter 7) and φ as shown in legend. Pe' is experimentally calculated from the applied frequency as shown in table 7.1.

The much smaller values of the displacements may be attributed to the beam width used in experiments, which is comparable to l^*. In this case of small beam width, there is a large contribution of short path light collisions giving a smaller rate of decorrelation and may consequently give smaller values of the diffusivities. Moreover, we may not be measuring particle self diffusivities/motions since firstly the particles are relatively small and secondly we are measuring a crystal, which significantly changes the structure factor and thus measured dynamics. The double scattering analysis of (Sorensen, Mockler et al., 1976) used for similar work on colloidal glasses (Petekidis, Vlassopoulos et al., 2003) produced results of similar Pe' dependence as the analysis of the simpler equation (7.3), although with values of an order of magnitude larger.

7.4 Chapter Conclusions

Through the use of the LS-Echo technique coupled with rheology, we have examined the shear-induced motions of glasses and their corresponding shear induced crystals and found strong correlations to the BD simulations results discussed in chapter 6. Comparing the glass and the crystal, we observe that although at low strains the crystal shows increased particle displacements than glass due to relative to the higher free volume around a particle (in-cage motion), at higher strains, the crystal shows reduced particle rearrangements due to the anisotropic sliding layer motion. A quantitative comparison between the crystal simulations

and the experiments was not possible at this stage. However, we qualitatively found good agreement at the high Pe' regime, where a characteristic minimum of shear induced diffusivities as a function of frequency is observed. Moreover, the use of a CCD camera and multispeckle correlation may allow measurements of the correlation function under shear at longer times and thus at lower frequencies, reaching the low Pe' regime.

7.5 References

Haw, M. D., W. C. K. Poon, P. N. Pusey, P. Hebraud and F. Lequeux (1998). "Colloidal glasses under shear strain." Phys. Rev. E **58** 4673.

Hébraud, P., F. Lequeux, J. P. Munch and D. J. Pine (1997). "Yielding and Rearrangements in Disordered Emulsions." Phys. Rev. Lett. **78**(24).

Koumakis, N. (2007). Shear Induced Crystallization of a Colloidal Glass. Department of Materials Science and Technology, University of Crete. **MSc**.

Koumakis, N., A. B. Schofield and G. Petekidis (2008). "Effects of shear induced crystallization on the rheology and ageing of hard sphere glasses." Soft Matter **4**: 2008 2008-2018.

Petekidis, G., A. Moussaid and P. N. Pusey (2002). "Rearrangements in hard-sphere glasses under oscillatory shear strain." Physical Review E **66**(5) 051402.

Petekidis, G., D. Vlassopoulos and P. N. Pusey (2003). "Yielding and flow of colloidal glasses." Faraday Discuss **123** 287-302.

Schaertl, W. and H. Sillescu (1994). "Brownian dynamics of polydisperse colloidal hard spheres: Equilibrium structures and random close packings." J. Stat. Phys. **77** 1007.

Smith, P. A., G. Petekidis, S. U. Egelhaaf and W. C. K. Poon (2007). "Yielding and crystallization of colloidal gels under oscillatory shear." Phys. Rev. E **76**(4) 041402.

Sorensen, C. M., R. C. Mockler and W. J. Sullivan (1976). Phys. Rev. A **14** 1520.

Weitz, D. A. and D. J. Pine (1993). Diffusing-wave spectroscopy. Dynamic Light Scattering: The Method and Some Applications W. Brown, Clarendon Press**:** 652–720.

Chapter 8 – Experimental Rheology of Attractive Colloids

Abstract

Steady and oscillatory rheology was utilized to study the mechanical response of colloidal glasses and gels with particular emphasis in their yielding behavior. We used a suspension of hard sphere colloidal particles with short-range depletion attractions induced by the addition of non-adsorbing linear polymer. While high volume fraction hard sphere glasses exhibit a single yield point due to cage breaking, attraction dominated glasses show a two-step yielding reflecting bond and cage breaking, respectively. Here we investigated the yielding behavior of frustrated colloid–polymer systems with equal attraction strength and range, varying the particle volume fraction, φ, spanning the region from an attractive glass (φ=0.6) to a low volume fraction (φ=0.1) attractive gel. Yielding throughout this range, probed both by oscillatory and steady shear, is found to remain a two step process until very low φ's.

The first yield strain related with in-cage or inter-cluster bond braking remains constant for φ>0.3, while the second yield strain, attributed to braking of cages or clusters into smaller constituents, increases as volume fraction is decreased due to enhancement of structural inhomogeneities in the gel. Steady shear tests indicated distinct shear rate regimes: At steady state, low and intermediate shear rates create denser or smaller flowing clusters, whereas high rates may lead to complete break-up into independent particles. When the range of attraction was increased, both yield strains increased scaling with the range of attraction and accompanied structural changes. The structural properties under shear are expected to be reflected by the non dimensional Pe_{dep} number, introduced as the ratio of depletion and shear forces/time scales. By increasing the range of attraction, linear viscoelastic properties are reduced due to weakening of the gel. Most importantly both yield strains increase as expected by the rationalization given.

Finally, we have shown that both the linear viscoelasticity and the stresses measured at step rates evolve with waiting time. For the latter an increase of the second stress overshoot over the first is observed at long times. This suggests that although initial particle bonding is quite fast, slower structural rearrangements lead to stronger clusters at longer times. We have extended these findings for van der Waals interactions and found that even small attractions,

$U \approx -1K_BT$, may cause long range restructuring and lead to the appearance of a second stress overshoot.

8.1 Introduction/Experimental

Introduction

Previous rheological experiments (Pham, Petekidis et al., 2006; Pham, Petekidis et al., 2008) in colloid-polymer mixtures at high particle volume fractions have shown that an attractive glass exhibits a two step yielding with increasing oscillatory strain amplitude as opposed to the single yielding in a repulsive glass (figure 8.1). The first step was attributed to bond breaking while the second one to cage breaking in the glassy state. As the strain amplitude is increased beyond the linear regime, particles are able to change bonding neighbors by escaping from interparticle attraction, thus leading to energy dissipation and partial yielding. When higher strains are applied to the system, the cages are distorted and finally break giving rise to a second yielding point.

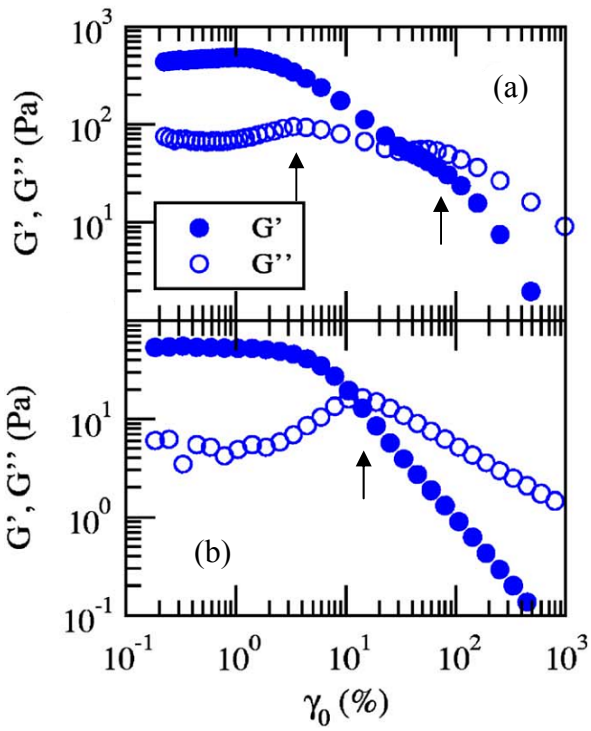

Figure 8.1: Dynamic strain sweeps at ω=1 rad s^{-1} for a) An attractive hard sphere glass and b) for a repulsive hard sphere glass five from the work of (Pham, Petekidis et al., 2008). The vertical arrows show the positions of the yield strains.

Here we rheologically investigate the transition, from a cage dominated to bond dominated kinetic arrest. This is achieved by probing samples that have the same attraction strength but different colloidal volume fraction. Thus by lowering the latter we

expected to eliminate the cage effect. In reality though, the transition from a glass to a gel has proven to be far from simple as particle cages turn into particle clusters and interconnected networks (Krall and Weitz, 1998; Lu, Conrad et al., 2006; Zaccarelli, 2007; Lu, Zaccarelli et al., 2008). In order to unravel this complexity, we additionally examined the time evolution (ageing) of linear and non linear mechanical properties and the changes caused by increasing the range of attraction. Through this work, the original simple bond and cage breaking idea (Pham, Petekidis et al., 2006; Pham, Petekidis et al., 2008) is refined for attractive glasses and extended to lower volume fraction gels (Koumakis and Petekidis, 2011).

Experimental

Here we have used Poly-methylmethacrylate (PMMA) particles sterically stabilized by chemically grafted poly-hydro-stearic acid (PHSA) chains (≈10nm) dispersed in cis-decalin. The hydrodynamic radius of particles was 130 nm with a size polydispersity of 23% measured by SEM(Pham, Petekidis et al., 2006; Pham, Petekidis et al., 2008). This high polydispersity removes the possible complications of crystallization under shear expected with monodisperse samples(Smith, Petekidis et al., 2007; Koumakis, Schofield et al., 2008). The added depletant was a non-adsorbing linear polystyrene with M_w=132900 gr/mol and R_g=10.8 nm. This gives an average size ratio $\xi_1=R_g/R_c=0.083$ in the dilute limit and a constant depletion attraction at contact of $U_{dep}/(k_BT)=-23.5\pm0.5$ as derived from the model of Asakura and Oosawa(Asakura and Oosawa, 1954; Aarts, Tuinier et al., 2002) also taking into account polymer coil-coil interactions. The overlap concentration for the polymer was calculated at $c^*=0.0427$ gr/ml while c_{pfree}, the polymer concentration in the free volume, was kept constant at approximately $1c^*$.

Taking into account the concentration dependence of the polymer and mesh size in the semidilute regime we have calculated a depletion range $\xi_1^*=0.043$ and $U_{dep}/(k_BT)=-15\pm1$ according to the generalized free volume theory (GFVT) (Lekkerkerker, Poon et al., 1992; Fleer and Tuinier, 2007). In order to examine the attraction range dependence, a larger polymer chain with M_w=1210700 gr/mol and R_g=35 nm was additionally used. This yields a ratio $\xi_2=0.27$ in the dilute regime and an overlap concentration of $c^*=0.0109$ gr/ml with ideal AO potential $U_{dep}/(k_BT)=-22\pm1$. The polymer concentration in the free volume is about $c_{pfree}/c^*=2.9$ which based on GFVT(Lekkerkerker, Poon et al., 1992; Fleer and Tuinier, 2007) leads to a depletion range $\xi_2^*=0.12$ and 0.17 with a depletion attraction at contact of –4.7kT and -2.9kT for the small and large volume fractions respectively. Table 8.1 shows the attraction strengths and parameters for all the samples used, as well as the ratio of Pe/Pe_{dep} as will be

discussed further in the text.

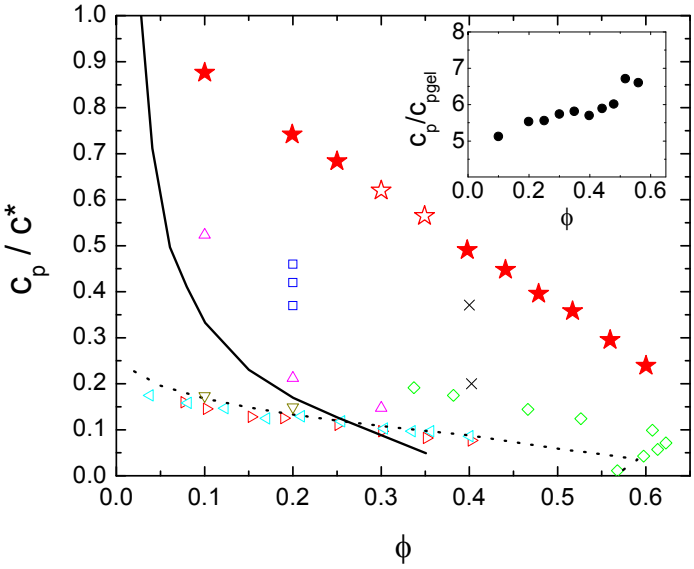

Figure 8.2: Samples studied (stars), along with gel/arrest transition points from literature. The examined samples follow a line of equal attraction strength, well within the gel/attractive glass regime. Solid and open stars are non-slip and time dependent slip samples respectively. Gel transition points are as follows: Squares are from (Dibble, Kogan et al., 2006) (ξ=0.043), left and right sided triangles are from (Shah, Chen et al., 2003) (ξ=0.061 for left sided and ξ=0.090 for right sided), slanted squares are from (Pham, Puertas et al., 2002; Pham, Egelhaaf et al., 2004) (ξ=0.08), slanted crosses are from (Laurati, Petekidis et al., 2009) (ξ=0.083) and triangles facing upwards and downwards are from (Poon, Starrs et al., 1999) (Upward triangles refer to transient gelation and downward to aggregates at ξ=0.06). The theoretical transition lines are taken from (Chen and Schweizer, 2004) (Solid line for ξ=0.09) and (Bergenholtz, Poon et al., 2003) (Dotted line for ξ=0.083). The inset shows c_p/c_{pgel} for the examined samples with the c_{pgel} taken from (Bergenholtz, Poon et al., 2003).

The rheometer used was an ARES-HR strain controlled instrument with a force balance transducer 10FRTN1 and a 25 mm cone-plate geometry (0.044 rad). As a standard protocol before each test a high strain dynamic shear rejuvenation (γ_0=1000 %, ω=1 rad s^{-1}) was performed for dynamic tests or high rate steady shear ($\dot{\gamma}$=100 s^{-1}) for steady shear experiments followed by a waiting time of typically 120s before the beginning of the experiment (unless stated otherwise). Slip was absent in all measurements in the range ($0.4<\varphi<0.6$), as verified by direct observation as well as the use of serrated plates (Ballesta, Besseling et al., 2008; Ballesta, Besseling et al., 2010), but was present in some cases for gels at lower φ ($0.20<\varphi<0.40$) as discussed below. During dynamic tests (frequency and strain sweeps) data were gathered by averaging over few cycles.

At T=293K, R_c=130nm			Ideal Polymers from Aarts (2002)			GFVT Fleer (2007)			Pe/Pe_{dep}= $-U_{dep}/(2q_s)$	
Mw	φ	Cp/C*	C_{pfree}/C^*	q_s, ξ^*	$U_{dep}(2R_c)$	C_{pfree}/C^*	q_s, ξ^*	$U_{dep}(2R_c)$	Ideal	Fleer
132900	0.100	0.842	0.968	0.091	-23.07	0.952	0.049	-16.07	127.45	165.59
132900	0.199	0.713	0.962	0.091	-22.92	0.927	0.049	-15.76	126.60	160.06
132900	0.250	0.658	0.973	0.091	-23.18	0.925	0.049	-15.74	128.08	159.74
132900	0.300	0.597	0.975	0.091	-23.24	0.913	0.050	-15.60	128.39	157.26
132900	0.349	0.543	0.990	0.091	-23.60	0.911	0.050	-15.57	130.39	156.76
132900	0.400	0.473	0.978	0.091	-23.30	0.881	0.051	-15.21	128.73	150.47
132900	0.439	0.430	0.991	0.091	-23.63	0.875	0.051	-15.13	130.52	149.26
132900	0.480	0.381	0.995	0.091	-23.71	0.858	0.051	-14.92	130.95	145.56
132900	0.517	0.344	1.026	0.091	-24.45	0.859	0.051	-14.94	135.07	145.92
132900	0.559	0.284	1.004	0.091	-23.92	0.813	0.053	-14.37	132.13	136.44
132900	0.601	0.231	0.992	0.091	-23.64	0.772	0.054	-13.85	130.62	128.11
1210700	0.433	0.505	2.816	0.289	-20.98	1.263	0.119	-4.67	36.34	19.59
1210700	0.600	0.067	3.080	0.289	-22.95	0.615	0.173	-2.86	39.74	8.27

Table 8.1: Table showing the characteristics of the studied samples of this work and calculations for the case of ideal polymers (Aarts, Tuinier et al., 2002) and the GFVT (Fleer and Tuinier, 2007). We additionally show the Pe/Pe_{dep} ratio as discussed in the text.

8.2 Oscillatory Rheology

A range of volume fractions, from 0.60 down to 0.10 with equal attraction strength was examined. The attraction range and strength of the attractive glass at φ=0.60 is the same as the most attractive sample studied by (Pham, Petekidis et al., 2008). Figure 8.2 depicts the samples studied at different volume fractions but with an equal attraction according to Asakura and Oosawa (Asakura and Oosawa, 1954; Aarts, Tuinier et al., 2002). All samples are well within the gel regime compared to the, gel/attractive glass transition points taken from previous experimental and theoretical studies on similar systems (Poon, Starrs et al., 1999; Pham, Puertas et al., 2002; Bergenholtz, Poon et al., 2003; Shah, Chen et al., 2003; Chen and Schweizer, 2004; Pham, Egelhaaf et al., 2004; Dibble, Kogan et al., 2006; Laurati, Petekidis et al., 2009). For some samples of intermediate volume fraction (samples with open symbols, fig. 8.2) we observed time dependent slip (Buscall, McGowan et al., 1993; Kamp and Kilfoil, 2009; Ballesta, Besseling et al., 2010) in the linear oscillatory measurements, where slip effects become more pronounced with elapsed waiting time. However, even for these samples steady start up tests were free of slip judging from a comparison with serrated plates data. In all measurements shown we have subtracted the viscous contribution of the

polymer solution, although the contribution is negligible for φ>0.20, while the corresponding suspensions with no polymer exhibits viscoelasticity below the torque limits.

Linear Viscoelasticity

The frequency dependence of G' and G'' in the linear regime is shown in Fig. 8.3a for different volume fractions. In the range of 0.40<φ<0.60 the samples show similar features of G' and G'', such as the weak increase of the storage modulus with frequency and the minimum of the loss modulus characteristic of colloidal glasses and gels (Derec, Ducouret et al., 2003; Prasad, Trappe et al., 2003; Koumakis, Schofield et al., 2008; Carrier and Petekidis, 2009; Laurati, Petekidis et al., 2009). At lower φ the system exhibits a liquid-like behavior; however the experimental data become scattered due to low torque signal. The characteristic relaxation time of about 6s, determined from the cross-over of G' and G'' at φ=0.2 (fig. 8.3b) represents the recombination time of inter-cluster bonds in the gel network similar to previous findings (Laurati, Petekidis et al., 2009).

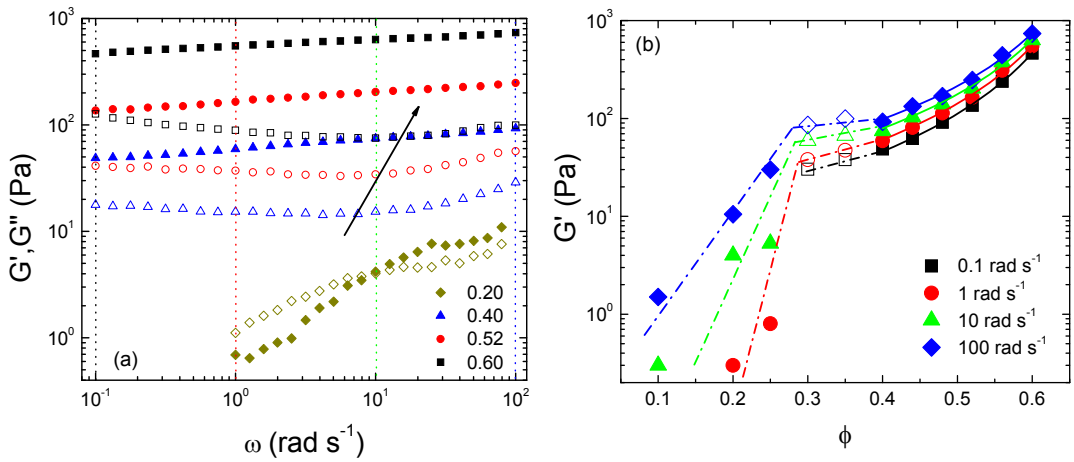

Figure 8.3: a) Dynamic frequency sweeps for four different volume fractions of equal attraction strength, i) 0.20, ii) 0.40, iii) 0.52 and iv) 0.60 with G' as solid and G'' as open symbols. The arrow notes the direction of the minimum of G''. b) Values of G' as a function of volume fraction at ω=0.1, 1, 10 and 100 rad s^{-1} specified by the vertical dashed lines in a). Open symbols indicate samples where a time dependent slip was detected at long times. Solid lines (φ=0.40 to 0.60) are fits to $G'=G_0(\varphi_{RCP}-\varphi)^{-c}$ with φ_{RCP}=0.7241 and c=2.41, 2.30, 2.18, 2.11 going from lower to higher ω. Dash-dot lines are guides to the eye.

The minimum of G'' in fig. 8.3a is related, within the MCT approach, with the transition from α to β relaxation (Mason and Weitz, 1995), or the characteristic time for a particle to explore its cage as has been discussed in previous chapters. As the volume fraction increases the minimum moves to higher frequencies and thus smaller time scales. This is

reasonable as higher volume fractions translate to stricter clusters and cages, smaller interparticle distances and thus less time for a particle to explore its surroundings (Koumakis, Schofield et al., 2008). Still the existence of a longer relaxation, related either with a diffusive or an activated process might be present at much lower frequencies.

Figure 8.3b shows the volume fraction dependence of the elastic modulus at various frequencies. Under constant depletion attraction (U_{dep}=-23.5 k_BT), G' increases with volume fraction exhibiting different behaviors at low and high φ's (>0.4). Below φ=0.3, G' follows an exponential increase with a viscoelastic liquid-like response typical for a cluster fluid (φ=0.1) or a transient percolated network (0.1<φ<0.3).

However for φ≥0.3 the system exhibits a solid-like response with no relaxation time within the measurement time window and an elastic modulus that can be described well by $G'=G_0(\varphi_{RCP}-\varphi)^{-\nu}$. Such behaviour resembles that of hard sphere glasses (Koumakis, Schofield et al., 2008) approaching close packing as well as the viscosity divergence when approaching a gel point (Trappe, Prasad et al., 2001) or a glass transition (Marshall and Zukoski, 1990; Smith and Zukoski, 2004). The random close packing volume fraction for a hard sphere sample, measured after centrifugation, was φ_{RCP}=0.724, a rather high value compared to the monodisperse φ_{RCP}=0.64, which can be attributed to the high particle polydispersity (Schaertl and Sillescu, 1994).

Here the exponent, ν, is weakly frequency dependent ranging from 2.4 at low frequencies to 2.1 at high ones. For comparison, hard sphere glasses (Koumakis, Schofield et al., 2008) exhibit an exponent of about 4. Thus gels with constant attraction strength have a weaker dependence on volume fraction than hard sphere glasses when approaching close packing. This behavior is similar to that found in colloid-polymer gels (Shah, Chen et al., 2003) under constant polymer concentration (c/c*), where the G' increase with φ was fitted by a power law, although the attraction strength was not constant.

We should note that a critical power law dependence, $G'=G_0'(\varphi-\varphi_{gel})^{\delta}$ with φ_{gel}, the gel transition volume fraction, that has been used in other studies at lower φ's (Trappe, Prasad et al., 2001) cannot describe the φ dependence here. Moreover, the ratio of c_p/c_{pgel}, with c_{pgel} taken from (Bergenholtz, Poon et al., 2003), remains approximately constant for φ>0.3 (inset of fig. 8.2). Hence it is reasonable to assume that the increase of the elastic modulus along a line of constant attraction strength is dominated by the volume fraction increase and thus should scale similarly with a hard sphere glass approaching close packing, yet with a different exponent.

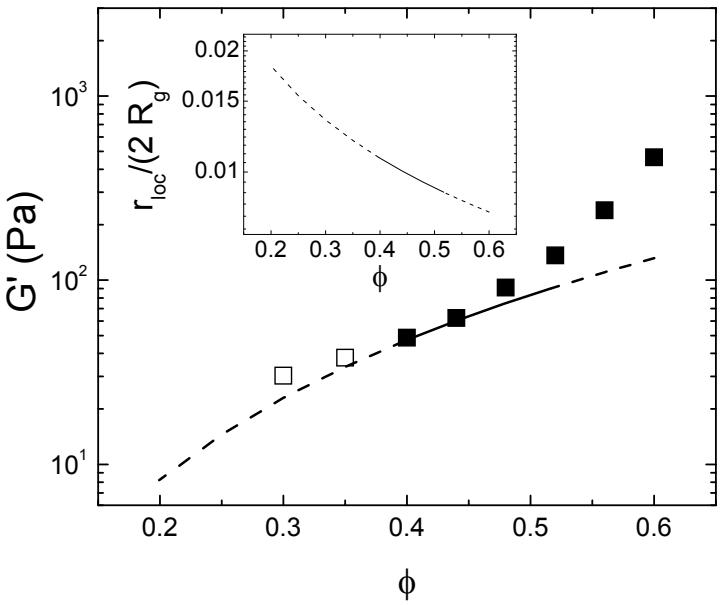

Figure 8.4: G' as a function of volume fraction at ω=0.1 rad s^{-1}. The line is the theoretical predictions from Chen and Schweitzer (2004) divided by a factor of 1500 in order to approach the experimental data. Inset shows the localization length along the line of equal attraction. In both the figure and the inset, the solid portions of the lines indicate data interpolated from the reference, while the dashed portions indicate extrapolated data.

In a more quantitative account of the data fig. 8.4 shows a comparison of the experimental G' at a low frequency (0.1 rad s^{-1}) with theoretical predictions for the zero frequency elastic modulus from combined MCT and two component PRISM theory (Shah, Chen et al., 2003; Chen and Schweizer, 2004; Laurati, Petekidis et al., 2009). Note that within this approach we have used values for the localization length (inset of fig. 8.4) along the line of equal attraction (or c/c_{pfree}) which were extracted from fig. 8 of (Chen and Schweizer, 2004). In agreement with what has been seen previously (Chen and Schweizer, 2004), this approach overestimates the elastic modulus; here by about three orders of magnitude. Such behavior was attributed to a characteristic cluster length-scale equal to several particle diameters that was not taken into account in theory (Chen and Schweizer, 2004). Therefore, the theoretical elastic modulus can be reduced by the average number of particles participating in a cluster, $G'_{exp}=G'_{MCT}/N_{cluster}$. In this way a satisfactory agreement with the experimental G' can be achieved using $N_{cluster}$=1500 originating from a characteristic radial cluster size of about 13 particle radii. Nevertheless, although the rescaled prediction agrees well for intermediate volume fractions (≈0.35) there is a clear deviation at low φ's (<0.25) where theory underestimates the elastic modulus as well as at high φ's (>0.4) where the experimental G' are larger than predicted. This suggests that if

such scaling holds, $N_{cluster}$ should be volume fraction dependent.

Non-linear dynamic response

The non-linear oscillatory response of the attractive glass and gels at various volume fractions is shown in figures 8.5a and 8.5b. Figure 8.5a shows a dynamic strain sweep (DSS) for five different volume fractions at ω=10 rad s^{-1}, spanning the phase diagram from the attractive glass regime at high φ down to a very low φ gel. At the highest volume fraction, well within the attractive glass region, there are two distinct peaks of G'' signifying yielding through the two mechanisms discussed previously (Pham, Petekidis et al., 2006; Pham, Petekidis et al., 2008), the first related to bond breaking and the second to cage breaking. At the same time, while G' starts at low strains larger than G'', it decreases below G'' with two distinct shoulders as the strain increases. As the volume fraction is decreased the second peak attributed to cage breaking, becomes broader and less pronounced, seemingly moving to higher strains, until it disappears at the lowest volume fraction. At low φ (≤0.20), G'' is larger than G' even at low strains, however as strain increases both moduli still decrease, exhibiting a complex shear thinning behavior.

Figure 8.5b shows G' and G'' as a function of increasing strain for a fixed φ of 0.40 and varying ω=1, 10 and 100 rad s^{-1}. The plots show a similar two step yielding, which seems independent of frequency while there is a slight increase of linear moduli with frequency as expected by the linear frequency sweep of fig. 8.3a.

In figure 8.6a and 8.6b we show the total stress, σ, and the elastic stress, γG', during dynamic measurements at ω=10 rad s^{-1} (same data with fig. 8.5a). In such a plot a linear increase of the stress with strain may indicate both an elastic response, with $\sigma \propto \gamma_0$, at low strains as well as a viscous behavior at large strain amplitudes where the sample is shear melted with $\sigma \propto \dot{\gamma} \sim \omega\gamma_0$. From these DSS we can again identify critical strains corresponding to the two yield mechanisms at the points where the stress curves become sub-linear or exhibits a peak, as indicated in fig. 8.6. The yield points can be defined more clearly in these plots again revealing that the second yield strain moves to higher strains and progressively dissipates with decreasing volume fraction. In the range of 0.40<φ<0.60, the first yield point attributed to bond breaking is quite pronounced and remains at a constant strain, but for φ<0.40 it moves to higher strains.

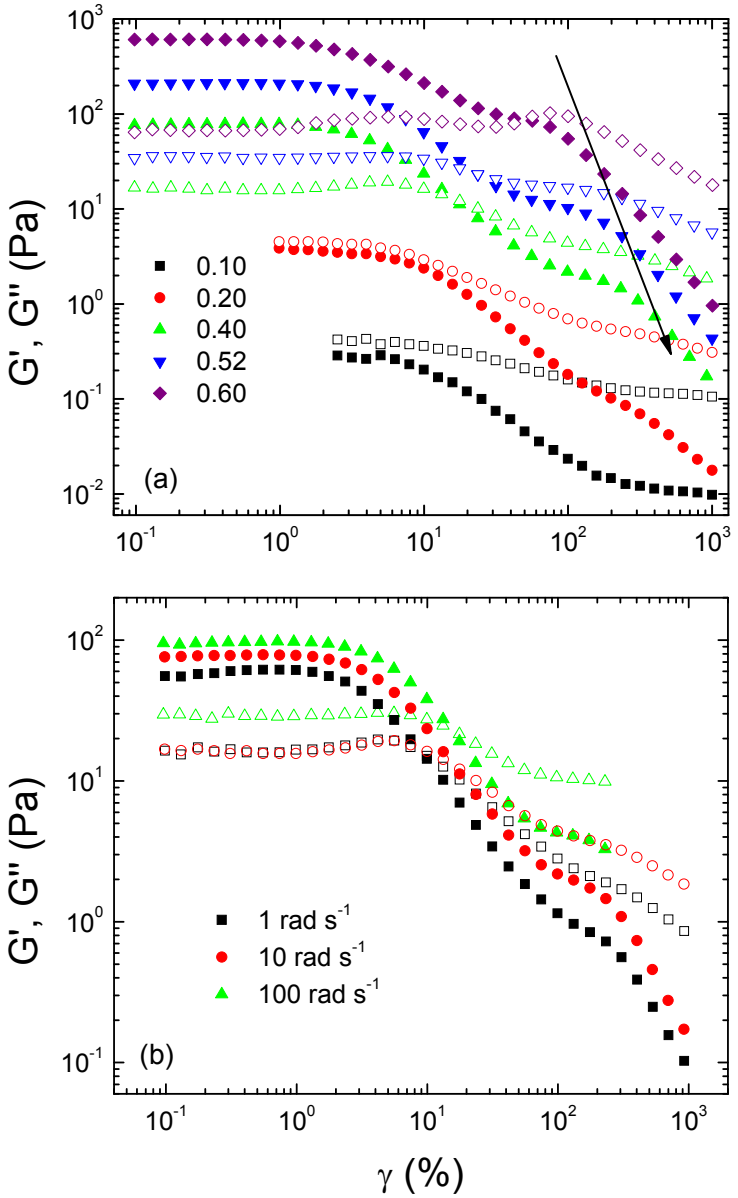

Figure 8.5: a) Dynamic strain sweep at ω=10 rad s^{-1} for five different volume fractions with equal attraction strength as indicated. The arrow shows the approximate shift of the second G'' peak with decreasing volume fraction. b) Dynamic strain sweep of φ=0.40 for three frequencies as indicated. (G': solid symbols, G'': open symbols)

By examining figures 8.5a, 8.6a and 8.6b and extracting the yield strains, we can separate them into three categories. The simplest one to extract is, γ_c, the crossover strain from figure 8.5a, which is the strain where G' becomes equal to G'' and the gel/glass is turning into a viscoelastic liquid. We can additionally determine the previously discussed first and second yield strains, γ_1 and γ_2, attributed to bond and cage breaking, either from figure 8.6a or 8.6b at the deflection points of the total stress or the peaks of the elastic stress. Although the values of γ_1 and γ_2 extracted from fig. 8.6a and 8.6b are not identical they are very similar and exhibit the same trends. Figure 8.7 depicts γ_1, γ_2 and γ_C at different frequencies as a function of the volume fraction but also the reciprocal of the

free volume $1/\varphi_{free}=1/(\varphi_{RCP}-\varphi)$, whith $\varphi_{RCP}=0.724$ as discussed previously. We also plot the yield strains for $\xi=0.27$ (only from $\gamma G'$) which will be discussed below.

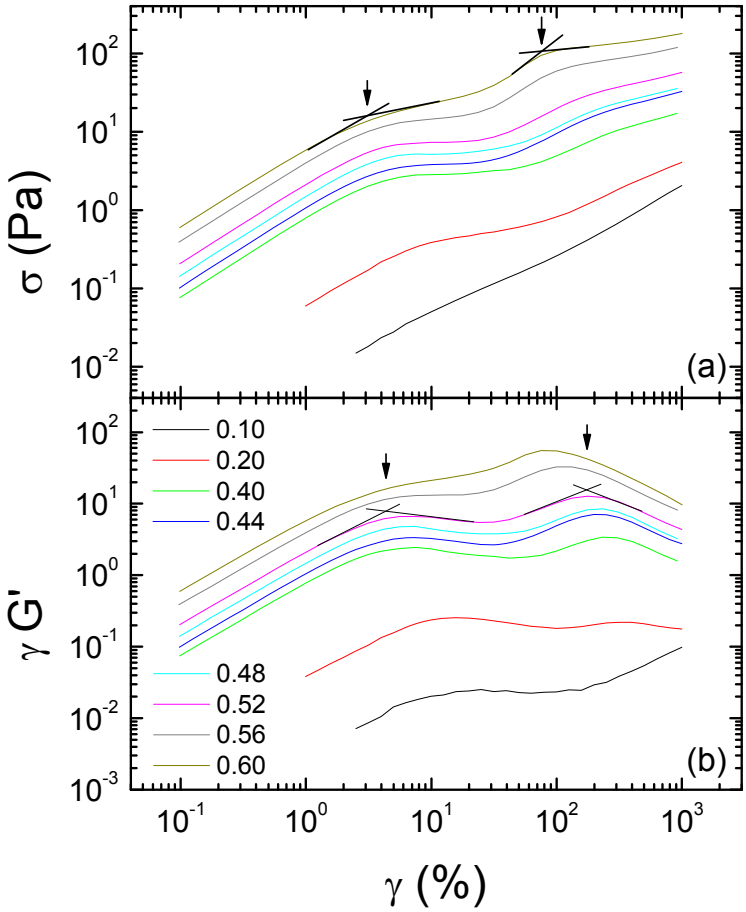

Figure 8.6: a) Stress, σ, during a dynamic strain sweep (fig. 8.5a) for several volume fractions as indicated at equal attraction strength decreasing from top to bottom. b) Elastic stress, $\gamma G'$, for the same data. Arrows indicate the yield strain according to non-linear onset of stress in a) and peak of $\gamma G'$ in b).

First yield strain, γ_1

The first yield strain, γ_1, seems separated in two regimes as indicated in fig. 8.7a; for $\varphi>0.40$ it is almost constant, whereas for $\varphi<0.40$ it exhibits higher values. This qualitatively concurs with theoretical predictions by Kobelev and Schweitzer (Kobelev and Schweizer, 2005), predicting a decrease of the yield strain as c_p/c_{pgel} increases. At high φ's c_p/c_{pgel} seems almost constant (inset of fig. 8.2), hence the yield strain is expected to remain the same. In contrast at low φ's c_p/c_{pgel} decreases when c_{pgel} is taken from simplified MCT/PRISM predictions (Chen and Schweizer, 2004) (figure 8.2) suggesting an increasing yield strain.

We could also argue that the first peak of G'', or equivalently the onset of non-linearities,

is linked to bonding neighbor distances and should manifest as a yield point when shear causes adjacent particles to collide and dissipate energy by breaking their bonds. In these samples, the bond length-scale remains constant and the peak remains unchanged at higher volume fractions. However, for $\varphi<0.40$ it moves to higher strains indicating that at lower particle densities there is higher structural and bonding flexibility that allows elongation and stretching before bonds break.

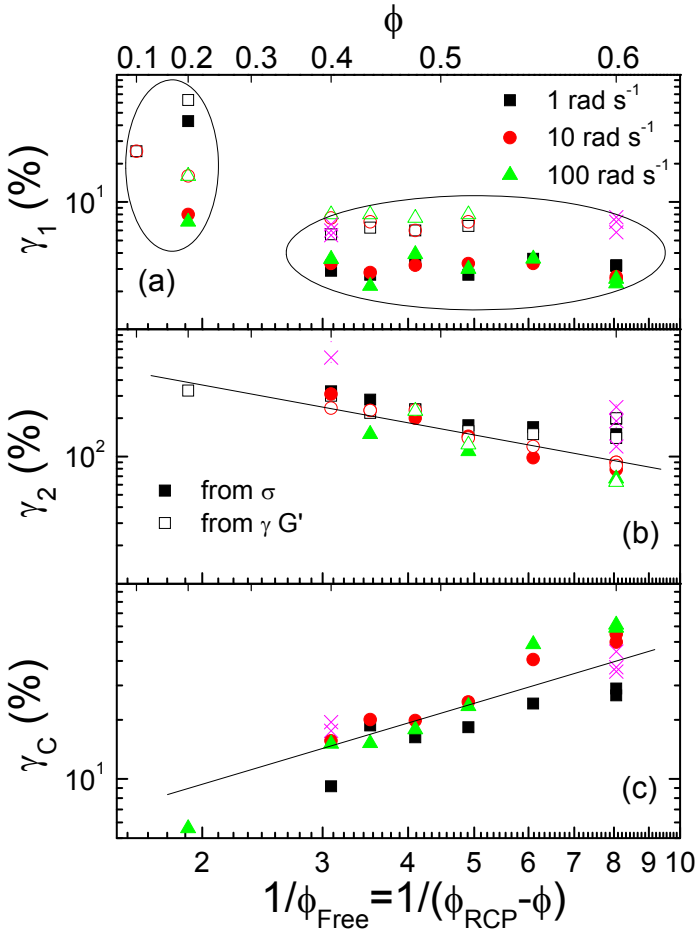

Figure 8.7: a) First yield strain versus distance from random close packing $1/(\varphi_{RCP}-\varphi)$ (bottom axis) or φ (top axis), at different frequencies, taken from dynamic strain sweeps (figures 8.6a and 8.6b). The ellipses indicate the low and high volume fraction regimes discussed in the text. b) The 2nd yield point plotted as in a). c) The crossover point (G'=G'') plotted as in a) and b) taken from figure 8.5a. The lines in b) and c) have power law exponents of -1 and 1 respectively. Magenta slanted crosses are yielding points for the ξ=0.27 sample (from γG'').

Second yield strain, γ_2

The second yield strain γ_2, shown in fig. 8.7b, decreases almost linearly with decreasing distance from maximum packing or $1/\varphi_{free}$. The volume fraction dependence of γ_2 is more difficult to explain than that of γ_1. At high volume fractions, the idea of bond and cage

breaking for γ_1 and γ_2 are acceptable as they relate to two distinct length scales and thus they introduce two distinct yielding processes. However as we lower the volume fraction the cages should vanish and thus one might also expect the second yield points to disappear. Hence a question on the exact origin of the secondary yield point arises. As the volume fraction is decreased, the glassy cages, which are distributed relatively homogeneously, turn into clusters of particles due to attractions and thus voids and inhomogenieties are created. This means that as φ is reduced the particles generally remain localized due to attractions. This increases the freedom of movement and flexibility of the interconnected clusters during shear and increases the yield strain of the system.

Figure 8.7b shows that the second yield strain, γ_2, related with the clusters/cages is inversely proportional to the distance from maximum packing, much like the behaviour of the yield strain in hard sphere glasses at high volume fractions(Petekidis, Moussaid et al., 2002; Koumakis, Schofield et al., 2008). We should point out however that in hard spheres the yield strain exhibits an non-monotonic behavior with φ, initially increasing upon entering the glassy regime and then decreasing above $\varphi \approx 0.61$ as random close packing is approached(Koumakis, Schofield et al., 2008). For the present system with constant attractions we only see a continuous decrease of γ_2 with φ since the system is always in a frustrated gel or an attractive glass. From figure 8.5a we can also see that not only does the yield strain increase with decreasing φ, but also the nonlinear regime around the yield point becomes broader reflecting a progressive process of breaking the clusters and loose networks of particles. Additionally, the yielding process of the less dense clusters and networks involves less energy dissipation, thus resulting in weaker peaks of the loss modulus.

The behavior prior to the second yield point can also be interpreted by involving cluster rotations due to the increase of free volume as φ decreases, much like observations in 2D gels under shear(West, Melrose et al., 1994; Hoekstra, Vermant et al., 2003; Masschaele, Fransaer et al., 2009). The complex two step yielding even at low $\varphi=0.20$ suggests significant contribution to the stress from chain like particle networks (Dibble, Kogan et al., 2006) even though the system is essentially a viscoelastic fluid. The second yield step disappears at $\varphi=0.10$, since probably at such concentrations there is no interconnected structure, although we still observe a thinning behaviour that can be attributed to the breaking of colliding clusters into smaller pieces.

Crossover yield strain, γ_C

The crossover strain (γ_C at G'=G'') (fig. 8.7c) is the strain above which the sample shows a viscoelastic liquid-like behaviour, although not necessarily that of a simple Newtonian liquid. The crossover transition shifts to higher strains as the volume fraction is increased along the line of equal attraction, while the system becomes a stronger solid with higher G' (fig. 8.3b). Lower volume fractions gels are shear melted closer to the first yield point, since clusters are less dense, thus once some inter-cluster bonds that keep the interconnected network solid break the sample may flow. As volume fraction increases though, the system has to break an increasing amount of clusters/cages to flow and so the crossover strain moves closer to the second yield point.

Since only the high φ attractive glass has G'<G'' for $\gamma>\gamma_2$ in contrast to the gels where this happens already at $\gamma_1<\gamma<\gamma_2$, one can argue that only the attractive glass yields truly in two steps, as above the onset of flow both mechanisms (bond and cage breaking) to required to act.

At high φ's, close and inside the attractive glass regime (φ≥0.58), the length scales for bond breaking and cage breaking come closer due to the shorter distance between particles determining the cages. Thus the two mechanisms might get coupled: Although bond breaking takes place first in some cases it may be accompanied by cage escape. At the same time during cage breaking, which is primarily related with the second yield point at larger strains few bonds may have to break. At lower φ's however breakage of specific inter-cluster bonds may lead to rupture of the solid network and creation of free floating clusters. The weakest bonds connecting the clusters are broken first at γ_1, while at γ_2 a further break up of the clusters into smaller pieces or independent particles takes place. Hence, although at high φ's (attractive glass regime) the shear melting of the sample generally requires both bond and cage escape, at lower volume fractions (attractive gels) the sample may flow (with G''>G') after in the interconnected network is broken to smaller pieces but not necessarily single particles. This is evidenced by the fact that $\gamma_c<\gamma_2$ below about φ=0.58 whereas in the attractive glass regime $\gamma_c\approx\gamma_2$.

In figure 8.8 we show G' and G'', similarly to fig. 8.5a, plotted however against the overall measured stress, which enables us to view the stress distribution during yield more clearly. Starting from the highest volume fractions we observe that the first yield point involves a wider distribution of stresses, which become narrower as φ decreases and appear as a very sharp transition at volume fractions around φ~0.4. For the lowest φ (≤0.20) the stress distribution broadens again. The relatively broad distribution of stresses

at the first yield transition in attractive glasses indicates a broad distribution of cage orientations and sizes. As φ is decreased though, the yield stress becomes specific and dependent on particle bonding stress. At the lowest φ (≤0.20) it broadens again as the open structures allow for cluster elongation and apparently variation of stress due to structural inhomogenieties.

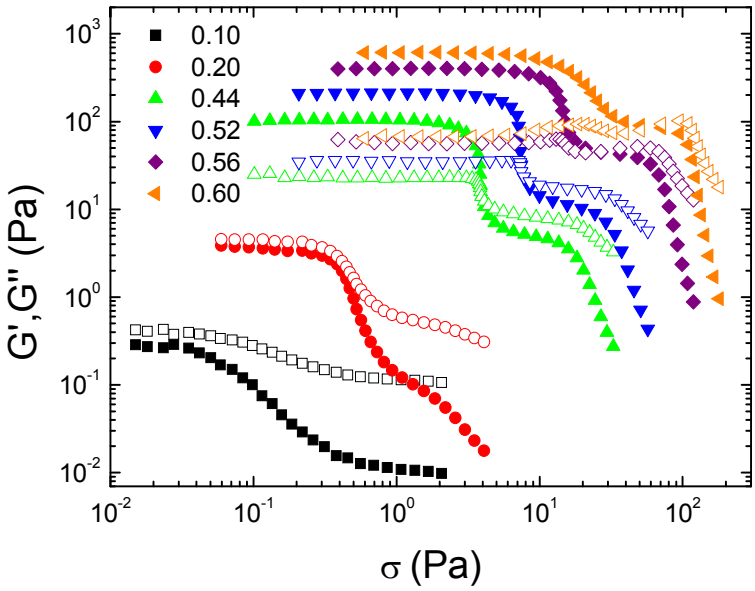

Figure 8.8: Dynamic strain sweep of six different volume fractions (as shown in legend) of equal attraction strength at ω=10 rad s^{-1} plotted by measured stress. Note the distribution of stresses needed for the different yield points at different φ.

The stresses involved in the second yield point however follow the opposite trend, revealing a quite sharp transition at high volume fractions which becomes smoother as φ is decreased. It starts off being sharp in the attractive glass, as the cage size distribution and relevant length-scales are better defined at high φ's. As φ is decreased, the cluster size distribution increases as voids replace high density areas, causing subsequent broadening of the second yield stress.

Yield Stresses

The yield stresses corresponding to the various yield points may be extracted from fig. 8.6a. Figure 8.9 shows all three yield stresses, σ_1, σ_2 and σ_c, determined at the corresponding yield strains γ_1, γ_2 and γ_c, both as a function of φ and the free volume. All yield stresses clearly increase with volume fraction following a power law dependence with exponents of 2.0, 2.3 and 3.4 respectively. This response is expected to be a combination of the G' increase with φ and the φ dependence of the yield strains (fig. 8.7). According to fig. 8.7, only γ_c increases with φ while γ_1 and γ_2 either remain constant or

decrease with φ. Hence the increase of the characteristic yield stresses is directly correlated with a stronger increase of the elastic modulus with φ along the line of equal attraction.

The strong increase of σ_1 with volume fraction from the gel to the attractive glass regime can not be quantitatively attributed to the increase of the number of existing bonds in the system. Thus the strong weakening of the gel relative to the attractive glass has to reflect the structural differences; the elasticity in the gel is determined by the elasticity of the network with characteristic length-scale that of the cluster, which is much larger than a particle leading to a weaker solid(Laurati, Petekidis et al., 2009; Zaccone, Wu et al., 2009).

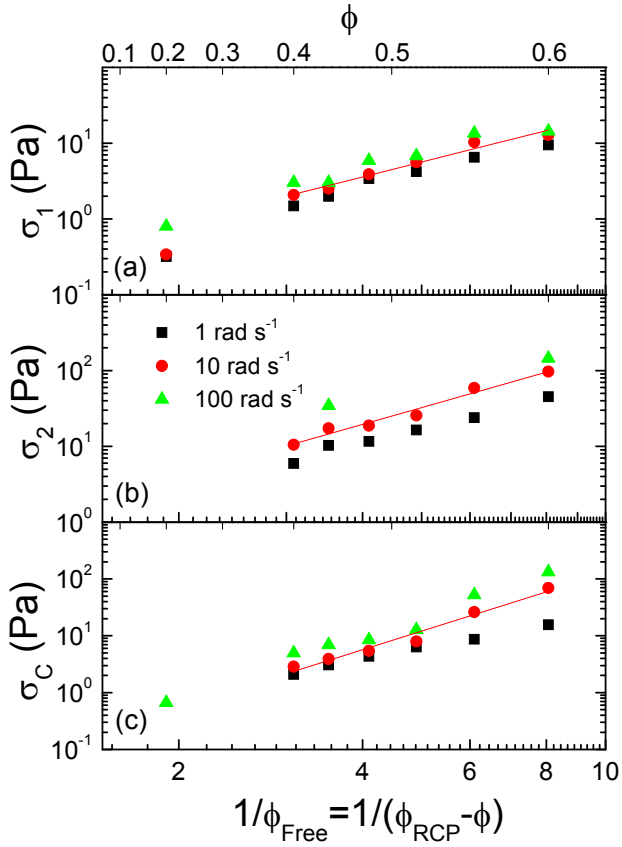

Figure 8.9: Stress corresponding to the yield strains of fig. 8.7 for a) the 1st yield point, b) the 2nd yield point and c) the crossover point (G'=G'') plotted against volume fraction (top axis) and the distance from random close packing $1/(\varphi_{RCP}-\varphi)$ (bottom axis). The lines are indicative power law fits in the high φ region (0.40 to 0.60) for ω=10 rad s^{-1}.

At low φ gels there are two length-scales present: the void size (or distance between network strands) and the thickness of the strands. The elasticity of the network in this

case is determined by the weakest contribution which is that of the mesoscopic network of clusters rather than the local, microscopic contribution of the bonds (Zaccone, Wu et al., 2009).

8.3 Steady Shear Rheology

Steady Shear response

Steady shear tests were also performed in order to probe the non-linear behavior of the samples. A steady rate was applied and the stress response was measured against strain (or equivalently time). These tests bear a strong resemblance to the step strain experiments carried out by (Pham, Petekidis et al., 2008), where an instantaneous strain was applied and the resulting stress peak was plotted with changing strain. Step rate experiments are simpler than oscillatory strain sweeps, as the rate remains constant throughout the test; although low strain information is lost when the inverse rate is lower than the rheometer acquisition time. Finally, since dynamic strain sweeps are time consuming, step rate tests are more suitable in examining the time dependence of non-linear properties.

In figure 8.10a we compare step rate tests for a high φ repulsive and attractive glass as well as a lower φ gel. In the hard sphere repulsive glass a single stress overshoot is observed. Peaks such as these have both been seen experimentally in a variety of soft matter systems such as polymers (Osaki, Inoue et al., 2000; Islam and Archer, 2001; Ravindranath and Wang, 2008), worm-like micelles (Padding, Boek et al., 2008), nanocomposites (Letwimolnun, Vergnes et al., 2007; Akcora, Liu et al., 2009), colloidal gels(Mohraz and Solomon, 2005) and colloidal glasses (Derec, Ducouret et al., 2003; Carrier and Petekidis, 2009) as well as predicted theoretically (Sollich, 1998) and probed by simulations (Rottler and Robbins, 2003; Padding, Boek et al., 2008; Zausch and et al., 2008). Although detailed explanation are system specific, the basic idea is of an elastic energy storage mechanism which causes increase of stress before the peak and a dissipative energy release mechanism after the peak leading to shear induced flow.

Whereas the hard sphere glass at φ=0.60 shows a single peak, both the attractive gel with φ=0.44 and the attractive glass at φ=0.60 reveal two distinct peaks as indicated by the vertical arrows. The single stress overshoot in the case of the hard sphere glass reflects the single yielding mechanism corresponding to cage breaking. In contrast, for the attractive gels and glasses two stress peaks are observed in agreement with the two step yielding processes found in oscillatory measurements.

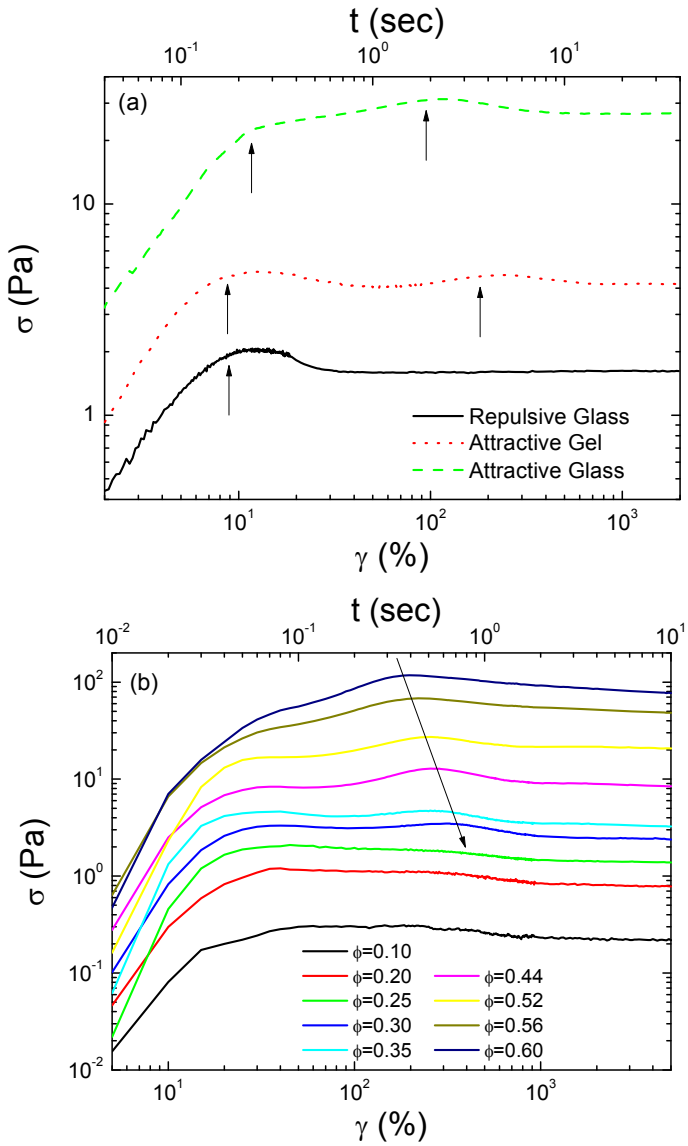

Figure 8.10: (a) Step rate test in a repulsive glass of φ=0.60, an attractive glass at φ=0.60 and a gel at φ=0.44 for a rate of 0.5 s^{-1}. Arrows indicate single and double yielding for repulsive and attractive glass/gel respectively. (b) Step rate tests showing stress response versus strain at a rate of 5 s^{-1} for various φ decreasing from top to bottom and indicated in the legend. The arrow shows the changing position of the second yield point with φ.

Step rate experiments at various φ's, measured along the line of equal attraction from the attractive glass down to the gel regime, are plotted in figure 8.10b at a rate of 5 s^{-1}. This rate was chosen in order to show the two peaks as clearly as possible for all volume fractions. As seen previously in dynamic measurements, the second peak becomes less pronounced at lower colloid volume fractions and moves to slightly higher strains, until dissipating at the lowest volume fraction measured (φ=0.1).

In figure 8.11, we plot step rate tests with increasing shear rates for an intermediate

volume fraction gel, φ=0.44 and an attractive glass, φ=0.60. In the gel the strain of the second peak is shear rate independent, although the stress value at the second stress overshoot rises much stronger than the first one with shear rate. For the highest φ attractive glass however, (fig. 8.11b) a change in the position of the second peak is observed, shifting to higher strains with increasing rate.

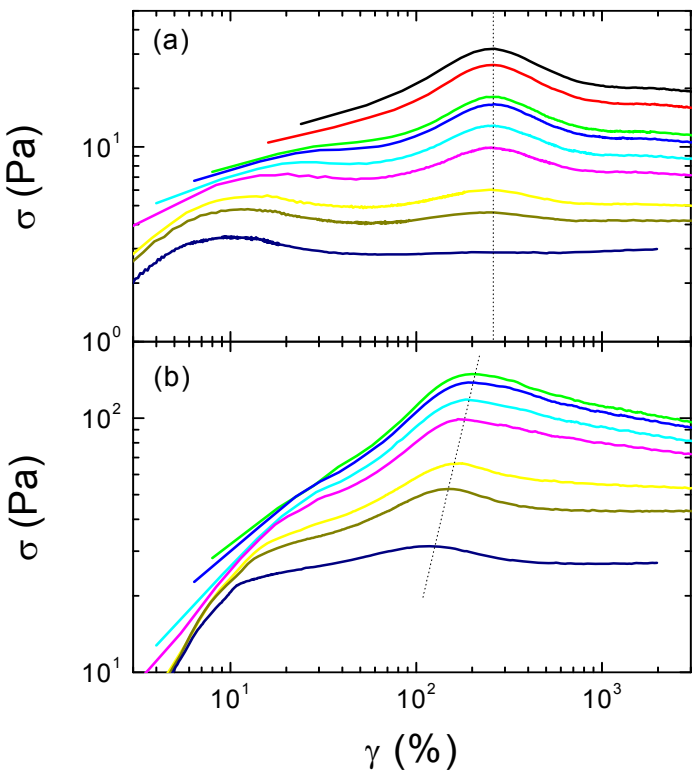

Figure 8.11: Step rate tests with increasing rates (0.1, 0.5. 1, 3, 5, 8, 10, 20, 30 s^{-1}) from bottom to top for (a) φ=0.44 and the same rates (0.1 – 10 s^{-1}) for (b) φ=0.60. The dotted lines denote the rate dependence of the second stress overshoot.

The dependence of the second yield point on φ and shear rate is shown in fig. 8.12. The stress at the second peak increases with rate following an apparent power law with an exponent of 0.5, which is almost φ independent. At the same time the second yield strain remains essentially constant for all φ's except for the highest that corresponds to an attractive glass (figs 8.11a, 8.11b and 8.12b) where it increases with shear rate. Moreover, as φ increases the second yield stress increases, while the second yield strain generally decreases in agreement with the findings of the oscillatory shear measurements.

The values of the stress at steady state, reached after the second stress overshoot is exceeded, is plotted in figure 8.13 together with typical flow curves measured by

progressively decreasing shear rate starting from high rates. The flow curve data are in good agreement with steady state stress values from step rate tests and can be fitted by Herschel–Bulkley, $\sigma = \sigma_y + \eta\dot{\gamma}^a$, with exponent α that varies with volume fraction from 0.71 at the lowest (φ=0.2) to 0.32 at the highest (φ=0.6). However these exponents are just indicative since the range of rates measured is rather limited, hindering the determination of terminal flow at high rates especially for the highest volume fractions.

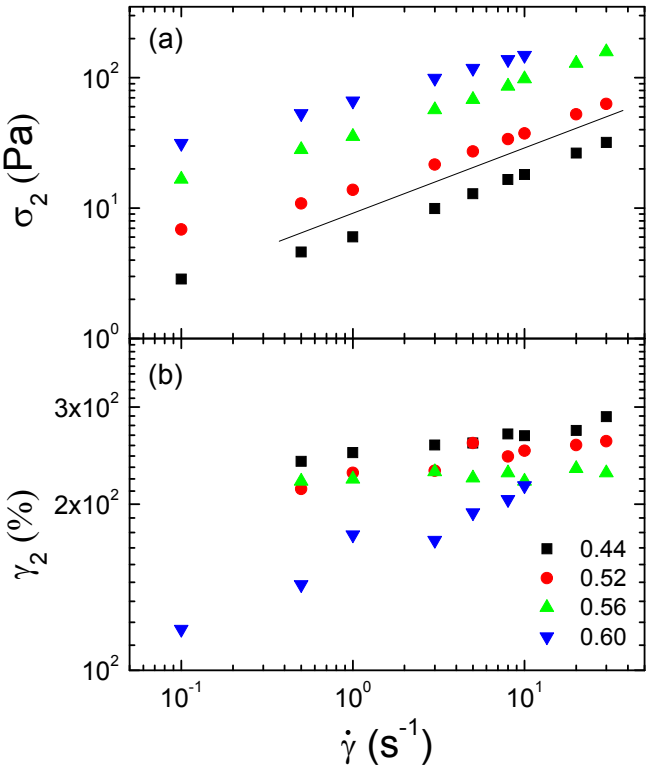

Figure 8.12: (a) Yield stress and (b) strain corresponding to the second peak in step rate tests of fig. 8.10 and of additional φ at a waiting time of 120 sec. The solid line indicates a power law increase with exponent of 0.5 in (a).

As will be discussed later, at the lowest rates the time scale for the creation of bonds is much shorter than the inverse shear rate. Hence after the first yield point, there is time for rotation and restructuring of clusters with minimum internal bond breaking, similar to 2D gels(West, Melrose et al., 1994; Hoekstra, Vermant et al., 2003; Masschaele, Fransaer et al., 2009). Thus at the lowest rates, the first yield mechanism dominates over the second one which at the limit of zero shear rate is absent (fig. 8.11a). At this limit inter-cluster bonds may break temporarily under shear so that broken clusters can flow past each other. However during this process bonds may reform, re-brake and so on. In addition we should note that at such low rates flow may not be homogenous; instead strong shear banding may occur when wall slip is eliminated(Ballesta, Besseling et al., 2008; Ballesta, Besseling et al., 2010).

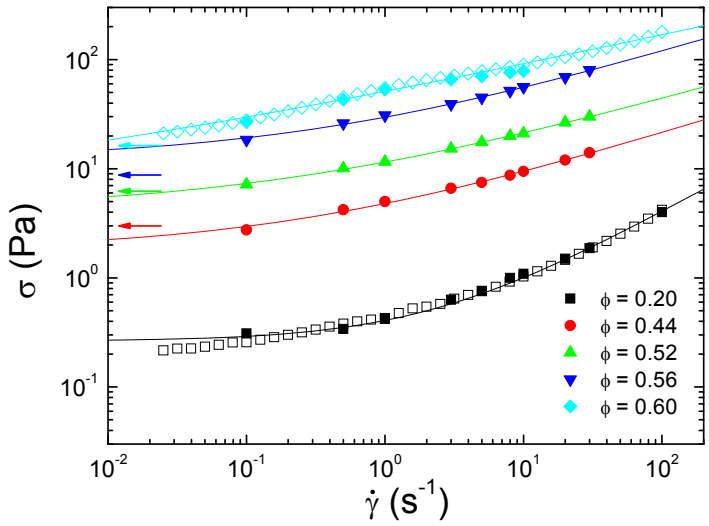

Figure 8.13: Flow curves with points taken from the steady state values of fig. 8.12 (solid) or with averaging time 20 seconds per point (open). Lines are Hershey-Buckley fits with exponents of 0.71, 0.41, 0.37, 0.39 and 0.28 from bottom to top. Arrows are values of γ_C determined at low frequency oscillatory measurements (ω=1 rad s^{-1}) in fig. 8.7.

As rate is increased, the imposed shear becomes important and is able to break an increasing amount of clusters/cages resulting in an enhancement of the second peak over the first. This happens for both the attractive glass and the lower volume fraction gels (figs 8.11 and 8.12a). However in case of the attractive glass we observe a change in the position of the second peak (γ_2) which shifts to slightly higher strains with increasing rate (figs 8.11 and 8.12b). Such an effect is most probably due to the time evolution of the second yield point as smaller rates take longer to reach the same strains than larger ones. This effect will be discussed further in the section on aging.

The first yield strain in attractive glasses and gels has been rationalized using the Kramer's type escape arguments(Smith, Petekidis et al., 2007; Laurati, Egelhaaf et al., 2010), where the probability of a particle to escape from an attractive well increases with shear induced displacements, while energy balance arguments have been used in charged stabilized suspensions to calculate the yield stress(Friend and Hunter, 1971). Here we formulate a simple argument to describe the shear rate dependence of cluster breaking into individual particles by introducing a dimensionless number, Pe_{dep}. We can argue that a cluster would break for rates above which the drag force acting on a particle becomes larger than the depletion attraction. Hence in a two particle cluster when one of them is displaced by shear flow it may drag along the other one if the viscous drag F_{visc} is smaller than the bonding force, F_{dep}. Otherwise if

$$F_{visc} = 6\pi\eta R\upsilon > F_{dep} \quad (8.1)$$

the bond will break and the particles will flow independently. The relative velocity in a shear flow for two particles in contact is of the order of $\dot{\gamma}R$. Such simple argument may be used to define a dimensionless number signifying the rates above which cluster are expected to fully break. By inserting a simple ramp potential:

$$F_{visc} / F_{dep} = \frac{6\pi\eta R\dot{\gamma}R}{\left(U_{dep(r=2R)} / 2\xi R\right)} = \frac{12\pi\eta\xi R^3}{U_{dep(r=2R)}}\dot{\gamma} \equiv Pe_{dep} \quad (8.2)$$

Here both diffusion and hydrodynamic lubrication effects are ignored and therefore the calculation is only suited for strong attractions. Then the ratio

$$Pe / Pe_{dep} = \frac{U_{dep(r=2R)}}{k_{\mathrm{B}}\mathrm{T}}(2\xi)^{-1} \quad (8.3)$$

indicates that the shear rate needed to fully break all clusters in a gel is related to the conventional Peclet number, Pe, by simply factoring in the attraction strength and range. Hence a Pe_{dep}=1 signifying a complete breakage of a cluster corresponds to Pe≈130. Such shear rates are however beyond the values reached in the present work, where a Pe=1 corresponds to $\dot{\gamma}$=30 s^{-1} suggesting that clusters may not be fully broken here.

In principal this argument may be used to calculate the equilibrium cluster size at lower shear rates. However, at this stage it is quite speculative and would require a systematic series of scattering or imaging experiments under steady shear to be verified. Nonetheless, it is worth mentioning that a limited set of confocal experiments under shear (Ballesta, Besseling et al., 2010) with similar hard spheres of larger size as well as Brownian Dynamics simulations (chapter 9) support such simple scaling.

In summary, oscillatory and steady shear rheology of attractive glasses and lower volume fraction gels have shown that the simple bond and cage breaking is proven to be more complicated than expected. When few inter-cluster bonds are broken due to shear induced particle collisions, the clusters constituting the interconnected network are released and allowed to flow (first yield point). As strain is increased further, collisions between flowing clusters dominate the nonlinear mechanical response (second yield point) which crucially depends on the shear rate.

As we increase volume fraction reaching inside the attractive glass regime, we should

seamlessly pass over to the two-step yielding previously described (Pham, Petekidis et al., 2006; Pham, Petekidis et al., 2008), comprising of initially breaking weaker bonds within cages (first yield point) and then breaking the strongly bonded cages (second yield point). Another characteristic result of the nonlinear response in these systems is the rate dependent shear induced structure. A schematic overview of the structural changes involved at different strains and shear rates (or frequencies) is attempted in figure 8.14 for a lower volume fraction gel (for clarity). The vertical axis can be thought of as either frequency of oscillation or the rate in steady shear and the horizontal axis as the maximum strain or elapsed strain. Different rows depict different shear rates, increasing from top to bottom with $Pe_{dep}<<1$, $Pe_{dep}\approx 1$ and $Pe_{dep}>>1$, respectively. Note that only cases (a) and (b) are realized experimentally here. Similarly the three schemes along the horizontal axis refer to regimes with $\gamma<\gamma_1$, then $\gamma_1<\gamma<\gamma_2$ and finally $\gamma>\gamma_2$.

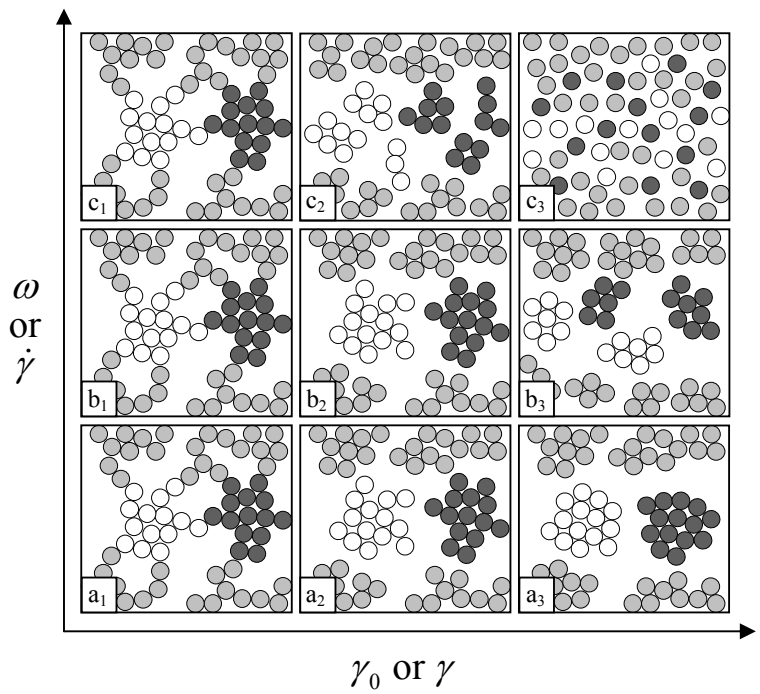

Figure 8.14: Structure representation of a lower φ gel at rest and under shear. Increasing from left to right is the applied strain in both steady (γ) and oscillatory (γ_0) experiments. Increasing from bottom to top is the shear rate ($\dot{\gamma}$) or frequency of oscillation. The scheme describes how different regimes of strain rate and applied strain lead to different structural properties under shear.

Under weak, linear deformations (a_1, b_1, c_1), both at dynamic or steady shear (prior to yield), the structure is expected to a first approximation to look similar to that at rest. Heterogeneities are present with two clusters highlighted. When the applied strain is increased under relatively low shear rates (a_2, b_2) beyond the first yield point,

interconnectivity between clusters is lost due to inter-cluster bond braking. At strains much higher than the first yield point and for shear rates slower than bond re-formation, cluster reformation is faster than shear induced breaking (a_3). Furthermore through rotation, clusters may compact enabling better flow past each other and lowering stresses. Thus the second stress peak originating from cluster-cluster interactions appears weaker compared to the first or not seen at all. This corresponds to the lowest rates shown in figure 8.10. Note that at low rates colloidal glasses and gels may exhibit shear banding (Besseling, Isa et al., 2010) and thus the picture above might become more complicated. However independent studies (Ballesta, Besseling et al., 2010) suggest that such effect might be weakly present only for the highest volume fraction (0.60) at the lowest rate measured here ($\dot{\gamma}$=0.1s^{-1}).

At high strains and intermediate rates, comparable to bond formation times (b_3), the breaking of clusters occurs through cluster collisions resembling a transient jamming of clusters that gives rise to the second stress peak. Clusters do not totally break down, but smaller more stable clusters are formed. As the rate increases, cluster collisions are more violent, the second peak stress, σ_2, increases and smaller clusters are created. This behavior corresponds to the higher rates in fig. 8.11 and the oscillatory measurements of figs 8.5, 8.6 and 8.8.

Finally, at very high shear rates where shear induced bond breaking is much faster than bond formation (c_2), intra-cluster bonding is not sufficient to keep the particles clustered as before. Large clusters break into smaller more stable clusters (or even individual particles at the highest rates) giving rise to a large initial peak. At high rates and large strains (c_3) any remaining clusters collide with each other and break down into individual particles, which would be related to the weak stress overshoot of the second yield point. Particles originating from different clusters intermix and the system is fully homogenized. In this case, it is expected that with increasing rate the second stress overshoot will decrease compared to the first one, as the previously strong clusters are broken at the start up of shear. These rates have not been achieved in the present experiments and this part of the discussion is speculative, but recent confocal microscopy measurements (Ballesta, Besseling et al., 2010) with larger spheres, as well as simulations (chapter 9) are in agreement with this picture.

8.4 Changing the Size Ratio and Aging Effects

Changing size ratio, ξ

In order to better understand the mechanisms behind yielding and its relation to bonding range, we changed the size ratio of the colloid-polymer mixture to ξ_2=0.27 as opposed to the previous ξ_1=0.083 (ξ_2/ξ_1=3.25 corresponding to ξ^*_2/ξ^*_1=1.6 in the free volume), retaining a similar attraction (U~-23k_BT) according to simple AO. We expect that such increase of the range of attraction will also reflect to the strain of the first and probably the second yield point. We studied two volume fractions, an attractive glass with φ=0.60 and a gel with φ=0.44. Figure 8.15 shows the linear viscoelastic response of four samples, with φ=0.60 and 0.44 for ξ=0.083 and 0.27.

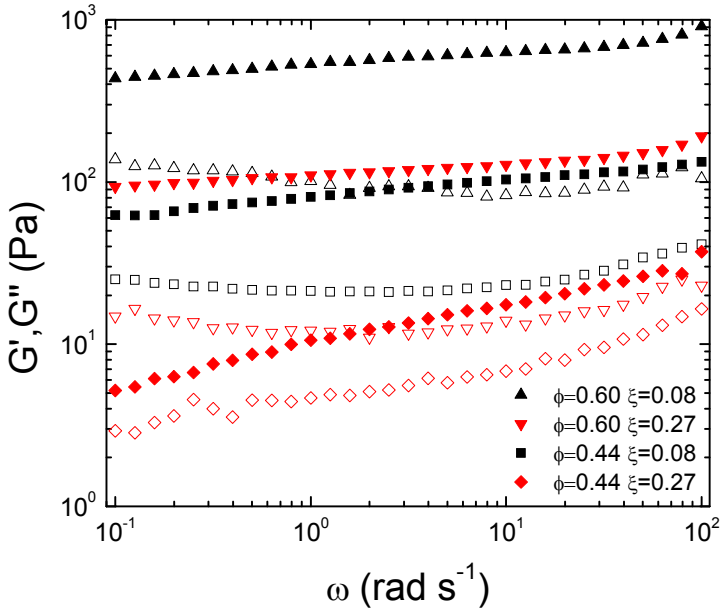

Figure 8.15: Dynamic frequency sweep showing G' (solid) and G'' (open) for samples with ξ_1=0.083 (black) and ξ_2=0.27 (red) at φ=0.60 (triangles) and φ=0.44 (squares) for the same attraction potential at contact (U= -19.1k_BT).

An initial observation in fig. 8.15 is the drop of both G' and G'' with increasing ξ at the same φ which is intuitively surprising as the attraction strength at contact was kept the same. According to the generalized Stokes-Einstein relation(Mason, Ganesan et al., 1997; Mason, 2000; Hoekstra, Vermant et al., 2003) the complex viscoelastic modulus, $G^*(\omega)$, is inversely proportional to the average particle mean squared displacement,$\langle\Delta r^2_{(t=2\pi/\omega)}\rangle$. Hence when the attraction range is increased but the attraction strength at contact, $U_{dep}(r=2R)$, remains the same, the particles are less localized and the depletion force, $F_{dep}=dU_{dep}/dr$, between them is weaker. Similarly, MCT-PRISM calculations for colloidal

gels up to about φ=0.4 yield a scaling of G' with the localization length of $G' \propto r_{loc}^{-2}$ (with r_{loc}~ξR) in agreement with experimental data(Shah, Chen et al., 2003), although the latter were performed at constant distance from gelation, rather than at constant attraction strength.

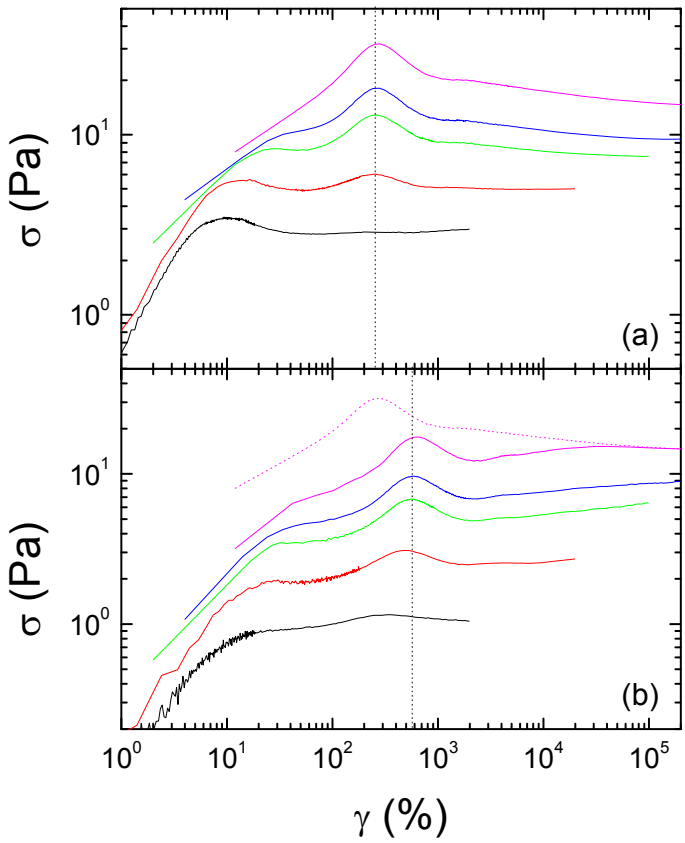

Figure 8.16: Step rate tests with increasing rates from bottom to top (0.1, 1, 5, 10, 30 s^{-1}) for φ=0.44 with (a) ξ_1=0.083 and (b) ξ_2=0.27. Vertical dotted lines show the approximate position of the second peaks for the two ξ's. Note the dotted curve in (b), which is the highest rate of (a), showing how the stresses of the different ξ come together at high rates and high strains, indicating the absence of bonding effects.

Thus the drop of elasticity for the longer range samples is direct consequence of the weaker localization that leads to weakening of the gel. Here the ratio of the elastic moduli of the two size ratio's measured at 1 rad s^{-1} (fig. 8.15) is about 4.9 for φ=0.60 and 7.7 for φ=0.44 suggesting a ratio of localization lengths (depletion ranges) of 2.65 and 2.77 respectively. This is in reasonable agreement the value at dilute concentrations, $\xi_2/\xi_1 \approx 3$, but larger than the one in the free volume $\xi^*_2/\xi^*_1 \approx 2$. Moreover, the attraction strength calculated by GVFT for the large size ratio at high concentrations is clearly lower (~2.7-4k_BT) than that for the small size ratio -15 k_BT). Hence the drop of the viscoelastic moduli may be related also with weaker attraction strength.

Another interesting finding seen in fig. 8.15 is that both G' and G'' exhibit a clear frequency dependence for the φ=0.44 and large depletion range (ξ_2=0.27) sample. This indicates that there is some restructuring of particles within the clusters probably due to their weaker localization.

Figure 8.16 shows the non linear response in step rate tests for the lower φ (=0.44) gel for both attraction ranges and different shear rates. Comparing fig. 8.16a with fig. 8.16b one can readily observe a shift of both stress peaks to higher strains with the increase of ξ. Such shift of γ_1 and γ_2 to higher strains is expected within the rationalization relating them with bond and cage/cluster breaking discussed above. More importantly however, the shift is similar to the range of attraction ratio, $\xi_2^{*}/\xi_1^{*}\approx 2$. A similar increase of the characteristic yield strains γ_1 and γ_2 is seen in oscillatory tests (figure 8.7) for both φ's. Surprisingly, the dynamic crossover strain (fig. 8.7c) seems to depend on φ, but not on ξ. This possibly happens as the increase of yield strain with ξ is cancelled out by the decrease of the elasticity (weakening of the gel) when the range of attraction is increased.

Shear induced structural rearrangements can be inferred by the non-linear stresses measured as discussed above for the smaller ξ. As the system is strained, some bonds may break initially, freeing particles within the cage or cutting loose clusters from the interconnected network and enhancing energy dissipation. Previous work on yielding of hard sphere glasses(Petekidis, Moussaid et al., 2002; Petekidis, Vlassopoulos et al., 2003; Petekidis, Vlassopoulos et al., 2004; Grand and Petekidis, 2008; Koumakis, Schofield et al., 2008), has shown that at high φ particle collisions take place easier as particles are closer together. Thus upon approaching random close packing the material becomes more brittle exhibiting a decreasing yield strain. In the same manner, when the depletion range increases, interparticle forces decrease and bonded particles are able to move elastically to larger distances under shear; thus the yield strain increases. However, the first yield strain related with bond breaking is bound by the cage size, or any other large length-scale imposed by the structure. For attractive glasses this would correspond to the hard sphere glass strain of approximately 10% to 15% (Lindemann, 1910; Petekidis, Vlassopoulos et al., 2003; Petekidis, Vlassopoulos et al., 2004; Koumakis, Schofield et al., 2008). Even though φ=0.44 is much lower than the glass transition volume fraction, the sample behaves in a similar fashion, as particles are mostly clustered together in regions with a higher local φ. In the case of the second yield point, when the attraction range is increased, the flowing clusters (for gels) or the cages (for attractive glasses) may be elongated more before breaking since intra-cluster/cage bonds have a longer range.

Thus the second yield point takes place at higher strains although it corresponds to length scales larger than the bond itself.

Figure 8.16b also reveals that at high rates (corresponding to Pe≈1) and at high strains, the curves for the two ξ converge to the same final stress value, in contrast to observations at lower rates. Thus it could be argued that a complete structural break down has occurred that has removed the bonding effects. However, since the value of Pe_{dep} is still much lower than unity (1/130 for ξ_1 and 1/38 for ξ_2), it is more likely that the shear rate has whittled down the clusters/cages for the two ξ's to a similar size, so as to give similar stress response.

A final noteworthy feature detected in fig. 8.15b is the clear but puzzling emergence of a third peak or shoulder for ξ_2. There is a similar but much weaker shoulder seen at higher rates for the smaller ξ_1 (fig. 8.16a). Such a peak may indicate an additional, tertiary, breaking of unbroken clusters/cages. The increase in ξ exacerbates the height of the third peak, possibly due to the occurrence of denser clusters(Lodge and Heyes, 1999; Videcoq, Han et al., 2007) and the subsequent difficulty in fully breaking them up.

Aging effects

It has been experimentally observed that time scales and viscoelastic properties of colloidal glasses and gels evolve with waiting time(d'Arjuzon, Frith et al., 2003; Manley, Davidovitch et al., 2005; Jabbari-Farouji, Atakhorrami et al., 2008; Yin and Solomon, 2008; Negi and Osuji, 2009; Negi and Osuji, 2010). In this section we discuss the linear and the non linear response of the aged gel and attractive glass. Probing an aged sample with non linear rheology, we aim to link the previously discussed findings on shear induced changes with evolving structures due to ageing.

In figures 8.17a and 8.18a we show the evolution of G' and G'' at ω=10 rad s^{-1} for both the gel with φ=0.44 and the attractive glass at φ=0.60 with ξ=0.083. The elastic modulus of the lower volume fraction gel revealed a clear strengthening with time (fig. 8.17a) while in the attractive glass a less substantial increase of G' is found (fig. 8.18a). In both cases G'' either decreases weakly or is almost constant. Figure 8.17b and 8.18b show the non-linear response in a step rate experiment for the same samples, at a rate of 0.5 s^{-1} for various waiting times after rejuvenation. Although the stresses of both peaks increase with waiting time, the second one shows a more pronounced rise than the first, as indicated (with star symbols) in figs 8.17a and 8.18a. Moreover, the inset of fig. 8.17b presents the stress response of the gel for various waiting times, normalized with the first

peak, in order to show the behavior of the second peak more clearly.

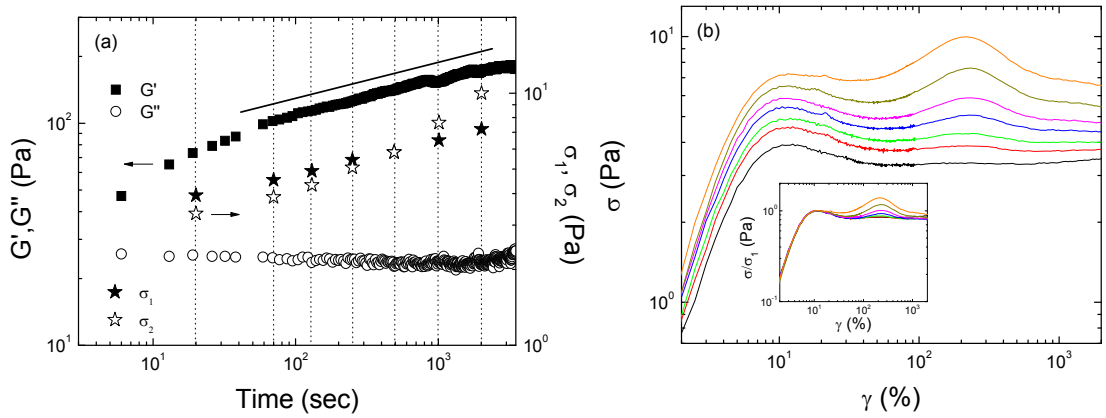

Figure 8.17: (a) Linear viscoelastic measurements at ω=10 rad s^{-1} for the φ=0.44 gel. Vertical doted lines correspond to the delay times in (b), and stars correspond to the first and second peak stresses shown in (b). Horizontal arrows point to the corresponding data axis. The solid line is a power law of 0.13. (b) Step rate tests showing stress response versus strain at a rate of 0.5 s^{-1} for the φ=0.44 gel for different delay times (20, 70, 130, 250, 500, 1000, 2000 s from bottom to top). Inset shows the data in (b) normalized by the stress of the first peak to reveal the increase of the second stress overshoot over the first.

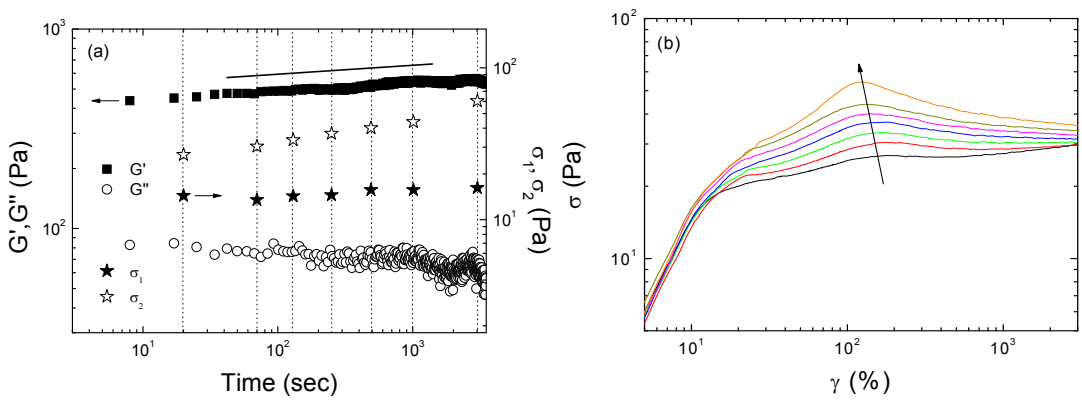

Figure 8.18: (a) Linear viscoelastic measurements at ω=10 rad s^{-1} for the φ=0.60 attractive glass. Vertical doted lines correspond to the delay times in (b), and stars correspond to the first and second peak stresses of (b). Horizontal arrows point to the corresponding data axis. The solid line is a power law of 0.03. (b) Step rate tests showing stress response versus strain at a rate of 0.5 s^{-1} for the φ=0.60 attractive glass for different delay times (20, 70, 130, 250, 500, 1000, 3000 s from bottom to top). The arrow follows the movement of the second peak with increasing delay time.

Since the first peak corresponds to the breaking of bonds its height represents the stress that can be stored in the network before it is released via inter-cluster bond breaking. The subsequent decay of the stress is therefore related to the number of bonds that break. The height of the first peak (σ_1) follows the increasing trend of the elastic modulus with

waiting time for both the gel and the attractive glass as seen in figs 8.17a and 8.18a. The value of σ_1 corresponds approximately to the stress the network can withstand before it starts being disrupted. Its increase with time suggests that either the stress of bond breaking or the number of bonds in the network increase. The stress of the individual bond is unlikely to change in such long times, as bond formation time is of the order of 10^{-2}s as previously calculated from Pe_{dep}. Hence the increase of the elasticity and σ_1 should be attributed to the coarsening of the gel and for the case of σ_1, the higher number of inter-cluster bonds. The strong correlation of σ_1 with the aging behavior of G' is perhaps to be expected, as the initial increase of stress at strains smaller than the first yield point in a step rate test is determined by the linear moduli of the related system at rest.

The second peak represents the breaking of clusters/cages. The fact that the second peak becomes larger than the first with time indicates that the strengthening of the gel occurs not only by increasing the number of particle bonds, but more importantly due to restructuring and creation of denser and stronger particle clusters. As discussed, since bond formation time at these attraction strengths should be very small, this rather long time scale suggests large scale, or long time structural changes. In other words, after the initial quench to the gel state the sample slowly progresses to deeper energetic minima via single particle, as well as, cooperative motions.

For the attractive glass in fig 8.18b, the second stress overshoot not only increases in height, but also the strain at which it occurs (γ_2) shifts to smaller strains with increasing waiting time in contrast to the lower volume fraction gels where it remains constant. The shift with time suggests that the cages become less flexible as the system slowly moves to deeper energetic minima and becomes more brittle. This behaviour concurs with the decrease of the second yield strain, γ_2, with rate (fig. 8.11b) since at low rates the glass reaches γ_2 after longer times during which the sample may have partly aged. Such behavior suggests that the higher φ attractive glass displays faster ageing with regard to its non linear response than the lower volume fraction gels. This might be expected since larger voids in gels require complex long range structural rearrangements that may require more time.

For ξ=0.27 (not shown), aging studies for both φ's studied, show that the first stress peaks are only slightly affected by aging and are correlated to the time evolution of linear properties in accordance with ξ=0.083. However, the second stress overshoot and the subsequent third shoulder gain in strength with waiting time. The third peak showed a

strong increase in the beginning, with the second dominating at the end. This indicates that the stronger and denser clusters giving rise to the third stress peak are created faster, but the weaker clusters corresponding to the second peak comprise the majority, although slower in their creation.

Rheological Detection of Attractions

From the findings of figure 8.17 and 8.18 it becomes clear that detection of attractions in a hard sphere system could take place by examining the non linear properties of the system at long delay times after rejuvenation. As has been discussed previously and seen in earlier work (Koumakis, 2007), even in the supposedly simple hard sphere system of this work, the refractive index mismatch between the particles and the solvent may produce small attractions. Specifically when using Octadecene there was some doubt if the particles truly were hard spheres or if some attractions were present due to van der Waals forces. We thus used a similar experimental protocol to examine the effect evolution of the non linear properties as a way of determining the existence of attraction through the detection of two step yielding.

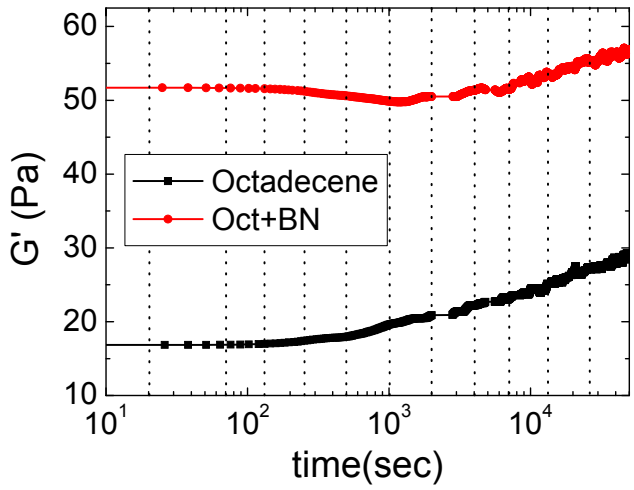

Figure 8.19: Linear dynamic measurements after rejuvenation at ω=1 rad s^{-1} of a simple repulsive glass (R=180nm) at φ=0.58 (from φ_{RCP}=0.66±0.01) showing simple aging in two different solvents, Octadecene and a mixture of Octadecene and Bromonaphthalene. Vertical doted lines correspond to the delay times in figure 8.20.

In figure 8.19 we show the linear aging properties after rejuvenation of polydisperse PMMA hard spheres (refractive index n=1.497) at φ=0.58 with R=180nm in two solvents; Octadecene (n=1.444) and a mixture of Octadecene and Bromonaphthalene (n=1.473) as discussed in chapter 2. The volume fractions for both samples have been estimated from random close packing and since they are different batches, their volume fractions may differ up to 1%. We see that after a few hundred seconds, aging sets in for both samples, showing no discernible

differences between the two. Greater interest lies in the non linear properties as a function of delay time as shown in figure 8.20, in the fashion of figures 8.17b and 8.18b. Although the sample in the mixture (8.20a) shows almost no secondary peak even at the longest delay time, the sample in Octadecene (8.20b) shows a strong appearance of a second peak with increasing delay time.

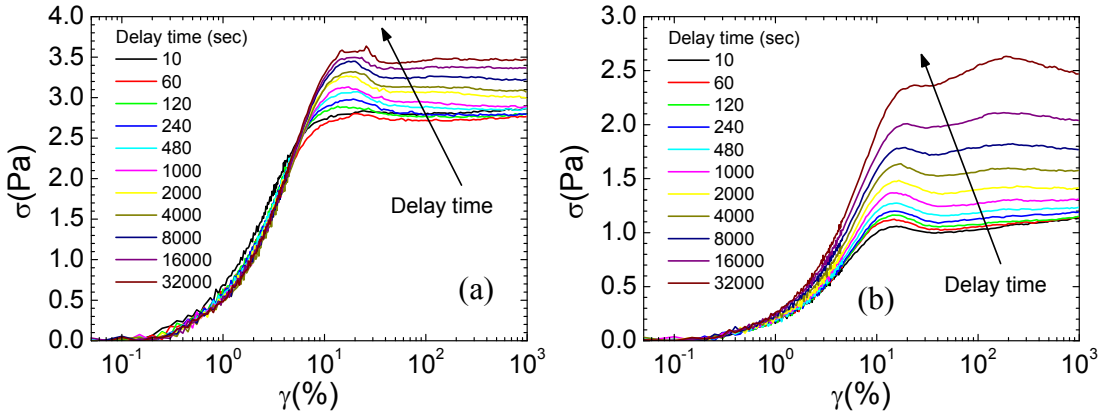

Figure 8.20: Step Rate Tests showing Stress response vs Strain at a rate of $0.05s^{-1}$ of a simple repulsive glass (R=180nm) at φ=0.575 (from φ_{RCP}=0.66) for different delay times as shown in the legend for particles in b) a mixture of Octadecene and Bromonaphthalene and b) Octadecene. The arrows follow the stress with the increase of delay time.

According to (Pusey, 1991; Hunter, 2001), a simple model shows Van der Waals attractions between two particles are given by the following formula:

$$U_A(r) = -\frac{A}{6}\left[\frac{2R^2}{r^2-4R^2}+\frac{2R^2}{r^2}+\log\left(1-\frac{4R^2}{r^2}\right)\right]$$
$$with\ \ A = \frac{3}{4}k_BT\left(\frac{\sqrt{n_1}-\sqrt{n_3}}{\sqrt{n_1}+\sqrt{n_3}}\right)^2+\frac{3h\nu_e}{16\sqrt{2}}\frac{\left(n_1^2-n_3^2\right)^2}{\left(n_1^2+n_3^2\right)^{3/2}} \qquad (8.4)$$

where r is the centre to centre separation, A is the Hamaker constant, n_1 is the refractive index of the particle and n_3 of the solvent, h is Plank's constant and ν_e is the main electronic absorption frequency in the ultraviolet with $\nu_e \approx 3x10^{15}$ s^{-1}. In this way, allowing for a 10nm steric repulsion layer, the attraction for Octadecene particles is calculated to be at maximum $U_A(2R) \approx 1K_BT$ for particles of about R=180nm, whereas for the mixture it is found to be approximately 20 times less.

Therefore we find that this type of test is extremely sensitive to even the smallest of attractions, even though the waiting time in order to see a secondary peak increases substantially, about two orders of magnitude, in comparison to the depletion attractions of

figures 8.17b and 8.18b. Especially in dense systems, the long range restructuring allows for the appearance of secondary peaks at very small attraction strengths.

8.5 Chapter Conclusions

To conclude, we have shown that the transition from a two step yielding attractive glass to a low volume fraction gel at equal attraction strength and range shows a complicated yielding process that remains two step until very low φ, where structural cohesion becomes impossible. Two types of tests were used to probe the non-linear behavior and determine the values of the first and second yield strain and stress, dynamic strain sweeps and step rate tests providing the frequency and the rate dependence in oscillatory and steady shear respectively. We have shown that the first yield point is due to the breaking of bonds within cages (at high φ) or between interconnected clusters (at low φ), while the second one is attributed to the breaking of cages or of clusters into smaller constituents. While the bonding strength is kept constant, the first yield point stays constant for all φ and increase only at the lowest one (φ=0.2), whereas the second yield strain increases as volume fraction is decreased. This effect is attributed to cages turning into looser clusters, as the introduction of voids increases the relevant to yielding length-scale, allows greater flexibility of bonds and introduces cluster rotation. Steady shear experiments indicated three distinct shear rate regimes determining the state of the system after the first yield point that breaks some inter-cluster or in-cage bonds. At the lowest rates the freed clusters may rotate slowly almost unperturbed, intermediate rates cause partial breakdown of the clusters through increased collisions and finally the highest rates break down the clusters into particles. With increasing rate the height of the second peak increases over the first, with clusters reducing to smaller sizes.

By increasing the range of attraction, linear viscoelastic properties are reduced due to weakening of the gel. Most importantly both yield strains increase as expected by the rationalization given. A third broader peak appearing in the longer attraction range sample is not fully understood, but could be related to an additional step that is necessary to break denser particle clusters.

Finally, we have shown that both the linear viscoelasticity and the stresses measured at step rates evolve with waiting time. For the latter an increase of the second stress overshoot over the first is observed at long times. This suggests that although initial particle bonding is quite fast, slower structural rearrangements lead to stronger clusters at longer times. For the high volume fraction attractive glass, as waiting time increases the

second yield strain decreases along with the peak stress increase due to tighter cages that create a more brittle material. We have extended these findings for van der Waals interactions and found that even small attractions, $U \approx -1K_BT$, may cause long range restructuring and lead to the appearance of a second stress overshoot.

8.6 References

Aarts, D. G. A. L., R. Tuinier and H. N. W. Lekkerkerker (2002). "Phase behaviour of mixtures of colloidal spheres and excluded-volume polymer chains." Journal of Physics Condensed Matter **14**(33) 7551-7561.

Akcora, P., H. Liu, S. K. Kumar, J. Moll, Y. Li, B. C. Benicewicz, L. S. Schadler, D. Acehan, A. Z. Panagiotopoulos, V. Pryamitsyn, V. Ganesan, J. Ilavsky, P. Thiyagarajan, R. H. Colby and J. F. Douglas (2009). "Anisotropic self-assembly of spherical polymer-grafted nanoparticles." Nature Materials **8**(4) 354-359.

Asakura, S. and F. Oosawa (1954). "On interaction between two bodies immersed in a solution of macromolecules." The Journal of Chemical Physics **22**(7) 1255-1256.

Ballesta, P., R. Besseling, L. Isa, G. Petekidis and W. C. K. Poon (2008). "Slip and flow of hard-sphere colloidal glasses." Physical Review Letters **101**(25) 258301.

Ballesta, P., R. Besseling, N. Koumakis, W. C. K. Poon and G. Petekidis (2010). "Slip of Colloidal Gels under Shear." In preparation.

Bergenholtz, J., W. C. K. Poon and M. Fuchs (2003). "Gelation in model colloid-polymer mixtures." Langmuir **19**(10) 4493-4503.

Besseling, R., L. Isa, P. Ballesta, G. Petekidis, M. E. Cates and W. C. K. Poon (2010). "Shear Banding and Flow-Concentration Coupling in Colloidal Glasses." Physical Review Letters **105**(26) 268301.

Buscall, R., I. J. McGowan and A. J. Morton-Jones (1993). "The rheology of concentrated dispersions of weakly attracting colloidal particles with and without wall slip." Journal of Rheology **37**(4): 621 621-641.

Carrier, V. and G. Petekidis (2009). "Nonlinear rheology of colloidal glasses of soft thermosensitive microgel particles." Journal of Rheology **53**(2) 245-273.

Chen, Y. L. and K. S. Schweizer (2004). "Microscopic theory of gelation and elasticity in polymer-particle suspensions." Journal of Chemical Physics **120**(15) 7212-7222.

d'Arjuzon, R. J. M., W. Frith and J. R. Melrose (2003). "Brownian dynamics simulations of aging colloidal gels." Physical Review E **67**(6) 061404.

Derec, C., G. Ducouret, A. Ajdari and F. Lequeux (2003). "Aging and nonlinear rheology in suspensions of polyethylene oxide–protected silica particles." Physical Review E **67**(6) 061403.

Dibble, C. J., M. Kogan and M. J. Solomon (2006). "Structure and dynamics of colloidal depletion gels: Coincidence of transitions and heterogeneity." Physical Review E **74**(4) 041403.

Fleer, G. J. and R. Tuinier (2007). "Analytical phase diagram for colloid-polymer mixtures." Physical Review E **76**(4) 041802.

Friend, J. P. and R. J. Hunter (1971). J. Colloid Interface Sci. **37**: 548

Grand, A. and G. Petekidis (2008). "Effects of particle softness on the rheology and yielding of colloidal glasses." Rheologica Acta **47**(5-6) 579-590.

Hoekstra, H., J. Vermant, J. Mewis and G. G. Fuller (2003). "Flow-Induced Anisotropy and Reversible Aggregation in Two-Dimensional Suspensions." Langmuir **19**(22) 9134-9141.

Hunter, R. J. (2001). Foundations of Colloid Science, Oxford University Press.

Islam, M. T. and L. A. Archer (2001). "Nonlinear rheology of highly entangled polymer solutions in start-up and steady shear flow." Journal of Polymer Science, Part B: Polymer Physics **39**(19) 2275-2289.

Jabbari-Farouji, S., M. Atakhorrami, D. Mizuno, E. Eiser, G. H. Wegdam, F. C. MacKintosh, D. Bonn and C. F. Schmidt (2008). "High-bandwidth viscoelastic properties of aging colloidal glasses and gels." Physical Review E **78**(6) 061402.

Kamp, S. W. and M. L. Kilfoil (2009). "Universal behaviour in the mechanical properties of weakly aggregated colloidal particles." Soft Matter **5**(12) 2438-2447.

Kobelev, V. and K. S. Schweizer (2005). "Nonlinear elasticity and yielding of depletion gels." Journal of Chemical Physics **123** 164902.

Koumakis, N. (2007). Shear Induced Crystallization of a Colloidal Glass. Department of Materials Science and Technology, University of Crete. **MSc**.

Koumakis, N. and G. Petekidis (2011). "Two step yielding in attractive colloids: transition from gels to attractive glasses." Soft Matter (In Press) DOI:10.1039/c0sm00957a.

Koumakis, N., A. B. Schofield and G. Petekidis (2008). "Effects of shear induced crystallization on the rheology and ageing of hard sphere glasses." Soft Matter **4**(10) 2008-2018.

Krall, A. H. and D. A. Weitz (1998). "Internal dynamics and elasticity of fractal colloidal gels." Physical Review Letters **80**(4) 778-781.

Laurati, M., S. U. Egelhaaf and G. Petekidis (2010). "Non-Linear Rheology of Colloidal Gels with Intermediate Volume Fraction." Journal of Rheology, submitted.

Laurati, M., G. Petekidis, N. Koumakis, F. Cardinaux, A. B. Schofield, J. M. Brader, M. Fuchs and S. U. Egelhaaf (2009). "Structure, dynamics, and rheology of colloid-polymer mixtures: From liquids to gels." Journal of Chemical Physics **130**(13) 134907.

Lekkerkerker, H. N. W., W. C. K. Poon, P. N. Pusey, A. Stroobants and P. B. Warren (1992). "Phase Behaviour of Colloid + Polymer Mixtures." Europhysics Letters **20**(6) 559.

Letwimolnun, W., B. Vergnes, G. Ausias and P. J. Carreau (2007). "Stress overshoots of organoclay nanocomposites in transient shear flow." Journal of Non-Newtonian Fluid Mechanics **141**(2-3) 167-179.

Lindemann, F. A. (1910). Phys. Z. **11** 609.

Lodge, J. F. M. and D. M. Heyes (1999). "Transient colloidal gels by brownian dynamics computer simulation." Physical Chemistry Chemical Physics **1**(9) 2119-2130.

Lu, P. J., J. C. Conrad, H. M. Wyss, A. B. Schofield and D. A. Weitz (2006). "Fluids of clusters in attractive colloids." Physical Review Letters **96**(2) 028306.

Lu, P. J., E. Zaccarelli, F. Ciulla, A. B. Schofield, F. Sciortino and D. A. Weitz (2008). "Gelation of particles with short-range attraction." Nature **453**(7194) 499-503.

Manley, S., B. Davidovitch, N. R. Davies, L. Cipelletti, A. E. Bailey, R. J. Christianson, U. Gasser, V. Prasad, P. N. Segre, M. P. Doherty, S. Sankaran, A. L. Jankovsky, B. Shiley, J. Bowen, J. Eggers, C. Kurta, T. Lorik and D. A. Weitz (2005). "Time-dependent strength of colloidal gels." Physical Review Letters **95**(4) 048302.

Marshall, L. and C. F. Zukoski (1990). "Experimental studies on the rheology of hard-sphere suspensions near the glass transition." Journal of Physical Chemistry **94**(3) 1164-1171.

Mason, T. G. (2000). "Estimating the viscoelastic moduli of complex fluids using the generalized Stokes-Einstein equation." Rheologica Acta **39**(4) 371-378.

Mason, T. G., K. Ganesan, J. H. vanZanten, D. Wirtz and S. C. Kuo (1997). "Particle tracking microrheology of complex fluids." Physical Review Letters **79**(17) 3282-3285.

Mason, T. G. and D. A. Weitz (1995). "Linear viscoelasticity of colloidal hard sphere suspensions near the glass transition." Physical Review Letters **75**(14) 2770-2773.

Masschaele, K., J. Fransaer and J. Vermant (2009). "Direct visualization of yielding in model two-dimensional colloidal gels subjected to shear flow." Journal of Rheology **53**(6) 1437-1460.

Mohraz, A. and M. J. Solomon (2005). "Orientation and rupture of fractal colloidal gels during start-up of steady shear flow." Journal of Rheology **49**(3) 657-681.

Negi, A. S. and C. O. Osuji (2009). "Dynamics of internal stresses and scaling of strain recovery in an aging colloidal gel." Physical Review E **80**(1) 010404.

Negi, A. S. and C. O. Osuji (2010). "Physical aging and relaxation of residual stresses in a colloidal glass following flow cessation." Journal of Rheology **54**(5) 943-958.

Osaki, K., T. Inoue and T. Isomura (2000). "Stress overshoot of polymer solutions at high rates of shear." Journal of Polymer Science, Part B: Polymer Physics **38**(14) 1917-1925.

Padding, J. T., E. S. Boek and W. J. Briels (2008). "Dynamics and rheology of wormlike micelles emerging from particulate computer simulations." The Journal of Chemical Physics **129**(7) 074903-11.

Petekidis, G., A. Moussaid and P. N. Pusey (2002). "Rearrangements in hard-sphere glasses under oscillatory shear strain." Physical Review E **66**(5) 051402.

Petekidis, G., D. Vlassopoulos and P. N. Pusey (2003). "Yielding and flow of colloidal glasses." Faraday Discussions **123** 287-302.

Petekidis, G., D. Vlassopoulos and P. N. Pusey (2004). "Yielding and flow of sheared colloidal glasses." Journal of Physics Condensed Matter **16**(38) S3955-S3963.

Pham, K. N., S. U. Egelhaaf, P. N. Pusey and W. C. K. Poon (2004). "Glasses in hard spheres with short-range attraction." Physical Review E **69**(1 1) 115031-1150313.

Pham, K. N., G. Petekidis, D. Vlassopoulos, S. U. Egelhaaf, W. C. K. Poon and P. N. Pusey (2008). "Yielding behavior of repulsion- and attraction-dominated colloidal glasses." Journal of Rheology **52**(2) 649-676.

Pham, K. N., G. Petekidis, D. Vlassopoulos, S. U. Egelhaaf, P. N. Pusey and W. C. K. Poon (2006). "Yielding of colloidal glasses." Europhysics Letters **75**(4) 624-630.

Pham, K. N., A. M. Puertas, J. Bergenholtz, S. U. Egelhaaf, A. Moussaïd, P. N. Pusey, A. B. Schofield, M. E. Cates, H. Fuchs and W. C. K. Poon (2002). "Multiple glassy states in a simple model system." Science **296**(5565) 104-106.

Poon, W. C. K., L. Starrs, S. P. Meeker, A. Moussaïd, R. M. L. Evans, P. N. Pusey and M. M. Robins (1999). Faraday Discussions **112** 143-154

Prasad, V., V. Trappe, A. D. Dinsmore, P. N. Segre, L. Cipelletti and D. A. Weitz (2003). "Rideal Lecture: Universal features of the fluid to solid transition for attractive colloidal particles." Faraday Discussions **123** 1-12.

Pusey, P. N. (1991). Liquids, Freezing and the Glass Transition. Les Houches Session 51. D. Lesvesque, J. P. Hansen and J. Zinn-Justin. North-Holland, Amsterdam.

Ravindranath, S. and S. Q. Wang (2008). "Universal scaling characteristics of stress overshoot in startup shear of entangled polymer solutions." Journal of Rheology **52**(3) 681-695.

Rottler, J. and M. O. Robbins (2003). "Shear yielding of amorphous glassy solids: Effect of temperature and strain rate." Physical Review E **68**(1) 011507.

Schaertl, W. and H. Sillescu (1994). "Brownian dynamics of polydisperse colloidal hard spheres: Equilibrium structures and random close packings." Journal of Statistical Physics **77** 1007.

Shah, S. A., Y. L. Chen, K. S. Schweizer and C. F. Zukoski (2003). "Viscoelasticity and rheology of depletion flocculated gels and fluids." Journal of Chemical Physics **119**(16) 8747-8761.

Smith, P. A., G. Petekidis, S. U. Egelhaaf and W. C. K. Poon (2007). "Yielding and crystallization of colloidal gels under oscillatory shear." Physical Review E **76**(4) 041402.

Smith, W. E. and C. F. Zukoski (2004). "Flow properties of hard structured particle suspensions." Journal of Rheology **48**(6) 1375-1388.

Sollich, P. (1998). "Rheological constitutive equation for a model of soft glassy materials." Physical Review E **58**(1) 738.

Trappe, V., V. Prasad, L. Cipelletti, P. N. Segre and D. A. Weitz (2001). "Jamming phase diagram for attractive particles." Nature **411**(6839) 772-775.

Videcoq, A., M. Han, P. Abélard, C. Pagnoux, F. Rossignol and R. Ferrando (2007). "Influence of the potential range on the aggregation of colloidal particles." Physica A **374**(2) 507-516.

West, A. H. L., J. R. Melrose and R. C. Ball (1994). "Computer simulations of the breakup of colloid aggregates." Physical Review E **49**(5) 4237.

Yin, G. and M. J. Solomon (2008). "Soft glassy rheology model applied to stress relaxation of a thermoreversible colloidal gel." Journal of Rheology **52**(3) 785-800.

Zaccarelli, E. (2007). "Colloidal gels: Equilibrium and non-equilibrium routes." Journal of Physics Condensed Matter **19**(32) 323101.

Zaccone, A., H. Wu and E. Del Gado (2009). "Elasticity of Arrested Short-Ranged Attractive Colloids: Homogeneous and Heterogeneous Glasses." Physical Review Letters **103**(20) 208301.

Zausch, J. and et al. (2008). "From equilibrium to steady state: the transient dynamics of colloidal liquids under shear." Journal of Physics Condensed Matter **20**(40) 404210.

Chapter 9 – Simulations of Sheared Attractive Gels: Stresses and Structure under Shear

Abstract

Using Brownian dynamics simulations we have examined the structural properties during yielding of hard sphere depletion gels with the application of steady shear. We have found that the non-linear stress response in a concentrated gel is strongly affected by the structural changes during shear. The first low strain peak is verified to refer to the initial particle collisions (bond breaking), while the second stress peak refers to larger scale structural rearrangements. As for experiments, at the lowest rates the stress peaks become smaller, while at intermediate rates the second peak increases with long range restructuring taking place. At the highest rates, the first peak becomes prominent as bond breaking occurs primarily at the smallest strains, while the second peak becomes insignificant.

We also find that the stress peaks are significantly dependent on the initial structural properties and rejuvenation protocol prior to the application of shear. Larger changes in the structure, from the initial state to the steady state, correspond to larger stress peaks, more so for the secondary peak. At the steady state under shear, the lowest rates show the collapse of clusters onto each other, creating large voids, while larger rates decrease inhomogeniety. Moreover, the steady state under shear appears to depend only on the applied rate and not the initial conditions. The structural properties under shear are found to be reflected by the non-dimensional Pe_{dep} number, the ratio of depletion of applied shear forces.

Technically, we have additionally used a new measure to monitor the heterogeneous gel structure, the void distribution function, which is a more efficient marker of long range heterogeneous structure than the Voronoi volume or the application of a pair distribution function. Barring extreme inhomogenieties, the average bonds/contacts per particle in this case also is found to be a good indication of heterogeneity.

9.1 Introduction/Implementation

The two step yielding of hard sphere dispersions with strong depletion attractions has been observed experimentally in both attractive glasses (Pham, Petekidis et al., 2006; Pham, Petekidis et al., 2008) and lower volume fraction gels (Laurati, Egelhaaf et al., 2010; Koumakis and Petekidis, 2011). Although it has been proposed that the first yield at

low strains is due to bond breaking and the second at higher strains due to cage/cluster breaking, microscopic information is not available to support this. Simulations of colloidal gels under transient (Whittle and Dickinson, 1997; Rzepiela, van Opheusden et al., 2004) and steady state shear (Whittle and Dickinson, 1997; Silbert, Melrose et al., 1999) have probed the shear induced disruption of the gel network as a function of shear rate. Still the yielding mechanisms in colloidal gels as a function of shear rate, especially in the intermediate particle volume fractions where multiple length scales are present are far from well understood.

In this chapter we examine results from Brownian Dynamics simulations on attractive particles. We study intermediate volume fraction gels under transient steady shear in order to elucidate the structural changes during the two step yielding process as seen experimentally in chapter 8. We additionally identify significant changes in the transient structure and stresses by varying the initial rejuvenation protocol.

Implementation

Depletion attractions were added in the simulations by using the simple form of the AO potential $U_{dep}(r) = \Pi \cdot V_{overlap}(r)$ (Asakura and Oosawa, 1954) expected to describe the experimental system of hard sphere colloids and linear polymer mixture and as discussed in chapter 2. Two parameters where used as input for the code in order to characterize the potential; the range of attraction (ξ) and the depth of the potential at contact ($U_{dep}(r = 2R)$).

Any applied external force on the spheres is counterbalanced by the Stokes drag on the particle during the course of its motion. Therefore, since the depletion force between particles is given by $F_{dep} = \frac{dU_{dep}}{dr}$ and the corresponding viscous drag $F_{visc} = 6\pi\eta R\frac{\Delta r}{\Delta t}$, we find that the displacements that arise for two particles due to depletion attractions are:

$$F_{dep} = F_{visc} \Leftrightarrow \Delta r = \frac{dU_{dep}}{dr}\frac{\Delta t}{6\pi\eta R} \qquad (9.1)$$

The stresses due to the depletion may be calculated from the particle positions and forces in each time step as $\boldsymbol{\sigma}_{\mathbf{Depl}} = \frac{\sum\left(\vec{r}\bullet\vec{F}_{dep}\right)}{V}$. Here we are interested in the xy of the stress tensor (shear stress):

$$\sigma_{Depl}^{xy} = \frac{\sum\left(r_x F_y\right)}{V} \qquad (9.2)$$

The overall stress response is the sum of the hard sphere interaction stresses, presented in the previous chapters, and the additional stresses due to the depletion forces. Thus:

$$\sigma = \sigma_{HS} + \sigma_{Depl} \qquad (9.3)$$

Two regimes of simulations are studied under shear with N=5405 monodisperse particles at a φ=0.44 and high attraction strengths exhibiting frozen dynamics and unchanging structures at rest. The first mirrors the experimental system with $U_{dep}(2R)$=-17KT and ξ=0.1, with the step rate tests performed by BD at Pe, that span a significant range of rates. The purpose of this study is the elucidation of the yielding processes as described in chapter 8 with changing rate and strain. The second system studied has larger attractions with $U_{dep}(2R)$=-30KT and ξ=0.05, while the Pe was varied in a smaller range and the rejuvenation conditions were changed. The larger attractions lead to increased attractive stresses and enabling us to examine the effect of the rejuvenation protocol on the structure and stress with BD. All the data shown are from single runs using three distinct initial configurations as described below, one for the first regime and two for the second. Initial probing of these regimes was perfomed with the use of 1005 particles giving similar results.

Before the application of shear, we run a simulation with an initial random configuration at rest, until steady state is achieved. Steady structure in this context is defined by a frozen structure that persists without any changes for a few t_B. In some cases instead of starting with a random state, we apply a rejuvenation protocol similar to the experiments (chapter 8), where the system is sheared at a specific rate until a steady state under shear is reached. The last particle configuration under shear is then extracted and a BD simulation at rest is run until it reaches a structurally steady state as determined by observation of the structure. Depending on the attraction strength, the initial configuration and φ this may extend to t/t_B=10.

In chapter 8 we define the ratio of Pe and Pe_{dep} numbers as $Pe / Pe_{dep} = -U_{dep}(r = 2R)/(2\xi k_B T)$, which indicates the shear rate needed to fully break all clusters in a gel in relation to the conventional Peclet number. This is according to a simple model which compares the viscous forces exerted on a pair of particles during shear with the depletion forces. Hence a Pe_{dep}=1 where a complete cluster break up might be expected corresponds to a Pe≈85 for the first regime of $U_{dep}(2R)$=-17KT, ξ=0.1 and a Pe≈300 for the second regime of $U_{dep}(2R)$=-30KT and ξ=0.05. Pe_{dep} is used in the following chapter as a method of identifying the structural changes in the steady state under shear as a function of rate.

Analysis Methods

While in previous chapters the analysis of the positional data from BD simulations consisted of both displacements and structural data, BD simulations of the attractive systems under shear do not allow for facile extraction of the dynamic data. This is mainly due to the cooperative motion of clusters during shear, reducing the available components for statistical averaging. Having a much larger box (or equivalently running many simulations) would provide information on the cooperative motions of clusters. Hence we are limited to examining the changes in the structural properties as well as the determination of shear stress. An example of the gel structures is seen in figure 9.1, where a two diameter thick slice of an intermediate φ gel is shown. In the case of gels, structural analysis cannot be accomplished though the use of pair distribution functions as the averaging will not be able to highlight the heterogeneity in the structures. The idea is then not to examine the particle positions themselves, but rather examine the structural properties of the space between them, i.e. the heterogeneous voids.

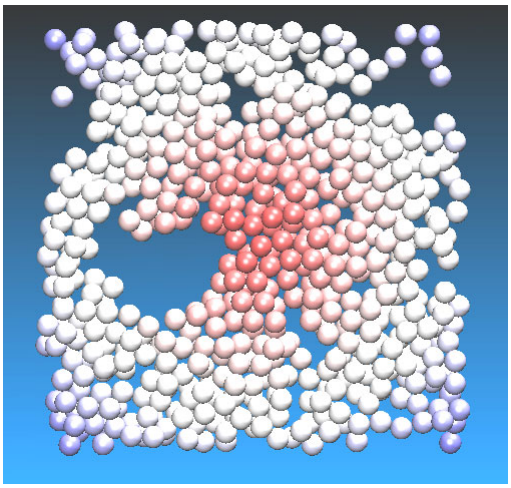

Figure 9.1: Image showing a two diameter thick slice of a long time configuration with φ=0.44, $U_{dep}(2R)$=-30KT and ξ=0.05 at rest. Particle colors reflect the current distance from the centre of the box.

The distribution of Voronoi volumes may be used as a tool to quantify the voids. A Voronoi volume around a particle is defined as the space closest to that particle originally proposed by Georgy Voronoi in 1907 (Voronoi, 1907). In colloidal literature it has been used to examine the correlation of local dynamics with local structure(Conrad, Starr et al., 2005), the structure of gels (Varadan and Solomon, 2002), gels under uniaxial shear (Varadan and Solomon, 2003) and hard sphere crystallization processes(Haw, 2006). Images of Voronoi areas and volumes are shown in figure 9.2. Although computationally efficient calculations of Voronoi volumes generally require volume calculations of complex geometric shapes, we have

adopted a much simpler method due to the difficulty of applying periodic boundary conditions under shear to existing free source algorithms. As we generally have small system sizes, in our analysis we simply divide the simulation space in small volumes dV ($dV \ll R^3$) and enumerate the distances to the particles.

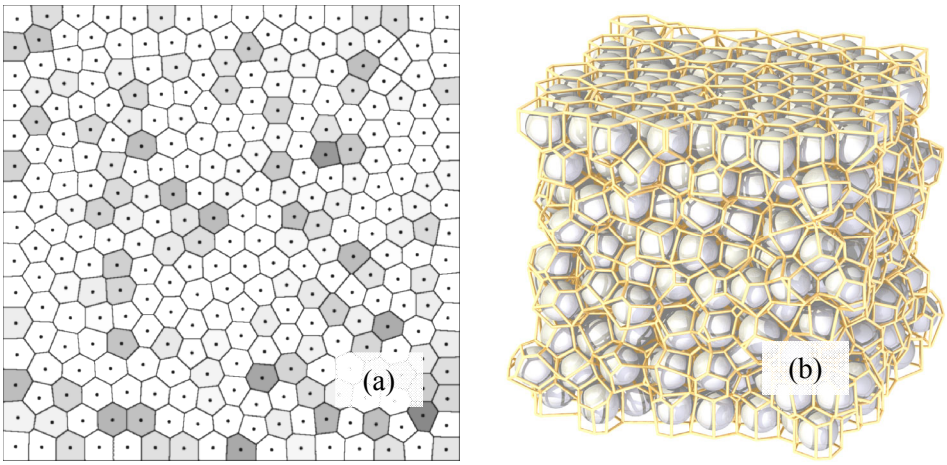

Figure 9.2: Schemes showing a) two dimensional Voronoi areas of points and b) three dimensional Voronoi volumes of spheres.

Even though the distributions of Voronoi volumes have been used successfully in the past to identify void structures, we have found that they return poor statistics for large void structures as seen in fig. 9.1. Therefore, we have are using a more specific method in identifying small changes in larger void structures. We define as a "void volume", the volume of a sphere having its centre in the void space, with a radius equal to the distance to the nearest particle surface, schematically shown in two dimensions in figure 9.3. If we divide the simulation space into small dV volumes as before, the radius of the void volume sphere, R_{void}, is given by:

$$R_{void} = \left|\vec{r}_{dV} - \vec{r}_{particle}\right| - R \qquad (9.4)$$

where R is the nearest particle radius, $\vec{r}_{dV}$ and $\vec{r}_{particle}$ are the positions of the dV volume and the nearest particle respectively. Instead of a void volume, we may also simply examine a "void distance", the radius of the void sphere, R_{void}, the one dimensional equivalent of the void volume. Unlike the Voronoi volume distribution which allocates the available space only once per examined configuration, by definition the void volume distribution may incorporate in its calculations a specific portion of space many times. Although this function may seem arbitrary, this method is much more robust in the mapping of the heterogeneous distribution of void sizes, as will be shown further. In some respects, the Voronoi volume is the inverse of the void volume distribution, as the former examines the available free space to each particle

or equivalently the average distance to the nearest particle, while the latter examines the distance of any empty position in space to the nearest particle.

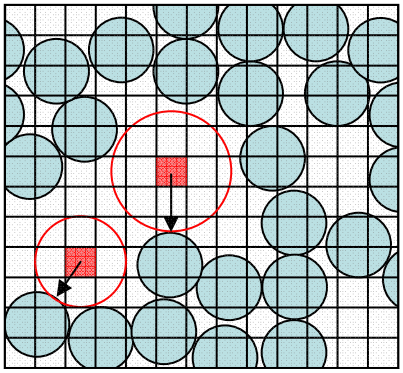

Figure 9.3: Scheme showing a two dimensional representation of the radius used in the calculation of the void volume distribution function as discussed in text. For purposes of clarity the division of the simulation space has been exaggerated.

9.2 Start-up Shear: Stresses

Shear Rate Dependence

We first discuss the start-up shear stress responses in various gels as a function of time (or equivalently strain) for different shear rates and then quantify these responses in terms of structural changes. The overall stress response from BD simulations for the first series of systems, at φ=0.44, $U_{dep}(2R)$=-17KT and ξ=0.1, (similar to the experimental samples of chapter 8), is shown in figure 9.4. Here the starting configuration is a state at rest being initialized from a random particle configuration as described previously. Simulations were performed in a range of Pe from 10^{-1} to 10^{4}, while the actual roughly estimated $Pe_{dressed}$ in experiments is of the order of 10^{-2} to 10^{1}. As described in chapter 2, $Pe_{dressed}$ is used to identify the relation of shear to the short-time self-diffusivity of a particle in the specific medium and φ. In the case of experimental colloid-polymer suspensions, where a high volume fraction of particles is immersed in a polymer solution, the hydrodynamic interactions are ill defined due to the change of solvent viscosity by the addition of polymer and the local hydrodynamic effects of particle clustering. Thus determination of $Pe_{dressed}$ is not straightforward.

Under these above conditions the detection of the two stress peaks s not obvious in the overall stress response of the BD simulations. Instead we find that at low rates an initial weak peak is followed by a “shoulder”, while as rates are increased, the initial peak dominates and the second weaker one disappears. This is not in qualitative agreement with the experimental data that shows the second stress peak increasing with rate, although the range of examined Pe is

different: (10^{-1}<Pe<10^4 in BD while 10^{-2}<$Pe_{dressed}$<10^1 in experiments). Additionally, the first peak differs in strain compared to that in experiments, as in the simulation it appears in the range of 1% strain, while experiments show peaks at about 10%. These differences will be discussed below in the context of the structural properties and the applied simulation potential. The stresses at Pe=10^4 are not shown for clarity, as it follows the same trends, although it is structurally analyzed further below.

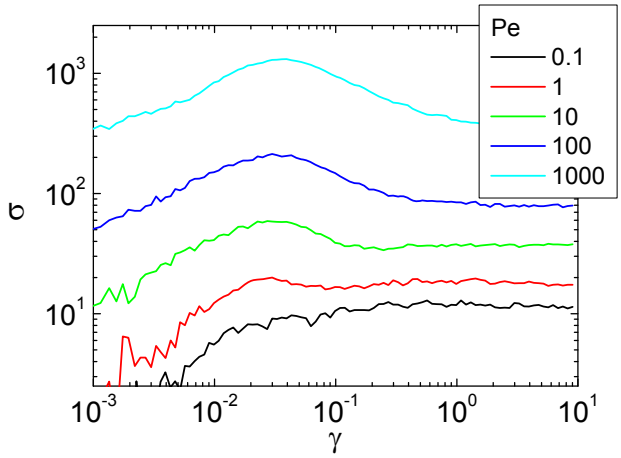

Figure 9.4: Overall stress response during step rate tests (start-up) for a large range of Pe (0.1-1000) at φ=0.44, $U_{dep}(2R)$=-17KT and ξ=0.1 as a function of absolute strain γ, using an initial random configuration.

The stresses of figure 9.4 are decomposed into the hard sphere stresses (9.5a) and the depletion potential stresses (9.5b). The hard sphere stresses are dominant at the high Pe regime (Pe>10) showing similar stress values to the overall stress. The depletion stresses keep the same order of magnitude for all applied rates and thus become important for the lowest rates probed where they are comparable to the hard sphere stresses. Based on the stress response shown in figure 9.5, the first peak at 1% strain seems to primarily originate from the hard sphere stresses, while the second peak at 100% and low Pe originates from the depletion stresses. It is interesting to note that we also detect negative stresses related to the attractions at the steady state for the highest rates.

With a first look, this result may seem to contrast the premise of chapter 8 where the first peak was attributed to bond breaking, while the second to cluster collisions and subsequent breaking. This is not the case though, as these stresses represent the nature of the yielding peaks in terms of the two particle potentials, the hard sphere potential and the depletion attraction potential. The discussion of bonds and clusters, however, refers to changes in the

structural properties. The correlation between the stresses and the structures will be examined in detail further in this chapter.

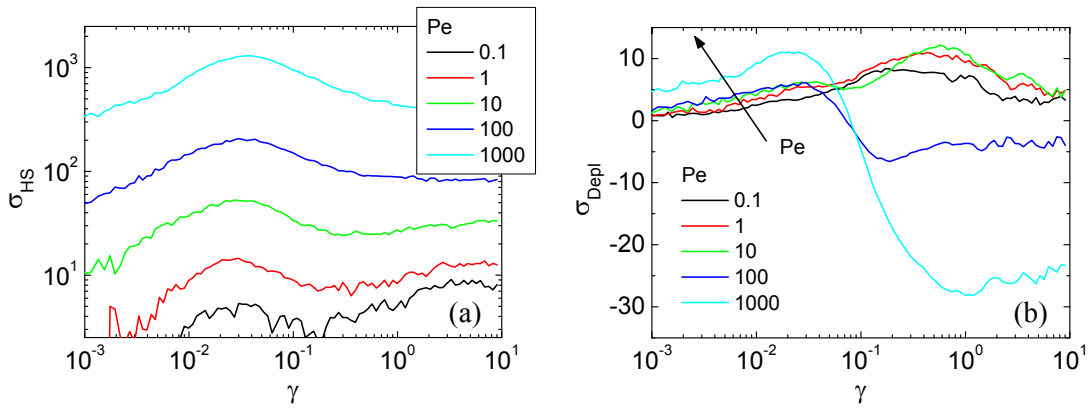

Figure 9.5: Decomposition of the stress response during the step rate test of previous figure (9.4) at φ=0.44, U_{dep}(2R)=-17KT and ξ=0.1 depicting a) the hard sphere contribution in a log-log plot and b) the depletion attraction contribution in a lin-log representation.

Although the depletion forces for U_{dep}(2R)=-17KT and ξ=0.1 are dominant when compared to Brownian motion and inhomogeneous gel structures are present, the two peaks were not as apparent as in the experimental data. We thus increased the depletion attraction at contact to U_{dep}(2R)=-30KT and decreased its range to ξ=0.05, closer to the expected experimental range. Again in this case, as before, the state at rest was initialized from a random particle configuration. The applied shear rates here are much closer to the experimental range going from Pe=0.2 up to 5. As seen in figure 9.6, the overall features are as before, although now the prominence of the second peak stress is much clearer at lower rates, while again the trends of the peaks show qualitative differences to the experiments (fig. 8.12 where the second peak increases over the first). As a technical note, the overall stresses may begin from negative values at small strains (fig. 9.6) as the initial structure may be frozen at rest in a slightly distorted, but random, state. Averaging on multiple runs of different starting structures may eliminate such minor artifacts.

Decomposing the stresses into the hard sphere repulsion and attraction stresses (fig. 9.7) yields similar results as before. The hard sphere stresses are the main component of the first peak, while the depletion stresses of the second peak. This narrow range of rates shows the first peak due to hard sphere repulsions becoming larger with rate, while depletion stresses only show a slight increase of the second peak. In this regime there is evidence that the first yielding is not only associated with the hard sphere repulsion stresses, but also with the depletion stresses showing an approximate 30% contribution to the peak at Pe=5.

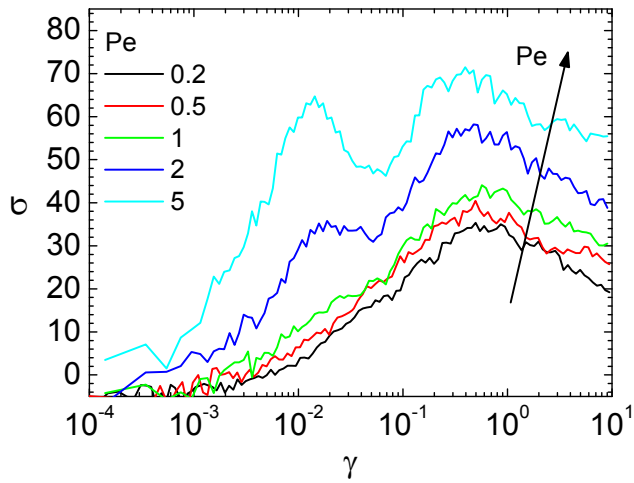

Figure 9.6: Step rates showing in a Lin-Log plot the overall stress response against absolute strain γ, for various Pe=0.2, 0.5, 1, 2 and 5 at φ=0.44, $U_{dep}(2R)$=-30KT and ξ=0.05, using an random initial configuration.

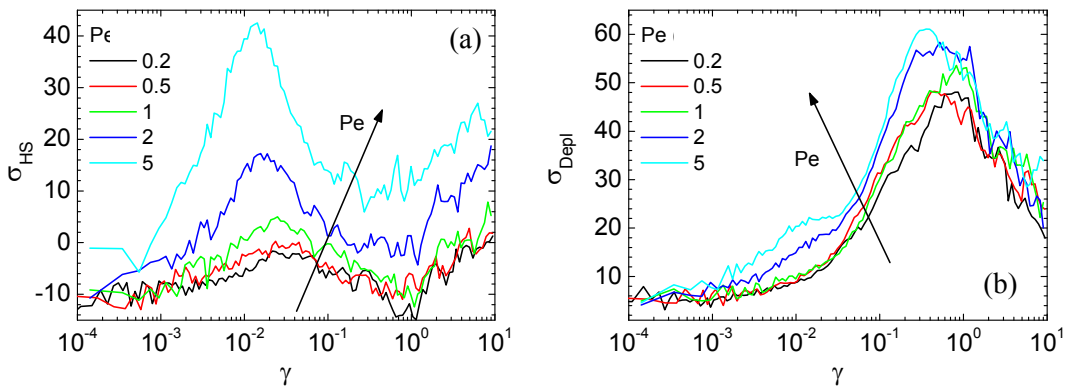

Figure 9.7: Decomposed stress response of the step rates of figure 9.6 at φ=0.44, $U_{dep}(2R)$=-30KT and ξ=0.05 show in a lin-log plot a) the hard sphere repulsion stresses and b) the contribution from depletion attraction stresses.

Rejuvenation Protocol and Stresses

We additionally examine the effect of rejuvenation on the start up shear simulations by applying a preshear before allowing the initial state to reach a steady state at rest. We use a preshear of Pe=10, which is approximate to the preshear used in the experiments and the same parameters as before with $U_{dep}(2R)$=-30KT and ξ=0.05, and perform BD simulations at the same applied rates. The overall stress responses of these simulations are shown in figure 9.8 and their decomposed stresses in fig 9.9. Qualitatively, as found before, we find that both the first and second peaks increase in stress with shear rate, although the second is weaker than the first. Substantial differences are observed, however, between the two rejuvenations by looking at the actual values of the peak stresses. Starting from a random configuration, as

opposed to a presheared configuration, we find smaller values of the first stress peak (σ_{HS}), while larger for the second peak (σ_{Depl}).

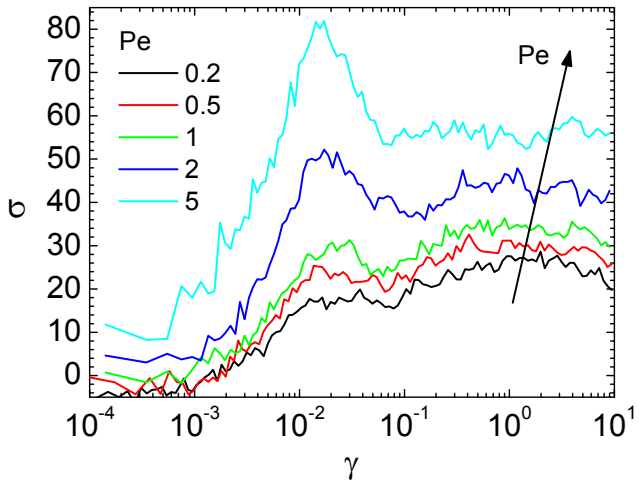

Figure 9.8: Overall stress response of step rates against strain γ, for various Pe=0.2, 0.5, 1, 2 and 5 at φ=0.44, U_{dep}(2R)=-30KT and ξ=0.05 using a shear rejuvenation of Pe=10 as done in experiments.

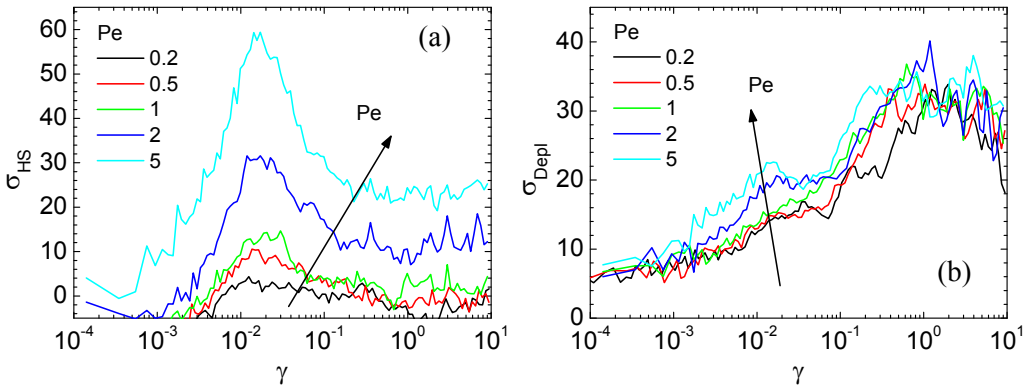

Figure 9.9: Decomposed stress response of the step rates of figure 9.8 at φ=0.44, U_{dep}(2R)=-30KT and ξ=0.05 showing in a lin-log plot a) the hard sphere repulsion stresses and b) the depletion attraction stresses.

9.3 Start up Shear: Structural Properties

Rejuvenation and Structures at Rest

Before examining the structural properties under shear and their correlation to stresses, we examine the structural properties of the states at rest to compare the two rejuvenation procedures and the different available analyses. Figure 9.10 shows data analysis for the structures occurring at rest from simulations at φ=0.44, U_{dep}(2R)=-30KT and ξ=0.05 for two initial starting points; one with particles having random uncorrelated positions in the simulation box (black), and another by using a preshear of Pe=10 (red). Images showing a slice of two diameters thick for the structures are shown in figures 9.10a (random, black) and

9.10b (presheared, red). The first realization intuitively refers to a random unbiased structure after steady state at rest is reached, while the second may show orientational or structural bias related to the external shear.

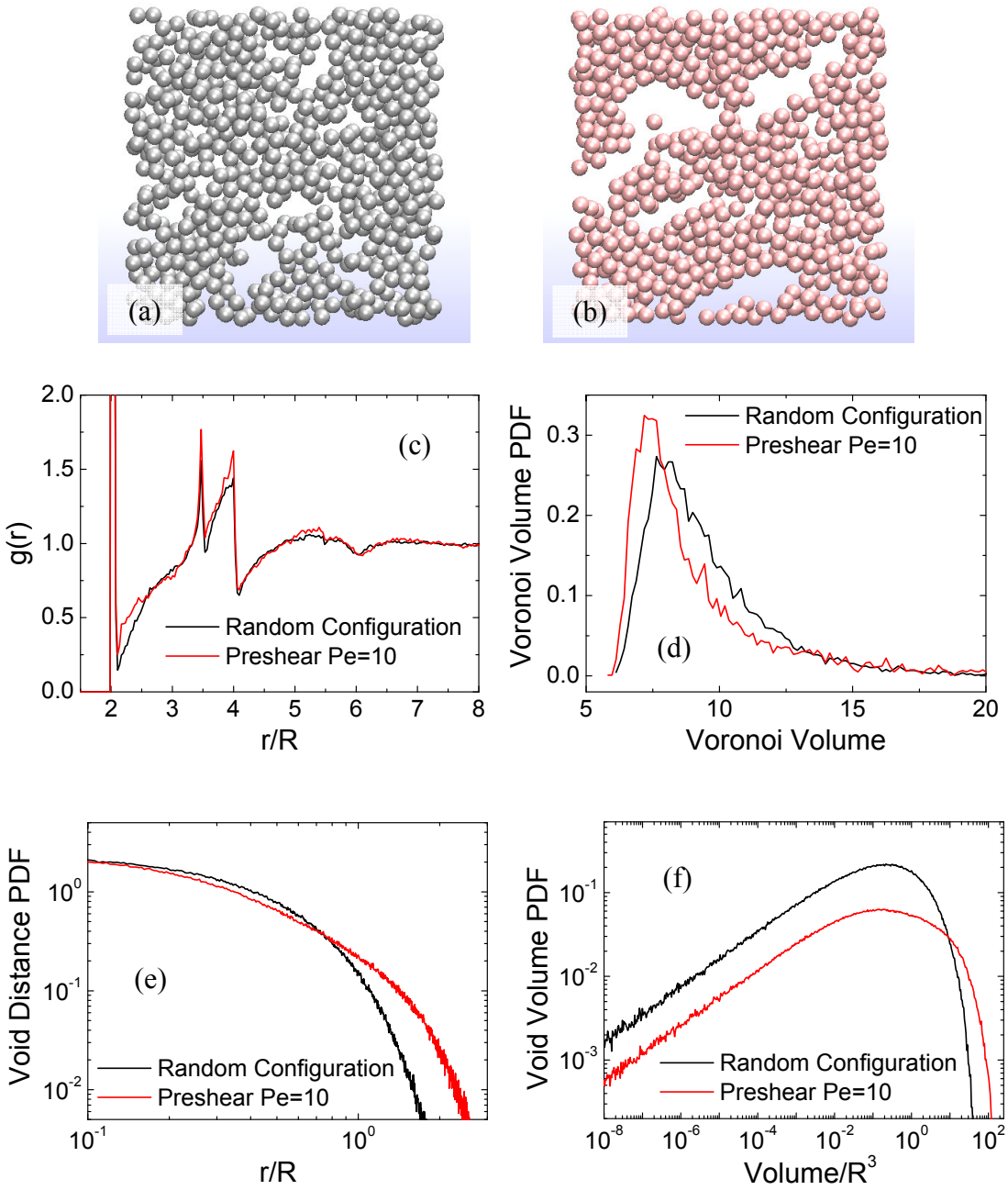

Figure 9.10: Data concerning the structure differences of φ=0.44, $U_{dep}(2R)$=-17KT and ξ=0.1, by starting the equilibration with a random configuration or a configuration that has been presheared at Pe=10. a) A two diameter thick slice of a random starting configuration and b) a configuration presheared at Pe=10. We also show c) the pair distribution function of the two structures, d) the Voronoi volume probability density function, e) the void distance probability density function and f) the void volume probability density function.

More specifically, we find that heterogeneities are present for both structures, although the presheared structure shows larger voids and thus more compact clusters. As will be seen later, the structures under shear depend on the applied rate and the final evolution of any structure at rest will correspond to the parameters of the applied preshear or initialization. Thus by simple observation we find differences between the initial structures, which as shown before, lead to significant differences for the stresses during start-up shear.

The pair distribution function is shown for the two structures in 9.10c. Both cases the g(r) show a peculiar g(r), reminiscent of a crystal with short range order due to the initial peaks and also an amorphous system at larger distances. The initial peaks come from the close proximity of the particles due to gelation, in connection with the well defined monodisperse radii, essentially capturing the structure of close packed clusters of a few particles. Since long range structure is amorphous, the peaks are smoothed out at larger ranges. Even though we have found the structures to be quite dissimilar by observation, the g(r) only shows minute differences between the two. The compact clusters in the presheared configuration are seen as a small increase of the correlation function at short ranges, while larger ranges show almost no differences at all. All in all, it could be argued that the differences in the curve are due to statistical noise.

This is not the case when looking at the Voronoi volume probability density function (PDF) of figure 9.10d. This graph essentially show the distribution of available volume for each particle and thus by extension is able to examine the heterogeneous structures. The curves show a peak in the Voronoi volume distribution roughly corresponding to the average volume available for each particle. Since the two curves refer to the same φ, a transition of the peak to lower volumes describes an increase in local cluster density, as is seen for the presheared configuration. Due to bad statistics though, information on the volumes of the larger voids is lost.

Figures 9.10e and 9.10f are two representations of the void volume distribution as discussed previously. Figure 9.10e has the one dimensional representation of the void size distribution using the radius of the void sphere, while figure 9.10f has the distribution of void volumes. In both cases, we see a reduction of the probability to find small/intermediate void sizes for the presheared configuration, while an increase of probability to find large voids. Small void sizes ($r/R<1$ or $Volume/R^3<1$) mostly represent the voids/spaces that are near particle surfaces and between close packed structures, while larger sizes represent actual voids. Hence, examining more compact clusters increases the probability of finding large void sizes and decreases the probability of voids found near the surface of particles. Although the two representations are

equivalent with concern to the information contained, the use of the volume representation (9.10f) highlights the differences between large and small void sizes (Bitsanis, 2010). Compared to the other techniques of characterizing heterogeneous structure shown in figure 9.10, it seems to us that the void volume probability density function (PDF) is the most compact, accurate and relevant method of analysis for the intended use of void characterization.

Structures under Shear: Rate Dependence

In continuation, we examine the structural properties of the steady state under shear as a function of changing rate. Here we study the structure under shear at a strain of γ=1000% for the stress responses shown in figures 9.4 and 9.5, on colloidal gels with φ=0.44, $U_{dep}(2R)$=-17KT and ξ=0.1 at various rates. Figure 9.11 shows images of the steady state at rest and under shear, exhibiting a collapse of structures at the lowest rates, while showing decreasing heterogeneities with increasing rate. The same information, but in more detail, can be seen in the Voronoi volume distribution of figure 9.12. As rates are increased, the Voronoi volume distribution shows the peak moving towards larger volumes indicating more homogeneous structure.

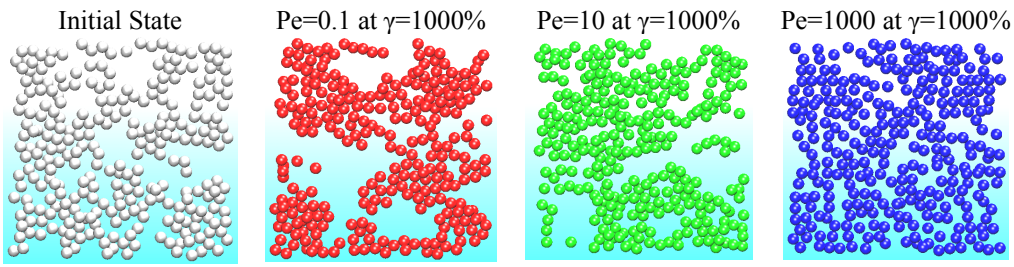

Figure 9.11: Images showing one diameter thick slices of long time configurations with φ=0.44, $U_{dep}(2R)$=-17KT and ξ=0.1 at rest and under shear as labeled.

In figure 9.13 we additionally show the void volume distribution of a simple liquid state at rest and the gel under shear. Here, the void volumes show a decrease in the probability of finding large voids with the increase of rate, again indicating homogenization of structure. We also see that by increasing the rate, the distributions move towards the liquid state. However, as we see from the equal distributions of Pe=1000 and 10000, they may not actually reach it. This is related to the structural anisotropy caused by high shear rate as will be discussed further and as seen in steady shear simulations of chapter 4 and work of (Foss and Brady, 2000), causing some structural heterogeneity in the xy plane.

The increase of heterogeneities with increasing rate is associated with the Pe_{dep} as discussed above and in the chapter 8, which for this case is Pe=85 for Pe_{dep}=1. At the highest rates with

Pe_{dep}>>1, the applied shear becomes much stronger than the attraction force and thus attraction effects are diminished, showing behavior that is equivalent to a sheared dispersion of the same φ and rate without attractions. At the lowest rates (Pe_{dep}<<1), bonds between particles are strong in comparison to shear and the application of shear allows the particles to spatially explore the surrounding landscape and collapse into large clusters. Besides the dependence on rate, the size of these clusters is additionally expected to be a complex function of volume fraction, attractions strength and range.

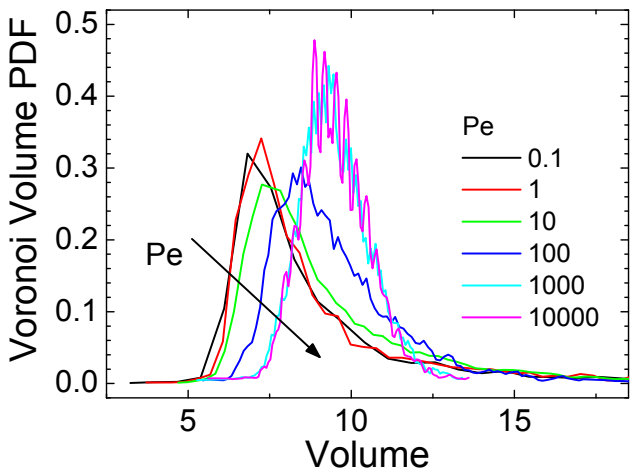

Figure 9.12: Voronoi volume PDF of φ=0.44, $U_{dep}(2R)$=-17KT and ξ=0.1 under shear at a strain γ=1000% and varying Pe as shown in legend.

Further analysis may be done by quantifying the average void volume from the probability density function as $\overline{V_{void}} = \int_0^\infty P(V)VdV$, where P(V) is the void volume PDF of figure 9.13. The results of this analysis can be seen in figure 9.14. As qualitatively discussed, the void volume decreases with increasing rate reaching a plateau value at the highest rates. Although lower rates in the simulation have not been examined, the trend of the curve implies that the average void volume will reach a constant value at the lowest rates. The average void size, which is a measure of heterogeneity, is expected to also be proportional to the size of particle clusters.

Structures under Shear: Strain Dependence

Using similar structural analysis, we additionally examine the transient behavior of the sheared states in order to correlate with the stress response. Again we study the structure under shear at various strains corresponding to the stress responses shown in figures 9.4 and 9.5, with φ=0.44, $U_{dep}(2R)$=-17KT and ξ=0.1 at various rates. In figure 9.15 we show the

microstructural evolution of the void volume for Pe=1, 10, 100 and 1000 for various selected strains. Low applied shear rates, Pe=1 and 10, show an increase in heterogeneity compared to the state at rest, while higher rates, Pe=100 and 1000, show a decrease of heterogeneities.

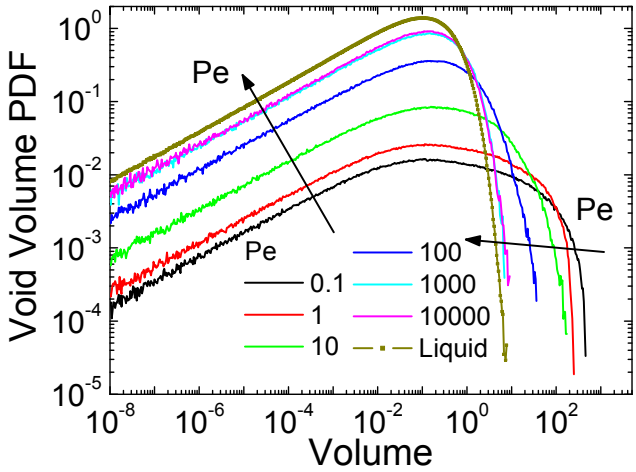

Figure 9.13: Void volume PDF of φ=0.44, $U_{dep}(2R)$=-17KT and ξ=0.1 under shear at a strain γ=1000% and varying Pe as shown in legend. The state for a liquid φ=0.44 with no attractions at rest is also plotted.

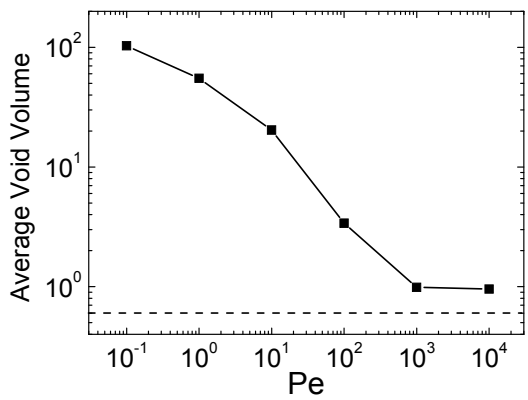

Figure 9.14: Average void volume as a function of Pe for φ=0.44, $U_{dep}(2R)$=-17KT and ξ=0.1 under shear at a strain γ=1000%. The state for a liquid φ=0.44 with no attractions at rest is shown with a dashed horizontal line.

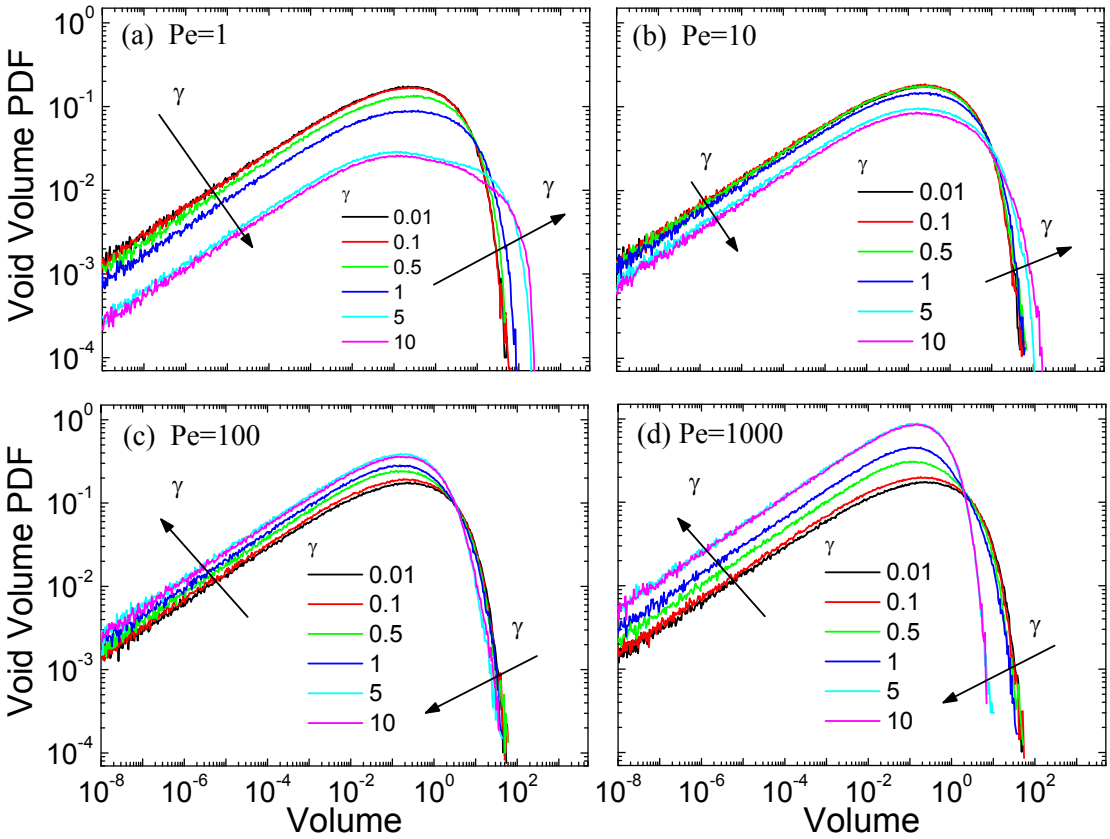

Figure 9.15: Microstructural evolution of φ=0.44, U_{dep}(2R)=-17KT and ξ=0.1 under shear with the absolute values of strain γ as shown in legend showing the void volume PDF at a) Pe=1, b) Pe=10, c) Pe=100 and d)Pe=1000.

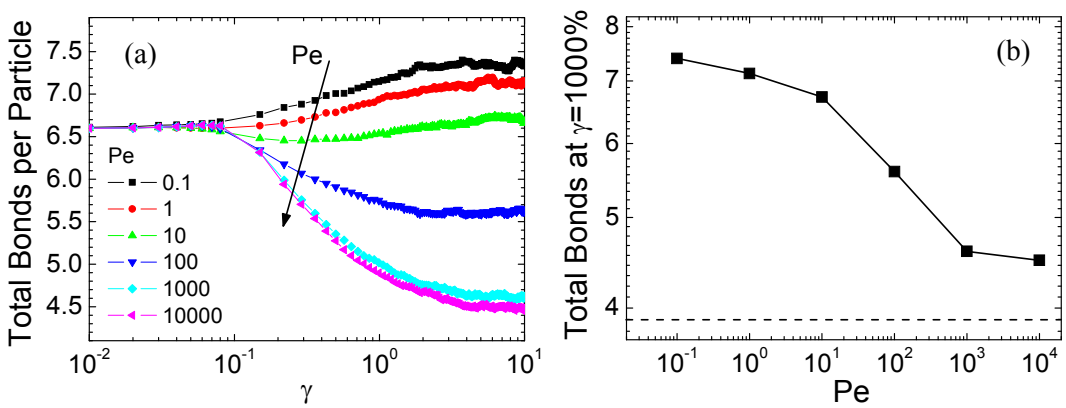

Figure 9.16: a) Microstructural evolution under shear showing the average bonds per particle versus γ of φ=0.44, U_{dep}(2R)=-17KT and ξ=0.1 with various Pe as shown in legend. The liquid state with no attractions for this φ and ξ gives 3.9 bonds per particle. b) The total bonds per particle at a strain of γ=1000%, with the bonds of the liquid state shown as a horizontal dashed line.

An additional way of characterizing inhomogeneous structure, although only regarding to the particle local structure, is to enumerate the average number of bonds or contacts for each

particle. We define that a pair of particles is bonded when the distance between them is less than 2R(1+ξ). Therefore in figure 9.16a we plot the average number of bonds per particle for the different rates as a function of strain. We find that the number of bonds is similar for all rates at low strains, while above γ=10%, they increase for Pe=0.1, 1 and 10 and decrease for Pe=100, 1000 and 10000. The calculation of the average number of bonds is very similar to that of the coordination number which gives the average number of neighbors. Instead of using the bond distance, the latter uses the first minimum of g(r) for the enumeration.

From both figure 9.15 and in more detail from 9.16a, we observe that for all rates, significant structural changes occur only after a strain of 10%, while also reaching a steady state at a strain of 500%. This is in agreement with the depletion stresses of figure 9.5b, which show variation of stresses for the same range of strains. Generally we find that as we increase strain and inhomogenieties increase, there are large peaks and positive values of stress, while reversely when inhomogenieties decrease we find negative stress values.

The negative depletion stresses can be explained by the pair correlation functions of figure 9.17 taken at the peak of depletion stresses at γ=100%. While many details for the lower rates are lost, the high rates, specifically Pe=1000, show a distinct anisotropy as in previous findings of chapter 4 (fig. 4.19) for glasses. Here we find that the attractive bonding stresses are negative since there are many more particles at contact in the compression axis, than in the extension axis. The same pair correlation reversely indicates large positive stresses for the hard sphere repulsion potential. Thus we find that when the attractive forces are small in comparison to shear forces (Pe_{dep}>1, Pe>85) and clusters begin to break down, then the anisotropy produced from particle collisions causes negative values of depletion stress.

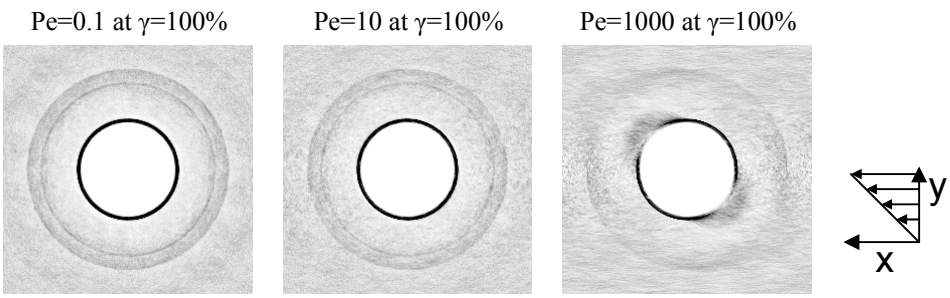

Figure 9.17: Pair correlation functions of xy plane as calculated in chapters 4 and 5 (inverted) of φ=0.44, U_{dep}(2R)=-17KT and ξ=0.1 with Pe=0.1, 10 and 1000 at a strain of γ=100%, the second stress peak.

For the lower rates, the pair correlation in the xy plane (fig 9.17) is not able to give information on the structural properties of the bonds, as the involved range (ξ=0.1) is too

small to discern differences in the specific images. Although based on the previous discussion of high rates, the collapse of the clusters under shear must somehow change the structural properties in such a way that we find fewer particles in the compression axis than in the elongation axis. It is clear though that depletion stresses, associated with the second peak, show a maximum when extensive rearrangements of clusters occur that increase heterogeneity. This observation is later verified when looking at different rejuvenation protocols.

The hard sphere repulsion stresses though are different, showing a peak at 1% strain, seemingly unrelated to structure. These come from the high proximity of the particles in the initial state as shown for the g(r) in figure 9.10c. With the smallest application of strain, the particles in the gel structure collide and cause a large increase in the repulsion stress. It may be that these stresses are an artifact of the specific sharp potentials used in the simulation, both for the repulsion and the attraction. In comparison a real experimental system would have a softer repulsive potential, perhaps even of comparable range to the depletion potential. This is not unreasonable, as the experimental stabilizing layer of the PMMA spheres of chapter 8 is of the order of 5% of the radius, of similar range as the attraction potential. If a softer potential is used in the simulations, although the particles in this case would still be trapped, they would not be frozen as with the steep potential, but would be allowed some "wiggle" room. Preliminary results using a modified potential to accommodate these effects have shown changes in the strain of the first peak bringing it closer to experimental results, without showing appreciable changes in other structural findings.

Even though the state at rest is dependent upon the initialization conditions, it may not be accidental that with random starting conditions and Pe>85 ($Pe_{dep}>1$) the structure becomes more homogeneous, while reversely with $Pe_{dep}<1$ there is collapse of the clusters. By the definition of Pe_{dep}, which refers to the balance of shear and depletion forces, we expect that any structure originating from the depletion attractions will start to deteriorate for rates larger Pe_{dep}. Thus by removing the effect of shear on the initial conditions, we may expect inhomogenieties to increase at $Pe_{dep}<1$ and a decrease for $Pe_{dep}>1$.

In figure 9.16b we also plot the average number of bonds at the steady state as a function of Pe, exhibiting a strong similarity to the average void volume of figure 9.14, generally decreasing with rate and showing plateau values at both high and low rates. These similarities show that although the void structure gives detailed information on the heterogeneous properties of the system, we may infer these same results by averaging the number of bonds from the local structure of each particle. Although, not examined, it may also be of interest to

separately enumerate the number of bonds in the compression and the extension axis under shear in order to better understand the first neighbor structure.

As discussed, the state under shear shows increasing inhomogenieties as rate is decreased. Hence, we qualitatively expect that when applied rates have a Pe_{dep} below unity and are stopped, the resulting structures will be increasingly inhomogeneous as rates are decreased, eventually reaching a constant level of inhomogeniety. For applied rates above $Pe_{dep}=1$, we expect the resulting structure to be equivalent to that of a random initial configuration. We base these speculations on the premise that on stopping shear at low rates, the heterogeneous structure will remain approximately unchanged, while at higher rates will increase in heterogeneity up to that of a random initial configuration

Structures under Shear: Effect of Rejuvenation

After examining the transient and steady state structural changes in a step rate test for a large range of rates, starting from an initial random state, we present a similar study where the starting point is a shear rejuvenated state. We examine an attractive system with $\varphi=0.44$, $U_{dep}(2R)=-30KT$ and $\xi=0.05$ starting with a state produced at Pe=10 (presented in figure 9.10). There we found that the random state shows less heterogeneity than the presheared state. Now for these two initial conditions we apply various rates from Pe=0.2 up to Pe=5 and examine the resulting structures.

Figures 9.18 and 9.19 show the void distribution functions and average bonds per particle respectively for these simulation conditions. As before, for both rejuvenation protocols we find that structural heterogeneities decrease with increasing rate. More importantly though, we find that the structural differences at the steady state under shear compared to the state at rest are larger when starting with a random configuration (9.18a and 9.19a) than with a presheared configuration (9.18b and 9.19b). Thus in correlation to the stress responses of figures 9.7b and 9.9b, we conclude that the stresses of the second peak become larger when more restructuring occurs. We also find that the structures under shear at the steady state are independent of the starting conditions.

Therefore we find that the structure before the application of shear dictates the non linear stress response. If the structure is more homogeneous due to a random configuration, (or the experimental equivalent of high shear rejuvenation), we find that the stress peaks are more pronounced. On the other hand, the more heterogeneous structure resulting from low shear rate rejuvenation exhibits weaker stress overshoots. Generally we observe that with larger restructuring during shear the stress peaks are stronger.

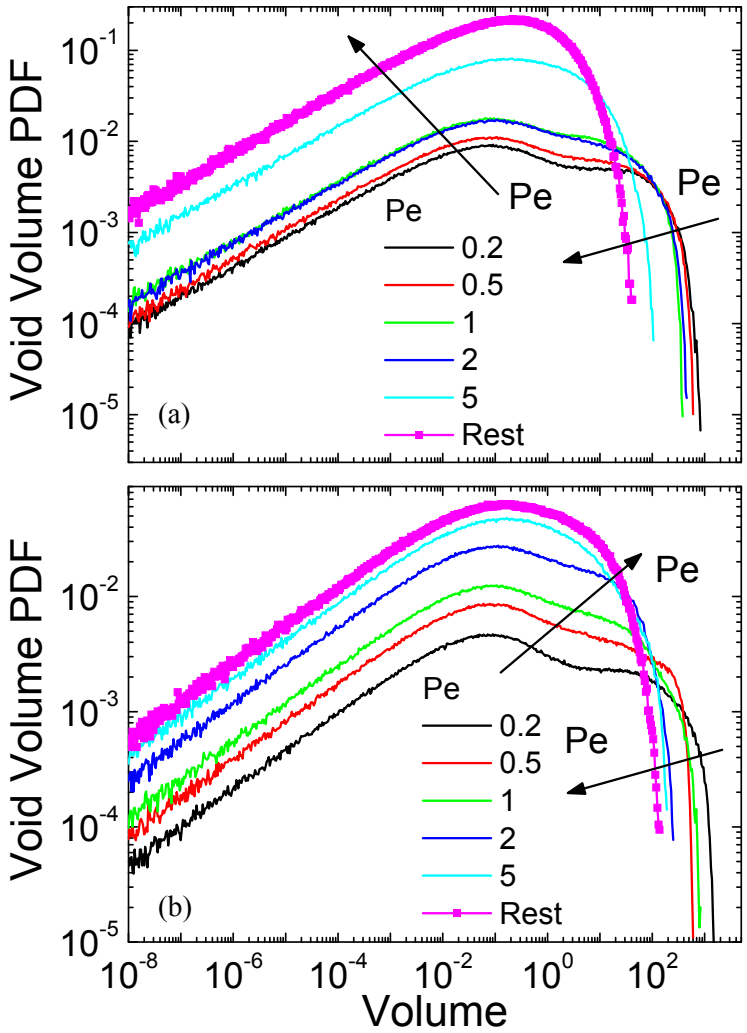

Figure 9.18: Void volume PDF of φ=0.44, $U_{dep}(2R)$=-30KT and ξ=0.05 under shear for various Pe at γ=1000% and at rest as shown in legend with a) using an initial simple liquid configuration instead of a shear rejuvenation and b) using a shear rejuvenation of Pe=10 as done in experiments.

In experiments, this may be the reason a relatively large waiting time is needed to see the peaks, the experimental protocol for most measurements (chapter 8) included a 120sec of waiting time which translates to approximately $t=350t_B$. Although the initial rejuvenated structure shows little or no peaks, ageing due to long range restructuring lead to a configuration which under shear clearly exhibits stronger stress peaks. In BD simulations however, a waiting time of more than a few t_B for such strong gels is meaningless as the system becomes frozen almost instantaneously. The simulation box is too small for long range restructuring as it is only a few clusters in size.

We should note that, these findings concern conditions where the rate of rejuvenation is larger than the applied rate. It is not clear what would happen for initial states at rest that are highly

heterogeneous, 'rejuvenated' at the limit of the lowest rates, which are then probed with a start-up test of larger rate. We do expect that at the steady state the initial heterogeneity will break down into more homogenous structures, as the initial conditions do not seem to change the steady state under shear, but we cannot predict the transient stress response.

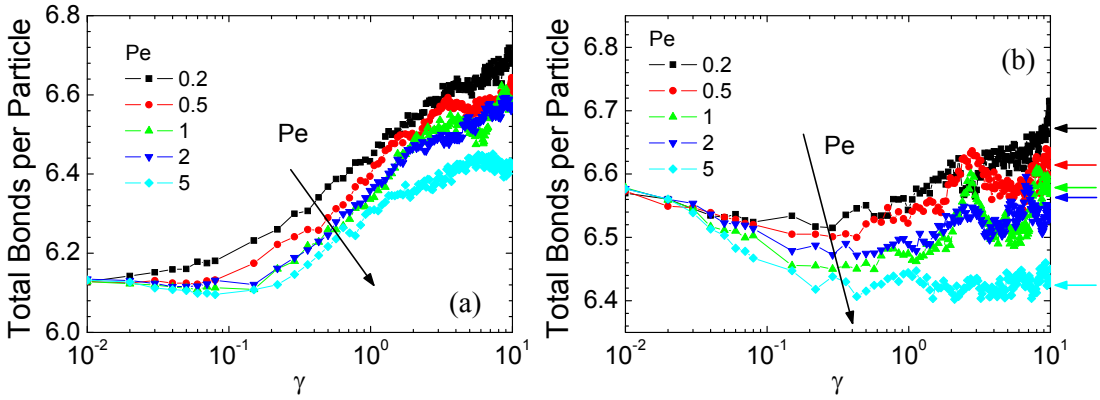

Figure 9.19: Microstructural evolution under shear showing the average bonds/contacts per particle versus strain γ of φ=0.44, $U_{dep}(2R)$=-30KT and ξ=0.05 with various Pe as shown in legend, a) with an initial random configuration and b)using a shear rejuvenation of Pe=10 as done in experiments. Horizontal arrows in b) note the final bonding states in a). The liquid state with no attractions for this φ and ξ gives 2.3 bonds per particle.

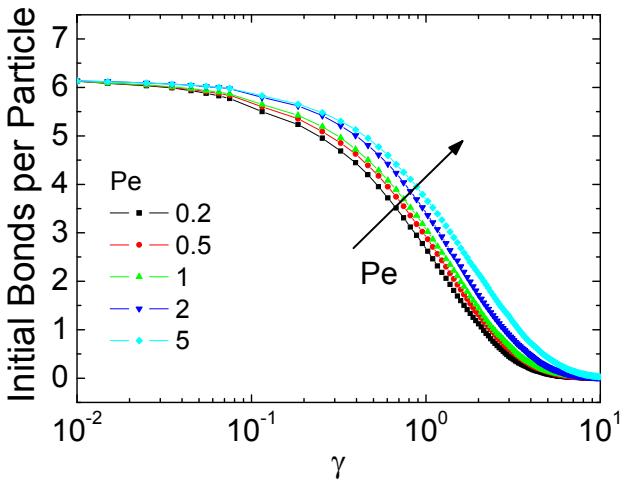

Figure 9.20: Microstructural evolution under shear showing the remaining initial bonds per particle versus strain γ of φ=0.44, $U_{dep}(2R)$=-30KT and ξ=0.05 with various Pe as shown in legend using an initial random configuration. Arrow shows the trend with increasing Pe.

Instead of enumerating and averaging the bonds per particle at every strain as done in figures 9.16 and 9.19, we may also identify the number of persisting bonds from the initial structure. This is done by identifying the bonds in the state at rest and then removing them from the

enumeration when they are broken for particle distances greater than $2R(1+\xi)$. In figure 9.20 we analyze the bonds in this way for an initial random configuration at $\varphi=0.44$, $U_{dep}(2R)=-30KT$ and $\xi=0.05$. We find that even at the lowest rates where depletion forces are dominant and heterogeneities are larger, none of the initial bonds remain at the steady state, while at lower rates the rate of decay is larger.

This result states that the structure during shear, although containing large clusters and heterogeneities, is varying constantly with clusters that restructure, break and reform, in a way that does not allow the persistence of bonds for large periods of time. The rate dependence actually suggests that larger heterogeneities cause more restructuring events to occur under shear. This may be partly due to the flexibility of the bonds with regard to their angle, as no energy or stress is needed for bond rotation. Hence much restructuring under shear can occur through bond rotation and sliding without changing the overall energy of the system.

Structures under Shear: General findings

We now show in figure 9.21 a schematic representation of the structural properties of gels under the application of steady shear as a function of strain and rate, which is a direct comparison to the schematic representation of the yielding processes of the previous experimental chapter 8 (fig. 8.15). This figure shows mapping of structure at different rates and strains, with the rows showing low rates at the bottom with $Pe_{dep}<<1$, high rates on the top with $Pe_{dep}>>1$ and intermediate rates in the middle with $Pe_{dep}\approx1$ while the columns show on the left small linear strains (below the first yield), on the right states above/during the second yield and in the middle strains between the two yield points.

The scheme already provided in chapter 8, gives an initial understanding, while the simulation images (fig. 9.21) show the actual structural details. At all rates below the first yield, we find that the initial structure has not changed. As strain is increased above the first yield, the highest rates show that the inhomogenieties and clusters are broken down into smaller constituents; the lowest rates show an initial cluster collapse, while intermediate rates show detachment of clusters. For the highest rates at the steady state, the structure becomes homogeneous, whereas at the lowest rates the clusters further collapse to form large heterogeneities, while the intermediate rates show the flow of medium sized clusters.

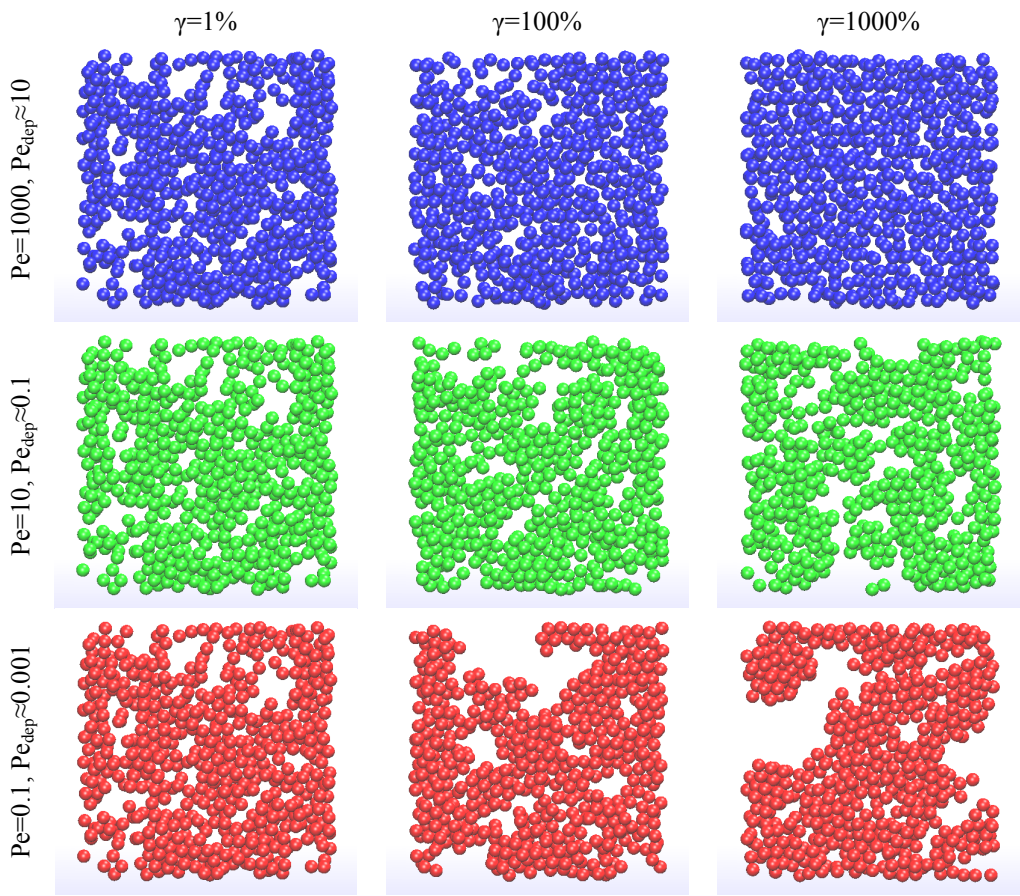

Figure 9.21: Images showing two diameter thick slices of configurations of φ=0.44, $U_{dep}(2R)$=-17KT and ξ=0.1 under shear for Pe=0.1, 10 and 1000 from bottom to top and strains of 1%, 100% and 1000% from left to right as labeled.

Addition of Hydrodynamic Interactions

Even for the state at rest, the work of (Tanaka and Araki, 2000; Furukawa and Tanaka, 2010) reveals that the addition of hydrodynamic interactions (HI) between attractive colloids may enhance the network-forming ability. While at certain low volume fractions the use of Brownian Dynamics leads to fluids of free floating aggregate clusters, the addition of hydrodynamics leads to percolated phase separation followed by gelation. With HI when colloidal particles start to aggregate and form clusters, lubrication effects retard the direct contact of colloids and tend to induce motions of transverse character. This is a direct consequence of the incompressible nature of the liquid in which colloids are suspended. The resulting particle motions of extensional character assist in the formation of elongated structures along the flow. Without HI, particles can straightforwardly aggregate without any interruption making highly dense clusters.

Since at rest the addition of hydrodynamic interactions causes structural alterations for some cases, it may be that under shear we recover different qualitative stresses and structural changes than for simple BD. Even without the addition of attractions, if two hard sphere particles at close proximity are sheared at high rate with HI, they will form a rotating doublet due to lubrication forces, whereas for BD they will simply come apart. In the more complex setting of clustered particles due to attraction forces, the addition of HI may be expected to hinder the restructuring of clusters under high shear rate.

Therefore, in order to elucidate the details of the stresses and structural changes under shear for the gels, Stokesian Dynamics (SD) (Foss and Brady, 2000) simulations were additionally attempted. Preliminary tests for the strong gels have shown qualitative similarities to BD simulations up to strains approaching the second peak. Above such strains, the code was unable to give results and must be modified to accommodate the increased pressures of multiple collisions and restructuring. As shown for simple hard sphere systems (Foss and Brady, 1999; Foss and Brady, 2000) the contributions of HI on particle motions become qualitatively important at rates of Pe>10, due to lubrication forces. Therefore we may argue that at rates below Pe=10, our findings on the stresses and the cluster restructuring under shear are valid. Future work may include the examination of structural changes with the addition of hydrodynamics either with SD or less computationally taxing algorithms such as Accelerated Stokesian Dynamics (ASD) (Sierou and Brady, 2001).

9.4 Chapter Conclusions

In conclusion we have found that the non linear stress response in a concentrated gel is affected by the structural changes during shear. The first low strain peak is found to refer to the initial particle collisions caused by close particle proximity due to bonding, while the second stress peak refers to larger scale structural rearrangements. As discussed in the experimental chapter 8, at the lowest rates the stress peaks become smaller, while at intermediate rates the second peak increases with long range restructuring taking place. At the highest rates, the first peak becomes prominent as bond breaking occurs primarily at the smallest strains, while the second peak becomes insignificant.

We also find that the stress peaks are significantly dependent on the initial structural properties and rejuvenation protocol before the application of shear. The larger the change in the structure, from the initial state to the steady state, the larger the stress peaks, more so for the secondary peak. Structurally at the steady state, for the lowest rates the clusters collapse onto each other, creating large inhomogeneities and voids, while larger rates generally create

more homogeneous structures. Moreover, the steady state under shear appears to depend only on the applied rate and not the initial conditions. The structural properties under shear reflect the non dimensional Pe_{dep} number, as described in chapter 8, which is a ratio of depletion and shear forces/time scales. Additionally, we have discovered that even at the lowest rates where the strongest inhomogenieties appear, no bonds are left undisturbed as there is constant restructuring during shear.

Technically, we have used a new measure to monitor the heterogeneous gel structure, the void distribution function, which is a more efficient marker of long range heterogeneous structure than the Voronoi volume or the application of a pair distribution function. Barring extreme inhomogenieties, the average bonds/contacts per particle in this case may also be a good indication of inhomogenieties.

Future work concerning the microscopic properties of the gels under shear may include study of the gel cluster size in the transient and steady state with applied shear rate and attraction strength. These structural properties may be examined either with simulations (BD, SD or ASD) or with confocal microscopy.

9.5 References

Asakura, S. and F. Oosawa (1954). "On interaction between two bodies immersed in a solution of macromolecules." The Journal of Chemical Physics **22**(7) 1255-1256.

Bitsanis, G. (2010). Private Communication.

Conrad, J. C., F. W. Starr and D. A. Weitz (2005). "Weak Correlations between Local Density and Dynamics near the Glass Transition." The Journal of Physical Chemistry B **109**(45) 21235-21240.

Foss, D. R. and J. F. Brady (1999). "Self-diffusion in sheared suspensions by dynamic simulation." J. Fluid Mech. **401** 243-274.

Foss, D. R. and J. F. Brady (2000). "Structure, diffusion and rheology of Brownian suspensions by Stokesian Dynamics simulation." Journal of Fluid Mechanics **407**(-1) 167-200.

Furukawa, A. and H. Tanaka (2010). "Key Role of Hydrodynamic Interactions in Colloidal Gelation." Physical Review Letters **104**(24) 245702.

Haw, M. D. (2006). "Void structure and cage fluctuations in simulations of concentrated suspensions." Soft Matter **2**(11) 950-956.

Koumakis, N. and G. Petekidis (2011). "Two step yielding in attractive colloids: transition from gels to attractive glasses." Soft Matter (In Press) DOI:10.1039/c0sm00957a.

Laurati, M., S. U. Egelhaaf and G. Petekidis (2010). "Non-Linear Rheology of Colloidal Gels with Intermediate Volume Fraction." Journal of Rheology, submitted.

Pham, K. N., G. Petekidis, D. Vlassopoulos, S. U. Egelhaaf, W. C. K. Poon and P. N. Pusey (2008). "Yielding behavior of repulsion- and attraction-dominated colloidal glasses." Journal of Rheology **52**(2) 649-676.

Pham, K. N., G. Petekidis, D. Vlassopoulos, S. U. Egelhaaf, P. N. Pusey and W. C. K. Poon (2006). "Yielding of colloidal glasses." Europhysics Letters **75**(4) 624-630.

Rzepiela, A. A., J. H. J. van Opheusden and T. van Vliet (2004). "Large shear deformation of particle gels studied by Brownian dynamics simulations." Journal of Rheology **48**(4) 863-880.

Sierou, A. and J. F. Brady (2001). "Accelerated Stokesian Dynamics simulations." Journal of Fluid Mechanics **448**(-1) 115-146.

Silbert, L. E., J. R. Melrose and R. C. Ball (1999). "The rheology and microstructure of concentrated, aggregated colloids." Journal of Rheology **43**(3) 673-700.

Tanaka, H. and T. Araki (2000). "Simulation Method of Colloidal Suspensions with Hydrodynamic Interactions: Fluid Particle Dynamics." Physical Review Letters **85**(6) 1338.

Varadan, P. and M. J. Solomon (2002). "Direct Visualization of Long-Range Heterogeneous Structure in Dense Colloidal Gels." Langmuir **19**(3) 509-512.

Varadan, P. and M. J. Solomon (2003). "Direct visualization of flow-induced microstructure in dense colloidal gels by confocal laser scanning microscopy." Journal of Rheology **47**(4) 943-968.

Voronoi, G. (1907). "Nouvelles applications des parametres continus a la theorie des formes quadratiques." Journal f˙ur die Reine und Angewandte Mathematik **133** 97-178.

Whittle, M. and E. Dickinson (1997). "Stress overshoot in a model particle gel." The Journal of Chemical Physics **107**(23) 10191-10200.

Chapter 10 – Conclusions and Outlook

This study has examined the non-linear transient and steady state properties under shear in comparison to the state at rest, both microscopic and rheological, of like model colloidal suspensions of hard spheres, encompassing the mechanically trapped glassy state, the entropically favorable shear induced crystal and the jammed attractive glass and gels states.

Chapter 4: Stresses, Dynamics and Structure during Transient Shear: Start-up and Cessation of Flow

The transient response of hard sphere glasses was examined in a start-up shear experiment with experimental rheology and Brownian Dynamics (BD) simulations, which exhibits a stress peak with elapsed time at the yield point of approximately 10% strain. The stress peak was found to increase in amplitude at high rates and lower φ, while the position of the peak increases with rate and generally remains unchanged with φ.

Although at rest the displacements of the glass show a plateau, the length scale of in-cage motion, at the steady state under shear BD Simulations generally show that long time motions become diffusive as the cages are broken and particles flow past each other. Moreover, the long time diffusion coefficient showed large dependence on applied rate, but much smaller dependence on the studied φ. At short times, the displacements decrease with elapsed strain when compared to the state at rest, the decrease being more pronounced with increasing φ and Pe. These short time motion constrictions are associated with the shear induced out of cage motion, as forcing a particle out of cage increases long time diffusivity, but also hinders in cage motion through spatial constriction.

A transient super diffusive regime is found to occur at intermediate time scale displacements, which becomes more pronounced with increasing φ. This is related to the transient nature of the start up shear and the transition from the displacements at rest to diffusive long time displacements under shear.

During examination of the structural properties under shear it was found that compared to the structure of other planes, the steady state g(r) in the xy plane (velocity – velocity gradient) is most affected becoming highly anisotropic. The transient g(r) of the xy plane at low strains is isotropic, turning into a distorted structure as strain increases and showing flow lines along the extension axis when strains increase above yield, signifying out of cage diffusion. While cage distortion is more significant at high rates, low rates still distort the structure although do

not elongate the cage. The peak of the stress response is found to be correlated to the inability of particles to escape their cages and relax the stress, before the maximum distortion of the cage occurs which forces them out due to applied shear.

The examination of the stress after cessation of shear showed relaxations which became more pronounced for larger rates while generally becoming slower as φ is increased and particle motions become hindered. The structure and the dynamics during relaxation were found to revert back to the state at rest at rates similar to the relaxation of stress.

Continuation of this work could include Stokesian dynamics simulations or equivalently confocal microscopy experiments as a validation of the BD simulations findings, especially at higher rates. Moreover, a more detailed examination of the relaxation processes can be made along similar lines.

Chapter 5: Oscillatory Shear on Glasses: Stresses, Structure and Dynamics

Examination of the non-linear oscillatory response of glassy hard sphere suspensions was also conducted, both experimentally with rheology and through Brownian dynamics simulations. We found two distinct regimes in terms of stress responses, dynamics and structure under shear, one for the lower frequencies and a second for the higher frequencies of oscillation, the transition related to the time scale of the in cage beta relaxation or equivalently the minimum of G'' in a linear frequency sweep. In terms of rheological response, dynamic strain sweeps going well into the non linear regime show maxima of G'' at strains of about 10% for low frequencies, while higher frequencies exhibit maxima at strains of 100%. The parameters which characterize the third harmonic stresses within the period, I_3/I_1 and δ_3, may quantify the transition between these regimes, the first through a characteristic minimum, while the second more reliably with a transition at high strains from a thinning to a hardening regime.

Furthermore, a dynamic strain sweep with what appeared to be two peaks of G'' and thus inferring two distinct yielding processes was observed in a narrow range of frequencies and high volume fraction. These yielding processes are found to be related to the non harmonic properties of the stress response by showing a transition from a low frequency response at low strains to a high frequency response at high strains.

The stress-strain Lissajous figures have characteristic shapes in each regime, with the low frequencies showing trapezoid like shapes, with an elastic stress increase for about 10% strain after the maxima and then almost constant stress. The higher frequencies show a distinct area

of reduced stresses after the maximum of strain, due to reduction of particle collisions, with a range of 50% strain, while additionally showing a viscous response for the rest of the curve.

When increasing the strain, displacements also increase as more particles are able to undergo out of cage motions, while spatial dynamic inhomogenieties and the non Gaussian parameter show an increase during yielding and then a decrease at larger strains. At the largest strains displacements are due to out of cage motion and occur homogenously throughout the system, while for strains around yield the particles are divided into two populations: one that exhibits in cage displacements and a second that exhibit out of cage displacements. For applied strains that cause the shear induced diffusivity to increase above the diffusivity at rest, we find super diffusive behavior, between the short and long time diffusivities under shear.

Diffusivity at high oscillatory strains shows a linear increase with frequency in the high frequency regime mirroring the viscous loss due to shear activated particle rearrangements. However, in the low frequency regime, diffusivity increases with a power law slope of less than one, depending on the distance from maximum packing, with Brownian activated out of cage displacements. Moreover, intermediate strains near yielding show a much more complex behavior of displacements, with particles showing out of cage diffusive behavior in the low frequency regime, but being trapped within their cages in the high frequency regime. Although in the latter case the non Gaussian parameter is large, the displacements are found to be spatially homogenous between particles in the system.

For a super cooled liquid near the glass transition and in the context of the BD simulations, we recognize three regimes for diffusivity and stresses under high strain or steady state shear. At the highest rates, diffusivity and stresses follow a power law slope of one with applied rate as the stress response is governed by interparticle collisions. For rates corresponding to the displacement plateau at rest, the stress slope is reduced to zero as the entropic cage plasticity is measured, with the diffusivity showing a slope of less than one. At the lowest rates, the long time diffusivity is probed, exhibiting a slope of zero for the diffusion and a slope of unity for the stresses as the system behaves as a fluid.

Lastly, new methods for analysis of the elastic and viscous components of stresses during oscillatory experiments were brought forward and examined against relaxations functions of elastic stresses. The comparison showed that although the new methods are an improvement upon existing decompositions, they still lack the necessary sophistication to extract meaningful physical properties for arbitrary stress responses.

Future work may include detailed rheological measurements of the two frequency regimes with using two sphere sizes and multiple volume fractions for scaling the results. Additionally, concerning the decomposition of elastic and viscous stresses within the period, removal of the rheometer filter and subsequent modeling of the transducer may be carried out, in order to access smaller timescales (an order of magnitude) during the relaxation and decompose stresses into instantaneous elastic and viscous components. By this decomposition one could in principle model the rheological data within the period onto the microscopic information. Other options could include Stokesian dynamics simulations, LS-Echo or equivalently confocal microscopy experiments for the microscopic examination of the higher frequencies during oscillatory shear of glassy φ and for the validation of the BD Simulations.

Chapter 6: Simulation of Hard Sphere Crystals under Oscillatory Shear

Using BD simulations, we compared the microscopic motions at rest and under oscillatory shear of a shear-induced crystal, oriented parallel to shear, and the same volume fraction glass. For the amorphous and crystalline structures at rest we found that although the short time MSD for the crystal is higher than that of the glass, the dynamic heterogeneities in the glass may allow increase of the MSD above those of the crystal for longer times. Thus while in the crystal particles are completely confined in their cage with the MSD showing a clear plateau, in the glass large scale out of cage motion is observed via dynamic heterogeneities.

When comparing the displacements of the crystal oriented parallel to shear and the glass under oscillatory shear we found that the crystal has anisotropic displacements compared to the isotropic displacements in the glass. The crystal displacements are due to cooperative motion of x-z layers of particles sliding over each other, thus exhibiting a yield strain less than that of the glass. Past the yield point, the long time shear induced displacements of the glass are found to be larger, while stresses are highly correlated to instantaneous shear induced displacements in both crystal and glass. Thus we concluded that during the experimental shear of a monodisperse glass, the large out of cage displacements allow the system to explore the energy landscape and find the minima in energy, stresses and displacements by configuring particles into a crystal oriented parallel to shear.

Through the examination of the parallel crystal under oscillatory shear, we have found that the MSD of the crystal increases with decreasing frequency, although showing qualitatively similar displacements as a function of applied strain. The yield strain of the crystal is less for lower oscillation frequencies as Brownian motion has time to act upon the system under shear and allow the sliding of the crystal layers. The equivalent of an effective diffusion coefficient was shown to exhibit a power law scaling with frequency of less that one at lower

frequencies, an effect of similar origin to the corresponding frequency dependence of a hard sphere glass, the slope being dependent on φ or more accurately the distance from maximum packing. The stress responses of the crystal under oscillatory shear in experiments and simulations are qualitatively similar at low frequencies, with the largest differences possibly occurring due to the lack of hydrodynamic interactions in the BD simulations as well as crystal defects of the experimental system.

Similarly, the low strain perpendicular and high strain parallel to shear crystals may occur due to minimization of stresses and displacements similarly to the shear induced crystallization of a glass. The crystal perpendicular to shear exhibits low stresses and MSD at low non linear strains (10%-20%), while parallel to shear shows slightly larger stresses in the same regions. At higher strains, the sliding layers of the parallel crystal are more efficient in minimizing stresses and the perpendicular crystal is no longer stable. Thus starting from an amorphous glassy system, at low strains a crystal perpendicular to shear is formed, which becomes unstable at larger strains and reorients into a crystal parallel to shear.

Chapter 7: Experimental Rheology and LS-Echo during the Shear Induced Crystallization of Hard Sphere Glasses

Through the use of the LS-Echo technique coupled with rheology, we have examined the shear-induced motions of glasses and their corresponding shear induced crystals and found strong correlations to the BD simulations results. Comparing the glass and the crystal, we observe that although at low strains the crystal shows increased particle displacements than glass due to relative to the higher free volume around a particle (in-cage motion), at higher strains, the crystal shows reduced particle rearrangements due to the anisotropic sliding layer motion. A quantitative comparison between the crystal simulations and the experiments was not possible at this stage. However, we qualitatively found good agreement at the high frequency regime, where a characteristic minimum of shear induced diffusivities as a function of frequency is observed.

The use of a CCD camera and multispeckle correlation may allow measurements of the correlation function under shear at longer times and thus at lower frequencies, reaching the low frequency regime. Additionally, modification of technique/setup to examine forward scattering and thus simple self diffusion may be done in order to scale and compare results to BD simulations. Alternately, Stokesian dynamics simulations or equivalently confocal microscopy experiments may be carried out in order to elucidate the microscopic properties during oscillatory shear.

Chapter 8: Experimental Rheology of Attractive Colloids

With the use of experimental rheology, we have shown that the transition from a two step yielding attractive glass to a low volume fraction gel at equal attraction strength and range shows a complicated yielding process that remains two step until very low φ, where structural cohesion becomes impossible. We have shown that the first yield point is due to the breaking of bonds within cages (at high φ) or between interconnected clusters (at low φ), while the second one is attributed to the breaking of cages or of clusters into smaller constituents. While the bonding strength is kept constant, the first yield point stays constant for all φ and increase only at the lowest one (φ=0.2), whereas the second yield strain increases as volume fraction is decreased.

This effect is attributed to cages turning into looser clusters, as the introduction of voids increases the relevant to yielding length-scale, allows greater flexibility of bonds and introduces cluster rotation. Steady shear experiments indicated three distinct shear rate regimes determining the state of the system after the first yield point that breaks some inter-cluster or in-cage bonds. At the lowest rates the freed clusters may rotate slowly almost unperturbed, intermediate rates cause partial breakdown of the clusters through increased collisions and finally the highest rates break down the clusters into particles. With increasing rate the height of the second peak increases over the first, with clusters reducing to smaller sizes. The structural properties under shear are expected to be reflected by the non dimensional Pe_{dep} number, introduced as the ratio of depletion and shear forces/time scales.

By increasing the range of attraction, linear viscoelastic properties are reduced due to weakening of the gel. Most importantly both yield strains increase as expected by the rationalization given.

Finally, we have shown that both the linear viscoelasticity and the stresses measured at step rates evolve with waiting time. For the latter an increase of the second stress overshoot over the first is observed at long times. This suggests that although initial particle bonding is quite fast, slower structural rearrangements lead to stronger clusters at longer times. We have extended these findings for van der Waals interactions and found that even small attractions, $U \approx -1K_BT$, may cause long range restructuring and lead to the appearance of a second stress overshoot.

In future work, rheological examination of the high rate yielding regime with larger particles may be done, possibly in conjunction with confocal microscopy in order to examine the

structural changes under shear. Similar yielding phenomena may be examined in depth for different attraction strengths and ranges, while also examining the effects of rejuvenation and aging on yielding. It would also be interesting to make a microscopic examination of the effects of aging on structure with confocal microscopy and their correlation to yielding properties.

Chapter 9: Simulations of Sheared Attractive Gels: Stresses and Structure under Shear

By examining a hard sphere depletion gel with BD simulations, we have found that the non linear stress response in a concentrated gel is affected by the structural changes during shear. The first low strain peak is verified to refer to the initial particle collisions (bond breaking), while the second stress peak refers to larger scale structural rearrangements. As discussed for the experiments, at the lowest rates the stress peaks become smaller, while at intermediate rates the second peak increases with long range restructuring taking place. At the highest rates, the first peak becomes prominent as bond breaking occurs primarily at the smallest strains, while the second peak becomes insignificant.

We also find that the stress peaks are significantly dependent on the initial structural properties and rejuvenation protocol before the application of shear. The larger the change in the structure, from the initial state to the steady state, the larger the stress peaks, more so for the secondary peak. At the steady state under shear, the lowest rates show the collapse of clusters onto each other, creating large voids, while larger rates decrease inhomogeniety. Moreover, the steady state under shear appears to depend only on the applied rate and not the initial conditions. The structural properties under shear are found to be reflected by the non dimensional Pe_{dep} number, the ratio of depletion and shear forces/time scales.

Technically, we have used a new measure to monitor the heterogeneous gel structure, the void distribution function, which is a more efficient marker of long range heterogeneous structure than the Voronoi volume or the application of a pair distribution function. Barring extreme inhomogenieties, the average bonds/contacts per particle in this case may also be a good indication of void sizes.

Future work concerning the microscopic properties of the gels under shear, other than already mentioned, may include study of the gel cluster size in the transient and steady state as a function of applied shear rate and attraction strength as an elucidation of the correspondence of structure to the non dimensional Pe_{dep} number. These structural properties may be examined either with simulations (BD or SD) or with confocal microscopy.

Appendix

A.1 Simulation Box anisotropy

In chapter 6, we analyzed the microscopic properties of a crystal under shear using a highly anisotropic simulation box instead of a simple cubic box. As stated in that chapter, in order to capture the yielding mechanisms of the crystal with applied oscillatory shear, a large number of layers (>100) as well as a random FCC stacking was needed due to confinement effects in the velocity gradient direction. Since creating an isotropic box of that many layers was computationally prohibitive, a highly anisotropic box was used to simulate the crystal under shear.

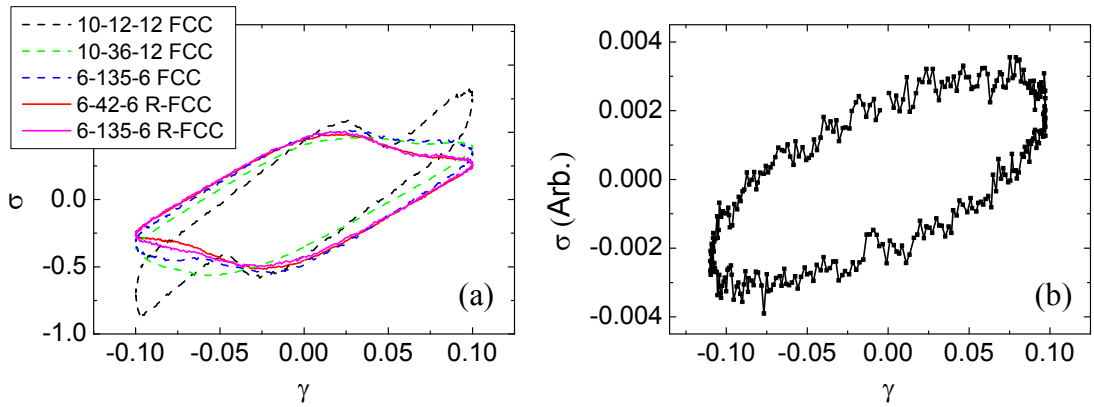

Figure A.1: a) Lissajous Stress-Strain curves at 10% Strain of crystal in the isotropic and anisotropic boxes, with FCC (Dashed) and random FCC (Solid) stacking as indicated in the figure. Notation refers to the number of particles in the x-y-z directions. b) Experimental Lissajous figure of 267nm spheres at φ=0.615 sheared at 1.6 Hz and γ_0=10%.

Figure A.1 shows the Lissajous stress response of simulation runs of Pe'=1 at γ_0=10%, around the yield where the shear space and stress responses are the most sensitive to the different anisotropies and crystal types. The legend uses the notation of chapter 6 for the box sizes, x-y-z or shear direction – velocity gradient – vorticity. Simulated boxes with few layers are found to constrict the crystal under shear in the y axis which causes sudden stress jumps and unrealistic (compared to experiments) yield strain values. Similar problems occur with a single sided FCC crystal as an initial condition, either of the FCC twin structures. Better averaging of stresses and results which qualitatively approach experiment are found, upon the introduction of many layers and applying the experimentally found random FCC (R-FCC), a mixture of FCC and HCP layering as discussed in chapter 1. The introduction of many layers simulates an actual sheared system and reduces effects caused by few layers.

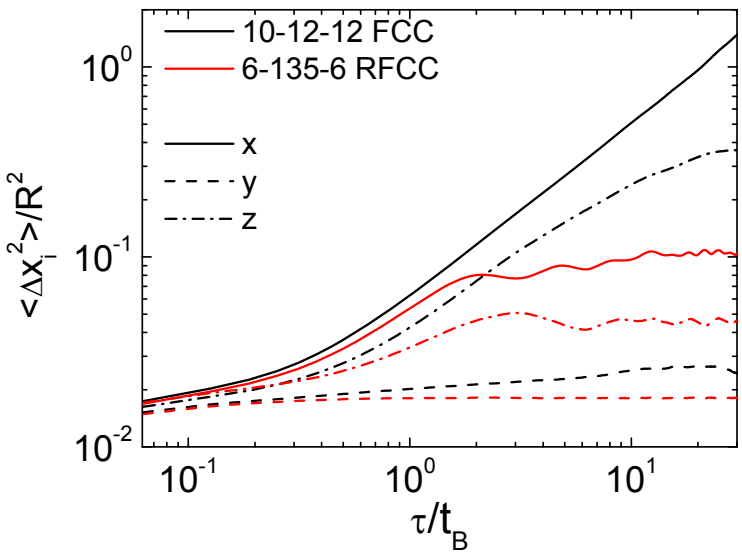

Figure A.2: Mean squared displacements of crystal in the isotropic 10-12-12 and highly anisotropic 6-135-6 boxes for a) 10% strain and Pe'=1

Since stresses and yielding are affected by number of layers, so are the calculated values of mean squared displacements, especially at intermediate strains near the yield strain as shown in figure A.2. This example shows how the yield strain, experimentally found to be less than 10% for the crystal, is increased above 10% with few layers. The yield strain in this case is defined at the strain above which $<\Delta x^2>$ becomes diffusive (slope of 1), thus layers slide over each other and the crystal rheologically flows. Although not shown, high oscillation frequencies and strains show no major differences. Thus we find that the MSD from a simulated crystal of only a few layers shows the suppression of yield and displacements. The physical interpretation of this effect can be found by examining a periodic boundary system of only two layers. This non physical system will yield very suddenly only once per 100% strain. In a real system of many layers, yielding occurs at about 10% which corresponds to the real structural length scale of the system.

As described above, the correction of stresses and MSDs near yielding are the main reasons for the implementation of the anisotropic box. Unfortunately, the anisotropy of the box causes some unexpected changes on the averaged MSD. Introduction of anisotropic box causes small but distinguishable fluctuations in the system at rest, which we believe to be Mermin-Wagner type long range fluctuations (Mermin, 1968), caused by the strong anisotropy of the periodic box. Figure A.3a shows that the fluctuations have a direct correlation to the anisotropic ratio of the box, while A.3b shows that the large axis of the box shows the smallest increase of

MSD due to fluctuations, independent of the structural properties of the system; i.e. glass or crystal of varying orientations have minimal effect on the occurrence of the fluctuations.

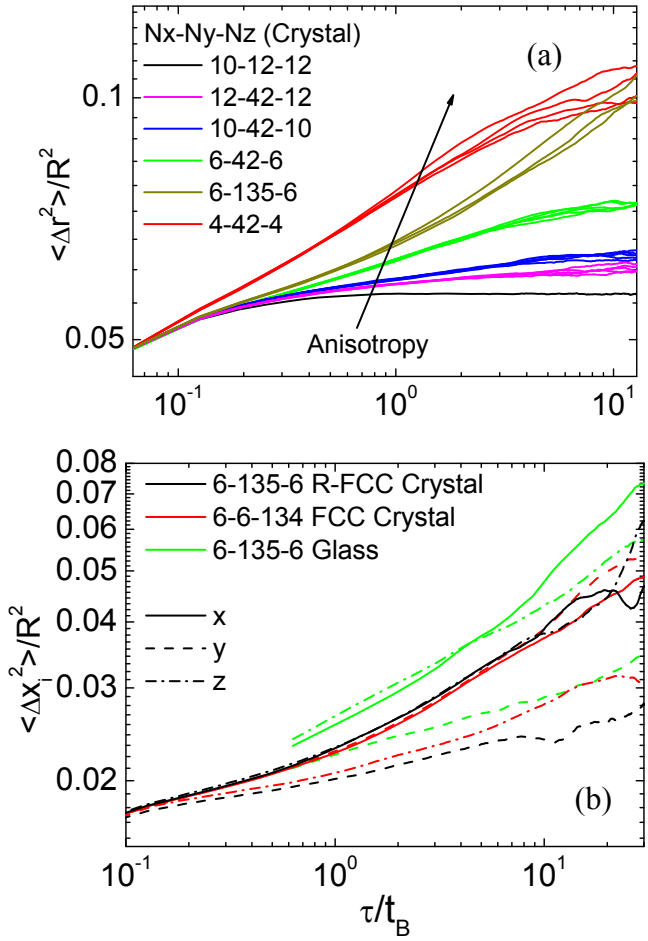

Figure A.3: a) Mean squared displacements of crystal in the isotropic 10-12-12, the highly anisotropic 6-135-6 and boxes of various anisotropic ratios at rest (Multiple Runs) and b) Mean squared displacements for individual axis in the highly anisotropic boxes of 6-135-6 and 6-6-134 with varying configurations of crystal and glass.

Figure A.4 also shows that these are long range fluctuations, as they disappear when compared to center of mass motion from the layer cages as also examined in chapter 6. This suggests that the use of the isotropic box is preferable at rest, although not under shear, especially not near the yield points. It is important to note, as can be seen from figure A.4, that the fluctuations produce only small increases of MSD, especially when compared to the shear induced displacements.

In figure A.5 we calculate the MSD of particles relative to another (cooperative motion). Thus we calculate the distance between two particles in the y-axis (gradient direction) belonging to different x-z layers with a specific distance in the y axis. In the context of figure A.4, we do

this as a measure of quantifying the length scale of the fluctuations. Since, when comparing to the first neighbors, there are no fluctuations, while when taking the average MSD the fluctuations are large, examining the comparison to neighbors of further distances can quantify the fluctuation length.

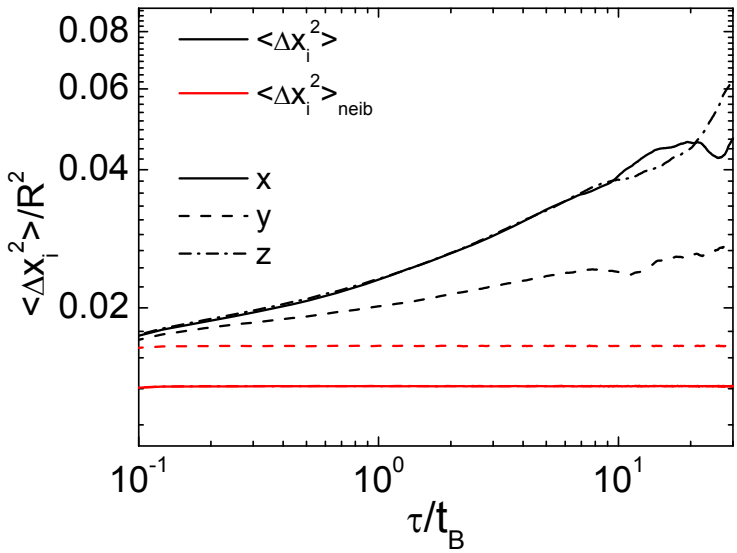

Figure A.4: Mean squared displacements in highly anisotropic 6-6-135 box by subtracting neighbor motions in the same y-z crystal plane

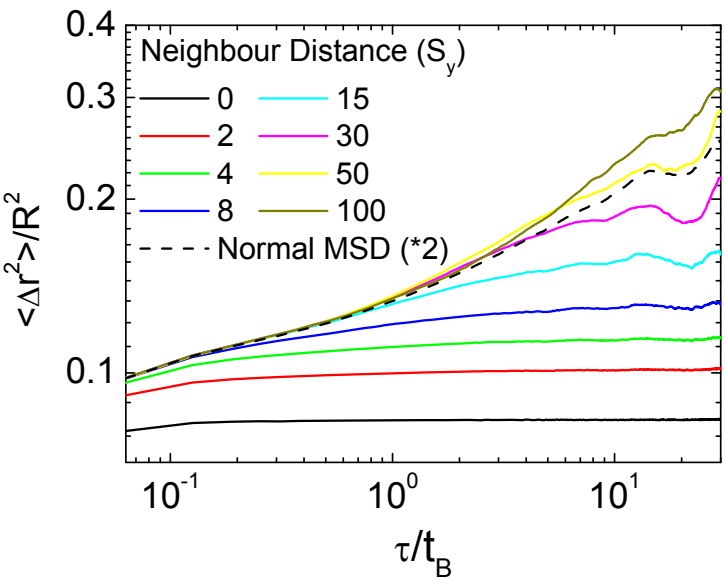

Figure A.5: Mean squared displacements of the crystal with φ=0.62 in the highly anisotropic 6-135-6 box at rest after subtracting the motion of a single particle. The particle which motion is subtracted is changed and examined at various distances in the y direction

When calculating the motion of one particle relative to the motion of another, the equation to calculate MSD may be modified as:

$$\left\langle \Delta x_{relative}{}^{2} \right\rangle_{\tau} = < \frac{1}{\mathrm{N}} \sum_{i=1}^{N} \left[\left(x_i(t+\tau) - x_i(t) \right) - \left(x_{k(i)}(t+\tau) - x_{k(i)}(t) \right) \right]^2 >_{\tau} \quad \text{(A.1)}$$

The *k* particles are identified as particles of a set initial y distance at the beginning of the simulation and remain the same throughout the calculation. Specifically, *k* particles are chosen from the initial configuration when satisfying the following conditions in relation to the *i* particles: $|x_i-x_k|$:min, $|z_i-z_k|$:min and $|y_i-y_k-S_y|$:min, where S_y is the required initial y-axis distance of the *k* and *i* particles.

Application of this type of MSD calculation for various values of S_y is shown in figure A.5 for the anisotropic box and crystal used in chapter 6, as a method of probing the length scales of the Mermin-Wagner fluctuations. Thus we see that larger distances in the y axis show larger fluctuations. By comparing to the average MSD we also find that the fluctuations in the y axis have an average range of the order of roughly 25 particle layers. In the isotropic box such an effect is absent.

Mermin – Wagner theory describes such fluctuations (Mermin, 1968) as long range fluctuations which arise in classical and quantum mechanical systems of lower dimensions (2D and 1D), which destroy long range order. Effectively the highly anisotropic simulation box has become a 1D system, although in our case crystallinity cannot be destroyed as particles at these volume fractions are spatially trapped in the crystal. Lower φ near the crystal transition, i.e. at φ=0.545, may actually revert to an amorphous configuration because of these fluctuations. For the calculation of MSD at rest these are quite important, but become insignificant at large strains, even in the x, z directions. Stresses are generally not expected to be adversely affected by this effect and comparisons of isotropic and anisotropic boxes at large strains has not shown any significant differences. Quantitatively, we find that when displacements under shear are more than one order of magnitude larger than at rest, the M-W fluctuations are insignificant for the purposes of our analysis.

An additional issue may arise due to the anisotropicity of the box due to repeated particle interactions. In the paper of (Sierou and Brady, 2004) on the diffusivities of non Brownian particles under shear, there is discussion on an artifact in the diffusivities due to the repeating interactions from the periodic boundary conditions under shear. As the simulation box is sheared in a non Brownian system, it was found that particles interact with the same particle images at intervals which are proportional to the size of the box in the direction of shear. Since the anisotropic box discussed here is small in the shear direction, there may be concern that a similar effect may alter calculated displacements. However, we argue that since the

displacements in the x-axis (shear direction) only occur as motions of whole xz plane particle layers (shear-vorticity), the particles interact only with their first neighbors at any point during shear. Therefore, as long as the size of the box is larger than a few particle diameters we find that there are no such effects. Further examination of the results of large strains for different boxes under shear has produced no evidence to the contrary.

A.2 Taylor Dispersion and Diffusivity Corrections

Taylor dispersion is an effect in which shear flow increases the diffusivity of particles in the flow direction (Taylor, 1954). As shear is applied in a dilute system, due to Brownian motion in the velocity gradient direction, particles change streamlines, effectively increasing the displacements in the flow direction. When the affine motion is subtracted for each time step though, in principal this effect is also subtracted. Therefore in the case of oscillatory shear, the calculations of the displacements in the flow direction with and without subtracting the affine motion produce different results for time scales equal to multiples of the period, even though one might expect that stroboscopic examination of particle positions at these time scales would be equivalent to subtracting the affine motion at each time step.

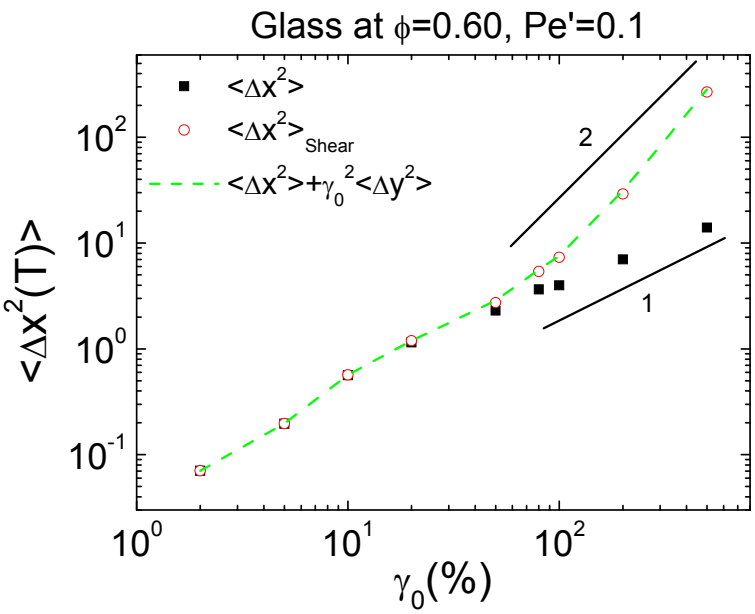

Figure A.6: Mean squared displacements for τ=T as a function of applied strain at Pe'=0.1, for a Glass under shear with φ=0.60 showing the non affine motion ($<\Delta x^2>_B$, black, squares, solid), the total motion under shear exhibiting the effect of Taylor dispersion ($<\Delta x^2>_A$, red, circles, open) and the simple scaling with strain as discussed in text (green, dashed line). Solid black lines show power law slopes of one and two.

In both dilute and concentrated systems under shear, which exhibit diffusive motion ($<\Delta r^2(\tau)>$ vs τ with a power law slope of 1), the mean squared displacements with and without the affine motions subtracted at timescales multiple to the period were found to follow a simple relation of $<\Delta x^2>_{Shear}=<\Delta x^2>+\gamma_0^2<\Delta y^2>$ as shown in figure A.6, where $<\Delta x^2>_A$ are the displacements without subtraction of the applied shear field and $<\Delta x^2>_B$ are the displacements after subtraction of the affine motion at every time step as generally shown in this work.

The total mean squared displacements, without subtraction of the affine motion, under simple steady shear for dilute suspensions is given by (Elrick, 1962; Sierou and Brady, 2004) as:

$$\left\langle \Delta x^2(t) \right\rangle_{Shear} = 2D_{xx}t + 2D_{xy}\dot{\gamma}t^2 + \tfrac{2}{3}D_{yy}\dot{\gamma}^2 t^3 \quad \text{(A.2)}$$

Although this equation would produce the correct effect of the Taylor dispersion in a diffusive system under steady shear, the more complicated case of oscillatory shear is not as simple. In essence, a rigorous calculation of the effect of oscillatory shear on the total mean squared displacement is needed.

In the case of crystals under shear, since the values of $<\Delta y^2>$ (velocity gradient) are generally quite small compared to $<\Delta x^2>$ (shear direction), the Taylor dispersion effect is expected to be small. Indeed, preliminary data analysis shows little effect on the x direction displacements of the crystal under shear. However, in the case of non diffusive motion in the glass, indicated by increased values of a_2 (chapter 5), the effects of Taylor dispersion are not as simple to scale, generally showing smaller values than the simple prediction above and occasionally even less than the non affine displacements. Further analysis along these lines is needed to clarify such behavior and will be the subject of further work.

Additionally, while in (Foss and Brady, 1999) diffusivities are calculated using the non affine displacements, as done in this work, the work of (Sierou and Brady, 2004) which deals with non Brownian suspensions, states that the correct calculation of the D_{xx} and D_{xy} diffusivities under shear need a 'correction' term which refers to a coupling between the applied shear and particle motions. This correction term is not to be confused with the term related to the affine motion. For small rates, Pe<10, this correction term is expected to be small, but the effect at larger rates may be important, although from the work of (Sierou and Brady, 2004), large φ close to those of this work show a diminishing effect. Nevertheless, a more rigorous examination is required as this correction term has not been examined in detail for the case of oscillatory shear.

A.3 High Pe' Crystal Stresses

As seen in figure A.7 when shearing the crystal in the simulations at high Pe' and large strains we retrieve Lissajous plot with large oscillations due to successive yielding events in the crystal. These findings do not agree with experiments as may be seen in chapter 7. In the latter such successive yielding events are probably smoothed out due to crystal defects or the effects of hydrodynamic interactions.

The implication of these successive high strain yielding events is that for a perfect random FCC crystal sheared in the (111) plane without hydrodynamic interactions, no breaking of the order may take place at any rates or strains. Since the crystal exhibits a simple sliding layer yielding, stresses are always shared equally between particles and no catastrophic events may occur to destabilize the crystal structure. Experimentally this is not the case, as the crystal is turned into an amorphous glass at high rates. Thus we surmise that the crystal experimentally breaks down at large rates and strains due to hydrodynamic interactions and more specifically the appearance of hydroclusters from lubrication stresses. Recent work on hard sphere crystals under steady shear shows that the break up of the crystal occurs through the appearance of amorphous domains (Yu, Derks et al., 2009). This may very well indicate the existence of hydroclusters.

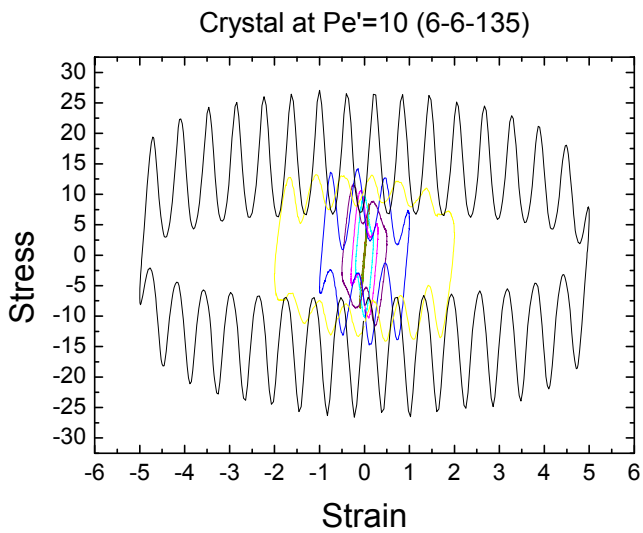

Figure A.7: High strain Lissajous Stress-Strain curves of crystal parallel to shear of φ=0.62 at Pe'=10

A.4 Rheometer Resonance

Using the ARES strain controlled rheometer at frequencies higher than 20 rad/sec we found that artificial higher harmonics may appear in the stress response of large applied strains related to the natural frequency of the transducer. The ratio of the third to the first harmonic, I_3/I_1, of several colloidal samples are shown in figures A.8 and A.9, showing a peak of intensity for values of 65rad/sec. Other systems and also micrometer sized particles also exhibit similar dependencies. The effect closely resembles a non linear mechanical resonance with a resonant frequency of about 200rad/sec, which is manifested as an increase of I_3/I_1 at about 65rad/sec.

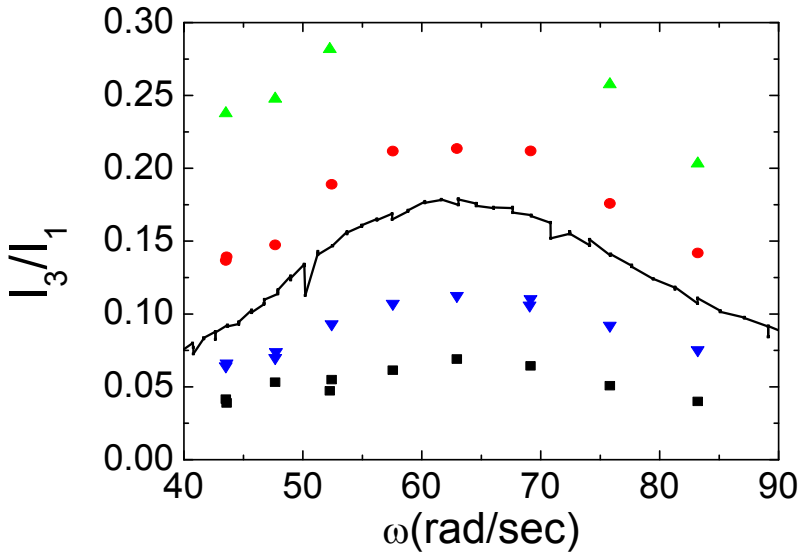

Figure A.8: Ratio of the third to the first harmonic at γ_0=30% versus frequency for a hard sphere system in Octadecene of R=130nm at φ=0.60 (line) and a concentrated aqueous star like micelle system of R=40nm at various temperatures (scattered symbols).

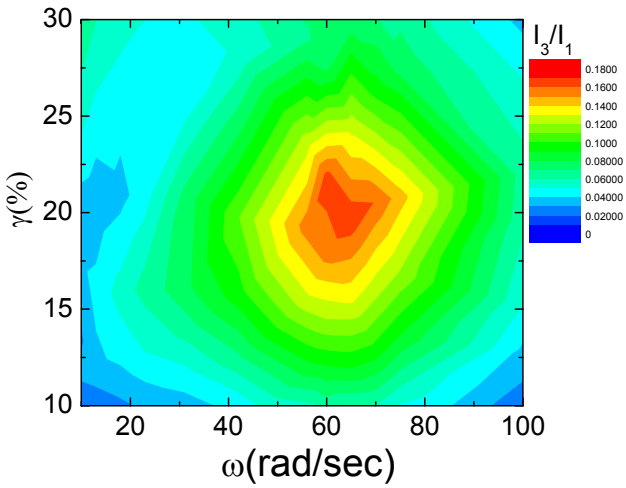

Figure A.9: Contour plot of the ratio of the third to the first harmonic vs γ_0 and frequency for a hard sphere system in Octadecene of R=130nm at φ=0.62.

The value of the peak is found to be dependent on the torque response of the sample as well as the actual viscoelastic properties. It seems that the resonance effect is not simply mechanical, but rather an effect related to the complex filtering and loop system of the transducer (Vermant, 2010).

A.5 References

Elrick, D. E. (1962). "Source functions for diffusion in uniform shear flow." Austral. J. Phys. **15** 283-288.

Foss, D. R. and J. F. Brady (1999). "Self-diffusion in sheared suspensions by dynamic simulation." J. Fluid Mech. **401** 243-274.

Mermin, N. D. (1968). "Crystalline Order in Two Dimensions." Physical Review **176**(1) 250.

Sierou, A. and J. F. Brady (2004). "Shear-induced self-diffusion in non-colloidal suspensions." Journal of Fluid Mechanics(506) 285-314.

Taylor, G. (1954). Conditions under Which Dispersion of a Solute in a Stream of Solvent can be Used to Measure Molecular Diffusion. **225:** 473-477.

Vermant, J. (2010). Private Communication.

Yu, L. W., D. Derks, A. Van Blaaderen and A. Imhof (2009). "Melting and crystallization of colloidal hard-sphere suspensions under shear." Proceedings of the National Academy of Sciences of the United States of America **106**(26) 10564-10569.